Crystallography Reports, Vol. 45, No. 4, 2000, pp. 529–536. Translated from Kristallografiya, Vol. 45, No. 4, 2000, pp. 583–590.
Original Russian Text Copyright © 2000 by Nizamutdinov, Vinokurov, Khakimov, Bulka, Galeev, Khasanova.

CRYSTALLOGRAPHIC SYMMETRY

Group–Theoretical Representation of Holohedral Forms of Crystals by Conjugated Simple Forms. Intergrowth of Crystals

N. M. Nizamutdinov*, V. M. Vinokurov*, E. M. Khakimov, G. R. Bulka*, A. A. Galeev*, and N. M. Khasanova***

* *Kazan State University, ul. Lenina 18, Kazan, 420008 Russia*[1]

** *Kazan State Pedagogical University, Kazan, Russia*

Received June 8, 1998; in final form, April 12, 1999

Abstract—The schemes for division of holohedral simple forms of crystals into conjugated simple forms are derived by decomposition of the symmetry group of the primitive sublattice into double cosets. The number of equivalently oriented simple forms in the intergrowth of crystals, whose primitive space sublattices are parallel to one another, is equal to the number of holohedral permutational conjugated simple forms, which has the value 992 for all the 32 symmetry classes. © *2000 MAIK "Nauka/Interperiodica".*

INTRODUCTION

If the point group G_K of the crystal does not coincide with the space group G_{sp} of the lattice, the faces of the crystal equivalently oriented with respect to the three-dimensional lattice are nonequivalently oriented with respect to the crystal structure. As a results of this nonequivalence, the holohedral form decomposes into conjugated simple forms allowed by the group G_K [1, 2]. The division of holohedral forms into conjugated simple ones was derived geometrically rigorously in [1–4] on the basis of the theory of crystal symmetry. The present study is aimed to derive the schemes of division of holohedral forms caused by lowering of the symmetry of the point group G_K with respect to the group of the primitive sublattice G_{ssp} (a holohedral group) by the group-theoretical method.

Under the condition that $G_K \subset G_{\text{ssp}}$, the crystal structure can have n_K equivalent orientations with respect to the primitive space sublattice [1]:

$$n_K \equiv [G_{\text{ssp}} : G_K] = g(G_{\text{ssp}})/g(G_K), \tag{1}$$

where $[G_{\text{ssp}} : G_K]$ is the index of the group G_K in G_{ssp}, and $g(G_{\text{ssp}})$ and $g(G_K)$ are the orders of the groups G_{ssp} and G_K, respectively. The number n_K is the number of individual crystals with parallel primitive sublattices in the intergrowth, called hereafter holohedral intergrowth. Various individual crystals in the intergrowth have different orientations and differently interact with applied magnetic fields. The possible formation of intergrown crystals of a substance is used in the interpretation of the nature of modulated crystal structures [5, 6] and is also taken into account in the studies of disymmetrization [7]. If the orientations of the space lattices of individual crystals of the intergrowth coincide, the detection of such crystals by the diffraction [6] and electron paramagnetic resonance (EPR) methods becomes rather difficult because their diffraction patterns and EPR spectra become indistinguishable. The present article is aimed at studying the intergrowth of individual crystals with the parallel primitive sublattices by the methods of the abstract theory of groups and representations. We also consider their possible detection by the EPR method. The study is performed in two main stages: (i) decomposition of the space group of the primitive space sublattice G_{ssp} into the adjacent classes with respect to the subgroup G_K and double cosets by modulus (G_K, G_H), where G_H is the group of a face of the holohedral simple form, and (ii) derivation of simple forms for cubic and rhombohedral crystals from their holohedral forms. The mathematical apparatus of the abstract group theory [8] used in our study corresponds to the merohedry method of the theory of crystal form [1, 2].

GROUP–THEORETICAL METHOD OF DERIVATION OF CONJUGATED SIMPLE FORMS OF CRYSTALS FROM THEIR HOLOHEDRAL FORMS

There are seven system space groups G_{sp} for crystals of various systems—C_i, C_{2h}, D_{2h}, D_{3d}, D_{4h}, D_{6h}, and O_h [9, 10]. Only for the trigonal system ($G_{\text{sp}} = D_{3d}$), the primitive sublattice is characterized by the group different from G_{sp} ($G_{\text{ssp}} = D_{6h}$), which reduces the number of holohedral groups to six [1, 2, 11, 12].

Consider the holohedral class of crystals, $G_K = G_{\text{ssp}}$. Let G_H be the symmetry group of the face of the holo-

---

[1] *e-mail: geod@pmkgu.kcn.ru*

hedral form. This face can be divided into g_H equivalent elementary (nonsymmetric) parts with respect to the symmetry elements of the group G_H, where g_H is the order of the group G_H. If one of these parts, f, is multiplied by the symmetry elements of the group G_H, we arrive at the face $G_H f$. Using the elements $h_i \in G_{\rm ssp}$ for $G_H f$, we arrive at all the other faces $h_i G_H f$ of the simple form, namely, $\sum h_i G_H f$. Applying the elements of the group $G_{\rm ssp}$ to f, we can also represent this simple form as $G_{\rm ssp} f$. Equating the holohedral forms obtained by these two methods, we obtain

$$G_{\rm ssp} = \sum_i h_i G_H, \quad 1 \le i \le n_H, \quad n_H = [G_{\rm ssp}: G_H], \tag{2}$$

where $h_i G_H$ is the right coset with respect to G_H [8]. To each face of the simple form in (2) there uniquely corresponds one coset. The index n_H of the subgroup G_H in $G_{\rm ssp}$ is equal to the number of faces of the holohedral simple form. Hereafter, for the sake of brevity, the simple forms are referred to as forms.

Let a crystal of the system $G_{\rm ssp}$ have the point group $G_K \subset G_{\rm ssp}$. In order to determine the number of conjugated forms l and their faces n_{KiH}, apply the group operations of G_K to the face $h_i G_H f$ of the holohedral form. With this aim, multiply $h_i G_H$ in (2) by G_K on the left-hand side. The product $G_K h_i G_H$ is the double coset by modulus (G_K, G_H) [8]. The product $G_K h_i G_H$ contains all the cosets corresponding to the faces equivalent with respect to G_K. The $G_K h_i G_H$ class uniquely corresponds to one simple form of the crystal with G_K. The number n_{KiH} equals the number of the right cosets with respect to G_H in the product $G_K h_i G_H$. Multiplying the left-hand side of (2) by G_K, we arrive at the expansion

$$G_K G_{\rm ssp} = \sum_{i=1}^{l} n_{KiH} G_K h_i G_H, \quad n_H = \sum_{i=1}^{l} n_{KiH}. \tag{3}$$

Expansion (3) is, in fact, the scheme for making the faces of the holohedral form nonequivalent. Using the conjugated groups $h_i G_H h_i^{-1}$, we can represent expansion (2) in the form

$$G_{\rm ssp} f = \sum_i (h_i G_H h_i^{-1})(h_i f), \quad 1 \le i \le n_H, \tag{4}$$

where the group $h_i G_H h_i^{-1}$ is the symmetry group of the ith face of the holohedral form, and $h_i f$ is one of the elementary parts of this face. The symmetry group of the face of the ith conjugated form (3) is determined as the intersection of the groups G_K and $h_i G_H h_i^{-1}$,

$$G_{KiH} = h_i G_H h_i^{-1} \cap G_K, \quad 1 \le i \le l. \tag{5}$$

The number n_{KiH} of the faces of the ith conjugated form is equal to the index $[G_K : G_{KiH}]$ of the group G_{KiH} in G_K:

$$n_{KiH} = g(G_K) : g(G_{KiH}) \equiv [G_K : G_{KiH}], \quad 1 \le i \le l. \tag{6}$$

The groups G_K of the crystals of the system under consideration are invariant subgroups of the group $G_{\rm ssp}$ and, therefore, expansion (3) acquires the form

$$G_K G_{\rm ssp} = \sum_{i=1}^{l} n_{KiH} h_i (G_K G_H). \tag{7}$$

The product $(G_K G_H)$ in (7), which acts onto the elementary part of f, yields one conjugated form

$$(G_K G_H) f = G_K (G_H f). \tag{8}$$

It follows from (7) and (8) that all the conjugated forms are of the same type. Therefore, we restrict our consideration to only one conjugated form $G_K(G_H f)$. The group of the face $G_{\rm F}$ of conjugated form (8) is determined as the intersection $G_{\rm F} = G_H \cap G_K$ (5). Form (8) can be obtained by multiplying the face $(G_{\rm F} f)$ with the aid of the coset representatives in the expansion of G_K with respect to the subgroup $G_{\rm F}$:

$$G_K = \sum_{j=1} h_j (G_H \cap G_K) = \sum_{j=1} h_j G_{\rm F}, \qquad 1 \le j \le [G_K : G_{\rm F}] = n_{KH}. \tag{9}$$

The number l of the conjugated forms is calculated by the formula

$$l = [g_{\rm ssp} : g_H] : [g_K : g_{\rm F}] \equiv [G_{\rm ssp} : G_H] : [G_K : G_{\rm F}]. \tag{10}$$

If $G_{K'} = G_K \times G$ and $G_{\rm F'} = G_{\rm F} \times G$ at $G \ne C_1$, then the substitution of G_K by $G_{K'}$ and $G_{\rm F}$ by $G_{\rm F'}$ in (9) does not change the system of the coset representatives $\{h_i\}$. In this case, the same form can be used for crystals with different symmetries, and the condition for the existence of the same simple form can be written as

$$G_K = \sum_i h_i G_{\rm F}, \quad G_{K'} = \sum_i h'_i G_{\rm F'}, \qquad h_i = h'_i, \quad 1 \le i \le n_{KH}. \tag{11}$$

If $G_{\rm F} = G_{\rm F'}$, then the condition for the admission of the same simple form reduces to the condition of "equal power" of the systems of representatives (11). In this case, the groups G_K and $G_{K'}$ are of the same order.

SIMPLE FORMS AND INTERGROWN CUBIC CRYSTALS

For the cubic system, $G_{\rm ssp} = G_{\rm sp} = O_h$. If $G_K = O_h$, all the simple forms—a cube, a rhombododecahedron, tetrahexahedron, octahedron, tetragon-trioctahedron, trigon-trioctahedron, and hexakis octahedron—are holohedral. The following holohedral forms possess the maximum number of faces having the highest possible symmetry.

A **cube** has the face group $G_H = G_{4V}$. At $G_K = O_h$, O, T_d, T_h, T the face groups are $G_F = G_H \cap G_K = C_{4V} \cap G_K$ – C_{4V}, C_4, C_{2V}, C_{2V}, and C_2, respectively. The decomposition (9) of the group G_K is performed with the use of the same system of the coset representatives $\{h_i\} = (1 + 3_1 + 3_1^2 + 3_2 + 3_2^2 + 2_x)$:

$$\begin{gathered} O_h = \{h_i\}C_{4V};\ O = \{h_i\}C_4;\ T_d = \{h_i\}C_{2V}; \\ T_h = \{h_i\}C_{2V};\ T = \{h_i\}C_2, \end{gathered} \tag{12}$$

whence it follows that a cube, being a simple form, can exist in crystals of all the five types of symmetry of the cubic system. The number n_K of individual crystals given by formula (1) in the intergrown crystals with $G_K = O_h$, O, T_d, T_h, T equals to the corresponding index:

$$\begin{gathered} [O_h : O_h] = 1;\ [O_h : O] = 2;\ [O_h : T_d] = 2; \\ [O_h : T_h] = 2;\ [O_h : T] = 4. \end{gathered} \tag{13}$$

It is seen from (13) that there are eleven different cubes.

The individual crystals of the intergrowth with G_K are transformed into one another by the coset representative in the decomposition of the group $G_{\text{ssp}} = O_h$ with respect to the subgroup G_K:

$$\begin{gathered} O_h = 1O_h,\ O_h = 1O + mO,\ O_h = 1T_d + m_yT_d, \\ O_h = 1T_h + m_{xy}T_h,\ O_h = 1T + m_xT + m_{xy}T + 4T, \end{gathered} \tag{14}$$

where m is the operation of reflection with respect to any of the symmetry planes of the group O_h; m_y is the reflection with respect to the symmetry plane normal to the crystallographic Y-axis; m_{xy} is the reflection with respect to the symmetry plane diagonal with respect to the crystallographic X- and Y-axes; and 4 is the rotation by an angle of $\pi/4$. The individual crystals of the intergrowth differ from one another (have differently hatched faces of the simple forms) [1].

The **rhombododecahedron** has $G_H = C_{2V}$. The subgroups of $G_H = C_{2V}$ in the groups $G_K = O_h$, O, T_d, T_h, T are the face groups: $G_F = C_{2V}$, C_2, C_{Syz}, C_{Sx}, C_1. The system of representatives $\{h_i\}$ in this case forms the group T:

$$\begin{gathered} O_h = \{T\}C_{2V};\ O = \{T\}C_2;\ T_d = \{T\}C_{Syz}; \\ T_h = \{T\}C_{Sx};\ T = \{T\}C_1. \end{gathered} \tag{15}$$

Decomposition (15) indicates that the crystals of all the five types of cubic-system symmetry can have a rhombododecahedron. According to (13), there are eleven different types of dodecahedra (differently hatched faces).

The **tetrahexahedron** has $G_H = C_{Sx}$. The decomposition of G_K with respect to the subgroup $G_F = C_{Sx} \cap G_K$ has the form

tetrahexahedra pentagon-dodecahedra

$$\begin{array}{ll} O_h = \{T_d\}C_{Sx} = \{O\}C_{Sx}, & \\ O = \{O\}C_1, & T_h = \{T\}C_{Sx},\ l = 2, \\ & T = \{T\}C_1,\ l = 2. \\ T_d = \{T_d\}C_1, & \end{array} \tag{16}$$

The system of the coset representatives (16) in the decomposition of O_h with respect to C_{Sx} coincides with the groups T_d or O. The decomposition of the groups O and T_d with respect to $G_F = C_1$ is provided by the use of the representatives of cosets $\{O\}$ and $\{T_d\}$, respectively. The crystals with $G_K = O_h$, O, T_d can have tetrahexahedra. In accordance with (13), there are five different types of tetrahexahedra. The number of representatives in the decomposition of T_h and T is two times less than O_h, and equals 12.

At $G_K = T_h$, pentagon-dodecahedra with the correspondingly hatched faces have the symmetry T_h. The combination of these conjugated forms has the symmetry group $G_{\text{ssp}} = O_h$. From the decomposition $O_h = T_h + m_{xy}T_h = \{T\}C_{Sx} + m_{xy}\{T\}C_{Sx}$ (14) and (16), it follows that two conjugated pentagon-dodecahedra are transformed into one another by the operation m_{xy} of the group O_h. The faces of these conjugated forms have different properties. In accordance with (14), a crystal with two conjugated pentagon-dodecahedra can consist of two individual crystals in the intergrowth that are also transformed into one another by the operation m_{xy}. Altogether, there are only twelve different pentagon-dodecahedra.

The **octahedron** has $G_H = C_{3V}$. The decomposition with respect to the group $G_F = C_{3V} \cap G_K$ has the form

octahedra tetrahedra

$$\begin{array}{ll} O_h = \{D_{2h}\}C_{3V} = \{D_4\}C_{3V}, & T_d = \{D_2\}C_{3V},\ l = 2, \\ O = \{D_4\}C_3, & T = \{D_2\}C_3,\ l = 2. \\ T_h = \{D_{2h}\}C_3, & \end{array} \tag{17}$$

For crystals with $G_K = T_d$, T, the holohedral form (octahedron) can be represented by two conjugated tetrahedra $l(T_d) = 2$ and $l(T) = 2$. According to (13), the number of various tetrahedra equals $l(T_d)[O_h : T_d] + l(T)[O_h : T] = 2 \times 2 + 2 \times 4 = 12$.

The **tetragon–trioctahedron** has $G_H = C_{Sxy}$. The decomposition of G_K with respect to $G_F = C_{Sxy} \cap G_K$ has the form

tetragon-trioctahedra trigon-tritetrahedra

$$\begin{array}{ll} O_h = \{O\}C_{Sxy} = \{T_h\}C_{Sxy}, & T_d = \{T\}C_{Sxy},\ l = 2, \\ O = \{O\}C_1, & T = \{T\}C_1,\ l = 2. \\ T_h = \{T_h\}C_1, & \end{array} \tag{18}$$

There are five types of tetragon-trioctahedra and twelve types of trigon-tritetrahedra, respectively.

The **trigon-trioctahedron** has $G_H = G_{Syz}$. The decomposition of G_K with respect to the subgroup $G_{\text{F}} = C_{Syz} \cap G_K$ takes the form:

trigon-trioctahedra tetragon-trioctahedra

$$\begin{array}{ll} O_h = \{O\}C_{Syz} = \{T_h\}C_{Syz}, & T_d = \{T\}C_{Syz},\ l = 2, \\ O = \{O\}C_1, & \\ T_h = \{T_h\}C_1, & T = \{T\}C_1,\ l = 2 \end{array} \quad (19)$$

with five types of trigon-trioctahedra and twelve types of tetragon-tritetrahedra.

The **hexakis octahedron** has $G_H = C_1$. Since the $G_{\text{F}} = C_1 \cap G_K = C_1$, the decomposition of the G_K system of the coset representatives coincide with the group G_K itself: $O_h = \{O_h\}C_1$ yields a hexakis octahedron,

$$\begin{array}{ll} O = \{O\}C_1, & l = 2 \text{ yield pentagon-trioctahera;} \\ T_d = \{T_d\}C_1, & l = 2 \text{ yields hexakis tetrahedra;} \\ T_h = \{T_h\}C_1, & l = 2 \text{ are didodecahedra;} \\ T = \{T\}C_1, & l = 4 \text{ yields pentagon-tritetrahedra.} \end{array} \quad (20)$$

SIMPLE FORMS AND CRYSTALS INTERGROWTHS OF TRIGONAL SYSTEM

In this case, $G_{\text{sp}} = D_{3d}$ and $G_{\text{ssp}} = D_{6h}$. The rhombohedral space lattices can have the crystals with $G_K = D_{3d}$, D_3, C_{3V}, C_{3i}, C_3. In accordance with G_K, the number n_K of individual crystals (1) can have the following values:

$$\begin{array}{c} [D_{6h} : D_{3d}] = 2;\ [D_{6h} : D_3] = 4; \\ [D_{6h} : C_{3v}] = 4; \\ [D_{6h} : C_{3i}] = 4;\ [D_{6h} : C_3] = 8. \end{array} \quad (21)$$

Simple holohedral forms are a pinacoid, hexagonal prisms of the $\{2\bar{1}\bar{1}0\}$ and $\{10\bar{1}0\}$ types, hexagonal dipyramids of the $\{2h\bar{h}\bar{h}l\}$ and $\{h0\bar{h}l\}$ types, a dihexagonal dipyramid, and a dihexagonal prism. The crystallographic *X*- and *Y*-axes are directed along the twofold axes of the group $G_{\text{sp}} = D_{3d}$ with the angle $\gamma = 120°$. The representations of these holohedral forms for crystals with $G_K \le D_{3d}$ are as follows.

The pinacoid has $G_H = C_{6V}$. The decomposition of G_K into cosets with respect to $G_{\text{F}} = C_{6V} \cap G_K$ takes the form $D_{6h} = (C_{2x})C_{6V} = (C_i)C_{6V}$ and $C_{2x} = (1 + 2_x)$:

pinacoids monohedra

$$\begin{array}{ll} D_{3d} = \{C_{2x}\}C_{3V}, & C_{3V} = \{C_1\}C_{3V},\ l = 2, \\ D_3 = \{C_{2x}\}C_3, & C_3 = \{C_1\}C_3,\ l = 2. \\ C_{3i} = \{C_i\}C_3, & \end{array} \quad (22)$$

A $\{2\bar{1}\bar{1}0\}$-type **hexagonal prism** has $G_H = C_{2xV}$. The decomposition has the form $D_{6h} = \{C_6\}C_{2xV} = \{C_{3V}\}C_{2xV} = \{C_{3i}\}C_{2xV}$:

hexagonal prisms trigonal prisms

$$\begin{array}{ll} D_{3d} = \{C_{3V}\}C_2 = \{C_{3i}\}C_2, & D_3 = \{C_3\}C_2,\ l = 2, \\ C_{3V} = \{C_{3V}\}C_1, & C_3 = \{C_3\}C_1,\ l = 2. \\ C_{3i} = \{C_{3i}\}C_1, & \end{array} \quad (23)$$

A $\{10\bar{1}0\}$-type **hexagonal prism** has $G_H = C_{2V}$. The decomposition of the G_K groups of the rhombohedral system with respect to the subgroup $G_{\text{F}} = C_{2V} \cap G_K$ has the form $D_{6h} = \{C_6\}C_{2V} = \{C_{3V}\}C_{2V} = \{C_{3i}\}C_{2V} = \{D_3\}C_{2V}$:

hexagonal prisms trigonal prisms

$$\begin{array}{ll} D_{3d} = \{D_3\}C_3, & C_{3V} = \{C_3\}C_S,\ l = 2, \\ C_{3i} = \{C_{3i}\}C_1, & C_3 = \{C_3\}C_1,\ l = 2. \\ C_3 = \{D_3\}C_1, & \end{array} \quad (24)$$

Dihexagonal prism has $G_H = C_S$. The decomposition yields the following prisms:

$$\begin{array}{rl} D_{3d} = \{D_{3d}\}C_1, & l = 1 \text{ dihexagonal;} \\ D_3 = \{D_3\}C_1, & l = 2 \text{ ditrigonal;} \\ C_{3V} = \{C_{3V}\}C_1, & l = 2 \text{ ditrigonal;} \\ C_{3i} = \{C_{3i}\}C_1, & l = 2 \text{ hexagonal;} \\ C_3 = \{C_3\}C_1, & l = 4 \text{ trigonal.} \end{array} \quad (25)$$

A $\{h0\bar{h}l\}$-type **hexagonal dipyramid** has $G_H = C_S$. The decomposition G_K with respect to the subgroup $G_{\text{F}} = C_S \cap G_K$ yields the following results $D_{6h} = \{D_6\}C_S = \{C_{6h}\}C_S$:

rhombohedra trigonal pyramids

$$\begin{array}{ll} D_{3d} = \{D_3\}C_S = \{C_{3i}\}C_2,\ l = 2, & C_{3V} = \{C_3\}C_S,\ l = 4, \\ D_3 = \{D_3\}C_1,\ l = 2, & C_3 = \{C_3\}C_1,\ l = 4. \\ C_{3i} = \{C_{3i}\}C_1,\ l = 2, & \end{array} \quad (26)$$

A $\{2h\bar{h}\bar{h}l\}$-type **hexagonal dipyramid** has $G_H = C_S$. The results of the decomposition of the groups G_K with respect to the subgroup $G_{\text{F}} = C_S \cap G_K$ are represented in the form $D_{6h} = \{D_6\}C_S = \{C_{6h}\}C_S = \{D_{3d}\}C_S$:

Table 1. Conjugated simple forms and their holohedral permutational varieties for cubic crystals

O_h, holohedry	O, enantiomorphic hemihedry	T_d, hemimorphic hemihedry	T_h, hemihedry	T, paramorphic tetartohedry	Form/conjugation ratio*
Cube	Cube	Cube	Cube	Cube	5/11
Rhombododecahedron	Rhombododecahedron	Rhombododecahedron	Rhombododecahedron	Rhombododecahedron	5/11
Tetrahexahedron	Tetrahexahedron	Tetrahexahedron	2 Pentagon-dodecahedra	2 Pentagon-dodecahedra	7/17
Octahedron	Octahedron	2 Tetrahedra	Octahedron	2 Tetrahedra	7/17
Tetragon-trioctahedron	Tetragon-trioctahedron	2 Trigon-tritetrahedra	Tetragon-trioctahedron	2 Trigon-tritetrahedra	7/17
Trigon-trioctahedron	Trigon-trioctahedron	2 Tetragon-tritetrahedra	Trigon-trioctahedron	2 Tetragon-tritetrahedra	7/17
Hexakis octahedron	Pentagon-trioctahedron	2 Hexakis tetrahedra	2 Didodecahedra	4 Pentagon-trioctahedron	11/29
$7 \times 1 = 7$**	$8 \times 2 = 16$**	$11 \times 2 = 22$**	$9 \times 2 = 18$**	$14 \times 4 = 56$**	49/119

* Number of simple forms conjugated with the given holohedral form divided into number of all the holohedral permutational conjugations.

** Number of conjugations multiplied by multiplicity n_K of the orientational degeneracy of the crystal structure with respect to holohedry equal to the number of the holohedral permutational conjugations.

$$D_{3d} = \{D_{3d}\}C_1 \text{ hexagonal dipyramid;}$$
$$C_{3i} = \{C_{3i}\}C_1, \quad l = 2 \text{ rhombohedra;}$$
$$D_3 = \{D_3\}C_1, \quad l = 2 \text{ trigonal pyramids;} \tag{27}$$
$$C_{3V} = \{C_{3V}\}C_1, \quad l = 2 \text{ hexagonal pyramids;}$$
$$C_3 = \{C_3\}C_1, \quad l = 4 \text{ trigonal pyramids.}$$

Dihexagonal dipyramid has $G_H = C_1$. The decomposition of the groups G_K is written in the form:

$$D_{3d} = \{D_{3d}\}C_1, \quad l = 2 \text{ trigonal scalenohedra;}$$
$$D_3 = \{D_3\}C_1, \quad l = 4 \text{ trigonal trapezohedra;}$$
$$C_{3V} = \{C_{3V}\}C_1, \quad l = 4 \text{ ditrigonal pyramids;} \tag{28}$$
$$C_{3i} = \{C_{3i}\}C_1, \quad l = 4 \text{ rhombohedra;}$$
$$C_3 = \{C_3\}C_1, \quad l = 8 \text{ trigonal pyramids.}$$

It is seen from (26) and (28) that in the transition from $G_{\text{ssp}} = D_{6h}$ to $G_{\text{sp}} = D_{3d}$, only the holohedral hexagonal and dihexagonal dipyramids are divided into rhombohedra and trigonal scalenohedra, respectively, because rhombohedra and trigonal scalenohedra can have different reticular densities [9]. The results of the decomposition for all the 32 crystal classes are given in Tables 1–5.

DISCUSSION AND CONCLUSIONS

Except for the rhombohedral system, the faces of various conjugated simple forms of crystals are characterized by the same nodal nets but have different structures. The holohedral form can conjugate and develop on crystals differently. This nonequivalence allows one to consider the crystal faceting for drawing certain conclusions about the type of crystal symmetry. This phenomenon underlies the theory of holohedry and merohedry [1, 2]. The empirical methods for dividing crystals into holohedral and merohedral classes were refined and developed by Gadolin [3] on the basis of 32 types of the crystal symmetry. The theory of merohedry, once the empirical method of crystal classification, has been developed into the theory of the external shape of crystalline materials. The abstract method of the group theory used in the present study relates the theory of crystal forms to the theory of representation of groups by transitive substitution groups [8]. Decomposition (3) is in fact the division of the system of cosets into the transitivity systems of the substitution groups.

The directional deposition of the substance onto a crystal can be described by the corresponding representations of the three-dimensional lattice by the methods of the group–theoretical analysis. Such a necessity can arise in the studies of intergrowths with $G_K = G_{\text{ssp}}$. It should be indicated that a three-dimensional lattice of cubic crystals can be represented by an orthorhombic lattice with respect to one of the threefold axes L_3. A rhombohedron in the unit cell of a primitive three-dimensional sublattice of the symmetry D_{6h} has two equivalent settings transformed into one another by a 180° rotation around the L_3 axis. This equivalence explains the wide spread occurrence of cubic twins with the common axis L_3 [13].

A three-dimensional lattice of trigonal crystals also possess two equivalent settings with respect to the sub-

Table 2. Conjugated simple forms and their holohedral permutational varieties for tetragonal crystals

D_{4h}	D_4	C_{4V}	C_{4h}	D_{2d}	S_4	C_4	Form/conjugation ratio*
Pinacoid	Pinacoid	2 Monohedra	Pinacoid	Pinacoid	Pinacoid	2 Monohedra	9/23
Tetragonal dipyramid	Tetragonal dipyramid	2 Tetragonal pyramids	Tetragonal dipyramid	Tetragonal dipyramid	2 Tetragonal tetrahedra	2 Tetragonal pyramids	10/27
Tetragonal prism {100}	Tetragonal prism	Tetragonal prism	Tetragonal prism	Tetragonal prism	Tetragonal prism	Tetragonal prism	7/17
Ditetragonal prism	Ditetragonal prism	Ditetragonal prism	2 Tetragonal prisms	Ditetragonal prism	2 Tetragonal prisms	2 Tetragonal prisms	10/27
Tetragonal prism {110}	Tetragonal prism	Tetragonal prism	Tetragonal prism	Tetragonal prism	Tetragonal prism	Tetragonal prism	7/17
Tetragonal dipyramid	Tetragonal dipyramid	2 Tetragonal pyramids	Tetragonal dipyramid	2 Tetragonal tetrahedra	2 Tetragonal tetrahedra	2 Tetragonal pyramids	11/29
Ditetragonal dipyramid	2 Tetragonal trapezohedron	2 Ditetragonal pyramids	2 Tetragonal dipyramids	2 Tetragonal scalenohedra	4 Tetragonal tetrahedra	4 Tetragonal pyramids	17/49
$7 \times 1 = 7$**	$8 \times 2 = 16$**	$11 \times 2 = 22$**	$9 \times 2 = 18$**	$9 \times 2 = 18$**	$13 \times 4 = 52$**	$14 \times 4 = 56$**	71/189

Note: for * and ** see Table 1.

Table 3. Conjugated simple forms and their holohedral permutational varieties for hexagonal crystals

D_{6h}, holohedry	D_{3h}, trigonal holohedry	D_6, enantiomorphic holohedry	C_{6V}, hemimorphic hemihedry	C_{6h}, paramorphic hemihedry	C_{3h}, trigonal paramorphic hemihedry	C_6, hemimorphic tetartohedry	Forms/conjugation ratio*
Pinacoid	Pinacoid	Pinacoid	2 Monohedra	Pinacoid	Pinacoid	2 Monohedra	9/23
Hexagonal dipyramid $\{2h\bar{h}\bar{h}l\}$	2 Trigonal dipyramids	Hexagonal dipyramid	2 Hexagonal pyramids	Hexagonal dipyramid	2 Trigonal dipyramids	2 Hexagonal pyramids	11/29
Hexagonal prism $\{2\bar{1}\bar{1}0\}$	2 Trigonal prism	Hexagonal prism	Hexagonal prism	Hexagonal prism	2 Trigonal prism	Hexagonal prism	9/23
Dihexagonal prism	2 Ditrigonal prism	Ditrigonal prism	Ditrigonal prism	2 Hexagonal prism	4 Trigonal prism	2 Hexagonal prism	13/37
Hexagonal prism $\{10\bar{1}0\}$	Hexagonal prism	Hexagonal prism	Hexagonal prism	Hexagonal prism	2 Trigonal prism	Hexagonal prism	8/21
Hexagonal dipyramid $\{h0hl\}$	Hexagonal dipyramid	Dihexagonal dipyramid	2 Hexagonal pyramids	Hexagonal dipyramid	2 Trigonal dipyramids	2 Hexagonal pyramids	10/27
Dihexagonal dipyramid	2 Ditrigonal dipyramid	2 Hexagonal trapezohedra	2 Ditrigonal pyramids	2 Hexagonal dipyramid	4 Trigonal dipyramids	4 Hexagonal pyramids	17/49
$7 \times 1 = 7$**	$11 \times 2 = 22$**	$8 \times 2 = 16$**	$11 \times 2 = 22$**	$9 \times 2 = 18$**	$17 \times 4 = 68$**	$14 \times 4 = 56$**	77/209

Note: * and ** see Table 1.

lattice of the symmetry D_{6h} [14]. This equivalence manifests itself, e.g., in twinning observed in calcite and dolomite crystals [6] and can be detected by the EPR method.

The centosymmetricity of the EPR spectra allows the use of this method only for crystals providing the modulated spectra from each individual crystal with equally oriented primitive cubic lattices. The EPR spectra can detect such twins only for cubic, hexagonal, and tetragonal crystals with several Laue classes.

Simple forms of the crystals are classified mainly by two methods [15]: (i) the derivation of less symmetric forms from more symmetric ones and (ii) the derivation of highly symmetric forms from less symmetric ones. Using the first method, one can determine the holohedral simple forms. The cubic, hexagonal, tetragonal, and orthorhombic systems have seven holohedral simple forms each. The monoclinic system has three simple forms, and the triclinic systems, only one. Among these 32 holohedral forms, only 18 are characterized by different symmetry groups: seven holohedral forms in the cubic system; hexagonal prism and dipyramid, dihexagonal prism and dipyramid in the hexagonal system; tetragonal prism and dipyramid, ditetragonal

Table 4. Conjugated simple forms and their holohedral permutational varieties for trigonal crystals

D_{3d}, rhombohedral holohedry	C_{3V}, hemimorphic hemihedry	C_{3i}, hexagonal tetartohedry	D_3, enantiomorphic hemihedry	C_3, rhombohedral tetartohedry	Form/conjugation ratio*
Pinacoid	2 Monohedra	Pinacoid	Pinacoid	2 Monohedra	7/34
Hexagonal dipyramids $\{2h\bar{h}\bar{h}l\}$	2 Hexagonal pyramids	2 Rhombohedra	2 Trigonal dipyramids	4 Trigonal pyramids	11/58
Hexagonal prism $\{2\bar{1}\bar{1}0\}$	Hexagonal prism	Hexagonal prism	2 Trigonal prisms	2 Trigonal prisms	7/34
Dihexagonal prism	2 Ditrigonal prisms	2 Hexagonal prism	2 Ditrigonal prisms	4 Trigonal prisms	11/58
Hexagonal prism $\{10\bar{1}0\}$	2 Trigonal prisms	Hexagonal prism	Hexagonal prism	2 Trigonal prisms	7/34
2 Rhombohedra	4 Trigonal pyramids	2 Rhombohedra	2 Rhombohedra	4 Trigonal pyramids	14/68
2 Trigonal scalenohedra	4 Ditrigonal pyramids	4 Rhombohedra	4 Trigonal trapezohedra	8 Trigonal pyramids	22/116
$9 \times 2 = 18$**	$17 \times 4 = 68$**	$13 \times 24 = 52$**	$14 \times 4 = 56$**	$26 \times 8 = 208$**	79/402

Note: for * and ** see table 1.

Table 5. Conjugated simple forms and their holohedral permutational varieties for orthorhombic, monoclinic, and triclinic crystals

Orthorhombic system

D_{2h}, holohedry	D_2, enantiomorphic hemihedry	C_{2V}, hemimorphism	Form/conjugation ratio*
Pinacoid {001}	Pinacoid	2 Monohedra	4/7
Rhombic prism {0*kl*}	Rhombic prism	2 Dihedra	4/7
Pinacoid {100}	Pinacoid	Pinacoid	3/5
Rhombic prism {*hk*0}	Rhombic prism	Rhombic prism	3/5
Pinacoid {010}	Pinacoid	Pinacoid	3/5
Rhombic prism {*h*0*l*}	Rhombic prism	2 Dihedra	4/7
Rhombic dipyramid	2 Rhombic tetrahedra	2 Rhombic dipyramid	5/9
$7 \times 1 = 7$**	$8 \times 2 = 16$**	$11 \times 2 = 22$**	26/45

Monoclinic system

C_{2h}, holohedry	C_2, hemihedry	C_S, hemimorphism	Form/conjugation ratio*
Pinacoid {001}	2 Monohedra	Pinacoid	4/7
Pinacoid {*hk*0}	Pinacoid	2 Monohedra	4/7
Rhombic prism	2 Dihedra	2 Dihedra	5/9
$3 \times 1 = 3$**	$5 \times 2 = 10$**	$5 \times 2 = 10$**	13/23

Triclinic system

C_i, holohedry	C_1, hemihedry	Form/conjugation ratio*
Pinacoid	2 Monohedra	3/5
$1 \times 1 = 1$**	$2 \times 2 = 4$**	3/5

Note: * and ** see Table 1.

prism and dipyramid, and orthorhombic dipyramid in the tetragonal system; rhombic dipyramid in the orthorhombic system; rhombic prism in the orthorhombic and monoclinic systems, and a pinacoid in all the systems except of the cubic system. The enclosure of each of the 32 holohedral forms into the corresponding G_K classes yields 318 [4] holoherally conjugated simple forms (Tables 1–5). In the cubic system, there are 49 such simple forms; in the hexagonal system, 156; in the tetragonal system, 71; in the orthorhombic system, 26; in the monoclinic system, 13; and in the triclinic system, 3 holohedral conjugated simple forms. Among 318 conjugations, 231 are nonequivalent with respect to the connectedness domain [16], 200 are holohedrally nonequivalent, and 146 are nonequivalent with respect to the normalizer of point groups [4, 17], and, finally, 47 conjugations are nonequivalent with respect to the complete symmetry group. Each of 318 conjugations can take n_K (1) holohedral permutational positions. The number of all the holohedral permutational conjugations for 32 crystal classes is equal to 992: 119 in the cubic system (Table 1), 189 in the tetragonal system (Table 2), 611 in the hexagonal system (Table 3), 45 in the orthorhombic system, 23 in the monoclinic system, and 5 in the triclinic system (Table 5).

The derivation of the simple forms from the holohedral ones corresponds to the crystal classification according to the scheme $G_{\mathrm{ssp}} \supseteq G_{\mathrm{sp}} \supseteq G_K$ and reflects the ability of crystals to intergrow. It also allows the graphic representation of holohedral permutational conjugated simple forms in terms of elementary parts of the holohedral simple form developed equivalently with respect to G_K [1].

REFERENCES

1. S. F. Glinka, *General Course of Crystallography* (Tsinzerling, St. Petersburg, 1902).
2. M. Bauer, *Lehrbuch der Mineralogie* (Nagelel, Stuttgart, 1904).
3. A. V. Gadolin, *Subdivisions Derivation, from a Single Common Origin, of All the Crystallographic Systems and Their Subdivisions* (Izd. Akad. Nauk SSSR, Moscow, 1954; first published in *Zap. Ross. Mineral. Obshchestva*, Ser. 2, **4** (2), 112 (1867)).
4. R. V. Galiulin, Kristallografiya **23** (6), 1125 (1978) [Sov. Phys. Crystallogr. **23** (6), 635 (1978)].
5. S. H. Chao and W. H. Taylor, Proc. Roy. Soc. London A **174**, 57 (1940).
6. H. R. Wenk, D. J. Barber, and R. J. Reeder, *Microstructures in Carbonates. Reviews in Mineralogy. Carbonates: Mineralogy and Chemistry* (1983), Vol. 11, p. 301.
7. V. M. Vinokurov, G. R. Bulka, N. M. Nizamutdinov, and N. M. Khasanova, Dokl. Akad. Nauk SSSR **237** (6), 1388 (1977).
8. M. Hall, *The Theory of Groups* (Macmillan, New York, 1959; Inostrannaya Literatura, Moscow, 1962).
9. O. Bravais, *Etudes Cristallographiques* (Gauthier-Villars, Paris, 1966; Nauka, Leningrad, 1974).
10. G. Ya. Lyubarskiĭ, *Group Theory and Its Application in Physics* (Gostekhizdat, Moscow, 1958; Pergamon Press, Oxford, 1960).
11. A. V. Shubnikov, Tr. Lab. Kristallogr. Akad. Nauk SSSR **2**, 3 (1940).
12. C. F. Nauman, *Elemente der Mineralogie* (Engelmann, Leipzig, 1855).
13. V. V. Dolivo-Dobrovol'skiĭ, *Course of Crystallography* (ONTI, Leningrad–Moscow, 1937).
14. *International Tables for Crystallography. Vol. A. Space-Group Symmetry*, Ed. by T. Hahn (Reidel, Dordrecht, 1989), 3rd. ed.
15. P. Groth, *Physikalische Krystallographie und Einleitung in die Krystallographische Kenntniss der wichtigsten Substanzen* (Engelmann, Leipzig, 1876; Rikker, St. Petersburg, 1897).
16. R. V. Galiulin, *Lectures on Geometric Foundations of Crystallography* (Chelyabinsk Univ., Chelyabinsk, 1989).
17. R. V. Galiulin, Tr. Mat. Inst. im. V.A. Steklova, Akad. Nauk. SSSR **148**, 82 (1978).

Translated by L. Man

Crystallography Reports, Vol. 45, No. 4, 2000, pp. 537–540. Translated from Kristallografiya, Vol. 45, No. 4, 2000, pp. 591–595.
Original Russian Text Copyright © 2000 by Palistrant.

Some Geometric Characteristics of Four-Dimensional Crystallographic Point Symmetry Groups and Their Subgroups

A. F. Palistrant
Moldova State University, ul. Matteevicha 60, Chisinau, 277009 Moldova

Received June 8, 1998

Abstract—Using three-dimensional point and tablet antisymmetry groups and also rosette and zero-dimensional groups of generalized antisymmetry that model all possible subgroups of four-dimensional crystallographic point groups, we determined the number of various symmetry groups forming the four-dimensional crystallographic classes for each category of such subgroups. These results allowed us to establish (without the use of the complete catalogue of the groups themselves) that 168 four-dimensional crystallographic classes preserve not only the point but also some other geometrical objects. The remaining 103 classes preserve only one invariant point of the four-dimensional Euclidean space. *© 2000 MAIK "Nauka/Interperiodica".*

1. Broun *et al.* [1] described the four-dimensional symmetry groups of the G_{40} category (four-dimensional crystallographic classes). Zamorzaev *et al.* [2] derived all kinds of their subgroups (hypercrystallographic with an invariant hyperplane and a singular point on it, i.e., the groups of the G_{430} category copying the groups of the G_{410} category; bi-rosette groups with an invariant two-dimensional plane and a point on it, i.e., the groups of the G_{420} category; hypertablet groups with an invariant hyperplane into which an invariant two-dimensional plane with singular point is embedded, i.e., the groups of the G_{4320} category coinciding with the groups of the G_{4210} and G_{4310} categories, and also the symmetry groups of the G_{43210} category). However, these groups and their subgroups need further structural study.

By definition, the four-dimensional crystallographic classes preserve at least one stationary point of the space. Clearly, among these groups, there are groups that preserve only one point of space. At the same time, there are also some groups that in addition to a point, preserve unchanged also some other geometrical objects of the four-dimensional space. However, the number of groups with the above properties among the four-dimensional crystallographic classes is unknown. It is also unknown how many four-dimensional crystal classes G_{40} are contained within each category of subgroups of four-dimensional point groups. The present paper is aimed at elucidating the above-mentioned geometrical features of the four-dimensional crystallographic classes and to determine all kinds of their nontrivial subgroups.

2. Zamorzaev *et al*. [2] interpreted all the groups of the G_{420} category in terms of the rosette groups of the symmetry G_{20} and the antisymmetry G_{20}^{1} and also of the Belov groups of complete color symmetry G_{20}^{p} and the Pawley color antisymmetry $G_{20}^{p'}$ at $p = 2, 3, 4, 6$ by applying a complex geometrical interpretation of signs "+" and "–," indices 1, …, p, or the indices with signs 1, …, p and $\bar{1}$, …, $\bar{p}$. This procedure is analogous to bringing into correspondence the one-dimensional point groups of P-symmetry G_{10}^{P} and the tablet groups of symmetry G_{320} in Table 1 from [3]. On the basis of the general theory and classification of the groups of P-symmetry (sections 2 and 3, ch. I [2]), and the results of calculations for the nontrivial generalization of the G_{20} category (sections 2 and 3, ch. II), one can see that $10G_{20}$ + (11M + 10C)G_{20}^{1} + (11M + 10C)G_{20}^{2} + (4M + 10C)G_{20}^{3} + (2 + 10 + 11)G_{20}^{4} (junior, senior, and 2-intermediate) + (2 + 10 + 11 + 4)G_{20}^{6} (junior, senior, 3-, and 2-intermediate) + (6 + 10 + 2 × 11)$G_{20}^{2'}$ (junior, senior, (1')- and 2-intermediate) + (4 + 10 + 11)$G_{20}^{3'}$ (junior, senior, and 3-intermediate) + (2 + 10 + 2 × 11 + 6)$G_{20}^{4'}$ (junior, senior, (2')-, 4-, and 2-intermediate) + (2 + 10 + 2 × 11 + 6 + 4)$G_{20}^{6'}$ (junior, senior, (3')-, 6-, 3-, and 2-intermediate) rosette groups (whose complete derivation is considered for the first time below) model 263 different four-dimensional symmetry groups that preserve two mutually orthogonal two-dimensional planes intersecting at the singular point (cf. with [4]). Note that not only one-to-one but also strong isomorphic correspondence exists between the indicated rosette groups G_{20}^{p} and the groups of the G_{420} category, i.e., the structure of each G_{20}^{P} group considered exactly reflects the structure of the corresponding G_{420} group [5].

Let us write the above-mentioned G_{20}^{P} groups, which interprete 263 different four-dimensional point symmetry groups of the G_{4201} category in Shubnikov's notation.[1]

G_{20}: 10 generating (1, 2, 3, 4, 6, m, $2 \cdot m$, $3 \cdot m$, $4 \cdot m$, $6 \cdot m$).

G_{20}^{1}: 11 junior (2', 4', 6', m', $2' \cdot m$, $2 \cdot m'$, $3 \cdot m'$, $4' \cdot m$, $4 \cdot m'$, $6' \cdot m$, $6 \cdot m'$), 10 senior ($1 \times 1'$, $2 \times 1'$, $3 \times 1'$, $4 \times 1'$, $6 \times 1'$, $m \times 1$, $2 \cdot m \times 1'$, $3 \cdot m \times 1'$, $4 \cdot m \times 1'$, $6 \cdot m \times 1'$).

G_{20}^{2}: 11 junior ($2^{(2)}$, $4^{(2)}$, $6^{(2)}$, $m^{(2)}$, $2^{(2)} \cdot m$, $2 \cdot m^{(2)}$, $3 \cdot m^{(2)}$, $4^{(2)} \cdot m$, $4 \cdot m^{(2)}$, $6^{(2)} \cdot m$, $6 \cdot m^{(2)}$), 10 senior ($1 \times 1^{(2)}$, $2 \times 1^{(2)}$, $3 \times 1^{(2)}$, $4 \times 1^{(2)}$, $6 \times 1^{(2)}$, $m \times 1^{(2)}$, $2 \cdot m \times 1^{(2)}$, $3 \cdot m \times 1^{(2)}$, $4 \cdot m \times 1^{(2)}$, $6 \cdot m \times 1^{(2)}$).

G_{20}^{3}: 4 junior ($3^{(3)}$, $3^{(-3)}$, $6^{(3)}$, $6^{(-3)}$), 10 senior ($1 \times 1^{(3)}$, $2 \times 1^{(3)}$, $3 \times 1^{(3)}$, $4 \times 1^{(3)}$, $6 \times 1^{(3)}$, $m \times 1^{(3)}$, $2 \cdot m \times 1^{(3)}$, $3 \cdot m \times 1^{(3)}$, $4 \cdot m \times 1^{(3)}$, $6 \cdot m \times 1^{(3)}$).

G_{20}^{4}: 2 junior ($4^{(4)}$, $4^{(-4)}$), 10 senior ($1 \times 1^{(4)}$, $2 \times 1^{(4)}$, $3 \times 1^{(4)}$, $4 \times 1^{(4)}$, $6 \times 1^{(4)}$, $m \times 1^{(4)}$, $2 \cdot m \times 1^{(4)}$, $3 \cdot m \times 1^{(4)}$, $4 \cdot m \times 1^{(4)}$, $6 \cdot m \times 1^{(4)}$), 11 2-intermediate ($2^{(4)}$, $4^{(4)} \times 1^{(2)}$, $6^{(4)}$, $2^{(4)} \cdot m$, $2 \cdot m^{(4)}$, $3 \cdot m^{(4)}$, $4^{(4)} \cdot m$, $4 \cdot m^{(4)}$, $6^{(4)} \cdot m$, $6 \cdot m^{(4)}$, $m^{(4)}$).

G_{20}^{6}: 2 junior ($6^{(6)}$, $6^{(-6)}$), 10 senior ($1 \times 1^{(6)}$, $2 \times 1^{(6)}$, $3 \times 1^{(6)}$, $4 \times 1^{(6)}$, $6 \times 1^{(6)}$, $m \times 1^{(6)}$, $2 \cdot m \times 1^{(6)}$, $3 \cdot m \times 1^{(6)}$, $4 \cdot m \times 1^{(6)}$, $6 \cdot m \times 1^{(6)}$), 11 3-intermediate ($2^{(2)} \times 1^{(3)}$, $4^{(2)} \times 1^{(3)}$, $6^{(2)} \times 1^{(3)}$, $m^{(2)} \times 1^{(3)}$, $2^{(2)} \cdot m \times 1^{(3)}$, $2 \cdot m^{(2)} \times 1^{(3)}$, $3 \cdot m^{(2)} \times 1^{(3)}$, $4^{(2)} \cdot m \times 1^{(3)}$, $4 \cdot m^{(2)} \times 1^{(3)}$, $6^{(2)} \cdot m \times 1^{(3)}$, $6 \cdot m^{(2)} \times 1^{(3)}$), 4 2-intermediate ($3^{(3)} \times 1^{(2)}$, $3^{(-3)} \times 1^{(2)}$, $6^{(3)} \times 1^{(2)}$, $6^{(-3)} \times 1^{(2)}$).

$G_{20}^{2'}$: 6 junior ($2^{(2} \cdot m^{\prime)}$, $2^{\prime)} \cdot m^{(2}$, $4^{(2} \cdot m^{\prime)}$, $4^{\prime)} \cdot m^{(2}$, $6^{(2} \cdot m^{\prime)}$, $6^{\prime)} \cdot m^{(2)}$), 10 senior ($1 \times 1^{(2} \cdot 1^{\prime)}$, $2 \times 1^{(2} \cdot 1^{\prime)}$, $3 \times 1^{(2} \cdot 1^{\prime)}$, $4 \times 1^{(2} \cdot 1^{\prime)}$, $6 \times 1^{(2} \cdot 1^{\prime)}$, $m \times 1^{(2} \cdot 1^{\prime)}$, $2 \cdot m \times 1^{(2} \cdot 1^{\prime)}$, $3 \cdot m \times 1^{(2} \cdot 1^{\prime)}$, $4 \cdot m \times 1^{(2} \cdot 1^{\prime)}$, $6 \cdot m \times 1^{(2} \cdot 1^{\prime)}$), 11 (1')-intermediate ($2^{(2} \cdot 1^{\prime)}$, $4^{(2} \cdot 1^{\prime)}$, $6^{(2} \cdot 1^{\prime)}$, $m^{(2} \cdot 1^{\prime)}$, $2^{(2} \cdot m \cdot 1^{\prime)}$, $2 \cdot m^{(2} \cdot 1^{\prime)}$, $3 \cdot m^{(2} \cdot 1^{\prime)}$, $4^{(2} \cdot m \cdot 1^{\prime)}$, $4 \cdot m^{(2} \cdot 1^{\prime)}$, $6^{(2} \cdot m \cdot 1^{\prime)}$, $6 \cdot m^{(2} \cdot 1^{\prime)}$), 11 2-intermediate ($2^{\prime)} \times 1^{(2}$, $4^{\prime)} \times 1^{(2}$, $6^{\prime)} \times 1^{(2}$, $m^{\prime)} \times 1^{(2}$, $2^{\prime)} \cdot m \times 1^{(2}$, $2 \cdot m^{\prime)} \times 1^{(2}$, $3 \cdot m^{\prime)} \times 1^{(2}$, $4^{\prime)} \cdot m \times 1^{(2}$, $4 \cdot m^{\prime)} \times 1^{(2}$, $6^{\prime)} \cdot m \times 1^{(2}$, $6 \cdot m^{\prime)} \times 1^{(2)}$).

$G_{20}^{3'}$: 4 junior ($3^{(3} \cdot m^{\prime)}$, $3^{(-3} \cdot m^{\prime)}$, $6^{(3} \cdot m^{\prime)}$, $6^{(-3} \cdot m^{\prime)}$), 10 senior ($1 \times 1^{(3} \cdot 1^{\prime)}$, $2 \times 1^{(3} \cdot 1^{\prime)}$, $3 \times 1^{(3} \cdot 1^{\prime)}$, $4 \times 1^{(3} \cdot 1^{\prime)}$, $6 \times 1^{(3} \cdot 1^{\prime)}$, $m \times 1^{(3} \cdot 1^{\prime)}$, $2 \cdot m \times 1^{(3} \cdot 1^{\prime)}$, $3 \cdot m \times 1^{(3} \cdot 1^{\prime)}$, $4 \cdot m \times 1^{(3} \cdot 1^{\prime)}$, $6 \cdot m \times 1^{(3} \cdot 1^{\prime)}$), 11 3-intermediate ($2^{\prime)} \cdot 1^{(3)}$, $4^{\prime)} \cdot 1^{(3)}$, $6^{\prime)} \cdot 1^{(3)}$, $m^{\prime)} \cdot 1^{(3}$, $2^{\prime)} \cdot m \cdot 1^{(3}$, $2 \cdot m^{\prime)} \cdot 1^{(3}$, $3 \cdot m^{\prime)} \cdot 1^{(3}$, $4^{\prime)} \cdot m \cdot 1^{(3}$, $4 \cdot m^{\prime)} \cdot 1^{(3}$, $6^{\prime)} \cdot m \cdot 1^{(3}$, $6 \cdot m^{\prime)} \cdot 1^{(3)}$).

$G_{20}^{4'}$: 2 junior ($4^{(4} \cdot m^{\prime)}$, $4^{(-4} \cdot m^{\prime)}$), 10 senior ($1 \times 1^{(4} \cdot 1^{\prime)}$, $2 \times 1^{(4} \cdot 1^{\prime)}$, $3 \times 1^{(4} \cdot 1^{\prime)}$, $4 \times 1^{(4} \cdot 1^{\prime)}$, $6 \times 1^{(4} \cdot 1^{\prime)}$, $m \times 1^{(4} \cdot 1^{\prime)}$, $2 \cdot m \times 1^{(4} \cdot 1^{\prime)}$, $3 \cdot m \times 1^{(4} \cdot 1^{\prime)}$, $4 \cdot m \times 1^{(4} \cdot 1^{\prime)}$, $6 \cdot m \times 1^{(4} \cdot 1^{\prime)}$), 11 (2')-intermediate ($2^{(4} \cdot 1^{\prime)}$, $4^{(4} \cdot 1^{(2} \cdot 1^{\prime)}$, $6^{(4} \cdot 1^{\prime)}$, $m^{(4} \cdot 1^{\prime)}$, $2^{(4} \cdot m \cdot 1^{\prime)}$, $2 \cdot m^{(4} \cdot 1^{\prime)}$, $3 \cdot m^{(4} \cdot 1^{\prime)}$, $4^{(4} \cdot m \cdot 1^{\prime)}$, $4 \cdot m^{(4} \cdot 1^{\prime)}$, $6^{(4} \cdot m \cdot 1^{\prime)}$, $6 \cdot m^{(4} \cdot 1^{\prime)}$), 11 4-intermediate ($2^{\prime)} \cdot 1^{(4}$, $4^{\prime)} \cdot 1^{(4}$, $6^{\prime)} \cdot 1^{(4}$, $m^{\prime)} \cdot 1^{(4}$, $2^{\prime)} \cdot m \cdot 1^{(4}$, $2 \cdot m^{\prime)} \cdot 1^{(4}$, $3 \cdot m^{\prime)} \cdot 1^{(4}$, $4^{\prime)} \cdot m \cdot 1^{(4}$, $4 \cdot m^{\prime)} \cdot 1^{(4}$, $6^{\prime)} \cdot m \cdot 1^{(4}$, $6 \cdot m^{\prime)} \cdot 1^{(4)}$), 6 2-intermediate ($2^{(4} \cdot m^{\prime)}$, $2^{\prime)} \cdot m^{(4}$, $4^{(4} \cdot m^{\prime)} \cdot 1^{(2}$, $4^{\prime)} \cdot m^{(4}$, $6^{(4} \cdot m^{\prime)}$, $6^{\prime)} \cdot m^{(4)}$).

$G_{20}^{6'}$: 2 junior ($6^{(6} \cdot m^{\prime)}$, $6^{(-6} \cdot m^{\prime)}$), 10 senior ($1 \times 1^{(6} \cdot 1^{\prime)}$, $2 \times 1^{(6} \cdot 1^{\prime)}$, $3 \times 1^{(6} \cdot 1^{\prime)}$, $4 \times 1^{(6} \cdot 1^{\prime)}$, $6 \times 1^{(6} \cdot 1^{\prime)}$, $m \times 1^{(6} \cdot 1^{\prime)}$, $2 \cdot m \times 1^{(6} \cdot 1^{\prime)}$, $3 \cdot m \times 1^{(6} \cdot 1^{\prime)}$, $4 \cdot m \times 1^{(6} \cdot 1^{\prime)}$, $6 \cdot m \cdot 1^{(6} \cdot 1^{\prime)}$), 11 (3')-intermediate ($2^{(2} \times 1^{(3} \cdot 1^{\prime)}$, $4^{(2} \times 1^{(3} \cdot 1^{\prime)}$, $6^{(2} \times 1^{(3} \cdot 1^{\prime)}$, $m^{(2} \times 1^{(3} \cdot 1^{\prime)}$, $2^{(2} \cdot m \times 1^{(3} \cdot 1^{\prime)}$, $2 \cdot m^{(2} \times 1^{(3} \cdot 1^{\prime)}$, $3 \cdot m^{(2} \times 1^{(3} \cdot 1^{\prime)}$, $4^{(2} \cdot m \times 1^{(3} \cdot 1^{\prime)}$, $4 \cdot m^{(2} \times 1^{(3} \cdot 1^{\prime)}$, $6^{(2} \cdot m \times 1^{(3} \cdot 1^{\prime)}$, $6 \cdot m^{(2} \times 1^{(3} \cdot 1^{\prime)}$), 11 6-intermediate ($2^{\prime)} \cdot 1^{(6}$, $4^{\prime)} \cdot 1^{(6}$, $6^{\prime)} \cdot 1^{(6}$, $m^{\prime)} \cdot 1^{(6}$, $2^{\prime)} \cdot m \cdot 1^{(6}$, $2 \cdot m^{\prime)} \cdot 1^{(6}$, $3 \cdot m \cdot 1^{(6}$, $4^{\prime)} \cdot m \cdot 1^{(6}$, $4 \cdot m^{\prime)} \cdot 1^{(6}$, $6^{\prime)} \cdot m \cdot 1^{(6}$, $6 \cdot m^{\prime)} \cdot 1^{(6)}$), 6 3-intermediate ($2^{(2} \cdot m^{\prime)} \cdot 1^{(3}$, $2^{\prime)} \cdot m^{(2} \cdot 1^{(3}$, $4^{(2} \cdot m^{\prime)} \cdot 1^{(3}$, $4^{\prime)} \cdot m^{(2} \cdot 1^{(3}$, $6^{(2} \cdot m^{\prime)} \cdot 1^{(3}$, $6^{\prime)} \cdot m^{(2} \cdot 1^{(3)}$), 4 2-intermediate ($3^{(3} \cdot m^{\prime)} \times 1^{(2}$, $3^{(-3} \cdot m^{\prime)} \times 1^{(2}$, $6^{(3} \cdot m^{\prime)} \times 1^{(2}$, $6^{(-3} \cdot m^{\prime)} \times 1^{(2)}$).

Note that the rosette symmetry groups G_{20} can be interpreted both as three- and four-dimensional symmetry groups [6].

3. Consider the category G_{420}. In addition to a point, the groups of symmetry transformations preserve two mutually orthogonal planes intersecting at the singular point indicated above. Let us check the number of point groups of the category G_{40} that the category G_{420} includes. It is clear that the above mutually orthogonal planes play different geometrical parts in the groups of the category G_{420}. However, they play the same part in the groups of the category G_{40}. Hence, the lists of the groups G_{20}, G_{20}^{1}, G_{20}^{p}, and $G_{20}^{p'}$ at $p = 2, 3, 4, 6$, which interpret the category G_{420}, contain numerous equivalent groups (connected to them by a tilde) under the assumption that they interpret the category G_{40}. For example, $2 \sim 1^{(2)} \sim m'$, $3 \sim 1^{(3)}$, $6 \sim 1^{(6)}$, $2 \times 1^{(3)} \sim 3 \times 1^{(2)}$ etc., and $2^{(4)} \sim 4^{(2)}$, $2^{(2)} \times 1^{(3)} = 2^{(6)} \sim 6^{(2)}$, $3^{(-3)} \times 1^{(2)} = 3^{(6)} \sim 6^{(3)}$, $3^{(3)} \times 1^{(2)} \sim 6^{(-3)}$, $4^{(2)} \times 1^{(3)} \sim 6^{(4)}$, $2 \cdot m^{\prime)} \sim m^{\prime)} \times 1^{(2}$, $3 \cdot m' \sim m^{\prime)} \cdot 1^{(3}$, $4 \cdot m' \sim m^{\prime)} \cdot 1^{(4}$, $6 \cdot m^{\prime)} \sim m^{\prime)} \cdot 1^{(6}$, $2 \times 1^{(2} \cdot 1^{\prime)} \sim 2 \cdot m \times 1^{(2)}$, $3 \cdot m^{(2} \cdot 1^{\prime)} \sim 2^{\prime)} \cdot m \times 1^{(3}$, $3 \cdot m \times 1^{(2)} \sim 2 \times 1^{(3} \cdot 1^{\prime)}$, $6^{(2} \cdot 1^{\prime)} \sim 2^{(2)} \cdot m \times 1^{(3)}$, etc.

As a result, we obtain that there are $152 G_{40}$ groups among $263 G_{420}$ groups. In particular, the groups from $263 G_{420}$ groups interpreting $152 G_{40}$ are the following: 1, 2, 3, 4, 6, m, $2 \cdot m$, $3 \cdot m$, $4 \cdot m$, $6 \cdot m$; 2', 4', 6', $2' \cdot m$, $2 \cdot m'$, $3 \cdot m'$, $4' \cdot m$, $4 \cdot m'$, $6' \cdot m$, $6 \cdot m'$; $3 \times 1'$, $4 \times 1'$, $6 \times 1'$, $2 \cdot m \times 1'$, $3 \cdot m \times 1'$, $4 \cdot m \times 1'$, $6 \cdot m \times 1'$; $2^{(2)}$, $4^{(2)}$, $6^{(2)}$, $2^{(2)} \cdot m$, $2 \cdot m^{(2)}$, $3 \cdot m^{(2)}$, $4^{(2)} \cdot m$, $4 \cdot m^{(2)}$, $6^{(2)} \cdot m$, $6 \cdot m^{(2)}$; $2 \times 1^{(2)}$, $3 \times 1^{(2)}$, $4 \times 1^{(2)}$, $6 \times 1^{(2)}$, $2 \cdot m \times 1^{(2)}$, $3 \cdot m \times 1^{(2)}$, $4 \cdot m \times 1^{(2)}$, $6 \cdot m \times 1^{(2)}$; $2^{(2} \cdot m^{\prime)}$, $2^{\prime)} \cdot m^{(2}$, $4^{(2} \cdot m^{\prime)}$, $4^{\prime)} \cdot m^{(2}$, $6^{(2} \cdot m^{\prime)}$, $6^{\prime)} \cdot m^{(2}$; $3 \times 1^{(2} \cdot 1^{\prime)}$, $4 \times 1^{(2} \cdot 1^{\prime)}$,

---

[1] Enantiomorphism of the two-dimensional point groups G_{20}^{p} and $G_{20}^{p'}$ corresponds to that of four-dimensional groups G_{420}.

$6 \times 1^{(2} \cdot 1^{\prime)}, 2 \cdot m \times 1^{(2} \cdot 1^{\prime)}, 3 \cdot m \times 1^{(2} \cdot 1^{\prime)}, 4 \cdot m \times 1^{(2} \cdot 1^{\prime)}, 6 \cdot m \times 1^{(2} \cdot 1^{\prime)}$; $4^{(2} \cdot 1^{\prime)}, 6^{(2} \cdot 1^{\prime)}, 2^{(2} \cdot m \cdot 1^{\prime)}, 2 \cdot m^{(2} \cdot 1^{\prime)}, 3 \cdot m^{(2} \cdot 1^{\prime)}, 4^{(2} \cdot m \cdot 1^{\prime)}, 4 \cdot m^{(2} \cdot 1^{\prime)}, 6^{(2} \cdot m \cdot 1^{\prime)}, 6 \cdot m^{(2} \cdot 1^{\prime)}$; $4^{\prime)} \times 1^{(2}, 6^{\prime)} \times 1^{(2}, 2 \cdot m^{\prime)} \times 1^{(2}, 3 \cdot m^{\prime)} \times 1^{(2}, 4^{\prime)} \cdot m \times 1^{(2}, 4 \cdot m^{\prime)} \times 1^{(2}, 6^{\prime)} \cdot m \times 1^{(2}, 6 \cdot m' \times 1^{(2}$; $3^{(3)}, 3^{(-3)}, 6^{(3)}, 6^{(-3)}$; $3 \times 1^{(3)}, 4 \times 1^{(3)}, 6 \times 1^{(3)}, 3 \cdot m \times 1^{(3)}, 4 \cdot m \times 1^{(3)}, 6 \cdot m \times 1^{(3)}$; $4^{(4)}, 4^{(-4)}$; $4 \times 1^{(4),}\ 6 \times 1^{(4)}, 3 \cdot m \times 1^{(4)}, 4 \cdot m \times 1^{(4)}, 6 \cdot m \times 1^{(4)}$; $4^{(4)} \times 1^{(2)}$; $6^{(4)}, 3 \cdot m^{(4)}, 4^{(4)} \cdot m, 4 \cdot m^{(4)}, 6^{(4)} \cdot m, 6 \cdot m^{(4)}$; $6^{(6)}, 6^{(-6)}$; $6 \times 1^{(6)}, 3 \cdot m \times 1^{(6)}, 4 \cdot m \times 1^{(6)}, 6 \cdot m \times 1^{(6)}$; $6^{(2)} \times 1^{(3)}, 3 \cdot m^{(2)} \times 1^{(3)}, 4^{(2)} \cdot m \times 1^{(3)}, 4 \cdot m^{(2)} \times 1^{(3)}, 6^{(2)} \cdot m \times 1^{(3)}, 6 \cdot m^{(2)} \times 1^{(3)}$; $6^{(3)} \times 1^{(2)}, 6^{(-3)} \times 1^{(2)}, 3^{(3} \cdot m^{\prime)}, 3^{(-3)} \cdot m^{\prime)}, 6^{(3} \cdot m^{\prime)}, 6^{(-3} \cdot m^{\prime)}$; $3 \cdot m \times 1^{(3} \cdot 1^{\prime)}, 4 \cdot m \times 1^{(3} \cdot 1^{\prime)}, 6 \cdot m \times 1^{(3} \cdot 1^{\prime)}$; $3 \cdot m^{\prime)} \cdot 1^{(3}, 4^{\prime)} \cdot m \cdot 1^{(3}, 4 \cdot m^{\prime)} \cdot 1^{(3}, 6^{\prime)} \cdot m \cdot 1^{(3}, 6 \cdot m^{\prime)} \cdot 1^{(3}$; $4^{(4} \cdot m^{\prime)}, 4^{(-4} \cdot m^{\prime)}$; $4 \cdot m \times 1^{(4} \cdot 1^{\prime)}, 6 \cdot m \times 1^{(4} \cdot 1^{\prime)}$; $4^{(4} \cdot 1^{(2} \cdot 1^{\prime)}, 4^{(4} \cdot m \cdot 1^{\prime)}, 4 \cdot m^{(4} \cdot 1^{\prime)}, 6^{(4} \cdot m \cdot 1^{\prime)}, 6 \cdot m^{(4} \cdot 1^{\prime)}$; $4 \cdot m^{\prime)} \cdot 1^{(4}, 6^{\prime)} \cdot m \cdot 1^{(4}, 6 \cdot m^{\prime)} \cdot 1^{(4}$; $4^{(4} \cdot m^{\prime)} \cdot 1^{(2}, 4^{\prime)} \cdot m^{(4}, 6^{(4} \cdot m^{\prime)}, 6^{\prime)} \cdot m^{(4}$; $6^{(6} \cdot m^{\prime)}, 6^{(-6} \cdot m^{\prime)}$; $6 \cdot m \times 1^{(6} \cdot 1^{\prime)}$; $6^{(2} \times 1^{(3} \cdot 1^{\prime)}, 6^{(2} \cdot m \times 1^{(3} \cdot 1^{\prime)}, 6 \cdot m^{2)} \times 1^{(3} \cdot 1^{\prime)}$; $6 \cdot m^{\prime)} \cdot 1^{(6}$; $6^{(2} \cdot m^{\prime)} \cdot 1^{(3}, 6^{\prime)} \cdot m^{(2} \cdot 1^{(3}$; $6^{(3} \cdot m^{\prime)} \times 1^{(2}, 6^{(-3} \cdot m^{\prime)} \times 1^{(2}$.

One can readily see that there are only 42 non-isomorphic groups among 152 groups of the category G_{40}. For example, such groups are: 1–4, 6, $2 \cdot m, 3 \cdot m, 4 \cdot m, 6 \cdot m$; $4 \times 1', 6 \times 1', 2 \cdot m \times 1', 4 \cdot m \times 1', 6 \cdot m \times 1'$; $4 \times 1^{(2} \cdot 1^{\prime)}, 6 \times 1^{(2} \cdot 1^{\prime)}, 2 \cdot m \times 1^{(2} \cdot 1^{\prime)}, 4 \cdot m \times 1^{(2} \cdot 1^{\prime)}, 6 \cdot m \times 1^{(2} \cdot 1^{\prime)}$; $3 \times 1^{(3)}, 4 \times 1^{(3)}, 6 \times 1^{(3)}, 3 \cdot m \times 1^{(3)}, 4 \cdot m \times 1^{(3)}, 6 \cdot m \times 1^{(3)}$; $4 \times 1^{(4)}, 6 \times 1^{(4)}, 3 \cdot m \times 1^{(4)}, 4 \cdot m \times 1^{(4)}, 6 \cdot m \times 1^{(4)}$; $6^{(4)} \cdot m, 6 \cdot m^{(4)}$; $6 \times 1^{(6)}, 3 \cdot m \times 1^{(6)}, 4 \cdot m \times 1^{(6)}, 6 \cdot m \times 1^{(6)}$; $3 \cdot m \times 1^{(3} \cdot 1^{\prime)}, 4 \cdot m \times 1^{(3} \cdot 1^{\prime)}, 6 \cdot m \times 1^{(3} \cdot 1^{\prime)}$; $4 \cdot m \times 1^{(4} \cdot 1^{\prime)}, 6 \cdot m \times 1^{(4} \cdot 1^{\prime)}, 6 \cdot m \times 1^{(6} \cdot 1^{\prime)}$.

The matrix representation of 32 crystallographic classes given in [7] can be readily extended to the four-dimensional crystallographic classes obtained in this study. For example, in terms of the orthogonal four-dimensional matrices, the groups $2^{(4)}$, $6^{(6} \cdot m^{\prime)}$, $4^{(2} \cdot m \times 1^{(3} \cdot 1^{\prime)}$ can be written as follows:

$$\left\{\begin{pmatrix} -1 & 0 & 0 & 0 \\ 0 & -1 & 0 & 0 \\ 0 & 0 & -1 & 0 \\ 0 & 0 & 1 & 0 \end{pmatrix}\right\},$$

$$\left\{\begin{pmatrix} 1/2 & -\sqrt{3}/2 & 0 & 0 \\ \sqrt{3}/2 & 1/2 & 0 & 0 \\ 0 & 0 & 1/2 & -\sqrt{3}/2 \\ 0 & 0 & \sqrt{3}/2 & 1/2 \end{pmatrix}, \begin{pmatrix} -1 & 0 & 0 & 0 \\ 0 & 1 & 0 & 0 \\ 0 & 0 & 1 & 0 \\ 0 & 0 & 0 & -1 \end{pmatrix}\right\},$$

$$\left\{\begin{pmatrix} 0 & -1 & 0 & 0 \\ 1 & 0 & 0 & 0 \\ 0 & 0 & -1 & 0 \\ 0 & 0 & 0 & -1 \end{pmatrix}, \begin{pmatrix} -1 & 0 & 0 & 0 \\ 0 & 1 & 0 & 0 \\ 0 & 0 & 1 & 0 \\ 0 & 0 & 0 & -1 \end{pmatrix},\right.$$

$$\left.\begin{pmatrix} 1 & 0 & 0 & 0 \\ 0 & 1 & 0 & 0 \\ 0 & 0 & -1/2 & -\sqrt{3}/2 \\ 0 & 0 & \sqrt{3}/2 & -1/2 \end{pmatrix}, \begin{pmatrix} 1 & 0 & 0 & 0 \\ 0 & 1 & 0 & 0 \\ 0 & 0 & 1 & 0 \\ 0 & 0 & 0 & -1 \end{pmatrix}\right\}.$$

4. Now, let us determine how many different G_{40} groups are interpreted by 125 symmetry groups of the category G_{4320}.

According to [2] (section 1, ch. IV), 125 groups of the category G_{4320} are interpreted by the symmetry and the antisymmetry groups of tablets G_{320}^{1} or by 125 groups of twofold rosette antisymmetry G_{20}^{2} described in detail in Table 11 [8]. To answer the question raised above, it is sufficient to write the G_{20}^{2} groups as the groups of (2')-symmetry (complete and incomplete, degenerating into (1')- and 2-symmetries) and to leave only one group of each set of the coinciding groups in the list thus obtained as the G_{40} groups.

All $125 G_{20}^{2}$ in the form of G_{20}, G_{20}^{1}, G_{20}^{2}, and $G_{20}^{2'}$ (complete *P*-symmetries) were written in section 2. Therefore, if all the G_{20}^{p} and $G_{20}^{p'}$ (at $p = 3, 4, 6$) groups from the list of $152 G_{420}$ groups interpreting different G_{40} are rejected, then the first 75 remaining groups will model different G_{40} included in the category G_{4320}. It is explained by the fact that the above-mentioned 152 G_{420} groups, which are different when modeling G_{40}, are singled out from the list of 263 G_{20}^{P} groups arranged in the sequence G_{20}, G_{20}^{1}, G_{20}^{2}, $G_{20}^{2'}$, G_{20}^{p}, and $G_{20}^{p'}$ (at $p = 3, 4, 6$) by removing from each group all the subsequent groups coinciding with it when modeling G_{40}.

Taking into account all the above arguments, it is easy to determine the number of four-dimensional point symmetry groups in the category G_{430} that are interpreted by 122 Shubnikov antisymmetry classes G_{30}^{1} [7, 8]. Indeed, all 16 G_{30}^{1} groups of cubic system model 16 different groups of the category G_{40}. The remaining 122 – 16 = 106 three-dimensional point groups of symmetry and antisymmetry correspond to tablet groups G_{320}^{1}. However, as has been pointed out, among $125 G_{320}^{1}$, there are only 75 groups as different as G_{40}. Hence, the category G_{430} includes altogether 75 + 16 = 91 different G_{40} groups.

5. Finally, let us determine the number of groups as different as G_{40} among $67G_{43210}$. According to [2], all the groups of the category G_{43210} are modeled by symmetry and antisymmetry groups of finite ribbons G^1_{3210}, or by symmetry and twofold antisymmetry groups of finite borders G^2_{210}, or by symmetry and threefold antisymmetry groups of segments G^3_{10}, or, finally, by symmetry and fourfold antisymmetry groups of asymmetric dot G^4_0 (these groups are listed in Table 12 [8]). The easiest way of solving our problem is to write all the fourfold antisymmetry groups of zero-dimensional space G^4_0 and to retain in the list obtained only the groups that interpret different G_{40}. Being fully classified (according to sections 1 and 2, ch. 2 [8]), all the G^4_0 groups are exhausted by the generating group and all kinds of the senior groups of certain species: G; C_1, C_2, C_3, C_4, C_{12}, C_{13}, C_{14}, C_{23}, C_{24}, C_{34}, C_{123}, C_{124}, C_{134}, C_{234}, C_{1234}; C_1C_2, C_1C_3, C_1C_4, C_1C_{23}, C_1C_{24}, C_1C_{34}, C_1C_{234}, C_2C_3, C_2C_4, C_2C_{13}, C_2C_{14}, C_2C_{34}, C_2C_{134}, C_3C_4, C_3C_{12}, C_3C_{14}, C_3C_{24}, C_3C_{124}, C_4C_{12}, C_4C_{13}, C_4C_{23}, C_4C_{123}, $C_{12}C_{13}$, $C_{12}C_{14}$, $C_{12}C_{34}$, $C_{12}C_{134}$, $C_{13}C_{14}$, $C_{13}C_{24}$, $C_{13}C_{124}$, $C_{14}C_{23}$, $C_{14}C_{123}$, $C_{23}C_{24}$, $C_{23}C_{124}$, $C_{24}C_{123}$, $C_{34}C_{123}$; $C_1C_2C_3$, $C_1C_2C_4$, $C_1C_2C_{34}$, $C_1C_3C_4$, $C_1C_3C_{24}$, $C_1C_4C_{23}$, $C_1C_{23}C_{24}$, $C_2C_3C_4$, $C_2C_3C_{14}$, $C_2C_4C_{13}$, $C_2C_{13}C_{14}$, $C_3C_4C_{12}$, $C_3C_{12}C_{14}$, $C_4C_{12}C_{13}$, $C_{12}C_{13}C_{14}$; $C_1C_2C_3C_4$ (altogether 67 groups).

According to Mackay [9], among the listed 67 zero-dimensional groups of four-fold antisymmetry, there are only 16 different groups: G; C_i, C_{ij}, C_{ijk}, C_{1234}; C_iC_j, C_iC_{jk}, C_iC_{jkl}, $C_{ij}C_{ik}$, $C_{ij}C_{kl}$, $C_{ij}C_{ikl}$; $C_iC_jC_k$, $C_iC_jC_{kl}$, $C_iC_{jk}C_{jl}$, $C_{ij}C_{ik}C_{il}$; $C_1C_2C_3C_4$. Of these groups only 5 groups are not isomorphic: G, C, C_2, C_3, and C_4, i.e., the generating and four senior of l independent species at $l = 1, 2, 3$, and 4 [8].

It is not difficult to prove that 16 G^4_0 groups singled out are also as different as G_{40}. With this aim, one has to write their matrix representation. Thus, among 67 groups of the category G_{43210} only 16 groups are different as of G_{40}, and only 5 of these 16 groups are nonisomorphic.

6. Using the planar point symmetry groups studied, one can consider some geometrical features of the four-dimensional crystallographic classes of G_{40}. Consider again the sets G_{430} and G_{420}. Now, assume that their elements are only groups as different as G_{40}. Let us introduce two more new elements, the junction $G_{430} \cup G_{420}$ and the intersection $G_{430} \cap G_{420}$. Further, we denote the capacity of these sets by the symbols $m|G_{430}|$, $m|G_{420}|$ etc. Since the category (G_{4320}) coincides with the intersection of the categories (G_{430}) and (G_{420}), one has $m|G_{430} \cap G_{420}| = m|G_{4320}|$. However, as is well-known, $m|G_{430} \cup G_{420}| = m|G_{430}| + m|G_{420}| - m|G_{4320}|$. Hence, $m|G_{430} \cup G_{420}| = 91 + 152 - 75 = 168$.

As a result, we obtain that among $271G_{40}$ groups, 168 groups preserve not only a point but also other geometrical objects. The remaining 271 – 168 = 103 groups preserve only a point.

Thus, knowing the number of groups different as G_{40} and contained in the point symmetry groups of the categories G_{420}, G_{430}, and G_{4320}, we established (without use of the catalogue of four-dimensional crystallographic classes) that 168 classes preserve not only zero-dimensional but also other nontrivial subspaces in the four-dimensional Eucledian space.

7. The results obtained in this paper can schematically be represented as follows:

$$\begin{tikzcd}
 & 122(91)G_{430} \arrow[dr] & \\
271G_{40} \arrow[ur] \arrow[dr] & & 125(75)G_{4320} \\
 & 263(152)G_{420} \arrow[ur] &
\end{tikzcd}$$

$$\longrightarrow 67(16)G_{43210},$$

where the coefficients not enclosed into parentheses and those in the parent theses before the category symbol denote the number of groups and the number of groups different as four-dimensional crystallographic classes contained by this category, respectively. The symbol $\longrightarrow$ indicates that the subsequent category is included into the previous one (cf. with Fig. 15 [2]).

REFERENCES

1. H. Broun, R. Bulow, J. Neubuser, H. Wondratschek, and H. Zassenhaus, *Crystallographic Groups of Four-Dimensional Space* (Wiley, New York, 1978).
2. A. M. Zamorzaev, É. I. Galyarskiĭ, and A. F. Palistrant, *Color Symmetry, Its Generalizations and Applications* (Shtiintsa, Kishinev, 1978).
3. A. F. Palistrant, Dokl. Akad. Nauk SSSR **254** (5), 1126 (1980) [Sov. Phys. Dokl. **25**, 797 (1980)].
4. A. M. Zamorzaev and A. F. Palistrant, Z. Kristallogr. **151** (3–4), 231 (1980).
5. A. M. Zamorzaev, Izv. Akad. Nauk Resp. Mold., Mat. **1**, 75 (1994).
6. A. V. Shubnikov, Kristallografiya **7** (4), 490 (1962) [Sov. Phys. Crystallogr. **7**, 394 (1962)].
7. V. A. Koptsik, *Shubnikov Groups* (Izd. Mosk. Gos. Univ., Moscow, 1966).
8. A. M. Zamorzaev, *Theory of Simple and Multiple Antisymmetry* (Shtiintsa, Kishinev, 1976).
9. A. M. Zamorzaev and A. F. Palistrant, *Studies on Discrete Geometry* (Shtiintsa, Kishinev, 1974).

Translated by A. Darinskiĭ

Crystallography Reports, Vol. 45, No. 4, 2000, pp. 541–544. Translated from Kristallografiya, Vol. 45, No. 4, 2000, pp. 596–599.
Original Russian Text Copyright © 2000 by Treushnikov.

DIFFRACTION AND SCATTERING OF X-RAYS AND SYNCHROTRON RADIATION

X-ray Diffraction from Ideal Mosaic Crystals in External Fields of Certain Types, Part II: Changes in the Temperature Factor and Diffraction Pattern[1]

E. N. Treushnikov
Moscow State Academy of Geological Prospecting, Moscow, Russia

Received July 8, 1998

Abstract—The changes in the X-ray temperature factor of a single crystal in external fields of running electromagnetic and acoustic waves has been analyzed. The evaluation of these changes shows the importance of a thorough choice of crystals and experimental conditions for recording the variations in the structure factors (intensities). The relationships derived allow one to predict the type of a diffraction pattern formed in a field of a standing wave applied to the crystal. The position, shape, and the height of the main and auxiliary peaks are analyzed as functions of the applied-field parameters. *© 2000 MAIK “Nauka/Interperiodica”.*

VARIATION OF TEMPERATURE FACTOR AS FUNCTION OF A HARMONIC FIELD APPLIED TO A CRYSTAL

The variation of a temperature factor in a crystal can be estimated using the expression for the isotropic temperature factor

$$T\left(\frac{\sin\theta}{\lambda}\right) = \exp\left(-8\pi^2\langle u^2\rangle\frac{\sin^2\theta}{\lambda^2}\right), \quad (1)$$

where $\langle u^2\rangle^{1/2}$ is the root-mean square deviation of structure atoms averaged over all the vibration directions and time, θ is the diffraction angle, and λ is the wavelength. It is assumed that the displacements of all the atoms in the crystal are equal. This approximation is sufficient for the estimates which will he made below.

Denote the instantaneous displacement of an atom caused by thermal vibrations in the absence of any external factor by $\mathbf{u}_T$, and the displacement of this atom, caused by an applied harmonic field of frequency ω_1, by $\mathbf{u}(\omega_1)$. Then the resulting displacement is $\mathbf{u}_1(\omega_1) = \mathbf{u}_T + \mathbf{u}(\omega_1)$, and, therefore, $\langle u_1^2(\omega_1)\rangle = \langle u_T^2\rangle + \langle u^2(\omega_1)\rangle$ (because all the cross products become zeroes upon averaging the harmonic terms over time). It is natural to assume that formula (1) would also be valid for a crystal in various electromagnetic and acoustic fields, therefore

$$T_1\left(\frac{\sin\theta}{\lambda}\right) = T\left(\frac{\sin\theta}{\lambda}\right)\exp\left(-8\pi^2\langle u^2(\omega_1)\rangle\frac{\sin^2\theta}{\lambda^2}\right), \quad (2)$$

where $T(\sin\theta/\lambda)$ is the temperature factor recorded in traditional X-ray studies (without external fields). Thus, the determination of the temperature-factor variations reduces to evaluation of $\langle u^2(\omega_1)\rangle$.

The case of a running wave $\mathbf{A}^{\mathrm{ext}} = \mathbf{A}_0^{\mathrm{ext}}\cos(\boldsymbol{\omega}_1 t - \boldsymbol{k}_1 \boldsymbol{x})$. Consider first an electromagnetic field, i.e., substitute $\mathbf{A}^{\mathrm{ext}}$ and $\mathbf{A}_0^{\mathrm{ext}}$ by $\mathbf{E}^{\mathrm{ext}}$ and $\mathbf{E}_0^{\mathrm{ext}}$, and evaluate $\langle u^2(\omega_1)\rangle$ for a linear dielectric and the refractive index $n(\omega_1)$ as a macroscopic parameter characterizing its properties. Then the polarizability is written as $\mathbf{P} = [n^2(\omega_1) - 1]\varepsilon_0\mathbf{E}$, where ε_0 is the dielectric constant, and $\mathbf{E}$ is the macroscopic field in the material. It is expedient to pass from the field $\mathbf{E}$ to $\mathbf{E}^{\mathrm{ext}}$. In accordance with the Fresnel formulas for a polarized wave incident onto the crystal at a small angle, we have $E_0 = [2/(n + 1)]E_0^{\mathrm{ext}}$, where E_0 is the amplitude of the wave E. Then

$$\mathbf{P} = 2\varepsilon_0[n(\omega_1) - 1]\mathbf{E}^{\mathrm{ext}}. \quad (3)$$

The total polarizability $\mathbf{P}$ under the effect of an external field is provided by the displacements of ions, $\mathbf{u}$, from different sublattices of the crystal with respect to one another (the photon polarization) and the displacements of electrons with respect to nuclei (the electron polarization). Thus, for optical phonons, we can write $\mathbf{P}_{\mathrm{ph}}(\omega_1) = NQ^*\mathbf{u}(\omega_1)$ where N is the number of atoms per unit volume and Q^* is the effective charge ([2], p. 198). Thus, we have

$$\langle u^2(\omega_1)\rangle^{1/2} = \frac{2\varepsilon_0}{NQ^*}[n(\omega_1) - 1]E_0^{\mathrm{ext}}. \quad (4)$$

It was assumed that the longitudinal and the transverse particle displacements in an elastic wave caused by the effect of an electromagnetic field are approximately equal.

---

[1] For Part I see [1].

A similar expression can also be written for the electron component, because $\mathbf{P}_e(\omega_1) = Nq_e\mathbf{u}_e(\omega_1)$ (where q_e is the atomic charge and $\mathbf{u}_e(\omega_1)$ is the displacement of electrons with respect to the nucleus), moreover, in some cases, $Q^* \approx q_e$ ([2], p. 199).

Assuming that in (4) $N \approx 10^{29}$ m^{-3}, $Q^* \approx q_e = 1.6 \times 10^{-19}$ C, and $n = 3$ (the nonresonance value), we see that in order to make $\langle u^2(\omega_1)\rangle$ and $\langle u_T^2\rangle$ of the same order of magnitude (with due regard for the fact that the value $\sim 10^{-2}$ Å^2 is often encountered in X-ray studies), one has to apply the field $E_0^{\text{ext}} \sim 5 \times 10^9$ V/m. For high refractive indices, such as $n \approx 50$ (e.g., for a tetragonal modification of a $BaTiO_3$ crystal ([3], p. 190)), we obtain $E_0^{\text{ext}} \approx 2 \times 10^8$ V/m. Since the field E_0 inside the specimen is less by a factor of $n/2$ than the external field E_0^{ext}, in order to create a field $E_0 \approx 8 \times 10^6$ V/m one has to apply the potential difference $U \approx 8$ kV to the opposite faces of the crystal (at the specimen thickness $l \approx 1$ mm), which seems to be quite a reasonable value.

It should be indicated that, because of the resonance, the value of $\langle u^2(\omega_1)\rangle$ in piezoelectrics can be increased by several orders of magnitude if the frequency of an applied electric field coincides with one of the natural frequencies of the mechanical oscillations of the specimen. Thus, for a quartz in a constant field $U \approx 3$ kV, the change in the plate thickness (length) $\Delta l = dU$ is as small as $\sim 7 \times 10^{-7}$ cm (where d is the corresponding piezoelectric modulus). However, in the case of the resonance, the vibration amplitude of the quartz X-cut increases by a factor of $\rho_0 c_0/\rho c(2k - 1)\pi$ with respect to the value for the static mode ($\rho_0 c_0$ and ρc are the wave resistances of the quartz plate and the medium where the acoustic waves are emitted, respectively, k is the number of the natural-frequency harmonic of the vibrating plate). Thus, if $l = 1$ mm and the frequency is $f_1 \sim 8 \times 10^6$ Hz, the value of k is about 3. If one assumes that the ultrasonic waves are emitted into the air, the vibration amplitude increases by a factor of 2×10^3, i.e., it attains a value of $\sim 1.4 \times 10^{-3}$ cm, which corresponds to $\langle u^2(\omega_1)\rangle \approx 5 \times 10^{-3}$ Å^2 (at the lattice parameter $a \sim 5$ Å). The latter can be recorded by the X-ray diffraction method, because $\sigma\langle u^2\rangle$ often has the value of the order of $\sim(10^{-4}$–$10^{-5})$ Å^2.

Thus, the above orders of quantities $\langle u^2(\omega_1)\rangle$ indicate the necessity of rigorous allowance for various factors that can affect the diffraction patterns from crystals.

Now, consider the variation of the temperature factor (in the nonresonance case) under the effect of a planar running acoustic wave incident onto a crystal. The mean square deviation is denoted as $\langle u_a^2(\omega_1)\rangle$. Then $\mathbf{u}_a(\omega_1)$ is understood as the vibrational displacement of the particles in the medium under the effect of a sonic-wave field. We should like to estimate $\langle u_a^2(\omega_1)\rangle$ and, therefore, as earlier, use the average characteristics. In particular, the properties of the medium are characterized by the average velocity c of wave propagation in the crystal having the density ρ. Instead of the stress tensor, we use the sound pressure p. The relation between the pressure p in the medium and the external pressure p^{ext} depends on the boundary conditions [4], §137. We assume that these boundary conditions are such that $p = p^{\text{ext}}$. Under these assumptions, the real amplitude of the vibrational displacement for a plane wave is $u = p_0^{\text{ext}}/\omega_1\rho c$. Thus, the averaged squared atomic displacement is

$$\langle u_a^2(\omega_1)\rangle = \frac{2I^{\text{ext}}}{\omega_1^2\rho c}, \tag{5}$$

where $I^{\text{ext}} = (p_0^{\text{ext}})^2/2\rho c$ is the intensity of sound. When averaging the displacements, we assumed that the atomic displacements caused by longitudinal and transverse vibrations are approximately equal. Then the sought estimates of $\langle u_a^2(\omega_1)\rangle$ follow from formula (5).

Let $I^{\text{ext}} \approx 5$ W/cm^2 (this is really observed in the microwave range in a magnetostriction frequency converter), $\rho \approx 5 \times 10^3$ kg/m^3, and $c \sim 5 \times 10^3$ m/s. Then, in the range of high ultrasonic frequencies $f_1 \approx 10^8$ Hz, we have $\langle u_a^2(\omega_1)\rangle \sim 1$ Å^2; at $f_1 \approx 10^9$ Hz, we have $\langle u_a^2(\omega_1)\rangle \approx 0.01$ Å^2; and in the range of hypersound $f_1 \approx 10^{11}$ Hz, we have $\sim 10^{-6}$ Å^2. Thus, in the frequency range we are most interested in, the intensity of the diffraction pattern can vary considerably in the range of moderate and high ultrasonic and low hypersonic frequencies. In the transition to hypersonic frequencies, one has to increase the intensity of the external field or use the resonance modes for vibrations of the crystal lattice and an applied acoustic field.

DIFFRACTION PATTERNS FROM A CRYSTAL IN A FIELD OF A STANDING WAVE

Let a standing wave $\mathbf{A}(x, t) = 2\mathbf{A}_0\cos k_1 x\cos\omega_1 t$ of an electromagnetic or an acoustic nature propagate in a crystal. The relation between the amplitudes A_0 and A_0^{ext} of running waves, for this case was considered earlier. The force field of the standing wave generates a standing wave of atomic displacements from their equilibrium positions: $\mathbf{u}(x, t) = 2\mathbf{u}(\omega_1)\cos k_1 x\cos\omega_1 t$. Upon raising $\mathbf{u}(x, t)$ to the second power and averaging it over time and vibration directions (at each point x of atom location), we obtain

$$\langle u^2(x, \omega_1)\rangle^{1/2} = q(\omega_1)A_0^{\text{ext}}\cos k_1 x, \tag{6}$$

where $\langle u^2(\omega_1)\rangle^{1/2}$ is expressed in terms of (4) and (5), and therefore the proportionality coefficient $q(\omega_1)$ equals $2\varepsilon_0(n-1)/NQ^*$ for the electromagnetic waves and $1/\omega_1\rho c$ for the acoustic waves. The amplitude A_0^{ext} plays the role of E_0^{ext} and p_0^{ext} in the above external fields. All the X-ray diffraction methods use the dimensionless coordinate x, and therefore the wave number k_1 has the sense of $k_1 = 2\pi a/\lambda_1$.

Under the effect of a standing-wave field, the initial periodicity of the crystal is disturbed and, therefore, similar to the case considered in part I of this article [1], we have to introduce the structure factor of scattering for a crystal, $F_{\text{cr}}(\mathbf{S})$. For the case of a standing wave, the expression for the structure factor of a crystal is written in the form

$$F_{\text{cr}}(\mathbf{S}) = \sum_{mnp}\sum_{s} f_s(\mathbf{S})T\exp\left(-8\pi^2\langle u_{mnp}^2(\omega_1)\rangle\frac{\sin^2\theta}{\lambda^2}\right) \times \exp i2\pi\mathbf{S}(\mathbf{R}_{mnp}+\mathbf{r}_s), \tag{7}$$

where the notation is the same as in [1].

In equation (7), the total displacement of the centers of gravity of atoms averaged over time is zero. Then, it is convenient to pass from summation over mnp in (7) to integration over the crystal volume v. This can be done because we assume that the number of unit cells in a real crystal is very large, whereas the function under the summation sign over mnp smoothly varies with the transition from one cell to another under the given value of $\mathbf{S}$ in the vicinity of the reciprocal lattice point. Now, introduce a new vector $\boldsymbol{\varepsilon} \equiv \mathbf{S} - \mathbf{H}$ to describe the distribution of the structure factor (intensity) in the vicinity of the reciprocal-lattice point $\mathbf{H}$. Then, (7) with due regard for (6), we can rewrite (7) in the form

$$F_{\text{cr}}(\mathbf{S}) = \frac{F(\mathbf{H})}{V}\int_{v}\exp\left[-8\left(\pi q\frac{\sin\theta}{\lambda}A_0^{\text{ext}}\cos k_1 x\right)^2\right] \times \exp(i2\pi\boldsymbol{\varepsilon}\mathbf{r})dv, \tag{8}$$

where V is the unit-cell volume. It is also assumed that, within a diffraction peak, the structure factor of scattering by the unit cell is $F(\mathbf{S}) \approx F(\mathbf{H})$ and that $\exp i2\pi\mathbf{S}\mathbf{R}_{mnp} = \exp i2\pi\boldsymbol{\varepsilon}\mathbf{R}_{mnp}$ (because the components of the vectors $\mathbf{H}$ and $\mathbf{R}_{mnp}$ are integers). Taking into account that in many particular cases, the exponent in the first term in (8) is small compared with unity (see the above estimates of $\langle u^2(\omega_1)\rangle$), we can retain only two first terms in its expansion. Then, one can represent $F_{\text{cr}}(\mathbf{S})$ in the form

$$F_{\text{cr}}(\mathbf{S}) = \prod_{l=1}^{3}\frac{\sin\pi\varepsilon_l M_l}{\pi\varepsilon_l}F(\mathbf{H}) - 8\left(\pi q A_0^{\text{ext}}\frac{\sin\theta}{\lambda}\right)^2 \times F(\mathbf{H})\prod_{l=2}^{3}\frac{\sin\pi\varepsilon_l M_l}{\pi\varepsilon_l}\int_{-\frac{M_1}{2}}^{+\frac{M_1}{2}}\cos^2 k_1 x\exp(i2\pi\varepsilon_1 x)dx. \tag{9}$$

The first term in (9) describes the diffraction peaks from unperturbed crystal. Their heights are equal to $F(\mathbf{H})$, the shapes are set by the function $\prod_{l=1}^{3}\sin\pi\varepsilon_l M_l/\pi\varepsilon_l$, and they are centered at positions $\varepsilon_l = 0$. The second term characterizes the changes in $F_{\text{cr}}(\mathbf{S})$ caused by the effect of an external standing-wave field. These changes are proportional to the squared amplitude of the external field $(A_0^{\text{ext}})^2$ and the structure factor $F(\mathbf{H})$ and also depend on $\sin^2\theta/\lambda^2$ and on the crystal properties set by the coefficient q. The schematic diffraction pattern along the $\mathbf{a}^*$-axis is determined by the functional dependence of the integral in (9) on s_1, and can be written as

$$\int_{-\frac{M_1}{2}}^{+\frac{M_1}{2}}\cos^2 k_1 x\exp(i2\pi\varepsilon_1 x)dx = \frac{1}{2}\left\{\frac{\sin\pi\varepsilon_1 M_1}{\pi\varepsilon_1} + \sum_{\pm}\frac{\sin[(k_1\pm\pi\varepsilon_1)M_1]}{2(k_1\pm\pi\varepsilon_1)}\right\}. \tag{10}$$

Expressions (9) and (10) determine the diffraction pattern in the space of structure factors. The above formulas do not take into account the divergence of the primary beam, the finite width of its spectral range, and other experimental characteristics. Obviously, the existence of these factors should broaden the diffraction peaks. However, the theoretical consideration should deal, first and foremost, with an ideal experiment, because the main quantities used in the theory are independent of the concrete details of the experimental setup.

Now, analyze formulas (9) and (10) for an ideal experiment. According to (9) and (10), there are three peaks around the reciprocal lattice point $\mathbf{H}$. The main peak is centered in the position $\mathbf{H}$, but its height is less than that for an unperturbed crystal and is equal to $F(\mathbf{H})[1 - 4(\pi q\sin\theta/\lambda A_0^{\text{ext}})^2]$. This reduced peak height shows itself mainly in high-angle reflections. At $\langle u^2(\omega_1)\rangle \approx (10^{-3}–10^{-2})$ Å^2 (see the above estimates), the peak height is ~(0.97–0.75) $F(\mathbf{H})$ and, therefore, the intensities of such reflections can be reduced by factors of ~(1.06–1.77) in comparison with the intensities of an unperturbed crystal. As earlier, the shape of this peak is

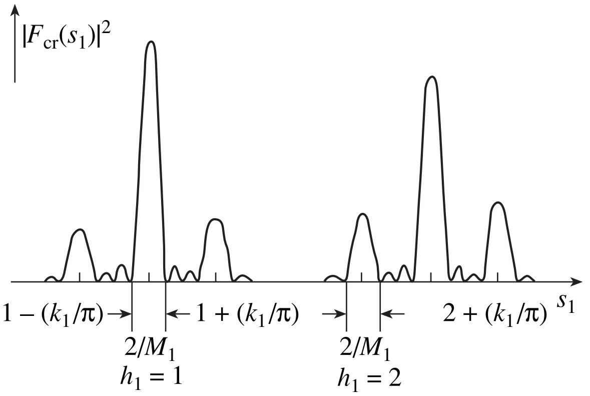

Schematic one-dimensional section of the peaks of the function $|F_{\rm cr}(\mathbf{S})|^2$ at two reciprocal-lattice points, $h_1 = 1$ and $h_1 = 2$, in an external field of a standing wave $\mathbf{A}^{\rm ext}(x, t) = 2\mathbf{A}_0^{\rm ext}\cos k_1 x \cos\omega_1 t$. The case $\lambda_1 < L_1$.

described by the function $\prod_{l=1}^{3}(\sin\pi\varepsilon_l M_l)/\pi\varepsilon_l$. Two other, auxiliary, maxima are centered in the positions $s_1 = h_1 \pm k_1/\pi$, $s_2 = h_2$, and $s_3 = h_3$; their heights are equal to $2(\pi q \sin\theta/\lambda A_0^{\rm ext})^2 F(\mathbf{H})$, and the shape along the $\mathbf{a}^*$-axis is set by the function $\sin[(k_1 \pm \pi\varepsilon_1)M_1]/(k_1 \pm \pi\varepsilon_1)$. The heights of the auxiliary maxima are determined by the parameter $\langle u^2(\omega_1)\rangle$. At the same orders of magnitude of $\langle u^2(\omega_1)\rangle \approx (10^{-3}–10^{-2})$ Å^2, the heights of these peaks are $\sim 1.2 \times (10^{-2}–10^{-1})F(\mathbf{H})$ (for high-angle reflections). Therefore, the auxiliary peaks can be experimentally recorded only with the use of either intense sources of X-ray radiation or at considerably longer exposures. Only if $\langle u^2(\omega_1)\rangle \approx 8 \times 10^{-2}$ Å^2 (see the above estimates for acoustic factors), the heights of auxiliary maxima can attain the values comparable with the value of the main maximum.

Formulas (9) and (10) yield the condition at which the main and the auxiliary maxima can overlap (an ideal experiment). The bases of the peaks start overlapping at $\lambda_1 = L_1$. In this case, a standing wave in a crystal has two antinodes (or two nodes). The maximum overlap is observed at $\lambda_1 = 2L_1$, i.e., in the situation where the center of an auxiliary maximum coincides with the edge of the main maximum, because a periodic effect of a standing wave under the conditions $\lambda_1 > 2L_1$ makes no sense at all. The auxiliary peaks on the diffraction pattern are explained by an additional periodicity provided by the dependence of the field amplitude of the standing wave on x. This situation is somewhat similar to the case of a periodic force field considered earlier, which resulted in the static atomic displacement from their equilibrium positions. However, in our case, an increase in the auxiliary-peak heights depends not on $\sin^2\theta/\lambda^2$ and an external-field amplitude but on their squared values, $\sin^2\theta/\lambda^2$ and $(A_0^{\rm ext})^2$, which is the manifestation of the specific features of modulation under the effect of the temperature factor and not of the displacement field of the atomic coordinates.

REFERENCES

1. E. N. Treushnikov, Kristallografiya **45**, 402 (2000) [Crystallogr. Rep. **45** (3), 360 (2000)].
2. P. Grosse, *Freie Electronen in Festkórpern* (Springer, Heidelberg, 1979; Mir, Moscow, 1982).
3. I. S. Zheludev, L. A. Shuvalov, A. A. Urusovskaya, I. A. Zheludev, *et al.*, *Modern Crystallography. Vol. 4. Physical Properties of Crystals*, Ed. by B. K. Vaĭnshteĭn, A. A. Chernov, and L. A. Shuvalov, 2dn ed. (Nauka, Moscow, 1981; Springer-Verlag, Berlin, 1988).
4. M. A. Isakovich, *General Acoustics* (Nauka, Moscow, 1973).

Translated by L. Man

Crystallography Reports, Vol. 45, No. 4, 2000, pp. 545–550. Translated from Kristallografiya, Vol. 45, No. 4, 2000, pp. 600–605.
Original Russian Text Copyright © 2000 by Treushnikov.

DIFFRACTION AND SCATTERING
OF X-RAYS AND SYNCHROTRON RADIATION

X-ray Diffraction from Ideal Mosaic Crystals in External Fields of Certain Types, Part III: Changes in Space Symmetry and Symmetry of Diffraction Pattern[1]

E. N. Treushnikov
Moscow State Academy of Geological Prospecting, Moscow, Russia

Received July 8, 1998

Abstract—The change in the space symmetry and the symmetry of the corresponding diffraction pattern occurring under the effect of uniform electric and magnetic fields applied to a crystal have been analyzed. The tables of point symmetry groups for various directions of applied magnetic fields are constructed. It is shown that in the absence of an external field, the diffraction patterns are described by nine possible point groups; in an electric field, they are described by eleven point groups; and in a magnetic field, by only five point groups. The theoretically calculated diffraction parameters are compared with the corresponding experimental values. © *2000 MAIK “Nauka/Interperiodica”.*

SPACE SYMMETRY AND SYMMETRY OF DIFFRACTION PATTERN OF CRYSTALS UNDER THE EFFECT OF EXTERNAL ELECTRIC AND MAGNETIC FIELDS

In order to determine the symmetry of a crystal in external fields, one has to invoke the Curie principle ([1], p. 44). If one applied a uniform electric field to a crystal, the Curie principle is used in the form

$$\Phi_1 = \Phi \cap \infty mm \otimes T_{\tau_1\tau_2\tau_3}, \qquad (1)$$

where Φ and Φ_1 are the space groups of the crystal symmetry prior to and upon the field application, ∞mm is the point symmetry group of an external field, and $T_{\tau_1\tau_2\tau_3}$ is the group of continuous three-dimensional translations. The signs $\cap$ and $\otimes$ denote the intersection and the direct multiplication, respectively.

If the initial space group of the crystal is known, condition (1) provides the determination of possible space groups under the effect of various external factors. It is clear that Φ_1 depends on the direction of an external field $\mathbf{E}^{\text{ext}}$ with respect to the **a**-, **b**-, and **c**-axes, which are assumed to be normal to the faces of a prismatic crystal. As an example, consider the space groups $P2_1/c$ and $Pca2_1$. If the external field $\mathbf{E}^{\text{ext}}$ is applied along the **a**- and **c**-axes, the sp. gr. $P2_1/c$ is changed to the sp. gr. Pc, if the field $\mathbf{E}^{\text{ext}}$ is applied along the **b**-axis, it is changed to $P2_1$. For the space group $Pca2_1$, the application of an external field along the **a**-, **b**-, and **c**-axes lead to the space groups Pa, Pc, and $Pca2_1$, respectively. The preservation of the translations in the newly formed Φ_1 groups is provided by the presence of the group of continuous translations $T_{\tau_1\tau_2\tau_3}$ in Eq. (1). Of course, if the initial space group Φ does not contain these translations, they cannot appear in new groups either. Thus, in the sp. gr. $P2/m$ and $Pmmm$, with the external field $\mathbf{E}^{\text{ext}}$ being applied along the **a**-, **b**-, or **c**-axes, these groups are transformed into Pm, $P2$, Pm and $P2mm$, $Pm2m$, and $Pmm2$, respectively. Thus, all the above space groups are transformed into noncentrosymmetric space groups. This is also the general rule in an applied electric field, because the field $\mathbf{E}^{\text{ext}}$ is described by a polar (and, therefore, noncentrosymmetric) vector. In a similar way, one can also analyze any of 230 space groups.

The symmetry of a diffraction pattern is determined by the point groups (crystallographic classes). The changes in the symmetry of the corresponding diffraction patterns of a crystal in various applied fields can also be obtained with the aid of the Curie principle in the form

$$K_1 = K \cap \infty mm, \qquad (2)$$

where K and K_1 are the point groups prior to and upon the application of an external field to the crystal. Since the structure factor is $F_1(\mathbf{H}) = F_1^*(-\mathbf{H})$, the symmetry of the diffraction pattern can be obtained by applying the center of inversion to the point group K_1. The possible symmetry groups of the diffraction pattern and also the point groups arising under the effect of an external uniform electric field applied along the **a**-, **b**-, and **c**-axes of the crystal are listed in Table 1. It is seen that the point symmetry of the crystal in a uniform elec-

---

[1] For parts I and II see [2] and [3].

Table 1. Effect of application of a uniform electric field, $\mathbf{E}^{\text{ext}}$, on the symmetry of the crystal and its diffraction pattern

Point symmetry group of crystal	Symmetry of diffraction pattern	Point symmetry group (left column) and the symmetry of the diffraction pattern (right column) in an external field					
without field		$\mathbf{E}^{\text{ext}} \parallel \mathbf{a}$		$\mathbf{E}^{\text{ext}} \parallel \mathbf{b}$		$\mathbf{E}^{\text{ext}} \parallel \mathbf{c}$	
1	$\bar{1}$	1	$\bar{1}$	1	$\bar{1}$	1	$\bar{1}$
$\bar{1}$		1	$\bar{1}$	1	$\bar{1}$	1	$\bar{1}$
2(‖**c**)	2/*m*	1	$\bar{1}$	1	$\bar{1}$	2	2/*m*
m(⊥**c**)		*m*	2/*m*	*m*	2/*m*	1	$\bar{1}$
2/*m*		*m*	2/*m*	*m*	2/*m*	2	2/*m*
*mm*2	*mmm*	*m*	2/*m*	*m*	2/*m*	*mm*2	*mmm*
222		2	2/*m*	2	2/*m*	2	2/*m*
mmm		2*mm*	*mmm*	*m*2*m*	*mmm*	*mm*2	*mmm*
3(‖**c**)	$\bar{3}$	1	$\bar{1}$	1	$\bar{1}$	3	$\bar{3}$
$\bar{3}$ (‖**c**)		1	$\bar{1}$	1	$\bar{1}$	3	$\bar{3}$
3*m**	$\bar{3}m$	1	$\bar{1}$	1	$\bar{1}$	3*m*	$\bar{3}m$
32		2	2/*m*	2	2/*m*	3	$\bar{3}$
$\bar{3}m$		2	2/*m*	2	2/*m*	3	$\bar{3}$
4(‖**c**)	4/*m*	1	$\bar{1}$	1	$\bar{1}$	4	4/*m*
$\bar{4}$ (‖**c**)		1	$\bar{1}$	1	$\bar{1}$	2	2/*m*
4/*m*		*m*	2/*m*	*m*	2/*m*	4	4/*m*
$\bar{4}2m$	4/*mmm*	2	2/*m*	2	2/*m*	*mm*2	*mmm*
4*mm*		*m*	2/*m*	*m*	2/*m*	4*mm*	4/*mmm*
422		2	2/*m*	2	2/*m*	4	4/*m*
4/*mmm*		2*mm*	*mmm*	*m*2*m*	*mmm*	4*mm*	4/*mmm*
6 (‖**c**)	6/*m*	1	$\bar{1}$	1	$\bar{1}$	6	6/*m*
$\bar{6}$ (‖**c**)		*m*	2/*m*	*m*	2/*m*	3	$\bar{3}$
6/*m*		*m*	2/*m*	*m*	2/*m*	6	6/*m*
$\bar{6}2m$	6/*mmm*	*m*	2/*m*	*m*	2/*m*	3*m*	$\bar{3}m$
6*mm*		*m*	2/*m*	*m*	2/*m*	6*mm*	6/*mmm*
622		2	2/*m*	2	2/*m*	6	6/*m*
6/*mmm*		2*mm*	*mmm*	*m*2*m*	*mmm*	6*mm*	6/*mmm*
23	*m*3	2	2/*m*	2	2/*m*	2	2/*m*
*m*3		2*mm*	*mmm*	*m*2*m*	*mmm*	*mm*2	*mmm*
$\bar{4}3m$	*m*3*m*	2*mm*	*mmm*	*m*2*m*	*mmm*	*mm*2	*mmm*
432		4	4/*m*	4	4/*m*	4	4/*m*
*m*3*m*		*mm*4(4‖**a**)	*mm*4/*m*	*m*4*m*(4‖**b**)	*m*4/*mm*	4*mm*	4/*mmm*

* Point group 3*m*. The crystallographic **a**- and **b**-axes lie between the planes *m*.

tric field is determined by ten noncentrosymmetric groups corresponding to ten polar classes ([1], p. 36). The symmetry of the corresponding diffraction patterns can be described by nine centrosymmetric point groups: $\bar{1}$, $2/m$, mmm, $\bar{3}$, $\bar{3}m$, $4/m$, $4/mmm$, $6/m$, and $6/mmm$, whereas in the absence of perturbations, it is described by eleven groups.

If a uniform magnetic field is applied to a crystal, the Curie principle is written in the form similar to Eq. (1), with the symbol of the point symmetry of an electric field being substituted by the symbol of the point symmetry of a magnetic field (∞/m).

Naturally, the groups Φ_1, in the case of a magnetic field, do not coincide with the groups in the case of an electric field. Thus, the application of a magnetic field along the **a**-axis results in the change of the groups analyzed above, $P2_1/c$, $Pca2_1$, $P2/m$, and $Pmmm$, to the groups $P\bar{1}$, Pc, $P\bar{1}$, and $P2/m$, respectively. The application of a magnetic field along the **b**-axis results in the change of the above groups to $P2_1/c$, Pa, $P2/m$, and $P2/m$, respectively, and, finally, the application of a magnetic field along the **c**-axis change these groups to $P\bar{1}$, $P2_1$, $P\bar{1}$, and $P2/m$, respectively. Unlike the case of an electric field, the application of a magnetic field can give rise to formation of both centrosymmetric and noncentrosymmetric groups, in full accordance with the initial space group of the crystal. This fact is explained by different symmetries of the polar, $\mathbf{E}^{\text{ext}}$, and axial, $\mathbf{H}^{\text{ext}}$, vectors.

The point group symmetry for the case of an external magnetic field is illustrated by Table 2. In this case, 32 point groups are transformed into 13 symmetry classes of magnetics ([1], p. 36). Then, the symmetry of the diffraction pattern is determined by five point groups $\bar{1}$, $\bar{3}$, $2/m$, $4/m$, and $6/m$. If both nonuniform electric and magnetic fields are applied to a crystal, the latter loses its property of periodicity. Then the symmetry of the crystal can be described by point groups. The Curie principle in this case has its conventional form ([1], p. 42).

The data listed in Tables 1 and 2 can also be used to select appropriate objects for study. Indeed, if the change in the diffraction-pattern symmetry under the effect of an applied field can be recorded experimentally, this shows that one can determine the field-induced changes in the diffraction parameters. The corresponding estimates of the intensity variations arising in this case were considered in [2].

COMPARISON OF THEORETICAL ESTIMATES OF DIFFRACTION PARAMETERS WITH THE CORRESPONDING EXPERIMENTAL DATA

A number of diffraction parameters were estimated in [2, 3]. These are the values of the averaged atomic displacements $\langle \Delta x \rangle$ numbered by the subscript s and the directions numbered by the subscript $l = 1–3$; the changes in the intensities $|\Delta I|$ of main and subsidiary peaks; the changes in the temperature factor ΔB, and some other parameters arising under the effect of various external factors. It is also expedient to compare these theoretical estimates with the corresponding experimentally determined values.

Fujimoto [4] performed the X-ray diffraction study of $LiNbO_3$ and $LiTaO_3$ crystals in an external electric field $E^{\text{ext}} \approx 50$ kV/cm using alternating positive and negative rectangular pulses at a frequency of 19 Hz. He measured the integrated intensities of a number of diffraction reflections under the effect of both positive and negative pulses. The displacements Δz of heavy Nb and Ta ions were of the order of 5.5×10^{-4} Å, whereas those of light Li ions were of the order of 1.3×10^{-3} Å.

It was indicated [2] that the most appropriate object for recording the variations in the atomic coordinates in an applied electric field are piezoelectrics, and first of all, displacive-type ferroelectrics (i.e., $LiNbO_3$ and $LiTaO_3$ [4]) possessing high values of the piezoelectric modulus d (here we do not use the tensor notation). Fujimoto also indicated how it is possible to estimate the average shifts in the atomic coordinates $\langle \Delta x \rangle$ at the given d and E^{ext} values and also some other parameters. Thus, for $LiNbO_3$ at the averaged values of the nonzero components of the piezoelectric modulus $\langle d \rangle \approx 2.3 \times 10^{-11}$ C/N, the hexagonal unit-cell parameter $\langle a \rangle \approx 8$ Å, dielectric constant $\langle \varepsilon \rangle \approx 45$ ([5], p. 22), and $E^{\text{ext}} \approx 50$ kV/cm, we obtain $\langle \Delta x \rangle \approx 0.2 \times 10^{-4}$ Å. Similar estimates were also made for $LiTaO_3$, $\langle \Delta x \rangle \approx 0.1 \times 10^{-4}$ Å. Thus, the numerical values of these estimates are considerably less than their experimental values, which can be explained as follows. First, the above estimates are macroscopic quantities, and, therefore, they include not only the displacements of the Nb, Ta, and Li atoms (ions) but also the displacements of oxygen atoms not taken into account in [4]. Second, since oxygen atoms form face-sharing octahedra, one can assume that the displacements of oxygen ions are insignificant. Third, it is very important that the refinement of the atomic coordinates was performed in [4] only over seven independent reflections, which, as a rule, is insufficient for the precision determination of coordinates.

The complete X-ray diffraction study of a $LiNbO_3$: Fe (0.01–0.02 at %) and triglycine sulfate $C_6H_{17}N_3O_{10}S$: Cr (0.002 at %) (TGS) single crystals was performed [6] under the effect of weak electromagnetic radiation ($\lambda = 532$ and 630 nm, the power density (0.2–0.3) W/cm^2). In this case [6], no variations in thermal or positional parameters of structure atoms structures were recorded. However, in both crystals, an increase of the extinction parameters responsible for the angular misorientation of the blocks of mosaics in the structure was recorded. Thus, the angular block misorientation upon the irradiation of a $LiNbO_3$: Fe

Table 2. Effect of applied uniform magnetic field $\mathbf{H}^{\text{ext}}$ on the symmetry of the crystal and its diffraction pattern

Point group of crystal	Symmetry of diffraction pattern	Point group of symmetry (left column) and symmetry of diffraction pattern (right column) in an external field					
without field		$\mathbf{H}^{\text{ext}} \parallel \mathbf{a}$		$\mathbf{H}^{\text{ext}} \parallel \mathbf{b}$		$\mathbf{H}^{\text{ext}} \parallel \mathbf{c}$	
1	$\bar{1}$	1	$\bar{1}$	1	$\bar{1}$	1	$\bar{1}$
$\bar{1}$		$\bar{1}$	$\bar{1}$	$\bar{1}$	$\bar{1}$	$\bar{1}$	$\bar{1}$
$2(\parallel \mathbf{c})$	$2/m$	1	$\bar{1}$	1	$\bar{1}$	2	$2/m$
$m(\perp \mathbf{c})$		1	$\bar{1}$	1	$\bar{1}$	m	$2/m$
$2/m$		$\bar{1}$	$\bar{1}$	$\bar{1}$	$\bar{1}$	$2/m$	$2/m$
$mm2$	mmm	m	$2/m$	m	$2/m$	2	$2/m$
222		2	$2/m$	2	$2/m$	2	$2/m$
mmm		$2/m$	$2/m$	$2/m$	$2/m$	$2/m$	$2/m$
$3(\parallel \mathbf{c})$	$\bar{3}$	1	$\bar{1}$	1	$\bar{1}$	3	$\bar{3}$
$\bar{3}\ (\parallel \mathbf{c})$		$\bar{1}$	$\bar{1}$	$\bar{1}$	$\bar{1}$	$\bar{3}$	$\bar{3}$
$3m$*	$\bar{3}\,m$	m	$2/m$	m	$2/m$	3	$\bar{3}$
32		2	$2/m$	2	$2/m$	3	$\bar{3}$
$\bar{3}\,m$		$2/m$	$2/m$	$2/m$	$2/m$	$\bar{3}$	$\bar{3}$
$4(\parallel \mathbf{c})$	$4/m$	1	$\bar{1}$	1	$\bar{1}$	4	$4/m$
$\bar{4}\ (\parallel \mathbf{c})$		1	$\bar{1}$	1	$\bar{1}$	$\bar{4}$	$4/m$
$4/m$		$\bar{1}$	$\bar{1}$	$\bar{1}$	$\bar{1}$	$4/m$	$4/m$
$\bar{4}\,2m$	$4/mmm$	2	$2/m$	2	$2/m$	$\bar{4}$	$4/m$
$4mm$		m	$2/m$	m	$2/m$	4	$4/m$
422		2	$2/m$	2	$2/m$	4	$4/m$
$4/mmm$		$2/m$	$2/m$	$2/m$	$2/m$	$4/m$	$4/m$
$6(\parallel \mathbf{c})$	$6/m$	1	$\bar{1}$	1	$\bar{1}$	6	$6/m$
$\bar{6}\ (\parallel \mathbf{c})$		1	$\bar{1}$	1	$\bar{1}$	$\bar{6}$	$6/m$
$6/m$		$\bar{1}$	$\bar{1}$	$\bar{1}$	$\bar{1}$	$6/m$	$6/m$
$\bar{6}\,2m$	$6/mmm$	m	$2/m$	m	$2/m$	$\bar{6}$	$6/m$
$6mm$		m	$2/m$	m	$2/m$	6	$6/m$
622		2	$2/m$	2	$2/m$	6	$6/m$
$6/mmm$		$2/m$	$2/m$	$2/m$	$2/m$	$6/m$	$6/m$
23	$m3$	2	$2/m$	2	$2/m$	2	$2/m$
$m3$		$2/m$	$2/m$	$2/m$	$2/m$	$2/m$	$2/m$
$\bar{4}\,3m$	$m3m$	$\bar{4}$	$4/m$	$\bar{4}$	$4/m$	$\bar{4}$	$4/m$
432		4	$4/m$	4	$4/m$	4	$4/m$
$m3m$		$4/m$	$4/m$	$4/m$	$4/m$	$4/m$	$4/m$

* For notation, see Table 1.

sample was 8.6(3)", whereas prior to irradiation, it was equal to 5.1(3)". The corresponding values for TGS crystals were 0.91(1)" and 0.61(1)".

It was indicated [2] that no atomic displacements occur in external electromagnetic fields. In [3], the mean square displacements of atoms from their equilibrium position $\langle u^2(\omega_1)\rangle^{1/2}$ were observed under the effect of the variation in ΔB. These displacements allow the estimation of the variation in ΔB; a considerable value of ΔB ($\sim 10^{-2}$ Å^2) can be obtained only in strong external fields ($E^{\text{ext}} \approx 10^8$ V/m). For the case under consideration, we obtain in weak external fields ($E^{\text{ext}} \approx 9 \times 10^2$ V/m) that $\Delta B \ll \sigma(\Delta B)$. Thus, the theoretical estimates made in [2, 3] are in good accord with the corresponding experimental values. The variations in the extinction parameters were not estimated, because their values depend on the growth conditions and can considerably vary for different specimens. However, one can readily predict an increase in the secondary-extinction parameter with an increase of the integrated intensity of the small-angle reflection [6]. It follows from the essence of the extinction phenomenon ([7], p. 74). Various methods for calculating the corresponding parameters were considered in [8], ch. 7.

The X-ray study of a $K_{0.30}MoO_3$ crystal with a quasi-one-dimensional conductivity in an alternating electric field (positive and negative current (voltage) pulses alternating at a certain frequency was performed in [9, 10]. The application of an external field to a crystal resulted in formation of satellite peaks associated with charge-density waves in the crystal [9, 10].

The type of the diffraction pattern formed due to application of an external force field of the form $A^{\text{ext}}(x) = A_0^{\text{ext}} \cos 2\pi k_1 x$ resulted in the periodic displacements of atoms from their equilibrium position [2] and the formation of an additional periodic electron density. This situation is analogous to that observed in [9, 10] and is caused by the formation in a crystal of a periodic structure of the charge-density waves induced by an alternating current (voltage) field. The analysis of the expression for the structure factor $F_{\text{cr}}(\mathbf{S})$ in this case revealed some additional satellite reflections on the diffraction pattern, which is quite consistent with the above experimental results. The positions and the intensities of satellites with respect to the main maxima were analyzed in [2, 9, 10].

The effect of an applied electric field (E^{ext} = 39 kV/cm) on the integrated intensities of a number of reflections for an organic 2-methyl-4-nitroaniline (MNA) crystal possessing high nonlinear optical characteristics was analyzed in [11]. It was shown that the relative changes in the integrated intensities of some reflections range within $\sim(0.03\text{–}1.81) \times 10^{-3}$, i.e., on the average, are equal to ~0.09%.

The analysis of the average atomic displacements and the corresponding changes in the integrated intensities in a crystals placed into an electric field was performed in [2]. For MNA crystals at $d \approx (38\text{–}250)$ pm/V ([12], p. 269) and $\varepsilon \approx 3$ (the dielectric constant for the related compounds considered elsewhere ([12], p. 418), we have that the relative displacement in atomic coordinates should be $(0.5\text{–}3.2) \times 10^{-4}$.

However, no atomic coordinate displacements were estimated in [1], probably because of a small number (six) of measured reflections. The theoretically calculated displacement yields the following relative variation in the integrated intensity $|\Delta I|/I \approx (0.004\text{–}0.2) \times 10^{-3}$ ($\Delta I = I_1 - I$, $\sin\theta/\lambda \approx 0.4$ Å^{-1}) or ~0.01%, which is nine times lower than the observed value. It was indicated [2], that, in some cases, the estimate of the change in the relative intensity $|\Delta I|/I$ provided by the atomic-coordinate displacements is a lower boundary of the relative change in the intensity under the effect of an external electric field. It can also indirectly indicate the considerable deformation of the electron density of chemical bonds of this organic compound occurring under the effect of an external electric field and provides an additional contribution to $|\Delta I|/I$. However, theoretically, it is impossible to estimate the effect of this factor on the intensity variation in our case.

The above estimates are very useful. They show that each reflection requires an exposure time of 1–2 days, which explains the small number of reflections recorded by the authors [11]. This estimate also allows one to develop an appropriate strategy of the experiment [2]. Indeed, if the study is aimed to obtain a most complete set of diffraction data for the detailed X-ray study, then it is necessary to use powerful synchrotron sources of X-ray radiation.

CONCLUSIONS

The presented cycle of studies ([2, 3] and the present article) provides the theoretical consideration of the basic problems of X-ray diffraction from ideal mosaic crystals in electric, magnetic, and electromagnetic fields and under acoustic perturbations. A more detailed consideration of these and some other problems can be found in [13] and include the intensity scattered by an electron, an atom, and a crystal; the modification of the Bragg equation, the expression for the integrated intensity, the allowance for the thermal vibrations of atoms and extinction in external fields.

The above theoretical analysis of the effect of external field on the diffraction parameters provides a more reasonable choice of objects for such studies and also the strategy and the tactics for experiments. Other useful data can be obtained from the analysis of the crystal symmetry and its variation under the effect of magnetic and electric fields.

In many instances, small displacements in atomic coordinates often recorded in various applied fields are themselves unimportant, but they can give rise to the considerable deformation of the outer (valence) electron density (see, e.g., [4]). The electron distribution can affect the optical, electric, and other properties of crystals (see the Hohenberg–Kohn theorem [14]). Therefore, the study of the electron-density distribution in crystals in applied fields seems to be of great importance.

The further detailed theoretical description should include the introduction of the characteristics of other external factors into the derived formulas and calculation of typical diffraction patterns from these formulas and estimation of their main parameters. In the study of highly intense external factors, one has to take into account all the nonlinear effects.

The above consideration can serve as the basis for studying dynamic X-ray diffraction in external fields. Indeed, one of the main theoretical parameters is the dielectric polarizability (susceptibility), $\chi(\mathbf{H})$. It is the variation of this parameter in external fields that determines the redistribution of X-ray intensities in the theory of dynamical diffraction in comparison with their distribution in the unperturbed case.

REFERENCES

1. L. A. Shuvalov *et al.*, *Modern Crystallography, Vol. 4. Physical Properties of Crystals*, Ed. by B. K. Vaĭnshteĭn, A. A. Chernov, and L. A. Shuvalov (Nauka, Moscow, 1981; Springer-Verlag, Berlin, 1988).
2. E. N. Treushnikov, Kristallografiya **45** (3), 402 (2000) [Crystallogr. Rep. **45,** 360 (2000)].
3. E. N. Treushnikov, Kristallografiya **45** (4), 541 (2000) [Crystallogr. Rep. **45** (2000)].
4. J. Fujimoto, Acta Crystallogr., Sect. A: Cryst. Phys., Diffr., Theor. Gen. Crystallogr. **38**, 337 (1982).
5. Yu. S. Kuz'minov, *Lithium Niobate and Thantalate. Materials for Nonlinear Optics* (Nauka, Moscow, 1975).
6. S. G. Zhukov, Author's Abstract of Candidate's Dissertation in Physics and Mathematics (Mosk. Gos. Univ., Moscow, 1990).
7. M. A. Poraĭ-Koshits, *Practical Course of X-ray Diffraction Analysis* (Mosk. Gos. Univ., Moscow, 1960).
8. L. A. Aslanov and E. N. Treushnikov, *Fundamentals of Theory of X-ray Diffraction* (Mosk. Gos. Univ., Moscow, 1985).
9. K. Tsutsumi, T. Tamegai, S. Kagoshima, and M. Sato, in *Proceedings of the International Conference on Charge Density Waves in Solids, Budapest, 1984*, p. 17.
10. T. Tamegai, K. Tsutsumi, S. Kagoshima, *et al.*, Solid State Commun. **56**, 13 (1985).
11. A. Pature, H. Graafsma, J. Baviatsis, *et al.*, Acta Crystallogr., Sect. A: Found. Crystallogr. **45**, FC25 (1989).
12. *Nonlinear Properties of Organic Molecules and Crystals*, Ed. by D. S. Chemla and I. Zyss (Academic, Orlando, 1987; Mir, Moscow, 1989), Vol. 1.
13. E. N. Treushnikov, Doctoral Dissertation in Physics and Mathematics (Nizhegorodskiĭ Gos. Univ., Nizhniĭ Novgorod, 1995).
14. W. Cohn and P. Vashishta, in *Theory of the Inhomogeneous Electron Gas*, Ed. by S. Lundqvist and N. H. March (Plenum, New York, 1983; Mir, Moscow, 1987).

Translated by L. Man

Crystallography Reports, Vol. 45, No. 4, 2000, pp. 551–554. Translated from Kristallografiya, Vol. 45, No. 4, 2000, pp. 606–610.
Original Russian Text Copyright © 2000 by Sardarly, Abdullaev, Guseĭnov, Nadzhafov, Éyubova.

Polymorphism and Phase Transitions in TlS

R. M. Sardarly[1], A. P. Abdullaev, G. G. Guseĭnov, A. I. Nadzhafov, and N. A. Éyubova

Radiation Research Department, Institute of Physics, Academy of Sciences of Azerbaijan,
pr. Dzhavida 31a, Baku, 370143 Azerbaijan

Received January 25, 1999; in final form, April 13, 1999

Abstract—The conditions for synthesis and the range of existence of the monoclinic TlS modification in the Tl–S system have been determined by means of differential thermal, X-ray diffraction, and microstructural analyses. It was shown that the monoclinic phase is a structural analogue of $TlGaSe_2$. Possible variants of formation of structural sheets and the nature of phase transitions in the monoclinic TlS modification are discussed. *© 2000 MAIK "Nauka/Interperiodica".*

As is well known, thallium halcogenides and their triple ABX_2 analogues, where A is Tl, B is Ga or In, and X is S, Se, or Te, crystallize in the tetragonal system and form chainlike structures [1]. The specific feature of these structures is the occurrence of thallium in mono- and trivalent states with the coordination numbers equal to eight and four (polyhedra in the shapes of cubooctahedra and tetrahedra), respectively. Substitution of Ga, In, Fe, etc., for Ta^{3+} and of K and Rb for Tl^+ results in the formation of a series of triple compounds, with different structures of the chainlike TlSe type, layer $TlGaSe_2$ type [2], or a close-packed type similar to the nonlayer low-symmetry variant of MoS_2 [3].

According to the data in [4, 5], the unit-call parameters of the monoclinic TlS modification at room temperature are $a = 11.018$, $b = 11.039$, $c = 4 \times 15.039$ Å; and $\beta = 100.69°$. The value of the c period indicates that the crystal structure is an eight-sheet polytype of the $TlGaSe_2$ structure. The polytype is characterized by the fourfold pseudoperiod along the c-axis. In view of this fact, one can expect the formation of a polytype with the double period $c = 2 \times 15.039$ Å. The temperature dependence of dielectric constant $\varepsilon(T)$ showed that the monoclinic TlS phase undergoes a first-order phase transitions at 318.6 K and then exists as an incommensurate phase up to 341.1 K [4]. At the latter temperature, a second-order phase transition is observed, and the pseudoperiod disappears.

The present study was aimed to establish (1) whether the low-temperature TlS phase is formed monoclinic (2) whether the $TlS_{monocl} \longleftrightarrow TlS_{tetr}$ transition really occurs and (3) if so, what are the conditions for this transition.

The phase diagrams of the Tl–S system reported in [5, 6] are inconsistent and should be refined since none of them reflects solid-state transformations in TlS. With this aim we synthesized a number of alloys with the 47–53 at. % S corresponding to the stoichiometric compositions TlS, TlS + 2% S, TlS + 4% S, and TlS + 6% S.

The synthesis was performed by alloying the components in evacuated quartz ampules at a residual pressure of 10^{-4} mm Hg and 623 K. The alloys were annealed for 45 days at 343 K. The annealed specimens were studied by the DTA, X-ray powder diffraction, and microstructural analyses. The X-ray diffraction pattern corresponding to the composition TlS + 4% S was closer to that from the monoclinic lattice than to the patterns of the remaining three types of the specimens synthesized. The polycrystals of this composition were ground, loaded into an evacuated ampule, and

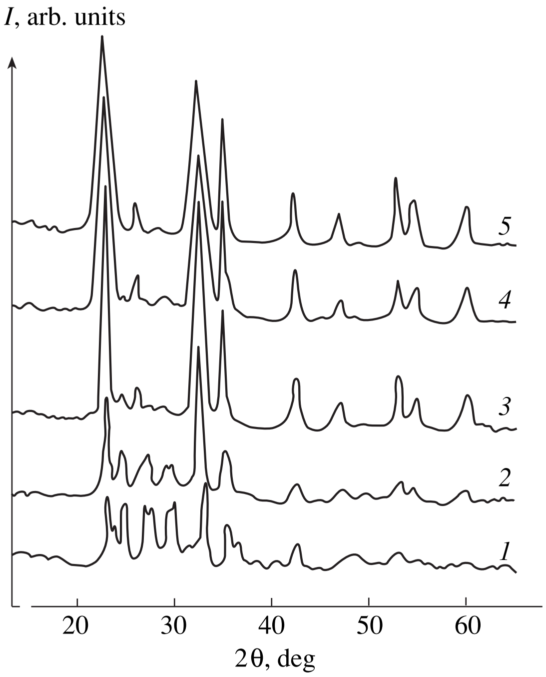

Fig. 1. X-ray diffraction patterns of the (TlS + 4 at % S) specimens annealed at the temperatures: (*1*) 261; (*2*) 303; (*3*) 323; (*4*) 373; and (*5*) 423 K.

---

[1] *e-mail: bahruz@usa.net*

Observed interplanar spacings of the (TlS + 4% S) specimens annealed at various temperatures

Present study						Data [7]	
d_{obs} (at 261 K)	*h k l*	d_{obs} (at 303 K)	*h k l*	d_{obs} (at 423 K)	*h k l*	d_{obs} (tetr. TlS)	*h k l*
4.9279	201	3.927	220	3.8277	200	3.893	200
3.7603	202	3.627	221	3.3958	002	3.396	002
3.6449	220	3.408	310	3.1160	211	3.080	211
3.5092	221	3.296	311	2.7587	220	2.746	220
3.3070	310	3.249	312	2.5384	202	2.557	202
3.1688	311	3.053	313	2.1283	222	2.140	222
3.0562	312	3.022	314	1.9458	400	1.946	400
2.9383	313	2.758	400	1.7371	420	1.745	420
2.9122	314	2.504	402	1.6867	402	1.691	402
2.8400	315	2.464	222	1.5537	422	1.550	422
2.6650	410	2.138	407			1.446	224
2.5481	331	1.949	440			1.374	440
2.5108	402	1.892	441			1.296	600
2.4057	314	1.834	442			1.277	442
2.3026	421	1.740	620			1.229	620
2.2496	422	1.680	623			1.212	124; 602
2.2251	423	1.553	629			1.156	622
2.1127	510						
1.87984	511						
2.85610	600						
1.77829	601						
1.72527	533						
1.67062	444						
1.59009	625						
1.53206	624						

annealed for 10 days at 261 K. Then diffraction patterns were recorded (Fig. 1, curve *1*). The measurements were performed on a DRON-3 diffractometer using CuK_α radiation. The interplanar spacings and reflection indices in the monoclinic subunit are listed in the table (the column of the data obtained in this study). Then, the same specimen was loaded into an evacuated ampule again, annealed for 10 days at 303 K, and subjected to the X-ray powder analysis (Fig. 1, curve *2*). Similar experiments were repeated at 323, 373, and 423 K. The corresponding X-ray diffraction patterns are shown in Fig. 1, curves *3*–*5*.

The DTA curves heated and cooled alloys annealed at 261, 303, 323, 373, and 423 K were recorded on a Q-derivatograph under the same conditions in the 286–623 K range. The error in the temperature measurements ranged within ±1 K.

The DTA curves recorded on cooling were used to construct the phase diagram of the Tl–S system in the range 47–53 at. % S (Fig. 2). According to the data obtained, the TlS compound is formed by the peritectic reaction at 460 K and undergoes solid-state transformations at 290 and 352 K. The Tamman triangle reveals the phase transition at 290 K in the alloys containing 50–51.7 at. % S. The maximum and minimum thermal effects are observed for compositions 51.2 at. % S (that is, TlS + 4 at. % S) and TlS, respectively. The temperature of the peritectic decomposition is lower than that reported in literature.

Thus, the data of X-ray powder and DTA analyses indicate that the specimens containing 50–51.2 at. % S are appropriate for studying solid-state transformations observed.

The microstructural analysis of the alloys annealed at 261, 303, 323, 373, and 423 K was performed on a MIM-7 microscope. It was found that layer and needle microstructures coexist in the specimens annealed at 303 K. In the alloys annealed at 423 K, only the needle microstructure is observed. The structures of all the specimens under study were characteristic of the alloys with the peritectic type of melting.

A visual examination of the diffraction spectra (Fig. 1) shows that they change when the temperature rises: a more complex spectrum of the low-temperature phase becomes simpler because of the disappearance of weak reflections. At 353 K, the specimen is transformed into the high-temperature phase, whose diffraction data completely agree with the literature data for the tetragonal TlS [7] (table). The differences between the diffraction spectra are insignificant. This indicates that no incommensurate phase was formed in our experiments. The simplest way of forming such phases in the structure type under consideration is the change in the thickness of the structural sheets caused by a larger number of polyhedral layers of Tl atoms.

Determination of possible variants of formation of structural sheets and an understanding of the nature of the phase transitions in the monoclinic TlS require detailed crystal-chemical analysis of the $TlGaSe_2$-type structure. Note that a crude crystallochemical analysis of the structures of this type was performed in [2, 8]. However, such an analysis is inadequate for the explanation of the details of the structural phase transition or the prediction of a possible formation of the incommensurate phase.

Each sheet consists of two identical layers of metal-atom polyhedra (Fig. 3) and is bound with other sheets by weak van der Waals interactions.

On one side of each polyhedral layer, all the halcogen atoms are located in the same plane (have the same *z* coordinate); on the other side of the layer, the halcogen atoms coordinating Tl^+ and Tl^{3+} (Ga) ions are at different *z* levels. The layers consist of the columns, which are formed by the Tl^+ prisms, and the chains of Tl^{3+} (Ga) tetrahedra. In $TlGaSe_2$, the adjacent layers are rotated by 90°. In the sheets, the tetrahedra share vertices to form (Tl_4S_{10}) Ga_4Se_{10} groups. The tetrahedral Tl_4S_{10} groups are arranged in a way to form octahedral voids (suitable for accommodation of Tl^+, In, Ga, Fe, and similar metals) and vacant semioctahedra “capping” one of the three faces of the prism (Fig. 3).

The prisms of Tl^+ ions form columns connected with chains of tetrahedra and, thus, form empty semioctahedra (“caps”) above the prism faces. In this case, the location of atoms inside the tetrahedra and prisms gives rise to considerable structural strain, since the resulting Tl^+–Tl^+ and Tl^+–Tl^{3+} distances are almost equal (≅3.80 Å), which is energetically unfavorable for the Tl^+ and Tl^{3+} ions having different radii (1.36 and 1.05 Å, respectively). Apparently, this fact partly explains the instability of the structure and formation of polytypes.

In addition to the above-described variant of the formation of sheets from identical polyhedral layers, three more variants of sheets can be modeled. In two of them, the width of the sheets and the *c* parameter are the same as in $TlGaSe_2$. In the first variant, two parallel layers are linked into the sheet without 90° rotation and the columns of prisms overlap in a way similar to that observed in the GaSe, MoS_2, and $TlInS_2$ III structures. In this variant, two sheets are formed by the layers having orientations (1) and (4) in Fig. 3. The tetrahedral Tl_4S_{10} groups share edges to form double tetrahedral ribbons with octahedral voids.

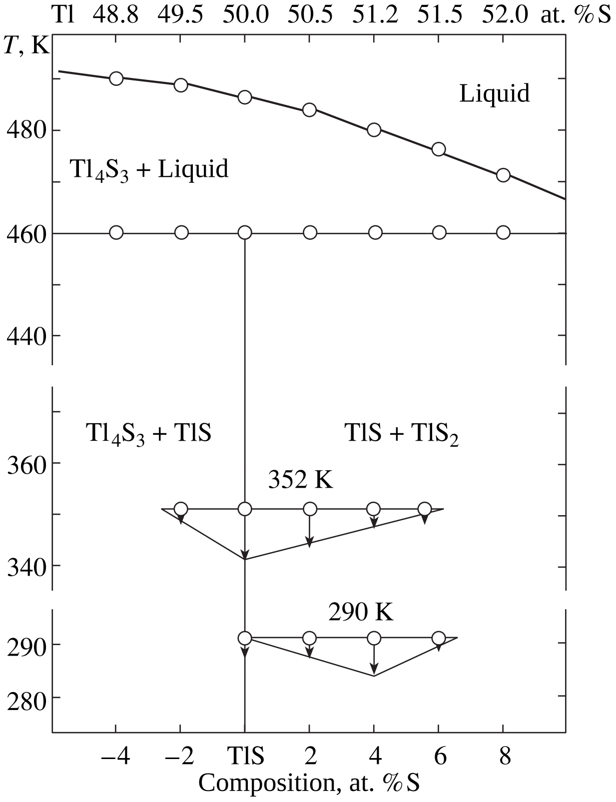

Fig. 2. Phase diagram of the Tl–S system in the range of existence of the monoclinic phase of TlS. (The Tamman triangles are based on the DTA data.)

The second sheet variant differs from the first one in the shift of its layers by the length of the prism or tetrahedron edge. Here, the prisms are interlinked by semioctahedra, and the coordination number of Tl^+ ions increases from six to seven. In the variants discussed, the monoclinicity angle of the cell apparently decreases, thus increasing the structure tetragonality.

Finally, the third variant is derived from the second by turning both polyhedral layers over 180° and linking the upper layer of the first sheet with the bottom layer of the second sheet [orientations (1) and (2) in Fig. 3]. In this case, the columns of prisms of Tl^+ ions are bound by the chains of tetrahedra of Tl^{3+} ions and form a sheet, whose thickness is slightly less than the thicknesses of the three previous variants. The thickness of this sheet changes, because halcogens of the prisms and the tetrahedra are located at different levels (spaced by ~1.75 Å). In the process of compound synthesis and single-crystal growth, one of the above variants is implemented or all the variants can coexist. Probably,

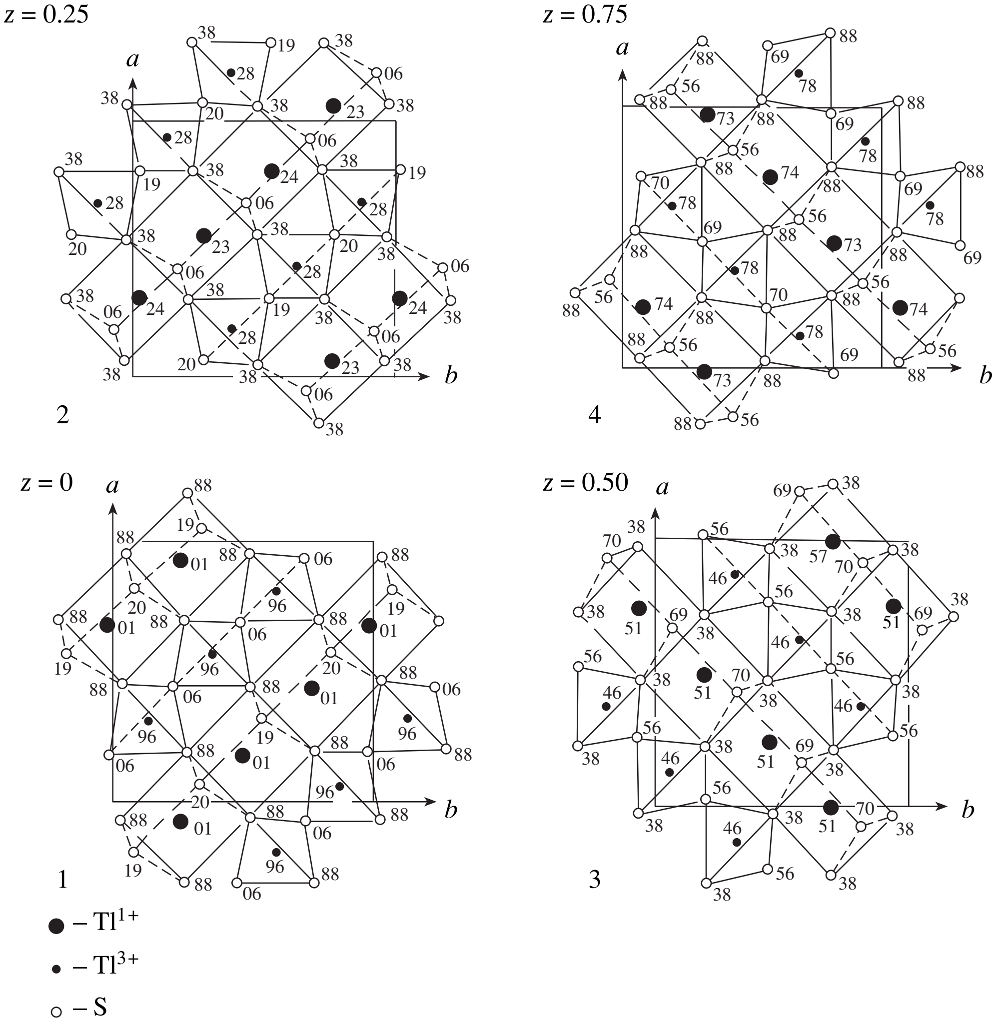

Fig. 3. Layers of polyhedra in the $TlGaSe_2$-type structure of the TlS compound at different z-levels. The atomic coordinates are given in fractions of the c-parameter multiplied by a factor of 10^2.

this can explain the inconsistent data on polytypism and phase transitions in the structures of this type and possible formation of incommensurate phases.

The diffractometry data for polycrystalline TlS specimens at varying temperature lead to the conclusions that (1) below 320 K, polycrystalline TlS is a polytype with parameter $c = 4 \times 15.04$ Å and that (2) the temperature rise decreases the pseudoperiod along the c-axis. The corresponding structure is a four- and two-sheet polytype. The structure transformation to the tetragonal phase is observed at about 353 K. Note that the transition of the monoclinic phase to the tetragonal one can proceed by levelling of the z-coordinates of Tl^{1+} atoms.

REFERENCES

1. H. Hahn and W. Kleingler, Z. Anorg. Chem. **260**, 110 (1949).
2. D. Muller and H. Hahn, Z. Anorg. Allg. Chem. **438**, 258 (1978).
3. W. H. Bragg, *Atomic Structure of Minerals* (1937), p. 77.
4. S. Kashida, K. Nakamura, and S. Katayama, Solid State Commun. **82**, 127 (1992).
5. M. Hansen and K. Anderko, *Constitution of Binary Alloys*, 2nd ed. (McGraw-Hill, New York, 1958; Metallurgizdat, Moscow, 1962), Vol. 2.
6. P. I. Feodorov, M. V. Mokhosoev, and F. P. Alekseev, *Chemistry of Gallium, Indium, and Thallium* (Nauka, Novosibirsk, 1977).
7. H. Hahn and W. Klinger, Z. Anorg. Chem. **260**, 116 (1949).
8. W. Henkel, H. D. Hocheiner, C. Carlone, *et al.*, Phys. Rev. **1326**, 3211 (1982).

Translated by I. Polyakova

Crystallography Reports, Vol. 45, No. 4, 2000, pp. 555–559. Translated from Kristallografiya, Vol. 45, No. 4, 2000, pp. 611–616.
Original Russian Text Copyright © 2000 by Lebedev, Michurin, Sluchinskaya, Demin, Munro.

Structure and Electric Properties of $InTe_{1-x}Se_x$, $In_{1-x}Ga_xTe$, and $In_{1-x}Tl_xTe$ Solid Solutions

A. I. Lebedev*[1], A. V. Michurin*, I. A. Sluchinskaya*, V. N. Demin, and I. Munro****

** Physics Department, Moscow State University, Vorob'evy gory, Moscow, 119899 Russia*

*** Daresbury Laboratory, Warrington, WA4 4AD United Kingdom*

Received March 22, 1999

Abstract—The local environment of Ga, Tl, and Se atoms in InTe-based solid solutions have been studied by the method of EXAFS spectroscopy. It is shown that these atoms can be regarded as substitutional impurities occupying the In(1), In (2), and Te positions in the InTe structure. Electric measurements showed that the $In_{1-x}Ga_xTe$ and $InTe_{1-x}Se_x$ solid solutions are semiconductors at $x > 0.24$ and $x > 0.15$, respectively. © *2000 MAIK "Nauka/Interperiodica".*

INTRODUCTION

An interest in InTe-based solid solutions is stimulated by the search for new narrow-band semiconductors that can be formed as a result of semimetal–semiconductor transitions occurring during the isoelectronic substitutions in these crystals. An example of such solid solution is $In_{1-x}Tl_xTe$, where substitution of some indium atoms by thallium results in the appearance of semiconductor properties at $x > x_c \approx 0.07$ [1, 2].

Since the physical properties of solid solutions are determined by the positions of introduced atoms, the structural studies of such solutions are quite timely.

Below, we report the results of the study of the InTe-based solid solutions of the compositions InTe: $In_{1-x}Ga_xTe$, $InTe_{1-x}Se_x$, and $In_{1-x}Tl_xTe$ crystallizing in the tetragonal system, sp. gr. $I4/mcm$ (the TlSe structure type).

Metal atoms in the InTe structure occupy two positions (Fig. 1). The In(1) atoms in the 4(*b*) position are tetrahedrally coordinated with four chalcogen atoms and form the chains along the *c*-axis. The In–Te bond in these chains is mainly of the covalent nature. The In(2) atoms in the position 4(*a*) also form chains, but they are surrounded with eight chalcogen atoms occupying the 8(*h*) positions. The atoms in the In(1) position have a valence +3, the atoms in the In(2) position, the valence +1.

The present study was aimed to substitute all the Te positions in InTe structure by the Se atoms in order to obtain the semiconductor properties. Proceeding from the data known for $InTlTe_2$ [3], we assumed that Tl^{+1} would substitute indium atoms in the position In(2), whereas small Ga^{3+} ions would occupy the In(1) positions.

The nearest environment of Ga, Se, and Tl atoms in the solid solutions were determined by the method of EXAFS spectroscopy [4]. The EXAFS data were complemented with the X-ray data and provided the determination of the existence range and the ranges of the variations of the crystal-lattice parameters for the above solid solutions.

SPECIMENS

Polycrystal and single crystal specimens of $InTe_{1-x}Se_x$, $In_{1-x}Ga_xTe$, and $In_{1-x}Tl_xTe$ solid solutions were synthesized from binary InTe, InSe, GaTe, and TlTe compounds in sealed quartz ampoules. The single-phase solid solutions were synthesized at compositions with $x \le 0.5$ for the first and the third solid solutions, and with $x \le 0.4$ for the second solid solution.

The EXAFS and X-ray measurements were performed on annealed polycrystal alloys. Prior to EXAFS measurements, the alloys were ground into powders, screened through a sieve, and then applied onto an adhesive plastic tape. The optimum thickness of the

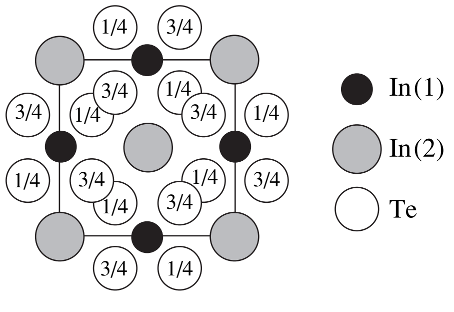

Fig. 1. InTe structure projected onto the *ab* plane. Indium atoms form chains along the *c*-axis and are located at heights 0 and 1/2.

---

[1] *e-mail: swan@mch.chem.msu.su, ail-f@scon.phys.msu.su*

1063-7745/00/4504-0555$20.00 © 2000 MAIK "Nauka/Interperiodica"

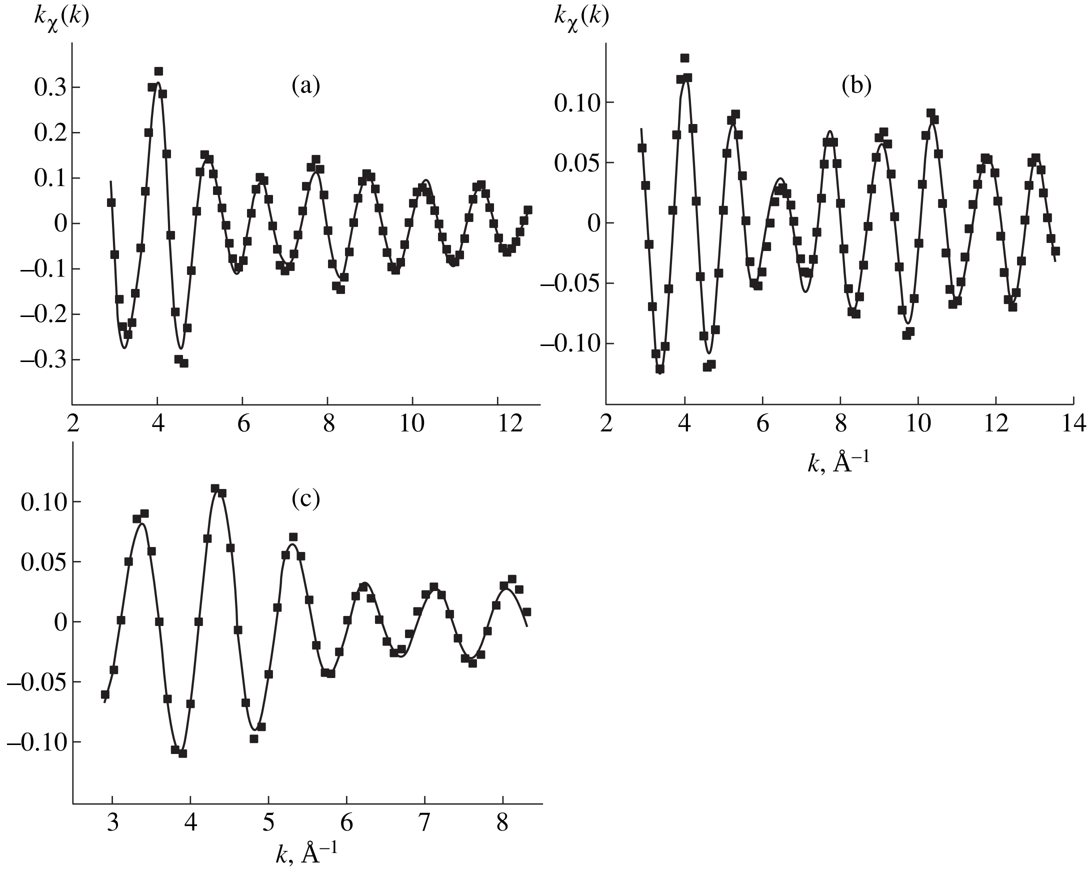

Fig. 2. EXAFS spectra obtained (a) at the *K*-absorption edge of Ga in an $In_{0.8}Ga_{0.2}Te$ specimen, (b) at the *K*-absorption edge of Se in an $InTe_{0.8}Se_{0.2}$ specimen, (c) at the L_{III} absorption edge of Tl atoms in an $In_{0.8}Tl_{0.2}Te$ specimen. Filled squares indicate the experimental data plotted on the theoretically calculated line.

absorbing layer was attained by folding the tape and usually consisted of eights layers.

Since the parameter x of the Bridgman-grown single crystals varied along the growth direction, the specimens of different compositions were prepared from various parts of the ingot. Prior to the determination of the specimen composition, we determined the *a*- and *c*-parameters by the X-ray diffraction method on a diffractometer (CoK_α radiation). The $a(x)$ and $c(x)$ dependences were calibrated using the standard $InTe_{1-x}Se_x$ and $In_{1-x}Ga_xTe$ specimens with $x = 0$, 0.1, 0.2, 0.3, 0.4, and 0.5. The $In_{1/2}Ga_{1/2}Te$ specimen ($x = 0.5$) consisted of several phases and, therefore, was not used for the construction of the calibration curves. The data obtained were processed by the least squares method and yielded the following lines:

$$a(x) = 8.4343 - 0.284x,$$

$$c(x) = 7.1452 - 0.381x \quad (InTe_{1-x}Se_x),$$

$$a(x) = 8.4320 - 0.084x,$$

$$c(x) = 7.1482 - 0.656x \quad (In_{1-x}Ga_xTe).$$

The composition parameter x was determined from the lattice parameter c strongly dependent on the composition. The error in the x determination did not exceed 2%.

The X-ray data showed that the composition parameter x in $InTe_{1-x}Se_x$ crystals increased along the ingot length, whereas in the $In_{1-x}Ga_xTe$ crystals, it slowly decreased along the ingot length.

The electric measurements were made by the four-probe method on specimens cleaved along the *c*-axis of the single crystals in the shape of 1 × 1 × 5-mm sticks. The low-resistance (closed) current and potential contacts were prepared by soldering with indium using the NH_4Cl fusing agent.

EXPERIMENTAL

The EXAFS measurements. The EXAFS spectra were measured in the transmission geometry at 80 K on the 7.1 station of the synchrotron radiation source (2 GeV, 240 mA) of the Daresbury Laboratory, UK. The spectra were obtained on *K*-absorption edges of Ga (10367 eV) and Se (12658 eV) and the L_{III}-absorption edge of Tl (12658 eV). The parameter S_0^2 (describing a decrease of the oscillation amplitude due to inelastic

Parameters of the local structure for InTe and InTe-based solid solutions

Specimen	InTe*	$In_{0.8}Ga_{0.2}Te$	$InTe_{0.8}Se_{0.2}$	$InTe_{0.7}Se_{0.3}$	$In_{0.8}Tl_{0.2}Te$**	$InTlTe_2^{**}$
Standard	InSb	Ga_2Te_3	InSe	InSe	TlI	TlI
R_1, Å	2.821(2)	2.643(4)	2.607(3)	2.605(3)	3.541(9)	3.561(6)
N_1	2.1(1)	4.2(3)	1.8(1)	1.7(1)	10.6(13)	12.3(14)
σ_1^2, Å^2	0.0021(3)	0.0043(5)	0.0016(4)	0.0013(4)	0.0138(15)	0.0134(8)
R_2, Å	3.541(8)	3.497(28)	3.526(43)	3.528(53)	4.313(25)	4.278(16)
N_2	6.4(4)	2.1(2)	3.5(2)	3.3(2)	4.2(5)	4.9(6)
σ_2^2, Å^2	0.0117(10)	0.0038(40)	0.049(10)	0.055(13)	0.0245(55)	0.0203(32)
R_3, Å	4.215(12)	4.272(28)	3.823(15)	3.821(16)		
N_3	6.4(4)	4.2(3)	1.8(1)	1.7(1)		
σ_3^2, Å^2	0.0136(19)	0.0179(56)	0.0027(14)	0.0015(15)		

* Spectra recorded at the *K*-absorption edge of In were obtained experimentally at the X23A2 NSLS station. When calculating the theoretical spectra, we took into account the fact that In atoms occupy two different positions and have different local environments.

** Processing the data obtained at the Tl-absorption edge, we assumed that eight Te atoms and two metal atoms are located at the same distance.

and multielectron effects [4]) necessary for the correct determination of the coordination numbers was measured on the standard compounds—InSe (the Se edge), Ga_2Te_3 (the Ga edge), and TlI (the Tl edge).

The details of the experiment and processing of EXAFS spectra were described elsewhere [5].

Figure 2a shows the characteristic EXAFS spectrum for the $In_{0.8}Ga_{0.2}Te$ specimen. The analysis of the first coordination sphere showed that gallium atoms are surrounded with four tellurium atoms at distances 2.64 Å (see table), which indicates that Ga atoms occupy the In(1) positions in the solid solution. These distances are close to the Ga–Te (2.61 Å) distances determined earlier for Ga_2Te_3, where Ga atoms are tetrahedrally coordinates with Te, which indicates the covalent character of the Ga–Te bonds in the solid solution studied. The location of Ga atoms is confirmed by the analysis of Ga positions in the second and third coordination spheres within the same chain along the *c*-axis and normally to it. The distances to these atoms obtained from the EXAFS data are consistent with the X-ray data. These distances are slightly shorter than the corresponding In–In distances in InTe, whereas the Ga–Te distance is shorter by 0.18 Å than the In(1)–Te distance in InTe (see table).

Figure 2b shows the typical EXAFS spectrum of the $InTe_{0.8}Se_{0.2}$ specimen, where Se atoms are surrounded with In atoms spaced by 2.61 Å. The latter distance is close to the length of the covalent In–Se bond in InSe (2.615 Å), which indicates that In–Se bond in the solid solution studied is also of the covalent nature. The same coordination numbers for Se and Te atoms in the InTe structure and the corresponding bond lengths lead to the conclusion that selenium atoms substitute Te atoms in the solid solution. The Se–In(1) distance is shorter by 0.22 Å than the Te–In(1) distance in InTe. The second coordination sphere of the selenium atom (four atoms in the In(2) position) is rather spread and is characterized by a surprisingly high value of the Debye–Waller factor. However, the analysis shows a considerable contributions from the atoms of the third coordination sphere (the closest chalcogen atoms in a slightly distorted square antiprism).

The analysis of the EXAFS spectrum of the $In_{0.8}Tl_{0.2}Te$ specimen (Fig. 2c) shows that Tl atoms substitute In in the In(2) position. The Tl–Te distances in the $In_{0.8}Tl_{0.2}Te$ solid solution and in the $InTlTe_2$ compound (isostructural to InTe)[2] are close to the In(2)–Te distance in InTe. One should pay attention on rather high values of the Debye–Waller factors obtained for the Tl–Se bonds.

Electrical properties. The $\rho(T)$ curves were studied for the $InTe_{1-x}Se_x$ and $In_{1-x}Ga_xTe$ solid solutions.[3]

Figure 3a shows the $\log\rho\,(10^3/T)$ curves for the $In_{1-x}Ga_xTe$ specimens. The temperature dependences of resistivity of all the specimens are of the thermoactivation nature. The curves have two clearly seen portions characterized by different activation energies and a kink in the vicinity of 140 K. We identified the high-temperature portion of the curve with intrinsic conductivity, and the low-temperature one, with impurity or hopping conductivity. The inset in Fig. 3a shows the band gap E_g (calculated as a double activation energy

---

[2] The $InTlTe_2$ compound is the limiting case of the $In_{1-x}Tl_xTe$ solid solution, where all the In(2) positions are occupied with Tl and all the In(1) positions, with indium.

[3] The electrical properties of the $In_{1-x}Tl_xTe$ solid solution are studied in detail elsewhere [1, 2, 6].

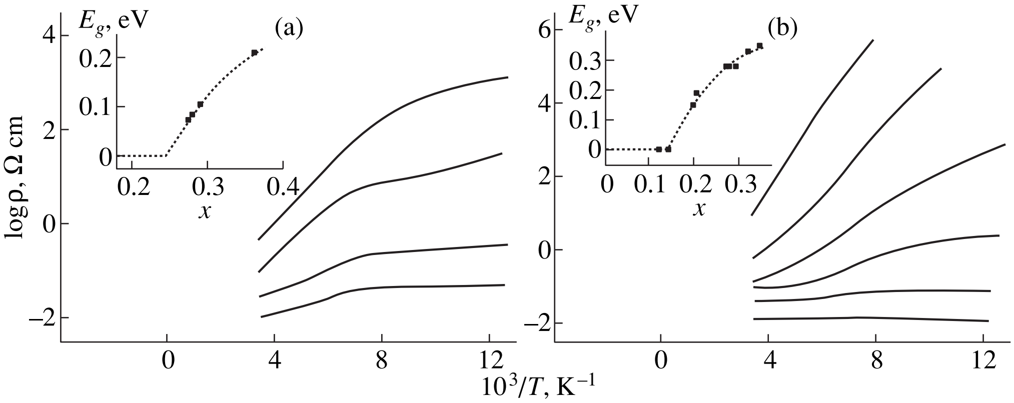

Fig. 3. Characteristic temperature dependences of resistivity for (a) $In_{1-x}Ga_xTe$ and (b) $InTe_{1-x}Se_x$ specimens. In the inset: the band gap as a function of the composition parameter.

on the high-temperature portion) as a function of the composition parameter x. Extrapolation of this dependence to the values $E_g \longrightarrow 0$ yielded composition parameter $x_c \approx 0.24$, above which the $In_{1-x}Ga_xTe$ crystals acquire semiconductor properties.

Figure 3b shows the $\log\rho\,(10^3/T)$ curves for the $InTe_{1-x}Se_x$ specimens. Various crystals showed both the thermoactivated $\rho(T)$ curves and the metallic (temperature-independent) ρ curves. The band gap (calculated as the double activation energy at the portion with the maximum slope) as a function of x is shown in the inset in Fig. 3b. It is seen that $InTe_{1-x}Se_x$ crystals acquire the semiconductor properties at $x > x_c \approx 0.15$.

DISCUSSION

The data obtained allow the determination of the atomic portions in InTe-type structures.

The EXAFS data show that Ga and Tl atoms occupy the highly symmetric In(1) and In(2) positions in the InTe structure, respectively. The positions of chalcogen atoms in the InTe structure are described by the parameter u. Unfortunately, the exact determination of this parameter in solid solutions is impossible because of the random character of atomic substitutions. Therefore, we considered the limiting compositions of the solid solutions studied, namely, the hypothetical compound of the composition $In_{1/2}Ga_{1/2}Te$,[4] in which all the In(1) positions are occupied by Ga atoms and also the hypothetical compound InSe with the InTe structure. In order to determine the parameter u, we used the crystal-lattice parameter and the Ga–Te and In(1)–Se distances determined by the EXAFS method. The a- and c-parameters of these hypothetical compounds were obtained by extrapolating the dependences of the lattice parameters determined for the solid solutions. The interatomic distances in the above compounds were assumed to be equal to the distances determined for the solid solutions. This approximation was based on the well known fact that the chemical bond length only weakly depends on the solid-solution composition, which is also confirmed by our experimental data.

The parameter for Te atoms in $In_{1/2}Ga_{1/2}Te$ was determined as $u_{Te} = 0.170$, whereas the calculated In(2)–Te distance is equal to 3.55 Å, i.e., almost coincides with that given for InTe (see table). In the hypothetical InSe compound with the InTe structure $u_{Se} = 0.172$, whereas the In(2)–Se distance equals 3.46 Å. Upon the Te $\longrightarrow$ Se substitution, In(1)–chalcogen distance is shortened by 0.22 Å, whereas the In(2)–chalcogen distance, only by ~0.1 Å.

The EXAFS data for the $InTlTe_2$ compound agree with the results of X-ray studies.[5] As was indicated above, the distance between the metal atom in the In(2) position and the tellurium atom in the $In_{1-x}Tl_xTe$ solid solution only slightly changes upon the substitution of indium by thallium and is less than the difference between the ionic radii of Tl^+ and In^+ (0.06 Å [9]).

The positions of chalcogen atoms determined indicate the distortions in the structures of the solid solutions studied. As is well known, a tetrahedron around In(1) atoms in the InTe structure is slightly elongated in the c-direction, and the corresponding Te–In(1)–Te (θ) angle equals 101°15′. In all the solid solutions, the tetrahedral distortion is more significant than in InTe: it is minimal for $In_{1/2}Tl_{1/2}Te$ ($\theta = 101°1'$), more pronounced in $In_{1/2}Ga_{1/2}Te$ ($\theta = 99°31'$), and is maximal in the hypothetical InSe with the InTe structure ($\theta = 99°2'$).

---

[4] The attempts to determine the structure of the $In_{1/2}Ga_{1/2}Te$ compound undertaken in [7] failed because the specimens contained several phases.

[5] Similar to [8], the small discrepancy between the Tl–Te distances determined from the EXAFS data (3.56 Å) and X-ray measurements (3.595 Å) can be explained by the static error in the calculation of the amplitudes and the phases for back scattering by heavy atoms in the FEFF program. The distances for the Pb atom (neighboring Tl in the Periodic table) determined from the EXAFS data are underestimated by 0.025 Å.

The results obtained clarify the role of atoms occupying the In(2) position in the InTe structure. High Debye–Waller factors determined from the EXAFS spectra for the In(2)–Te distances in InTe and $InTe_{1-x}Se_x$, and the Tl–Se distances in $In_{1-n}Tl_xTe$ (see table), the surprisingly small change in the distance between the metal in the In(2) position and the chalcogen upon the In $\longrightarrow$ Tl (<0.04 Å) and Te $\longrightarrow$ Se (about 0.1 Å) substitutions indicate weak chemical bonding between the metal atoms in this position with the surrounding chalcogen atoms. In other words, the In(2) position in the InTe structure plays the part of a specific cavity for single-charged ions in order to provide the electrical neutrality of the specimen as a whole. This role of the In(2) position allows the interpretation of the experimental fact that the substitution of In(2) atoms with the single-charged ions with considerably different radii (Na, K, and Tl) provides the preservation of the InTe structure.

It seems that a drastic increase of the Debye–Waller factor for the In(2)–Se distances in the $InTe_{1-x}Se_x$ solid solution is associated with the noticeable displacement of In(2) atoms from the highly symmetric position because of the changed symmetry of their environment caused by random substitution of chalcogen atoms. The low values of the small Debye–Waller factor for the In(1)–Se and Se–chalcogen distances show that the displacement of In(1) and chalcogen atoms in the solid solution is insignificant.

Comparing the electric properties of various InTe-based solid solutions, one cannot help but notice the anomalous behavior of the $\rho(T)$ curves in the $InTe_{1-x}Se_x$ specimens showing the semiconductor properties. In the high-temperature range, these curves considerably deviate from the expected thermoactivation dependences (this was never observed for the $In_{1-x}Ga_xTe$ and $In_{1-x}Tl_xTe$ solid solutions [2]). High values of the Debye–Waller factors for atoms in the In(2) position in all the studied solid solution, and surprisingly large In(2)–Se distances in the hypothetical InSe compound with the InTe structure, indicate a considerable increase of the size of the cavity filled with In(2) atoms. A considerable increase of the anharmonicity of In(2) motion can make the temperature variation in the band gap nonlinear, which, finally, results in the deviation of the $\rho(T)$ curves from thermally activated curves in the high-temperature range.

Concluding the article, we should like to indicate that all the InTe-based solid solutions have a characteristic feature. The substitutions of atoms in all the positions result in the formation of semiconductor properties. Qualitatively, this can be interpreted in the following way. The character of filling of the energy bands in indium telluride is close to that in semiconductors. However, some individual characteristics of the constituent atoms make the bottom of the conduction band in InTe slightly lower than the ceiling of the valence band, which results in a semimetal behavior. The strengthening of covalent bonding (because of a reduction of interatomic bonds within tetrahedra) upon the substitution of atoms in the $In_{1-x}Ga_xTe$ and $InTe_{1-x}Se_x$ solid solutions increases the splitting of the hybridized orbitals, "opens" the energy gap in the electron spectrum, and finally provides the appearance of semiconductor properties. In the $In_{1-x}Tl_xTe$ solid solution, the covalent bond lengths remain constant, and the semiconductor properties are caused by another reason. Since the contribution of the *s*-states into the states of the valence band are usually more pronounced than they are to the states of the conduction band, and 6*s* states of Tl are deeper than the 5*s* states of In (because of considerable relativistic corrections), the In $\longrightarrow$ Tl substitutions shift the valence band lower, an energy gap is formed in the electron spectrum, and crystals acquire semiconductor properties.

REFERENCES

1. C. A. Gaw and C. R. Kannewurf, J. Appl. Phys. **38**, 634 (1981).
2. B. A. Akimov, A. V. Albul, A. V. Davydov, *et al.*, Fiz. Tverd. Tela (Leningrad) **28**, 2680 (1986) [Sov. Phys. Solid State **28**, 1502 (1986)].
3. D. Müller, G. Eulenberger, and H. Hahn, Z. Anorg. Allg. Chem. **398**, 207 (1973).
4. D. I. Kochubeĭ, Yu. A. Babanov, K. I. Zamaraev, *et al.*, *X-ray Spectral Method for Studying Structures of Amorpheres Bodies: EXAFS Spectroscopy* (Nauka, Novosibirsk, 1988).
5. A. I. Lebedev, I. A. Sluchinskaya, V. N. Demin, and I. H. Munro, Izv. Ross. Akad. Nauk, Ser. Fiz. **60** (10), 46 (1996).
6. B. A. Akimov, A. V. Albul, N. B. Brandt, *et al.*, Fiz. Tverd. Tela (Leningrad) **29**, 16 (1987) [Sov. Phys. Solid State **29**, 8 (1987)].
7. H.-J. Deiseroth, D. Müller, and H. Hahn, Z. Anorg. Allg. Chem. **525**, 163 (1985).
8. A. I. Lebedev, I. A. Sluchinskaya, V. N. Demin, and I. H. Munro, Pis'ma Zh. Éksp. Teor. Fiz. **63**, 600 (1996) [JETP Lett. **63**, 635 (1996)].
9. *Properties of Inorganic Compounds*, contributions by A. I. Efimov *et al.* (Khimiya, Leningrad, 1983).

Translated by L. Man

Crystallography Reports, Vol. 45, No. 4, 2000, pp. 560–562. Translated from Kristallografiya, Vol. 45, No. 4, 2000, pp. 617–619.
Original Russian Text Copyright © 2000 by Kyazumov.

STRUCTURE OF INORGANIC COMPOUNDS

Polytypism and Superstructure in $CoInGaS_4$

M. G. Kyazumov[1]

Institute of Physics, Academy of Sciences of Azerbaidzhan, pr. Narimanova 33, Baku, 370143 Azerbaidzhan

Received June 10, 1998; in final form, March 29, 1999

Abstract—It is established that a one-layer polytype 1*T* with the unit-cell parameters $a = 3.758$, $c = 12.135$ Å, sp. gr. $P3m1$ and the structure module ${}_hT_hO_hT_hE$ is mixed with the three-layer polytype 3*R* with the unit-cell parameters $a = 3.758$, $c = 36.405$ Å, sp. gr. $R3m$ and the structure module ${}_hT_cO_cT_hE$, where T and O are two-dimensional nets of tetrahedra and octahedra, respectively, E is the empty intermediate layer, and h and c indicate the hexagonal and cubic packings of atomic planes S. The microdiffraction pattern in the hexagonal basis shows a monoclinic superlattice with the parameters $A = \sqrt{19}\,a$, $B = \sqrt{13}\,a$, $\gamma = 110.485°$ related to the main hexagonal lattice as $A = [520]$ and $B = [\bar{1}30]$. © *2000 MAIK “Nauka/Interperiodica”.*

The $CoInGaS_4$ compound was obtained by the sintering of CoS and $GaInS_3$ in the equimolecular ratio in a sealed ($p \leq 10^{-2}$ Pa) quartz ampule. The solid-phase synthesis was performed for 120 h at the temperature 1100 K. Then the temperature in the furnace was decreased (at a rate of 30 K/h) to 900 K. To provide the completion of the solid-state reaction, the ampule was kept for 240 h at 900 K, then the temperature in the furnace was lowered to 600 K, the reaction products were annealed at this temperature for quite a long time.

The specimens for electron diffraction study were obtained by precipitating microcrystals from the aqueous suspension onto the metal grid coated with a celluloid film with the thickness of about several tens of angstroms. Electron diffraction patterns were obtained in an electron diffraction camera (produced at Institute of Geology of Ore Deposits, Petrography, Mineralogy, and Geochemistry, RAS), the microdiffraction pattern was obtained in a BS-500 electron microscope (Czechoslovakia).

The oblique-texture type electron diffraction patterns (Fig. 1) showed that $CoInGaS_4$ consists of two polytypes 1*T* and 3*R* [1] also observed in the layer compounds $ZnIn_2S_4$ [2, 3] and $CdInGa(Al)S_4$ [4, 5]. In our case, the one-layer hexagonal 1*T* polytype had the unit-cell parameters $a = 3.758$, $c = 12.135$ Å, $\gamma = 120°$, sp. gr. $P3m1$ and the structure module ${}_hT_hO_hT_hE$. The three-layer 3*R* polytype has the lattice parameters $a = 3.758$, $c = 36.405$ Å, sp. gr. $R3m$ and the structure module ${}_hT_cO_cT_hE$, where T and O indicate tetrahedra and octahedra, respectively, E is the empty intermediate layer, h and c indicate the atomic planes S in the hexagonal and cubic close packings [1].

The microdiffraction pattern of the basis plane (Fig. 2) shows a system of weak reflections against the background of strong ones. The weak net corresponds to the major periodicity of the atomic packing S and is a two-dimensional hexagonal lattice in the reciprocal space with the parameters $a_1^* = a_2^* = a^*$ and the angle $\gamma^* = 60°$. The unit cell of the first lattice can be chosen by six ways that differ by rotation for angles multiple to 60°. The second net corresponds to the superperiodicity rationally related to the periodicity of the first net, because the reflections of the first net coincide with some reflections of the second net. The unit cell of the second net A^*, B^*, γ^* is monoclinic and can be chosen by a large number of ways. If the first cell is chosen with the angle γ^* close to 90°, then, in accordance with the spot-type electron-diffraction pattern shown in Fig. 2, the unit-cell parameters of these lattices are related as $\mathbf{a}_1^* = 5\mathbf{A}^* - \mathbf{B}^*$ and $\mathbf{a}_2^* = 2\mathbf{A}^* + 3\mathbf{B}^*$ and characterized by the matrix (5, –1/2, 3) with the determinant equal to 17.

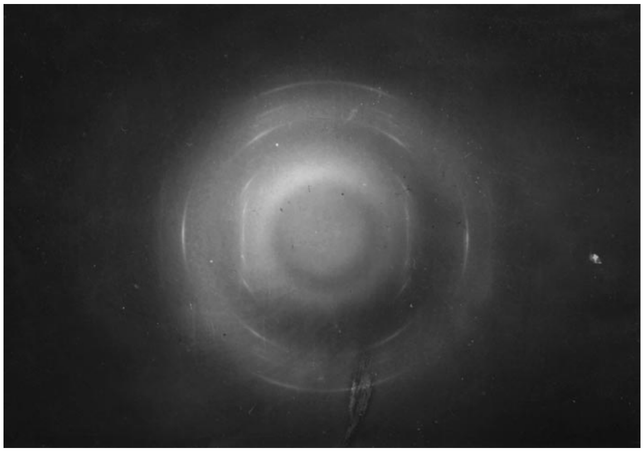

Fig. 1. Texture-type electron diffraction pattern from $CoInGaS_4$.

---

[1] *e-mail: physic@lan.ab.az*

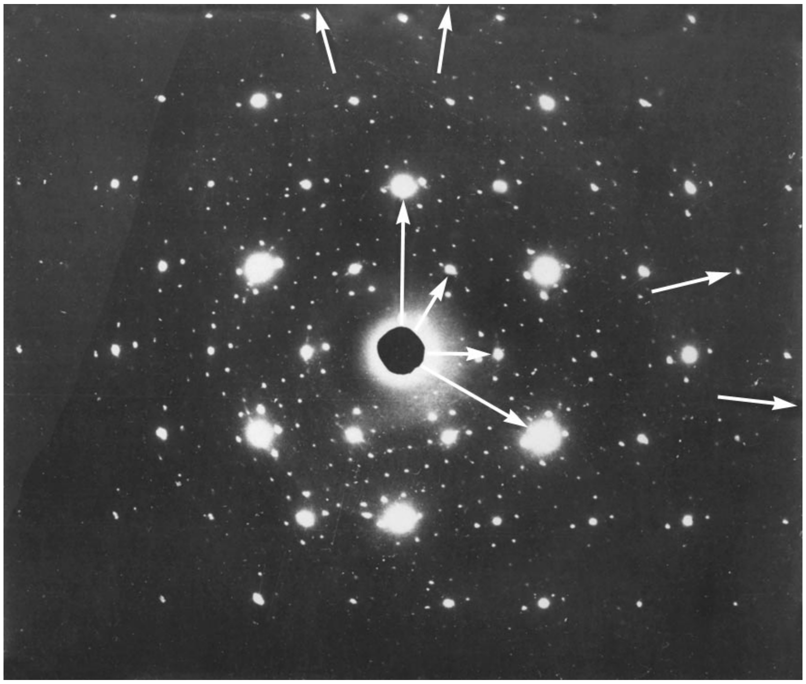

Fig. 2. Electron diffraction patterns from a $CoInGaS_4$ single crystal.

The inverse transformation at $a_1^* = a_2^* = a^*$ yields

$$\mathbf{A}^* = (3\mathbf{a}_1^* + \mathbf{a}_2^*)/17 = [31]\mathbf{a}^*/17,$$

$$\mathbf{B}^* = (-2\mathbf{a}_1^* + 5\mathbf{a}_2^*)/17 = [\bar{2}5]\mathbf{a}^*/17.$$

Indeed, the spot-type electron diffraction pattern in Fig. 2 has some weak superreflections along the [31]- and [25]-directions which divide the distances between the main reflections by 17 equal parts. This provides the determination of the superlattice $\mathbf{A}^*$, $\mathbf{B}^*$ at the fixed parameters $\mathbf{a}_1^*$, $\mathbf{a}_2^*$ of the main cell.

Using the well-known formulas of the electron diffraction analysis [6], we established that the above linear equations correspond to the following relationships between the lattice parameters in the direct space (which are characterized by the transposed matrices)

$$\mathbf{A} = 5\mathbf{a}_1 + 2\mathbf{a}_2 = [52]a, \quad \mathbf{a}_1 = (3\mathbf{A} - 2\mathbf{B})/17,$$

$$\mathbf{B} = -\mathbf{a}_1 + 3\mathbf{a}_2 = [\bar{1}3]a, \quad \mathbf{a}_2 = (A + 5B)/17.$$

The formation of a superperiodicity in the basis plane for similar compounds studied earlier [1, 7] was interpreted as the result of ordering of vacancies and isomorphous substitutions in the T and O nets and partial filling of an empty intermediate layer. Similar to the initial unit cells, the supercells were hexagonal and were multiple to three, four or seven primitive cells (multiplicity $N = 3$, 4, and 7). One crystal can have different N values for different substructures consisting either of T- or O-nets alone.

One can readily see that calculating the absolute magnitudes of the vectors by the vector relationships, one can obtain their scalar and vector products with due regard for the hexagonal basis ($a_1 = a_2 = a = 3.758$ Å, $\cos\gamma = -1/2$) and the direct and reciprocal lattice parameters:

$$A^* = \frac{\sqrt{13}}{17}a_1^*, \quad B^* = \frac{\sqrt{19}}{17}a_2^*,$$

$$\gamma^* = A^*B^* = 69.515^\circ,$$

$$A = \sqrt{19}a, \quad B = \sqrt{13}a, \quad \angle(A, B) = 110.485^\circ.$$

The area of the superlattice is equal to

$$S = [A * B] = [a_1\ a_2]\begin{vmatrix} 5 & 2 \\ \bar{1} & 3 \end{vmatrix} = 17[a_1\ a_2] = 17s.$$

Thus, unlike the case described in [1, 7], in our case, the formation of a monoclinic superlattice on the basis of the hexagonal lattice was observed. This monoclinic superlattice is related to the initial lattice by the above linear vector equations illustrated for the direct and the reciprocal lattice vectors against the background of the hexagonal point net in Fig. 3. In fact, this net cannot be the same for the direct and the reciprocal vectors. On an arbitrary scale, it can only show the relation between their directions (perpendicularity of A and B^*, etc.).

According to the formula of the compound, the superperiodicity in the absence of vacancies can be

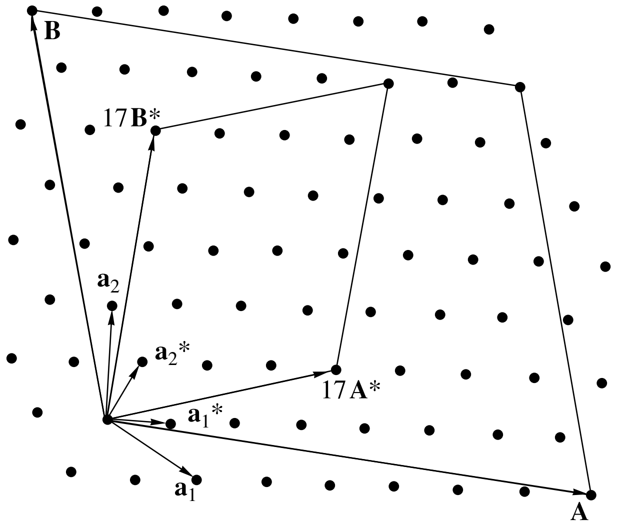

Fig. 3. Schematic hexagonal net for main spot-type reflections in the microdiffraction pattern shown in Fig. 2 and the linear relationships for the $\mathbf{a}_1^*$, $\mathbf{a}_2^*$ and 17**A***, 17**B*** vectors and also, on an arbitrary scale, for the $\mathbf{a}_1$, $\mathbf{a}_2$ and **A**, **B** vectors (for a more clear representation, weak superreflections are omitted).

explained by ordering and isomorphous substitutions of Co, In, and Ga cations, which results in various occupancies of primitive unit cells within the superlattice, so that these cells stop being identical. If such ordering occurred by different laws for each of the T- and the O-nets, then the substructures with different superlattices would have overlapped. Then these superlattices would have differed not only by orientations [1, 7, 8] and multiplicities N [1, 7], but also, as it became clear in this study, by their geometries (monoclinic, orthogonal). Although we observed no such combinations, in principle they are quite possible in similar compounds.

ACKNOWLEDGMENTS

The author is grateful to A. M. Fominenkov for his help in taking electron diffraction patterns and to A. S. Avilov for his valuable remarks.

REFERENCES

1. B. B. Zvyagin and M. G. Kyazumov, Izv. Ross. Akad. Nauk, Ser. Fiz. **57** (2), 22 (1993).
2. F. G. Donika, S. I. Radautsan, S. A. Semiletov, *et al.*, Kristallografiya **15** (4), 813 (1970) [Sov. Phys. Crystallogr. **15** (4), 695 (1970)].
3. F. G. Donika, S. I. Radautsan, G. A. Kiosse, *et al.*, Kristallografiya **15** (4), 816 (1970) [Sov. Phys. Crystallogr. **15** (4), 698 (1970)].
4. M. G. Kyazumov, A. P. Zhukhlistov, A. M. Fominenkov, and B. B. Zvyagin, in *Proceedings of the All-Union Conference on Electronic Microscopy, Sumy, 1987*, Vol. 2, p. 453.
5. A. G. Abdyllayev and M. G. Kyazumov, Thin Solid Films **190**, 303 (1990).
6. N. V. Belov, *Structural Crystallography* (Izd. Akad. Nauk SSSR, Moscow, 1951).
7. B. B. Zvyagin and M. G. Kyazumov, Kristallografiya **35** (5), 1290 (1990) [Sov. Phys. Crystallogr. **35** (5), 761 (1990)].
8. B. B. Zvyagin and K. Fichter, Bull. Mineral. **109**, 45 (1986).

Translated by L. Man

Crystallography Reports, Vol. 45, No. 4, 2000, pp. 563–567. Translated from Kristallografiya, Vol. 45, No. 4, 2000, pp. 620–624.
Original Russian Text Copyright © 2000 by Kosterina, Rybakov, Kemnitz, Troyanov.

STRUCTURE OF INORGANIC COMPOUNDS

Crystal Structures of Two Modifications of Sodium Pentahydrogendiphosphate $NaH_5(PO_4)_2$

E. V. Kosterina*, V. B. Rybakov*, E. Kemnitz, and S. I. Troyanov***
** Chemistry Department, Moscow State University, Vorob'evy gory, Moscow, 119899 Russia*
*** Institut für Chemie, Humboldt Universität, Berlin, Germany*

Received January 10, 2000

Abstract—Two crystalline modifications of $NaH_5(PO_4)_2$ are obtained by the reaction of Na_2CO_3 with an excess of orthophosphoric acid. The crystal structures of α- and β-$NaH_5(PO_4)_2$ are determined by X-ray diffraction analysis. The crystal data are $a = 8.484(4)$ Å, $b = 7.842(3)$ Å, $c = 10.353(4)$ Å, $\beta = 90.50(3)°$, $V = 689.3(3)$ Å^3, space group $P2_1/c$, $Z = 4$, and $R_1 = 0.0250$ for the α modification and $a = 7.127(2)$ Å, $b = 13.346(4)$ Å, $c = 7.177(2)$ Å, $\beta = 95.5(2)°$, $V = 679.5(3)$ Å^3, space group $P2_1/c$, $Z = 4$, and $R_1 = 0.0232$ for the β modification. Based of the hydrogen-bond system, the formulas of the α and β modifications can be represented as $Na(H_2PO_4)(H_3PO_4)$ and $Na[H(H_2PO_4)_2]$, respectively. They correspond to the stable and metastable forms of the compound. *© 2000 MAIK "Nauka/Interperiodica".*

Formation of alkali-metal and ammonium "superacid" phosphates with the $MH_5(PO_4)_2$ composition was first observed many years ago in the studies of the ternary M_2O–H_2O–P_2O_5 systems at high P_2O_5 concentrations [1–4]. Early structural studies of pentahydrogendiphosphates were performed by Norbert [5–8] and were confined to determining the unit cell parameters and possible space groups and included indexing the powder diffraction patterns. Later, the crystal structures of potassium [9], rubidium [10], cesium [11], and thallium [12] pentahydrogendiphosphates were determined by single-crystal X-ray diffraction analysis. A single crystal of $KH_5(PO_4)_2$ was studied by neutron diffraction [13] in order to reveal the positions of hydrogen atoms and to characterize the hydrogen-bond system. Recently, the crystal structure of $(NH_4)H_5(PO_4)_2$ was determined, and the structural phase transition was observed in this material at 180–210 K [14].

Although the majority of "superacid" phosphates have been characterized rather completely, the only data available in the literature on the sodium salt $NaH_5(PO_4)_2$ are the unit-cell parameters [5, 6]. Apparently, the incompleteness of data is a consequence of the difficulties encountered in performing the experimental studies with the compound that readily hydrates and, as a result, decomposes in air. In the present work, we made an attempt to fill this gap with the X-ray single-crystal structure analysis of two crystalline modifications of $NaH_5(PO_4)_2$.

EXPERIMENTAL

Synthesis. A 83% solution of orthophosphoric acid (Merck) and sodium carbonate (analytical grade), preliminarily calcined to a constant mass, were used as the starting reactants for the preparation of sodium pentahydrogendiphosphate. The modification of $NaH_5(PO_4)_2$, which is described in the literature [5] and denoted in the present study as the α modification, is usually formed as colorless needles upon slow crystallization from an aqueous solution. The α modification was synthesized in a solution containing a 40% excess of H_3PO_4 according to the procedure described in [6]. Single crystals suitable for X-ray structure analysis were prepared by allowing the solution to stand in an evacuated desiccator under P_2O_5 for two months. The formation of the single-phase product containing only the α modification was verified by comparison of its X-ray powder diffraction pattern with the data reported in [6]. Colorless prismatic crystals of the metastable β modification were obtained from a saturated solution within several hours upon rapid cooling from 85°C to room temperature. It was found that crystals of the α modification separated from the mother liquor are stable for a long time. On the contrary, crystals of the β modification contacting the mother liquor transform into the stable α modification for 1–2 days. Both modifications of $NaH_5(PO_4)_2$ easily hydrate in air. Hence, we prepared the samples for X-ray powder diffraction analysis and chose single crystals in a dry box.

X-ray diffraction study. The X-ray structure analysis of single crystals that were chosen under a polarizing microscope and loaded in capillaries was performed at room (298 K) and low (180 K) temperatures. The X-ray diffraction data were collected at room temperature on an Enraf–Nonius CAD4 four-circle automated diffractometer and at a low temperature on a Stoe STADI4 four-circle automated diffractometer (in

Table 1. Crystal data, data collection, and refinement parameters for the α and β modifications of $NaH_5(PO_4)_2$

Modification	α	β
Crystal system	Monoclinic	Monoclinic
Space group	$P2_1/c$	$P2_1/c$
a, Å	8.484(4)	7.127(2)
b, Å	7.842(3)	13.346(4)
c, Å	10.353(4)	7.177(2)
β, deg	90.50(3)	95.51(2)
V, Å^3	689.3(3)	679.5(3)
Z	4	4
ρ(calcd), g/cm^3	2.100	2.131
μ(MoK_α), cm^{-1}	6.96	7.06
Crystal size, mm	0.8 × 0.2 × 0.2	0.5 × 0.3 × 0.3
θ range, deg	2.4–28.0	2.9–31.0
No. of unique reflections	1395	2153
No. of reflections and parameters in the least-squares refinement	1243/121	1897/129
No. of reflections with $I > 2\sigma(I)$	1166	1772
R_1	0.0250	0.0232
$wR_2(F^2)$	0.0590	0.0619

both cases, MoK_α radiation, graphite monochromator, and ω/2θ scan mode). For both modifications of $NaH_5(PO_4)_2$, the results of the low- and room-temperature studies closely agree. Below, we report only the data of the low-temperature studies, which are characterized by slightly lesser R factors.

The crystallographic parameters and details of structure refinement are summarized in Table 1. The data were corrected for absorption by using ψ-scans of 6–8 reflections and a numerical method allowing for the real crystal shape. Further calculations were performed with the corrected data sets that resulted in lesser R factors.

The non-hydrogen atoms were located by the direct method (SHELXS86 [15]) and refined in the anisotropic approximation (SHELXL93 [16]). Low values of the residual electron density allowed location and isotropic refinement of all the hydrogen atoms in both structures. In the structure of the β modification, two hydrogen atoms appeared to be disordered over two positions each with 0.5 occupancy.

The atomic coordinates and equivalent (isotropic for H atoms) thermal parameters in crystal structures of α- and β-$NaH_5(PO_4)_2$ are listed in Table 2.

RESULTS AND DISCUSSION

Crystallization of metastable modifications is not an uncommon phenomenon; nonetheless, it has not been

Table 2. Atomic coordinates and equivalent thermal parameters (U_{iso} for H atoms) in the structures of the α and β modifications of $NaH_5(PO_4)_2$

Atom	x	y	z	U_{eq}/U_{iso}, Å^2
α-$NaH_5(PO_4)_2$				
Na	0.2210(1)	0.5869(1)	0.6633(1)	0.013(1)
P(1)	0.4158(1)	0.0056(1)	0.6939(1)	0.010(1)
P(2)	0.0388(1)	0.7416(1)	0.9299(1)	0.009(1)
O(1)	0.4879(2)	0.1474(2)	0.6162(1)	0.014(1)
O(2)	0.2607(2)	0.0556(2)	0.7550(1)	0.014(1)
O(3)	0.3853(2)	−0.1570(2)	0.6096(1)	0.016(1)
O(4)	0.5369(2)	−0.0478(2)	0.8012(2)	0.016(1)
O(5)	0.1047(2)	0.5869(2)	0.8656(1)	0.012(1)
O(6)	0.1504(2)	0.8965(2)	0.9396(1)	0.013(1)
O(7)	−0.1137(2)	0.8046(2)	0.8580(1)	0.014(1)
O(8)	0.0016(2)	0.7145(2)	1.0756(1)	0.013(1)
H(1)	0.426(3)	−0.151(4)	0.548(3)	0.033(8)
H(2)	0.526(4)	−0.131(5)	0.832(4)	0.06(1)
H(3)	0.173(4)	0.947(4)	0.868(3)	0.051(9)
H(4)	−0.155(3)	0.721(4)	0.818(3)	0.036(8)
H(5)	−0.023(3)	0.635(4)	1.087(3)	0.017(9)
β-$NaH_5(PO_4)_2$				
Na	0.3218(1)	0.1175(1)	0.1428(1)	0.013(1)
P(1)	0.7977(1)	0.1407(1)	0.0276(1)	0.009(1)
P(2)	0.2584(1)	0.1084(1)	0.6205(1)	0.011(1)
O(1)	0.8547(1)	0.2373(1)	−0.0584(1)	0.015(1)
O(2)	0.6957(1)	0.0659(1)	−0.1073(1)	0.013(1)
O(3)	0.6615(1)	0.1582(1)	0.1845(1)	0.014(1)
O(4)	0.9826(1)	0.0914(1)	0.1219(1)	0.011(1)
O(5)	0.3685(1)	0.1133(1)	0.8125(1)	0.015(1)
O(6)	0.0795(1)	0.0454(1)	0.6357(1)	0.014(1)
O(7)	0.3762(1)	0.0698(1)	0.4683(1)	0.015(1)
O(8)	0.1956(1)	0.2170(1)	0.5628(2)	0.017(1)
H(1)	0.710(3)	0.191(2)	0.268(3)	0.036(6)
H(2)	0.960(4)	0.049(2)	0.180(3)	0.037(7)
H(3)	0.079(4)	0.221(2)	0.525(4)	0.046(7)
H(4)*	0.595(4)	0.081(3)	−0.130(7)	0.03(1)
H(5)*	0.481(8)	0.095(4)	0.818(8)	0.05(1)
H(6)*	0.028(7)	0.022(4)	0.550(7)	0.03(1)
H(7)*	0.440(7)	0.029(3)	0.506(7)	0.05(2)

* Site occupancy is 0.5.

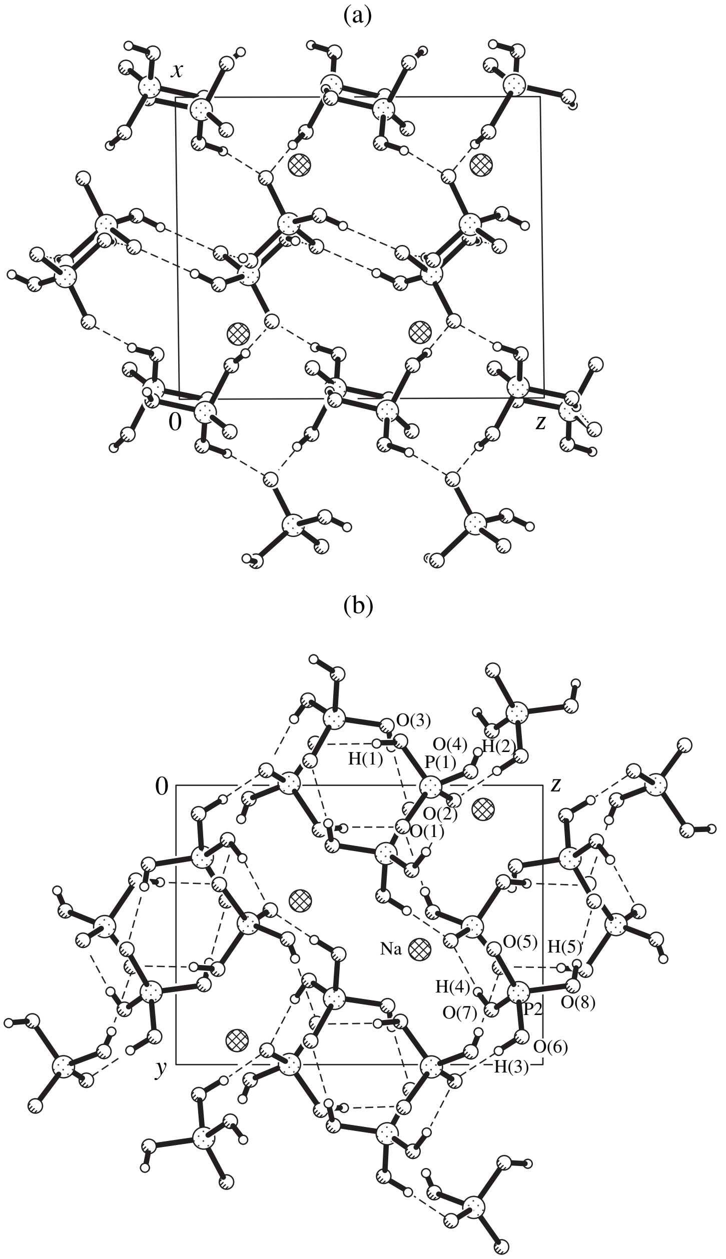

Fig. 1. Projections of the crystal structure of α-$NaH_5(PO_4)_2$ along (a) the *x*-axis and (b) the *y*-axis. Hydrogen bonds are shown by dashed lines.

observed for “superacid” salts in the $M_2O–H_2O–P_2O_5$ systems, where *M* is an alkali metal or ammonium. A reversible structural phase transition was found only for the ammonium salt $(NH_4)H_5(PO_4)_2$: it occurs in the temperature range 180–210 K and is accompanied by minor changes in the hydrogen-bond system [14]. In distinction to this, the crystalline modifications of $NaH_5(PO_4)_2$ differ in mutual arrangement of the structural units.

The structure of the α modification of $NaH_5(PO_4)_2$ is built of independent structural units such as the Na^+ cations, $H_2PO_4^-$ ions (*P*1), and H_3PO_4 molecules (P_2); therefore, the formula of the compound can be represented as $Na(H_2PO_4)(H_3PO_4)$. The Na^+ cation is coordinated by the O atoms, which form a distorted octahedron with the Na–O distances of 2.324(2)–2.586(2) Å. There are two shorter P–O distances [1.506(2) and 1.517(2) Å] and two longer P–OH distances [1.564(2) and 1.566(2) Å] in the $H_2PO_4^-$ anion. These distances differ fundamentally and are comparable to the corresponding values in K, Rb, and Cs pentahydrogendiphosphates, in which the shorter and

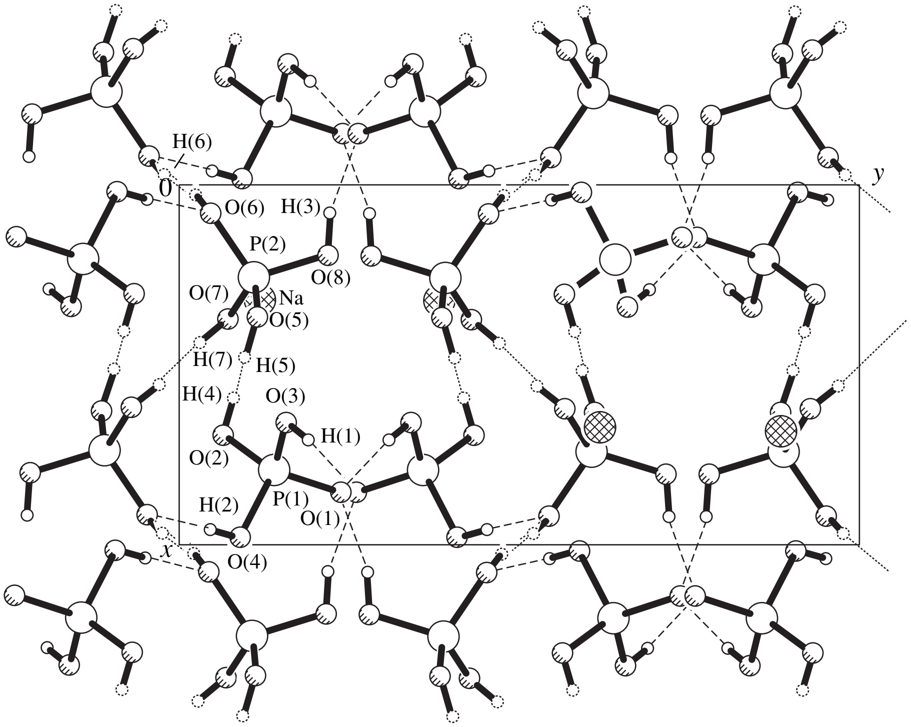

Fig. 2. Projection of the crystal structure of β-$NaH_5(PO_4)_2$ along the *z*-axis. The hydrogen bonds involving the ordered and disordered H atoms are shown by dashed and dotted lines, respectively. The H···O contacts in the hydrogen bonds are as follows: H(1, 2, 3)···O(1, 6, 1), 1.74(3)–1.81(3) Å; H(4)···O(5), 1.69(3) Å; H(5)···O(2), 2.01(6) Å; H(6)···O(6)^a, 1.73(4) Å, and H(7)···O(7)^a, 1.86(3) Å.

longer distances fall in the ranges 1.503–1.518 and 1.550–1.563 Å, respectively [9–11]. In the H_3PO_4 molecule, one P–O distance is short [P(2)–O(5), 1.495(2) Å] and three P–OH distances are longer (1.543–1.567 Å). All the hydrogen atoms are ordered and involved in the O–H···O hydrogen bonds. The lengths of these bonds (2.48–2.59 Å) indicate that they are strong or very strong. One of the hydrogen bonds is slightly shorter than the others [O(6)–H(3)···O(2), 2.475 Å]. Consideration of the structural functions of the O atoms in the formation of hydrogen bonds (a donor or an acceptor of an H atom) allows us to explain the difference in the P–O bonds. The longest P–O bonds involve the O atoms, which acts as donors of the H atoms. The P–O bonds with the O(1) and O(2) atoms, which serve as acceptors in two hydrogen bonds each, are significantly shorter. The shortest P–O bond is formed by the O(5) atom, which withdraws a hydrogen atom in one hydrogen bond. Additional participation in the coordination of sodium cations has no noticeable effect on the lengths of the P–O bonds.

In the structure of α-$NaH_5(PO_4)_2$, the centrosymmetric dimers are distinguished. They consist of two identical tetrahedra interlinked by two hydrogen bonds. Thus, the H_2PO_4 tetrahedra are linked into the *P*1–*P*1 dimers by pairs of the O(3)–H(1)···O(1) hydrogen bonds (2.585 Å), and the H_3PO_4 tetrahedra form the *P*2–*P*2 dimers through two O(8)–H(5)···O(5) hydrogen bonds (2.604 Å) (Fig. 1a). The O(4)–H(2)···O(1) hydrogen bonds (2.548 Å) link the *P*1–*P*1 dimers into layers, which are aligned parallel to the *yz* plane and pass at the height *x* = 0.5. The *P*2–*P*2 dimers are located in parallel planes at the height *x* = 0. The *P*1–*P*1 and *P*2–*P*2 dimers of the neighboring layers are linked by the O(6)–H(3)···O(2) (2.475 Å) and O(7)–H(4)···O(2) (2.591 Å) hydrogen bonds into a three-dimensional network (Fig. 1b).

The structural units of the β modification are the sodium cation and two independent $H_2PO_4^-$ ions linked by a hydrogen bond into the $[H(H_2PO_4)_2]^-$ anionic complex; therefore, the formula of this modification is represented as $Na[H(H_2PO_4)_2]$. A distorted octahedral environment of the sodium cation is formed by oxygen atoms at the Na–O distances (2.417–2.464 Å). There are three types of interatomic P–O distances in the structure: the short P(1)–O(1) distance (1.501 Å), four intermediate distances (1.520–1.540 Å), and three long distances (1.561–1.573 Å). These differences in the P–O distances are due to the different functions of the O atoms in the hydrogen bonds. By the type of ordering of the H atoms, the hydrogen bonds in the structure can be divided into three types (Table 2). The H(1), H(2), and H(3) atoms occupy ordered positions, and the remaining two H atoms are disordered over two positions each with 0.5 occupancy. The H(6) and H(7) atoms participate in the symmetric hydrogen bonds O(6)···O(6)^a and O(7)···O(7)^a, respectively, which are characterized by two maxima of electron density. The H(4) and H(5) atoms (both with 0.5 occupancy) are involved in the asymmetric O(2)···O(5) hydrogen bond, which is also characterized by two maxima.

The system of hydrogen bonds in β-$NaH_5(PO_4)_2$ is more complex than that in the α modification. We could not distinguish here the layers similar to those in the structure of the α modification. Let us consider the system of hydrogen bonds in the decreasing order of their strength. The strongest hydrogen bond O(2)···O(5) is 2.431 Å long; it links the $P(1)O_4$ and $P(2)O_4$ tetrahedra into the *P*1–*P*2 dimers (Fig. 2). The O(6)–H(6)···O(6)^a hydrogen bond is the next in strength; it is 2.474(2) Å long and links the dimers into the *P*1–*P*2···*P*2–*P*1 tetramer “clusters.” The remaining hydrogen bonds [2.574(2)–2.600(1) Å] link the tetramers into a complex three-dimensional system.

Thus, the α and β modifications of sodium pentahydrogendiphosphate crystallize in the same space group $P2_1/c$, but their structures are quite different as is expressed by the formulas $Na(H_2PO_4)(H_3PO_4)$ and $Na[H(H_2PO_4)_2]$. The unit cell parameters are also quite different. It is remarkable that the volume per formula unit for the stable α modification is noticeably larger than that for the metastable β modification (172.3 and 169.9 Å^3, respectively). The difference in the volumes by 1.4% observed at 180 K remains approximately the same at room temperature. Note that the phase transitions from an unstable to a stable modification are rarely accompanied by an increase in the unit cell volume.

The incongruent melting of the compound should be considered among the factors responsible for the formation of the metastable modification of $NaH_5(PO_4)_2$. According to the phase diagram of the Na_2O–H_2O–P_2O_5 system [4], crystals of NaH_2PO_4 (rather than crystals of the starting salt) precipitate first from the liquid phase obtained by melting sodium pentahydrogendiphosphate. Sodium dihydrogenphosphate also crystallizes in the monoclinic space group $P2_1/c$, and its unit cell parameters are close to those of the β modification of $NaH_5(PO_4)_2$ (Table 1): a = 6.808 Å, b = 13.491 Å, c = 7.331 Å, and β = 92.9° [17]. Since the tetrahedral $PO_2(OH)_2$ groups and the sodium cations in both structures form similar arrangements, it seems fairly probable that the formation of the β modification is initiated by microcrystals of NaH_2PO_4 during relatively rapid crystallization from the saturated solution.

REFERENCES

1. B. A. Muromtsev, Kaliĭ, No. 1, 36 (1937).
2. B. A. Muromtsev and L. A. Nazarova, Izv. Akad. Nauk SSSR 177 (1938).
3. R. Flatt, G. Brunisholz, and S. Charius-Gottreux, Helv. Chim. Acta **34**, 683 (1951).
4. B. Wendrow and K. A. Kobe, Ind. Eng. Chem. Res. **44**, 1439 (1952).
5. A. Norbert, Rev. Chim. Miner. **3**, 1 (1966).
6. A. Norbert, C. R. Seances Acad. Sci., Ser. C **266**, 705 (1968).
7. A. Norbert and D. André, C. R. Seances Acad. Sci., Ser. C **270**, 1718 (1970).
8. A. Norbert and D. André, C. R. Seances Acad. Sci., Ser. C **270**, 723 (1970).
9. É. Philippot and O. Lindqvist, Acta Chem. Scand. **25**, 512 (1971).
10. V. A. Efremov, É. N. Gudinitsa, I. Matsichek, and A. A. Fakeev, Zh. Neorg. Khim. **28**, 1725 (1983).
11. V. A. Efremov, V. K. Trunov, I. Matsichek, *et al.*, Zh. Neorg. Khim. **26**, 3213 (1981).
12. P. Y. Oddon, J.-R. Vignalou, A. Tranquard, and G. Pépe, Acta Crystallogr., Sect. B: Struct. Crystallogr. Cryst. Chem. **34**, 3510 (1978).
13. É. Philippot and M. Maurin, C. R. Seances Acad. Sci., Ser. C **274**, 518 (1972).
14. S. I. Troyanov, E. M. Snigireva, and E. Kemnitz, Z. Kristallogr. (2000) (in press).
15. G. M. Sheldrick, *SHELXS86: Program for the Solution of Crystal Structures* (Univ. of Göttingen, Germany, 1986).
16. G. M. Sheldrick, *SHELXL93: Program for the Refinement of Crystal Structures* (Univ. of Göttingen, Germany, 1993).
17. M. Gatti and G. Ferraris, Acta Crystallogr., Sect. B: Struct. Crystallogr. Cryst. Chem. **30**, 1 (1974).

Translated by I. Polyakova

Crystallography Reports, Vol. 45, No. 4, 2000, pp. 568–571. Translated from Kristallografiya, Vol. 45, No. 4, 2000, pp. 625–628.
Original Russian Text Copyright © 2000 by Murashova, Chudinova.

STRUCTURE OF INORGANIC COMPOUNDS

Sodium–Manganese Cyclopentaphosphate: Synthesis and Crystal Structure

E. V. Murashova and N. N. Chudinova

Kurnakov Institute of General and Inorganic Chemistry, Russian Academy of Sciences,
Leninskiĭ pr. 31, Moscow, 117907 Russia

Received June 18, 1998

Abstract—The $Na_2MnP_5O_{15}$ compound containing a cyclopentaphosphate anion was obtained for the first time by the direct synthesis from the melt of polyphosphoric acids in the presence of Na^+ and Mn^{4+} ions. The parameters of the monoclinic unit cell are $a = 5.176$, $b = 13.541$, and $c = 8.771$ Å; $\beta = 103.61°$; sp. gr. $P2_1/m$, and $Z = 2$. The cyclopentaphosphate anions and the manganese atoms in the structure are octahedrally coordinated with oxygen atoms and are linked into layers. Sodium anions crosslink the neighboring layers into a three-dimensional framework. *© 2000 MAIK “Nauka/Interperiodica”.*

This study continues our investigation of metal compounds of condensed phosphates with different forms of anions synthesized by crystallization from melts of polyphosphoric acids. We aimed to synthesize and study the structure of the $Na_2MnP_5O_{15}$ cyclopentaphosphate.

The only cyclopentaphosphate reported in literature is $NH_4Na_4P_5O_{15} \cdot 4H_2O$ [1, 2]. It was obtained by multiple fractionation of the Graham salt (vitreous sodium polyphosphate) containing 0.2% sodium cyclopentaphosphate along with other forms of condensed phosphates. Until now, all the attempts of direct synthesis of cyclopentaphosphates were unsuccessful.

Synthesis of $Na_2MnP_5O_{15}$

With the aim to obtain the $Na_2MnP_5O_{15}$ cyclopentaphosphate, we studied the low-temperature region (230–320°C) of the $Na_2O–MnO_2–P_2O_5–(H_2O)$ system. At higher temperatures (350–400°C), we obtained $Na_3Mn^{III}P_8O_{23}$ ultraphosphate [3] and $NaMn^{II}(PO_3)_3$ polyphosphate [4]. The initial compounds were sodium nitrate, manganese dioxide, and 85% phosphoric acid. The mixture of these substances with the Na : Mn : P = 5 : 1 : 15 atomic ratio was heated in a Teflon crucible at 230°C to yield gaseous nitrogen dioxide, oxygen, and some water. In the homogeneous melt formed, the oxidation state of manganese reduced from four to three, whereas the phosphoric acid exists as a combination of condensed forms. After three days, a crystalline substance precipitated from the melt. It consisted of brown crystals of an unknown compound and an admixture of colorless $Na_2H_2P_4O_{12}$ crystals (JCPDS 9-100). The X-ray diffraction study revealed that the brown compound was $Na_2MnP_5O_{15}$ cyclopentaphosphate. The precipitate was washed with hot water to remove the melt of polyphosphoric acids and then was dried in air. In order to separate $Na_2H_2P_4O_{12}$, the specimen was treated with hot hydrochloric acid readily dissolving $Na_2H_2P_4O_{12}$, but not reacting with $Na_2MnP_5O_{15}$. Thus, new condensed phosphate, $Na_2MnP_5O_{15}$ cyclopentaphosphate, was prepared by the direct synthesis and isolated as a single-phase substance. Single crystals of $Na_2MnP_5O_{15}$ for X-ray structure analysis were obtained at a higher temperature (320°C); however, in this case, the reaction product contained admixtures of $Mn(PO_3)_3$, $NaMn(PO_3)_3$, and $Na_3MnP_8O_{23}$, which could not be removed by any chemical method. Therefore, the optimum temperature for obtaining pure $Na_2MnP_5O_{15}$ is 230–250°C. The X-ray diffraction pattern calculated with the use of the atomic coordinates known for $Na_2MnP_5O_{15}$ coincided with the pattern obtained for the brown crystals synthesized at 230–250°C and treated with HCl (Guinier–de Wolf camera, CuK_α radiation, and Ge-standard).

Crystal Structure of $Na_2MnP_5O_{15}$

The parameters of the data collection and the main crystallographic characteristics are summarized in Table 1. The positions of the P and Mn atoms were determined from the Patterson map, and the remaining atoms were located on a difference Fourier map (SHELXS86 [5]). All the atoms were refined in the anisotropic approximation by the least-squares procedure using the SHELXL93 program [6]. The atomic coordinates and thermal parameters are listed in Table 2. Selected interatomic distances and angles are given in Table 3.

The structure is built by layers consisting of cyclic phosphate anions $P_5O_{15}^{5-}$ and MnO_6-octahedra and linked by common oxygen vertices, which are perpendicular to the [001]-direction (Fig. 1). The pentaphosphate rings located in the layers are arranged in such a way that the plane of the ring is perpendicular to the layer and the "diameter" of the ring determines the layer width (Fig. 2). Sodium cations are located between these corrugated layers and are surrounded with six oxygen atoms. An anion of cyclic phosphate consists of five PO_4-tetrahedra interlinked by bridging O(3), O(4), and O(7) atoms. The crystallographic symmetry of this anion is *m*. As shown in Fig. 1, the $P(2)O_4$ tetrahedron shares two terminal oxygen atoms with the manganese octahedra; in the $P(1)O_4$-tetrahedron, only the O(1) atom lies within the coordination sphere of manganese, whereas the O(2) atom is bound to the sodium atom. Two sodium atoms of the $P(3)O_4$-tetrahedron, O(8) and O(9) are coordinated with sodium atoms. Table 3 shows that the external cationic environment of the phosphorus–oxygen tetrahedra significantly affects the phosphorus–oxygen bond lengths in PO_4 tetrahedra: these bonds lengths are shortened in the row P–O(P), P–O(Mn), P–O(Na) because of a decrease in electronegativity of atoms in passing from phosphorus to manganese and sodium. The P–O–P angles in the ring increase in the row P(1)–O–P(3) to P(1)–O–P(2) and to P(2)–O–P(2), which can also be attributed to the difference in the external cationic environment of phosphorus–oxygen tetrahedra.

Four of the six manganese–oxygen distances in the Mn-octahedron are equal, whereas two distances are longer because of the Jahn–Teller effect. The sodium atom has six nearest neighbors. One of the Na–O distances is significantly longer than the remaining ones (2.84 and 2.380–2.529 Å, respectively).

RESULTS AND DISCUSSION

The $Na_2MnP_5O_{15}$ cyclopentaphosphate is the first cyclophosphate with an odd number of phosphorus atoms in the ring (>3) obtained by the direct synthesis from melt of polyphosphoric acids. Up to now, this procedure was successfully used to prepare metal cyclophosphates with even numbers (four, six, eight, ten, and twelve) of phosphorus atoms in the ring. Among them, there are double and triple cyclophosphates that synthesized earlier—cyclotetraphosphates $M^IM^{III}P_4O_{12}$, where M^I = Cs or NH_4^+ and M^{III} is a rare-earth element of the cerium subgroup [7]; cyclohexaphosphates $CsM^{II}M^{III}P_6O_{18}$ (M^{II} = Co, Mg, Zn, or Mn and M^{III} = V, Ga, Fe, or Mn) and $Cs_3M_3^{II}M^{III}(P_6O_{18})_2$ (M^{II} = Zn, Cd, or Mg and M^{III} = Mn, In, or V) [8, 9]; cyclooctaphosphates $M_2^IM_2^{III}P_8O_{24}$ (M^I = K or Rb and M^{III} = Ga, V, or Fe) [10]; and cyclododecaphosphates $Cs_3M_3^{III}P_{12}O_{36}$ (M^{III} = Ga, V, or Fe) [10]—and the $Ba_2Zn_3P_{10}O_{30}$ cyclododecaphosphate synthesized by Bagieu-Beucher *et al.* [11]. We see that metal cations with a similar size

Table 1. Main crystallographic data and the parameters of data collection and structure refinement

Crystal system	Monoclinic
a, Å	5.1768(6)
b, Å	13.541(2)
c, Å	8.771(1)
β, deg	103.61(1)
Sp. gr.	$P2_1/m$
Z	2
V, $Å^3$	597.6(1)
ρ_{calc}, g/cm^3	2.755
μ, mm^{-1}	1.94
$2\theta_{max}$, deg	60
Crystal dimensions, mm	1.2 × 0.3 × 0.2
Diffractometer*	Enraf-Nonius CAD-4
Scan mode	ω/2θ
N_a^{**}	1750
N_o^{**}	1696
N_p^{**}	112
*R*1	0.033
*wR*2	0.072
Gof	1.036
w	$1/(\sigma^2(F) + 0.0001\,F^2)$

* λMoK_α, graphite monochromator and ψ-correction of the data set.

** N_a is the number of reflections with $F > 0$, N_o is the number of reflections with $F > 4\sigma(F)$, and N_p is the number of parameters in the refinement.

Table 2. Atomic coordinates and thermal parameters

Atom	*x*/*a*	*y*/*b*	*z*/*c*	B_{eq}, $Å^2$
Mn(1)	1/2	1/2	1/2	0.659(9)
Na(1)	0.0781(3)	0.3910(1)	1.1291(1)	1.73(2)
P(1)	0.3499(1)	0.42147(5)	0.8095(1)	0.74(1)
P(2)	–0.0176(1)	0.35938(4)	0.5127(1)	0.66(1)
P(3)	0.5438(2)	1/4	1.0050(1)	0.83(2)
O(1)	0.4929(4)	0.4869(1)	0.7157(2)	1.01(3)
O(2)	0.2163(4)	0.4698(1)	0.9190(2)	1.15(3)
O(3)	0.5607(4)	0.3414(1)	0.8874(2)	1.19(3)
O(4)	0.1382(4)	0.3554(1)	0.6897(2)	1.26(3)
O(5)	–0.3066(4)	0.3787(1)	0.5067(2)	1.11(3)
O(6)	0.1204(4)	0.4226(1)	0.4181(2)	0.92(3)
O(7)	0.0082(5)	1/4	0.4581(3)	0.81(4)
O(8)	0.2834(6)	1/4	1.0451(3)	1.46(5)
O(9)	0.7936(6)	1/4	1.1254(3)	1.44(5)

Table 3. Selected interatomic distances (*d*, Å) and angles (ω, deg)

Bond	*d*	Angle	*d*
Mn(1)–O(1)	1.909(2) × 2	P(2)–O(4)	1.573(2)
Mn(1)–O(5)	1.918(2) × 2	P(2)–O(5)	1.507(2)
Mn(1)–O(6)	2.193(2) × 2	P(2)–O(6)	1.487(2)
Na(1)–O(1)	2.845(2)	P(2)–O(7)	1.572(1)
Na(1)–O(2)	2.380(2)	P(3)–O(3)	1.627(2) × 2
Na(1)–O'(2)	2.398(2)	P(3)–O(8)	1.471(3)
Na(1)–O(6)	2.529(2)	P(3)–O(9)	1.464(3)
Na(1)–O(8)	2.384(2)		
Na(1)–O(9)	2.407(2)	Angle	ω
P(1)–O(1)	1.515(2)	P(1)–O(3)–P(3)	131.6(1)
P(1)–O(2)	1.464(2)	P(1)–O(4)–P(2)	137.9(1)
P(1)–O(3)	1.575(2)	P(2)–O(7)–P(2)	140.9(2)
P(1)–O(4)	1.601(2)		

and equal charge vary within each type of compounds with the only exception—$Ba_2Zn_3P_{10}O_{30}$.

Our attempts to prepare $Na_2MnP_5O_{15}$ cyclopentaphosphate analogues with other of alkaline and trivalent metal cations failed, although it is well known that in condensed phosphates, Mn(III) is easily replaced by Fe(III), V(III), Cr(III), and other cations. Possibly, our failure is associated with the stressed state of the $Na_2MnP_5O_{15}$ structure caused by nonequivalent links of

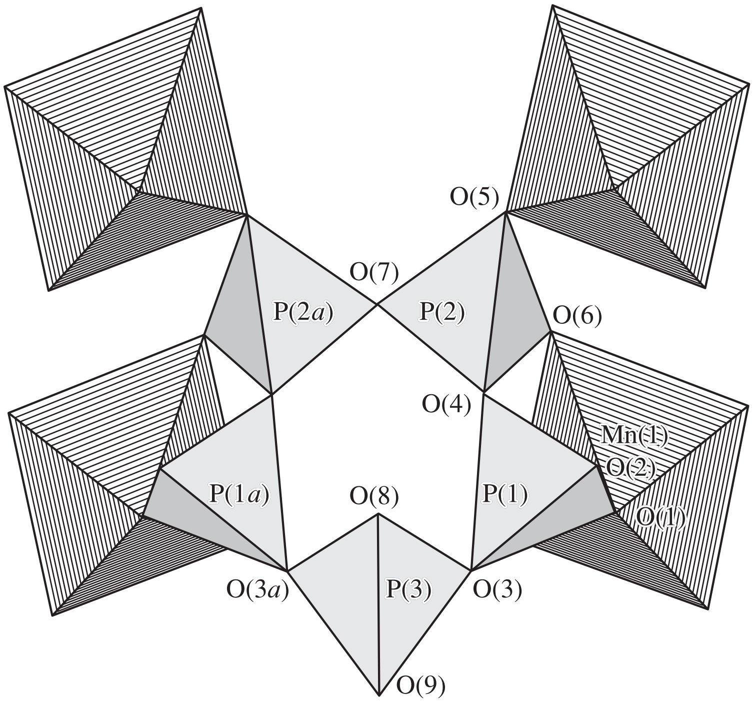

Fig. 1. Fragment of the $Na_2MnP_5O_{15}$ structure.

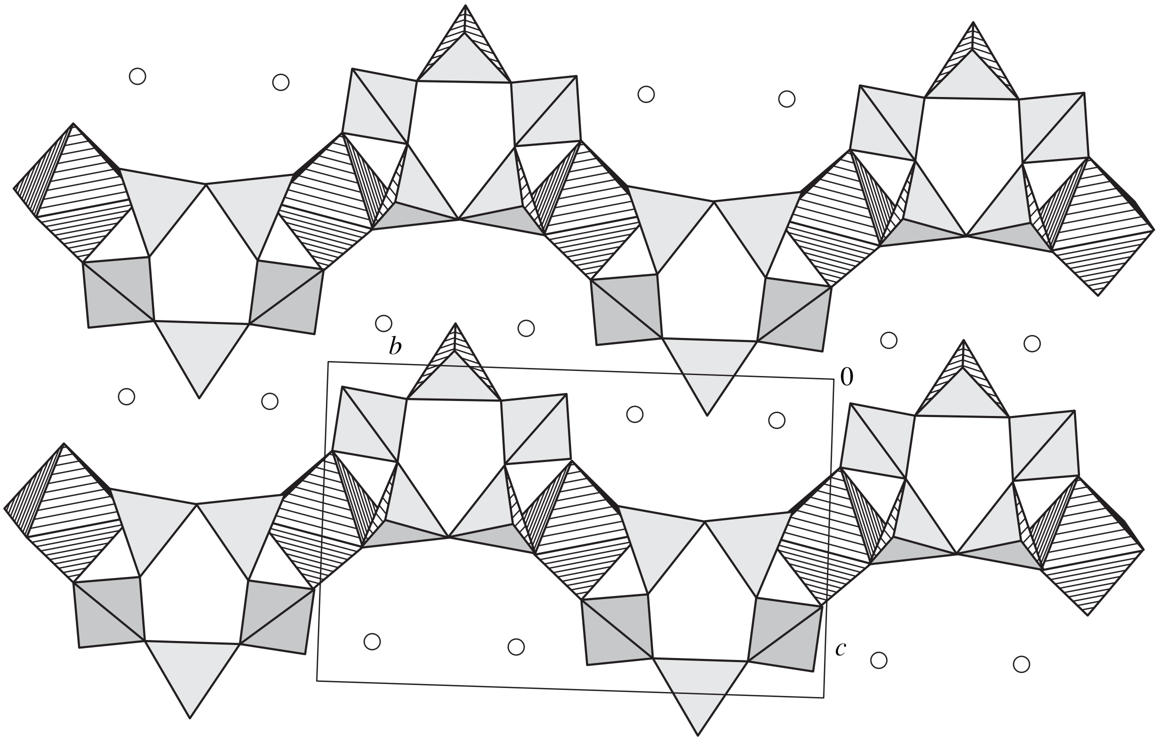

Fig. 2. $Na_2MnP_5O_{15}$ structure projected along [100].

the pentaphosphate ring. The same reasons seem to explain the hydrolytic instability of the $P_5O_{15}^{5-}$ ring in aqueous solutions and the low content of cyclopentaphosphate in comparison with cyclotetra- and cyclohexaphosphates in the Graham salt observed in [1, 2].

ACKNOWLEDGMENTS

This study was supported by the Russian Foundation for Basic Research, project no. 98-03-32695.

REFERENCES

1. E. Thilo and U. Schulke, Z. Anorg. Allg. Chem. **341** (5–6), 293 (1965).
2. K. H. Jost, Acta Crystallogr., Sect. B: Struct. Crystallogr. Cryst. Chem. **28** (3), 732 (1972).
3. N. N. Chudinova, E. V. Murashova, and N. B. Karmanovskaya, Zh. Neorg. Khim. **39** (11), 1769 (1994).
4. E. V. Murashova and N. N. Chudinova, Kristallografiya **42** (3), 416 (1997) [Crystallogr. Rep. **42** (3), 370 (1997)].
5. G. M. Sheldrick, Acta Crystallogr., Sect A: Found. Crystallogr. **46**, 467 (1990).
6. G. M. Sheldrick, *SHELXTL 93: Program for the Refinement of Crystal Structures* (Univ. of Göttingen, Germany, 1993).
7. K. K. Palkina, N. N. Chudinova, B. N. Litvin, and N. V. Vinogradova, Izv. Akad. Nauk SSSR, Neorg. Mater. **17** (8), 501 (1981).
8. E. V. Murashova and N. N. Chudinova, Kristallografiya **41** (2), 254 (1996) [Crystallogr. Rep. **41** (2), 236 (1996)].
9. E. V. Murashova and N. N. Chudinova, Kristallografiya **41** (2), 248 (1996) [Crystallogr. Rep. **41** (2), 230 (1996)].
10. I. Gruntse, N. N. Chudinova, and Kh. Gruntse, Izv. Akad. Nauk SSSR, Neorg. Mater. **25** (6), 886 (1989).
11. M. Bagieu-Beucher, A. Durif, and J. C. Guintel, J. Solid State Chem. **40** (2), 248 (1981).

Translated by I. Polyakova

Crystallography Reports, Vol. 45, No. 4, 2000, pp. 572–577. Translated from Kristallografiya, Vol. 45, No. 4, 2000, pp. 629–634.
Original Russian Text Copyright © 2000 by Krzhizhanovskaya, Kabalov, Bubnova, Sokolova, Filatov.

STRUCTURE OF INORGANIC COMPOUNDS

Crystal Structure of the Low-Temperature Modification of α-RbB_3O_5

M. G. Krzhizhanovskaya*, Yu. K. Kabalov, R. S. Bubnova***,**
E. V. Sokolova*, and S. K. Filatov*

** St. Petersburg State University, Universitetskaya nab., St. Petersburg, 199164 Russia*
*** Moscow State University, Vorob’evy gory, Moscow, 119899 Russia*
**** Grebenshchikov Institute of Silicate Chemistry, Russian Academy of Sciences,*
ul. Odoevskogo 24/2, St. Petersburg, 199155 Russia

Received March 12, 1998

Abstract—The crystal structure of α-RbB_3O_5 was refined by the Rietveld method with due regard for anisotropic vibrations of rubidium atoms to $R_p = 2.93$, $R_{wp} = 3.80$, $R_B = 2.53$, $R_F = 2.84$, and $s = 1.54$. The compound is isostructural to CsB_3O_5: it is orthorhombic, sp. gr. $P2_12_12_1$, $a = 8.209(1)$, $b = 10.092(1)$, $c = 5.382(1)$ Å, and $V = 445.9$ Å^3. The framework structure is formed by the boron–oxygen $[B_2^{III}B^{IV}O_5]^-$ rings consisting of two $[BO_3]$-triangles and a $[BO_4]$-tetrahedron. The rings are linked to form systems of helical chains running along the twofold screw axes parallel 2_1 to the *a*- and *b*-axes and infinite channels parallel to the *a*- and *c*-axes, which accommodate Rb atoms. The data were collected on an ADP-2 diffractometer [CuK_α radiation, Ni-filter, $12.00° < 2\theta < 110.00°$, a step in 2θ equal to 0.02°, count time 8 s per step, and 711 reflections ($\alpha_1 + \alpha_2$)]. All the calculations were performed using version 3.3 of the WYRIET program. The comparison of the structures of α- and β-RbB_3O_5 and CsB_3O_5 revealed that the type of deformations in the framework structures of alkali-metal borates due to the changes of the temperature or the substitution of cations is determined by the role played by metal atoms, and especially, by large and heavy ions. *© 2000 MAIK “Nauka/Interperiodica”.*

INTRODUCTION

A possible existence of polymorphic modifications of RbB_3O_5 was first discussed in [1–2]. It was found that the earlier unindexed Debye patterns of compound RbB_3O_5 were, in fact, the combinations of either two modifications of RbB_3O_5 [3] or $Rb_2B_8O_{13}$ and two modifications of RbB_3O_5 [4]. The powder data obtained showed [1, 2, 5] that the low-temperature α-RbB_3O_5 modification is isostructural to CsB_3O_5, and has a framework structure. The determination of the structure of the high-temperature β-RbB_3O_5 modification [5–7] revealed that, although the structural types of two modifications are different, their boron–oxygen frameworks are topologically identical. *In situ* thermal X-ray studies [5, 6] showed that the polymorphic transformation proceeds through partial amorphization with a jumpwise change of the volume, but without a rupture of the boron–oxygen framework.

Similar to other alkali-metal borates with the general formula MB_3O_5, where M = Li, Na, K, Rb, or Cs, the α- and β-RbB_3O_5 modifications belong to the compounds with mixed anions, because boron atoms in the structures are located in the $[BO_3]^{3-}$ triangles and the $[BO_4]^{5-}$ tetrahedra. The most characteristic structural unit of these compounds is the boron–oxygen $[B_3O_5]$ ring (the so-called triborate group, whose structural formula is written as $[B_2^{III}B^{IV}O_5]^-$ [8]) formed by condensation of two triangles and a tetrahedron.

The frameworks of alkali-metal borates with such stoichiometry (the oxide ratio $M_2O : B_2O_3$ is 1 : 3), the only exception being sodium borate, are topologically identical and built by only such triborate rings despite the large difference in the cation sizes (the ionic radii of Li^+ and Cs^+ are 0.90 and 1.95 Å, respectively [9]). Although CsB_3O_5 [10, 11] and α- and β-RbB_3O_5 [1, 6, 7] represent different structural types, their crystals belong to the same space group $P2_12_12_1$ and the rings in their frameworks are linked to form the systems of helical boron–oxygen chains and channels running along two directions; the channels are populated with alkali-metal cations. The space groups of the LiB_3O_5 ($Pna2_1$) [12, 13] and KB_3O_5 ($P2_1/c$) structures [14] contain only one system of twofold screw axes; therefore, the helical chains of the boron–oxygen rings and the channels filled with alkali cations are formed only along one direction.

In this study, the α-RbB_3O_5 structure was refined by the Rietveld method with the use of the atomic coordinates of CsB_3O_5. The results are compared with the corresponding data for the β-RbB_3O_5 and CsB_3O_5 structures.

Table 1. Characteristics of the experiments and crystallographic data for α- and β-RbB_3O_5 and CsB_3O_5

Formula	α-RbB_3O_5 (present study)	β-RbB_3O_5 [7]	CsB_3O_5 [11]
System	Orthorhombic	Orthorhombic	Orthorhombic
Sp. gr.	$P2_12_12_1$	$P2_12_12_1$	$P2_12_12_1$
a, Å	8.209(1)	8.438(6)	8.521(1)
b, Å	10.092(1)	8.719(4)	9.170(2)
c, Å	5.382(1)	6.240(3)	6.213(1)
V, Å^3	445.9	459.1(8)	485.5
Z	4	4	4
ρ_{calc}, g/cm^3	3.097	2.863(5)	3.357
Radiation	MoK_α	MoK_α	CuK_α
Method of data collection	Rietveld	Syntex $P2_1$	Picker
Number of reflections	711*	980	1262
R_F	0.028	0.065	0.039
R_P	0.029		
R_{wp}	0.038		
R_B	0.025		
s**	0.015		

* Number of reflections ($\alpha_1 + \alpha_2$).
** $s = R_{wp}/R_{exp}$, where R_{exp} is the expected value of R_{wp}.

EXPERIMENTAL

A polycrystalline α-RbB_3O_5 specimen was synthesized by the solid-state reaction by heating the charge for two weeks at 600°C. Rubidium carbonate and boric acid (both of reagent grade) were used as starting materials. An X-ray pattern obtained on a DRON-2 diffractometer was indexed using the program for automatic indexing (written by A.D. Krasil'nikov from the *Burevestnik* Research and Production Association) in the orthorhombic system; the unit-cell parameters were determined as a = 8.217(3), b = 10.095(3), and c = 5.391(2) Å. The comparison of the unit-cell parameters and relative intensities of the patterns from α-RbB_3O_5 and CsB_3O_5 led to the assumption on their isostructurality (Table 1).

The X-ray diffraction spectra were obtained on an ADP-2 diffractometer (CuK_α, Ni-filter) by 2θ scans at a step of 0.02° and count time of 8 s. All the computations were performed with the WYRIET program, version 3.3 [15]. The structure was refined within the sp. gr. $P2_12_12_1$ using the unit-cell parameters calculated for α-RbB_3O_5 and the atomic coordinates of CsB_3O_5 [11]. The refinement of the scale coefficient, unit-cell parameters, zero point, background, and the displacement of the sample from the goniometer axes was followed by the refinement of the structural and profile parameters. The peak shapes were described with the use of the pseudo-Voigt function at 6FWHM.[1] Asymmetry was refined at $2\theta < 40°$. In calculations, we used the scattering functions for ions. The refinement was performed by a gradual addition of the parameters at a continuous graphical modeling of the background until the attainment of stable R factors of the parameters refined. The structural parameters were refined in two stages: first, we refined the positional atomic parameters; then, the positional parameters simultaneously with the isotropic thermal parameters, and, finally, anisotropic thermal parameters of Rb atoms and site occupancies. The occupancies of all the positions were equal to unity (within an error of 0.05). The observed (dots) and calculated (solid curve) X-ray diffraction spectra of α-RbB_3O_5 are shown in Fig. 1. The crystallographic data and the parameters of the experiment are represented in Table 1. The final atomic coordinates and isotropic thermal parameters are listed in Table 2. Unfortunately, the accuracy in the determination of thermal parameters from powder data, especially for light boron atoms, was rather low.

DESCRIPTION OF THE STRUCTURE

Similar to CsB_3O_5, the compound α-RbB_3O_5 has a framework structure. It is built by boron–oxygen groups of one type ([B_3O_5]-rings). The channels formed accommodate alkali-metal cations. Each ring consists of two [BO_3]-triangles and a [BO_4]-tetrahedron (Fig. 2) and is connected with four other rings in such a way that the triangles alternate with the tetrahedra of the neighboring rings; all the oxygens are bridging atoms. The rings are linked into the chains with a

---

[1] FWHM is the mean width of a peak at its half-maximum height.

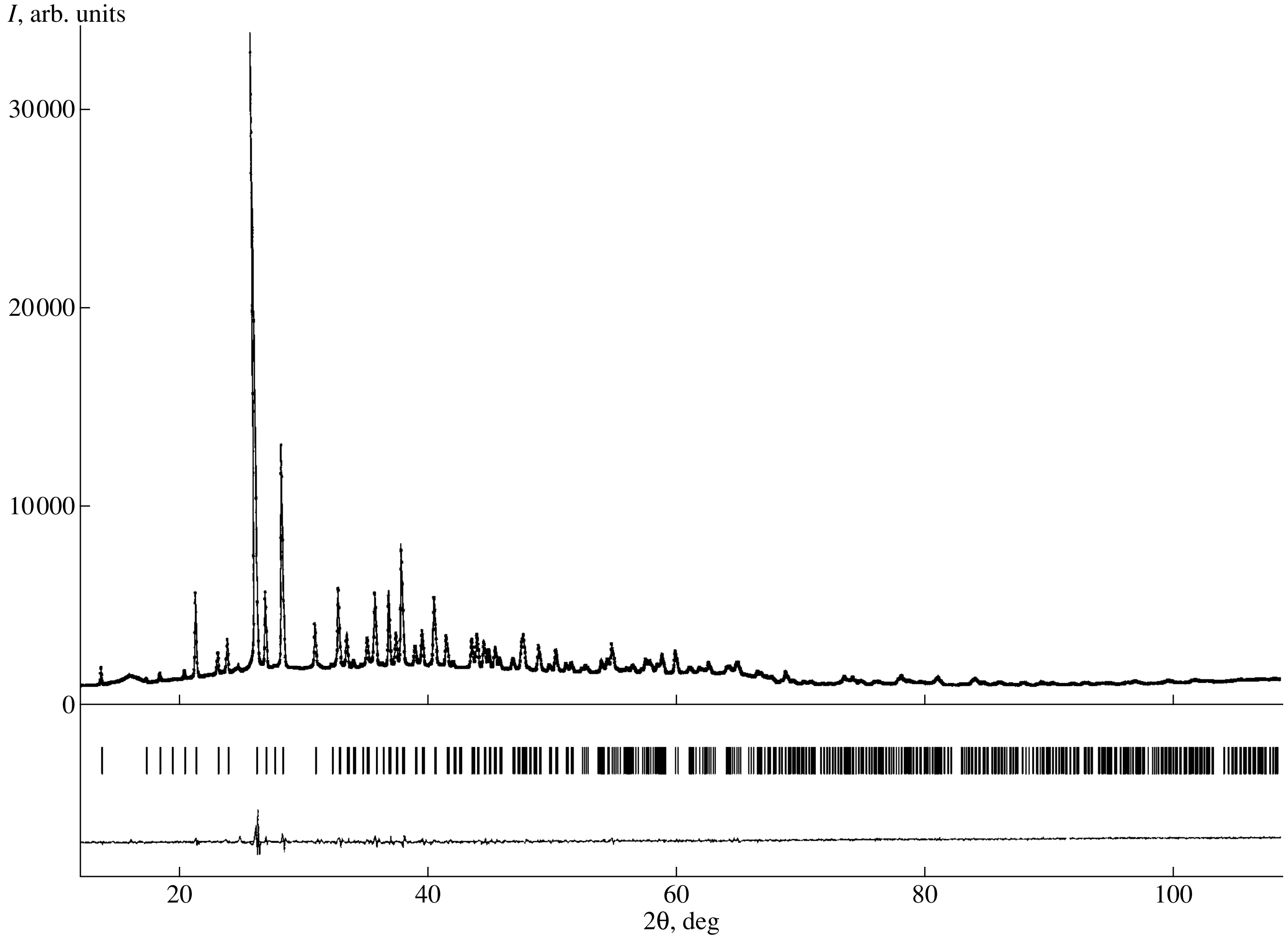

Fig. 1. Measured (dots) and calculated (solid curve) X-ray diffraction spectra for α-RbB_3O_5.

period of two rings along the twofold screw axes parallel to the *a*- and *c*-directions of the structure (Fig. 2). The chains running along the *a*-axis are relatively stretched ($a = 8.209$ Å), and the chains running in the *c* direction are considerably corrugated ($c = 5.382$ Å). Wide channels with columns of rubidium atoms are also formed along the *a*- and *c*-axes (Figs. 2, 3).

Table 2. Atomic coordinates and thermal parameters in α-RbB_3O_5

Atom	*x*/*a*	*y*/*b*	*z*/*c*	B_{iso}/B_{eq}
Rb	2942(2)	1310(2)	992(1)	2.90(4)*
O(1)	555(1)	056(1)	432(2)	0.6(1)
O(2)	544(1)	257(1)	705(2)	0.3(1)
O(3)	727(2)	072(1)	815(2)	0.8(1)
O(4)	777(1)	213(1)	431(2)	0.9(1)
O(5)	996(1)	090(1)	632(2)	0.6(1)
B(1)	885(4)	030(3)	775(5)	3.1(3)
B(2)	942(3)	182(2)	472(7)	1.8(3)
B(3)	644(3)	153(2)	600(4)	0.4(3)

* $B_{eq} = \frac{1}{3}[B_{11}a^{*2}a^2 + \ldots + 2B_{12}\, a^*\, b^*\, a\, b\cos(\gamma) + \ldots]$.

The mean B–O bond lengths are within the allowed range (1.36 and 1.52 Å for triangles and tetrahedra, respectively). However, the mean bond length in the tetrahedron is larger than the bond lengths in rubidium borates (1.47–1.48 Å) reported earlier [7] or the corresponding bond length in CsB_3O_5 [11]. Note that the spread in bond lengths and angles (1.31–1.40 Å and 112°–126° for triangles; 1.44–1.58 Å and 104°–116° for tetrahedra) is more pronounced than usually observed for polyhedra of this type in single-crystal studies.

The rubidium atoms are located inside wide channels in such a way that it is difficult to single out their coordination polyhedra. Assuming that Rb–O distances differing by the value of 0.25 Å form different coordination spheres, the coordination number of rubidium is 9. The rubidium atoms most closely approaching each other are related by a twofold screw axis. They are separated by a distance of 3.841 Å and form zigzag col-

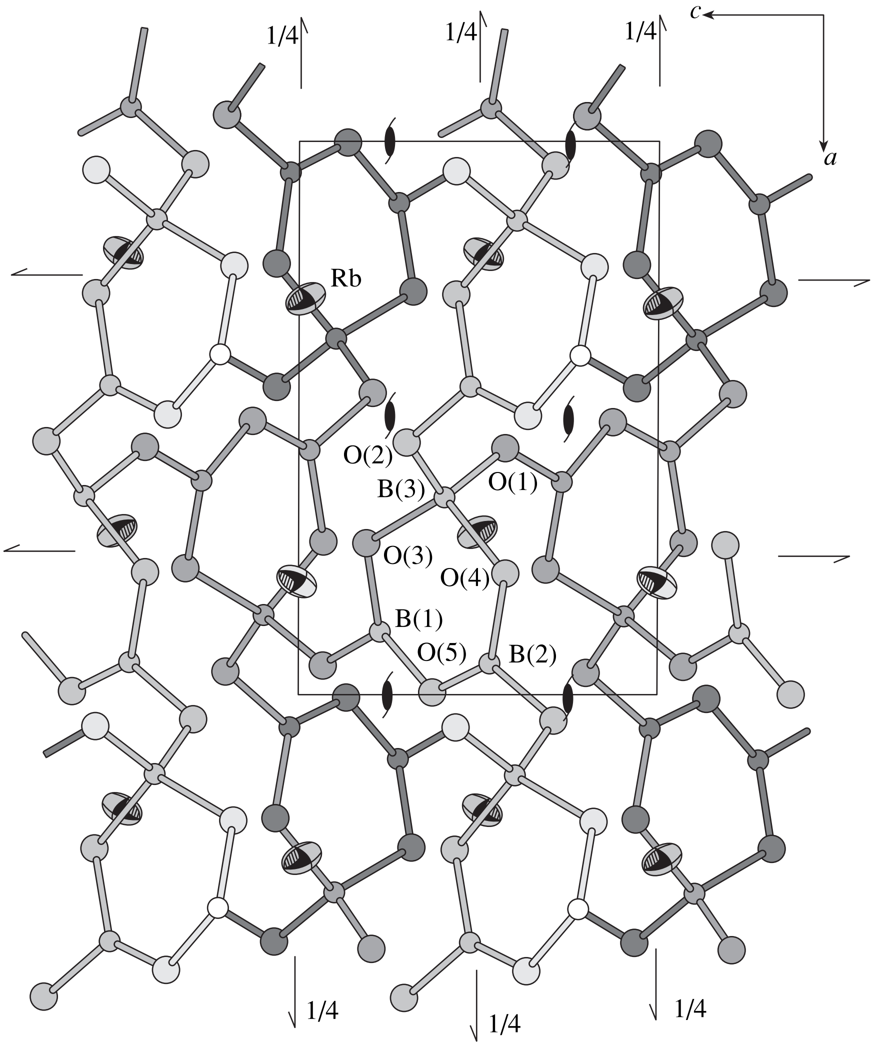

Fig. 2. Projection of the α-RbB_3O_5 structure onto the *ac* plane.

umns along the *c*-axis (Figs. 2, 3a). In the columns parallel to the *a*-axis, the distances between the rubidium atoms are 4.756 Å. The ellipsoids of thermal vibrations of rubidium atoms have two relatively long axes and are flattened along the direction close to the direction of the *a*-axis.

COMPARISON OF THE α- AND β-RbB_3O_5 AND CsB_3O_5 STRUCTURES

In different compounds of the MB_3O_5 series with the size of the alkali cation varying from 0.90 (Li^+ with c.n. = 6) to 1.95 Å (Cs^+ with c.n. = 10) [9], the boron–oxygen frameworks are topologically identical. In four structures (LiB_3O_5, α- and β-RbB_3O_5, and CsB_3O_5), two of which are the end members of the series, such framework is formed by helical chains of triborate groups with a period of two groups. In the structures containing large cations, the helical chains of triborate groups are formed along two directions: in α-RbB_3O_5 and CsB_3O_5, such chains and channels are filled with cations and are parallel to the *a*- and *c*-axes; in β-RbB_3O_5, the chains are parallel to the *a*- and *b*-axes and the channels, to the *a*- and *c*-axes. It is somewhat surprising that CsB_3O_5 is isostructural to the low-temperature α-RbB_3O_5 modification and not to the high-temperature one. It was expected that with an increase of the temperature, the amplitudes of atomic vibrations have also to increase, thus making the size of rubidium atoms closer to that of cesium atoms. As a result, the compound CsB_3O_5 should have been isostructural rather to β-RbB_3O_5. The substitution of the Cs^+ ion (R = 1.95 Å for c.n. = 10) for the smaller Rb^+ ion (R = 1.80 Å for c.n. = 10) [9] results in an increase of the unit-cell volume from 445.9 to 485.5 $Å^3$. As was expected, the *a* parameter increased from 8.209 Å in α-RbB_3O_5 to 8.521 Å in CsB_3O_5. The changes in two other unit-cell parameters are surprising again: *b* is

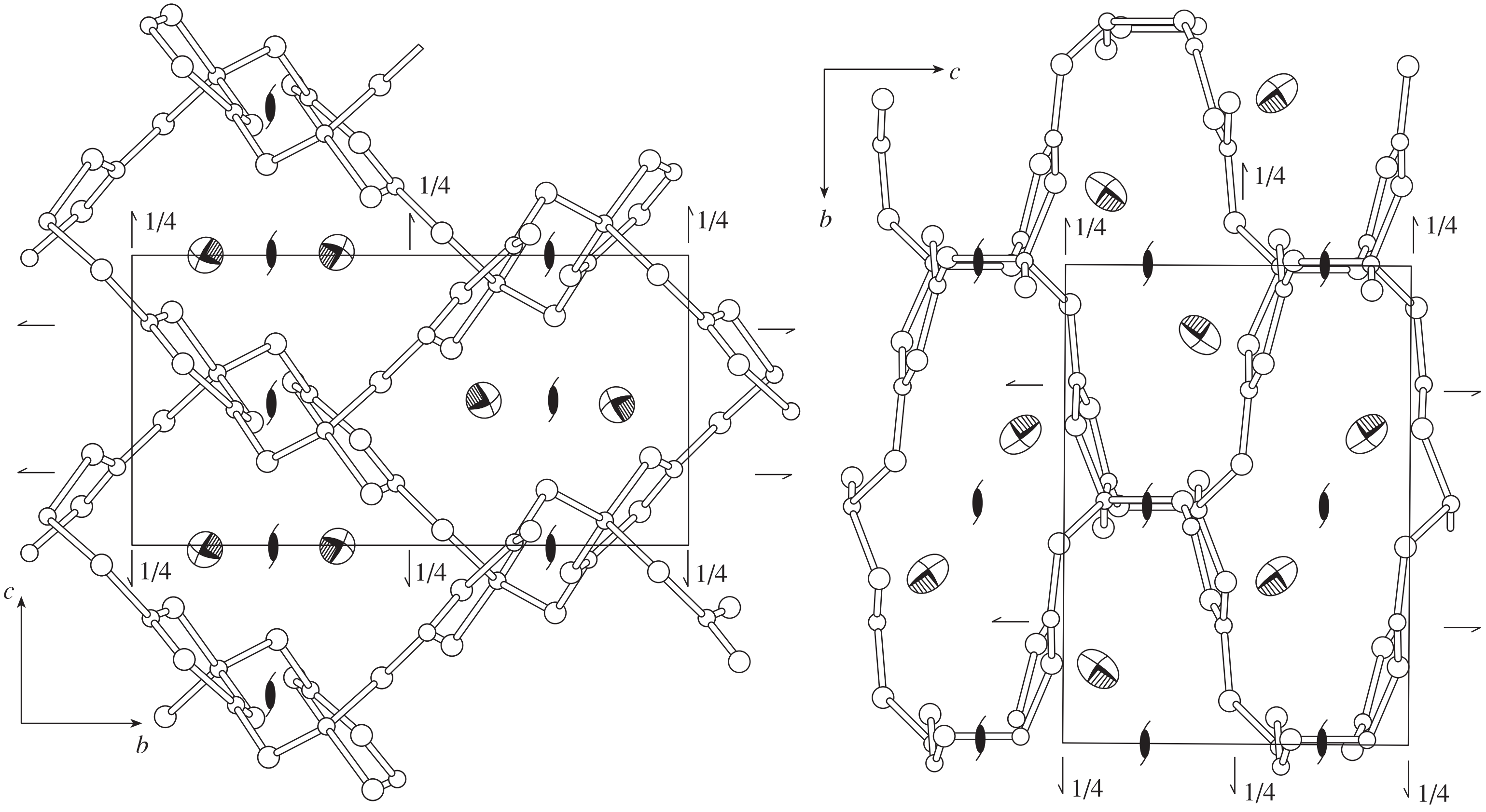

(a)

(b)

Fig. 3. Illustrating the continuous orientational changes during the α–β transformation of RbB_3O_5: (a) α-phase and (b) β-phase.

reduced by almost 1 Å (from 10.092 to 9.170 Å), whereas c increases by 1 Å (from 5.382 to 6.213 Å). Apparently, the pronounced anisotropy of lattice deformation on the substitution of cesium for rubidium cannot be attributed to the difference in the ion sizes alone.

The atomic coordinates in α-RbB_3O_5 and CsB_3O_5 are close; the largest difference (0.4 Å) is observed in the y coordinate of the cation. Apparently, such a considerable displacement of the large metal ion is responsible for the pronounced anisotropy of lattice deformations in CsB_3O_5, including the lattice contraction along the b-axis in comparison with the case of α-RbB_3O_5 [5, 6, 16].

The restructuring of RbB_3O_5 at the α–β transformation leads to even more pronounced anisotropy. Figure 3 shows the projections of these structures showing the orientational behavior of the structure due to transformation: the channels with a rhomboid cross section in the structure of the α-modification (Fig. 3a) are transformed into the channels with an oval cross section in the β-phase (Fig. 3b). Following the contour of each channel, one can see their topological identity. The difference between the structures consists in the location of the cations. In the polymorphic α–β transformation, these cations change their location in the jumplike manner, which results in severe deformations of the framework and the whole structure: $c_\alpha = 5.382$ Å $\longrightarrow b_\beta =$ 8.719 Å, $b_\alpha = 10.092$ Å $\longrightarrow c_\beta = 6.240$ Å, and $a_\alpha =$ 8.209 Å $\longrightarrow a_\beta = 8.438$ Å.

The above consideration confirms the earlier assumption [7, 16, 17] that the deformation in the framework structures of alkali-metal borates observed under temperature changes, and the cation substitution is determined by the role played by metal atoms and, especially, by large and heavy ions.

As seen from Figs. 2 and 3, the location of the metal ions inside the wide channels in the framework is caused by their “adhesion” to the channel walls. Obviously, the sites of “adhesion” are discrete and are considerably spaced. Jumping from one position to another, ions can severely distort the boron–oxygen framework, which, finally, results in the transformation of the structure into another polymorphic modification.

ACKNOWLEDGMENTS

This work was supported by the Russian Foundation for Basic Research, project no. 99-03-32524.

REFERENCES

1. R. S. Bubnova, M. G. Krzhizhanovskaya, V. B. Trofimov, *et al.*, in *Collected Abstracts of Int. Conf. on X-ray Diffraction Analysis of Real Structure of Matter, Slovakia, Liptovsky Mikolas, 1995*, p. 67.
2. S. K. Filatov, R. S. Bubnova, M. G. Krzhizhanovskaya, and I. G. Polyakova, in *Abstracts of XVII Congress IUCr, Seattle, 1996*, p. C-400.
3. M. M. Shul’ts, N. M. Vedishcheva, B. A. Shakhmatkin, *et al.*, Fiz. Khim. Stekla **12** (6), 651.
4. J. Kocher, Bull. Soc. Chim. Fr., No. 3, 919 (1968).
5. R. S. Bubnova, M. G. Krzhizhanovskaya, and S. K. Filatov, in *Proceedings of National Conference on Application of X-ray and Synchrotron Radiation, Neutrons, and Electrons to Study of Materials* (JINR, Dubna, 1997), Vol. 1, p. 112.
6. M. G. Krzhizhanovskaya, R. S. Bubnova, V. S. Fundamenskiĭ, *et al.*, in *Proceedings of National Conference on Application of X-ray and Synchrotron Radiation, Neutrons, and Electrons to Study of Materials* (JINR, Dubna, 1997), Vol. 1, p. 51.
7. M. G. Krzhizhanovskaya, R. S. Bubnova, V. S. Fundamenskiĭ, *et al.*, Kristallografiya **43** (1), 26 (1998) [Crystallogr. Rep. **43** (1), 21 (1998)].
8. J. Krogh-Moe, Phys. Chem. Glasses **3** (3), 101 (1962).
9. R. D. Shannon, Acta Crystallogr., Sect. A: Cryst. Phys., Diffr., Theor. Gen. Crystallogr. **32** (5), 751 (1976).
10. J. Krogh-Moe, Acta Crystallogr., Sect. B: Struct. Crystallogr. Cryst. Chem. **13**, 889 (1960).
11. J. Krogh-Moe, Acta Crystallogr., Sect. B: Struct. Crystallogr. Cryst. Chem. **30**, 1178 (1974).
12. H. Koenig and R. Hoppe, Z. Anorg. Allg. Chem. **439**, 71 (1978).
13. S. V. Radaev, E. A. Genkina, V. A. Lomonov, *et al.*, Kristallografiya **36** (6), 1419 (1991) [Crystallogr. Rep. **36** (6), 803 (1991)].
14. R. S. Bubnova, V. S. Fundamenskiĭ, I. I. Bannova, *et al.*, in *Collected Abstracts Int. Conf. “Spectroscopy, X-ray Diffraction Analysis, and Crystal Chemistry of Minerals,” Kazan, 1997* (Izd. Kazan. Univ., Kazan, 1997), p. 52.
15. J. Shneider, in *Profile Refinement on IBM-PC’s. IUCr. Int. Workshop on the Rietveld Method, Petten, 1989*, p. 71.
16. R. S. Bubnova, I. G. Polyakova, S. K. Filatov, and M. G. Krzhizhanovskaya, in *Borate Glasses Crystals and Melts*, Eds. A. C. Wright, S. A. Feller, and A. C. Hannon (Alden, Oxford, 1997), p. 120.
17. M. G. Krzhizhanovskaya, R. S. Bubnova, I. I. Bannova, and S. K. Filatov, Kristallografiya **42** (2), 264 (1997) [Crystallogr. Rep. **42** (2), 226 (1997)].

Translated by I. Polyakova

Crystallography Reports, Vol. 45, No. 4, 2000, pp. 578–584. Translated from Kristallografiya, Vol. 45, No. 4, 2000, pp. 635–641.
Original Russian Text Copyright © 2000 by Yakubovich, Kireev, Mel'nikov.

STRUCTURE OF INORGANIC COMPOUNDS

Refinement of Crystal Structure of a Ge-Analogue of Natisite $Na_2\{TiGeO_4\}$ and Prediction of New Phases with Anionic $\{MTO_5\}$ Radicals

O. V. Yakubovich*, V. V. Kireev, and O. K. Mel'nikov***** †
* Moscow State University, Vorob'evy gory, Moscow, 119899 Russia
** Moscow State Academy of Fine Chemical Technology, Moscow, Russia
*** Shubnikov Institute of Crystallography, Russian Academy of Sciences, Leninskiĭ pr. 59, Moscow, 117333 Russia

Received March 4, 1999; in final form, October 25, 1999

Abstract—The crystal structure of the synthetic Ge-modification of the mineral natisite, $Na_2\{TiOGeO_4\}$, has been refined by X-ray diffraction method (a four-circle diffractometer, $2\theta/\theta$ scanning, MoK_α-radiation, θ_{max} = 50°: $a = 6.658(1)$, $c = 5.161(1)$ Å, sp. gr. $P4/nmm$, $Z = 2$, $\rho_{calcd} = 3.58$ g/cm^3, $R1 = 0.030$, $s = 1.131$, $wR(F^2) = 0.058$ (352 reflections with $I \geq 2\sigma I$). The comparative crystallochemical analysis of the related (including hypothetical) phases with the anionic $\{MTO_5\}$ radicals (M = Ti, V, Ge; T = Ge, Si, P) is performed with the aim of revealing a possible relationship between the composition and the structure type of the compounds. *© 2000 MAIK "Nauka/Interperiodica".*

INTRODUCTION

A considerable interest in the studies of titanium-containing crystalline compounds is associated with their valuable physical properties, of which the most important are the nonlinear optical properties. Most often, titanium in crystalline oxygen-containing compounds is characterized by the coordination number six (the coordination polyhedron is an octahedron), although some compounds also show the tetrahedral or the fivefold titanium coordination [1]. The relationship between the nonlinear optical characteristics of the Ti-containing oxosalts [one of the typical representative of which is an acentric $KTiOPO_4$ (KTP) phase] and the distorted Ti-octahedron is confirmed by numerous studies, e.g., [2].

According to [3], the bond between the transition metal and oxygen is the most important parameter of nonlinear-optical materials with the composition indicated above. From this standpoint, of great interest are the compounds with the structures close to that of the mineral natisite $Na_2TiOSiO_4$ [4]. The distortion of Ti-octahedra in the structures of such compounds is so pronounced that the coordination polyhedron of Ti can be considered as a tetragonal pyramid with four close Ti–O bonds (≈1.97 Å) and one shortened Ti–O bond (≈1.70 Å) (the sixth Ti–O distance exceeds 3 Å). The deformation electron density in Ti-octahedra in titanite ($CaTiOSiO_4$) with the similar distribution of Ti–O bonds [5] justifies the separation of a such titanyl group characterizing the anomalously strong interaction between the titanium atom and one of the oxygen atoms in the minerals and synthetic phases.

The solution of the structure of the acentric orthorhombic modification of the low-temperature $Na_2TiOSiO_4$ modification [6], a synthetic analogue of the mineral paranatisite [7], allowed the interpretation of this phase as a probable nonlinear-optical material. The test for the second-harmonic generation showed the positive result over the wide temperature range (up to T = 800°C).

The well known ability of germanium to be located in both octahedra and tetrahedra (even within one structure) is explained by the amphoteric properties of its oxocomplexes, which can perform both the cationic (octahedra) and the anionic (tetrahedral complex GeO_4 anions) functions. Single crystals of the tetragonal Ge-analogue of the mineral natisite were obtained in the crystallization of the orthorhombic $Na_2TiOGeO_4$ modification, a phase isostructural to the orthorhombic $Na_2TiOSiO_4$ crystals, which can possess high nonlinear optical properties.

The crystal structure of the Ge-analogue of natisite [8] synthesized under the hydrothermal conditions was solved by the photographic method (the *0kl*–*4kl* and *hk0*–*hkl* layer lines) and then refined up to R_{hkl} = 12.8% in 1970. We undertook the structure refinement of the tetragonal $Na_2TiOGeO_4$ phase belonging to this structure type because of its promising physical properties. The results of this refinement and the comparative crystallochemical analysis of the related phases were performed with the aim of establishing the dependence between the composition of the compound and its structure type.

---

† Deceased.

EXPERIMENTAL. STRUCTURE REFINEMENT

Ge-natisite was synthesized in the shape of flattened prismatic colorless transparent crystals with the pyramidal end faces. The crystal lengths varied from 0.1 to 0.2 mm. The crystals were grown by the hydrothermal method from an alkaline solution (the NaOH concentration was equal to ≈25%) at $P = 900$ atm and $T = 450°C$. The composition of the initial charge was 10 g GeO_2 and 10 g TiO_2 per 30 ml of the solvent. The experiment was performed for 14 days in titanium-lined steel autoclaves.

The data of the X-ray spectral analysis and the diffractometric powder measurements allowed us to identify the samples as $Na_2TiOGeO_4$. The tetragonal unit-cell parameters and the crystal symmetry were refined on an isometric ~0.1 mm-long crystal on a four-circle SINTEX $P\bar{1}$ diffractometer. The crystallographic characteristics of the crystals, the data on processing of the experimental data, and the refined structure parameters are listed in Table 1.

All the computations were performed by the SHELXL programs [9]. We used the atomic scattering curves and introduced the corrections for anomalous dispersion [10]. The structure was refined in the full-matrix anisotropic approximation up to $R = 0.0304$. The coordinates of the basis atoms with the equivalent temperature factors are listed in Table 2.

DISCUSSION OF RESULTS

The coordination polyhedron of a Ti atom in the Ge-natisite, $Na_2TiOGeO_4$, is a hemioctahedron (a tetragonal pyramid). In accordance with its symmetry, D_{4v}, four oxygen atoms are located at equal distances from titanium (Ti–O(1) = 1.993(2) Å), and one more oxygen atom is located at the pyramid vertex and is characterized by a somewhat shortened distance, Ti–O(2) = 1.708(5) Å. The corresponding interatomic Ti–O distances in the pyramid base of the isostructural synthetic natisite, $Na_2TiOSiO_4$ [4], are equal to Ti–O 1.990(2) Å, whereas the Ti–O distance characterizing of the titanyl group is 1.695(5) Å. In addition to sodium-containing phases, there are two lithium-containing isotypes: $Li_2TiOSiO_4$ [11] and Li_2VOSiO_4 [12]. In the first compound, four Ti–O distances in the pyramid base are equal to 1.967(1) Å, the distance to the vertex equals 1.698(3) Å. The corresponding interatomic distances in the five-vertex polyhedron are shorter—1.955(3) and 1.623(6) Å, respectively. As is seen, the vanadyl group in Li_2VOSiO_4 is recorded even more accurately than the titanyl group in the titanium-containing phases of this structure type.

Table 1. Crystallographic characteristics of Ge-natisite and parameters of the diffractometric experiment and the structure refinement

Crystallographic characteristics	
Chemical formula	$Na_2\{TiO[GeO_4]\}$
Absorption, μ, mm^{-1}	8.42
Sp. gr.	$P4/nmm$
Unit-cell parameters, Å	
a	6.658(1)
c	5.161(1)
Z	2
Density ρ_{calc}, g/cm^3	3.578
Characteristics of diffractometric measurements	
Crystal dimensions, mm	0.1 × 0.1 × 0.1
Diffractometer	SINTEX $P\bar{1}$
Monochromator	Graphite
Radiation	MoK_α
Scanning mode	$2\theta : \theta$
$2\theta_{max}$, deg	100
Number of measured reflections	369
Number of independent reflections with $I \geq 2\sigma(I)$	352
Parameters of structure refinement	
Absorption correction	DIFABS
T_{max}, T_{min}	1.000, 0.760
Program complex	SHELXL97 (refinement by F^2)
Extinction coefficient	0.001(2)
$R1$	0.0304
s	1.131
$wR(F^2)$	0.0576

Table 2. Coordinates of basis atoms and equivalent temperature factors ($Å^2$)

Atom	x/a	y/b	z/c	U_{eq}
Ge	0.75	0.25	0.5	0.0053(1)
Ti	0.25	0.25	0.5743(2)	0.0056(2)
Na	0.5	0	0	0.0167(4)
O(1)	0.75	0.0346(3)	0.3062(4)	0.0081(4)
O(2)	0.25	0.25	0.2432(9)	0.0141(9)

The Ge–O distances in almost regular germanium tetrahedra in the $Na_2TiOGeO_4$ structure are equal to 1.748(2) Å. There are two groups of the cation–oxygen distances describing the centrosymmetric Na-octahedra (with the symmetry C_{2h}): Na–O(1) = 2.307(1) (four distances) and Na–O(2) = 2.669(2) Å (two distances), with the average distance being ⟨2.428 Å⟩.

The crystal structure of sodium titanogermanate has anionic layers of the mixed $\{TiO[GeO_4]\}$-type, which are topologically identical to the Ti,Si-layers formed by Ti-hemioctahedra and Ge-tetrahedra located in the

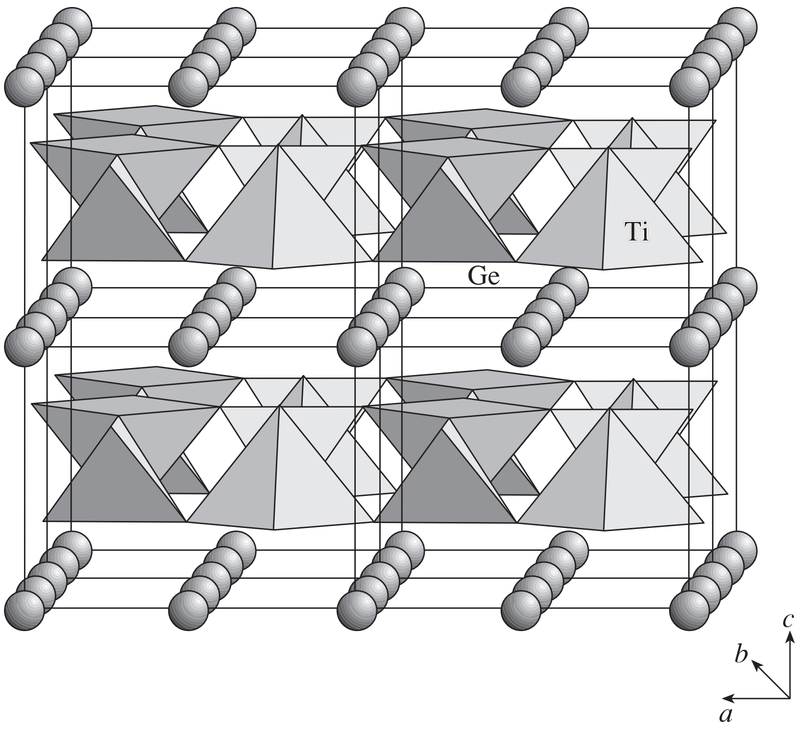

Fig. 1. $Na_2\{TiOGeO_4\}$ crystal structure. Sodium atoms are shown by spheres.

chess-board like manner in the *ab* plane and connected via the oxygen vertices. Along the *c*-axis, these layers alternate with layers of Na^+-cations occupying the octahedra sharing edges and vertices (Fig. 1).

As indicated above, four phases are crystallized in the natisite structure type (sp. gr. *P*4/*nmm*). They form a morphotropic series of isotypes described by the general formula $A_2\{MTO_5\}$, where *A* is the alkali metal (Na, Li) occupying an octahedron, *M* is the transition metal (Ti, V) occupying a five-vertex polyhedron, and *T* is Ge or Si occupying a tetrahedron. It should be emphasized that the complete isostructurality in this series is preserved upon the substitution of atoms in all the three types of cationic positions: in *A* position ($Na_2TiOSiO_4$–$Li_2TiOSiO_4$), in the *M* position ($Li_2TiOSiO_4$–Li_2VOSiO_4), and in the *T* position ($Na_2TiOGeO_4$–$Na_2TiOSiO_4$).

The crystallochemical characteristics, and, first of all, the charges and the ionic radii of the elements forming the mixed $\{MTO_5\}$-layers in the natisite structure type ($R_{Ti}^{4+} = 0.68$, $R_{V}^{4+} = 0.63$, $R_{V}^{5+} = 0.59$, $R_{Ge}^{4+} = 0.53$, $R_{Si}^{4+} = 0.42$, and $R_{P}^{5+} = 0.35$ Å) are such that a wide spectrum of potential isotypes and structurally related phases can be formed. Let us construct a composition tetrahedron for probable compounds with the anionic radicals of the mixed $\{MTO_5\}$-type. With this aim, place the *M* and *A* atoms (the already considered set of monovalent cations is complemented with potassium) at the vertices, and place the *T* atoms at the centers of the edges of the basis face (Fig. 2). Thus, we arrive at the complete list of the natural, synthesized, and hypothetical phases described by the formulas $A_2\{MTO_5\}$ and $A\{MTO_5\}$. Taking into account the amphoteric nature of germanium, this list can be considerably increased if one assumes that the Ge^{4+} cations fill not only tetrahedral (*T*), but also the octahedral (hemioctahedral) positions (*M*).

As is seen from Fig. 2, no $A_2\{GeTO_5\}$ compounds crystallizing in the natisite structure type are known. In the crystal structures of the lithium and sodium natisite analogues, $Li_2\{GeGeO_5\}$ [13], $Li_2\{(Ge, Si)_2O_5\}$ [14], and $Na_2\{GeGeO_5\}$ [15], Ge^{4+} cations can occupy only tetrahedra, and, therefore, their structure types differ from natisite. The $Li_2\{GeGeO_5\}$ and $Na_2\{GeGeO_5\}$ crystal structures with tetrahedrally-coordinated germanium are the layer network structures built by germanium tetrahedra separated by the layers of Li- or Na-polyhedra (Fig. 3). The tetrahedral nets in the sodium-containing phase (the $Na_2Si_2O_5$ structure type [16]) can be considered as fragments of the β-tridymite structure.

Among the structure types with the anionic $\{MTO_5\}$-type radicals [17], the most widespread are

(1) the natisite structure type, in which all the above four phases ($Na_2TiOSiO_4$, $Na_2TiOGeO_4$, $Li_2TiOSiO_4$, and Li_2VOSiO_4) and the mineral natisite are crystallized;

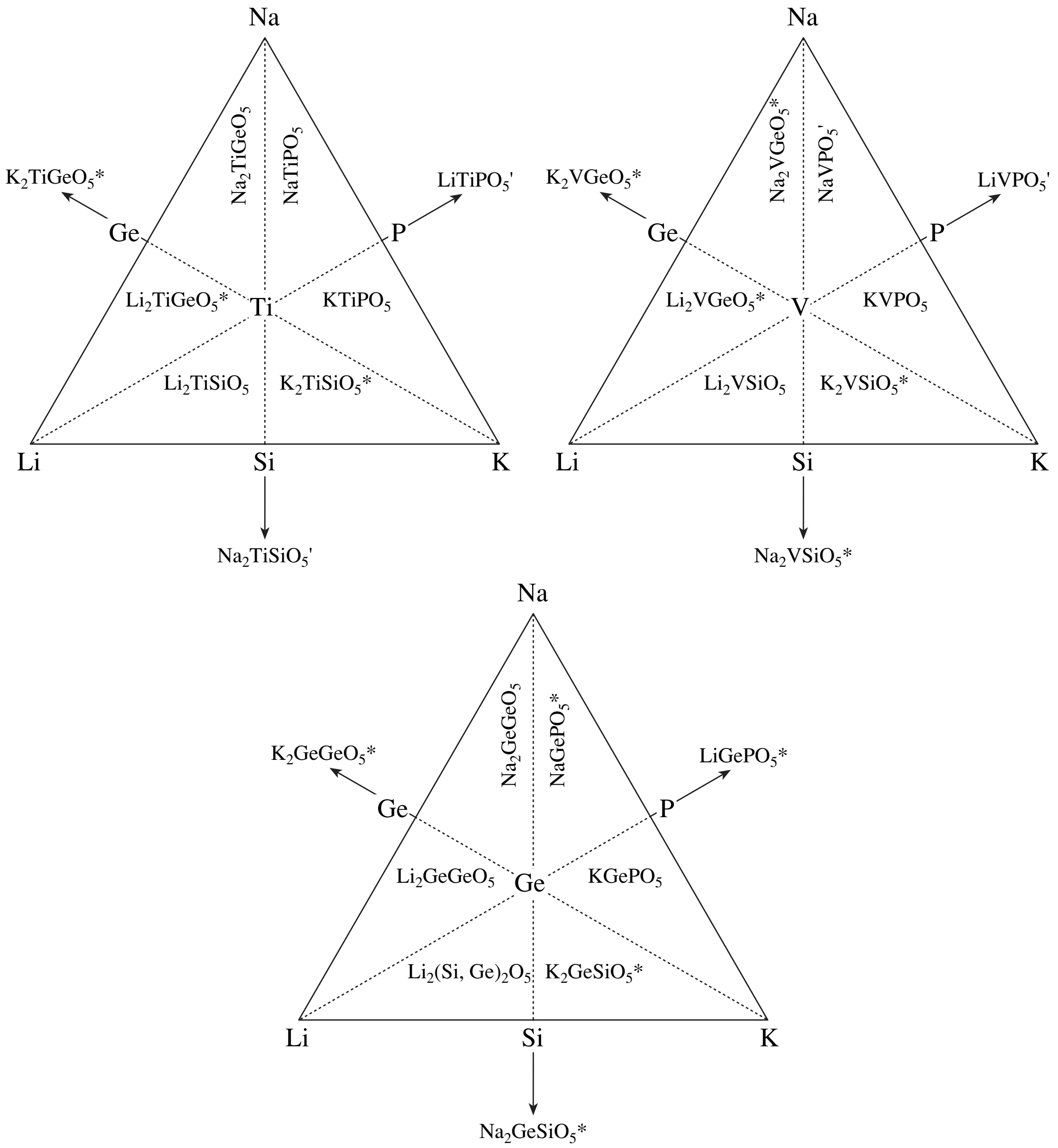

Fig. 2. Composition tetrahedra showing the existing and the hypothetical phases. The anionic $\{MTO_5\}$-radical is indicated in parentheses. The vertices of the tetrahedron bases are occupied by *A* atoms; the fourth vertex of the tetrahedron is occupied by an *M* atom, and *T* atoms are located in the middles of the base edges. Any *ATM*-triangle of the composition tetrahedron indicates the corresponding phase composition. Asterisks indicate unknown phases, primes indicate that the phases have two polymorphs.

(2) the titanite structure type $CaTiOSiO_4$ characteristic of isotypes $NaTiOPO_4$ [18] and $NaVOPO_4$ [19] with the space group of sphene, $P2_1/c$, and lithium phosphates—$LiTiOPO_4$ [20, 21] and $LiVOPO_4$ [22, 23]—both having the orthorhombic (sp. gr. *Pnma*) and triclinic (sp. gr. $P\bar{1}$) modifications, which are topologically identical to the structure of the mineral titanite (sphene);

(3) the KTP structure type ($KTiOPO_4$) known for the compound $KTiOPO_4$ (after which this structure type is named) and also for $KVOPO_4$ [24] and $KGeOPO_4$ [25]. In the latter case, since a more active phosphorus readily forms PO_4 groups, Ge^{4+} cations are located in octahedra.

In addition to the above four structure types, a new structure type was established for the low-temperature $Na_2TiOSiO_4$ modification (an orthorhombic polymorph also occurring in nature as mineral paranatisite) [6]. The crystal structure of the synthetic analogue of paranatisite is described by the acentric sp. gr. $Pmc2_1$ and consists of the same structural elements as its tetragonal modification, namely, of Ti-hemioctahedra, Si-tetrahedra, and Na-octahedra. The interatomic Ti–O distances in two independent five-vertex polyhedra of the symmetry C_s are such that each five-vertex polyhedron has four close distances [Ti(1)–O = 1.951(5) × 2,

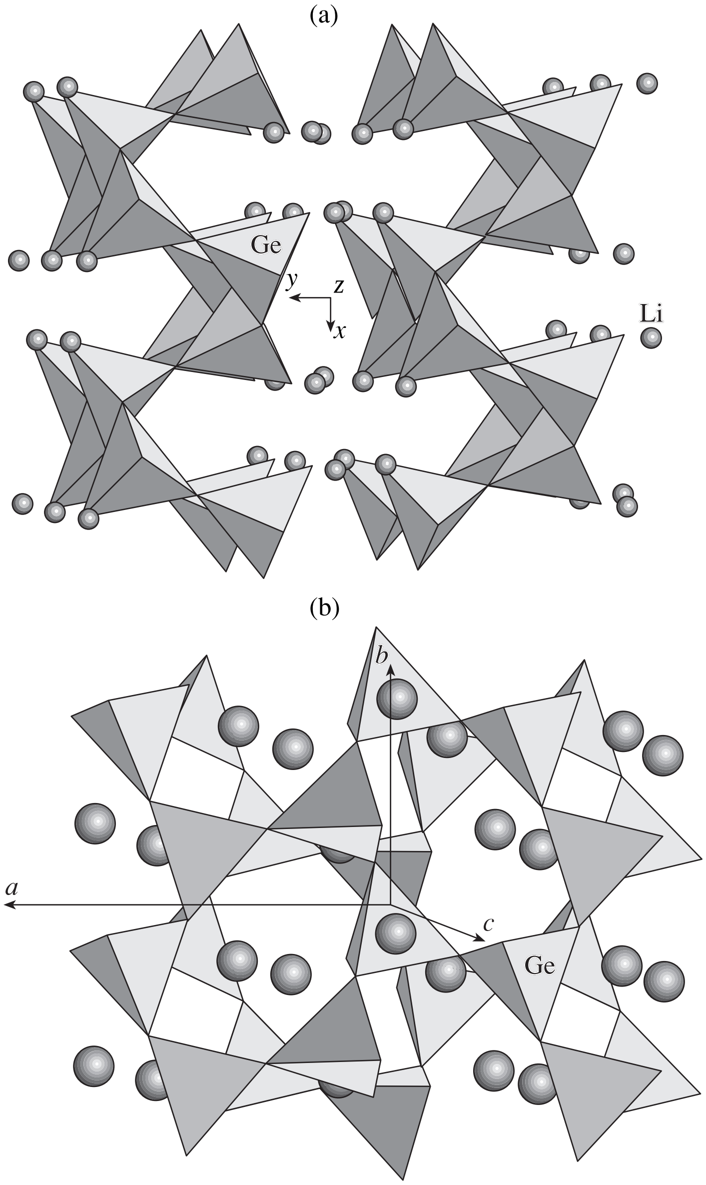

Fig. 3. $A_2\{\mathrm{Ge}T\mathrm{O}_5\}$ crystal structures, where T = Ge, Si (the formula analogues of the mineral natisite with tetrahedrally coordinated Ge atoms in both positions). (a) $Li_2Ge_2O_5$ and (b) $Na_2Ge_2O_5$.

Ti(1)–O = 1.974(5) × 2, Ti(2)–O = 1.964(5) × 2, and Ti(2)–O = 1.990(5) × 2 Å] and one shortened distance [Ti(1)–O = 1.705(7) and Ti(2)–O = 1.703(8) Å, respectively] characterizing the titanyl groups. The sixth oxygen atoms, which build-up the Ti-polyhedra to octahedra, are spaced by 3.110(7) and 3.481(8) Å from the Ti(1) and Ti(2), respectively. Both orthorhombic and tetragonal $Na_2TiOSiO_4$ polymorphs have similar structural fragments (polysomes). These are ribbons of tetragonal Ti-pyramids located on the four-angle faces and edge-oriented Si-tetrahedra of the edge orientation. Each Ti-hemioctahedron in the ribbon shares four basis vertices with four Si-tetrahedra. In the tetragonal modification, each SiO_4-tetrahedron is shared by two such ribbons elongated in the [110]-direction, which results in the formation of the layers parallel to the *ab* plane formed by alternating Ti-hemioctahedra and Si-tetrahedra along the *a*- and *b*-axes (Fig. 1). The anionic $\{TiOSiO_4\}^{2-}$-layers alternate with the layers of Na-octahedra along the *c*-axis.

The relationship between the unit-cell parameters of the tetragonal and orthorhombic polymorphs can roughly be determined from the following vector relationships: $\mathbf{a}_0 \approx \mathbf{c}_0 \approx \mathbf{a}_t$ and $\mathbf{b}_0 \approx \mathbf{c}_t$. The crystal structure of the orthorhombic phase consists of the ribbons described above and located along *c*-axis in the *ac*-plane and along the *b*-axis in the *ab*-plane. Each SiO_4-tetrahedron shares two vertices with the neighboring

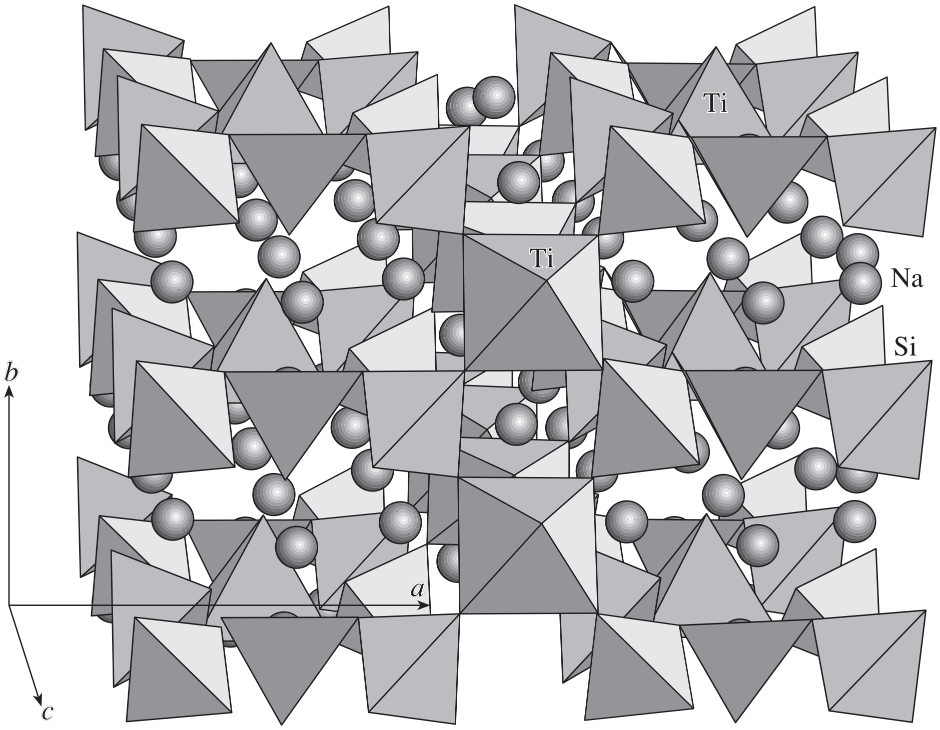

Fig. 4. Crystal structure of the orthorhombic modification of $Na_2\{TiOSiO_4\}$ in the axonometric projection.

hemioctahedra of one ribbon and two other vertices with the neighboring hemioctahedra of the other perpendicular ribbon. Displacing the hemioctahedron along the diagonal of the *ab* face of the tetragonal phase by a half of the second diagonal in the same plane and then displacing it downward along the *c*-axis (and thus changing the vertex orientation to the face orientation), we arrive at the orthorhombic $Na_2TiOSiO_4$ structure, in which the mixed anionic layers consisting of Si-tetrahedra and Ti-hemioctahedra are transformed into the framework described by the same formula $\{TiOSiO_4\}^{2-}$ (Fig. 4).

The framework structure, with the parameters very close to those of the tetragonal unit cell described by the same space group and topologically identical to the natisite structure in the basis projection, is characteristic of vanadyl phosphate $VOPO_4$ (the α-phase) [26]. Removing the layer of monovalent cations from the layer natisite (or Li_2VOSiO_4) structure and simultaneously substituting silicon in tetrahedra by phosphorus, we arrive at the situation where (V, P) layers along the *c*-axis are combined together, and V^{4+} hemioctahedra are transformed into V^{5+} octahedra. The phase thus obtained can be interpreted as another (quasimorphotropic) member of the natisite structural series.

REFERENCES

1. Yu. A. Pyatenko, A. A. Voronkov, and Z. V. Pudovkina, *Mineralogical Crystal Chemistry of Titanium* (Nauka, Moscow, 1976).
2. G. D. Stucky, M. L. F. Phillips, and T. E. Gier, Chem. Mater. **1**, 492 (1989).
3. C. R. Jego and G. D. Boyd, J. Appl. Phys. **41**, 2741 (1970).
4. H. Nyman and M. O'Keeffe, Acta Crystallogr., Sect. B: Struct. Crystallogr. Cryst. Chem. **34**, 905 (1978).
5. V. S. Urusov, N. N. Eremin, and O. V. Yakubovich, Kristallografiya **40** (3), 485 (1995) [Crystallogr. Rep. **40** (3), 442 (1995)].
6. A. Ziadi, H. Hillebrecht, G. Thiele, and B. Elouadi, J. Solid State Chem. **123**, 324 (1996).
7. A. P. Khomyakov, L. I. Polezhaeva, and E. V. Sokolova, Zap. Vses. Mineral. O–va **126**, 133 (1992).
8. V. Ya. Verkhovskiĭ, É. A. Kuz'min, V. V. Ilyukhin, and N. V. Belov, Dokl. Akad. Nauk SSSR **190**, 91 (1970).
9. G. M. Sheldrick, *SHELXL 97: Program for the Refinement of Crystal Structures from Diffraction Data* (Univ. of Göttingen, Germany, 1997).
10. *International Tables of Crystallography,* Ed. by T. Hahn (Kluwer, Dordrecht, 1995), Vol. A, 4th ed.
11. A. Ziadi, G. Thiele, and B. Elouadi, J. Solid State Chem. **109**, 112 (1994).
12. K. K. Rangan, Y. Piffard, O. Joubert, and M. Tournoux, Acta Crystallogr., Sect C: Cryst. Struct. Commun. **54**, 176 (1998).
13. H. Voellenkle and A. Wittmann, Monatsh. Chem. **99**, 251 (1968).
14. H. Voellenkle, A. Wittmann, and H. Nowotny, Z. Kristallogr. **126**, 37 (1968).
15. K. Kemiya *et al.*, Mater. Res. Bull. **14**, 641 (1979).

16. A. K. Pant, Acta Crystallogr. **24**, 1077 (1968).
17. P. A. Sandomirskiĭ and N. V. Belov, *Crystal Chemistry of Anionic Radicals* (Nauka, Moscow, 1984).
18. M. L. F. Phillips, W. T. A. Harrison, G. D. Stucky, *et al.*, Chem. Mater. **4**, 222 (1992).
19. K. H. Lii, C. H. Li, C. Y. Cheng, and S. L. Wang, Z. Kristallogr. **197**, 67 (1991).
20. P. G. Nagornyĭ, A. A. Kapshuk, N. V. Stus’, *et al.*, Zh. Neorg. Khim. **36**, 2766 (1991).
21. I. N. Geĭfman, N. G. Furmanova, P. G. Nagornyĭ, *et al.*, Kristallografiya **38** (6), 88 (1993) [Crystallogr. Rep. **38** (6), 759 (1993)].
22. K. H. Lii, C. H. Li, C. Y. Cheng, and S. L. Wang, J. Solid State Chem. **95**, 352 (1991).
23. A. V. Lavrov, V. P. Nikolaev, G. G. Sadikov, and M. A. Poraĭ-Koshits, Dokl. Akad. Nauk SSSR **266**, 343 (1982) [Sov. Phys. Dokl. **27**, 680 (1982)].
24. M. L. F. Phillips, W. T. A. Harrison, T. E. Gier, *et al.*, Inorg. Chem. **29**, 2158 (1990).
25. V. I. Voronkova, V. K. Yanovskiĭ, N. I. Sorokina, *et al.*, Kristallografiya **38** (5), 147 (1993) [Crystallogr. Rep. **38** (5), 662 (1993)].
26. B. D. Jordan and C. Calvo, Acta Crystallogr., Sect. B: Struct. Crystallogr. Cryst. Chem. **32**, 2894 (1976).

Translated by L. Man

Crystallography Reports, Vol. 45, No. 4, 2000, pp. 585–590. Translated from Kristallografiya, Vol. 45, No. 4, 2000, pp. 642–648.
Original Russian Text Copyright © 2000 by Yamnova, Egorov-Tismenko, Zlykhenskaya, Khomyakov.

Refined Crystal Structure of Iron-Rich Triclinic Astrophyllite

N. A. Yamnova*, Yu. K. Egorov-Tismenko*,
I. V. Zlykhenskaya*, and A. P. Khomyakov**

** Moscow State University, Vorob'evy gory, Moscow, 119899 Russia*[1]

*** Institute of Mineralogy, Geochemistry, and Crystal Chemistry of Rare Elements,*
Russian Academy of Sciences, ul. Veresaeva 15, Moscow, 121327 Russia

Received July 1, 1998

Abstract—Crystal structure of Fe-rich triclinic astrophyllite $K_2NaFe_7[Ti_2Si_8O_{26}F](OH)_4$ is refined (a Syntex $P\bar{1}$ automatic diffractometer, 3809 reflections, $2\theta/\theta$ scan, $R = 0.041$): $a = 5.365(2)$, $b = 11.88(1)$, $c = 21.03(2)$ Å, $\alpha = 84.87(6)°$, $\beta = 92.25(5)°$, $\gamma = 103.01(4)°$, sp. gr. $A\bar{1}$, $Z = 2$, $d_{\text{calcd}} = 3.29$ g/cm^3. The refined structure is identical to that reported earlier. The structure is built by three-layer *TOT* sheets in which an *O* layer of Fe-octahedra is sandwiched between the *T* layers consisting of Si-tetrahedra and Ti-octahedra. It is established that differently chosen unit cells of the mineral are interrelated. *© 2000 MAIK "Nauka/Interperiodica".*

INTRODUCTION

Astrophyllite, a mica-like titanium silicate, is known to have several polymorphic modifications with different symmetries and compositions. The crystal structure of the monoclinic modification was determined in [1, 2], and that of one of the triclinic modifications, in [3]. Yet, the quality of crystal samples used in [3] was low. As a result, it was impossible to determine the positional parameters with a sufficient accuracy (one of the parameters was roughly estimated). The final reliability factor was $R = 0.10$. These facts and the discrepancy of the unit-cell parameters of triclinic astrophyllites determined from numerous X-ray data stimulated a new refinement of the crystal structure of this mineral.

The astrophyllite samples studied were obtained from the crystals from the Khibiny deposit (Cola Peninsula). Their composition is described by the approximate formula

$$Na_2(K_{3.95}Ba_{0.01}Na_{0.04})_{\Sigma 4}(Fe^{2+}_{1.52}Fe^{3+}_{0.48})_{\Sigma 2}$$
$$\times(Fe^{2+}_{2.00}Mn_{1.04}Ca_{0.76}Na_{0.20})_{\Sigma 4}(Fe^{2+}_{6.76}Mg_{1.24})_{\Sigma 8}$$
$$\times(Ti_{3.95}Nb_{0.03}Zr_{0.02})_{\Sigma 4}(F_{1.20}OH_{0.80})$$
$$\times[(Si_{15.70}Al_{0.30})_{\Sigma 16}O_{48}]O_4(OH)_8$$

(microprobe analysis data).

The mineral is the richest in Fe and poorest in Mn and Al, compared with all the other astrophylites from the Khibiny deposit. It is thus the sample closest to the end compound of the series that has the composition $NaK_2Fe_7Ti_2Si_8O_{26}F(OH)_4$.

DIFFRACTION EXPERIMENT AND STRUCTURE REFINEMENT

The sample was a 0.1 × 0.15 × 0.3 mm-large astrophyllite single crystal.

The symmetry and unit-cell parameters of the triclinic unit cell were determined by the photomethod and then were refined on a Syntex $P\bar{1}$ automatic single-crystal diffractometer: $a' = 21.498(1)$, $b' = 11.884(2)$, $c' = 5.365(2)$ Å, $\alpha' = 103.08(4)°$, $\beta' = 102.19(5)°$, and $\gamma' = 82.73(6)°$. The crystal data collected in the trigonal setting are given in Table 1. The calculation of the $|F_{hkl}|$ amplitudes from the reflection intensities and all the other computations were performed by the AREN complex of programs [4]. The extinction laws for the *hkl* reflections (with $h + k = 2n$) indicated the base-centered Bravais lattice and, correspondingly, two possible space groups, $C1$ and $C\bar{1}$. Since the unit-cell parameters measured were different from those reported in [3], the structure of the mineral was solved by a direct method with the use of the automatic procedure of model selection and successive approximations. The final structure refinement was performed by the least squares method, within in the centrosymmetric space group $C\bar{1}$ in the isotropic approximation to $R_{\text{iso}} = 0.067$. The distribution of K^+, Na^+, Fe^{2+}, Fe^{3+}, Mn^{2+}, Mg^{2+}, and Ca^{2+} over the crystallographic positions was determined upon the refinement of the occupancies of these positions at the fixed B_{iso} with the use of appropriate mixed atomic-scattering curves and with due regard for the data of chemical analysis, the effective ionic radii, the average cation–oxygen distances, and the values of the temperature factors. The minimum reliability factor $R_{\text{aniso}} = 0.041$ was obtained for the formula

---

[1] *e-mail: elbel@geol.msu.ru*

Table 1. Numerical characteristics of the diffraction experiment on Fe-rich astrophyllite

Sample dimensions	0.1 × 0.15 × 0.3 mm	
Automatic single-crystal diffractometer	Syntex $P\bar{1}$	
Radiation	MoK_α	
Monochromator	Graphite	
Sp. gr.	$C\bar{1}$	$A\bar{1}$
Unit-cell constants (Å, deg) of the initial structure model for which the data were collected (left) and of the transformed structure model for which the final positional atomic parameters were determined (on the right)	a' = 21.50(2) b' = 11.88(1) c' = 5.365(2) α' = 103.08(4)° β' = 102.19(5)° γ' = 82.73(6)°	a = 5.365(2) b = 11.88(1) c = 21.03(2) α = 84.87(6)° β = 92.25(5)° γ = 103.01(4)°
Number of formula units per unit cell, Z	V = 1300.5(1)	2
Scan	2θ : θ	
Maximum sinθ/λ	1.08	
Scan rate	6–24 deg/min	
Number of measured reflections with $I > 1.96\sigma(I)$	3809	
Number of reflections used in the final least-squares procedure	3778	
Complex of programs	AREN	
Final reliability factor $R_{(hkl)}$:		
isotropic approximation	0.067	
anisotropic approximation	0.041	
Weighting scheme used in the least-squares procedure	$w = 1/(A + F + BF^2)$ $A = 2F_{\min} B = 2/F_{\max}$	

Table 2. Unit-cell constants (Å, deg) of some variants of triclinic astrophyllite structure and the matrices of the corresponding transformations

Initial, experimentally determined unit cell C, sp. gr. $C\bar{1}$	Unit cell A (sp. gr. $A\bar{1}$) obtained by the transformation of the C-cell using the matrix: $M_{C\to A} = \begin{pmatrix} 0 & 0 & \bar{1} \\ 0 & 1 & 1 \\ 1 & 0 & 1 \end{pmatrix}$	Unit cell A (sp. gr. $A\bar{1}$) suggested in [3]	Primitive unit cell (sp. gr. $P\bar{1}$) obtained by the transformation of A unit-cell from [3] using the matrix: $M_{A\to P} = \begin{pmatrix} 1 & 0 & 0 \\ 0 & 1 & 0 \\ 1 & \frac{1}{2} & \frac{1}{2} \end{pmatrix}$
a' = 21.498, α' = 103.08°	a = 5.365, α = 84.87°	a_w = 5.36, α_w = 85.13°	a'_w = 5.36, α'_w = 64.85°
b' = 11.884, β' = 102.19°	b = 11.881, β = 92.25°	b_w = 11.76, β_w = 90.00°	b'_w = 11.76, β'_w = 72.09°
c' = 5.365, γ' = 82.73°	c = 21.029, γ = 103.01°	c_w = 21.08, γ_w = 103.22°	c'_w = 13.06, γ'_w = 103.22°
Primitive unit cells obtained by transformation of the C-cell using various matrices			
Variant 1 $M_{C\to P} = \begin{pmatrix} 0 & 0 & \bar{1} \\ 0 & 1 & 1 \\ \frac{1}{2} & \frac{1}{2} & 0 \end{pmatrix}$	Variant 2 $M_{C\to P} = \begin{pmatrix} 0 & 0 & \bar{1} \\ 0 & 1 & 1 \\ \frac{1}{2} & \frac{1}{2} & 1 \end{pmatrix}$	Variant 3 $M_{C\to P} = \begin{pmatrix} 0 & 0 & \bar{1} \\ 0 & 1 & 1 \\ \frac{1}{2} & \frac{\bar{1}}{2} & \bar{1} \end{pmatrix}$	Variant 4 $M_{C\to P} = \begin{pmatrix} 0 & 0 & \bar{1} \\ 0 & 1 & 1 \\ \frac{1}{2} & \frac{\bar{1}}{2} & 0 \end{pmatrix}$
a_1 = 5.365, α_1 = 63.97°	a_2 = 5.365, α_2 = 56.69°	a_3 = 5.365, α_3 = 118.13°	a_4 = 5.365, α_4 = 115.52°
b_1 = 11.881, β_1 = 73.76°	b_2 = 11.881, β_2 = 98.03°	b_3 = 11.881, β_3 = 61.47°	b_4 = 11.881, β_4 = 85.43°
c_1 = 12.924, γ_1 = 103.01°	c_2 = 12.531, γ_2 = 103.01°	c_3 = 13.168, γ_3 = 103.01°	c_4 = 11.605, γ_4 = 103.01°

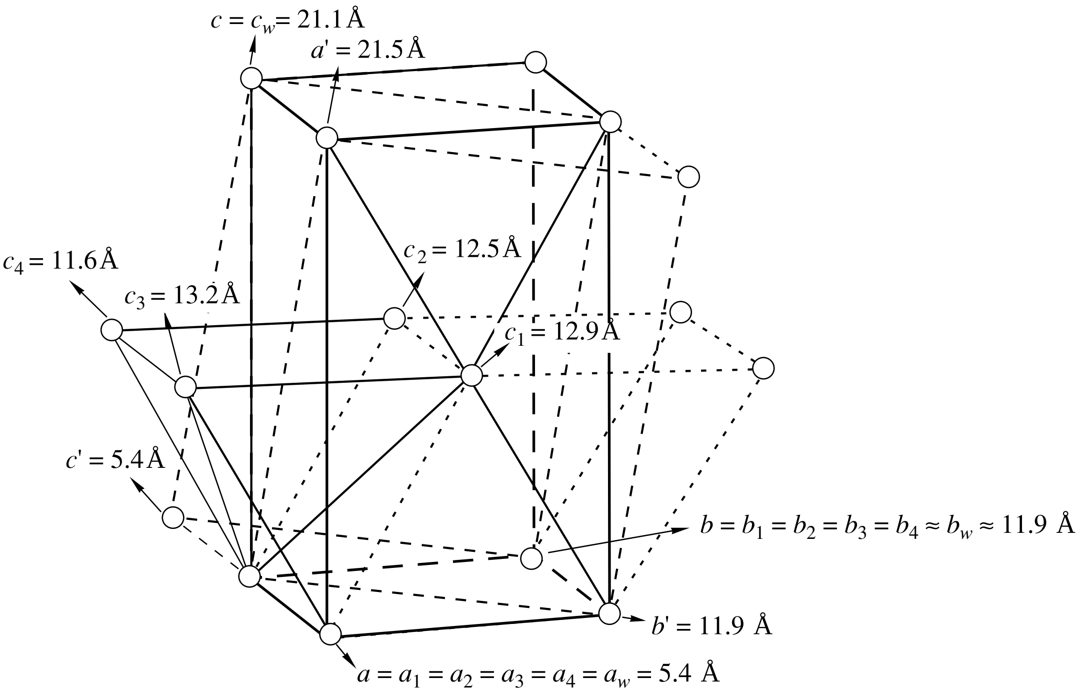

Fig. 1. Primitive and centered unit cells possible for triclinic astrophyllite. The *a*, *b*, and *c* parameters coincide with those given in Table 2.

$(K_{0.85}Na_{0.15})_2(Na_{0.73}K_{0.27})(Fe^{2+}_{0.84}Mg_{0.16})_4(Fe^{2+}_{0.76}Fe^{3+}_{0.24}) \cdot (Fe^{2+}_{0.50}Mn_{0.26}Ca_{0.19}Na_{0.05})_2[(Ti_{0.99}(Nb, Zr)_{0.01})_2(Si_{0.98}Al_{0.02})_8 \cdot O_{26}(OH, F)](OH)_4$ ($Z = 2$, $d_{calcd} = 3.29$ g/cm^3). The idealized formula is $K_2NaFe_7[Ti_2Si_8O_{26}F](OH)_4$. The substitution of Al for Si and Nb and Zr for Ti was established by the chemical analysis. The substituents in such low concentrations could not be detected by X-ray methods.

The O^{2-} and OH^- (F^-) positions were separated by calculating the local balance of bond strengths with due regard for the cation–anion distances [5]. The positional and thermal parameters of two independent hydrogen atoms were determined from the three-dimensional difference electron-density map and were refined by the least-squares method.

The comparison of our structure model with the model described in [3] in terms of crystal chemistry showed their identity. However, the comparison of the base-centered structure (sp. gr. $C\bar{1}$, unit-cell parameters *a*', *b*', and *c*'; see Table 2), suggested and refined in the present study with the face-centered structure (sp. gr. $A\bar{1}$, unit-cell parameters a_w, b_w, and c_w; see Table 2) suggested in [3], made it necessary to consider first the primitive triclinic structure (sp. gr. $P\bar{1}$) with the unit-cell parameters a'_w, b'_w, and c'_w (Table 2) and compare it with the initially chosen four primitive structures (Fig. 1). The unit-cell parameters of one of these primitive structures, a_1, b_1, and c_1, are close to a'_w, b'_w, and c'_w. Then, the appropriate matrix of the *C*–*A* transformation (Table 2) was determined, and the corresponding recalculation of the unit-cell parameters was performed. Finally, the atomic coordinates (Table 3) were calculated with respect to the common reference point of both structures under the assumption that the center of inversion coincides with the position of a Fe atom from the layer of Fe-octahedra. As is seen from Table 3, the atomic parameters of both structures differ insignificantly, which indicates that our samples and the samples examined in [3] have identical structures. The average cation–oxygen distances in the coordination polyhedra are: 2.125, 2.186, 2.153, and 2.138 Å for the Fe(1)-, Fe(2)-, Fe(3)-, and Fe(4)-octahedra, respectively; 1.954 Å for the Ti-octahedhra; 2.601 Å for ten-apex Na-polyhedra; and 3.199 Å for nine-apex K-polyhedra. The Si–O distances in Si tetrahedra are within the standard limits. The lengths and the angles of oxygen–hydrogen bonds are given in Table 4.

DISCUSSION OF RESULTS

Table 2 and Fig. 1 show that the structure under consideration can be described by different unit cells with close *a*, *b*, and *c* parameters. This explains the diversity of published data and the difficulty in choosing the structure variant to compare it with that considered in [3].

The unit cell of triclinic astrophyllite suggested in [6] ($a = 13.14$, $b = 12.82$, $c = 5.42$ Å, $\alpha = 93°34'$, $\beta = 101°40'$, $\gamma = 113°38'$) is the closest to the primitive unit cell of variant 4 (Table 2).

The projection of the mineral structure given in [6] seems to be consistent with our refined model, despite

Table 3. Positional and thermal atomic parameters of Fe-rich astrophyllite

Atom	Position multiplicity	Position occupancy	*x*/*a*	*y*/*b*	*z*/*c*	B_{eq}, Å^2
Fe(1)	2	Fe	0	0	0	0.92(1)
Fe(2)	4	0.5Fe + 0.26Mn + 0.19Ca + 0.05Na	0.8574(1)	0.7159(1)	0.991(1)	0.73(2)
			0.86	0.716	0.99	
Fe(3)	4	0.84Fe + 0.16Mg	0.7127(1)	0.4272(1)	0.0046(1)	0.64(1)
			0.71	0.426	0.006	
Fe(4)	4	0.84Fe + 0.16Mg	0.4296(1)	0.8596(1)	0.9942(1)	0.60(1)
			0.43	0.859	0.993	
Ti	4	Ti	0.5069(1)	0.7373(1)	0.8511(1)	0.62(1)
			0.51	0.738	0.847	
Si(1)	4	Si	0.0941(1)	0.9053(1)	0.8656(1)	0.64(2)
			0.09	0.904	0.865	
Si(2)	4	Si	0.0742(1)	0.4354(1)	0.1327(1)	0.64(2)
			0.09	0.436	0.132	
Si(3)	4	Si	0.7699(1)	0.8309(1)	0.1247(1)	0.66(2)
			0.76	0.83	0.122	
Si(4)	4	Si	0.7930(1)	0.7973(1)	0.3765(1)	0.61(2)
			0.81	0.799	0.38	
Na	2	0.73Na + 0.27K	0	0.25	0.25	1.00(4)
K	4	0.85K + 0.15Na	0.6333(3)	0.5199(1)	0.2480(1)	2.83(3)
			0.60	0.515	0.248	
O(1)	4	O	0.7631(4)	0.8458(2)	0.0478(1)	0.83(4)
			0.76	0.843	0.047	
O(2)	4	O	0.0944(4)	0.8767(2)	0.9429(1)	0.90(4)
			0.10	0.874	0.944	
O(3)	4	O	0.2035(4)	0.7125(2)	0.0460(1)	0.88(4)
			0.19	0.713	0.048	
O(4)	4	O	0.4889(5)	0.2744(2)	0.0639(1)	0.97(4)
			0.47	0.276	0.063	
O(5)	4	(OH)	0.6633(5)	0.0107(2)	0.9500(1)	0.97(4)
			0.67	0.015	0.951	
O(6)	4	O	0.0557(5)	0.4295(2)	0.0557(1)	0.94(4)
			0.05	0.429	0.057	
O(7)	2	(OH, F)	0.5	0.25	0.25	1.56(7)
O(8)	4	O	0.0116(5)	0.7390(2)	0.3485(1)	1.50(5)
			0.03	0.735	0.349	
O(9)	4	O	0.1616(7)	0.0460(2)	0.8453(1)	1.85(6)
			0.19	0.051	0.848	
O(10)	4	(OH)	0.6250(4)	0.5694(2)	0.0468(1)	1.08(5)
			0.62	0.572	0.046	
O(11)	4	O	0.4893(5)	0.7637(3)	0.1519(1)	1.55(7)
			0.48	0.756	0.152	
O(12)	4	O	0.1478(7)	0.0694(2)	0.6525(1)	1.88(8)
			0.12	0.071	0.651	
O(13)	4	O	0.7040(6)	0.6228(3)	0.8360(1)	2.49(9)
			0.79	0.64	0.836	
O(14)	4	O	0.1920(7)	0.1230(3)	0.3346(1)	2.32(8)
			0.27	0.106	0.335	
O(15)	4	O	0.8185(7)	0.8568(3)	0.8341(1)	2.36(8)
			0.80	0.872	0.835	
O(16)	4	O	0.6933(6)	0.1439(3)	0.1673(1)	2.36(8)
			0.71	0.157	0.167	
H(1)	4	H	0.328(5)	0.503(1)	0.597(1)	6.6(1)
H(2)	4	H	0.383(5)	0.936(1)	0.412(1)	4.6(1)

Note: Thermal parameters of hydrogen atoms are isotropic; the positional parameters indicated in the second row of each entry were derived from those given in [3].

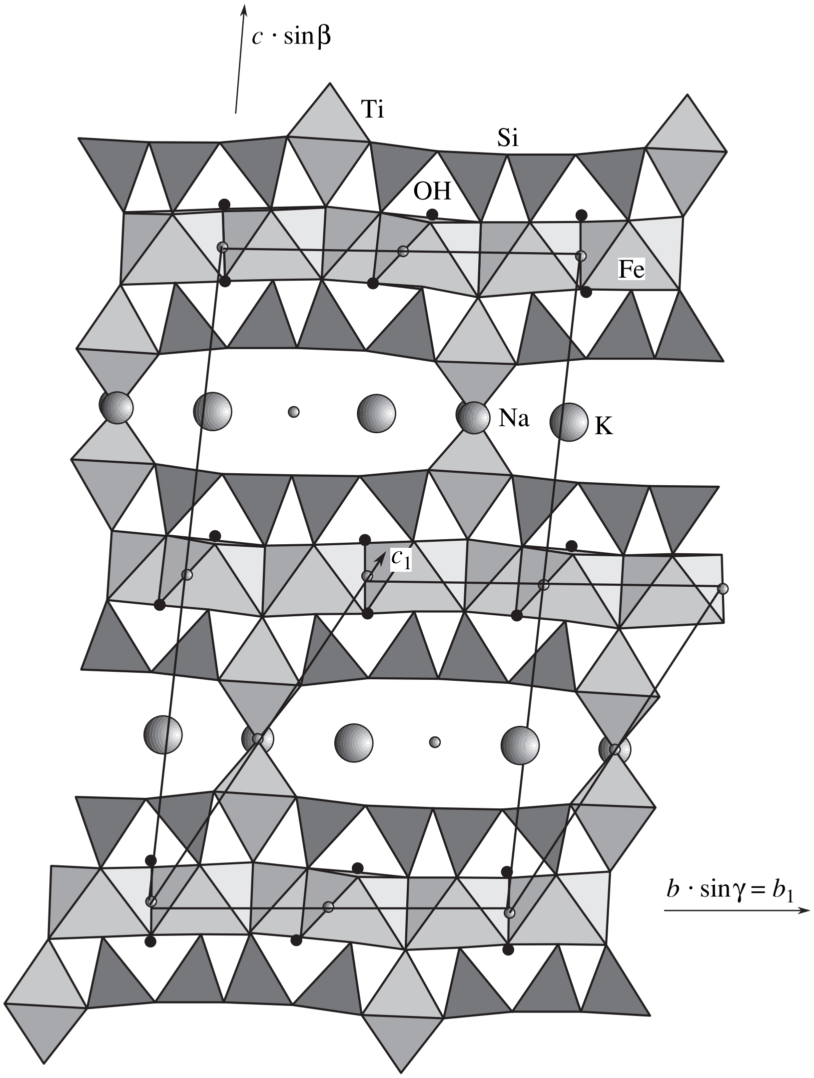

Fig. 2. Projection of the astrophyllite structure along the [100] direction in the $A\bar{1}$ setting. The b_1 and c_1 parameters are those of the primitive unit cell of variant 1 (Table 2). Centers of inversion are denoted by small open circles.

the fact that the authors of [6] indicated no positional parameters.

The crystal structure of mica-like triclinic astrophyllite consists of three-layer *TOT* sheets parallel to the (001) plane (Fig. 1). The central sheet layer (*O*) is formed by Fe octahedra. The peripheral layers are built of ribbonlike silicon–oxygen radicals $[Si_4O_{12}]^{8-}$ located along the shortest (5.4 Å) unit-cell parameter and linked via the Ti-octahedra (Fig. 2). Three-layer sheets linked by Ti-octahedra sharing the (OH, F)-apices and large K and Na cations in the intersheet cavities form a three-dimensional framework of the structure.

The triclinic astrophyllite structure established in the present study is identical to that of the most probable the polytypic astrophyllite modifications suggested by Zvyagin [7]. This modification, denoted as modification (3) in [7], is characterized by uniform Ti distribution caused by the mutual shifts of (Si, Ti) networks on both sides of the octahedron layer. The

Table 4. Parameters of H-bonds in Fe-rich astrophyllite

D–H·····*A*	*D*–H, Å	H–*A*, Å	*D*–*A*, Å	*D*–H–*A*, deg
O(5)–H(1)·····O(9)	1.03(2)	2.85(3)	3.458(4)	118.2(2)
O(10)–H(2)····O(12)	0.86(2)	2.92(3)	3.455(4)	121.5(1)

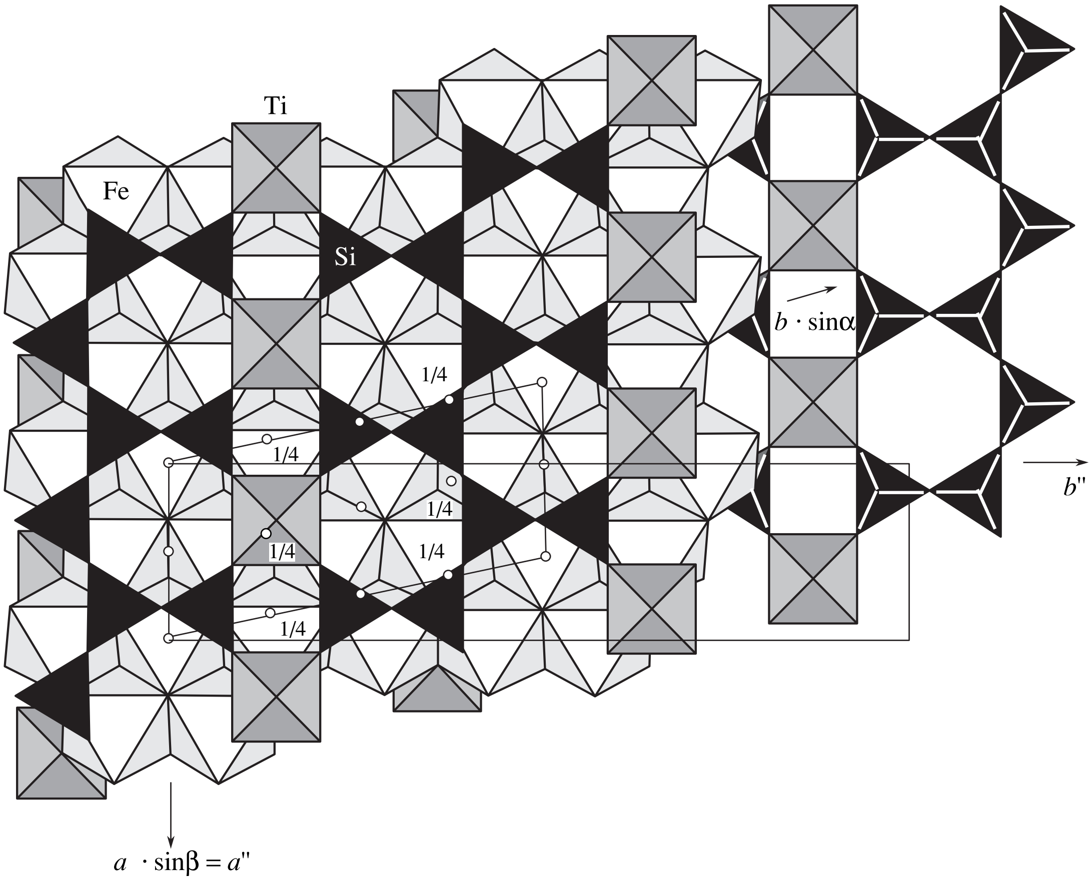

Fig. 3. Idealized fragment of the triclinic astrophyllite structure showing a *TOT* sheet projected along the [001] direction and the monoclinic unit cell with the parameters a'' and b''.

monoclinic symmetry is also established for another polytype, which is denoted as modification (1) in [7] and seems to be the least stable one. This modification is enriched with Na (the excessive Na^+ ions are located in the layer of octahedra) and differs from the triclinic one by the arrangement of *T* layers with respect to one another and to the central *O* layer of in the three-layer sheet. The monoclinic astrophyllite modification is described by the formula $K_2NaNa(Fe, Mn)_4Mg_2Ti_2[Si_4O_{12}]_2(OH)_4(OH,F)_2$; its parameters are $a = 5.322(1)$, $b = 23.129(5)$, $c = 10.842(3)$ Å, $\beta = 109.40(2)°$, $Z = 2$, sp. gr. $C2$ [1, 2]. In this structure, *T* layers lying on both sides of the *O* layer are bound by the twofold rotation axis lying in the plane of the *O* layer. Two of the three unit-cell parameters of the monoclinic and triclinic unit cells (those parallel to the mica-like layer (Fig. 3)) are related as $\mathbf{a}'' = \mathbf{a} = 5.4$ and $\mathbf{b}'' = \mathbf{a} + 2\mathbf{b} = 23$ Å. The third unit-cell parameter is determined in each structure independently because of different mutual arrangement of the adjacent shifted *TOT* sheets. Yet, since this parameter is determined by the translation of *TOT* sheets along the *c* axis, it can be assumed that $c'' \approx 1/2c$ (21 : 2 = 10.5 Å).

ACKNOWLEDGMENTS

The authors are grateful to E. L. Belokoneva for her help in the experiment and G. K. Krivokoneva who participated in the primary X-ray studies and discussed the results.

This study was supported by the Russian Foundation for Basic Research and the National Scientific Foundation of China, joint project no. 99-05-39019.

REFERENCES

1. J. Peng and Z. Ma, Scientia Sinica **12**, 272 (1963).
2. N. Shi, Z. Ma, G. Li, *et al.*, Acta Crystallogr. Sect. B: Struct. Sci. **54**, 109 (1998).
3. P. J. Woodrow, Acta Crystallogr. **22**, 673 (1967).
4. V. I. Andrianov, Kristallografiya **32** (1), 228 (1987) [Sov. Phys. Crystallogr. **32** (1), 130 (1987)].
5. Yu. A. Pyatenko, Kristallografiya **17** (4), 773 (1972) [Sov. Phys. Crystallogr. **17** (4), 677 (1972)].
6. J. Peng and Z. Ma, Scientia Sinica **13**, 949 (1964).
7. B. B. Zvyagin and Z. V. Vrublevskaya, Kristallografiya **21** (5), 949 (1976) [Sov. Phys. Crystallogr. **21** (5), 542 (1976)].

Translated by A. Mel'nikova

Crystallography Reports, Vol. 45, No. 4, 2000, pp. 591–594. Translated from Kristallografiya, Vol. 45, No. 4, 2000, pp. 649–652.
Original Russian Text Copyright © 2000 by Rastsvetaeva, Khomyakov.

Crystal Structure of a New Mn, Na-Ordered Analogue of Eudialyte with the Symmetry *R*3

R. K. Rastsvetaeva*[1] and A. P. Khomyakov**

** Shubnikov Institute of Crystallography, Russian Academy of Sciences,*
Leninskiĭ pr. 59, Moscow, 117333 Russia
*** Institute of Mineralogy, Geochemistry, and Crystal Chemistry of Rare Elements,*
Russian Academy of Sciences, ul. Veresaeva 15, Moscow, 121327 Russia

Received August 19, 1999

Abstract—The crystal structure of a new representative of the eudialyte family was studied. This mineral is characterized by a low calcium content and by ordering the elements that isomorphically replace calcium, which lowers the symmetry from *R*3*m* to *R*3. The structure of the sample under study consists of the six-membered rings with two octahedra of substantially different volumes, one occupied mainly by manganese and the other, mainly by sodium and characterized by the average distances of 2.22 and 2.45 Å, respectively. The formation of such octahedra is the most characteristic structural feature of the third low-symmetry mineral of the eudialyte family. *© 2000 MAIK "Nauka/Interperiodica".*

In recent years, the eudialyte family has been complemented with several new representatives, including minerals with an unusually low symmetry, *R*3 [1, 2]. Such a low symmetry of the eudialyte structural type is explained by the deficiency of calcium and a differentiation of the elements isomorphically replacing calcium in the octahedra entering six-membered rings. In this work, the crystal structure of a new mineral of the eudialyte family with an anomalously low calcium content was studied. This mineral was found in alkaline-, volatile-, and rare-element supersaturated pegmatites at the Alluaiv mountain of the Lovozero alkaline massif (the Kola Peninsula). The mineral occurs as pinkish-yellow grains of sizes ranging from 3 to 5 mm. The grains are optically uniaxial positive crystals with *No* = 1.610 and *Ne* = 1.619; ρ_{calcd} = 2.8 g/cm^3. The major structural

Table 1. Structural data and details of X-ray diffraction study

Characteristic	Value
Unit-cell parameters, Å	$a = 14.205(7)$, $c = 30.265(15)$
Unit-cell volume, Å^3	$V = 5288.8$
Sp. gr., *Z*	*R*3; 3
Radiation, λ, Å	MoK_α; 0.71073
Crystal dimensions, mm	0.15 × 0.20 × 0.28
Diffractometer	Syntex $P2_1$
Scanning mode	ω/2θ
sinθ/λ, Å^{-1}	<0.77
Range of data collection	$-21 < h < 21, -21 < k < 21, 0 < l < 46$
R_{int} for equivalent reflections	0.014
Total number of reflections	6788 $I > 2\sigma(I)$
Number of independent reflections	4004 $\lvert F\rvert > 4\sigma(F)$
Program used for calculations	AREN [3]
Absorption correction	DIFABS [4]
Number of independent positions	69
R factor for anisotropic refinement	0.036

---

[1] *e-mail: rast@rsa.crystal.msk.su*

1063-7745/00/4504-0591$20.00 © 2000 MAIK "Nauka/Interperiodica"

Table 2. Atomic coordinates, equivalent thermal parameters, multiplicities (*Q*), and occupancies (*q*) of the positions

Atom	*x*/*a*	*y*/*b*	*z*/*c*	B_{eq}, Å^2	*Q*	*q*
Zr(1)	0.3334(1)	0.1582(1)	0.1666(1)	1.89(1)	9	1
M(1)*	–0.0001(1)	0.2726(1)	–0.0002(1)	1.41(1)	9	1
M(1)'*	0.2435(1)	0.2435(1)	–0.0003(1)	1.52(1)	9	1
Si(1)	–0.0108(2)	0.6090(1)	0.0965(1)	1.47(3)	9	1
Si(1)'	–0.0050(1)	0.3968(1)	0.0963(1)	1.40(3)	9	1
Si(2)	0.1403(1)	0.0571(1)	0.0811(1)	1.60(5)	9	1
Si(3)	0.0634(1)	0.3285(1)	0.2374(1)	1.42(4)	9	1
Si(3)'	0.2754(1)	0.3223(1)	0.2373(1)	1.46(4)	9	1
Si(4)	0.2085(1)	0.4170(1)	0.0750(1)	1.77(4)	9	1
Si(5)	0.5264(1)	0.2499(1)	0.2528(1)	1.61(4)	9	1
Si(6)	0.4581(1)	0.5419(1)	0.2586(1)	1.81(4)	9	1
O(1)	0.1709(3)	0.3593(3)	0.0288(1)	2.3(2)	9	1
O(2)	0.1840(3)	0.3537(3)	0.2210(1)	2.3(1)	9	1
O(3)	0.6259(3)	0.5837(3)	0.0446(1)	3.2(5)	9	1
O(3)'	0.6367(4)	0.0407(3)	0.0452(1)	2.2(2)	9	1
O(4)	0.2557(4)	0.0224(3)	0.2071(1)	2.6(1)	9	1
O(4)'	0.2630(3)	0.2269(3)	0.2060(1)	3.3(5)	9	1
O(5)	0.4758(4)	0.2220(4)	0.2042(1)	4.3(3)	9	1
O(6)	0.2250(4)	0.0918(4)	0.0417(1)	3.2(3)	9	1
O(7)	0.1914(3)	0.0797(4)	0.1293(1)	2.8(3)	9	1
O(8)	0.1070(4)	0.3937(5)	0.1076(1)	3.5(3)	9	1
O(8)'	0.2726(3)	0.3708(3)	0.1058(1)	2.1(2)	9	1
O(9)	0.4423(4)	0.1996(4)	0.2922(1)	2.8(3)	9	1
O(10)	0.6167(3)	0.2104(3)	0.2569(1)	3.0(3)	9	1
O(11)	0.0729(3)	0.1233(3)	0.0772(1)	3.2(4)	9	1
O(12)	0.0579(5)	0.4379(4)	0.2261(1)	3.1(4)	9	1
O(12)'	0.3948(3)	0.4310(3)	0.2282(1)	2.1(2)	9	1
O(13)	0.0255(3)	0.5045(3)	0.3053(1)	2.4(1)	9	1
O(14)	0.4048(4)	0.2978(4)	0.1280(1)	3.2(5)	9	1
O(14)'	0.4115(4)	0.1011(4)	0.1267(1)	2.5(2)	9	1
O(15)	0.0454(3)	0.3002(3)	0.2895(1)	2.3(4)	9	1
O(15)'	0.2625(3)	0.2926(3)	0.2885(1)	1.9(2)	9	1
O(16)	0.0210(3)	0.5175(3)	0.1125(1)	2.3(2)	9	1
O(17)	0.2861(5)	0.5465(4)	0.0714(2)	5.9(4)	9	1
O(18*a*)	0.2095(6)	0.610(1)	0.2534(4)	2.9(2)	9	0.41(1)
O(18*b*)	0.374(1)	0.590(1)	0.2669(3)	3.5(2)	9	0.59(1)
Si(7*a*)	0.3333	0.6667	0.0435(1)	2.1(1)	3	0.64(1)
Si(7*b*)	0.3333	0.6667	0.0882(3)	2.7(2)	3	0.36(1)
Si(8*a*)	0.3333	0.6667	0.2458(3)	1.9(1)	3	0.25(1)
Si(8*b*)*	0.3333	0.6667	0.2897(1)	2.19(5)	3	0.75(1)
M(2*a*)*	0.1842(2)	0.3526(2)	0.3315(1)	2.27(5)	9	0.40(1)
M(2*b*)*	0.460(1)	0.528(1)	0.0035(3)	2.7(1)	9	0.10(1)
Fe	0.0162(1)	0.5163(1)	0.0013(1)	3.1(1)	9	0.50(1)

Table 2. (Contd.)

Atom	*x*/*a*	*y*/*b*	*z*/*c*	B_{eq}, Å^2	*Q*	*q*
Na(1*a*)	0.189(2)	0.621(2)	0.1601(7)	8.1(4)	9	0.20(1)
Na(1*b*)	0.186(1)	0.577(1)	0.1499(5)	5.3(3)	9	0.25(1)
Na(1*c*)	0.245(1)	0.515(1)	0.1819(6)	5.0(3)	9	0.25(1)
Na(1*d*)	0.227(2)	0.573(2)	0.1647(7)	6.1(3)	9	0.20(1)
Na(2*a*)*	0.1201(3)	0.2300(4)	0.1521(1)	2.5(1)	9	0.46(1)
Na(2*b*)	0.092(2)	0.177(2)	0.1668(5)	5.3(5)	9	0.22(1)
Na(2*c*)	0.105(1)	0.206(1)	0.1552(4)	4.9(3)	9	0.32(1)
Sr	0.2346(7)	0.1127(7)	0.2820(3)	4.1(1)	9	0.10(1)
Na(3)	0.1988(3)	0.0966(2)	0.2883(1)	3.2(1)	9	0.90(1)
Na(5*a*)	0.4411(5)	0.2165(4)	0.0510(2)	3.1(1)	9	0.52(1)
Na(5*b*)*	0.4722(3)	0.2334(3)	0.0420(1)	2.7(1)	9	0.48(1)
Na(6*a*)	0.5607(3)	0.1081(3)	0.1806(1)	2.7(1)	9	0.67(1)
Na(6*b*)	0.5729(8)	0.4128(9)	0.1689(5)	2.5(4)	9	0.14(1)
Na(6*c*)	0.605(2)	0.431(2)	0.166(1)	7(5)	9	0.19(1)
OH(1)	0.0	0.0	0.3304(8)	5.8(4)	3	0.52(3)
OH(2)	0.3333	0.6667	0.1390(7)	3.2(5)	3	0.37(3)
OH(3)	0.3333	0.6667	0.1889(7)	3.2(3)	3	0.39(2)
OH(4*a*)	0.609(3)	0.387(3)	–0.0064(8)	6.9(4)	9	0.40(1)
OH(4*b*)	0.6667	0.3333	0.007(2)	7.3(6)	3	0.70(1)
OH(5)	0.408(2)	0.603(2)	0.0029(8)	4.9(7)	9	0.30(3)
H_2O(1*a*)	0.0	0.0	0.2348(8)	3.6(5)	3	0.47(3)
H_2O(1*b*)	0.0	0.0	0.268(3)	9(1)	3	0.25(4)
H_2O(3*a*)	0.6667	0.3333	0.1033(7)	4.2(6)	3	0.50(3)
H_2O(3*b*)	0.6667	0.3333	0.141(2)	8(1)	3	0.20(2)
Cl(1*a*)*	0.6667	0.3333	0.0437(7)	3.7(3)	3	0.30(2)
Cl(1*b*)	0.6667	0.3333	0.080(1)	3.7(3)	3	0.10(2)

Note: The notation of the atomic positions correspond to that used in [1]; the positions crystallographically independent in the sp. gr. *R*3 are primed.

* The position compositions are as follows: *M*(1) = 0.7Mn + 0.24Ca + 0.06Ce; *M*(1)' = 0.45Na + 0.35Ca + 0.15Ce + 0.05Sr; *M*(2*a*) = 0.21Zr + 0.19Na; *M*(2*b*) = 0.056Ti + 0.044Nb; Si(8*b*) = 0.65Si + 0.1Al; Na(2*a*) = 0.4Na + 0.06K; Na(5*b*) = 0.43Na + 0.05Sr; Cl(1*a*) = 0.2Cl + 0.1H_2O.

characteristics and the details of single-crystal X-ray diffraction study are summarized in Table 1. The atomic coordinates are listed in Table 2.

The preliminary data on the chemical composition of the mineral (the microprobe analysis) correspond to the empirical formula (with respect to 26(Si + Al)) $\mathrm{Zr_{3.63}Ti_{0.12}Nb_{0.34}Hf_{0.04}Ca_{1.75}Mn_{1.91}Si_{25.91}Al_{0.09}Fe_{1.55}K_{0.12} \cdot Na_{16.34}Sr_{0.53}Ce_{0.63}}$.

The crystallochemical formula of the sample (*Z* = 3),

$$\mathrm{Zr_3[(Mn_{2.1}Ca_{0.72}Ce_{0.18})(Na_{1.35}Ca_{1.05}Ce_{0.45}Sr_{0.15})] \times [Si_3O_9]_2[Si_9O_{27}]_2[\overset{[IV]}{Fe}_{1.55}(\overset{[V]}{Zr}_{0.6}\overset{[VI]}{Na}_{0.58})(Ti_{0.15}Nb_{0.12})^{[V]}] \times [Si_{1.9}\overset{[VI]}{Al}_{0.1}](Na_{14}Sr_{0.4}K_{0.2})(OH, O)_4(F, Cl)_{0.7} \cdot 1.1H_2O},$$

reflects the ordered distribution of Mn and Na atoms over two crystallographically independent sites of the six-membered ring (the first square brackets). The average cation–anion distances in the Ca-octahedra of eudialytes are in the range of 2.32–2.37 Å, whereas the replacement of Ca cations by smaller Mn cations reduces this distance to 2.26 Å [1]. On the contrary, the presence of larger cations, along with Ca cations, results in an increase of the octahedron dimensions. For example, the corresponding distance in the structure studied in [1] is 2.41 Å. The sample studied consists of six-membered rings built by octahedra of considerably

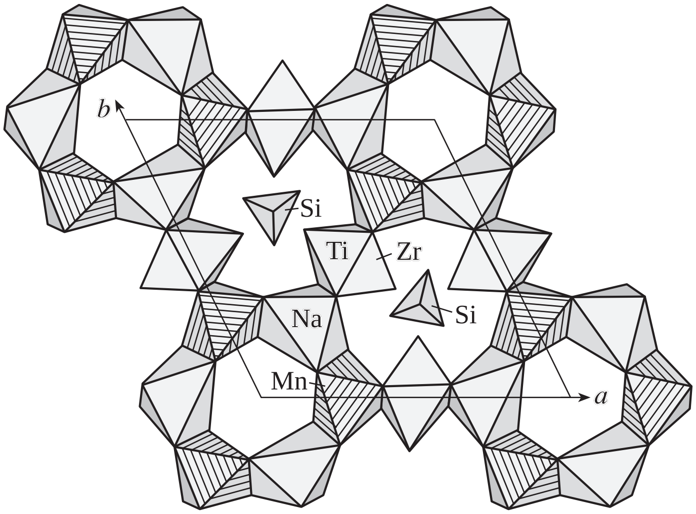

Fragment of the crystal structure projected onto the (001) plane. The octahedra occupied mainly by manganese atoms entering six-membered rings are hatched with solid lines. The Si(7,8)-tetrahedra are located on threefold axes.

different volumes. These octahedra are occupied mainly by manganese and sodium atoms and are characterized by the average distances of 2.22 and 2.45 Å, respectively. The presence of such octahedra is the most characteristic structural feature of the third representative of the eudialyte family with the symmetry *R*3 (figure). The sample under study is also characterized by a high silica content, which favors the transformation of the nine-membered Si-rings into ten-membered planar radicals containing statistically disordered additional Si-tetrahedra.

ACKNOWLEDGMENTS

This work was supported by the Russian Foundation for Basic Research, project no. 99-05-65035.

REFERENCES

1. R. K. Rastsvetaeva and A. P. Khomyakov, Kristallografiya **44** (5), 824 (1999) [Crystallogr. Rep. **44** (5), 765 (1999)].
2. O. Johnsen and J. D. Grice, in *Abstracts of the 17th IMA General Meeting, Toronto, 1998*, p. A108.
3. V. I. Andrianov, Kristallografiya **32** (1), 228 (1987) [Sov. Phys. Crystallogr. **32** (1), 130 (1987)].
4. N. Walker and D. Stuart, Acta Crystallogr., Sect. A: Found. Crystallogr. **39**, 158 (1983).

Translated by T. Safonova

Crystallography Reports, Vol. 45, No. 4, 2000, pp. 595–600. Translated from Kristallografiya, Vol. 45, No. 4, 2000, pp. 653–658.
Original Russian Text Copyright © 2000 by V. Rau, T. Rau, Lebedev, Kurkutova.

STRUCTURE OF COORDINATION COMPOUNDS

Geometrical Model of the Structure of the Heterocomplex Compound $[Cr(OCN_2H_4)_6]^{3+}[Co(DH)_2(NO_2)_2]_3^- \cdot 2H_2O$

V. G. Rau, T. F. Rau, G. O. Lebedev, and E. N. Kurkutova
Vladimir State Pedagogical University, Vladimir, Russia

Received November 25, 1997; in final form, March 16, 1999

Abstract—The structural organization of the new heterocomplex compound with carbamide has been considered on the basis of division of the crystal space into Dirichlet polyhedra of the system of Delone points (centers of the complex ions). It is demonstrated that the coordination numbers for all domains (Dirichlet domains) of the complex ions in the structure obey the “rule of fourteen,” whereas the polyhedra providing the structural organization of the crystal are distorted Fedorov cuboctahedra. © *2000 MAIK “Nauka/Interperiodica”.*

Generally, investigations of crystal structures of various substances are based on a certain geometrical model of these structures, which approximate the real structure taking into account some specific conditions. Thus, the ionic compounds, in particular, minerals, are considered on the basis of a polyhedral model of the crystalline state (the so-called Pauling–Belov polyhedra [1]). This crystalline state of these objects is analyzed by considering their anionic or cationic packing. The crystals consisting of organic molecules are usually considered on the basis of the principle of intermolecular polyhedra suggested by Fischer and Koch [2] and generalizing the Kitaigorodsky’s ideas [3]. Galiulin suggested the most general geometrical approach for studying the structural organization of crystals, which is based on the construction of a Delone partition and Dirichlet partition dual to Delone partition for the Delone point system [4]. The result of such an analysis depends on the choice of the system “points” (localized electron density, atomic nuclei, centers of mass of the structural fragments, complex-forming atoms, etc.). The use of the terms “packing of complex anions” and “packing of complex cations” instead of “packing of anions and cations” [5] resulted in a new concept of the intercoordination complex polyhedron (ICP) [5]. It is evident that the presence of an integral number of ICP’s densely filling the space in the unit cell of a crystal, i.e., of packing polyhedra with the known shape provides, in fact, the knowledge of the structural organization of the crystal. At the microlevel, the structure is determined by individual elements of the intercoordination polyhedron.

Over a number of years, Rau *et al.* [5] studied the structures of complicated heterocomplex compounds built by various complex anions—from relatively simple, such as Cl^-, $(I_3)^-$, $(NO_3)^-$, $(SO_4)^{2-}$, and $(ClO_4)^-$, to rather complicated such as $[Cr_2O_7]^{2-}$, $[Co(NH_3)_2(NO_2)_4]^-$, $[Co(DH)_2(NO_2)_2]^-$ (where *D*H is the dimethylglyoxonium ion, $[PtCl_5OH]^{2-}$, and the octahedral $[M(OCN_2H_4)_6]^{2+,3+}$ cations of di- and trivalent *M* metals (Co, Mg, Ni, Zn, Cr, etc.) with carbamide). These studies demonstrated that the major form of intercoordination polyhedron for cations of bivalent metals is characterized by four-fold coordination, and of trivalent metals, by a hexagonal anionic prism with the complex cation located on the axis of this prism. When analyzing coordination, the neutral water molecules were ignored. In fact, the use of the concept of an intercomplex polyhedron continues the common practice of employing Belov’s polyhedra at the macrolevel. Nevertheless, this approach can be combined with the Fischer and Koch approach [2] if the “molecules” are understood as complex anions, complex cations, and neutral molecules of water or a solvent. In this case, we are concerned with heteromolecular compounds, and packing can be analyzed within the framework of the discrete-modeling method [6], successfully used in the description of the crystalline state of homomolecular compounds. The method is based on the concept of the packing space and three-dimensional polyominoes, either dividing this space or filling it at a given packing coefficient [7]. The main problems facing the method at the present stage of its development is the approximation of molecules with three-dimensional polyominoes and determination of the coordination numbers for each molecule, which present some difficulties for real structures.

To solve the latter problem, we use below the method for constructing Dirichlet domains for complex ions. The package of programs was designed and first used by Panov for describing homomolecular organic compounds [8]. It appeared that the potentialities of this procedure were so promising that we used it to describe the structure of a new heterocomplex compound with carbamide $[Cr(OCN_2H_4)_6]^{3+}[Co(DH)_2(NO_2)_2]_3^- \times 2H_2O$. The determination of the coordination polyhedron (Fischer’s and Koch’s terminology [2]) at the final stage of

Coordinates of nonhydrogen atoms (×10^4) and hydrogen atoms (×10^3) and equivalent isotropic thermal parameters B_{eq}

Atom	*x*	*y*	*z*	B_{eq}, Å^2
Cr(1)	0	0	0	0.86(1)
Co(2)	5000	5000	0	0.79(1)
Co(3)	2501(1)	–2481(1)	4873(1)	1.29(1)
O(1)	1909(2)	185(2)	–160(1)	1.23(5)
O(2)	–314(2)	101(2)	1396(1)	1.33(5)
O(3)	283(2)	–1780(1)	62(1)	1.37(5)
O(101)	4814(2)	3266(2)	1560(1)	1.21(5)
O(102)	4047(2)	2593(1)	197(1)	1.22(5)
O(201)	1537(2)	–3949(2)	6567(1)	1.72(6)
O(202)	2916(2)	–3155(2)	2921(1)	1.76(6)
O(301)	3401(2)	–1009(2)	3190(1)	1.52(5)
O(302)	2113(2)	–1860(2)	6823(1)	1.88(6)
O(11)	2875(2)	6681(2)	472(1)	1.44(6)
O(12)	2357(2)	4917(2)	1108(1)	1.50(5)
O(21)	–183(2)	–1880(2)	5713(1)	1.47(6)
O(22)	371(2)	–1595(2)	4188(1)	2.25(6)
O(31)	5210(2)	–2887(2)	4039(1)	1.69(6)
O(32)	4613(2)	–3463(2)	5511(2)	1.97(6)
O(01)	–464(2)	–4512(2)	1810(1)	1.85(6)
O(02)	6485(2)	–754(2)	–1738(2)	2.09(6)
N(1)	3203(2)	5607(2)	602(1)	1.23(6)
N(2)	676(2)	–1914(2)	4935(2)	1.67(7)
N(3)	4328(2)	–3021(2)	4798(2)	1.50(7)
N(101)	5167(2)	4407(2)	1203(2)	0.92(6)
N(102)	5707(2)	6404(2)	373(1)	0.88(5)
N(201)	1867(2)	–3910(2)	5610(1)	1.12(6)
N(202)	2538(2)	–3529(2)	3860(2)	1.33(6)
N(301)	3122(2)	–1050(2)	4140(2)	1.29(6)
N(302)	2497(2)	–1468(2)	5891(2)	1.22(6)
N(11)	3796(2)	–706(2)	33(2)	1.44(6)
N(12)	3053(2)	–1184(2)	–1252(2)	1.63(7)
N(21)	408(2)	287(2)	2697(2)	1.66(7)
N(22)	871(2)	–1491(2)	1875(2)	1.55(7)
N(31)	839(2)	–3586(2)	–627(2)	2.05(7)
N(32)	–1145(2)	–2591(2)	–661(2)	1.42(6)
C(1)	2899(2)	–557(2)	–454(2)	0.96(7)
C(2)	310(2)	–377(2)	1937(2)	1.39(7)
C(3)	–13(2)	–2639(2)	–405(2)	1.13(7)
C(101)	5648(2)	5133(2)	1688(2)	1.08(7)
C(102)	5954(2)	6330(2)	1202(2)	1.25(7)
C(103)	5885(2)	4795(2)	2626(2)	1.73(9)
C(104)	6481(2)	7334(2)	1634(2)	1.65(8)
C(201)	1830(2)	–4876(2)	5139(2)	1.11(7)
C(202)	2204(2)	–4641(2)	4093(2)	1.23(7)
C(203)	1489(2)	–6089(2)	5615(2)	1.47(8)
C(204)	2195(3)	–5594(2)	3397(2)	1.50(8)
C(301)	3220(2)	–104(2)	4621(2)	1.28(8)
C(302)	2848(2)	–357(2)	5661(2)	1.19(8)
C(303)	3630(3)	1096(2)	4152(2)	2.10(9)
C(304)	2872(3)	582(2)	6370(2)	1.91(9)
H(11)	361(3)	–31(2)	55(2)	
H(12)	445(3)	–120(2)	–11(2)	
H(13)	371(3)	–175(2)	–144(2)	
H(14)	247(3)	–113(3)	–152(2)	
H(21)	–15(3)	91(3)	282(2)	
H(22)	74(3)	–9(3)	313(2)	
H(23)	82(3)	–188(2)	142(2)	
H(24)	131(3)	–184(3)	229(2)	
H(31)	66(3)	–419(3)	–92(2)	
H(32)	148(3)	–358(3)	–46(2)	
H(33)	–140(3)	–323(2)	–84(2)	
H(34)	–170(3)	–204(2)	–45(2)	
H(1)	441(3)	297(3)	99(3)	
H(2)	313(3)	–237(3)	297(3)	
H(3)	185(3)	–279(3)	679(3)	
H(131)	590(3)	402(3)	274(2)	
H(132)	531(3)	523(3)	312(3)	
H(133)	673(3)	499(3)	263(3)	
H(141)	650(3)	802(3)	125(2)	
H(142)	592(3)	745(3)	230(2)	
H(143)	736(3)	712(3)	165(3)	
H(231)	60(3)	–604(3)	607(2)	
H(232)	145(3)	–665(3)	518(2)	
H(233)	220(3)	–631(3)	595(2)	
H(241)	284(3)	–619(3)	343(2)	
H(242)	135(3)	–600(3)	359(2)	
H(243)	237(3)	–520(3)	280(2)	
H(331)	445(3)	103(3)	364(2)	
H(332)	378(3)	162(3)	453(2)	
H(333)	290(3)	146(3)	392(2)	
H(341)	224(3)	123(3)	629(2)	
H(342)	262(3)	24(3)	699(2)	
H(343)	372(3)	91(3)	626(3)	
H(101)	–68(3)	–486(3)	234(2)	
H(102)	42(3)	–451(3)	164(2)	
H(201)	643(3)	–20(3)	–232(3)	
H(202)	749(3)	–118(3)	–197(3)	

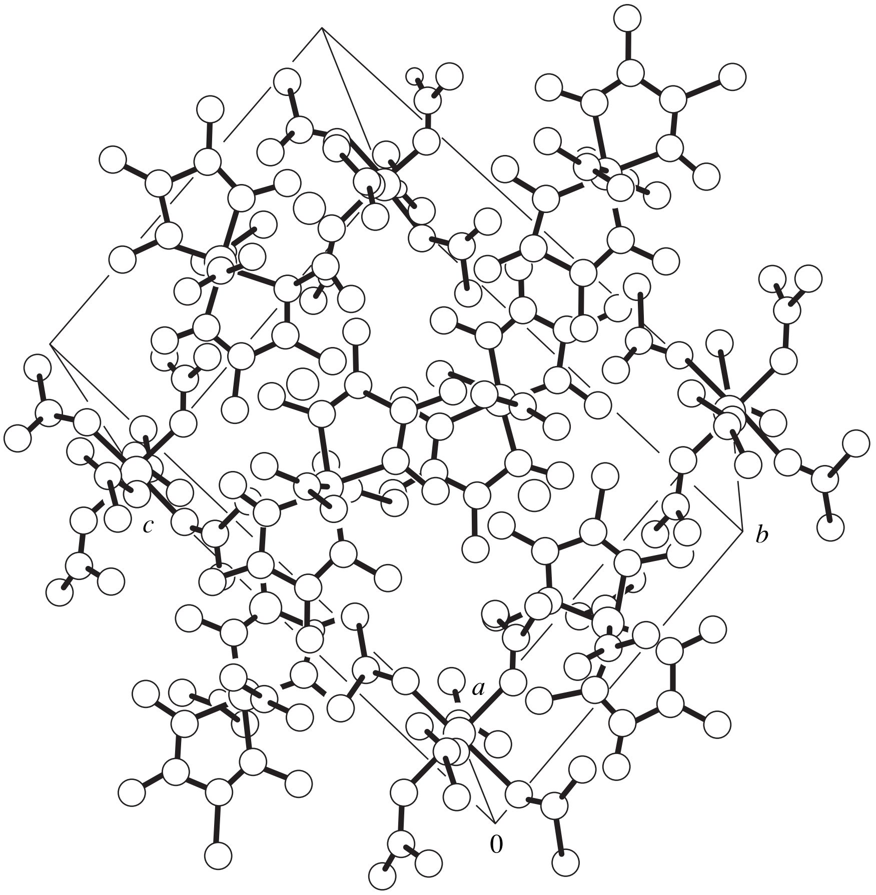

Fig. 1. The unit cell of the crystal structure and the system of points–atoms.

the study leads, in essence, to the global Delone system of points, where "points" are understood as molecules and complexes rather than as individual atoms. Performing Delone triangulation, one can describe the structural organization of any chosen compound. The theoretical grounds of this approach call for special analysis and are beyond the scope of the present study.

Consider the stages of geometrical analysis of the crystal structure under consideration. These are:

System of points (atoms) (Fig. 1)

↓

Dirichlet polyhedra for atoms (Fig. 2)

↓

Dirichlet domains for complex ions (Fig. 3)

↓

Delone system of points
(centers of complex ions)

↓

Dirichlet polyhedra for the centers
of complex ions (Fig. 4)

We believe that such an analysis would provide the complete description of the structure.

The X-ray diffraction data were collected by Bondar' and Potekhin and processed to $R_{hkl} = 0.025$ (4822 reflections). Then these data were used for subsequent structure determination and establishment of the geometric features of the heterocomplex compound. The unit cell with the parameters $a = 10.389(4)$, $b = 10.974(4)$, $c = 14.523(4)$ Å, $\alpha = 87.46(3)°$, $\beta = 73.92(3)°$, $\gamma = 86.98(3)°$, $V = 1588$ Å^3, sp. gr. $P\bar{1}$ contains two formula units of the above-mentioned composition. The atomic coordinates are given in the table. The structure contains two independent complex anions $[Co(2, 3)(DH)_2(NO_2)_2]^-$ (Co–N, 1.887–1.943 Å) and the cation $[Cr(1)(OCN_2H_4)_6]^{3+}$ (Cr–O, 1.953–1.969 Å). The three-dimensional crystal structure is shown in Fig. 1.

The nonequivalent complex anions Co(3) and Co(2) that occupy the general and the special positions at the center of inversion (1/2, 1/2, 0) have similar structures with the octahedral coordination of Co atoms. The NO_2 groups occupy the *trans*-positions in the octahedra. Both $(N_2O_2C_4H_7)^-$ dimethylglyoxonium ions lie in the

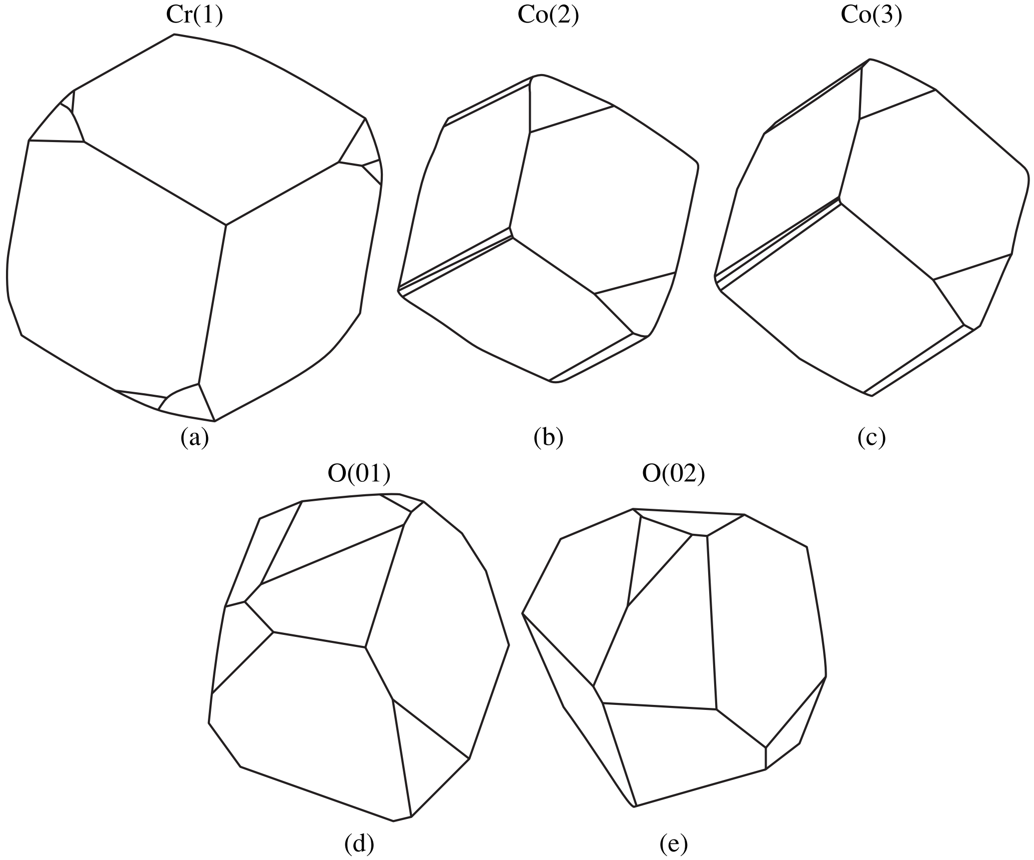

Fig. 2. Dirichlet domains for the (a) Cr(1), (b) Co(2), and (c) Co(3) complex-forming atoms and (d) O(01) and (e) O(02) atoms of water molecules.

same plane (within 0.02 Å). The differences in the structure of the complex anions are reflected in the types of the Dirichlet regions for the central Co(2) and Co(3) atoms (Figs. 2b, 2c). It is evident that the Co(2) polyhedron has a higher approximate symmetry, 2/*m*. The polyhedron of Cr(1) in the center of the complex cation (Fig. 2a) at the origin of the coordinate system is even more symmetrical. Similar to the complex cation as a whole, the core of this complex has the symmetry $\bar{3}$ and not 32, as was the case in the $[Cr(OCN_2H_4)_6][Co(NH_3)_2(NO_2)_4][Co(DH)_2(NO_2)_2]$ structure [9]. The shapes of the Dirichlet regions for water molecules located in the general nonequivalent positions in the unit cell are essentially different. Nevertheless, the average dimensions of their faces and volumes are close (Figs. 2d, 2e). Figures 2a–2e are drawn on the same scale.

The structural organization of crystals is determined by the type, dimensions, and coordination of the Dirichlet domains characterizing the volumes of the unit-cell parts occupied by each complex anion, cation, and water molecule. For comparison, Figs. 3b and 3c present the domains of Co(2) and Co(3) projected onto the plane perpendicular to the N–Co–N' vector of NO_2 groups in the *trans*-positions. The approximate symmetry of the domains of the Co(2) and Co(3) complex anions is the same, *mmm*, despite the different positions occupied by these anions in the unit cell. The Cr(1) domain is projected along a threefold axis of the oxygen octahedron about the Cr atom (Fig. 3a). The coordination numbers of each anion and cation domains were determined upon discarding the boundary areas of the polyhedra (less than 2% of its total surface) and neglecting water molecules. Our calculations demonstrated that the numbers of "neighbors" for all the structure domains obeys the "rule of fourteen" [10].

At this stage, one can pass to the Dirichlet polyhedra of complexes in accordance with the geometrically rigorous definition of a polyhedron within the framework of the crystallographic geometry [4] (i.e., the distances between the points of the Delone system are divided into two). Then, the Delone system of points is a set of the centers of the complex-ion domains, i.e., coincides with the positions of the Cr(1), Co(2), and Co(3) atoms. In molecular compounds, such centers are not necessarily the positions of the real atoms. The construction of Dirichlet polyhedra for the Delone system of domain centers is illustrated by Figs. 4a–4c. In all the cases,

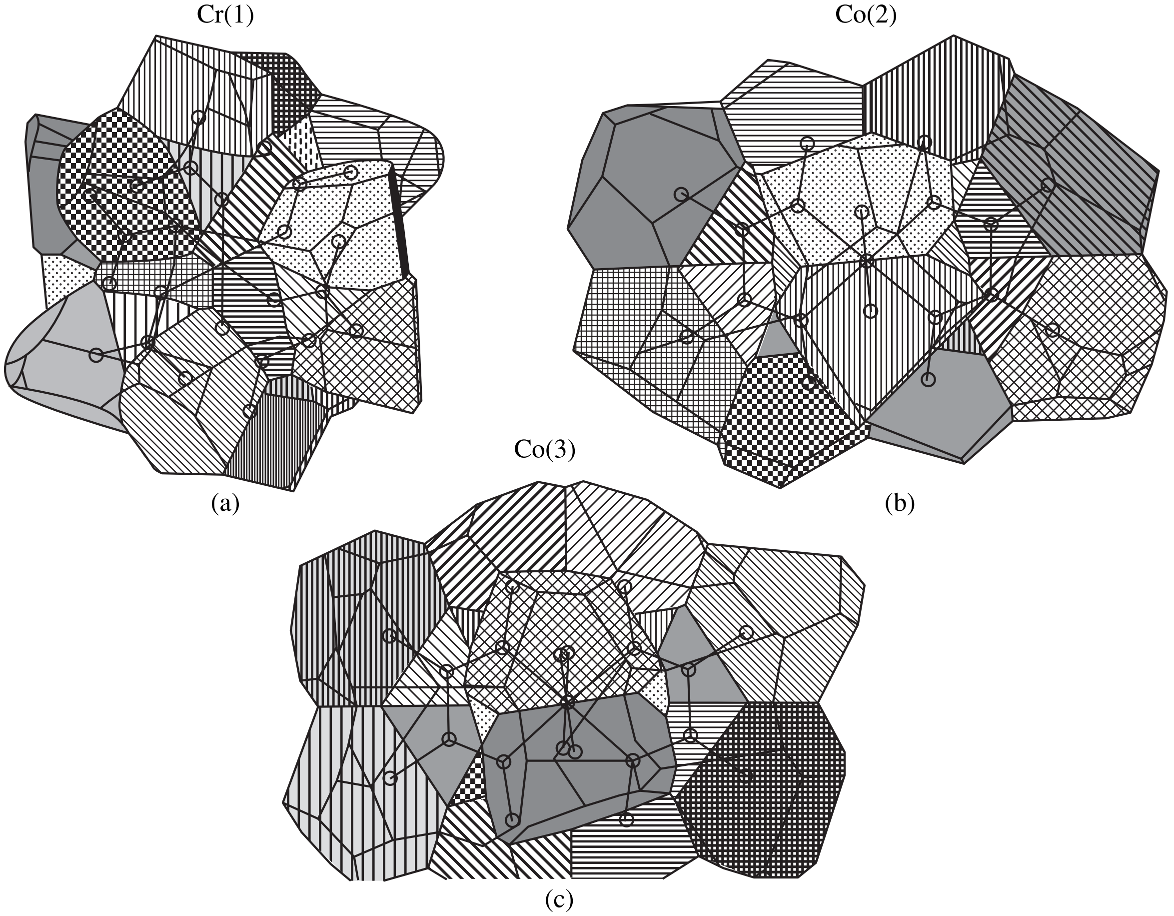

Fig 3. Dirichlet domains for the complexes containing (a) Cr(1), (b) Co(2), and (c) Co(3) complex-forming atoms.

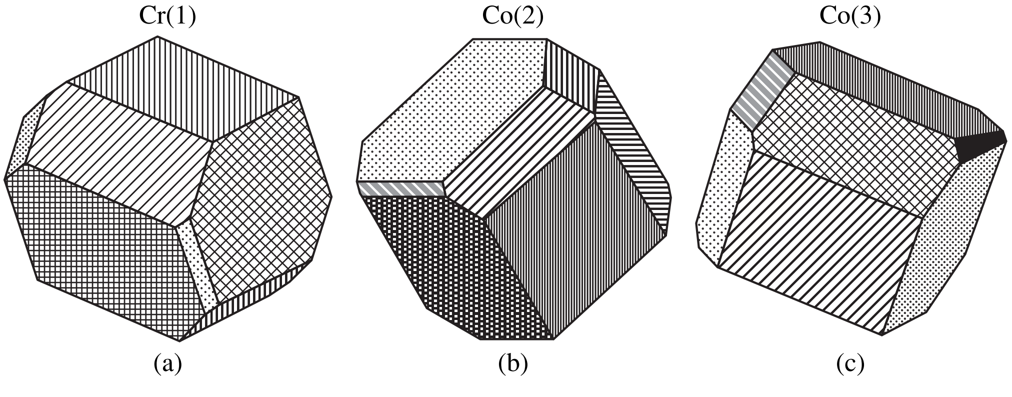

Fig. 4. Dirichlet polyhedra around the centers of the (a) Cr(1), (b) Co(2), and (c) Co(3) complex ions.

these polyhedra are distorted Fedorov cuboctahedra. The set of cuboctahedra for the Cr(1), Co(2), and Co(3) complex ions determines the structural organization of a single crystal of the heterocomplex compound under study.

ACKNOWLEDGMENTS

We thank R. V. Galiulin for a useful discussion of the relationship between the Delone and the Dirichlet systems in the description of crystal structures.

REFERENCES

1. N. V. Belov, *Structures of Ionic Crystals and Metal Phases* (Akad. Nauk SSSR, Moscow, 1947).
2. W. Fischer and E. Koch, Z. Kristallogr. **150**, 245 (1979).
3. A. I. Kitaĭgorodskiĭ, *Molecular Crystals* (Nauka, Moscow, 1971).
4. R. V. Galiulin, *Crystallographic Geometry* (Nauka, Moscow, 1984).
5. V. G. Rau, V. I. Bondar’, T. F. Rau, and S. V. Stepanov, *Problems of Crystal Chemistry* (Nauka, Moscow, 1990), pp. 99–110.
6. A. V. Maleev, V. G. Rau, K. A. Potekhin, *et al.*, Dokl. Akad. Nauk SSSR **315** (6), 1382 (1990).
7. A. V. Maleev, Kristallografiya **40** (3), 394 (1995).
8. Yu. É. Ovchinnikov, K. A. Potekhin, V. N. Panov, and Yu. T. Struchkov, Dokl. Ross. Akad. Nauk **340** (1), 62 (1995).
9. V. I. Bondar’, V. G. Rau, S. P. Rozman, *et al.*, Dokl. Akad. Nauk SSSR **255** (3), 569 (1980).
10. V. A. Blatov, A. P. Shevchenko, and V. N. Serezhkin, Dokl. Ross. Akad. Nauk **335** (6), 742 (1994).

Translated by T. Safonova

Crystallography Reports, Vol. 45, No. 4, 2000, pp. 601–603. Translated from Kristallografiya, Vol. 45, No. 4, 2000, pp. 659–661.
Original Russian Text Copyright © 2000 by Diacon, Donu, Chapurina.

Crystal Structures of Copper(II) Compounds with Racemic Threonine

I. A. Diacon*, S. V. Donu*, and L. F. Chapurina**

** Institute of Applied Physics, Academy of Sciences of Moldova, Academiei 5, Chisinau, 20-28 Moldova*
*** Institute of Chemistry, Academy of Sciences of Moldova, Academiei 3, Chisinau, 20-28 Moldova*

Received July 8, 1998; in final form, April 26, 1999

Abstract—Crystals structures of two modifications of the copper(II) compound with racemic threonine Cu(*D*-Tre)(*L*-Tre) are determined by the electron diffraction technique. The unit cell parameters, space group, and number of formula units per unit cell for the crystals of two modifications are as follows: $a = 11.10(3)$ Å, $b = 9.56(2)$ Å, $c = 5.11(2)$ Å, $\gamma = 92.6(2)°$, space group $P2_1/b$, and $Z = 2$ (**I**); and $a = 22.20(3)$ Å, $b = 9.56(2)$ Å, $c = 5.11(2)$ Å, $\gamma = 92.6(2)°$, space group $C2_1/b$, and $Z = 4$ (**II**). The structures are polytypic modifications of the same compound. *© 2000 MAIK "Nauka/Interperiodica".*

Earlier [1–3], we studied a series of copper(II) coordination compounds with racemic forms of α-amino acids. The results of our studies of copper(II) salts with *DL*-threonine were reported in [1]. Crystals of a hydrate form Cu(*D*-Tre)(*L*-Tre) · $4.5H_2O$ and three anhydrous modifications of this compound were investigated.

In the course of these studies, the crystal structures of two anhydrous modifications with the Cu(*D*-Tre)(*L*-Tre) composition were determined by the electron diffraction technique. Since threonine contains two chiral centers, it can exist in four stereoisomeric forms (two optical antipodes due to α-carbon, and two optical antipodes, to β-carbon). Therefore, from the crystal-chemical standpoint, it is of interest, on one hand, to reveal the arrangement of the threonine antipodes relative to the copper ion and, on the other hand, to determine the conformation of the threonine residues.

CRYSTAL STRUCTURE OF Cu(*D*-Tre)(*L*-Tre), MODIFICATION I

Crystals of Cu(*D*-Tre)(*L*-Tre) are monoclinic. The unit cell parameters are $a = 11.10(3)$ Å, $b = 9.56(2)$ Å, $c = 5.11(2)$ Å, $\gamma = 92.6(2)°$, space group $P2_1/b$, and $Z = 2$. The *b* and *c* parameters were determined from the point electron diffraction patterns, and the *a* and γ parameters were found using the electron diffraction patterns taken from the textures [4–6]. More than 260 reflections revealed on the electron diffraction patterns of the textures were used to determine the coordinates of the non-hydrogen atoms in the structure. At first stage, the coordinates of the copper atoms were determined from the analysis of the three-dimensional Patterson function. Next, the remaining non-hydrogen atoms in the structure were located from the Fourier maps. A series of iterations of the structure refinement [4–8] resulted in $R = 16\%$. The atomic coordinates are listed in the table, and a fragment of the structure is shown in the figure.

The crystal structure of Cu(*D*-Tre)(*L*-Tre) (modification **I**) consists of discrete centrosymmetric complexes. In the complexes, the *trans* octahedral coordination of the copper ions is formed by two carboxyl oxygen atoms and two nitrogen atoms of the bidentate *D*- and *L*-threonine ligands and two carboxyl oxygen atoms of the threonine residues of the neighboring complexes (figure).

A specific feature of the structure is its layered type. The structure consists of identical layers formed by the Cu(*D*-Tre)(*L*-Tre) complexes. The layers are aligned parallel to the *bc* coordinate plane and repeat at a period of *a* ($a = 11.10$ Å). Within the layer, the arrangement of the complexes follows a pattern of the centered rectan-

Coordinates ($\times 10^3$) of non-hydrogen atoms in the crystal structure of Cu(*D*-Tre)(*L*-Tre), modification **I**

Atom	*x*/*a*	*y*/*b*	*z*/*c*
Cu	000	000	000
O(1)	–47(6)	157(6)	–196(6)
O(2)	–171(6)	337(6)	–208(6)
O(3)	–327(6)	–16(6)	–88(6)
N(1)	–127(6)	48(6)	242(6)
C(1)	–131(8)	229(8)	–116(8)
C(2)	–194(8)	154(8)	117(8)
C(3)	–324(8)	123(8)	18(8)
C(4)	–397(8)	124(8)	284(8)

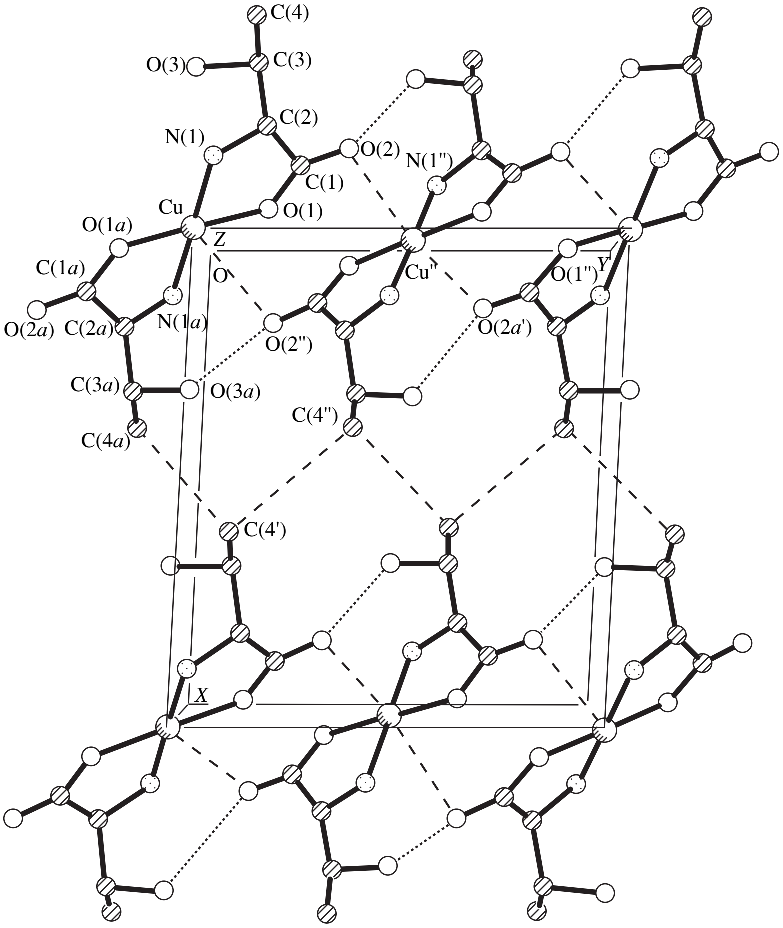

Crystal structure of Cu(*D*-Tre)(*L*-Tre), modification **I**.

gular motif; the neighboring complexes are linked by the bonds between copper ions and oxygen atoms of the carboxyl groups [Cu''···O(2) and Cu''···O(2*a*'), 2.83 Å], as well as by the network of hydrogen bonds [O(3*a*)–H···O(2''), 2.51; N(1'')–H···O(2), 3.15; and N(1'')–H···O(1''), 2.82 Å]. All the above bonds arrange the complexes within the layer in such a way that the C(4*a*)H_3, C(4')H_3, and C(4'')H_3 methyl groups of the threonine residues are located in the interlayer space and form interlayer contacts C(4*a*)H_3···C(4')H_3 (3.90 Å) and C(4')H_3···C(4'')H_3 (4.25 Å). Each methyl group of a layer contacts two methyl groups of the neighboring layer to form an infinite ···C(4*a*)H_3···C(4')H_3···C(4'')H_3··· chain.

CRYSTAL STRUCTURE OF Cu(*D*-Tre)(*L*-Tre), MODIFICATION II

The unit cell of the Cu(*D*-Tre)(*L*-Tre) crystals (modification **II**) was determined from the electron diffraction patterns taken from the single crystals and textures. The unit cell is twice as large as the unit cell of modification **I**: $a = 22.20(3)$ Å, $b = 9.56(2)$ Å, $c = 5.11(2)$ Å, $\gamma = 92.6(2)°$, space group $C2_1/b$ (in a nonstandard setting), and $Z = 4$. The positions of the non-hydrogen atoms were determined with the same procedure as those in the structure of modification **I**. For both structures, the numbers of the reflections used and the discrepancy factors *R* almost coincide.

Analysis of the structural data obtained by electron diffraction showed that the crystal structure of modification **II** is formed from the centrosymmetric Cu(*D*-Tre)(*L*-Tre) complexes, which are the same as in the structure of modification **I**. These complexes are packed in similar layers that repeat parallel to the coordinate plane *bc* at a period of 1/2*a* ($a = 22.20$ Å). However, the repetition patterns in the structures of modifications **II** and **I** differ from each other. In the crystal structure of modification **II**, the neighboring layers are shifted by 1/2*b* relative to each other. At the same time, the spacings between the layers and the conditions of their neighborhood [C(4*a*)H_3···C(4')H_3, 4.06 and C(4')H_3···C(4'')H_3, 4.12 Å] are identical in both modifications. Thus, the two structures studied are polytypic modifications of the same compound.

SPECIFIC FEATURES OF THE ELECTRON DIFFRACTION PATTERNS FROM TEXTURES OF TWO MODIFICATIONS OF THE Cu(*D*-Tre)(*L*-Tre) CRYSTALS

It was shown in [5, 6, 9] that, due to the specific geometry of three-dimensional sets of reflections and the regularity in distribution of intensities, the electron diffraction patterns taken from the textures serve as an efficient experimental base for revealing and describing the polytypic crystal structures. Below, by concrete examples of the above copper compounds with racemic threonine, we illustrate how the difference in polytypic crystal structures is reflected in the electron diffraction patterns from the textures.

The unit cells of the two modifications differ only by the a parameters, one of which is twice as large as the other. The identity of the b, c, α, and β parameters appears on the electron diffraction patterns from the textures of both modifications as identical sets of ellipses. The electron diffraction patterns are also similar in systematic absences of $hk0$ reflections with $k = 2n + 1$ and $00l$ reflections with $l = 2n + 1$. These similarities of the diffraction patterns characterize the identical symmetry of the mutual arrangement of the centrosymmetric Cu(*D*-Tre)(*L*-Tre) complexes within the layers that constitute both structures. The structural data obtained indicate that the studied modifications of the structure differ only by the shifts of the neighboring layers along the b-axis. For the crystals of modification **I**, the shifts along the b-axis are zero, and for the crystals of modification **II**, the shifts are $\pm 1/2b$. The electron diffraction patterns from the textures clearly revealed the diffraction differences resulting from the shifts of the layers. In the diffraction pattern of the crystals of modification **II**, the hkl reflections with $h + k = 2n + 1$ are absent, whereas in the diffraction pattern of the crystals of modification **I**, this type of systematic absences is not observed. Note also identical splittings of the corresponding reflections in the electron diffraction patterns from the textures, which indicate that unique angles of the unit cells in both modifications are identical.

REFERENCES

1. L. F. Chapurina, A. V. Ablov, I. A. D'yakon, and S. V. Donu, Zh. Neorg. Khim. **21** (1), 158 (1976).
2. B. K. Vaĭnshteĭn, I. A. D'yakon, and A. V. Ablov, Dokl. Akad. Nauk SSSR **193** (2), 330 (1970) [Sov. Phys. Dokl. **15** (7), 645 (1970)].
3. I. A. D'yakon, S. V. Donu, L. A. Chapurina, and L. N. Kaĭryak, Kristallografiya **37** (6), 1391 (1992) [Sov. Phys. Crystallogr. **37** (6), 751 (1992)].
4. B. K. Vaĭnshteĭn, *Electron Diffraction Structure Analysis* (Akad. Nauk SSSR, Moscow, 1956).
5. B. B. Zvyagin, *Electron Diffraction Analysis and Structure Crystallography of Clay Minerals* (Nauka, Moscow, 1964).
6. B. B. Zvyagin, Z. V. Vrublevskaya, A. N. Zhukhlistov, O. V. Sidorenko, S. V. Soboleva, and A. F. Fedotov, *High-Voltage Electron Diffraction Analysis of Laminated Minerals* (Nauka, Moscow, 1979).
7. A. S. Avilov, R. M. Imamov, and S. A. Semiletov, Prib. Tekh. Éksp., No. 3, 214 (1976).
8. A. S. Avilov, Kristallografiya **21** (6), 1117 (1976) [Sov. Phys. Crystallogr. **21** (6), 646 (1976)].
9. B. B. Zvyagin, Kristallografiya **32** (3), 673 (1987) [Sov. Phys. Crystallogr. **32** (3), 394 (1987)].

Translated by I. Polyakova

Crystallography Reports, Vol. 45, No. 4, 2000, pp. 604–610. Translated from Kristallografiya, Vol. 45, No. 4, 2000, pp. 662–668.
Original Russian Text Copyright © 2000 by Panov, Potekhin, Struchkov, Shishkina, Dem'yanovich, Zefirov.

STRUCTURE OF ORGANIC COMPOUNDS

Molecular and Crystal Structures of (*S*,*S*)-[*o*-(α-Dimethylaminoethyl)phenyl]phenylarylcarbinols

V. N. Panov*, K. A. Potekhin*, Yu. T. Struchkov†, I. N. Shishkina***,**
V. M. Dem'yanovich*, and N. S. Zefirov*****

** Vladimir State University, Vladimir, 600000 Russia*

*** Nesmeyanov Institute of Organoelement Compounds, Russian Academy of Sciences,*
ul. Vavilova 28, Moscow, 117813 Russia

**** Chemistry Department, Moscow State University, Vorob'evy gory, Moscow, 119899 Russia*

Received June 10, 1998

Abstract—The crystal structures of (*S*,*S*)-*o*-(α-dimethylaminoethyl)phenyl]phenyl-2,4-dimethylphenylcarbinol (**I**) and (*S*,*S*)-*o*-(α-dimethylaminoethyl)phenyl]phenyl-2,4,5-trimethylphenylcarbinol (**II**) are determined by X-ray diffraction. The molecular and crystal structures of **I** and **II** are similar. The crystal structures of **I** and **II** are compared based on the analysis of the geometric characteristics of the Voronoĭ–Dirichlet packing polyhedra. The circular dichroism spectra of amino alcohols **I** and **II** revealed a strong positive Cotton effect in the region of 230 nm, which correlates with the *S*-configuration of the chiral carbinol center. *© 2000 MAIK “Nauka/Interperiodica”.*

INTRODUCTION

In recent years, considerable attention has been given to the search for new chiral reagents for asymmetric synthesis [1, 2]. The properties of these reagents are determined by their structure and configuration of their asymmetric centers.

Condensation of lithiated (*S*)(–)-*N*,*N*-dimethyl-α-phenylethylamine with 2,4-dimethyl- [3] or 2,4,5-trimethylbenzophenones affords (*S*,*S*)-*o*-(α-dimethylaminoethyl)phenyl]phenyl-2,4-dimethylphenylcarbinol (**I**) or (*S*,*S*)-*o*-(α-dimethylaminoethyl)phenyl]phenyl-2,4,5-trimethylphenylcarbinol (**II**), respectively. A specific feature of the circular dichroism (CD) spectra of these two amino alcohols is a strong positive Cotton effect in the region of 230 nm.

In order to establish correlations between the absolute configuration and the CD data, we determined the single-crystal structures of these δ-amino alcohols by X-ray diffraction.

An analysis of structures **I** and **II** revealed their similarity on the molecular and crystal-packing level. The quantitative evaluation of the degree of distinction between molecular packings of compounds **I** and **II** was made by comparing the geometric characteristics of the Voronoĭ–Dirichlet packing polyhedra of their molecules.

EXPERIMENTAL

Crystals **I** are orthorhombic; at 20°C, $a = 8.315(2)$ Å, $b = 8.367(3)$ Å, $c = 30.239(8)$ Å, $V = 2104(2)$ Å^3, space group $P2_12_12_1$, $Z = 4$, and $d_{\text{calcd}} = 1.14$ g/cm^3. Crystals **II** are orthorhombic; at –120°C, $a = 8.276(7)$ Å, $b = 8.511(5)$ Å, $c = 30.63(1)$ Å, $V = 2157(2)$ Å^3, space group $P2_12_12_1$, $Z = 4$, and $d_{\text{calcd}} = 1.15$ g/cm^3. The unit cell parameters and the intensities of diffraction reflections (1586 and 1457 unique reflections with $I > 2\sigma(I)$ for **I** and **II**, respectively) were measured on a Siemens P3/PC automated diffractometer (λMoK_α, $\theta/2\theta$ scan mode, $\theta < 23°$). Both structures were solved by the direct method. The correct enantiomorphs were chosen based on the known absolute configuration of one of the two asymmetric centers in the molecules.

The hydrogen atom of the hydroxyl group was located on a difference map of electron density, and the positions of the remaining H atoms were calculated. The refinement of the structures in the anisotropic approximation (isotropic for the hydroxyl H atom), with the remaining hydrogen atoms treated within the riding-atom model at fixed values of the isotropic thermal parameters, led to $R = 0.060$ and $R_w = 0.062$ for structure **I**, and $R = 0.052$ and $R_w = 0.050$ for structure **II**. The coordinates and equivalent isotropic thermal parameters U_{eq} of the non-hydrogen atoms are listed in Tables 1 and 2.

---

† Deceased.

Table 1. Coordinates ($\times 10^4$) and equivalent isotropic thermal parameters ($Å^2 \times 10^3$) of non-hydrogen atoms in structure **I**

Atom	*x*	*y*	*z*	U_{eq}
O	4141(5)	4398(6)	1694(1)	49(1)
N	6587(6)	5108(7)	2309(2)	56(2)
C(1)	5010(6)	3856(7)	1308(2)	38(2)
C(2)	6330(7)	2680(7)	1469(2)	39(2)
C(3)	7574(7)	3185(7)	1764(2)	40(2)
C(4)	8655(8)	2032(8)	1908(2)	55(2)
C(5)	8549(8)	449(9)	1789(2)	63(3)
C(6)	7339(8)	–29(8)	1505(2)	57(2)
C(7)	6261(7)	1092(7)	1349(2)	45(2)
C(8)	7702(7)	4885(9)	1928(2)	49(2)
C(9)	9445(8)	5425(10)	2012(2)	70(3)
C(10)	6332(11)	6779(10)	2411(3)	95(4)
C(11)	7066(8)	4249(11)	2709(2)	79(3)
C(12)	5639(6)	5271(7)	1037(2)	36(2)
C(13)	4666(7)	6590(7)	936(2)	43(2)
C(14)	5265(8)	7794(8)	661(2)	52(2)
C(15)	6814(8)	7741(8)	480(2)	51(2)
C(16)	7757(8)	6439(7)	581(2)	50(2)
C(17)	7187(7)	5215(8)	847(2)	44(2)
C(18)	2947(7)	6808(9)	1100(2)	63(2)
C(19)	7401(10)	9106(9)	200(2)	80(3)
C(20)	3788(7)	2995(7)	1010(2)	41(2)
C(21)	2330(8)	2436(9)	1178(2)	63(3)
C(22)	1282(8)	1614(11)	906(3)	85(3)
C(23)	1664(9)	1302(10)	471(3)	79(3)
C(24)	3086(8)	1878(8)	301(2)	57(2)
C(25)	4149(7)	2719(8)	568(2)	49(2)

Table 2. Coordinates ($\times 10^4$) and equivalent isotropic thermal parameters ($Å^2 \times 10^3$) of non-hydrogen atoms in structure **II**

Atom	*x*	*y*	*z*	U_{eq}
O	6917(4)	6702(3)	776(1)	30(1)
N	7653(5)	9098(5)	178(1)	34(1)
C(1)	6378(5)	7546(5)	1160(2)	26(1)
C(2)	5206(5)	8854(5)	1001(1)	24(1)
C(3)	5712(5)	10073(5)	714(2)	26(1)
C(4)	4584(6)	11170(5)	578(2)	33(2)
C(5)	2966(6)	11075(6)	701(2)	38(2)
C(6)	2477(6)	9887(6)	971(2)	33(1)
C(7)	3578(6)	8784(5)	1116(2)	28(1)
C(8)	7453(5)	10197(5)	551(2)	26(1)
C(9)	8009(6)	11884(6)	469(2)	38(2)
C(10)	9356(8)	8816(8)	81(2)	56(2)
C(11)	6787(8)	9532(6)	–215(2)	45(2)
C(12)	7816(5)	8188(5)	1422(1)	24(1)
C(13)	9167(6)	7234(5)	1515(2)	28(1)
C(14)	10380(6)	7852(6)	1778(2)	30(1)
C(15)	10338(6)	9369(6)	1954(2)	33(2)
C(16)	8988(6)	10303(6)	1864(2)	30(2)
C(17)	7764(6)	9677(5)	1607(2)	27(1)
C(18)	9402(6)	5582(6)	1340(2)	38(2)
C(19)	11748(7)	9992(7)	2212(2)	50(2)
C(20)	8859(7)	11946(6)	2038(2)	45(2)
C(21)	5522(6)	6345(5)	1458(2)	26(1)
C(22)	4942(6)	4931(6)	1296(2)	37(2)
C(23)	4159(7)	3875(6)	1569(2)	45(2)
C(24)	3921(7)	4219(6)	2000(2)	44(2)
C(25)	4486(6)	5627(6)	2169(2)	35(2)
C(26)	5285(6)	6670(5)	1894(2)	30(2)

COMPARISON OF MOLECULAR STRUCTURES I AND II

Perspective views of molecules **I** and **II** and the atomic numberings are shown in Fig. 1. There are two asymmetric centers in both molecules. The absolute configuration of the carbinol C(1) center was determined as *S* on the basis of the known *S*-configuration of the C(8) asymmetric center.

Molecules **I** and **II** differ in that the methyl group in **II** substitutes for the H(16) hydrogen atom in **I**. The following two factors are apparently responsible for the absence of a fundamental difference in the geometric structure of the molecules upon substitution. First, the above methyl group in molecule **II** is “external;” that is, it has no short intramolecular nonbonded contacts with other atoms of the molecule, except the C(19) atom. The C(19)···C(20) contact is a 1···4-type contact between the substituents of the aryl ring. Therefore, its formation can result only in the deformation of the aryl ring but cannot change the conformation of the molecule as a whole. Second, as shown below, both molecules are rather rigid; that is, the rotation of their fragments about single bonds is essentially hindered by short intramolecular nonbonded contacts.

Both molecules involve the intramolecular O–H···N bond (O···N, 2.820(8) and 2.809(5); H···N, 2.1 (1) and 1.84(6) Å; and O–H···N, 163(5)° and 153(3)° in **I** and **II**, respectively). This hydrogen bond closes the seven-membered C(1)C(2)C(3)C(8)NH(1)O heterocycle and, as a consequence, fixes the orientation of the C(2)C(3)C(4)C(5)C(6)C(7) aryl ring (ring *A*) relative to the C(1)–C(2) bond [the O–C(1)–C(2)–C(3) torsion

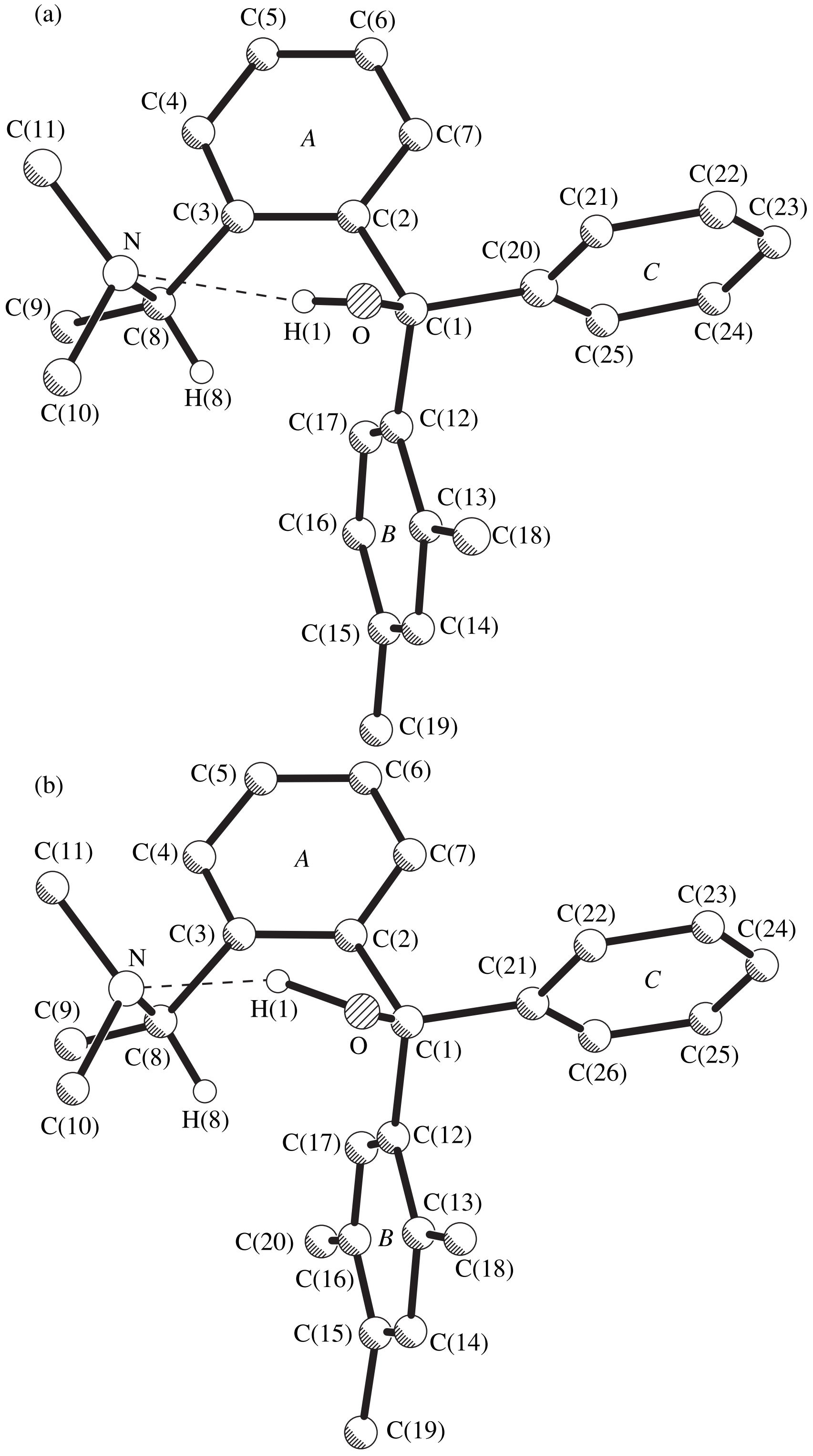

Fig. 1. Perspective views of molecules (a) **I** and (b) **II**. All hydrogen atoms, except those of the hydroxyl group and the C(8) asymmetric center, are omitted. The intramolecular hydrogen bond is denoted by the dashed line.

angle is –61.5(6)° in both molecules]. This orientation of ring *A* gives rise to a short intramolecular nonbonded contact of the 1···5 type between atoms C(8) and C(12). The C(8)···C(12) distances are 3.21 and 3.18 Å in molecules **I** and **II**, respectively, whereas the double van der Waals radius of the carbon atom is 3.42 Å [4].

The orientation of the C(12)C(13)C(14)C(15)C(16)C(17) aryl ring (ring *B*) relative to the C(1)–C(12) bond is also rigidly fixed: the O–C(1)–C(12)–C(13) torsion angles are –46.1(6)° and –46.2(5)° in molecules **I** and **II**, respectively. Changes of this torsion angle [the rotation of ring *B* relative to the C(1)–C(12) bond] are hindered by an intramolecular nonbonded 1···6-type contact between atoms C(8) and C(17) and two 1···5-type contacts O···C(18) and C(3)···C(17). The C(8)···C(17) distances are 3.31 and 3.28 Å, and the C(3)···C(17) distances are 3.27 and 3.24 Å in molecules **I** and **II**, respectively. The O···C(18) distances are 2.88 and 2.85 Å in **I** and **II**, whereas the mean-statistic value of the van der Waals O···C contact is 2.97 Å [4].

The orientation of the phehyl ring (ring *C*) in molecules **I** and **II** is also fixed by intramolecular nonbonded contacts. The O–C(1)–C(20)–C(21) torsion angle in molecule **I** is –19.2(6)°, and the corresponding O–C(1)–C(21)–C(22) angle in molecule **II** is –20.0(5)°. A decrease in this angle is hindered by the C(7)···C(25) contact (3.24 Å) in molecule **I** and the C(7)···C(26) contact (3.30 Å) in molecule **II**, and an increase in this angle is hindered by the C(17)···C(25) contact (3.38 Å) in molecule **I** and the C(17)···C(26) contact (3.40 Å) in molecule **II**.

Thus, the orientations of all three rings (*A*, *B*, and *C*) are fixed rather rigidly in both molecules, and, as a consequence, molecules **I** and **II** have almost identical geometric forms.

The intramolecular hydrogen bond and a large number of short intramolecular nonbonded contacts (including the 1···4-type contacts) result in the deformation of bond lengths and angles in molecules **I** and **II**. As an example, note an increase in the C(9)–C(8)–N bond angle to 114.9(5)° in **I** and 115.5(4)° in **II** and the elongation of the C(2)–C(3) bond to 1.429(8) in **I** and 1.422(6) Å in **II** in comparison with the mean C_{ar}–C_{ar} bond length (1.390 Å) for these two molecules.

COMPARISON OF CRYSTAL STRUCTURES I AND II

As noted above, molecules **I** and **II** are close in geometric structure. Substitution at the C(16) atom (methyl group for hydrogen) increases the volume of crystal space per molecule by only 2.5%. However, the similarity of the molecular packings **I** and **II** is not evident even for the structures characterized by the same space group and small difference in the corresponding parameters of the unit cells.

In order to reveal the specific features of molecular packings and to describe quantitatively the degree of distinction between the packings, we compared the Voronoĭ–Dirichlet packing polyhedra [5, 6] of molecules **I** and **II**.

It was found that the coordination numbers of molecules are fourteen in both structures, and, moreover, the coordination polyhedra belong to the same 2(4)8(5)4(6)I packing type (according to Fischer and Koch [6]). Therefore, the packing polyhedra of molecules (PPM) **I** and **II** have 14 boundary surfaces each (the boundary surface (BS) is an assembly of faces shared by two packing polyhedra of the adjacent molecules). The area of a BS and the areas of its constituent faces are determined by the relative positions of atoms of the adjacent molecules in the crystal. Therefore, the difference in areas of the corresponding BS can be considered as an indicator of distinction between the molecular packings [7].

To characterize the degree of distinction between two molecular packings belonging to the same packing type, it is expedient to use the D_t coefficient of noncoincidence of the relative BS areas

$$D_t = \frac{1}{2}\sum_i \left|\frac{S_{1i}}{S_1} - \frac{S_{2i}}{S_2}\right|, \qquad (1)$$

where S_{1i} and S_{2i} are the areas of the *i*th BSs; and S_1 and S_2 are the areas of the PPM surfaces in the first and the second structures, respectively. It is evident that comparison between two crystal structures by using formula (1) is possible only if the BSs of their packing polyhedra show a one-to-one correspondence. Moreover, as a rule, if this correspondence even exists, we do not know about it *a priori*. Therefore, it is necessary to find out preliminarily if this correspondence exists and to consider all possible ways of having the two PPMs coincide.

The existence of the one-to-one correspondence between the BSs of the packing polyhedra of molecules in crystal structures **I** and **II** follows from the same packing type of the coordination polyhedra in these structures. For the 2(4)8(5)4(6)I packing type, there are only four topologically equivalent ways of bringing into coincidence two coordination polyhedra (and, hence, the packing polyhedra also). Calculation of the D_t coefficients for each of the four variants of PPM coincidence revealed that one of the variants [$D_t(1)$] significantly differs from the others: $D_t(1) = 0.02$, $D_t(2) = 0.11$, $D_t(3) = 0.13$, and $D_t(4) = 0.16$. A small value of the $D_t(1)$ coefficient indicates that crystal structures **I** and **II** are very close in geometry. Based on the correspondence between the PPMs, we can establish the correspondence between the crystallographic axes in structures **I** and **II**: $x_{\mathbf{I}} \longrightarrow y_{\mathbf{II}}$, $y_{\mathbf{I}} \longrightarrow x_{\mathbf{II}}$, and $z_{\mathrm{I}} \longrightarrow -z_{\mathbf{II}}$. Figure 2 shows the projections of crystal structures **I** and **II** along the $x_{\mathbf{I}}$- and $y_{\mathbf{II}}$-axes, respectively.

A more detailed analysis shows that we can establish the correspondence between not only BSs, but separate PPM faces of **I** and **II** also. This allows the use of three more coefficients—d_i, D_S, and ν_i [7]—which are more sensitive than D_t to the distinctions in the mutual arrangement of molecules relative to one another in the compared crystal structures.

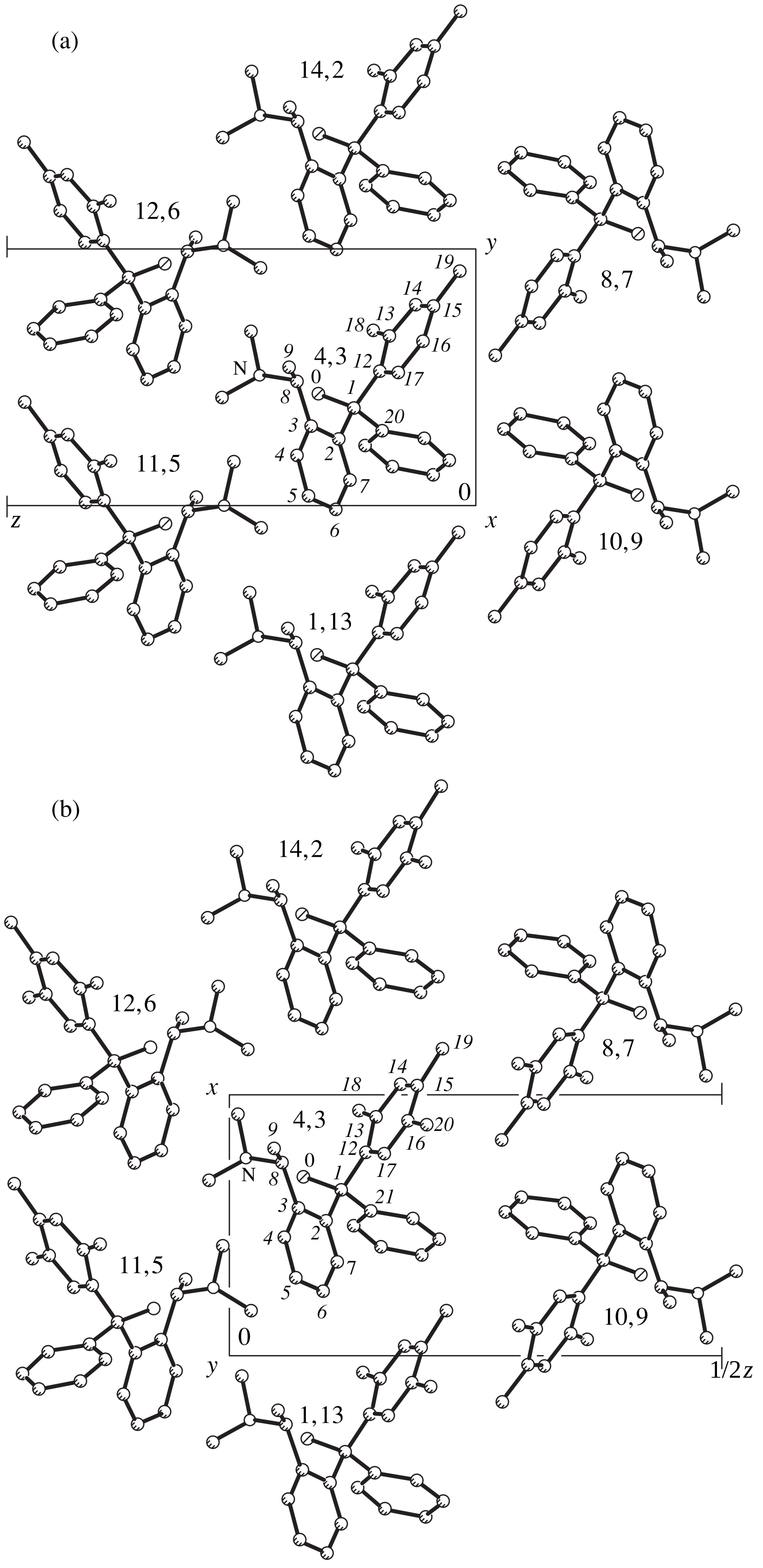

Fig. 2. Projections of crystal structures (a) **I** along the *x*-axis and (b) **II** along the *y*-axis. Numbering of the molecules that surround the reference molecules corresponds to that in Table 3.

Table 3. Characteristics of the boundary surfaces of the packing polyhedra of molecules in structures **I** and **II**

BS number *i*	Position of the *i*th molecule		BS area		ΔS, Å^2	d_i	ν_i, %
	I	**II**	S_{1i}, Å^2	S_{2i}, Å^2			
1	*x*, *y* – 1, *z*	*x* – 1, *y*, *z*	53.1	52.8	–0.3	0.07	4.3
2	*x*, *y* + 1, *z*	*x* + 1, *y*, *z*					
3	*x* – 1, *y*, *z*	*x*, *y* – 1, *z*	41.3	45.4	4.1	0.31	16.2
4	*x* + 1, *y*, *z*	*x*, *y* + 1, *z*					
5	1 – *x*, *y* – 1/2, 1/2 – *z*	*x* – 1/2, 3/2 – *y*, –*z*	39.6	40.2	0.6	0.04	1.8
6	1 – *x*, *y* + 1/2, 1/2 – *z*	*x* + 1/2, 3/2 – *y*, –*z*					
7	*x* – 1/2, 3/2 – *y*, –*z*	2 – *x*, *y* – 1/2, *z*	28.2	28.0	–0.2	0.48	16.2
8	*x* + 1/2, 3/2 – *y*, –*z*	2 – *x*, *y* + 1/2, *z*					
9	*x* – 1/2, 1/2 – *y*, –*z*	1 – *x*, *y* – 1/2, *z*	22.2	21.0	–1.2	0.28	7.2
10	*x* + 1/2, 1/2 – *y*, –*z*	1 – *x*, *y* + 1/2, *z*					
11	2 – *x*, *y* – 1/2, 1/2 – *z*	*x* – 1/2, 5/2 – *y*, –*z*	21.9	21.6	–0.3	0.03	0.8
12	2 – *x*, *y* + 1/2, 1/2 – *z*	*x* + 1/2, 5/2 – *y*, –*z*					
13	*x* – 1, *y* – 1, *z*	*x* – 1, *y* – 1, *z*	8.5	11.0	2.5	0.29	3.4
14	*x* + 1, *y* + 1, *z*	*x* + 1, *y* + 1, *z*					
Total			429.7	439.7	10.0	D_S = 0.19	100.0

Coefficients of relative distinction between the boundary surfaces are defined as

$$d_i = \frac{\sum_j |\sigma_{1j} - \sigma_{2j}|}{S_{1i} + S_{2i}}, \qquad (2)$$

where σ_{1j} and σ_{2j} are the areas of the *j*th faces; and S_{1i} and S_{2i} are the areas of the *i*th BSs of the packing polyhedra in the first and the second structures, respectively. Summation is made over all pairs of faces of the *i*th BSs.

The coefficient of noncoincidence of packings D_S is defined as

$$D_s = \frac{\sum_i d_i(S_{1i} + S_{2i})}{S_1 + S_2}, \qquad (3)$$

where summation extends over all BSs; and S_1 and S_2 are the areas of the PPM surfaces in the first and the second structures, respectively.

The contribution of the *i*th BS to the coefficient of noncoincidence of packings D_S is defined as

$$\nu_i = \frac{d_i(S_{1i} + S_{2i})}{D_s(S_1 + S_2)}. \qquad (4)$$

Table 3 represents the characteristics of the boundary surfaces of PPMs: the position of the adjacent molecule sharing the BS under consideration with the reference molecule (the position of the reference molecule in the unit cell is *x*, *y*, *z*); the BS areas S_{1i} and S_{2i} for the first and the second structures, respectively; and the difference between these areas ΔS_i. The last two columns contain the relative differences in the areas of the BS faces d_i and contribution ν_i of a BS to the coefficient of noncoincidence of packings D_S (expressed in percent). All the BSs are divided into pairs, since those related by a translation or a twofold screw axis have identical numerical characteristics.

The areas of most PPM boundary surfaces in structures **I** and **II** differ insignificantly; the exception is provided by BSs 13, 14 (ΔS_i = 2.5 Å^2) and 3, 4 (ΔS_i = 4.1 Å^2). However, the BS area is not a rigorous characteristic of the degree of distinction between mutual arrangements of adjacent molecules, since approximate equality of the BS areas may conceal large differences in the areas of separate constituent faces.

A more sensitive characteristic of the distinction between the corresponding BSs is the d_i coefficient. As is seen from Table 3, the largest differences are observed for BSs 3, 4 (d_i = 0.31) and 7, 8 (d_i = 0.48). This result is explained by the structural distinctions between molecules **I** and **II**. The differences in the areas of the faces that characterize the contacts of the "surplus" methyl group of molecule **II** are the main contributors to the d_i coefficient for the above BS pairs—81% (3 and 4) and 71% (7 and 8). It is also notable that the least difference is observed between BSs 11, 12 (d_i = 0.03) and 5, 6 (d_i = 0.04), whose faces do not involve the "surplus" methyl group.

The above four BSs (3, 4, 7, and 8) with the largest d_i values are the largest contributors to the coefficient of noncoincidence of packings (ν_i = 16.2%). Almost 65%

of the distinctions between PPMs of **I** and **II** are due to these BSs.

The integral coefficient of noncoincidence of packings of D_S for crystal structures **I** and **II** is equal to 0.19. It is comparable with the same criterion ($D_S = 0.16$) for the crystal structures of (+)-3-diazacamphor and (+)-3-bromocamphor [7], which also have close molecular packings despite the difference in molecular structure.

Thus, compounds **I** and **II** have similar crystal structures characterized by the same packing type. Moreover, there is the correspondence between separate faces of the packing polyhedra of their molecules. A strong positive Cotton effect observed in the region of 230 nm of the CD spectra of **I** and **II** correlates with the *S*-configuration found in the chiral carbinol center of molecules **I** and **II**. This allows application of the CD method to determination of the absolute configuration of the carbinol center in δ-amino alcohols—the diaryl- and triarylcarbinol derivatives.

REFERENCES

1. J. Eilers, J. Wilken, and J. Martens, Tetraherdon: Asymmetry **7** (8), 2343 (1996).
2. V. Peper and J. Martens, Chem. Ber. **129** (6), 691 (1996).
3. V. M. Dem'yanovich, I. N. Shishkina, K. A. Potekhin, *et al.*, Dokl. Akad. Nauk **333** (2), 183 (1993).
4. Yu. V. Zefirov and P. M. Zorkiĭ, Usp. Khim. **64** (5), 446 (1995).
5. R. V. Galiulin, *Crystallographic Geometry* (Nauka, Moscow, 1984).
6. W. Fischer and E. Koch, Z. Kristallogr. **150**, 245 (1979).
7. V. N. Panov, K. A. Potekhin, and A. V. Goncharov, Kristallografiya **42**, 389 (1997) [Crystallogr. Rep. **42**, 351 (1997)].

Translated by I. Polyakova

Crystallography Reports, Vol. 45, No. 4, 2000, pp. 611–614. From Kristallografiya, Vol. 45, No. 4, 2000, pp. 669–672.
Original English Text Copyright © 2000 by Rajnikant, Gupta, Attar Singh.

STRUCTURE OF ORGANIC COMPOUNDS

X-ray Structure Analysis of 5*N*-Ethyl-8-Carboxy-9-Oxo-11-Methyl-Pyrido[2,1-*b*]quinazoline[1]

Rajnikant,[2] V. R. Gupta, and Attar Singh

X-ray Crystallography Laboratory, Department of Physics, University of Jammu, Jammu Tawi, 180006 India

Received March 4, 1999; in final form, April 26, 1999

Abstract—The crystal structure of 5*N*-ethyl-8-carboxy-9-oxo-11-methyl-pyrido[2,1-*b*]quinazoline ($C_{16}H_{16}N_2O_3$) has been determined by X-ray diffraction analysis. The compound crystallizes in the monoclinic crystal system (space group $P2_1/c$) with the unit cell parameters a = 9.775(1) Å, b = 15.868(1) Å, c = 9.799(1) Å, β = 113.50(1)°, Z = 4. The benzene ring is planar, the pyrimidine ring exists in 11β-sofa conformation, and the pyridone ring deviates slightly from planarity. The crystal packing exhibits intra- and intermolecular interactions of the O–H···O, C–H···O, and C–H···N types. © *2000 MAIK "Nauka/Interperiodica".*

5*N*-ethyl-8-carboxy-9-oxo-11-methyl-pyrido[2,1-*b*]quinazoline has been prepared by refluxing 2,4-dimethyl-2,3-dihydroquinazoline and diethyl ethoxy methylene malonate [1]. The present work has been undertaken as a part of our systematic research on the crystallographic analysis of several important organic molecules [2–12].

EXPERIMENTAL

Rectangular shaped crystals of 5*N*-ethyl-8-carboxy-9-oxo-11-methyl-pyrido[2,1-*b*]quinazoline were grown from chloroform at room temperature. Three-dimensional intensity data were collected on an Enraf–Nonius CAD4 single-crystal X-ray diffractometer at the Indian Institute of Technology (Chennai). The unit cell parameters were refined by the least-squares procedure. The data were corrected for Lorentz and polarization factors, but no absorption or extinction corrections were made.

The crystal structure has been determined by direct methods using the SHELXS86 software package [13]. The full-matrix least-squares refinement of the structure has been carried out by using the SHELXL93 software package [14]. All the H atoms were located from the difference Fourier map. Three cycles of refinement of the positional and anisotropic thermal parameters for the non-hydrogen atoms and the positional and isotropic thermal parameters for the hydrogen atoms yielded R = 0.048. The crystallographic data are summarized in Table 1.

Table 1. Crystal data and experimental details

Crystal habit	Light yellow rectangular	Absorption coefficient, mm^{-1}	0.777
Chemical formula	$C_{16}H_{16}N_2O_3$	$F(000)$	600
Molecular weight	284.3	Crystal size, mm	0.40 × 0.25 × 0.20
Crystal system	Monoclinic	Refinement of unit cell	25 reflections, $26° \le 2\theta \le 42°$
Unit cell parameters		θ range for entire data collection	$1° \le \theta \le 70°$
a, Å	9.775(1)	No. of measured reflections	2852
b, Å	15.868(1)	No. of unique reflections	2580
c, Å	9.799(1)	No. of observed reflections $[F > 4\sigma(F)]$	2578
β, deg	113.50(1)	No. of parameters refined	255
Unit cell volume, $Å^3$	1393.9	Final R-factor	0.048
Density (calculated), g/cm^3	1.355	wR	0.143
No. of molecules per unit cell	4	Weighting scheme	$1/[\sigma^2(F_{eq})^2 + 0.0774P^2 + 0.35P]$
Space group	$P2_1/c$	Final residual electron density $e \cdot Å^{-3}$	−0.21–+0.22
Wavelength λ	CuK_α	Maximum ratio	−0.105[xH(2)]

---

[1] This article was submitted by the authors in English.

[2] Author for correspondence; *e-mail: rajni_kant_verma@hotmail.com*

1063-7745/00/4504-0611$20.00 © 2000 MAIK "Nauka/Interperiodica"

Table 2. Atomic coordinates and equivalent isotropic (isotropic for hydrogen atoms) thermal parameters (Å^2)

Atom	x	y	z	U_{eq}/U_{iso}^*	Atom	x	y	z	U_{eq}/U_{iso}^*
C(1)	0.5204(2)	0.7712(1)	–0.0278(2)	0.057(1)	C(16)	0.4116(3)	0.4466(1)	–0.2562(3)	0.062(1)
O(1)	1.1543(2)	0.4009(1)	0.3496(2)	0.079(1)	C(17)	1.1039(2)	0.4718(1)	0.3288(2)	0.055(1)
C(2)	0.3694(3)	0.7822(1)	–0.1095(3)	0.068(1)	C(18)	0.8398(2)	0.7315(1)	–0.0643(2)	0.053(1)
O(2)	1.1695(2)	0.5331(1)	0.4262(2)	0.074(1)	H(1)	0.577(2)	0.812(1)	0.050(2)	0.06(1)
C(3)	0.2914(2)	0.7235(1)	–0.2150(3)	0.065(1)	H(2)	0.325(3)	0.832(2)	–0.089(3)	0.09(1)
O(3)	0.9898(1)	0.6410(1)	0.2639(1)	0.057(1)	H(3)	0.189(3)	0.731(2)	–0.276(3)	0.09(1)
C(4)	0.3606(2)	0.6521(1)	–0.2393(2)	0.055(1)	H(4)	0.308(2)	0.611(1)	–0.308(2)	0.06(1)
N(5)	0.5906(2)	0.5678(1)	–0.1687(1)	0.042(1)	H(6)	0.715(2)	0.418(1)	–0.099(2)	0.06(1)
C(6)	0.7689(2)	0.4597(1)	–0.0346(2)	0.046(1)	H(7)	0.925(2)	0.379(1)	0.105(2)	0.06(1)
C(7)	0.8928(2)	0.4384(1)	0.0903(2)	0.046(1)	H(11)	0.796(2)	0.716(1)	0.122(2)	0.05(1)
C(8)	0.9703(2)	0.4967(1)	0.1974(2)	0.043(1)	H(151)	0.586(2)	0.477(1)	–0.315(2)	0.06(1)
C(9)	0.9236(2)	0.5822(1)	0.1770(2)	0.042(1)	H(152)	0.454(2)	0.544(1)	–0.380(2)	0.05(1)
N(10)	0.7968(1)	0.6018(1)	0.0500(1)	0.038(1)	H(161)	0.463(3)	0.410(1)	–0.177(3)	0.07(1)
C(11)	0.7588(2)	0.6927(1)	0.0239(2)	0.042(1)	H(162)	0.335(3)	0.477(2)	–0.220(3)	0.11(1)
C(12)	0.5929(2)	0.7013(1)	–0.0520(2)	0.043(1)	H(163)	0.361(3)	0.409(2)	–0.335(4)	0.10(1)
C(13)	0.5131(2)	0.6409(1)	–0.1554(2)	0.043(1)	H(17)	1.113(3)	0.586(2)	0.381(3)	0.10(1)
C(14)	0.7177(2)	0.5424(1)	–0.0532(2)	0.038(1)	H(181)	0.812(2)	0.703(1)	–0.164(2)	0.06(1)
C(15)	0.5132(2)	0.5076(1)	–0.2899(2)	0.048(1)	H(182)	0.820(2)	0.790(2)	–0.077(2)	0.07(1)
					H(183)	0.951(3)	0.722(1)	–0.004(3)	0.07(1)

* $U_{eq} = (1/3)\sum_i \sum_j U_{ij} a_i^* a_j^* (\mathbf{a}_i \cdot \mathbf{a}_j)$.

Table 3. Torsion angles (deg) for non-hydrogen atoms and dihedral angles (deg) between the planes of benzene (1), pyrimidine (2), and pyridone (3) rings of the molecule (e.s.d.'s are given in parentheses)

C(12)–C(1)–C(2)–C(3)	–0.0(3)	C(6)–C(7)–C(8)–C(9)	–1.7(3)
C(2)–C(1)–C(12)–C(13)	–1.9(3)	C(7)–C(8)–C(9)–N(10)	2.2(3)
C(1)–C(2)–C(3)–C(4)	1.4(3)	C(8)–C(9)–N(10)–C(14)	0.1(2)
C(2)–C(3)–C(4)–C(13)	–0.8(3)	C(14)–N(10)–C(11)–C(12)	37.3(2)
C(3)–C(4)–C(13)–C(12)	–1.1(3)	C(9)–N(10)–C(14)–C(6)	–2.8(2)
C(14)–N(5)–C(13)–C(12)	23.5(2)	C(11)–N(10)–C(14)–N(5)	–9.5(2)
C(13)–N(5)–C(14)–N(10)	–23.1(2)	N(10)–C(11)–C(12)–C(13)	–36.0(2)
C(14)–C(6)–C(7)–C(8)	–1.1(3)	C(1)–C(12)–C(13)–C(4)	2.4(3)
C(7)–C(6)–C(14)–N(10)	3.3(3)	C(11)–C(12)–C(13)–N(5)	8.6(3)

Plane	Plane	Angle
1	2	16.12(5)
1	3	28.61(5)
2	3	12.77(5)

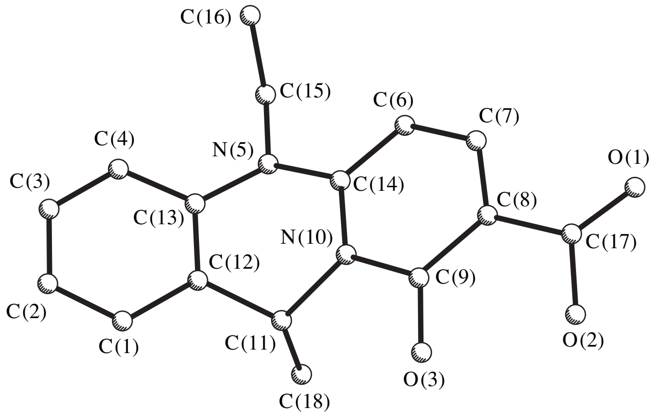

A general view of the molecule and atomic numbering scheme.

RESULTS AND DISCUSSION

The final atomic coordinates and equivalent isotropic thermal parameters for the non-hydrogen (isotropic for hydrogen) atoms are given in Table 2. The endocyclic torsion angles and dihedral angles between different least-squares planes are listed in Table 3. A general view of the molecule and the atomic numbering scheme [15] is shown in the figure.

The bond distances of the molecule, on the whole, agree with the values reported for some analogous structures containing quinazoline or pyrimidine rings [16–19]. The mean value [1.392(2) Å] of the two $C(sp^2)$–N bonds, i.e., N(5)–C(13) [1.419(2) Å] and N(5)–C(14) [1.366(2) Å], is in agreement with the standard mean value of 1.385 Å[20]; the length of the bond N(5)–C(13) is close to the values obtained in *E*- and *Z*-isomers of 1-(-2-amino-1-cyano-2-thioethylene)pyridinium-ylide [21]. The C(9)=O(3) bond length [1.255(2) Å] is greater than its theoretical value [1.199 Å], and it may probably be due to the strong intramolecular O(2)–H(17)···O(3) hydrogen bond. The benzene ring is perfectly planar, and the pyridone ring deviates slightly from planarity [the maximum deviation is –0.023 Å for the C(14) atom]. The pyrimidine ring has an 11β-sofa conformation with the asymmetry parameter ΔC_s [C(11)] = 0.87 [22]. The dihedral angle between the least squares plane of benzene and pyridone rings is 28.61(5)°, indicating that the molecule is somewhat folded, may be due to the sofa conformation of the pyrimidine ring.

Table 4. Inter- and intramolecular hydrogen bonds

Bond *D*–H··*A*	H··*A*, Å	*D*··*A*, Å	*D*–H··*A*, deg
C(11)–H(111)···O(3)	2.19(2)	2.658(2)	109(1)
C(18)–H(183)···O(3)	2.81(2)	3.285(2)	109(2)
O(2)–H(17)···O(3)	1.56(3)	2.514(2)	156(3)
C(15)–H(152)···O(2)$^{(i)}$	2.67(2)	3.426(2)	131(1)
C(4)–H(4)···O(2)$^{(i)}$	2.70(2)	3.594(2)	159(2)
C(16)–H(162)···N(10)$^{(ii)}$	2.78(4)	3.479(4)	123(2)

Note: Symmetrical transformations: (*i*) –1 + *x*, *y*, –1 + *z*; (*ii*) 1 – *x*, 1 – *y*, –*z*).

The molecular packing in the crystal is of the *herring-bone* type. The following intra- and intermolecular bonds have been found to contribute to the stability of the crystal structure: O–H··O, C–H··O, and C–H··N (Table 4).

ACKNOWLEDGMENTS

Rajnikant is grateful to Dr. K. L. Dhar, Scientist, Natural Products Chemistry Division, Regional Research Laboratory, Jammu Tawi, for supplying the samples. He further acknowledges the financial support received under Special Assistance Program (SAP) of the University Grants Commission (DSA-Phase III), Government of India, New Delhi.

REFERENCES

1. B. Mahajan, Ph. D. Thesis (Regional Research Laboratory, Jammu Tawi, 1995).
2. Rajnikant, D. Watkin, and G. Tranter, Acta Crystallogr., Sect. C: Cryst. Struct. Commun. **51**, 1452 (1995).
3. Rajnikant, D. Watkin, and G. Tranter, Acta Crystallogr., Sect. C: Cryst. Struct. Commun. **51**, 2071 (1995).
4. V. K. Gupta, K. N. Goswami, V. S. Yadava, *et al.*, Z. Kristallogr. **210**, 154 (1995).
5. Rajnikant, V. K. Gupta, A. Singh, *et al.*, Acta Crystallogr., Sect. C: Cryst. Struct. Commun. **52**, 2272 (1996).
6. Rajnikant, V. K. Gupta, A. Singh, *et al.*, Mol. Mater. **6**, 227 (1996).
7. Rajnikant, V. K. Gupta, M. Lal, *et al.*, Mol. Mater. **6**, 199 (1996).
8. Rajnikant, M. Lal, V. K. Gupta, *et al.*, Crystallogr. Rep. **43**, 448 (1998).
9. Rajnikant, V. K. Gupta, A. Singh, *et al.*, Mol. Mater. **9**, 227 (1998).
10. Rajnikant, V. K. Gupta, M. Lal, *et al.*, Mol. Mater. **9**, 131 (1998).
11. Rajnikant, V. K. Gupta, A. Kumar, *et al.*, Mol. Cryst. Liq. Cryst. (in press).
12. Rajnikant, V. K. Gupta, R. Gupta, *et al.*, Crystallogr. Rep. **45**, 98 (2000).
13. G. M. Sheldrick, *SHELXS86: Program for the Solution of Crystal Structures* (Univ. of Göttingen, Germany, 1986).

14. G. M. Sheldrick, *SHELXL93: Program for the Refinement of Crystal Structures* (Univ. of Göttingen, Germany, 1993).
15. W. D. S. Motherwell and W. Clegg, *PLUTO: Program for Plotting Molecular and Crystal Structures* (Univ. of Cambridge, Cambridge, 1978).
16. A. A. Freer, D. J. Robins, and G. N. Sheldrake, Acta Crystallogr., Sect. C: Cryst. Struct. Commun. **43**, 1119 (1987).
17. A. T. Johnson, D. A. Keszler, K. Sakuma, and J. D. White, Acta Crystallogr., Sect. C: Cryst. Struct. Commun. **45**, 1114 (1989).
18. K. Djinovic, L. Golic, and I. Leban, Acta Crystallogr., Sect. C: Cryst. Struct. Commun. **46**, 281 (1990).
19. P. Pecorari, M. Renaldi, and L. Antolini, Acta Crystallogr., Sect. C: Cryst. Struct. Commun. **48**, 2027 (1992).
20. F. H. Allen, O. Kennard, D. G. Watson, *et al.*, J. Chem. Soc., Perkin Trans. 2, S1 (1987).
21. E. Fischer, M. Knippel, K. M. Wollin, *et al.*, J. Prakt. Chem. **325**, 261 (1983).
22. W. L. Duax and D. A. Norton, *Atlas of Steroid Structures* (Plenum, New York, 1975), Vol. 1.

Crystallography Reports, Vol. 45, No. 4, 2000, pp. 615–618. Translated from Kristallografiya, Vol. 45, No. 4, 2000, pp. 673–676.
Original Russian Text Copyright © 2000 by Polyakova, Neĭkovskiĭ, Sergienko.

STRUCTURE OF ORGANIC COMPOUNDS

Crystal and Molecular Structures of (1,3,4-Thiadiazolyl-2)aminodipropionic and (5-Methyl-1,3,4-Thiadiazolyl-2)aminodipropionic Acids

I. N. Polyakova*, S. I. Neĭkovskiĭ, and V. S. Sergienko***
** Kurnakov Institute of General and Inorganic Chemistry, Russian Academy of Sciences,*
Leninskiĭ pr. 31, Moscow, 117907 Russia
*** Pridneprov'e State Academy of Civil Engineering and Architecture, Dnepropetrovsk, Ukraine*

Received July 8, 1998

Abstract—Crystal structures of (1,3,4-thiadiazolyl-2)aminodipropionic (**I**) and (5-methyl-1,3,4-thiadiazolyl-2)aminodipropionic (**II**) acids are determined [R = 0.0363 and 0.0529 for 2706 and 1614 reflections with $I > 2\sigma(I)$ for **I** and **II**, respectively]. The similarity and distinctions in the hydrogen-bond systems and molecular-packing motifs of crystals **I** and **II** are discussed. © *2000 MAIK "Nauka/Interperiodica".*

(5-*R*-1,3,4-Thiadiazolyl-2)aminodipropionic acids are new aminocarboxylate ligands containing a specific heterocyclic substituent. The synthesis of these compounds with R = H, *Me*, and *iso*-Pr, their IR spectra, and complex formation with Zn^{2+}, Cd^{2+}, and Hg^{2+} ions were described in [1–3]. In the present work, we report the results of the X-ray diffraction study of (1,3,4-thiadiazolyl-2)aminodipropionic (**I**) and (5-methyl-1,3,4-thiadiazolyl-2)aminodipropionic (**II**) acids. Our data can serve as a basis for the correct interpretation of the spectra.

EXPERIMENTAL

Crystals of compounds **I** and **II** are triclinic, space group $P\bar{1}$, and $Z = 2$.

Compound **I**: $C_8H_{11}N_3O_4S$, a = 5.2080(8), Å b = 9.975(2) Å, c = 10.156(2) Å, α = 91.03(2)°, β = 92.25(1)°, γ = 103.31(2)°, V = 512.8(2) A^3, d_{calcd} = 1.588 g/cm^3, and μ(Mo) = 0.32 mm^{-1} (CAD-4 diffractometer, $\lambda \text{Mo}K_\alpha$, graphite monochromator, ω scan mode, $2\theta_{max}$ = 64°).

Compound **II**: $C_9H_{13}N_3O_4S$, a = 7.144(1) Å, b = 8.921(2) Å, c = 10.494(2) Å, α = 72.71(2)°, β = 73.97(2)°, γ = 67.82(1)°, V = 581.1(2) Å^3, d_{calcd} = 1.482 g/cm^3, and μ(Mo) = 0.29 mm^{-1} (Syntex $P2_1$ diffractometer, $\lambda \text{Mo}K_\alpha$, graphite monochromator, $\omega/2\theta$ scan mode, $2\theta_{max}$ = 56°).

Both structures were solved by the direct method with the SHELXS86 program [4]. The hydrogen atoms were located from difference Fourier syntheses. Structure **I** was refined by the least-squares procedure in the anisotropic approximation for the non-hydrogen atoms and in the isotropic approximation for hydrogen atoms with the SHELXL93 program [5]. The discrepancy factors were $R1$ = 0.0491 and $wR2$ = 0.1245 for a complete set of 3300 unique reflections and $R1$ = 0.0363 and $wR2$ = 0.1168 for 2706 reflections with $I > 2\sigma(I)$, and S = 1.121. In structure **II**, the non-hydrogen atoms were refined in the anisotropic approximation. The hydrogen atoms were refined within the riding-atom model, and their thermal parameters U_{iso} were fixed by the values of 0.01 Å^2 larger than the U_{eq} values of the atoms to which they are attached. The refinement for a set of 1614 unique reflections with $I > 2\sigma(I)$ led to R = 0.0529, wR = 0.0733, and S = 1.0885 (SHELX76 [6]).

The atomic coordinates and parameters of thermal vibrations for structures **I** and **II** are listed in the table. Fragments of crystal structures **I** and **II** are shown in Figs. 1 and 2, respectively.

RESULTS AND DISCUSSION

The five-membered thiadiazole rings in molecules **I** and **II** are planar within ±0.002 and ±0.008 Å, respectively. In **I**, the N(3) atom deviates from the plane of the ring by 0.029 Å. In **II**, the N(3) and C(9) substituents deviate from the plane of the ring in opposite directions, by 0.047 and 0.033 Å, respectively. The dihedral angle between the plane defined by the C(1), C(3), and C(6) atoms that form the environment of the N(3) atom and the plane of the five-membered ring is 1.4° in **I** and 6.3° in **II**. The environment of the N(3) atom has a flattened pyramidal configuration with a pyramid height of 0.041 Å in **I** and 0.188 Å in **II**. The heights of the N(3) pyramids correlate with the N(3)–C(1) bond lengths [1.343(2) and 1.369(6) Å in **I** and **II**, respectively]: the flatter pyramid in **I** corresponds to a shorter bond. Both factors indicate that the lone electron pair of the N(3) atom in **I** is conjugated with the thiadiazole ring to a greater extent than in **II**.

1063-7745/00/4504-0615$20.00 © 2000 MAIK "Nauka/Interperiodica"

Atomic coordinates and equivalent thermal parameters U_{eq} (for H atoms, U_{iso}) in structures **I** and **II**

Atom	x	y	z	U_{eq}/U_{iso}, Å^2
		I		
S(1)	0.3827(1)	0.2433(1)	−0.0089(1)	0.031(1)
O(1)	0.5428(3)	0.3060(1)	0.6779(1)	0.038(1)
O(2)	0.2844(2)	0.4402(1)	0.6053(1)	0.028(1)
O(3)	0.2489(3)	−0.0598(2)	0.1643(1)	0.047(1)
O(4)	0.1485(3)	−0.1371(1)	0.3649(1)	0.042(1)
N(1)	0.5688(2)	0.4026(1)	0.1884(1)	0.024(1)
N(2)	0.7498(2)	0.4373(1)	0.0915(1)	0.029(1)
N(3)	0.1667(2)	0.2491(1)	0.2309(1)	0.023(1)
C(1)	0.3628(2)	0.3011(1)	0.1513(1)	0.021(1)
C(2)	0.6784(3)	0.3641(2)	−0.0146(1)	0.030(1)
C(3)	0.1687(3)	0.3135(1)	0.3619(1)	0.023(1)
C(4)	0.3580(3)	0.2657(1)	0.4586(1)	0.024(1)
C(5)	0.4005(3)	0.3403(1)	0.5911(1)	0.023(1)
C(6)	−0.0610(3)	0.1396(1)	0.1883(1)	0.025(1)
C(7)	−0.0944(3)	0.0145(1)	0.2750(2)	0.026(1)
C(8)	0.1202(3)	−0.0630(1)	0.2607(1)	0.026(1)
H(2O)	0.354(6)	0.513(3)	0.695(3)	0.065(8)
H(4O)	0.264(7)	−0.191(4)	0.341(3)	0.077(9)
H(2)	0.766(6)	0.368(3)	−0.092(3)	0.054(7)
H(3*A*)	0.205(4)	0.404(2)	0.350(2)	0.023(4)
H(3*B*)	−0.013(4)	0.283(2)	0.394(2)	0.031(5)
H(4*A*)	0.304(5)	0.174(3)	0.475(2)	0.040(6)
H(4*B*)	0.527(4)	0.273(2)	0.420(2)	0.036(5)
H(6*A*)	−0.217(4)	0.177(2)	0.192(2)	0.035(5)
H(6*B*)	−0.035(5)	0.116(3)	0.100(2)	0.039(6)
H(7*A*)	−0.257(5)	−0.044(3)	0.244(2)	0.040(6)
H(7*B*)	−0.112(4)	0.036(2)	0.367(2)	0.029(5)
		II		
S(1)	0.2779(2)	−0.0968(2)	−0.2798(1)	0.0296(6)
O(1)	−0.2500(7)	0.4338(6)	−0.0524(4)	0.043(2)
O(2)	−0.4887(7)	0.5092(5)	−0.1784(4)	0.045(2)
O(3)	0.2671(8)	−0.0360(5)	0.1626(4)	0.055(2)
O(4)	0.2110(8)	0.2019(5)	0.2178(4)	0.049(2)
N(1)	0.1872(8)	0.1806(5)	−0.4528(4)	0.031(2)
N(2)	0.2353(8)	0.0553(6)	−0.5207(4)	0.032(2)
N(3)	0.1752(7)	0.2135(5)	−0.2359(4)	0.028(2)
C(1)	0.2064(8)	0.1182(6)	−0.3255(5)	0.024(2)
C(2)	0.2839(9)	−0.0926(7)	−0.4472(5)	0.029(2)
C(3)	0.0785(9)	0.3922(6)	−0.2808(5)	0.030(2)
C(4)	−0.1446(9)	0.4448(7)	−0.2918(5)	0.034(2)
C(5)	−0.2981(9)	0.4621(7)	−0.1623(5)	0.033(2)
C(6)	0.157(1)	0.1354(7)	−0.0907(5)	0.032(2)
C(7)	0.229(1)	0.2145(7)	−0.0118(5)	0.034(2)
C(8)	0.2384(9)	0.1097(7)	0.1321(5)	0.032(2)
C(9)	0.335(1)	−0.2460(7)	−0.4978(6)	0.042(3)
H(2O)	−0.591	0.520	−0.105	0.055
H(4O)	0.264	0.125	0.296	0.059
H(3*A*)	0.158	0.442	−0.362	0.040
H(3*B*)	0.095	0.449	−0.220	0.040
H(4*A*)	−0.167	0.375	−0.325	0.059
H(4*B*)	−0.003	0.124	−0.043	0.042
H(6*A*)	−0.171	0.542	−0.350	0.059
H(6*B*)	0.261	0.029	−0.091	0.042
H(7*A*)	0.392	0.226	−0.061	0.044
H(7*B*)	0.150	0.318	−0.007	0.044
H(9*A*)	0.202	−0.285	−0.466	0.052
H(9*B*)	0.458	−0.331	−0.482	0.052
H(9*C*)	0.398	−0.206	−0.615	0.052

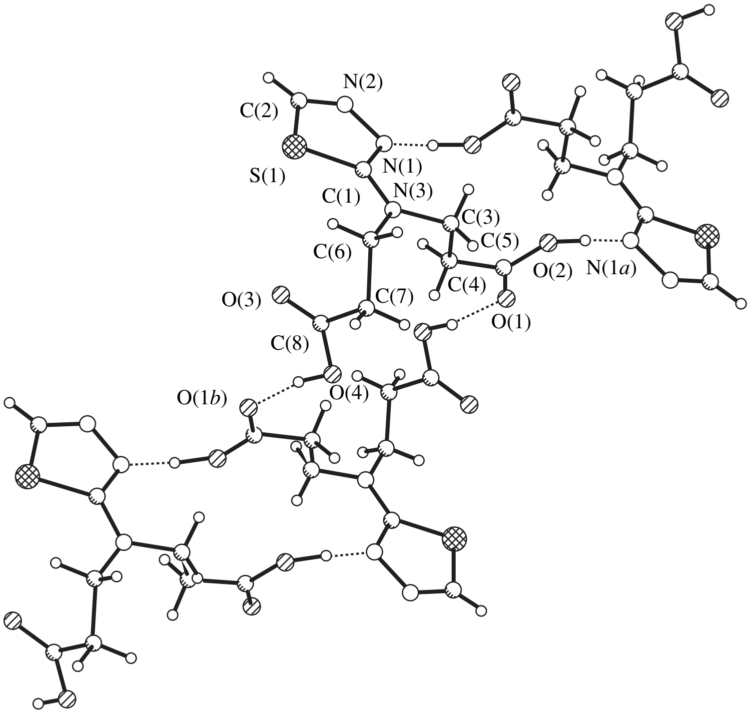

Fig. 1. A fragment of structure **I**.

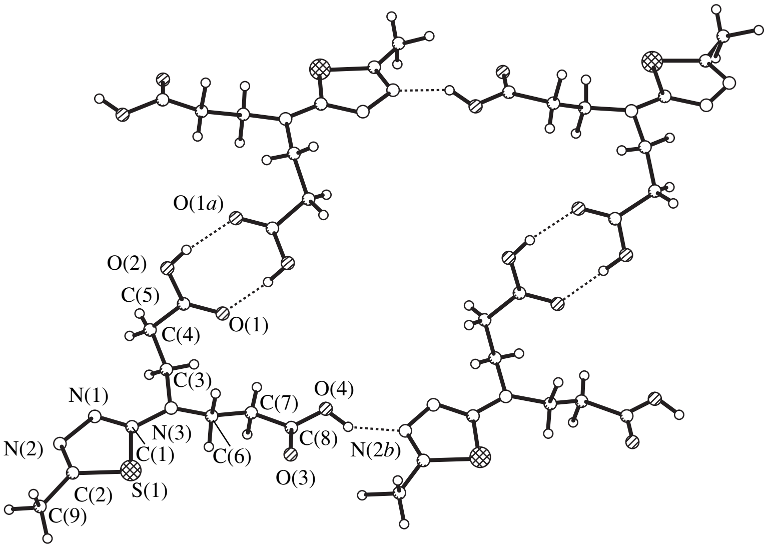

Fig. 2. A fragment of structure **II**.

In the unsubstituted 1,3,4-thiadiazole [7] and its symmetrically substituted 2,5-dimethyl [8] and 2,5-diamino [9] derivatives, the five-membered rings have a symmetric structure (in the first two compounds, the molecules occupy special positions). Asymmetric substitution in the thiadiazole ring results in the inequality of the endocyclic C–N bonds and the SCN and NNC angles. The N(2)–C(2) bond lengths in **I** and **II** are approximately identical [1.283(2) and 1.286(7) Å]. The N(1)–C(1) bonds are elongated; this elongation is more distinct in **I** than in **II** [1.331(2) and 1.310(6) Å]. The N(1)–N(2) bonds in both molecules [1.382(2) and 1.387(6) Å] are shortened relative to the standard single N–N bond (1.420 Å [10]). As noted earlier [11, 12], this shortening indicates the conjugation of bonds in the ring. The endocyclic CNN and SCN angles in **I** and **II** differ noticeably (by 2.2°–3.0°). The geometric parameters of the thiadiazole ring in **II** are close to the corresponding values in 2-amino-5-methyl-1,2,4-thiadiazole [13]. As far as we know, crystal structures of monosubstituted 1,2,4-thiadiazoles have not been studied.

In structures **I** and **II**, molecules are linked by the hydrogen bonds into double chains differing in the pattern of their arrangement. In **I**, the chains are formed by the alternation of centrosymmetric pairs of bonds of two types: O(2)–H(2O)···N(1) ($1 - x$, $1 - y$, $1 - z$) [O···N, 2.577(2); O–H, 1.15(3); H···N, 1.43(3) Å; and OHN, 177(3)°] and O(4)–H(4O)···O(1) ($1 - x$, y, $1 - z$) [O ···O, 2.625(2); O–H, 0.93(3); H···O, 1.70(4) Å; and OHO, 170(3)°]. In **II**, the O(4)–H(4O)···N(2) (x, y, z + 1) hydrogen bonds [O···N, 2.689(6); O–H, 0.96; H···N, 1.82 Å; and OHN, 149°] link the molecules related by the translation along the z-axis into chains, and the O(2)–H(2O)···O(1) ($-x - 1$, $1 - y$, $-z$) bonds [O···O, 2.670(6); O–H, 0.91; H···O, 1.79 Å; and OHO, 164°] link the chains in pairs. In structure **II**, the O–H···O bonds are formed between the same carboxyl groups, thus closing eight-membered centrosymmetric OCOHOCOH rings. In **I**, the O–H···O bonds are formed between different carboxyl groups; and due to these bonds, twenty-membered centrosymmetric $(HOC_3NC_3O)_2$ rings are closed. Different atoms—N(1) and N(2)—serve as acceptors in the O–H···N hydrogen bonds in structures **I** and **II**, respectively. The rings closed by the O–H···N hydrogen bonds also differ in size: the sixteen-membered $(NCNC_3OH)_2$ ring in **I** and the 38-membered (including the O–H···O bonds) $(N_2CNC_3OHOC_3NC_3OH)_2$ ring in **II**. Both hydrogen bonds in compound **I** are shorter than those in compound **II**.

ACKNOWLEDGMENTS

We are grateful to the Russian Foundation for Basic Research for the financial support (project no. 96-07-89187) in the payment of the licence for using the Cambridge Structural Database, which was employed in analysis of the structural results obtained in this work.

REFERENCES

1. S. I. Neĭkovskiĭ and V. V. Alyab’eva, Izv. Vyssh. Uchebn. Zaved., Khim. Khim. Tekhnol. **40** (1), 93 (1997).
2. S. I. Neĭkovskiĭ and V. V. Alyab’eva, Izv. Vyssh. Uchebn. Zaved., Khim. Khim. Tekhnol. **40** (2), 55 (1997).
3. S. I. Neĭkovskiĭ and V. V. Alyab’eva, Izv. Vyssh. Uchebn. Zaved., Khim. Khim. Tekhnol. **40** (2), 58 (1997).
4. G. M. Sheldrick, Acta Crystallogr. A **46** (6), 467 (1990).
5. G. M. Sheldrick, *SHELXL93: Program for the Refinement of Crystal Structures* (Univ. of Göttingen, Göttingen, 1993).
6. G. M. Sheldrick, *SHELX76: Program for Crystal Structure Determination* (Univ. of Cambridge, Cambridge, 1976).
7. T. Cour, Acta Crystallogr. B **30** (6), 1642 (1974).
8. Z. P. Povet’eva and Z. V. Zvonkova, Kristallografiya **16** (5), 1032 (1971) [Sov. Phys. Crystallogr. **16** (5), 899 (1971)].
9. H. Senda and J. Maruha, Acta Crystallogr. C **43** (2), 347 (1987).
10. F. H. Allen, O. Kennard, D. G. Watson, *et al.*, J. Chem. Soc., Perkin Trans. 2, S1 (1987).
11. G. Alzuet, S. Ferrer, J. Borrás, and X. Solans, Acta Crystallogr. C **47** (11), 2377 (1991).
12. M. Mathew and G. J. Palenik, J. Chem. Soc., Perkin Trans. 2, No. 5, 532 (1974).
13. L. Antolini, A. Cornia, A. C. Fabretti, and W. Malavasi, J. Crystallogr. Spectrosc. Res. **23**, 967 (1993).

Translated by I. Polyakova

Crystallography Reports, Vol. 45, No. 4, 2000, pp. 619–625. Translated from Kristallografiya, Vol. 45, No. 4, 2000, pp. 677–683.
Original Russian Text Copyright © 2000 by Tishchenko, Zhukhlistova.

STRUCTURE OF ORGANIC COMPOUNDS

Crystal and Molecular Structure of the Membrane-Active Antibiotic Enniatin *C*

G. N. Tishchenko[†] and N. E. Zhukhlistova

Shubnikov Institute of Crystallography, Russian Academy of Sciences,
Leninskiĭ pr. 59, Moscow, 117333 Russia

Received July 13, 1998

Abstract—The crystal structure of the cyclic hexadepsipeptide antibiotic enniatin *C* *c*[-(*L*-MeLeu-*D*-Hyi)$_3$-], $C_{34}H_{59}N_3O_9$, was established by X-ray structure analysis (sp. gr. $P2_1$, a = 20.205(5) Å, b = 8.702(2) Å, c = 25.587(6) Å, γ = 97.0(5)°, V = 4465.3(18) Å^3, Z = 4, R = 0.089 for 3601 reflections with $I > 2\sigma(I)$). The unit cell contains two independent molecules of enniatin *C*, one ethanol molecule disordered over two positions, and approximately two water molecules occupying four positions and forming hydrogen bonds with each other. The independent antibiotic molecules adopt virtually identical conformations similar to those observed in the structures of enniatin *B* and its Na,Ni-complex. These conformations are characterized by alternating upward and downward orientations of the carbonyl groups and pseudoequatorial orientations of side radicals. The Leu residues have stretched conformations. The *N*-methylamide groups of the independent antibiotic molecules face each other, whereas the molecules are displaced by approximately 8.4 Å with respect to each other along the mean planes of the rings. © *2000 MAIK "Nauka/Interperiodica".*

INTRODUCTION

Enniatin *C* is a representative of antibiotics of the enniatin series, which also includes enniatin *A*, enniatin *B*, and beauvericin. All these antibiotics are cyclic hexadepsipeptides and contain alternating residues of amino and oxy acids. For enniatin *C*, acids are residues of *N*-methylleucine and α-oxyisovaleric acid.

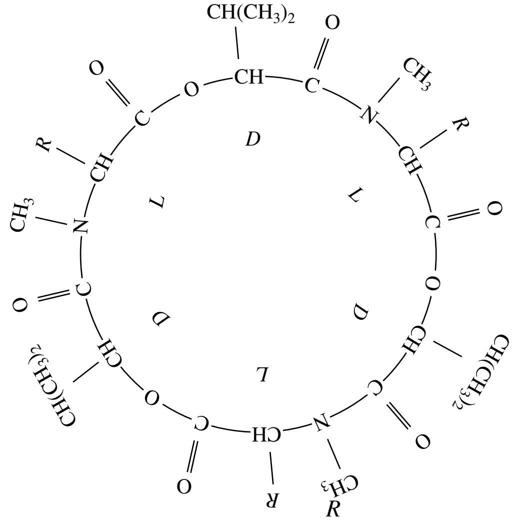

(1) Enniatin *A*—$CH(CH_3)C_2H_5$
(2) Enniatin *B*—$CH(CH_3)_2$
(3) Enniatin *C*—$CH_2CH(CH_3)_2$
(4) Enniatin—$CH_2C_6H_5$

The physiological function of enniatin on ionophorous antibiotics is to induce the transport of alkali and alkaline-earth metal ions through biological membranes. Molecules of these antibiotics adopt two preferential conformations, namely, the *N* conformation typical of the nonpolar media and the *P* conformation characteristic of polar media [1] and the crystalline state [2–5]. According to the results of IR and NMR spectroscopy, both conformations have *trans*-*N*-methylamide bonds [1, 6]. Ultrasonic absorption measurements demonstrated that the *N* conformation is a mixture of two conformers which undergo rapid interconversion [7, 8]. The theoretical analysis of enniatins revealed five possible asymmetric low-energy conformations, namely, *N*1–*N*5 [9], and one symmetrical *P* conformation [9, 10], whose conformational parameters of were calculated. According to the CD spectral curves, enniatins adopt the *P* conformation upon the formation of complexes with metal ions [11, 12]. Actually, enniatin *B* has such a conformation in the crystal of its complex with KI [13] and in the Na,Ni-complex [14]. The same conformation was also observed in the crystals of hydrated synthetic enniatin *B* [4–6] and natural enniatin *B* [15].

The enniatin *B* was repeatedly studied, whereas the crystal structure of enniatin *C* was not studied at all. However, proceeding from the fact that the chemical structures of these two compounds are similar, one can expect that the crystals of enniatin *C* grown in the presence of KSCN would also adopt the *P* conformation. In this study, we established the crystal structure of enniatin *C* by the method of X-ray diffraction analysis.

[†] Deceased.

1063-7745/00/4504-0619$20.00 © 2000 MAIK "Nauka/Interperiodica"

Table 1. Atomic coordinates and thermal parameters

Atom	*x*/*a*	*y*/*b*	*z*/*c*	U_{eq}
Molecule **I**				
N(1)	0.5830(4)	–0.0415(9)	0.3028(4)	0.059(2)
C(1*A*)	0.6421(6)	0.0426(13)	0.2783(4)	0.066(3)
C(1')	0.6238(7)	0.1242(15)	0.2310(6)	0.079(4)
O(1)	0.5709(5)	0.1024(12)	0.2083(5)	0.111(3)
C(1)	0.5493(7)	–0.1789(16)	0.2766(5)	0.088(4)
C(1*B*)	0.6941(6)	–0.0689(14)	0.2641(6)	0.079(3)
C(1*G*)	0.7143(6)	–0.1612(14)	0.3097(6)	0.088(4)
C(1*D*1)	0.7655(8)	–0.2683(19)	0.2932(8)	0.114(5)
C(1*D*2)	0.7437(7)	–0.0660(15)	0.3574(5)	0.084(4)
O(2')	0.6740(4)	0.2219(10)	0.2116(4)	0.080(2)
C(2*A*)	0.6637(6)	0.3056(14)	0.1627(5)	0.074(3)
C(2')	0.6145(5)	0.4224(15)	0.1752(5)	0.064(3)
O(2)	0.6282(5)	0.5134(11)	0.2089(5)	0.100(3)
C(2*B*)	0.7306(9)	0.3775(18)	0.1433(8)	0.115(6)
C(2*G*1)	0.7764(9)	0.2478(26)	0.1328(10)	0.152(8)
C(2*G*2)	0.7198(10)	0.4709(28)	0.0936(11)	0.160(9)
N(3)	0.5623(4)	0.4325(9)	0.1420(3)	0.056(2)
C(3*A*)	0.5206(7)	0.5529(15)	0.1551(6)	0.086(4)
C(3')	0.4545(6)	0.4778(20)	0.1823(5)	0.070(3)
O(3)	0.4283(5)	0.3567(14)	0.1781(5)	0.107(3)
C(3)	0.5399(7)	0.3196(19)	0.1037(5)	0.099(4)
C(3*B*)	0.4991(9)	0.6356(23)	0.1046(6)	0.125(7)
C(3*G*)	0.5552(12)	0.6936(27)	0.0709(11)	0.168(11)
C(3*D*1)	0.5304(15)	0.7642(43)	0.0212(10)	0.240(18)
C(3*D*2)	0.6011(12)	0.8241(28)	0.1029(15)	0.206(16)
O(4')	0.4350(4)	0.5917(10)	0.2121(3)	0.078(2)
C(4*A*)	0.3737(5)	0.5577(13)	0.2422(4)	0.060(3)
C(4')	0.3926(6)	0.4701(13)	0.2907(5)	0.061(3)
O(4)	0.4355(4)	0.5297(10)	0.3202(4)	0.088(3)
C(4*B*)	0.3468(7)	0.7046(15)	0.2564(4)	0.078(3)
C(4*G*1)	0.3342(9)	0.7943(15)	0.2045(7)	0.109(5)
C(4*G*2)	0.2832(8)	0.6698(16)	0.2892(7)	0.113(6)
N(5)	0.3590(4)	0.3294(10)	0.3040(4)	0.065(3)
C(5*A*)	0.3801(5)	0.2487(12)	0.3498(4)	0.057(3)
C(5')	0.4216(6)	0.1248(13)	0.3348(6)	0.064(3)
O(5)	0.4285(6)	0.0783(11)	0.2922(4)	0.103(3)
C(5)	0.3102(8)	0.2468(17)	0.2695(7)	0.109(5)
C(5*B*)	0.3194(7)	0.1866(17)	0.3849(6)	0.091(4)
C(5*G*)	0.2804(8)	0.3049(26)	0.4058(8)	0.122(6)
C(5*D*1)	0.2180(11)	0.2190(51)	0.4373(20)	0.344(32)
C(5*D*2)	0.3199(15)	0.4272(32)	0.4415(10)	0.175(11)
O(6')	0.4484(3)	0.0693(9)	0.3769(3)	0.071(2)
O(6*A*)	0.4902(5)	–0.0516(13)	0.3680(5)	0.071(3)
C(6')	0.5576(6)	0.0347(17)	0.3406(5)	0.069(3)
O(6)	0.5800(5)	0.1544(12)	0.3611(5)	0.110(4)
C(6*B*)	0.5061(8)	–0.1085(19)	0.4235(6)	0.105(5)
C(6*G*1)	0.4360(8)	–0.2001(37)	0.4438(10)	0.197(14)
C(6*G*2)	0.5532(9)	–0.2230(23)	0.4218(7)	0.127(6)
Molecule **II**				
N(1)	0.2474(4)	0.3901(9)	0.0635(4)	0.053(2)
C(1*A*)	0.2293(5)	0.2505(10)	0.0950(5)	0.056(3)
C(1')	0.1965(6)	0.2888(14)	0.1445(5)	0.063(3)

Table 1. (Contd.)

Atom	*x*/*a*	*y*/*b*	*z*/*c*	U_{eq}
Molecule **II**				
O(1)	0.2111(5)	0.4033(10)	0.1723(4)	0.095(3)
C(1)	0.3013(6)	0.5037(12)	0.0842(5)	0.075(4)
C(1*B*)	0.2870(5)	0.1571(13)	0.1071(4)	0.063(3)
C(1*G*)	0.3263(6)	0.1126(13)	0.0597(5)	0.073(3)
C(1*D*1)	0.3832(7)	0.0212(19)	0.0776(7)	0.105(5)
C(1*D*2)	0.2864(7)	0.0290(18)	0.0176(6)	0.101(4)
O(2')	0.1508(4)	0.1737(7)	0.1596(3)	0.065(2)
C(2*A*)	0.1159(5)	0.1827(12)	0.2070(4)	0.058(3)
C(2')	0.0524(5)	0.2616(15)	0.1970(5)	0.068(3)
O(2)	0.0127(5)	0.1955(10)	0.1652(4)	0.095(3)
C(2*B*)	0.0972(5)	0.0209(12)	0.2281(5)	0.068(3)
C(2*G*1)	0.1600(7)	−0.0577(13)	0.2347(7)	0.094(4)
C(2*G*2)	0.0578(9)	0.0290(17)	0.2781(6)	0.102(5)
N(3)	0.0414(5)	0.3965(10)	0.2206(4)	0.064(3)
C(3*A*)	−0.0192(5)	0.4657(14)	0.2071(4)	0.067(3)
C(3')	0.0000(7)	0.6012(10)	0.1703(4)	0.051(3)
O(3)	0.0549(5)	0.6617(9)	0.1628(4)	0.089(3)
C(3)	0.0912(5)	0.4801(12)	0.2561(5)	0.067(3)
C(3*B*)	−0.0561(8)	0.5150(16)	0.2560(6)	0.098(5)
C(3*G*)	−0.0713(7)	0.3936(18)	0.2956(7)	0.098(5)
C(3*D*1)	−0.0935(8)	0.4677(25)	0.3469(7)	0.124(6)
C(3*D*2)	−0.1170(12)	0.2669(30)	0.2769(11)	0.171(11)
O(4')	−0.0548(4)	0.6434(9)	0.1493(3)	0.079(2)
C(4*A*)	−0.0447(6)	0.7765(15)	0.1145(5)	0.075(3)
C(4')	−0.0088(7)	0.7245(15)	0.0654(4)	0.070(3)
O(4)	−0.0331(5)	0.6053(11)	0.0441(4)	0.093(3)
C(4*B*)	−0.1150(6)	0.8216(16)	0.1014(6)	0.091(4)
C(4*G*1)	−0.1495(9)	0.8655(25)	0.1525(8)	0.137(7)
C(4*G*2)	−0.1089(8)	0.9614(19)	0.0659(6)	0.111(5)
N(5)	0.0442(4)	0.8203(8)	0.0461(3)	0.049(2)
C(5*A*)	0.0779(5)	0.7665(13)	0.0025(4)	0.063(3)
C(5')	0.1381(5)	0.6932(11)	0.0219(5)	0.054(3)
O(5)	0.1607(4)	0.6926(10)	0.0634(4)	0.083(2)
C(5)	0.0759(7)	0.9570(13)	0.0749(5)	0.077(3)
C(5*B*)	0.0934(5)	0.8903(13)	−0.0399(4)	0.059(3)
C(5*G*)	0.0351(6)	0.9732(12)	−0.0581(5)	0.066(3)
C(5*D*1)	0.0609(7)	1.0907(17)	−0.0988(6)	0.093(4)
C(5*D*2)	−0.0173(7)	0.8664(21)	−0.0811(7)	0.110(5)
O(6')	0.1652(3)	0.6286(8)	−0.0213(3)	0.063(2)
C(6*A*)	0.2263(6)	0.5542(13)	−0.0105(4)	0.065(3)
C(6')	0.2091(6)	0.4169(12)	0.0229(4)	0.050(3)
O(6)	0.1625(4)	0.3228(10)	0.0086(3)	0.077(2)
C(6*B*)	0.2545(6)	0.5159(11)	−0.0642(4)	0.061(3)
C(6*G*1)	0.2687(6)	0.6592(20)	−0.0980(7)	0.108(5)
C(6*G*2)	0.3166(7)	0.4341(16)	−0.0583(5)	0.083(4)
O(*al*)	0.1462(20)	0.6709(50)	0.4918(13)	0.312(19)
C(1*al*)	0.1274(20)	0.6822(26)	0.4330(14)	0.210(15)
C(2*al*1)	0.1054(31)	0.5233(77)	0.4194(26)	0.048(37)
C(2*al*2)	0.1571(38)	0.8188(73)	0.3866(36)	0.422(55)
O(*w*1)	0.6092(20)	0.4709(49)	0.3231(13)	0.224(24)
O(*w*2)	0.5290(14)	0.4238(37)	0.3941(19)	0.241(24)
O(*w*3)	−0.0623(42)	0.3127(53)	0.0809(33)	0.279(43)
O(*w*4)	0.0164(12)	0.3244(37)	0.0063(25)	0.278(29)

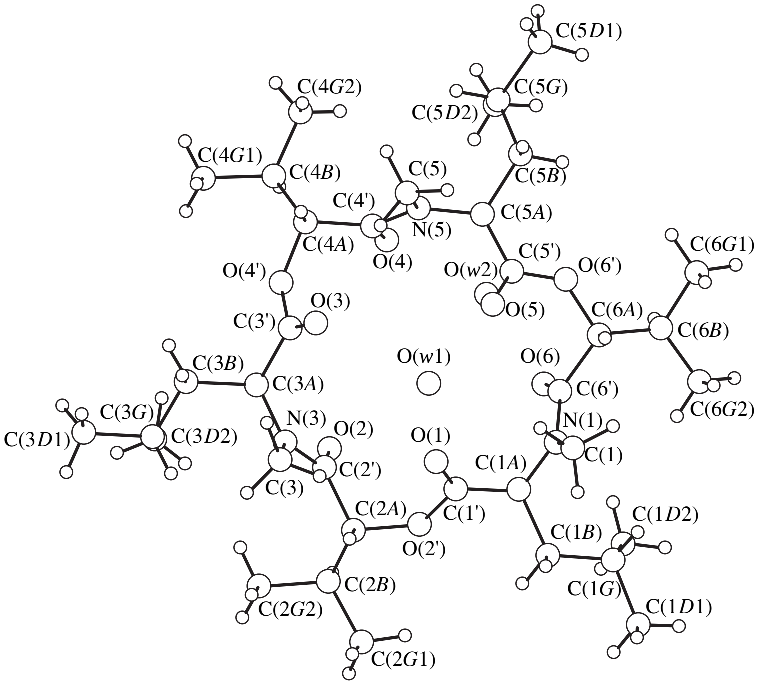

Fig. 1. Conformation of a molecule (**I**) of enniatin *C* in the crystal structure.

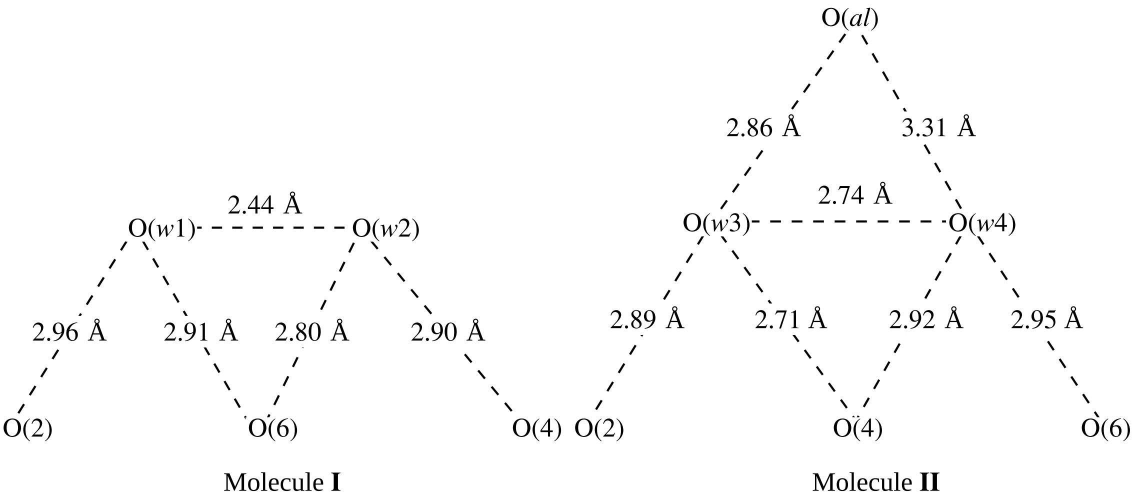

Fig. 2. Scheme of hydrogen bonding in the structure of enniatin *C*.

EXPERIMENTAL

Colorless crystals of the nominal composition enniatin $C \cdot n$KSCN, grown at the Shemyakin–Ovchinnikov Institute of Bioorganic Chemistry of the Russian Academy of Sciences, belong to the sp. gr. $P2_1$, $a = 20.205(5)$, $b = 8.702(2)$, $c = 25.587(6)$ Å, $\gamma = 97.0(5)°$, $V = 4465.3(18)$ Å^3, $Z = 4$. There are two formula units per asymmetric unit. The reflection intensities were measured on a four-circle Syntex-$P2_1$ diffractometer (CuK_α radiation, graphite monochromator, $d \geq 1.0$ Å, $\theta/2\theta$ scanning technique). Of the total 4936 measured reflections, 3601 reflections with $I > 2\sigma(I)$ were used in further computations.

The structure was solved by the direct method using the MULTAN84 program [16] and was then refined using the SHELXL93 program package [17]. The electron density syntheses revealed all the atomic positions of two independent enniatin *C* molecules and also a number of additional peaks. Proceeding from the nominal composition (enniatin $C \cdot n$KSCN), we made an attempt to reveal K, S, C, and N atoms. However, the refinement of the structure and the analysis of the geometry of the arrangement and the weights of the

Table 2. Conformational angles (deg) in molecules **I** and **II** of enniatin *C*

Molecule **I**

Angle	*i* = 1	*i* = 2	*i* = 3	*i* = 4	*i* = 5	*i* = 6
φ_i	–95.4(12)	69.1(13)	–102.1(12)	79.6(11)	–99.9(11)	71.1(12)
ψ_i	170.1(10)	–133.4(10)	154.1(10)	–126.5(10)	170.6(8)	–140.5(10)
ω_i	177.2(10)	–176.6(9)	179.5(9)	178.7(9)	–180.0(8)	178.4(9)
χ_i	–55.5(13)		–57.4(12)		60.0(16)	
δ_i^1	–179.5(11)		177.2(22)		175.8(21)	
δ_i^2	–57.4(14)		–63.7(18)		–61.3(20)	
χ_i^1		60.6(19)		57.5(13)		70.6(17)
χ_i^2		–178.6(14)		–178.7(11)		–175.2(13)

Molecule **II**

Angle	*i* = 1	*i* = 2	*i* = 3	*i* = 4	*i* = 5	*i* = 6
φ_i	–101.8(10)	89.0(11)	–102.9(11)	68.9(12)	–95.9(10)	66.7(10)
ψ_i	147.2(9)	–119.3(11)	166.9(8)	–134.5(10)	174.2(8)	–136.0(8)
ω_i	176.7(9)	177.5(9)	177.6(9)	177.5(8)	178.2(8)	178.6(9)
χ_i	–53.1(13)		–53.7(18)		–50.9(13)	
δ_i^1	179.3(10)		165.0(13)		178.7(10)	
δ_i^2	–54.5(14)		–63.8(18)		–62.4(14)	
χ_i^1		57.5(13)		60.9(16)		57.6(12)
χ_i^2		–177.9(10)		–179.4(12)		–178.4(9)

Note: The conformational parameters φ_i, ψ_i, ω_i, χ_i^1, χ_i^2, δ_i^1, and δ_i^2 correspond to the angles: C(*i*'–1)–N(*i*)[O(*i*')]–C(*iA*)–C(*i*'), N(*i*)[O(*i*')]–C(*iA*)–C(*i*')–O(*i*' + 1) [N, (*i*')], C(*iA*)–C(*i*')–O(*i*')[N(*i*)]–C[(*i* + 1)*A*], N(*i*)[O(*i*')]–C(*iA*)–C(*iB*)–*C*(*iG*1), N(*i*)[O(*i*')]–C(*iA*)-C(*iB*)–C(*iG*2), C(*iA*)–C(*iB*)–C(*iG*)–C(*iD*1), and C(*iA*)–C(*iB*)–C(*iG*)–C(*iD*2), where *i* is the number of a residue.

localized peaks revealed only a disordered ethanol molecule and about two water molecules (occupying four positions) along with the antibiotic molecules, but no potassium ions and rhodano groups. The final electron-density synthesis revealed 104 non-hydrogen atoms. These atoms were refined anisotropically. The hydrogen atoms of the antibiotic molecules were placed in positions calculated and isotropically refined using the riding model. The *R* factor, calculated over 3601 reflections with $I > 2\sigma(I)$, was 0.089. The atomic coordinates and equivalent thermal parameters are given in Table 1.

RESULTS AND DISCUSSION

The unit cell of the structure under study contains two crystallographically independent molecules (**I** and **II**) of enniatin *C*, a disordered ethanol molecule, and about two water molecules occupying four positions. One of the enniatin molecules (**I**) is shown in Fig. 1. The ethanol molecule is disordered over two positions, characterized by different angles of rotation about the O–C bond and the occupancies 0.86 and 0.14, respectively. The water molecules are distributed over four positions, (O(*w*1), O(*w*2), O(*w*3), and O(*w*4), with the occupancies of 0.60, 0.65, 0.33, and 0.49, respectively). The pairs of these positions (O(*w*1) and O(*w*2); O(*w*3) and O(*w*4)) are located in the vicinity of antibiotic molecules **I** and **II**, respectively. The water molecules are linked to the enniatin *C* molecules via weak H bonds (2.71(6)–2.96(4) Å) formed by the carbonyl oxygen atoms of the peptide groups (Fig. 2). One of the carbonyl oxygen atoms of each enniatin *C* molecule forms hydrogen bonds with two adjacent water molecules, while each of the remaining two carbonyl oxygen atoms forms a hydrogen bond only with one water molecule. The water molecules (with partial occupancies of the positions) are linked in pairs through strong hydrogen bonds O(*w*1)···O(*w*2) (2.44(6) Å) and

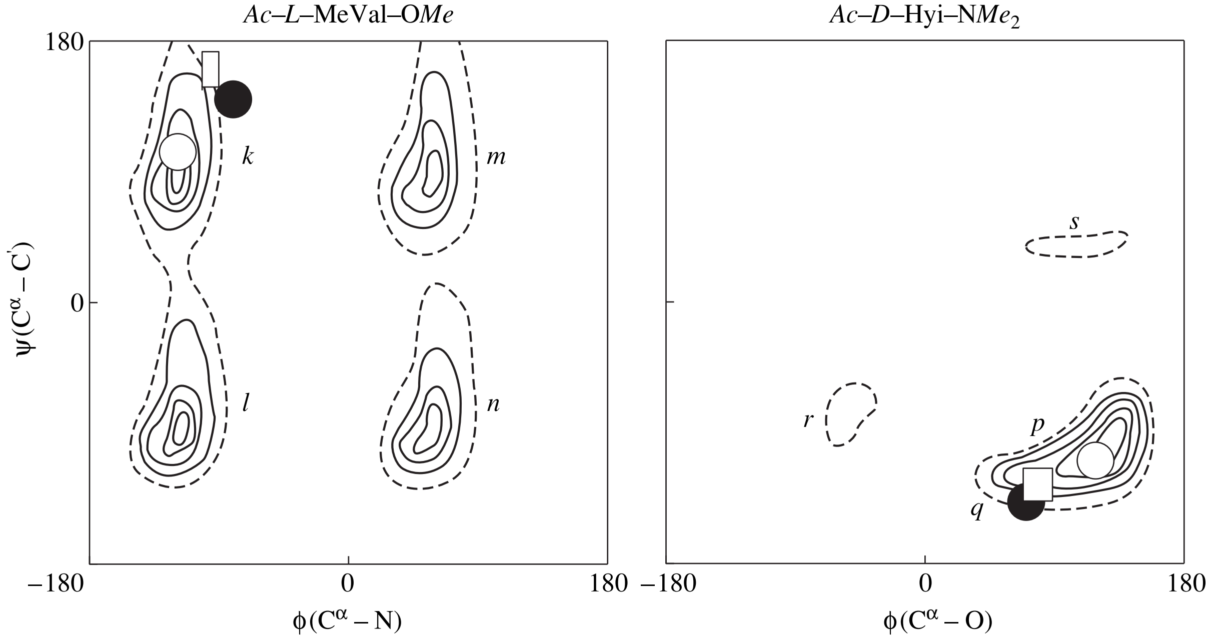

Fig. 3. Conformational maps for the amino- and oxy-acid residues of enniatin *C* molecules (rectangles), crystal hydrate of enniatin *B* (empty circles), and its Na,Ni-complex (solid circles) in the crystal structures.

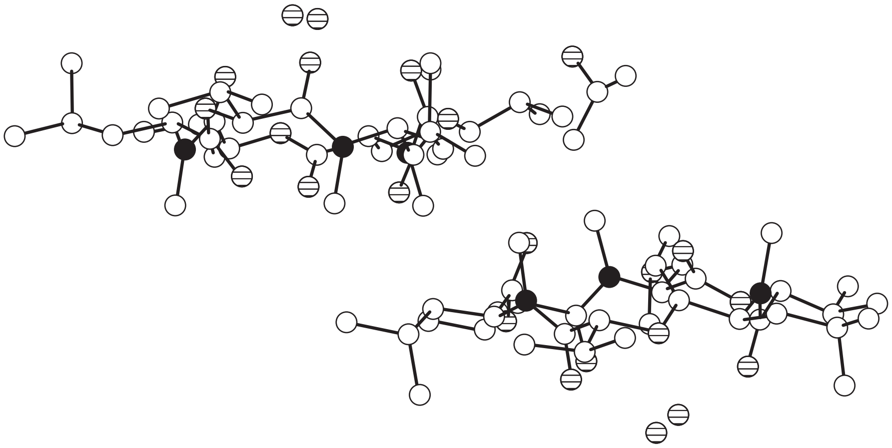

Fig. 4. Projection of the structure of enniatin *C* along the plane passing through N atoms of molecule **I**. The N, O, and C atoms of the structure are represented by solid, hatched, and empty circles, respectively.

O(*w*3)···O(*w*4) (2.48(11) Å). The water molecules of the second pair form weak hydrogen bonds with the O(*al*) atom of the alcohol molecule [the O(*al*)···O(*w*3) and O(*al*)···O(*w*4) distances are 2.86(8) and 3.31(5) Å, respectively]. Apparently, these interactions are responsible for the low occupancies of the positions of the O(*w*3) and O(*w*4) molecules, compared to those of the O(*w*1) and O(*w*2) molecules.

In the crystal structure, both enniatin *C* molecules adopt virtually identical conformations, which are similar to those of the enniatin *B* molecule in the hydrated state [4, 5, 15] and in its Na,Ni complex [14]. The enniatin *C* molecules are characterized by alternating upward and downward orientations of the carbonyl groups, pseudoequatorial orientations of the side valine radicals, and by stretched conformations of the side chains of the leucine residues with a pseudoequatorial arrangement of the C^{α}–C^{β}–C^{γ} fragments.

All amino acid residues adopt similar conformations in both independent enniatin *C* molecules (Table 2). The φ and ψ angles characterizing these conformations range from –95.4° to –103.0° and from 147.2° to 170.6°, respectively. The same is true for the oxy acid residues for which the φ and ψ angles range from 66.7° to 89.0° and from –119.4° to –140.5°, respectively. The corresponding points in the conformation maps for the model compounds *Ac*–*L*-MeVal–O*Me* and *Ac*–*D*-Hyi–NMe_2 [18] fall within the regions restricted by rectangles (Fig. 3) displaced to the periphery, and they are close to the *k* minimum for the angles of the amino acid residues and to the *q* border of the *p*–*q* minimum for the angles of the oxy acid residues.

Noteworthy is the fact that the rectangles are located much closer to the φ, ψ points for the Na,Ni complex of enniatin *B* [14] (solid circles) than to the φ, ψ points for hydrated enniatin *B* [4, 5] (empty circles). In other words, the "bottom" of the enniatin *C* molecule is more open than the "bottom" of the molecule of native enniatin *B* [4]. Undoubtedly, this is associated with somewhat different molecular packings of the molecules in the crystals and with their different interactions with water molecules.

The mutual arrangement of two crystallographically independent molecules of enniatin *C* and alcohol and water molecules in the crystal structure is shown in Fig. 4. Molecules **I** and **II** of enniatin *C* are almost parallel to each other. Their slightly open *N*-methylamide "bottoms" and the valine radicals face each other. The molecules are displaced by about 8.4 Å with respect to each other along the mean plane of molecule **I**. The carbonyl oxygen atoms of the *N*-methylamide groups that form the polar edge are located on the other sides of molecules **I** and **II** (where also pairs of water molecules are located). The disordered alcohol molecule is located between the antibiotic molecules. The bond lengths and the bond angles in of enniatin *C* molecules **I** and **II** are similar to those observed in the structures of hydrated enniatin *B* [4, 5], anhydrous enniatin *B* [19], and its Na,Ni-complex [14, 19]. As was expected, these parameters for the structure under study coincide most closely with the values obtained for the first two compounds.

ACKNOWLEDGMENTS

We are grateful to Yu. A. Ovchinnikov and V. T. Ivanov for providing the crystals and Yu. V. Nekrasov for collecting X-ray diffractometry data.

This work was supported by the Russian Foundation for Basic Research, project no. 96-04-48898.

REFERENCES

1. Yu. A. Ovchinnikov, V. T. Ivanov, A. V. Evstratov, *et al.*, Int. J. Pept. Protein Res. **6**, 465 (1974).
2. A. J. Geddes and D. Akrigg, Acta Crystallogr., Sect. B: Struct. Crystallogr. Cryst. Chem. **32**, 3164 (1976).
3. G. N. Tishchenko, Z. Karimov, B. K. Vainshtein, *et al.*, FEBS Lett. **65**, 315 (1976).
4. G. N. Tishchenko, A. I. Karaulov, and Z. Karimov, Kristallografiya **26** (5), 984 (1981) [Sov. Phys. Crystallogr. **26** (5), 559 (1981)].
5. G. N. Tishchenko, A. I. Karaulov, and Z. Karimov, Cryst. Struct. Commun. **11**, 451 (1982).
6. D. B. Davies and M. A. Khaled, Tetrahedron Lett. 2829 (1973).
7. T. Funk, F. Eggers, and E. Grell, Chimia **26**, 632 (1972).
8. E. Grell, T. Funk, and F. Eggers, *Molecular Mechanisms of Antibiotic Action on Protein Biosynthesis and Membranes* (Elsevier, Amsterdam, 1972), p. 646.
9. E. M. Popov and G. M. Lipkind, *Conformation Computations for Complicated Molecules* (Izd. inst. teplo- i massoobmena Akad. Nauk BSSR, Minsk, 1970), p. 120.
10. R. Maigret and B. Pullman, Theor. Chim. Acta **37**, 17 (1973).
11. Yu. A. Ovchinnikov, V. T. Ivanov, A. V. Evstratov, *et al.*, Biochem. Biophys. Res. Commun. **37**, 668 (1969).
12. M. N. Shemyakin, Yu. A. Ovchinnikov, V. T. Ivanov, *et al.*, Membr. Biol. **1**, 402 (1969).
13. N. E. Zhukhlistova, G. N. Tishchenko, L. Refaat, and M. M. Woolfson, Kristallografiya **43** (1), 50 (1998) [Crystallogr. Rep. **43** (1), 45 (1998)].
14. N. E. Zhukhlistova and G. N. Tishchenko, Kristallografiya **26** (6), 1232 (1981) [Crystallogr. Rep. **26** (6), 700 (1981)].
15. N. E. Zhukhlistova, G. N. Tishchenko, I. V. Tolstykh, and V. A. Zenkova, Kristallografiya **44** (1), 12 (1999) [Crystallogr. Rep. **44** (1), 8 (1999)].
16. P. Main, L. Lessinger, G. G. Germain, and M. M. Woolfson, *MULTAN84: A Computer Program for the Direct Determination of Crystal Structures* (Univ. of York, England, 1984).
17. G. M. Sheldrick, *SHELXTL-93: Program for the Refinement of Crystal Structures* (Univ. of Göttingen, Germany, 1993).
18. E. M. Popov, G. M. Lipkind, V. Z. Pletnev, and S. F. Arkhipova, Khim. Prir. Soed., No. 2, 184 (1971).
19. N. E. Zhukhlistova, G. N. Tishchenko, V. I. Andrianov, and R. Main, Kristallografiya **40** (3), 532 (1995) [Crystallogr. Rep. **40** (3), 486 (1995)].

Translated by T. Safonova

Crystallography Reports, Vol. 45, No. 4, 2000, pp. 626–632. Translated from Kristallografiya, Vol. 45, No. 4, 2000, pp. 684–691.
Original Russian Text Copyright © 2000 by Ilyushin, Dem'yanets.

Crystal Chemistry of Germanates: Characteristic Structural Features of Li,Ge-Germanates

G. D. Ilyushin and L.N. Dem'yanets

Shubnikov Institute of Crystallography, Russian Academy of Sciences,
Leninskiĭ pr. 59, Moscow, 117333 Russia

Received April 13, 1998; in final form, August 25, 1999

Abstract—Crystallochemical classification of eleven compounds from the Li-germanate family is suggested. Depending on the set of the primary building units (PBU) (*M*-octahedra of the composition [GeO_6] and *T*-tetrahedra of the composition [GeO_4]) and the type of their “condensation,” these germanates are divided into three crystallochemical groups: framework *MT*-structures (four phases), condensed *MT*-structures (two phases), and tetrahedral *T*-condensed structures (five phases). The structural characteristics of the framework Li,Ge-germanates are considered, i.e., their symmetry, crystallographically independent sets of the primary building units, framework architecture, and the types of chains and layers of the (Ge,O)-radicals. © *2000 MAIK “Nauka/Interperiodica”.*

INTRODUCTION

The family of Li-germanates includes eleven compounds [1–9] and is the largest of all the families of *A*-germanates/silicates (*A* = Li, Na, K, Rb, and Cs). Lithium germanates include the compounds containing anionic groups in the form of [GeO_4]-tetrahedra—the main characteristic used for classification of oxygen-containing salts. The Li/Ge ratio in these germanates ranges over the wide ranges from 8 : 1 to 2 : 7. The structural variety of these germanates is explained by (a) the possible simultaneous localization of germanium in *M*-octahedra of the composition [GeO_6], and the *T*-tetrahedra of the composition [GeO_4], i.e., by the formation of two types of primary building units (PBU) by Ge atoms of two types and (b) the geometric variety of polyhedron condensation in three-dimensional crystal structures (vertex- or edge-sharing polyhedra). No natural lithium germanates have been observed. All the compounds analyzed in this article were synthesized under laboratory conditions by the methods of solid-phase synthesis, crystallization from low- and high-temperature aqueous solutions, and crystallization from melt. Germanates of various compositions are of great interest for establishing the crystallochemical analogy in the behavior of germanium atoms under “milder” temperatures and pressures, and silicon atoms under high temperatures and pressures existing in the depth of the earth crust.

Of special interest for crystal chemistry are Ge- germanates, the compounds, where germanium is located in both octahedra and tetrahedra. Such behavior is characteristic only of germanium and manifests itself in the interaction of GeO_2 with oxides of one-, two, and three-charged metal cations. Using the analogy with silicates, the crystallochemical systematization of the 20 Ge-germanates known by 1985 (including four Li-germanates) and based on the separation of the motif of [GeO_4]-tetrahedra (ortho- and diorthotetrahedra, chains, and layers) was suggested in [10]. At present, the number of Ge-germanates, including alkali and alkali earth germanates, amounts to forty.

The structural determinations of Li- germanates provided the establishment of all the atomic coordinates (with the only exception of $Li_3HGe_4^{VI}Ge_3^{IV}O_{16} \cdot 3H_2O$, for which the Li positions have not been determined).

The present study was aimed to the crystallochemical classification of the family of Li-germanates, establishing their structural characteristics (symmetry, the crystallographically independent sets of primary building units, framework architecture, and geometric types of tetrahedral Ge-radicals). At the same time, we also analyzed the bond lengths of the behavior of framework-forming octahedrally-coordinated Ge^{VI} atoms and the tetrahedrally-coordinated Ge^{IV} atoms. The classification of Li-germanates continues our studies on the crystal chemistry of ternary Na*Me*-germanates/silicates and K, *Me*-silicates (*Me* = Ti, Zr, Sn, and K) [11–14].

CRYSTALLOCHEMICAL CLASSIFICATION OF Li-GERMANATES

The analysis of the known structural data on Li-germanates shows that their structures always contain one of two possible sets of primary building units PBU represented by either *M* and *T* (six compounds) or only by *T* (five compounds). Unlike alkali metal titanates, there are no germanates containing only *M*-octahedra. The condensation of primary building units—[Ge,O]-tetrahedra and octahedra—occurs only along the shared vertices and edges. Depending on the type of condensation and the PBU sets, all the germanates can be divided into three crystallochemical groups: framework *MT*-structures, *MT*-condensed structures, and tetrahedral *T*-structures. The compositions of these phases are indicated in Fig. 1.

The group of framework *MT*-structures (PBU: *M* and *T*, condensation only at vertices) consists of four germanates: $Li_2Ge^{VI}Ge^{IV}_6O_{15}$ ($Li_2Ge_7O_{15}$), $Li_4Ge^{VI}_2Ge^{IV}_7O_{20}$ ($Li_4Ge_9O_{20}$), $Li_2Ge^{VI}Ge^{IV}_3O_9$ ($Li_2Ge_4O_9$), and $Li_2Ge^{VI}Ge^{IV}_2O_6(OH)_2$ ($Li_2Ge_3O_6(OH)_2$). The detailed analysis of their structures is given below.

The group of *MT*-condensed structures (PBU: *M* and *T*; condensation of (*M* + *M*) along the edges and (*M* + *T*) along vertices) consists of the $Li_3HGe^{VI}_4Ge^{IV}_3O_{16} \cdot 3H_2O$ ($Li_3HGe_7O_{16} \cdot 3H_2O$) and $Li_4Ge^{VI}_3Ge^{IV}_2O_{12}$ ($Li_4Ge_5O_{12}$) germanates. The structures of these germanates allow the substitution of Li by Na, K, Rb, and Cs (the structural type of alkali-free pharmacosiderite $Fe^{VI}_4As^{IV}_3O_{12}(OH)_4 \cdot 5H_2O$).

The group of tetrahedral and *T*-condensed structures (a PBU: *T*; condensation occurs only at vertices) includes $Li_2Ge^{IV}_2O_5$, $Li_2Ge^{IV}O_3$, $Li_6Ge^{IV}_2O_7$, $Li_4Ge^{IV}O_4$, $Li_8Ge^{IV}O_6$ ($Li_8O_2GeO_4$) germanates. The analogous of for all the germanates are the well-known $Li_2Si_2O_5$, Li_2SiO_3, $Li_6Si_2O_7$, Li_4SiO_4 and Li_8SiO_4 silicates with the same type of the *T*-radical (Si_2O_5-layers, [SiO_3]-chains, [Si_2O_7] diorthogroups, and [SiO_4] orthotetrahedra).

Below, we consider the structural characteristics of framework germanates in the order of an increase in the tetrahedral component within the framework of the atomic–polyhedral model, with the separation of polyhedra only for the framework-forming Ge atoms and with lithium atoms being statistically or orderly distributed over the framework voids.

STRUCTURES OF THE FRAMEWORK Li,Ge-GERMANATES

The $Li_2Ge^{VI}Ge^{IV}_2O_6(OH)_2$ germanate (*q* = *T*/*M* = 2). The crystal structure with the unit-cell parameters *a* = 9.988, *b* = 5.151, and *c* = 11.701 Å, γ = 110.79° was refined in the anisotropic approximation up to *R* = 0.03 (575 reflections), sp. gr. *B*2/*b* [1]. The crystallographically independent PBU set consists of one *M*-octahedron, one *T*-tetrahedron, and two Li atoms. Hydrogen atoms were localized in [2], *R* = 0.042 (865 reflections).

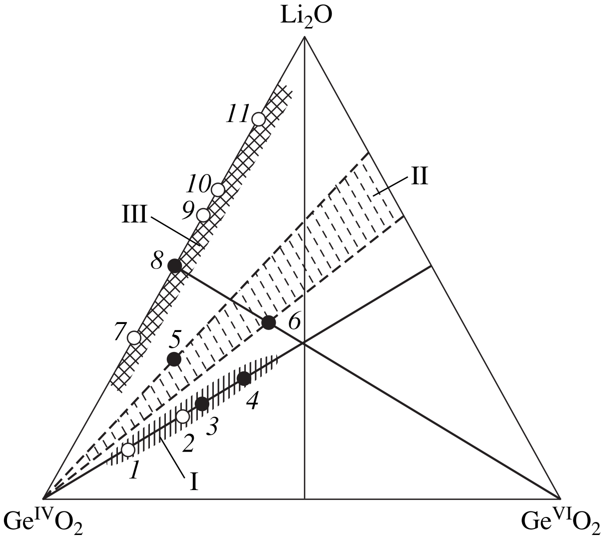

Fig. 1. The $Li_2O–Ge^{IV}O_2–Ge^{VI}O_2–H_2O$ system. The composition tetrahedron projected onto the $Li_2O–Ge^{IV}O_2–Ge^{VI}O_2$ plane. The regions of formation of (I) *MT*-framework structures, (II) *MT*-condensed structures, (III) tetrahedral *T*-structures are hatched in different ways. Black circles show the phases synthesized under the hydrothermal conditions: (*1*) $Li_2Ge^{VI}Ge^{IV}_6O_{15}$, (*2*) $Li_4Ge^{VI}_2Ge^{IV}_7O_{20}$, (*3*) $Li_2Ge^{VI}Ge^{IV}_3O_9$, (*4*) $Li_2Ge^{VI}Ge^{IV}_2O_6(OH)_2$, (*5*) $Li_3HGe^{VI}_4Ge^{IV}_3O_{16} \cdot 3H_2O$, (*6*) $Li_4Ge^{VI}_3Ge^{IV}_2O_{12}$, (*7*) $Li_2Ge^{IV}_2O_5$, (*8*) $Li_2Ge^{IV}O_3$, (*9*) $Li_6Ge^{IV}_2O_7$, (*10*) $Li_4Ge^{IV}O_4$, (*11*) $Li_8Ge^{IV}O_6$.

A fragment of the crystal structure projected onto the *XZ* plane is shown in Fig. 2. The structure consists of isolated [$GeO_4(OH)_2$]-octahedra with two OH-vertices not participating in the condensation of Ge-polyhedra. The *T*-radical consists of infinite [GeO_3]-chains. The *M*-octahedra of the composition [$GeO_4(OH)_2$] are connected to four endless chains normal to the drawing plane located at the heights *x* = 0.25 and 0.75 in the *YZ* plane and forming the *MT*-framework. The chains are parallel to the *Y*-axis, with their tetrahedra looking at one another; the repetition period equals two.

The geometric model. The Li and Ge^{VI} atoms in the structure form the layers of the composition (2Li + Ge) in the *YZ* plane at a height of *x* = 0.50. The layers are separated by the [GeO_3]-chains. Within the framework of the geometric model with the layer and chain structural fragments alternating along the *Y*-axis, the structure can be represented as:

	(2Li + Ge)-layer	–	[GeO_3]-chains	–	(2Li + Ge)-layer	–	[GeO_3]-chains
located at the heights *X*:	0		0.25		0.50		0.75

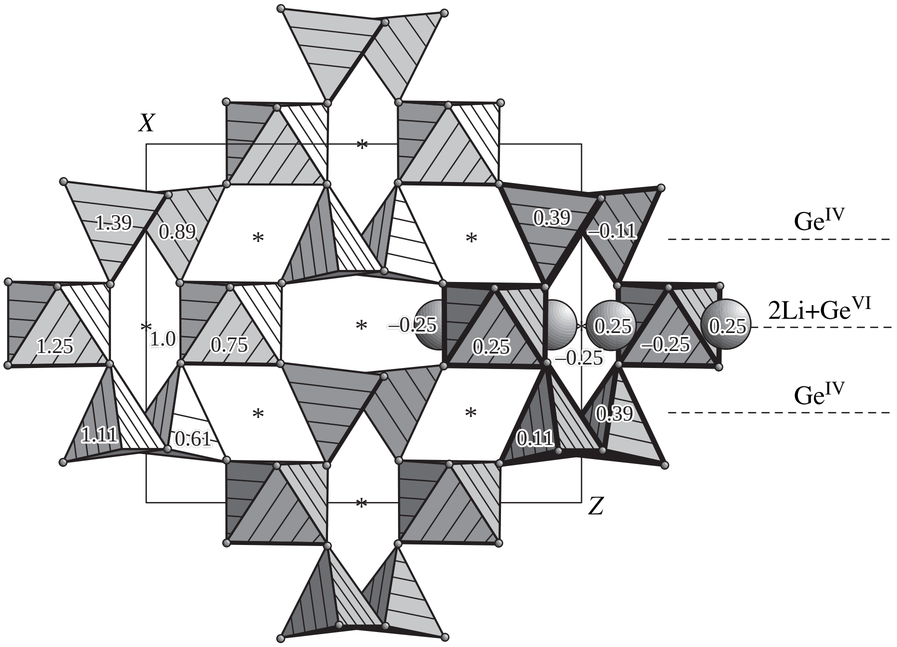

Fig. 2. $\mathrm{Li_2Ge^{VI}Ge_2^{IV}O_6(OH)_2}$. A fragment of the structure projected onto the *XZ* plane. The $(2\mathrm{Li} + \mathrm{Ge^{VI}})$ layers are located normally to the drawing plane at a height of $x = 0.50$ (circles denote Li-atoms, Ge-atoms are located in octahedra). The layers are connected by $[\mathrm{Ge}_n\mathrm{O}_{3n}]$-chains running along the *Y*-axis. The structurally equivalent fragments located at various heights are differently shadowed and hatched. The solid lines single out the repeating structural fragment of the composition M_2T_4. The figures indicates the coordinates of metal atoms along the *Y* axis.

The model with the localized hydrogen atoms [2] is characterized by narrow ranges of the Ge–O bond lengths, with the pronounced difference between the $\mathrm{Ge^{IV}}$–O bond lengths for the end (1.727–1.737 Å) and bridging (1.769–1.789 Å) O-atoms in *T*-tetrahedra and difference between the bond lengths for germanium atoms localized in the *T*- and *M*-polyhedra. Two O-atoms in the OH groups form $\mathrm{Ge^{VI}}$–O bonds (1.855 Å) shortened in comparison with all the other bonds (1.890–1.896 Å).

The $\mathrm{Li_2Ge^{VI}Ge_3^{IV}O_9}$ germanate ($q = T/M = 3$). The complete structural study was performed only for the germanate of the composition $\mathrm{LiNaGe^{VI}Ge_3^{IV}O_9}$ [3–5]. The first structural data for $\mathrm{Li_2Ge^{VI}Ge_3^{IV}O_9}$ (formed together with four other germanates by solid-phase reactions in the $\mathrm{Li_2O}$–$\mathrm{GeO_2}$ system) were published in [3]. The structure of the $\mathrm{LiNaGe^{VI}Ge_3^{IV}O_9}$ phase (a member of the $\mathrm{Li_2Ge^{VI}Ge_3^{IV}O_9}$–$\mathrm{Li_{1.5}Na_{0.5}Ge^{VI}Ge_3^{IV}O_9}$–$\mathrm{LiNaGe^{VI}Ge_3^{IV}O_9}$ row) was refined up to $R = 0.086$, sp. gr. *Pcca* in [4]. The parameters of the orthorhombic unit cell are $a = 9.31$, $b = 4.68$, $c = 15.88$ Å. The crystallographically independent set of PBU consists of one *M*-octahedron, two *T*-tetrahedra, one Li-, and one Na-atom.

A fragment of the structure projected onto the *XZ* plane is shown in Fig. 3 and consists of isolated $[\mathrm{GeO_6}]$-octahedra. The *T*-radical is represented by infinite $[\mathrm{GeO_3}]$-chains. All the polyhedra share vertices. The model suggested in [4] has a split Li(1)-position and a fully occupied Na-position. The *M*-octahedra ($y = 0.5$), connected by $[\mathrm{GeO_3}]$-chains lying in the *XZ*-plane at heights $y = 0$ and 1, form the *MT*-framework. The corrugated chains run along the *X*-axis. The repetition period is much larger (six) in comparison with that in $\mathrm{Li_2Ge^{VI}Ge_2^{IV}O_6(OH)_2}$ germanate (two).

The geometric model. The Li-, Na-, and $\mathrm{Ge^{VI}}$-atoms form the layers in the *XZ*-plane at the height $y = 0.5$ and are separated by $[\mathrm{GeO_3}]$-chains. Within the geometric model with alternating structural fragments along the *Y*-axis lying at the heights $y = 0$ and $y = 0.5$, the structure of this germanate can be represented as:

$$[\mathrm{GeO_3}]_\infty\text{-chains—(Na + Li + Ge)-layers.}$$

Similar to the case of the refined model of $\mathrm{LiNaGe^{VI}Ge_3^{IV}O_9}$, the structure of the orthorhombic $\mathrm{Li_2Ge^{VI}Ge_2^{IV}O_6(OH)_2}$ is characterized by rather close Ge–O distances. The $\mathrm{Ge^{IV}}$–O distances for the end O-atoms (1.716–1.758 Å) and the bridging O-atoms (1.757–1.789 Å) in the *T*-tetrahedra are essentially different. The Ge–O distances in the *T*- and *M*-polyhedra are also different.

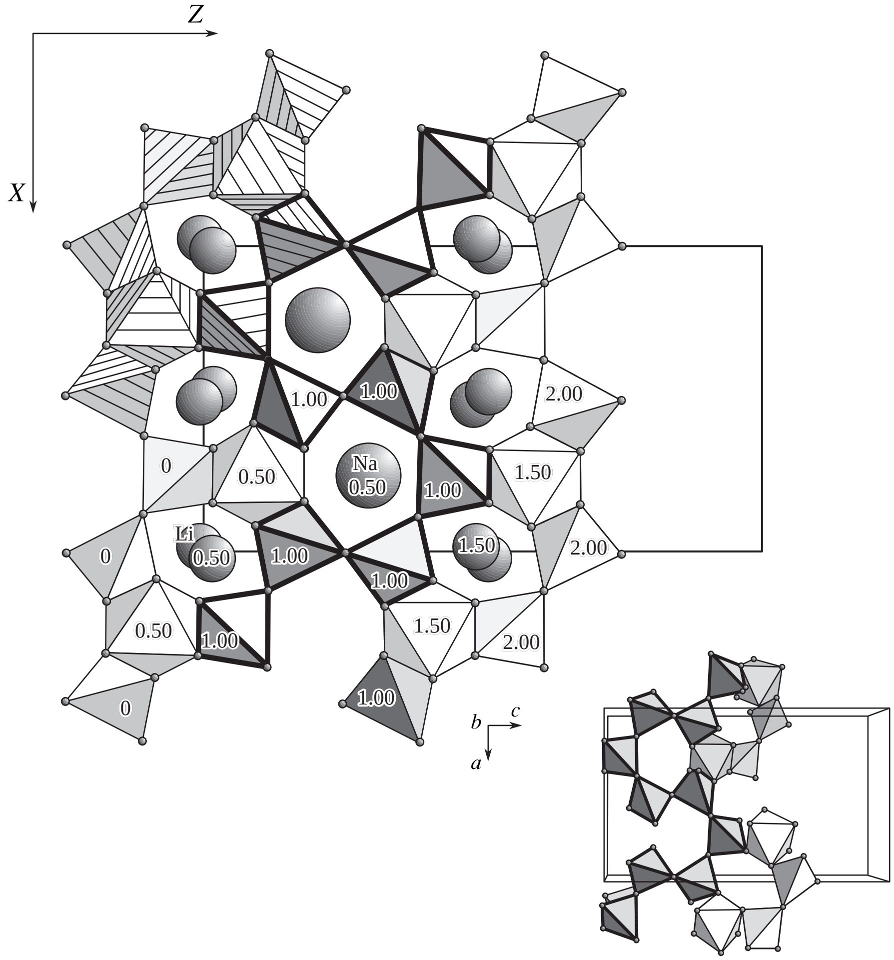

Fig. 3. $\mathrm{LiNaGe^{VI}Ge_3^{IV}O_9}$. A fragment of the structure projected onto the *XZ*-plane. The Li- (small circles), Na- (large circles), and $\mathrm{Ge^{VI}}$-atoms (in octahedra) form the (Li + Na + Ge) layers in the *XZ*-plane at a height of $y = 0.50$, connected by corrugated $[\mathrm{Ge}_n\mathrm{O}_{3n}]$-chains ($n = 6$, solid lines) along the *X*-axis in the *XZ* plane. The repeated structural fragment of the composition M_2T_6 is hatched. Figures indicate the heights along the *y*-axis; the figures at Li-atoms show the heights of the centers of split positions. The inset shows that all the polyhedra share vertices (the Ge–O bonds).

The $\mathrm{LiNaGeGe_3O_9}$ structure is characterized by its low symmetry, sp. gr. $Pca2_1$ [5]. The structure model is characterized by fully occupied Li- and Na-positions. The structure was refined to $R = 0.071$ (560 reflections). Within the framework of this model, the accuracy of the determined positional parameters of the atoms is comparatively low, which, in turn, deteriorates the geometric characteristics of PBU. The Ge–O bond lengths for Ge in the tetrahedron (1.67–1.80 for the end O atoms and 1.71–1.86 Å for bridging ones) and in the octahedron (1.81–1.93 Å) are very close. Therefore, in what follows, we use only the centrosymmetric model of $\mathrm{LiNaGeGe_3O_9}$ suggested in [4].

The $\mathbf{Li_4Ge_2^{VI}Ge_7^{IV}O_{20}}$ germanate ($q = T/M = 3.5$). The crystal structure was refined to $R = 0.082$ [6]. The parameters of the monoclinic unit cell are $a = 12.43$, $b = 8.00$, $c = 7.49$ Å, $\beta = 91.0°$. The structure was solved within the sp. gr. *C*2. The crystallographically independent PBU set consists of one *M*-octahedron, four *T*-tetrahedra, and three Li-atoms.

The fragment of the structure projected onto the *XZ*-plane is shown in Fig. 4. The structure is characterized by isolated $[\mathrm{GeO_6}]$-octahedra. The *T*-radical consists of a $[\mathrm{Ge_7O_{20}}]$-layer formed by (Ge,O)-chains. The model has two fully occupied Li-positions. Two Li-atoms are located in positions on the twofold axis (at heights $y = 0.17$ and $y = -0.20$); one Li-atom occupies the general position (Fig. 3, $y = -0.12$). The *M*-octahedra of the composition $[\mathrm{GeO_6}]$ are connected by Ge,O-chains and form the *MT*-framework. The $[\mathrm{Ge_7O_{20}}]$-layers are parallel to the (210) plane. The repetition periods for a $[\mathrm{GeO_4}]$-tetrahedron located on the 2-axis in the (Ge,O) net is 8 (along the *b*-axis) and 10 (along the translation vector (**a** + **b**)).

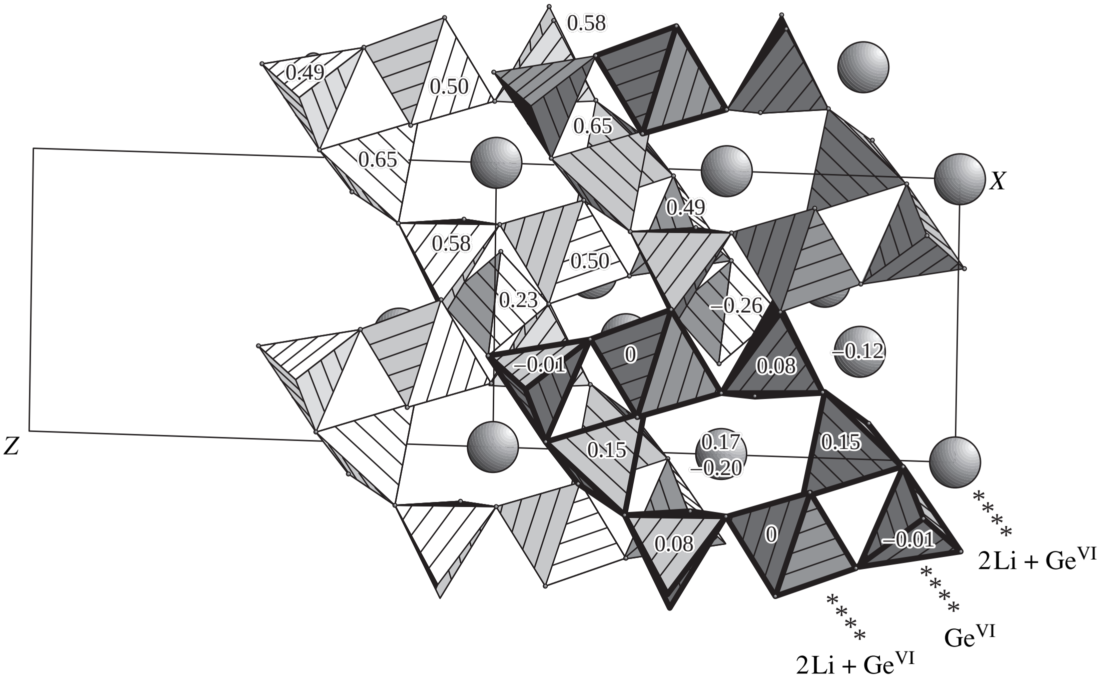

Fig. 4. $Li_4Ge_2^{VI}Ge_7^{IV}O_{20}$. A fragment of the structure projected onto the *XZ*-plane. Asterisks indicate the sections of the (210) planes in which the Li and Ge^{VI} atoms form the (2Li + Ge)-layers connected by (Ge,O)-layers also parallel to the (210)-planes. The structurally-equivalent fragments lying at different heights along the *Y*-axis are differently shadowed and hatched. The repeating structural M_2T_6-unit is indicated by solid lines.

The geometric model. The Li(1)-, Li(2)-, Li(3)-, and Ge^{VI}-atoms in the structure form the (2Li + Ge)-layers parallel to the (210) plane. These layers are separated by the Ge^{VI},O-layers. Within the geometric model with layer structural fragments alternating along the (210) direction, the structure can be represented as a sequence of the layers

	(2Li + Ge)-layers	–	Ge_7O_{20}-layers	–	(2Li + Ge)-layers	–	Ge_7O_{20}-layers
With the heights along the (210) direction equal to	0		0.25		0.50		0.75

Unlike $LiGe^{VI}Ge_2^{IV}O_6(OH)_2$, the structure of the monoclinic germanate under consideration is characterized by considerable scatter in all the Ge–O bond lengths for the end (1.713–1.800 Å) and bridging (1.711–1.815 Å) O-atoms in the *T*-tetrahedra, and almost equal to Ge–O distances in the *T*- and *M*-polyhedra. Within the framework of the sp. gr. *C*2, the geometric characteristics of the model, in particular the ranges of Ge–O length variations, should be further refined. The average values of the Ge–O bond lengths in octahedra and tetrahedra are quite reasonable.

The $Li_2Ge^{VI}Ge_6^{IV}O_{15}$ germanate ($q = T/M = 6$). The crystal structure of this germanate was solved in [7] by X-ray diffraction methods within the sp. gr. *Pbcn*, $R = 0.072$. The neutron diffraction determination was performed on single crystals in the anisotropic approximation to $R = 0.067$ (1580 reflections) [8]. The parameters of the orthorhombic unit cell are $a = 7.369$, $b = 16.736$, and $c = 9.710$ Å. The structure was solved under the assumption that the Li(2)-position is slightly split, and confirmed the model suggested in [7]. The set of crystallographically independent PBU consists of one *M*-octahedron, three *T*-tetrahedra, and two Li-atoms.

A fragment of the structure projected onto the *YZ* plane is shown in Fig. 5. The structure is characterized by isolated $[GeO_6]$-octahedra. The *T*-radical consists of infinite Ge,O-chains forming the corrugated layer of the composition $[Ge_6O_{15}]$. Similar to the $LiNaGe^{VI}Ge_3^{IV}O_9$ model, the model suggested in [8] has a slightly split Li(2)-position (in Fig. 5, the Li(2)-atoms are located in the center) and a fully occupied Li(1)-position. The *M*-octahedra $[GeO_6]$ we linked by four infinite $[GeO_3]$-chains in the *YZ* plane at heights $x = 0.3$ and 0.7, and form the *MT*-framework. The chains are aligned along the *Z*-axis and the repetition period equals 6.

The geometric model. The Li(1), Li(2) and Ge^{VI}-atoms in the structure form the chain-like substructures

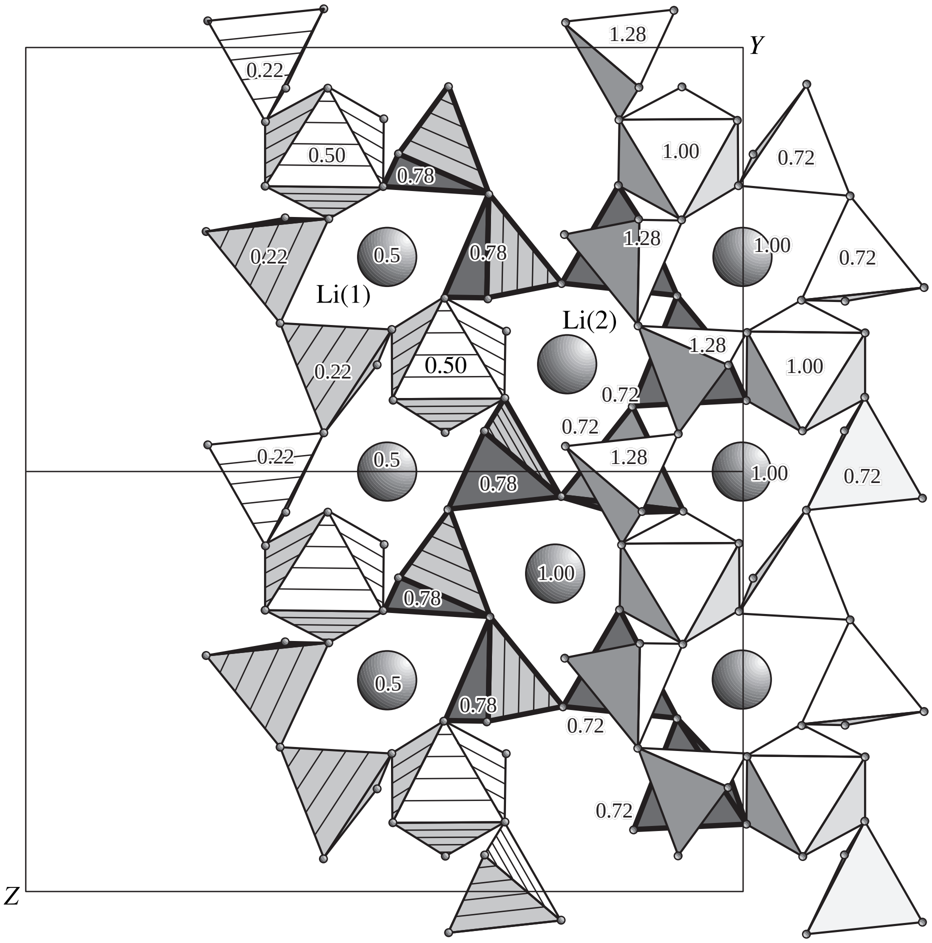

Fig. 5. $Li_2Ge^{VI}Ge_6^{IV}O_{15}$. A fragment of the structure projected onto the *YZ*-plane. The chains of Ge-tetrahedra at heights $x = 0.78$ and $x = 0.72$ (solid lines) connect isolated [GeO_6]-octahedra. The Li- and Ge^{VI}-atoms form the substructures related by the 2_1-axis in the *YZ*-plane at heights $x = 0.50$ and $x = 1.0$.

of the composition (2Li + Ge) in the *YZ*-plane at the height of $x = 0.5$. These chains are related by the 2_1-axes.

The results obtained in [8] indicate the considerable reduction of all the of bond-length ranges for the end and bridging O-atoms in the *T*-tetrahedra compared with the data indicated in [7], and also the pronounced difference between the Ge–O bond lengths in the *T*- and *M*-polyhedra.

DISCUSSION

The analysis of the structures of the framework Li,Ge-germanates revealed three characteristic features distinguishing them from similar *A*, Me^{4+}-germanates/silicates (A = Li, Na, K, Rb, Cs; Me^{4+} = Ge, Ti, Zr, Sn).

Nonisotrucurality of germanates. All the germanates have original structures and have no analogues among alkali *A*, *Me*(IV)-germanates/silicates. Nor do they have analogues among alkali-free phosphates or sulfates. It should be emphasized that germanates of other alkali metals, e.g., three from five known Na,Zr-germanates with framework structures, have the structural analogues among alkali-free compounds [11], whereas two well-known K,Zr-germanates have no analogues at all.

Type of *T*-radical. The *T*-radical is represented by isolated infinite chains of [GeO_4]-tetrahedra (in two cases) and by the same chains forming layers (in two other cases). The repetition periods in the chain or in the layer range from 2 to 10. In five framework structures of Na,Zr-germanates [11], all the *T*-radicals are of the island-type and are [GeO_4]-orthotetrahedra, [Ge_2O_7]-diorthogroups, and five-link [Ge_5O_{16}]-chains. In two K,Zr-germanates [12], the *T*-radicals are [Ge_2O_7]-diorthogroups and [Ge_3O_9]-rings, respectively [12].

Content of the *T*-component. Unlike the case of Na,Zr-germanates (q = 1, 1.5, 2, 2.5) and K,Zr germanates (q = 2, 3), the q ratio equal to the number of [GeO_4]-tetrahedra to the number of [GeO_6]-octahedra in Li,Ge-germanates, $q = T/M$, varies in a wider range (q = 2, 3, 3.5, 6).

At the minimum q-value, $q = 2$, the tetrahedra in the $LiGe^{VI}Ge_2^{IV}O_6(OH)_2$ framework forms chains with the repetition period 2*T*. Similar chains are also typical of Li,Al(Sc,Fe)-silicates with close "PBU stoichiometry" (2[SiO_4][AlO_6]), although they form the *MT* condensed structures of the pyroxenetype $LiAlSi_2O_6$ instead of *MT* framework structures.

At $q = 3$, the end compounds in the row of alkali germanates $Li_2Ge^{VI}Ge_3^{IV}O_9$–$LiNaGe^{VI}Ge_3^{IV}O_9$–$Na_2Ge^{VI}Ge_3^{IV}O_9$ have different Ge,O-radicals. The [Ge_3O_9]-chains in two first phases and the three-membered [Ge_3O_9]-rings in the Na-containing phase are explained by the different structures of the main crystal-forming complexes [10].

The framework $Li_4Ge_2^{VI}Ge_7^{IV}O_{20}$ structure ($q = 3.5$) is characterized by the T/M ratio never encountered earlier in the crystal chemistry of the *M*, *T*-frameworks—$T/M = 3.5$ (7 : 2).

The *MT*-framework of the composition MT_6 is often encountered among alkali silicates ($LiNaZrSi_6O_{15}$, $K_2ZrSi_6O_{15}$, $Na_2LnSi_6O_{15}$, *Ln*–RE, etc.). There are more than ten topologically different variants of such frameworks. The Li-germanate of the composition $Li_2Ge^{VI}Ge_6^{IV}O_{15}$ has its own variant of PBU condensation and its own MT_6-framework.

The geometric criteria of the structural-solution quality for germanates are: the existence of narrow ranges of Ge–O distance variations within each type of polyhedra; the clearly pronounced difference between the distances to the end and the bridging O-atoms in *T*-tetrahedra; and a considerable difference in the Ge–O distances for germanium located in tetrahedra and octahedra. In this approach, a lower *R*-factor for a less symmetric space group is not the necessary decisive factor for the choice of the final structure.

Three geometric models of germanates considered above satisfy these criteria. The monoclinic $Li_4Ge_2^{VI}Ge_7^{IV}O_{20}$ and $LiNaGeGe_3O_9$ do not satisfy it: the symmetry is lowered from *Pcca* to $Pca2_1$ [8], which results in three-to-five times broadening of the range of all the Ge–O distances—for both end and bridging O-atoms in tetrahedra and octahedra in comparison with the distances conventionally observed in germanates.

The analysis of the crystallochemical characteristics of the framework lithium germanates (symmetry, PBU sets, framework architecture, geometric types of tetrahedral Ge-radicals) is the basis for the further study of the crystallization processes of germanates. Earlier, a similar analysis and the simulation of the processes of structure formation were performed for Na,*Me*-germanates [10].

The structural data show that the framework Li-germanates are crystallized within low-symmetric space groups—monoclinic *C*2 and *B*2/*b* and orthorhombic *Pcca* and *Pbcn*. One structure is described by the acentric group *C*2, the other structures are described by the centrosymmetric groups. All the structures are characterized by a relatively low number of crystallographically independent PBU in the unit cell—only one *M*-octahedron, one-to-four *T*-tetrahedra, and two-to-three Li-atoms.

It seems that the most important fact is that all the [GeO_6]-octahedra in the unit cell are related by Symmetry elements. This fact is of great importance for the simulation of the process of forming germanate structures in the solution by combining secondary building units (SBU) (the simplest combinations of the primary building units), i.e., of *M*-octahedra, *T*-tetrahedra, and Li-atoms. Thus, the secondary building units for simulating the crystallization processes of Li,Ge-germanates should be selected with due regard for the obligatory symmetric relations at all the stages of formation of secondary structural building units, the precursors of the crystal-structure formation of framework germanates.

ACKNOWLEDGMENTS

This study was supported by the Russian Foundation for Basic Research, project no. 98-05-64883.

REFERENCES

1. N. N. Nevskiĭ, L. N. Ivanova, V. V. Ilyukhin, and N. V. Belov, Dokl. Akad. Nauk SSSR **242** (6), 1330 (1978) [Sov. Phys. Dokl. **23**, 705 (1978)].
2. R. Klaska and R. Jendryan, Z. Kristallogr. **162** (1–4), 129 (1983).
3. A. Wittmann and E. Modern, Monatsch. Chem. **92** (2), 581 (1965).
4. H. Völlenkle, A. Wittamann, and H. Nowotny, Monatsch. Chem. **100** (1), 79 (1969).
5. R. G. Matveeva, V. V. Ilyukhin, and N. V. Belov, Dokl. Akad. Nauk SSSR **213** (3), 584 (1973).
6. H. Völlenkle, A. Wittamann, and H. Nowotny, Monatsch. Chem. **102** (1–4), 361 (1971).
7. H. Völenkle, A. Wittamann, and H. Nowotny, Monatsch. Chem. **101** (1), 56 (1970).
8. Y. Iwata, N. Koyano, and I. Shibuya, Annual. Rep. Res. React. Inst., Kyoto Univ. **19**, 11 (1986).
9. B. L. Greenberg and G. M. Loiacono, Acta Crystallogr. Sect. C: Cryst. Struct. Commun. **46**, 2021 (1990).
10. D. Yu. Pushcharovskiĭ, *Structural Mineralogy of Silicates and Their Synthetic Analogues* (Nedra, Moscow, 1986).
11. G. D. Ilyushin and L. N. Dem'yanets, Itogi Nauki Tekh., Ser. Kristallokhim. **22**, 174 (1989).
12. G. D. Iljushin and L. N. Demianets, in *Growth of Crystals*, Ed. by E. I. Givargisov and A. M. Melnikova (Consultant Bureau, New York; London, 1996), Vol. 20, p. 89.
13. G. D. Ilyushin and L. N. Dem'yanets, Kristallografiya **42** (6), 1124 (1997) [Crystallogr. Rep. **42** (6), 1047 (1997)].
14. G. D. Iljushin and L. N. Demianets, in *Collected Abstract of 17th Congress and General Assembly International Union of Crystallography, 1996*, PS 08.00.17, p. 315.

Translated by L. Man

Crystallography Reports, Vol. 45, No. 4, 2000, pp. 633–639. Translated from Kristallografiya, Vol. 45, No. 4, 2000, pp. 692–698.

CRYSTAL CHEMISTRY

Analysis of Molecular Cl···Cl Interactions in Pentachlorobezene and Hexachlorobenzene Crystals

O. V. Grineva and P. M. Zorky

Moscow State University, Vorob'evy gory, Moscow, 119899 Russia

Received July 9, 1998

Abstract—The concept of Cl-aggregation in chlorine-containing organic compounds and the principles of their classification are briefly discussed. The method for singling out Cl-aggregates in substances with high chlorine content is considered, using the examples of hexachlorobenzene and pentachlorobenzene. It is established that Cl-aggregates in these compounds are three dimensional (i^3-aggregates) and contain subaggregates of lower dimensionalities. The results obtained agree with the earlier assumptions about an important role of the chlorophobic effect in Cl-aggregation. © *2000 MAIK "Nauka/Interperiodica".*

The present article is part of the crystallochemical study of the structural characteristics of chlorine-containing organic crystals. Earlier [1], on the basis of energy calculations, we put forward the hypothesis of an important role of the *chlorophobic effect* in Cl-*aggregation*. Below, we analyze the manifestation of the chlorophobic effect in crystals with high chlorine content, using examples of the crystal structures of hexaclorobenzene and pentachlorobezene.

SHORTENED Cl···Cl DISTANCES AND Cl-AGGREGATION

With the accumulation of new X-ray diffraction data, the systematic study of organic crystals becomes ever more informative. The analysis of these data leads to conclude that they are characterized by shortened intermolecular Cl···Cl distances in comparison with double van der Waals radii characteristic of chlorine-containing organic crystals [2], and that some crystal properties (i.e., the ability to photochemical reactions) are dependent on the existence of such distances [3]. The specific features of chlorine-containing organic crystals were repeatedly studied, but the authors often used the reduced value of the van der Waals radius of a chlorine atom (1.76 Å) [4] and, thus, considered only the shortest (less than 3.5 Å) intermolecular Cl···Cl distances. For many years, the study of chlorine-containing organic crystals reduced to the statistical analysis of the geometric characteristics of the Cl···Cl contacts (e.g., the review article [5]). A rather formal classification of the structures with short intermolecular Cl···Cl distances was suggested in [6] and then was refined and developed in [7–9] (this classification will be considered in detail later). The Cl···Cl contacts obtained by a number of researchers were reviewed elsewhere [8, 9].

However, is seems that the formation of the structure depends not only on the presence of some shortened Cl···Cl distances, but also on the arrangement of all the chlorine atoms in the crystal space. The analysis of organic crystals shows that the specific contacts have a tendency toward *aggregation*, including the *aggregation* of short intermolecular Cl···Cl distances [10, 11]. It should be emphasized that we mean here not only the shortest Cl···Cl distances, but also those distances which only slightly exceed the double value of the "normal" van der Waals radius of a chlorine atom (1.9 Å [12]). In other words, the crystal structure has a number of rather short (about 4.2–4.3 Å) distances nonuniformly distributed in the space, i.e., located only within certain regions.

The specific manifestations of this effect in the crystal structures of three substances (chlorobenzene and two dichloronaphthalenes with low chlorine content) were discussed in [13], undertaken with the aim to study Cl-aggregation. In an earlier study [14], the author indicated the characteristic feature of three modifications of *p*-dichlorobenzene—the layers formed due to Cl···Cl interactions. Studying the thermal expansion of the crystals, Wheeler and Colson [14] concluded that the layers in *p*-dichlorobenzene polymorphs are formed due to attractive interactions between chlorine atoms. However, the results obtained in our previous study to the effect [1] led us to another assumption—Cl-aggregation, at least in some cases, is caused by the chlorophobic effect, which reduces to the following. Since the most energetically advantageous interactions are those between the benzene rings, chlorine atoms are "pushed away" from the regions of these interactions, which, in turn, results in the formation of Cl-aggregates.

In this connection, we performed the crystallochemical analysis of the structures with both low and high chlorine content. In the latter case, the chlorophobic effect resulted in a grouping of the intermolecular Cl···Cl distances in only some regions of the crystalline substance, whereas purely attractive interactions between chlorine atoms would have resulted in their

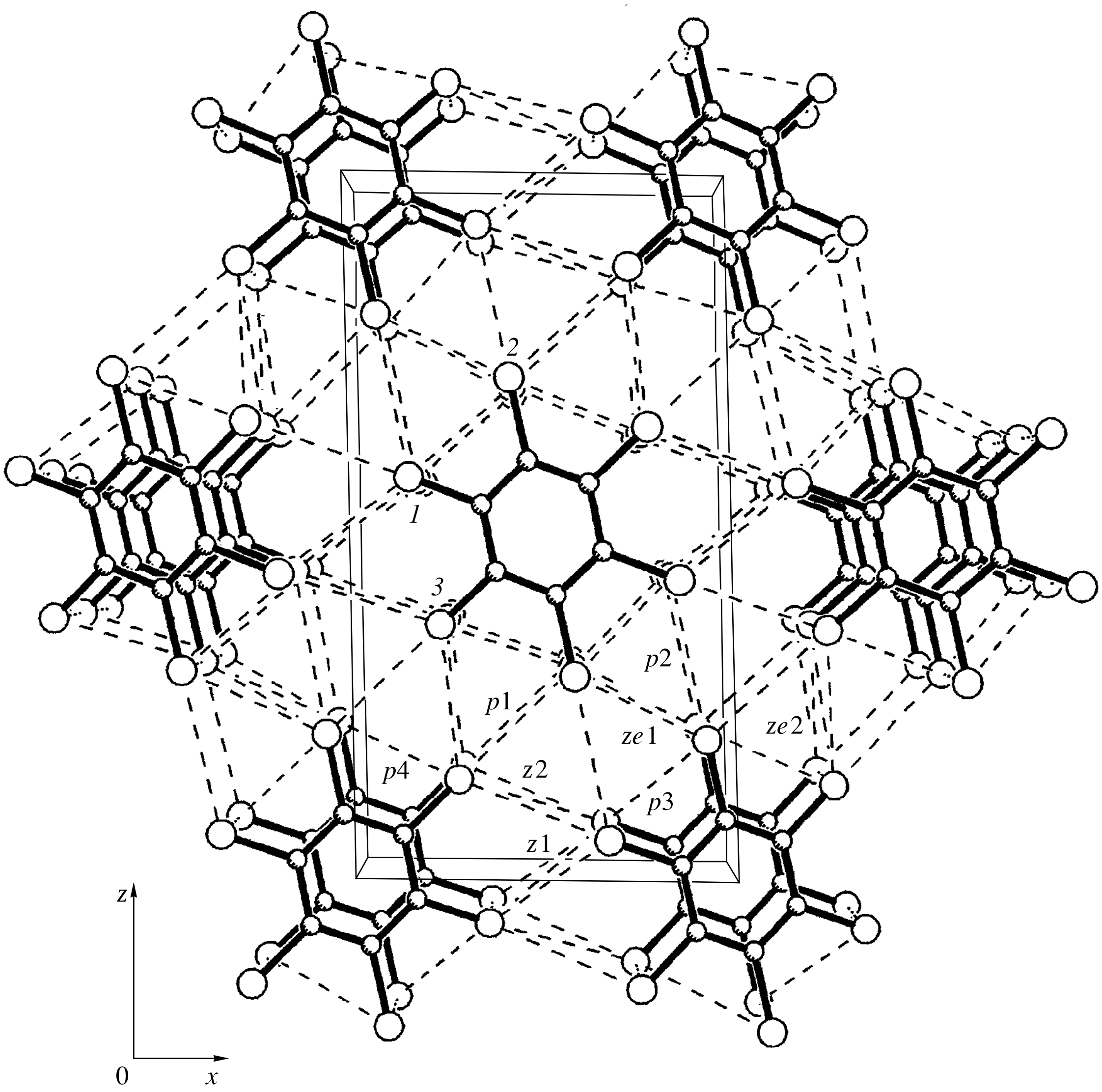

Fig. 1. Hexaclorobenzene (viewed along the *Y*-axis). The dashed lines in Figs. 1–5 indicate intermolecular Cl···Cl contacts; figures indicate independent chlorine atoms. For notation of ribbons forming Cl-aggregates, see Fig. 3; the ribbons are numbered in the order of an increasing *d* or d_1 distance.

homogeneous distribution over the crystal space. Our assumption is justified only if the interactions between chlorine atoms produce a strong influence on the formation of the crystal structure. Obviously, the arrangement of molecules in a crystal is determined by a number of factors, and the Cl··Cl interactions do not necessarily play the decisive role in the structure formation.

The phenomenon of Cl-aggregation is almost unstudied, and no Cl-aggregates formed by shortest intermolecular Cl··Cl distances are classified. As already indicated, Sarma and Desiraju [6, 7] suggested a classification of structures with short intermolecular Cl··Cl distances. They invoked the concept of the β-structure (or 4 Å-structure) first introduced by Schmidt [3] for structures in which the shortest lattice period was equal to ~4 Å. These structures (of which most are formed by planar aromatic molecules) are often encountered among chlorine-containing organic crystals. The classification suggested in [6–9] is based on several typical two-dimensional motifs stabilized by attractive Cl··Cl interactions. These motifs are formed by planar ribbons, planar layers, corrugated layers, and double-corrugated layers, whose short Cl··Cl intermolecular distances lie almost in the molecule plane. The fragments thus constructed are connected via stacking of benzene rings, and form a 4 Å-structure. Desiraju [8] considers hexachlorobenzene and the β-modification (triclinic) of 1,4-dichlorobenzene as representatives of the structures with ribbons and planar layers. According to Desiraju [8], the pentachlorobenzene structure has a double corrugated layer. In our opinion, an essential shortcoming of this classification is the rather formal attempt to find some relation between the space groups and the two-dimensional motifs (e.g., an orthogonal structure and a double corrugated layer). In some cases, this leads to a rather unusual description of the structures. This is true for both compounds considered in the present study, and especially, for hexachlorobenzene.

It should be indicated that Desiraju and his coauthors give different definitions of short Cl⋅⋅Cl distances. Analyzing the number of short distances per molecule, Sarma and Desiraju [6] use a somewhat ambiguous criterion of selecting short Cl⋅⋅Cl distances, which states that the atoms in the structure should be spaced by a distance shorter than the distance providing an –0.05 kJ/mol energy contribution to the crystal stabilization. Unfortunately, they did not indicated this distance, but, the indirect data allowed us to assume that it ranged within 3.8–3.9 Å. It was also indicated [6] that the distances exceeding 3.6 Å existed in both 4 Å-structures and structures not related to this type. Therefore, these distances could not be structure-forming and were ignored. However, refining their classifications for chlorine-containing 4 Å-structures, Sarma and Desiraju [7] included into consideration Cl⋅⋅Cl distances up to 4.1 Å, whereas, somewhat later, calculating the Cl⋅⋅Cl contacts, Desiraju and Parthasarathy [15] took into account Cl⋅⋅Cl distances less than 3.52 Å.

OBJECTS OF STUDY

In the present study, we analyzed the data of the X-ray diffraction study of hexachlorobenzene [16, 17] and pentachlorobenzene [18] in terms of crystal chemistry. Desiraju *et al*. [6–9] and considered the data of the first complete structural determination of crystalline hexaclorobenzene [16], where most of the short intermolecular Cl⋅⋅Cl distances were indicated, although we used more accurate results from a more recent study [17]. It should be indicated that the difference between the unit-cell parameters in [16] and [17] ranges within 0.03–0.05 Å. For most of the intermolecular Cl⋅⋅Cl distances, the maximum discrepancy is 0.13 Å. However, arranging the Cl⋅⋅Cl distances in the order of their increase, we revealed that, in three instances, the distances given in [16] and [17] are slightly inconsistent. March and Williams [18] claimed that their aim was to obtain a more detailed information on Cl⋅⋅Cl intermolecular interactions in organic crystals, but, in fact, they discussed in detail only the molecule geometry. The major data on the crystal structures of hexachlorobenzene and pentachlorobenzene are as follows:

Substance	Structure class	*a*	*b*	*c*	β	Number of independent Cl atoms
Hexaclorobenzene	$P2_1/n$, $Z = 2(\bar{1})$	8.0476	3.8363	14.8208	92.134	3
Pentachlorobezene	$Pca2_1$, $Z = 4(1)$	16.802	3.856	13.279		5

It was shown [19] that benzene rings make three main types of the contacts: sandwich-type, oblique, and orthogonal contacts. In turn, each of these contacts has several stereotypes. Below, we use the concept of the *S*-structure, i.e., the structure with aggregation of sandwich-type contacts (in this case the difference between the stereotypes is ignored). These structures are formed by stacks of benzene rings. As is seen from Figs. 1 and

Short intermolecular distances in the hexachlorobenzene and pentachlorobenzene structures

Hexaclorobenzene			Pentachlorobezene			Hexaclorobenzene			Pentachlorobezene		
$r_{(\mathrm{Cl}\cdots\mathrm{Cl})}$ Å	Cl⋯Cl	type $r_{(\mathrm{Cl}\cdots\mathrm{Cl})}$	$r_{(\mathrm{Cl}\cdots\mathrm{Cl})}$ Å	Cl⋯Cl	type $r_{(\mathrm{Cl}\cdots\mathrm{Cl})}$	$r_{(\mathrm{Cl}\cdots\mathrm{Cl})}$ Å	Cl⋯Cl	type $r_{(\mathrm{Cl}\cdots\mathrm{Cl})}$	$r_{(\mathrm{Cl}\cdots\mathrm{Cl})}$ Å	Cl⋯Cl	type $r_{(\mathrm{Cl}\cdots\mathrm{Cl})}$
			3.447	1…3	*inter*	3.885	3…3	*inter*	3.885	1…2	*intra*
3.516	2…3'	*inter*	3.539	2…4	*inter*	3.917	1…2	*intra*	3.891	3…5	*inter*
3.563	1…2	*inter*	3.562	1…4	*inter*	3.963	1…3'	*inter*	3.985	2…5	*inter*
3.701	2…2	*inter*	3.700	1…4	*inter*				4.001	4…5	*intra*
3.711	1…1'	*inter*	3.709	1…5	*inter*				4.049	4…5	*inter*
3.736	1…1'	*inter*	3.748	2…5	*inter*	4.155	2…3'	*intra*	4.181	2…3	*intra*
3.779	1…3'	*inter*	3.829	1…3	*inter*	(4.413)	2…3'		(4.412)	3…5	
3.836		period	3.856		period	(4.662)	1…2		(4.638)	1…5	

Note: Cl⋯Cl distances between the benzene-ring stacks are indicated as*inter*, those inside such stacks are indicated as *intra*.

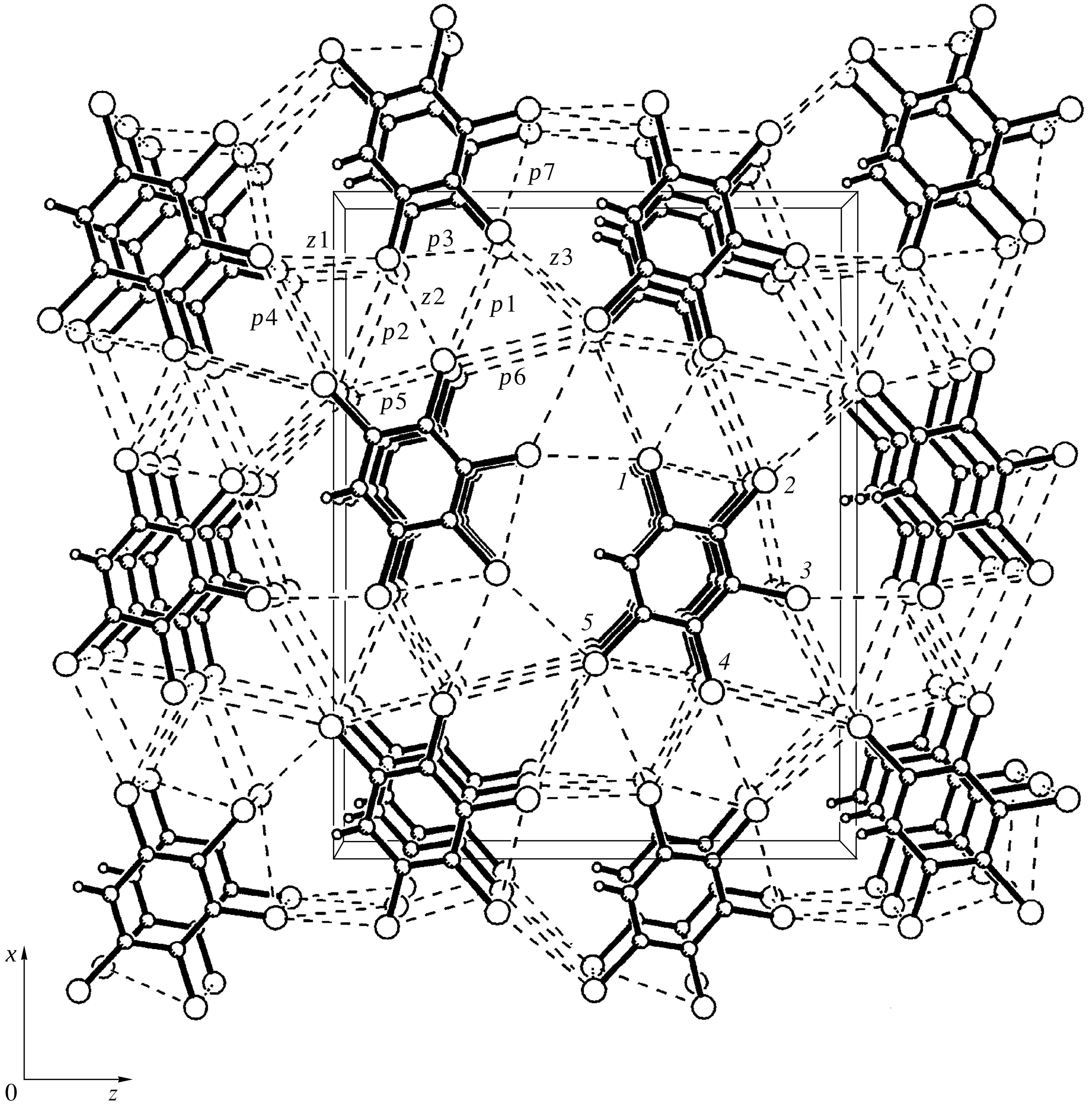

Fig. 2. Pentachlorobezene (viewed along the *y*-axis).

2, the hexachlorobenzene and pentachlorobenzene structures belong to the *S*-group, and, therefore, it is natural to assume that the mutual stack orientation is determined mainly by Cl··Cl interactions.

METHODS OF CRYSTALLOCHEMICAL ANALYSIS AND MAIN RESULTS

We believe that studying the structural characteristics of chlorine-containing organic crystals, it is preferable to classify them by the type of Cl-aggregates formed by intermolecular Cl··Cl contacts. A Cl-aggregate can be finite or infinite in one, two or three dimensions (the i^1-, i^2-, and i^3-aggregates, respectively). Thus, the study of chlorine aggregation is based on the separation of intermolecular Cl··Cl distances, which are called *short* Cl··Cl *distances or* Cl··Cl *contacts* and which form Cl-aggregates.

We do not use energy characteristics for selecting Cl··Cl distances because the potentials indicated by various authors are inconsistent and lead to obvious ambiguities. Moreover, the contributions to the crystal energy come not only from Cl··Cl interactions, but also from the Cl··C and Cl··H interactions. Therefore, as follows from [1], the dependence between the energy contributions of the interactions with participation of chlorine atoms and the Cl··Cl distances is somewhat ambiguous.

We calculated the intermolecular distances from each symmetrically independent chlorine atom of the

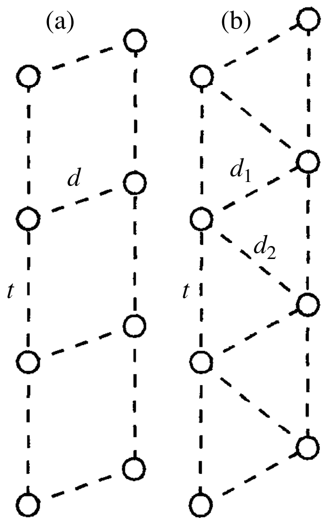

Fig. 3. Elements of Cl-aggregates characteristic of chlorine-containing crystals of the *S*-type: (a) *p*-type ribbons, (b) *z*-type ribbons for $d_1 \neq d_2$ and *ze*-type ribbons for $d_1 = d_2$; *t* is the stack period (the shortest translation).

initial hexachlorobenzene and pentachlorobezene molecules to all the chlorine atoms of the molecules in the nearest environment. These values are listed in the table in the order of their increase. In parentheses, the shortest of the long distances are also indicated. It is seen that the total number of the shortest intermolecular Cl··Cl distances and their values are rather close. In the pentachlorobenzene crystal, the short and the long distances considerably differ—up to the distance 4.18 Å, the difference between two neighboring distances does not exceed 0.14 Å; the next distance is longer by 0.23 Å. For hexachlorobenzene, the longest of short distances can be selected as either 3.963 Å (the gap to the next distance equal to 0.19) or as 4.155 Å (the gap of 0.26 Å). The longest of the short distances for hexachlorobenzene is chosen to be 4.155 Å. The allowance for all the contacts indicated in the table leads to the formation of a i^3-aggregate.

We described Cl-aggregates in *S*-structures with the aid of two main elements—ribbons of two types (Fig. 3) running along the stacks. It has already been

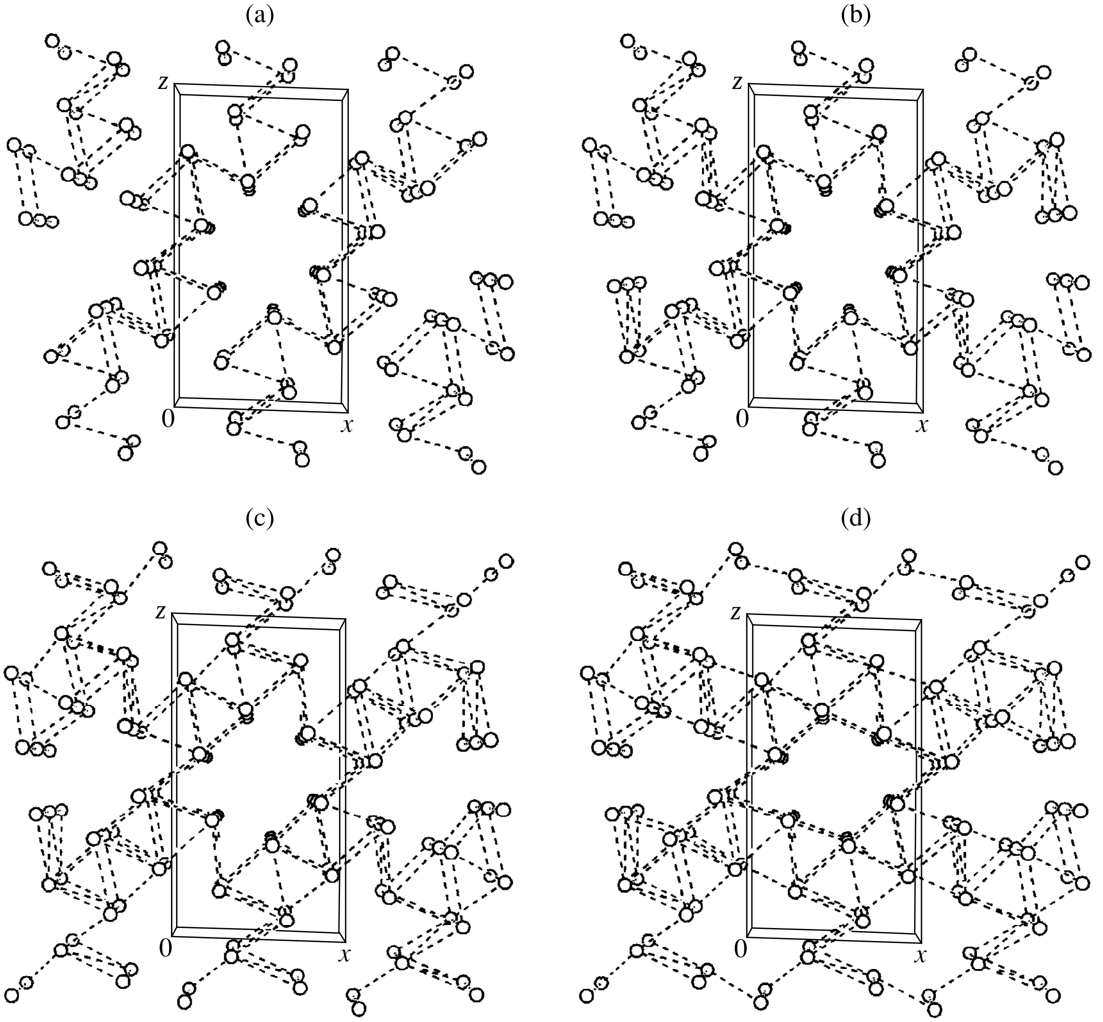

Fig. 4. Cl-aggregates in hexachlorobenzene at different lengths of the contact under consideration. The maximum contact lengths (a) 3.836, (b) 3.885, (c) 3.963, and (d) 4.155 Å.

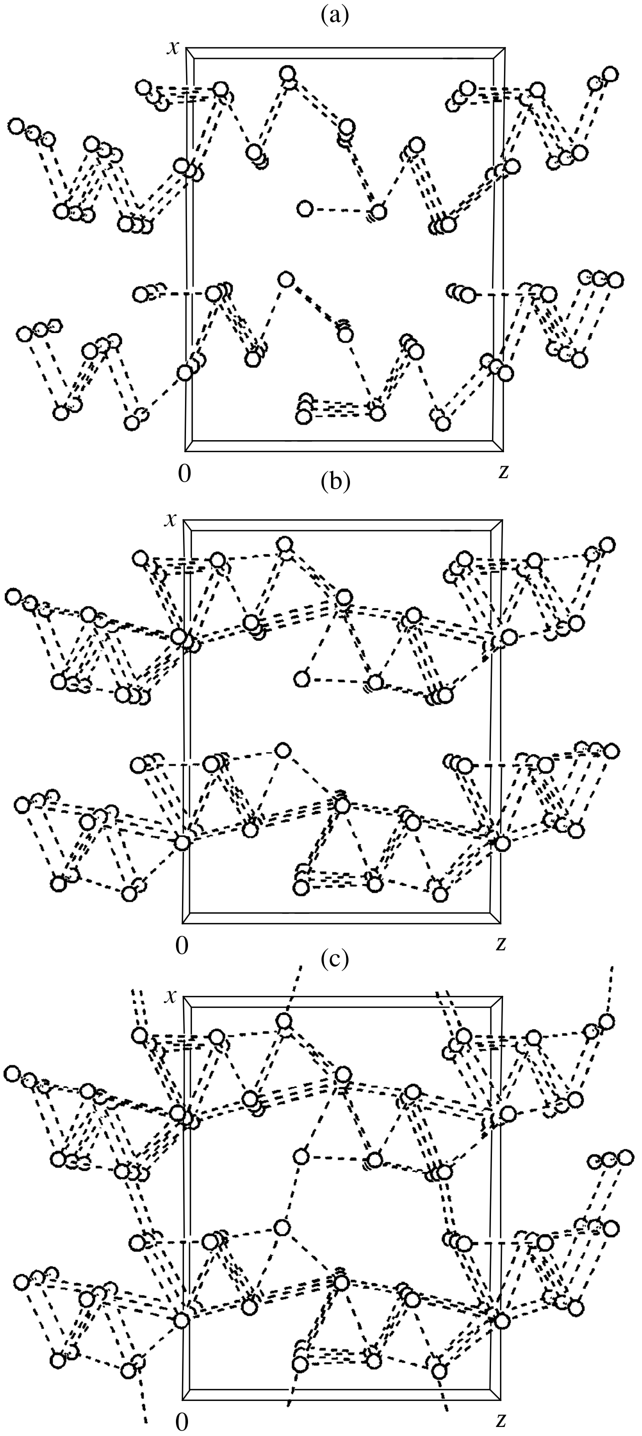

Fig. 5. Cl-aggregates in pentachlorobenzene at different lengths of the contact under consideration. The maximum contact lengths (a) 3.856, (b) 4.049, (c) 4.181 Å.

indicated that, to a large extent, the Cl··Cl interactions determine the mutual stack orientations. Therefore, we considered first Cl-aggregates formed by the shortest *S-inter*-contacts (the contacts between the stacks). As is seen from table, all the contacts in both crystals shorter than the translation *t* are *S-inter*-contacts, and, therefore, we considered Cl-aggregates formed by the contacts either shorter than or equal to *t*. Moreover, in hexachlorobenzene, we also considered a Cl-aggregate with due regard for the first contact exceeding *t* because it is also an *S-inter*-contact. As is seen from Figs. 4a and 5*a*, Cl-aggregates formed by the contacts *t* are periodic only in two dimensions (i.e. are i^2-aggregates). In hexachlorobenzene, the allowance for the next *S-inter*-contact results in the formation of a i^3 aggregate (Fig. 4b). It should also be noted that, according to [16], a i^3 aggregate in hexachlorobenzene can be singled out by considering the contacts of lengths $\leq t$ alone. Thus, the allowance for only the shortest *S-inter*-contacts does not change the dimensionality of a Cl-aggregate in hexachlorobenzene, but reduces its dimensionality in pentachlorobenzene.

Since the longest contacts in the pentachlorobenzene and hexachlorobenzene structures differ from the preceding ones (and are, in fact, *S-intra*-contacts, i.e., the contact inside the stack), we considered Cl-aggregates containing all the Cl··Cl contacts except for the longest one. It was established that, in this case as well, a Cl-aggregate in pentachlorobenzene is periodic in two dimensions and, thus, is a complex layer (Fig. 5b) which can be represented as a set of edge-sharing rods. Similar rods are also present in a Cl-aggregate in hexachlorobenzene (Fig. 4c) with only one difference: in the latter case, they are connected by *z*- and *ze*-ribbons along two directions (Fig. 3). Thus, a i^3-aggregate in pentachlorobenzene (Fig. 5c) is formed only with the participation of the longest contact 4.181 Å: these layers are connected by the *p*-type ribbons. In hexachlorobenzene, a i^3-aggregate (with due regard for all the contacts, Fig. 4d) resembles the corresponding aggregate in pentachlorobenzene: the layers, which can be called two-row corrugated layers are connected by the *z*-type ribbons. It should also be indicated that in pentachlorobenzene and hexachlorobenzene, the shortest of the long distances also lie in such layers.

Thus, the study of Cl-aggregation in pentachlorobenzene and hexachlorobenzene shows that Cl-aggregates in these crystals are heterogeneous, i.e., most of the Cl··Cl contacts are located within the subaggregates of lower dimensionality, and only a small number of the contacts connect subaggregates into an aggregate. Also, despite the fact that the chlorine positions in molecules are distributed rather uniformly (especially in hexachlorobenzene) and the chlorine concentration is rather high, the crystals also contain well-pronounced subaggregates. Our study shows that the contacts providing the merge of these subaggregates can be either the longest ones (pentachlorobenzene) or can also be of moderate lengths (hexachlorobenzene). The first variant seems to be more typical, whereas the second variant is provided by a high symmetry of the molecule.

The existence of subaggregates in Cl-aggregates of higher dimensionality is consistent with the assumption that the key role in the formation of these Cl-aggregates is played by the chlorophobic effect [1], which provides the most compact arrangement of the shortest intermolecular Cl··Cl contacts.

ACKNOWLEDGMENTS

This study was supported by the Russian Foundation for Basic Research, project no. 98-03-32171a.

REFERENCES

1. O. V. Grineva and P. M. Zorky, Zh. Fiz. Khim. **72**, 714 (1998).
2. T. Sakurai, M. Sundaralingam, and G. A. Jeffrey, Acta Crystallogr. **16**, 354 (1963).
3. G. M. J. Schmidt, Pure Appl. Chem. **27**, 647 (1971).
4. A. Bondi, J. Phys. Chem. **68**, 441 (1964).
5. A. É. Masunov and P. M. Zorky, Zh. Fiz. Khim. **66**, 60 (1992).
6. J. A. R. P. Sarma and G. R. Desiraju, Chem. Phys. Lett. **117**, 160 (1985).
7. J. A. R. P. Sarma and G. R. Desiraju, Acc. Chem. Res. **19**, 222 (1986).
8. G. R. Desiraju, in *Organic Solid State Chemistry* (Elsevier, Amsterdam, 1987), p. 519.
9. G. R. Desiraju, *Crystal Engineering* (Elsevier, Amsterdam, 1989), Chap. 6.
10. P. M. Zorky and O. N. Zorkaya, in *Proceedings of the 16th European Crystallographic Meeting, Lund, Sweden, 1995*, p. 87.
11. P. M. Zorky, in *Abstracts of the 10th International Symposium on Organic Chemistry, Poznan–Rydzyna, Poland, 1997*, p. 24.
12. Yu. V. Zefirov and P. M. Zorky, Zh. Strukt. Khim. **15**, 118 (1974).
13. I. S. Neretin, O. N. Zorkaya, and P. M. Zorky, Vestn. Mosk. Univ., Ser. 2: Khim. **38**, 235 (1997).
14. G. L. Wheeler and S. D. Colson, J. Chem. Phys. **65**, 1227 (1976).
15. G. R. Desiraju and R. Parthasarathy, J. Am. Chem. Soc. **111**, 8725 (1989).
16. I. N. Strel'tsova and Yu. T. Struchkov, Zh. Strukt. Khim. **2**, 312 (1961).
17. G. M. Brown and O. A. Strydom, Acta Crystallogr. Sect. B: Struct. Crystallodr. Cryst. Chem. **30**, 801 (1974).
18. P. Marsh and D. E. Williams, Acta Crystallogr. Sect. B: Struct. Crystallodr. Cryst. Chem. **37**, 705 (1981).
19. P. M. Zorky and O. N. Zorkaya, Adv. Mol. Struct. Res. **3**, 147 (1997).

Translated by L. Man

Crystallography Reports, Vol. 45, No. 4, 2000, pp. 640–646. Translated from Kristallografiya, Vol. 45, No. 4, 2000, pp. 699–706.
Original Russian Text Copyright © 2000 by Petukhov.

LATTICE DYNAMICS

Kinetics of State Switching in a Disordered Linear System

B. V. Petukhov

Shubnikov Institute of Crystallography, Russian Academy of Sciences,
Leninskiĭ pr. 59, Moscow, 117333 Russia[1]

Received July 9, 1998

Abstract—The Kolmogorov approach is used to describe the transition from the metastable to the stable state of a linear system, as a statistical process of multiple formations of nuclei of a new state and their merging. Within the framework of the model of a *random-force* field decelerating the motion of the boundaries between various states, it is shown that the kinetics of state switching undergoes a drastic change in the vicinity of a certain critical driving-force $F = F_c$. At $F < F_c$ the switching process is considerably decelerated because of the anomalous boundary motion. The theory can also be used to calculate the influence of defects on the interphase domain boundaries on substrates, crystal growth by step mechanism, plastic flow of materials due to dislocation motion in the Peierls–Nabarro relief, and kinetics of their physical processes. *© 2000 MAIK “Nauka/Interperiodica”.*

INTRODUCTION

The kinetics of state switching in linear systems determines the characteristics of many physical processes such as the dynamics of spin chains, polymers, domain boundaries on two-dimensional substrates [1], crystal growth via step motion on the surface [2], plastic flow of materials due to dislocation motion in the Peierls–Nabarro relief [3], etc.

The characteristics of state switching in a linear system with several degrees of freedom are essentially different from the well known exponential kinetics of relaxation of one-dimensional systems $Q(t) = Q_0\exp(-t/\tau)$, where $Q(t)$ is the fraction of the initial state at the moment t. As shown by A.N. Kolmogorov in 1937 [4], the mutual effect of various degrees of freedom changes the temporal law of relaxation even in spatially-homogeneous materials.

For example, consider a spin chain. Leaving aside the fluctuations, one can state that there are two states—with all the spins being directed either upward or downward. These states are separated by an energy barrier. In the absence of a magnetic field, these states are degenerate. The application of a magnetic field makes one of these states more favorable and aligns the spins along the field. The change of the magnetic-field sign makes this state metastable and gives rise to a driving force for spin reorientation (switching) and to a transient process of state switching. In other systems, the driving force can be of another physical nature, but the process proceeds similarly.

We shall also consider mixed states, i.e., the situations where some parts of the system are in different states, i.e., can be considered as different phases. A great contribution to the kinetics of state switching in linear systems comes from the motion of the so-called kink–solitons or simply kinks [5], which are, in fact, interphase boundaries. These boundaries can be considered as specific one-dimensional quasiparticles. If the driving force is relatively weak, the process is quasiequilibrium, i.e., proceeds via the motion of kinks–solitons, which are in the thermal equilibrium. However, below, we consider rather pronounced driving forces and essentially nonequilibrium processes, so that the contribution of thermal kinks can be ignored.

Switching the global state of the system proceeds in two stages. First, a thermal fluctuation gives rise to a local transition of a small portion of the system, which overcomes an energy barrier equal to the energy of the formation of two boundaries between the phases, and takes quite a long time. This portion can be considered as a “nucleus” of a new state, limited by two kinks separating different states. Then, under the effect of the applied external force, the kinks spread over the linear system until they meet the kinks from another nuclei formed statistically independently and are annihilated. Upon the merging of all the nuclei, the switching process is completed.

The problem of state switching kinetics in spatially homogeneous material (for a system of any dimension) was solved by A.N. Kolmogorov [4]. If the frequency of nucleus formation per unit length per unit time is denoted by J and the velocity of kink spreading, by v, the fraction of the initial phase $Q(t)$ by the moment t can be written as [4]:

$$Q(t) = \exp(-Jvt^2). \qquad (1)$$

In real materials, kink motion is affected by defects because of the one-dimensional nature of quasiparticles (in the one-dimensional case, quasiparticles cannot go around a barrier). A well-known example of the anom-

---

[1] *e-mail: petukhov@ns.crys.ras.ru*

alous behavior of a one-dimensional particle in random potentials is the quantum localization of such particles [6]. In [7], a specific classical analogue of this phenomenon was predicted—with a decrease of the driving force F, a particle should demonstrate the anomalous drift:

$$x(t) \sim t^{\delta(F)} \quad (\delta(F) < 1). \tag{2}$$

In the presence of a broad spectrum of random barriers and at $F = 0$, the particle should undergo anomalous diffusion [8]

$$x(t) \sim \ln^2(t). \tag{3}$$

There are numerous review articles to this effect [9–11]. This phenomenon is also known as “quasilocalization” [9], nonlinear drift in a “field of a random force” [10, 12], the motion in the “creep phase” [13], and the “heterogeneous dynamics” [14]. Recently, the anomalous drift of dislocation kinks was observed in experiments on the dislocation mobility in Ge [15].

We aimed to study the effect of point defects on the switching kinetics in linear systems. Randomly arranged point defects and their accumulations create a spectrum of random barriers that decelerate the kink motion and change the characteristics of the switching process. The calculation of these characteristics requires the further development of the probabilistic approach to the description of the statistical process of multiple formation and merge of nuclei. This approach will allow, in particular, the study of the transition from the mode of the normal kink drift (the Kolmogorov case) to the anomalous drift with the corresponding change of the general kinetics of the global-state switching of the system. Because of the microscopic nature of the kinks, the study of the general kinetics of state switching is often the only possibility of obtaining the information on kink dynamics.

If the times of a free-kink motion between the barriers are short in comparison with the times of their pinning at the barriers, the kinetics can be considerably different. Below, we consider just this situation, and therefore the contribution of the free-drift time of the kink to the total time of kink motion can be ignored.

KINETICS OF STATE SWITCHING FOR AN ARBITRARY SPECTRUM OF THE KINK-MOTION BARRIERS

Consider the changes in the system state at a certain arbitrarily chosen point with time. It is convenient to divide the system into the intervals of length Δl comparable to the typical size of the barrier (the details will be considered later). A kink τ_i is characterized by the delay time characteristic of each interval, whereas the density of the delay-time distribution, $P(\tau)$, is assumed to be the same in all the intervals. The total delay time for a kink passed n intervals equals $T_n = \sum_{i=1}^{n} \tau_i$.

By the moment t, an arbitrarily chosen reference point will be in a new “switched” state if the boundary of a new state of the nucleus generated at a moment of time t' within a certain interval n has enough time to attain the point under consideration prior to the moment t, or, in other words, if the delay time T_n during the kink motion from the site of its generation to the point under consideration is shorter than $t - t'$. The probability of nucleus generation within the time interval $\Delta t'$ equals $J\Delta l^{(n)}\Delta t'$. The additional quantity $(1 - J\Delta l^{(n)}\Delta t')$ is the probability that, within the given length and time intervals, no nucleus is generated. The probability $q_n(t)$ that the nth interval would not be a source of the state switching at all equals the product of the probabilities that no nuclei would be generated in all the time intervals between the moments $t' = 0$ and $t' = t - T_n$, i.e.,

$$q_n(t) = \prod_{\alpha} (1 - J\Delta l^{(n)}\Delta t'_{\alpha}) \approx \exp(-J\Delta l^{(n)}(t - T_n)). \tag{4}$$

The total probability of the preservation of the initial state $Q(t)$ at the given point is the product of the probabilities that no nuclei appear in any intervals for which the time necessary for the kink to reach the chosen point is less than t. The sets of such intervals exist both on the left and on the right of the point under consideration. Since the barriers are independent, $Q(t)$ can be represented as the probability product, $Q(t) = q_0(t)Q^+(t)Q(t)$, where $q_0(t) = \exp(-J\Delta lt)$ is the probability that no nucleus can appear in the interval to which the point under consideration belongs. The probability $Q^+(t)$ that no nuclei appearing on one side of the point (e.g., only on the right-hand side) can change the state (and, in a similar way $Q^-(t)$) is a product of probabilities $q_n(t)$ (for all the intervals $\Delta l^{(n)}$ from unity to the maximum value N satisfying the condition $T_N < t < T_{N+1}$)

$$\begin{aligned} Q^+(t) &= \prod_{n=1}^{N} \exp(-J\Delta l(t - T_n)) \\ &= \exp\left(-J\Delta l\left(N(t - T_N) + \sum_{i=1}^{N} i\tau_i\right)\right). \end{aligned} \tag{5}$$

The exponent in Eq. (5) was transformed with due regard for the relationships

$$\begin{aligned} \sum_{n=1}^{N} T_N &= \sum_{n=1}^{N}\sum_{i=1}^{n} \tau_i = \sum_{i=1}^{N} (N - i)\tau_i \\ &= NT_N - \sum_{i=1}^{N} i\tau_i. \end{aligned} \tag{6}$$

The probability $Q^+(t)$, averaged over all the points of the system or, which is the same, over all the possible barrier positions and the equal value of the averaged probability $Q^{-}(t)$ are written in the form

$$\langle Q^{+}(t)\rangle = \langle Q^{-}(t)\rangle = \sum_{N=1}^{\infty}\int\prod_{m=1}^{N}P(\tau_m)d\tau_m Q^{+}(t)P_1(t-T_N). \tag{7}$$

Here, $P(\tau)d\tau$ is the probability that the delay time range within τ and $\tau + d\tau$. Integration is performed over all the τ_m whose sum is less than t and $P_1(t) = \int_t^{\infty}P(\tau)d\tau$ is the probability that the delay time would exceed t. By definition of N, the factor $P_1(t - T_N)$ takes into account the fact that the interval following the Nth interval will have the delay time, which, being added to T_N, would exceed t.

Now, calculate the characteristic function for $Q^{+}(t)$, which is the Laplace transform of $\langle Q^{+}(t)\rangle$:

$$\hat{Q}(s) = \int_0^{\infty}dte^{-st}\langle Q^{+}(t)\rangle dt = \int_0^{\infty}dte^{-st} \times \sum_{N=1}^{\infty}\int e^{-J\Delta lN(t-T_N)}P_1(t-T_N)\prod_{m=1}^{N}e^{-J\Delta lm\tau_m}P(\tau_m)d\tau_m. \tag{8}$$

Changing the integration order with respect to t, and the summation order with respect to N, we can calculate the integral over t with due regard for the condition $t > T_N$:

$$\int_{T_N}^{\infty}dte^{-(s+J\Delta lN)t+J\Delta lNT_N}P_1(t-T_N) = e^{-sT_N}\int_0^{\infty}dt'e^{-(s+J\Delta lN)t'}\int_{t'}^{\infty}P(\tau)d\tau = e^{-sT_N}(1-\hat{P}(s+J\Delta lN))/(s+J\Delta lN).$$

Here $\hat{P}(s)$ is the Laplace transform of $P(\tau)$, and $\hat{P}(s) = \int_0^{\infty}e^{-s\tau}P(\tau)d\tau$.

The remaining integral over $\{\tau_m\}$ is the product of integrals and can be readily expressed in terms of the product of the Laplace transforms $\hat{P}(s)$:

$$\hat{Q}(s) = \sum_{N=1}^{\infty}((1-\hat{P}(s+J\Delta lN))/(s+J\Delta lN)) \times \prod_{m=1}^{N}\hat{P}(s+J\Delta lm). \tag{9}$$

GAUSSIAN FIELD OF A RANDOM FORCE

A kink moves in a potential consisting of a randomly varying energy of the interactions between the system and defects, $U(x)$, during the change of the state within the length x, and a regular term $-Fx$ due to the driving force F. In the model under consideration, $U(x)$ is a random quantity performing "the Brownian motion" with the "diffusion coefficient" σ on the energy scale. The examples of the physical implementation of the model of a random potential, the so-called "field of a random force," are considered in [7–13]. Thus, for point defects randomly distributed in the system with the average linear density ρ, the change in the energy of their interaction with the system during its state switching is $\pm u$, $\sigma = \rho u^2$.

Consider a certain barrier formed by the peak of the potential $U(x)$, and calculate the delay time of a kink due to this potential. The kink can overcome the barrier due only to a favorable thermal fluctuation. The expectation time τ of such thermal activation is described by the formula [16, 17]

$$\tau = (\Delta l/D_k)\int_0^{\infty}e^{(U(x)-Fx)/kT}dx. \tag{10}$$

Here D_k is the diffusion coefficient of the kink and Δl is the characteristic dimension of the kink localization in front of the barrier determined by the length at which the potential is changed by a value of the order of the heat energy kT. We are not interested in the exact value of the preexponential factor in Eq. (10) and restrict ourselves to a mere estimation of Δl proceeding from the following simple considerations. The potential in Eq. (10) is a sum of an arbitrarily diffusing component of $U(x)$ whose typical amplitude increases with x as $(\sigma x)^{1/2}$ and a regular "drift term" Fx. At small lengths, the potential shows the "diffusion behavior," whereas at $x \sim x_{\mathrm{b}} = \sigma/F^2$, it behaves differently, and, at $x > x_{\mathrm{b}}$, the contribution of Fx starts prevailing. In the latter case, Δl is estimated from the relationship $F\Delta l \sim kT$ as $\Delta l \sim kT/F$. The condition of the applicability of this estimate is $\Delta l > x_{\mathrm{b}}$, i.e., $\delta = kTF/\sigma > 1$. In the other limiting case, $\delta < 1$, the value of Δl is estimated from the relationship $(\sigma\Delta l)^{1/2} \sim kT$ as $\Delta l \sim (kT)^2/\sigma$.

For the distribution function $P(\tau)$, the following relationship was obtained [7, 10]

$$P(\tau) = \frac{\exp(-1/(s_0\tau))}{\Gamma(\delta)s_0^{\delta}\tau^{\delta+1}}, \tag{11}$$

where $s_0 = \sigma D_k/((kT)^2\Delta l)$ and $\Gamma(\delta) = \int_0^{\infty}x^{\delta-1}e^{-x}dx$. The Laplace transform $P(\tau)$ is written as

$$\hat{P}(s) = (2/\Gamma(\delta))(s/s_0)^{\delta/2}K_{\delta}(2(s/s_0)^{1/2}). \tag{12}$$

Here $K_{\delta}(x)$ is Macdonald's function [18]. To calculate the product in (9), one has to know the behavior of $\hat{P}(s)$

at small values of the argument. Using the expansion of K_δ, we obtain

$$\hat{P}(s) \approx 1 + s/(s_0(1-\delta)) - (s/s_0)^{\delta}\frac{\Gamma(1-\delta)}{\Gamma(1+\delta)}. \qquad (13)$$

We retain two s-dependent terms of the expansion, because we are also interested in the region $\delta \sim 1$, where the contributions of these terms are competing. Using the above formula, we obtain

$$\prod_{m=1}^{N}\hat{P}(s + J\Delta lm) \approx \exp\left\{\int_0^N dm \ln \hat{P}(s + J\Delta lm)\right\}$$

$$= \exp\left\{-\frac{\lambda}{\varepsilon}\left(\frac{s}{J\Delta l}N + \frac{1}{2}N^2\right) + \frac{\lambda^{\delta}}{\varepsilon}\frac{\Gamma(2-\delta)}{\Gamma(2+\delta)}\right. \qquad (14)$$

$$\left.\times\left[\left(\frac{s}{J\Delta l} + N\right)^{\delta+1} - \left(\frac{s}{J\Delta l}\right)^{\delta+1}\right]\right\}.$$

Here $\lambda = J\Delta l/s_0$ and $\varepsilon = \delta - 1$. The parameter $\lambda = J\Delta l/s_0$, determined by the probability of generation of a nucleus within one microscopic interval Δl for the time $1/s_0$, is assumed to be small. The switching time is determined by the generation of nuclei at system portions large compared to Δl. Thus, only large N-values are important in the sum of Eq. (9), and therefore the summation over m in Eq. (14) can be substituted by integration. Moreover, in the same approximation, we have

$$\frac{1-\hat{P}(s+J\Delta lN)}{s+J\Delta lN} \approx \frac{1}{s_0\varepsilon}\left[1-\left(\frac{s+J\Delta lN}{s_0}\right)^{\varepsilon}\frac{\Gamma(2-\delta)}{\Gamma(1+\delta)}\right]. \qquad (15)$$

Consider the case of high ($\delta > 1$) and low ($\delta < 1$) values of the driving force.

1. The case $\delta > 1$. The last term in expansion (13) can be ignored everywhere with the exception of a narrow neighborhood of small ε (which deserves a special consideration). Thus, we have

$$\hat{Q}(s) \approx \sum_{N=1}^{\infty}\frac{1}{s_0\varepsilon}\exp\left\{-\frac{\lambda}{2\varepsilon}\left(\frac{s}{J\Delta l} + N\right)^2 + \frac{\lambda}{2\varepsilon}\left(\frac{s}{J\Delta l}\right)^2\right\} \qquad (16)$$

$$\approx \frac{1}{s_0}\sqrt{\frac{\pi}{2\lambda\varepsilon}}\exp\left(\frac{\lambda}{2\varepsilon}\left(\frac{s}{J\Delta l}\right)^2\right)\operatorname{erfc}\left(\sqrt{\frac{\lambda}{2\varepsilon}}\frac{s}{J\Delta l}\right).$$

The inverse Laplace transformation yields [19]

$$\langle Q^{\pm}(t)\rangle = \exp\left(-\frac{\varepsilon}{2}s_0 J\Delta l t^2\right). \qquad (17)$$

At $\Delta l = kT/F$, the above expression can be written as $\langle Q^{\pm}(t)\rangle = \exp\{-(1/2)(1 - 1/\delta)v_0 Jt^2\}$, where $v_0 = D_k F/(kT)$ is the velocity of the free kink drift. Thus, if $\delta \gg 1$ (the effect of a random energy addition to the potential in which the kink moves is negligible), the expression obtained is consistent with Kolmogorov formula (1). (We should like to remind that $\langle Q(t)\rangle = \langle q_0(t)Q^{+}(t)Q^{-}(t)\rangle$). In this case, the switching time is short in comparison with the time of nucleus formation within one interval, and therefore, $q_0(t) \approx 1$ and $\langle Q(t)\rangle \approx \langle Q^{\pm}(t)\rangle^2$. At $\delta \sim 1$, the formula has the same form as the Kolmogorov formula, but the kink velocity is renormalized, $v = (1 - 1/\delta)v_0$. The procedure of averaging the fraction of the initial state over the barrier spectrum reduces to the simple substitution of the kink velocity by its average value.

Thus, in this range of parameters, the kink deceleration by random barriers results in a reduction of the average kink velocity, and the dependence of the kink velocity on the driving force acquires a certain threshold. This process is accompanied by a noticeable deceleration of the switching process (Fig. 1). At a certain critical value of the driving force, $F = F_c$, determined by the condition $\delta(F_c) = 1$, the average kink velocity goes to zero, and the character of the kink motion is changed. The region under the driving-force threshold requires special consideration.

2. The case $\delta < 1$. In this case, the major contribution to $\hat{Q}(s)$ comes from the third term of (13). Then

$$\hat{Q}(s) = t_a \exp\left((st_a)^{1+\delta}\right)\Gamma\left(\frac{\delta}{1+\delta}, (st_a)^{1+\delta}\right), \qquad (18)$$

where

$$t_a = \frac{1}{s_0}\left[\frac{\Gamma(2-\delta)}{\Gamma(2+\delta)\lambda(1-\delta)}\right]^{\frac{1}{1+\delta}}, \quad \Gamma(a, z) = \int_z^{\infty} x^{a-1}e^{-x}dx.$$

At $\delta \longrightarrow 1$, expression (18), with due regard for the relationship $\Gamma(1/2, x^2) = (\pi)^{1/2}\operatorname{erfc}(x)$, acquires functional form Eq. (16), and the inverse Laplace transformation leads to the Kolmogorov dependence $\langle Q(t)\rangle = \exp(-\text{const}\cdot t^2)$, but with the coefficient in the exponent differing from that in the case $\varepsilon > 0$ (17). The cause of such a jump will be discussed later.

As is seen from Eq. (18), the dependence of the averaged switching kinetics on the parameter λ enters only the scale factor t_a. The same will also be true upon the inverse Laplace transformation $\langle Q^{\pm}(t)\rangle = f_\delta(t/t_a)$, where $f_\delta(x)$ is the function dependent on the parameter δ alone. Using the asymptotic expansion of $\hat{Q}(s)$ Eq. (18) at high and low s values, one can readily obtain the explicit analytical expression for $f_\delta(x)$ at high and low values of the argument

$$f_\delta(x) \approx \frac{1+\delta}{\Gamma(1-\delta)}x^{-(1+\delta)}, \quad x \longrightarrow \infty, \qquad (19)$$

$$f_\delta(x) \approx 1 - \frac{1}{(1+\delta)\Gamma(2+\delta)}x^{1+\delta}, \quad x \longrightarrow 0. \qquad (20)$$

Formulas (19) and (20) provide a sufficiently complete description of the kinetics of the state switching for a linear system characterized by the average frac-

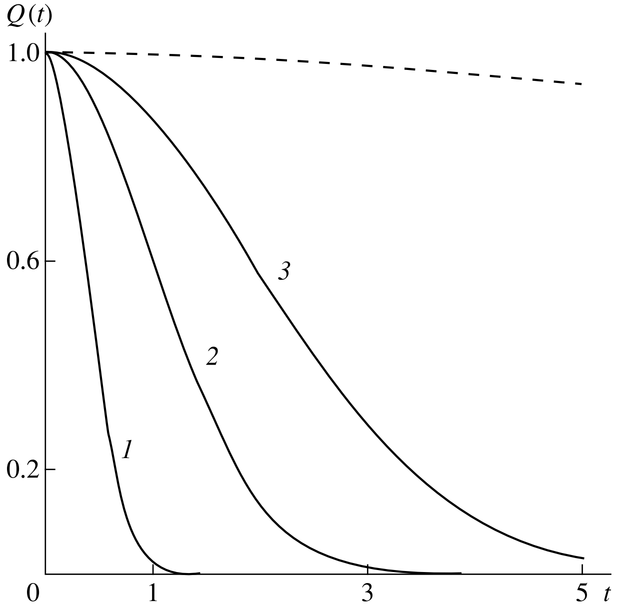

Fig. 1. Decrease of the initial state fraction $Q(t)$, with time at various values of the driving force $F > F_c$ characterized by the parameter $\delta = kTF/\sigma$. δ = (*1*) 5, (*2*) 1.5, (*3*) 1.1. Time is measured in the $1/(s_0(\lambda)^{1/2})$ units. For comparison, the dashed line shows the switching kinetics at $\delta = 0.8$ ($F < F_c$).

tion of the initial state $\langle Q(t)\rangle = \exp(-J\Delta lt)\langle Q^{\pm}(t)\rangle^2$. The behavior of such a system is illustrated by Fig. 2 (with the use of the numerical calculation at the intermediate $t \sim t_a$ values).

With a decrease of δ to values lower than unity, the switching process is decelerated. At high t values, the exponential dependence of Kolmogorov type (1) is changed to power dependence of type (19).

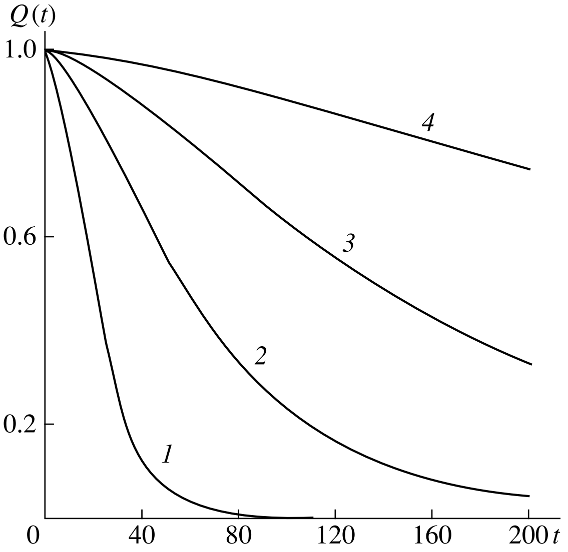

Fig. 2. Switching kinetics at the prethreshold value of the driving force. δ = (*1*) 0.8, (*2*) 0.6, (*3*) 0.5, and (*4*) 0.4. Time is measured in the $1/(s_0(\lambda)^{1/2})$ units; $\ln(1/\lambda) = 25$.

The case of an extremely strong effect of a random field $\delta \longrightarrow 0$ deserves special consideration. At $\delta \ll 1$, the quantity $\hat{Q}(s)$ (18) is transformed to the form

$$\hat{Q}(s) \approx \frac{1}{s\lambda}\exp\left(\frac{s}{J\Delta l}\right)E_1\left(\frac{s}{J\Delta l}\right), \tag{21}$$

where $E_1(x) = \int_x^{\infty} e^{-t}\frac{dt}{t}$ and the inverse Laplace transformation yields [19]

$$\langle Q^{\pm}(t)\rangle = \frac{1}{1 + J\Delta lt}. \tag{22}$$

As is seen from (22), the characteristic switching time in this particular case becomes comparable with the generation time of the nucleus of a new state, within the minimum length interval $t_0 = 1/(J\Delta l)$. At large δ-values, the switching time is much shorter than t_0 and is determined mainly by "sweeping" of a new state with the boundaries of nuclei generated far from the point under consideration. In this instance, the characteristic switching time is equal to the average switching time.

SWITCHING TIME

An important integral characteristic of the kinetics of system-state change is the average switching time determined by the formula

$$\langle t\rangle = \int_0^{\infty}\langle Q(t)\rangle dt. \tag{23}$$

At $\delta > 1$, the use of the explicit form of $\langle Q(t)\rangle$ (17)

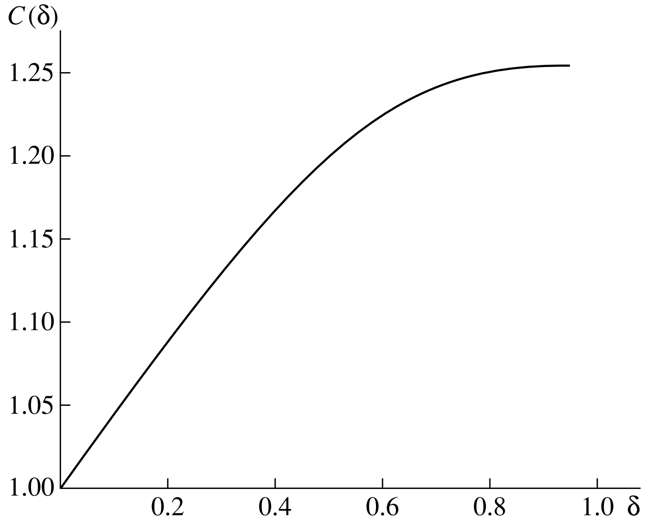

Fig. 3. Normalization factor for the average time $\langle t\rangle$ of state switching described by (25) for $0 < \delta < 1$.

yields

$$\langle t\rangle = \int_0^\infty e^{-J\nu t^2}dt = \frac{1}{2}\left(\frac{\pi}{J\nu}\right)^{1/2}. \qquad (24)$$

At $\delta < 1$, the dependence of the average time on t_a can also be obtained in the explicit form with the aid of the scale analysis

$$\langle t\rangle = C(\delta)t_a = C(\delta)\frac{1}{s_0}\left[\frac{\Gamma(2-\delta)}{\Gamma(2+\delta)\lambda(1-\delta)}\right]^{\frac{1}{1+\delta}}, \qquad (25)$$

where $C(\delta) = \int_0^\infty f_\delta^2(x)dx$. The numerical calculation shows (Fig. 3) that C depends on δ and varies within a narrow range of the values from unity to $(\pi/2)^{1/2}$ at the δ varying from 0 to 1.

Of a certain interest is also the average time of the "one-sided sweep" of the reference point by the boundaries of the nuclei t_1 formed on one side of this point

$$t_1 = \int_0^\infty \langle Q^\pm\rangle dt = \hat{Q}(s = 0). \qquad (26)$$

It is seen from Eq. (18) that if $\delta < 1$, then $t_1 = \Gamma(\delta/(1 + \delta))t_a$. The Gaussian form of $\langle Q(t)\rangle$ at $\delta \longrightarrow 1$ yields

$$\langle t\rangle = t_1/\sqrt{2} = \sqrt{2}\hat{Q}(s = 0). \qquad (27)$$

With the use of general formulas (13)–(15) that yield $\hat{Q}(s)$ at both $\delta > 1$ and $\delta < 1$, relationship (27) provides a more accurate description of the transitional region $\delta \longrightarrow 1$. For $\varepsilon \ll 1$, we have

$$\begin{aligned}\langle t\rangle &= \frac{1}{\sqrt{2}s_0\lambda\varepsilon}\int_0^\infty dz(1-z^\varepsilon)\exp\left(-\frac{z^2}{2\lambda\varepsilon}(1-z^\varepsilon)\right) \\ &\approx \left(\frac{1}{s_0}\right)\left(\frac{\pi(1-\lambda^{\varepsilon/2})}{4\lambda\varepsilon}\right)^{1/2}.\end{aligned} \qquad (28)$$

The above equation describes the continuous transition from the region $\varepsilon > 0$ to the region $\varepsilon < 0$, i.e., provides the smooth transformation of Eq. (24) into (25). Eq. (28) shows that the dependence of the average switching time on the driving force is considerably changed in the vicinity of $\delta = 1$, and, at $\varepsilon < 0$, $|\varepsilon| > 1/\ln(1/\lambda)$, we arrive at the exponential increase of $\langle t\rangle$ with ε, namely, $\langle t\rangle \sim 1/\lambda^{\varepsilon/4} = \exp(|\varepsilon|)\ln(1/\lambda)/4)$. The dimension of the transitional region can be estimated as $\Delta|\varepsilon| \sim 2/\ln(1/\lambda)$, i.e., the transitional region is quite narrow.

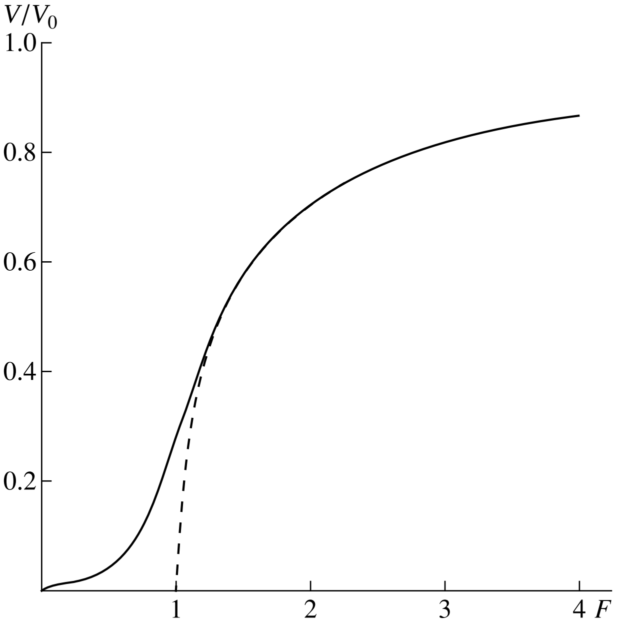

Fig. 4. Dependence of the state-switching rate $V \sim 1/\langle t\rangle$ on the driving force F in the anomalous region, $F \sim F_c$. The rate V is normalized to V_0 (the switching rate in the absence of decelerating barriers); F is measured in the σ/kT units.

In the problems of step, domain boundary, and dislocation motion, where, in the absence of the driving force, the system state is multiply degenerate with the period equal to the crystal-lattice parameter a, the quantity $\langle t\rangle$ determines the characteristic time necessary for the system displacement for one period. This allows one to estimate the rate V of the system "translation" while considering with the "switching on" of the driving force

$$V \sim a/\langle t\rangle. \qquad (29)$$

Figure 4 illustrates the dependence of the translation rate of the system on the driving force in the transitional region $F \sim F_c$. This dependence is characterized by a smooth threshold.

CONCLUSION

Thus, it was shown that the process of state switching in a disordered linear system shows considerable changes at certain critical values of the driving force $F = F_c$. At $F > F_c$, the process can be described by the Kolmogorov kinetics with the renormalized kink velocity $v = (1 - 1/\delta)v_0$ (compared to that of the free kink drift). The formula containing a "threshold term," $1 - 1/\delta(F)$, shows that the character of the kink motion is changed with a decrease of δ down to unity with the corresponding changes of the problem parameters, e.g., of F. It was established [7] that this is associated with the fact that the average time necessary for a kink to overcome a barrier, $\langle\tau\rangle = \int_0^\infty \tau P(\tau)d\tau$, tends to infinity, because of a slow decrease of the distribution function $P(\tau)$ for large τ at $\delta \le 1$. As a result, the kink deceleration is determined not by all the barriers, but mainly by the highest ones encountered at the kink path with the probability of the order of unity (the heterogeneous deceleration). Therefore, the temporal variation in the kink paths with time can be determined from the relationship $(x(t)/\Delta l)P_1(t) \sim 1$, whence, in accordance with (11), it follows that at large t, we have $x(t) \sim t^{\delta}(\delta \le 1)$ [i.e., (2)].

To avoid any misunderstanding, we should like to emphasize the probabilistic character of the so-called law of nonlinear drift. Thus, trying to generalize the Kolmogorov formula (1) by the changing the law of linear drift $x(t) = vt$ by relationship (2), one arrives at $Q(t) = \exp(-\mathrm{const}\, t^{1+\delta})$ inconsistent with a more rigorous calculation (see formula (19)). This indicates a considerable contribution to the switching kinetics of fluctuations in the distribution of the barriers decelerating the kinks. Therefore, statistical fluctuations present in the barrier distribution should rigorously be taken into account when calculating switching kinetics.

Thus, the calculation of the kinetics of state switching for a disordered linear system provided the establishment of the transition from the exponential Kolmogorov-type kinetics to the diffuse kinetics with the asymptotic power behavior at the late stages of the process. This transition is caused by the changes in the kink–soliton motion from the homogeneous (on the average) drift, with a finite velocity to the heterogeneous deceleration by the highest barriers on the kink paths. The dependence of the average state switching rate, $V \sim 1/\langle t \rangle$, on the driving force F is obtained. At $F > F_c$, this dependence is characterized by a certain threshold. In the narrow vicinity of F_c, the threshold becomes rather smooth, and, at $F < F_c$, the rate V exponentially decreases with a decrease of the driving force. Such behavior qualitatively agrees with the experimentally observed dislocation mobility in Ge crystals [20].

ACKNOWLEDGMENTS

This study was supported by the INTAS, project no. 96-363.

REFERENCES

1. I. F. Lyuksyutov and V. L. Pokrovskiĭ, Pis'ma Zh. Éksp. Teor. Fiz. **33**, 343 (1981) [JETP Lett. **33**, 326 (1981)].
2. A. A. Chernov, Usp. Fiz. Nauk **73**, 277 (1961).
3. J. P. Hirth and J. Lothe, *Theory of Dislocations* (McGraw-Hill, New York, 1967; Atomizdat, Moscow, 1972).
4. A. N. Kolmogorov, Izv. Akad. Nauk SSSR, Ser. Mat., No. 3, 355 (1937).
5. R. K. Dodd, J. C. Eilbeck, J. Gibbon, and H. C. Morris, *Solitons and Nonlinear Wave Equations* (Academic Press, New York, 1982; Mir, Moscow, 1988).
6. N. F. Mott and W. D. Twose, Adv. Phys. **10**, 1492 (1961).
7. B. V. Petukhov, Fiz. Tverd. Tela **13**, 1445 (1971) [Sov. Phys. Solid State **13**, 1204 (1971)].
8. Ya. G. Sinaĭ, Teor. Veroyatn. Primen. **28**, 247 (1982).
9. S. Alexander, J. Bernasconi, W. R. Schneider, and R. Orbach, Rev. Mod. Phys. **53**, 175 (1981).
10. J.-P. Bouchaud and A. Georges, Phys. Rep. **195**, 127 (1990).
11. J. W. Haus and K. W. Kerr, Phys. Rep. **150**, 263 (1987).
12. V. M. Vinokur, J. Phys. (Paris) **47**, 1425 (1986).
13. J.-P. Bouchaud and A. Georges, Comments Condens. Matter Phys. **15**, 125 (1991).
14. B. V. Petukhov, Fiz. Tverd. Tela **35**, 1121 (1993) [Phys. Solid State **35**, 571 (1993)].
15. Yu. L. Iunin, V. I. Nikitenko, V. I. Orlov, and B. V. Petukhov, Phys. Rev. Lett. **78**, 3137 (1997).
16. A. P. Kazantsev and V. L. Pokrovskiĭ, Zh. Éksp. Teor. Fiz. **58**, 677 (1970) [Sov. Phys. JETP **31**, 362 (1970)].
17. N. G. van Kampen, *Stochastic Processes in Physics and Chemistry* (North Holland, Amsterdam, 1981).
18. *Handbook of Mathematical Functions*, Ed. by M. Abramowitz and I. A. Stegun (Dover, New York, 1965; Nauka, Moscow, 1979).
19. *Higher Transcendental Functions (Bateman Manuscript Project)*, Ed. by H. Bateman and A. Erdelyi (McGraw-Hill, New York, 1953; Nauka, Moscow, 1969).
20. Yu. L. Iunin, V. I. Nikitenko, V. I. Orlov, and B. Ya. Farber, Fiz. Tverd. Tela **33**, 1262 (1991) [Sov. Phys. Solid State **33**, 715 (1991)].

Translated by L. Man

Crystallography Reports, Vol. 45, No. 4, 2000, pp. 647–649. Translated from Kristallografiya, Vol. 45, No. 4, 2000, pp. 707–709.
Original Russian Text Copyright © 2000 by Katkova, Nosov, Chuprunov, Belokoneva.

Pseudosymmetry and Ferroelectric Phase Transitions in the KTP Structure Type

M. R. Katkova*, S. S. Nosov*, E. V. Chuprunov*, and E. L. Belokoneva**

** Nizhniĭ Novgorod State University, pr. Gagarina 23, Nizhniĭ Novgorod, 603600 Russia*
*** Faculty of Geology, Moscow State University, Vorob'evy gory, Moscow, 119899 Russia*[1]

Received October 13, 1998

Abstract—The characteristic pseudosymmetry observed in the crystal structures of $KTiOPO_4$-type ferroelectrics have been analyzed. The low-symmetry phases of all the crystals under consideration are characterized by a pronounced pseudosymmetry. The transition temperature monotonically decreases with an increase of the pseudosymmetry parameter of the crystal structure of the ferroelectric phase. The approach suggested to evaluate the transition temperature is more precise and universal than the Abrahams–Jamieson–Kurtz criterion. *© 2000 MAIK "Nauka/Interperiodica".*

INTRODUCTION

The establishment of the relationship between the atomic structure of a crystal and its physical properties involves the determination of integrated geometric parameters of the atomic structure, determining some properties of the crystal, and the examination of the mechanism of this effect. One of the integrated geometric parameters is symmetry, i.e., the invariance of the atomic structure with respect to a particular group of isometric transformations. Symmetry determines a possible spectrum of physical properties of the crystal, irrespectively of its chemical composition, with the symmetry group determining only some necessary conditions providing the manifestation of different properties. In the search for the geometric parameters that influence physical properties of the crystal but do not depend on the chemical composition, it is reasonable to analyze fine features of the symmetry of the crystal structure. One of such features is the Fedorov pseudosymmetry, i.e., the invariance of a substantial portion of the electron density with respect to a particular space supergroup of the symmetry group of the crystal [1]. In pseudosymmetrical crystals, the specific structural features manifest themselves as symmetrical characteristics, which allows one to analyze them and their effect on the physical properties by the group-theoretical and crystallophysical methods.

RESULTS AND DISCUSSION

Consider the role of Fedorov pseudosymmetry in the description of second-order structural phase transitions in crystals. It is well known [2] that such phase transitions can be characterized by a scalar, a vector, or a tensor quantity, continuously varying in the course of the phase transition and describing the distortion of the structure of a high-symmetry phase. This quantity, or the so-called order parameter, also characterizes the change in the symmetry in the course of the phase transition. Generally, the order parameter is determined by the displacements of a relatively small number of atoms in the crystal unit cell [2]. This signifies that a rather large number of atoms are still related by the symmetry operations of the highly symmetric phase, whereas the structure as a whole is invariant only with respect to the symmetry group of the low symmetric phase.

Comparing the electron densities of the highly and low symmetric structures, one can state that a substantial portion of the electron density remains undistorted and is described by the symmetry group of the highly symmetric phase. The use of a quantitative parameter relating the symmetrical and the asymmetrical portions of the electron density allows one to evaluate the order parameter irrespectively of its form—scalar, vector, or tensor—and thus describe the degree of structure distortion in the course of the phase transition. On the other hand, it is evident that the transition to the phase with a symmetry described by the supergroup of the space group of the initial phase, which is accompanied by small structural distortions, can occur only if a considerable portion of the electron density of the initial phase obeys the symmetry of the highly symmetric phase, i.e., if it is pseudosymmetrical.

One can use as the quantitative structural characteristic of the crystal pseudosymmetry the following functional proposed in [3]:

$$\eta_{\mathbf{t}}[\rho(\mathbf{x})] = \int\limits_V \rho(\mathbf{x})\rho(\mathbf{tx})dV \Big/ \int\limits_V \rho^2(\mathbf{x})dV,$$

where $\rho(\mathbf{x})$ is the function of the electron density in the crystal, and $\mathbf{t}$ is the symmetry operation, which belongs to the symmetry group of the high-symmetry phase and is absent in the symmetry group of the low-symmetry phase.

---

[1] *e-mail: elbel@geol.msu.ru*

If $\rho(\mathbf{x})$ is fully invariant with respect to the operation $\mathbf{t}$, then $\eta_{\mathbf{t}}[\rho(\mathbf{x})] = 1$. If $\eta_{\mathbf{t}}[\rho(\mathbf{x})] = 0$, then $\rho(\mathbf{x})$ is fully asymmetric with respect to the $\mathbf{t}$ operation.

This approach was applied to the analysis of the 25 best studied pyroelectric crystals (tourmaline, barium and lead titanates, $Li_2B_4O_7$, etc.) [4]. It was shown that on the constructed diagram most of these crystals are located in the vicinity of the pseudosymmetry region (0.9–1.0).

We studied the pseudosymmetry of the atomic structures on the $KTiOPO_4$-type (KTP) crystals. The $KTiOPO_4$ crystals are essentially nonlinear-optical material widely used in practice in recent years. All crystals of this structure type are characterized by the temperature-induced second-order ferroelectric phase transition, which proceeds with the change of the polar space group $Pna2_1$ to a nonpolar space group.

The determination of the pseudosymmetry crystal structure of the initial ferroelectric phase, the space group of the paraphase (*Pnan*), and the symmetries of all the atomic positions were first reported in [5, 6]. The mixed framework formed by P-tetrahedra and Ti-octahedra in the ferroelectric phase was successfully described by the above-mentioned supergroup with the only exception—the K(1) and K(2) atoms did not obey this symmetry. The pseudopositions of the K(I) and K(II) atoms, related to the initial positions either by a twofold pseudosymmetry axis parallel to the *b*-axis or by the pseudoplane *n* perpendicular to the *c*-axis shown in the polyhedra, are shown in the figure published in [5]. It is obvious that K cations undergo considerable displacements and, to a great extent, are responsible for the phase transition to the high-temperature modification.

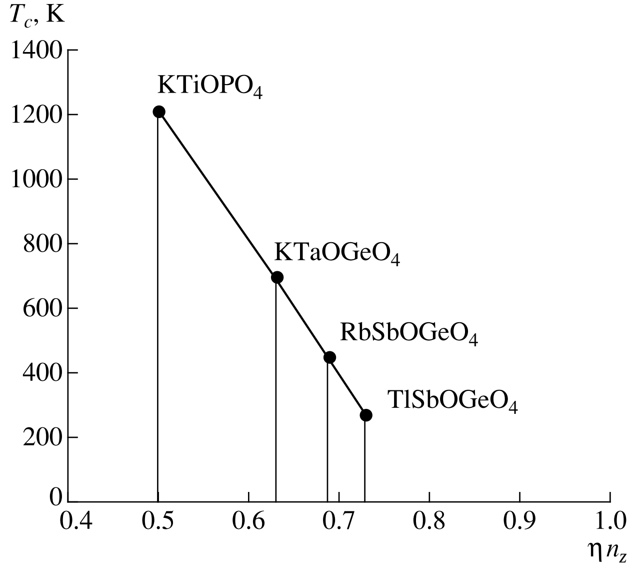

Temperature of the phase transition in KTP-type crystals as a function of the degree of pseudosymmetry with respect to the glide symmetry plane n_z.

The paraphase of $TlTiOPO_4$ was first studied in [7], where it was concluded that the second-order phase transition is of the displacive type. The splitting of one Tl-position (instead of two positions in the space group with a higher symmetry) was not established owing to poor quality of the experimental data. The splitting of the K positions in the high-temperature $KTiOPO_4$ modification studied in [8] was not examined at all, although the pronounced anisotropy of thermal vibrations of cations along the *c*-axis was revealed in both cited structure refinements. However, such splitting was established for the $TlSbOGeO_4$ structure that possessed the parastate ($T_c = 292$ K) even at room temperature [9].

The detailed studies of phase transitions in germanates, (KTP analogues) [10] demonstrated that the phase transitions are of dual nature,—they demonstrate both displacive and order–disorder transitions, because the positions of large cations in all the high-temperature phases appeared to be split. The distances between these positions in the series of $TlSbOGeO_4$, $RbSbOGeO_4$, and $KTaOGeO_4$ increase from 0.56 Å for Tl to 0.71 and 0.99 Å for Rb and K, respectively. The transition temperatures increase from 272 to 700 K in parallel with an increase in the above-mentioned distances, which is associated with the degree of pseudosymmetry in the crystal structure. The larger the displacements in the course of the phase transition to the ferroelectric phase, the more pronounced the distances between the split positions in the high-temperature phase and the higher the transition temperatures [10]. The $TlSbOGeO_4$ crystal structure, which possesses the lowest transition point among all the crystals considered above, is characterized by the smallest atomic displacements in the ferroelectric phase compared to those in the high-temperature phase and by the least marked splitting of the cationic positions in the high-symmetry phase. The ferroelectric low-temperature phase of this compound exhibits the most pronounced pseudosymmetry of all the three compounds considered above.

It is of interest to evaluate the degree of pseudosymmetry in the KTP-type crystal structures with the polar phase, with respect to the glide plane *n* perpendicular to the *c*-axis at $z = 0.5$. We calculated the degree of pseudosymmetry using the results of X-ray diffraction studies of four compounds—$TlSbOGeO_4$, $RbSbOGeO_4$, $KTaOGeO_4$, and $KTiOPO_4$—whose Curie points lie within the temperature range of 272–1207 K [6, 9, 11].

The calculations performed by the above equation demonstrated that the degree of pseudosymmetry is 0.73, 0.69, 0.63, and 0.50 for $TlSbOGeO_4$ ($T_c = 272$ K), $RbSbOGeO_4$ ($T_c = 450$ K), $KTaOGeO_4$ ($T_c = 700$ K), and $KTiOPO_4$ ($T_c = 1207$ K), respectively.

Figure illustrates the relationship between the above values and the transition temperature. The energy spent in distorting the crystal structure linearly depends on the parameter describing this distortion. The smaller the distortion of the low-symmetry phase compared with the high-symmetry phase, the lower the energy spent for displacing the atoms in the course of the phase transition. This fact agrees with the assumptions [12] about the relationships between the low T_c values and the pronounced pseudosymmetry in the series of germanate analogues of KTP crystals.

CONCLUSIONS

In 1968, Abrahams suggested evaluating the relation between the transition temperature (Curie point T_c) and the atomic displacements by the following equation: $T_c = (K/2k)(\Delta z)^2$ K, where K is the force constant, k is the Boltzmann constant, and Δz is the value characterizing the atomic displacements along the direction of spontaneous polarization [13]. In this case, the temperature is given in Kelvins. However, it is evident that the atomic displacements responsible for the phase transition (for germanate analogs of KTP, the displacements of large cations differ by an order of magnitude from those of the cations located in the octahedra [10]), cannot occur only along one axis. Also, the structure as a whole is distorted, which is difficult to take into account within this approach. The attempts to calculate the group displacements encounter the difficulty in the choice of the coordinate origin. Algorithm (1) proposed in this work is free from the above-mentioned drawbacks. The approach developed is universal and provides a rigorous solution of the problem. Moreover, the fact that the phase transitions considered are not a pure displacive type (as is implied by the Abrahams algorithm) but are dual natured, does not complicate the solution of the problem with the use of the algorithm suggested in the present study.

Therefore, the example of the KTP crystals shows that the pseudosymmetry of the crystal structures in the low-symmetry phase is a necessary condition for the occurrence of the second-order phase transitions. It was also shown that functionals of type (1) can successfully be used for the evaluation of structural distortions (the order parameters) observed in the course of phase transitions.

REFERENCES

1. M. R. Katkova, N. Yu. Novikova, M. A. Faddeev, and E. V. Chuprunov, Kristallografiya **43** (1), 9 (1998) [Crystallogr. Rep. **43** (1), 5 (1998)].
2. V. A. Strukov and A. P. Levanyuk, in *Physical Grounds of Ferroelectric Phenomena in Crystals* (Fizmatgiz, Moscow, 1983).
3. E. V. Chuprunov, E. A. Soldatov, and T. N. Tarkhova, Kristallografiya **33** (3), 759 (1988) [Sov. Phys. Crystallogr. **33** (3), 446 (1988)].
4. V. A. Ivanov, M. A. Faddeev, and M. A. Chuprunov, in *XVI Scientific Readings in Memory of Academician N.V. Belov. Collected Abstracts* (Nizhniĭ Novgorod, 1997), p. 90.
5. E. L. Belokoneva, O. V. Yakubovich, V. G. Tsirel'son, and V. S. Urusov, Izv. Akad. Nauk SSSR, Neorg. Mater. **26**, 595 (1990).
6. P. A. Thomas, A. M. Glaser, and B. E. Watts, Acta Crystallogr., Sect. B: Struct. Sci. **46**, 333 (1990).
7. W. T. A. Harrison, T. E. Gier, G. D. Stuky, and A. J. Schulz, J. Chem. Soc. Chem. Commun., No. 4, 540 (1990).
8. J. A. Kaduk, J. Faber, S. Pei, and R. H. Jahrman, in *Collected Abstract of the ACA Meeting, Atlanta, 1994*, PIN27, p. 141.
9. E. L. Belokoneva and B. V. Mill', Zh. Neorg. Khim. **37**, 252 (1992).
10. E. L. Belokoneva, K. S. Knight, W. I. David, and B. V. Mill, J. Phys.: Condens. Matter, No. 9, 3833 (1997).
11. E. L. Belokoneva and B. V. Mill', Zh. Neorg. Khim. **37**, 998 (1992).
12. E. L. Belokoneva, Usp. Khim. **63**, 559 (1994).
13. S. Abrahams, Acta Crystallogr., Sect. A: Fundam. Crystallogr. **50**, 658 (1994).

Translated by T. Safonova

Crystallography Reports, Vol. 45, No. 4, 2000, pp. 650–654. Translated from Kristallografiya, Vol. 45, No. 4, 2000, pp. 710–714.
Original Russian Text Copyright © 2000 by Stupina, Katsnelson.

Effects of Structure Instability of a V_3Si Single Crystal from X-ray Scattering Data

N. N. Stupina and A. A. Katsnelson
Moscow State University, Vorob'evy gory, Moscow, 119899 Russia

Received February 9, 1999

Abstract—Diffuse X-ray scattering from a V_3Si single crystal was studied at room temperature. It was demonstrated that the structure possesses instability regions associated with the formation of a new phase. The characteristic features of the q dependence of diffuse scattering are indicative of the presence of two-types of domains—those randomly distributed over the crystal and those forming a spatially periodic distribution. *© 2000 MAIK "Nauka/Interperiodica".*

INTRODUCTION

The V_3Si compound belongs to crystals characterized by the lattice instability. The instability manifested itself as a rather weak martensite transformation from the cubic to the tetragonal system at $T \approx 27$ K [1]. Below this temperature, a gradual increase in the parameter $c \cong 4.7185$ Å is observed, being especially fast at $T \approx 21$ K. The saturation was attained for $c_{\max} \approx 4.7258$ Å at about $T_c \approx 17$ K (the temperature of the superconducting transition). The parameter a slightly decreased. In the tetragonal phase, we have $(c/a)_{\max} = 1.0024 \pm 0.0002$ at $a_{\min} \cong 4.7145$ Å and $a/b = 1.0 \pm 0.00006$ (Figs. 6, 8 in [1]). Upon transformation from the cubic to the tetragonal system, the single-crystal structure of the sample is not retained, instead a twin domain structure is formed.

Above the phase transition point, V_3Si crystals strongly exhibit a temperature dependence of magnetic susceptibility up to room temperature [2]. The character of this dependence in the vicinity of room temperature is similar to that observed for systems containing localized electrons with the uncompensated magnetic moment. The physical nature of this unusual situation is, most likely, associated with defects in the real structure of this compound. In this connection, this work aimed to obtain experimental data necessary for making conclusions about the mutual arrangement of these defects, their size, shape, and symmetry.

This work is the second part of a combined X-ray diffraction study of the decrease in the intensity of diffraction maxima I_1 and the intensity distribution of X-ray diffuse scattering I_2 from a V_3Si single crystal at 300 K. In the first part of our investigations [3], we showed that this crystal is characterized by partly ordered defects of different types, giving rise to oriented displacement fields. According to the $\Gamma_{15(+)}$ and $\Gamma_{12(+)}$ irreducible representations of the cubic group, which were found in [3], the displacements of the V atoms from their ideal positions in the unit cell may be associated with pronounced antiphase fluctuations.

The above effects noticeably change the diffuse scattering pattern. The study of this pattern makes it possible to reveal characteristic signs of lattice instability.

EXPERIMENTAL AND DATA ANALYSIS

Measurements of the intensity distribution of X-ray diffuse scattering from a V_3Si single crystal were made on an X-ray diffractometer, using the monochromated CuK_α radiation, according to a procedure reported in [4]. The scattering from a platelet-like single-crystal sample with the surface being cut parallel to the (120) plane was recorded in the (001) plane of the reciprocal space. The measured intensities were converted to electronic units by comparing them with the scattering intensity from amorphous quartz. The fluorescence radiation was eliminated with the aid of a Ni filter placed before the counter.

Diffuse scattering I_2 consists of scattering caused by thermal atomic vibrations in the crystal (I_T) and of additional scattering I_{ST} resulting from static lattice defects. The measured diffuse scattering also involves the Compton scattering and other secondary components, which were eliminated by well known techniques [5]. The distribution of the scattering intensity I_T, about each reciprocal-lattice point (relpoints), can be calculated from the elastic moduli of the crystal reported in [4, 6]. The distribution of the scattering intensity I_{ST} can involve different components depending on the type, concentration, strength, and symmetry of defects, as well as on the diffraction ($\mathbf{Q}$) and wave ($\mathbf{q}$) vectors.

Thus, according to [7], the contribution of symmetrical Huang scattering $I_H \approx q^{-2}$ should predominate in the vicinity of relpoints. The presence of randomly distributed strong defects in the material under study leads to a contraction of the region, where the dependence

$I_H \approx q^{-2}$ is fulfilled. It is also possible to establish the range of the q values for the asymptotical scattering $I_A \approx q^{-4}$. The transition point q_0, between regions with different scattering laws, I_H and I_A, is related to the defect radius R_0 by the approximate relationship $q_0 \approx R_0^{-1}$. If defects are aligned along particular directions in the crystal, one can expect a more gradual decrease in the displacement fields than that leading to the Huang scattering. In this case, the scattering should obey the law $I_{ST} \approx q_1^{-(2-B)}$, where q_1 is the projection of $\mathbf{q}$ onto the plane perpendicular to the crystallographic directions along which the defects are located. The wave vector can be written as $\mathbf{q} = \mathbf{Q} - \mathbf{H}$, where $Q = 4\pi\sin\theta_{hkl}/\lambda$, θ_{hkl} is the Bragg angle, and $\mathbf{H}$ is the reciprocal-lattice vector. In other words, to observe this intensity dependence, one has to make measurements in the reciprocal-space plane perpendicular to the line of defect alignment. Here, $B = 4\pi n(C^2H^2/t_{\parallel})\{(1/\nu)\sum_{\alpha=1}^{\nu}[1-(\mathbf{mn}_\alpha)^2]\}$, where C is the defect strength, $\mathbf{m} = \mathbf{Q}/Q$, $\mathbf{n}_\alpha$ are the unit vectors parallel to the lines α, ν is the number of the systems of lines, and $t_{\parallel}$ is the average distance between possible defects located on a straight line. The expression in square brackets demonstrates that the B value strongly depends not only on the reciprocal-lattice vector, but also on the mutual orientation of the diffraction vector $\mathbf{Q}$ and the separated lines.

RESULTS OF MEASUREMENTS

In this study, the diffuse-scattering intensity in the vicinity of the 040, 220, and 330 relpoints in the (001) plane of the reciprocal space was measured for a V_3Si single crystal at room temperature. The choice of the relpoints for the analysis is dictated by the fact that the relationships between the quasi-Debye factor D and the diffraction vector for these relpoints appeared to be different [3]. Thus, for the 040 relpoint, this dependence was quadratic ($D = M = M_0Q^2$), whereas for the 220 and 330 relpoints, it took the form $D = M + M'$. Here, the addition $M' \cong B[\ln(L/\zeta R^0)]$ (where L is crystal dimension, $\zeta \approx 1$, and R^0 is the largest of the $\mathbf{C}Q/t_{\parallel}$ and R_0 values) is indicative of the existence of regions with partly ordered defects [7]. The M' value for the 220 relpoint is three times lower than for the 330 relpoint [3].

The measured diffuse-scattering intensity from the sample was rather high. Therefore, the elimination of the spurious components and the thermal diffuse scattering component (calculated from the elastic moduli [8]) did not noticeably changed the intensity distribution of diffuse scattering. In this experiment, these factors became noticeable only at $q \approx 0.1$ Å^{-1}. For all the dependences shown in the figures, the experimental errors lie within the dots of experimentally measured values.

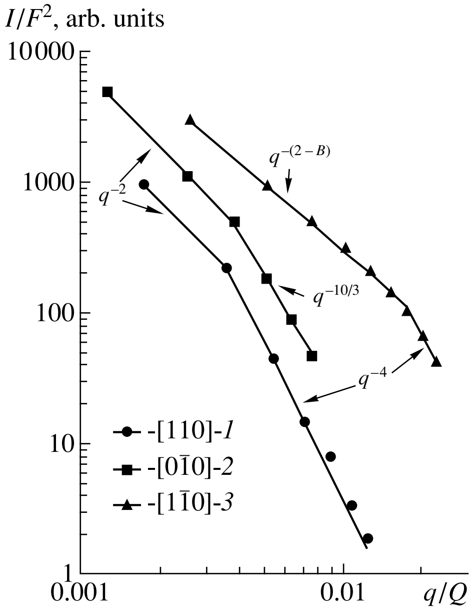

Fig. 1. Typical q/Q dependence of the X-ray diffuse-scattering intensity in a V_3Si single crystal (*1* and *2*) in the vicinity of the 040 relpoint corresponding to planar randomly distributed defects and (*3*) in the vicinity of the 220 relpoint corresponding to defects located along the [001] direction.

The diffuse scattering patterns in the vicinity of different relpoints in the crystal structure of V_3Si were dissimilar and rather complex. The pronounced Huang scattering ($I_H \approx q^{-2}$) was observed at small q only in the vicinity of the 040 relpoint in the [110] and [0$\bar{1}$0] directions. With an increase of q, the scattering intensity along the [110] direction is changed, $I_A \approx q^{-4}$ (Fig. 1), which indicates that the sample contains strong randomly distributed defects. The transition point $q_0/Q \approx 0.0037$ corresponds to $q_0 \approx 0.02$ Å^{-1}, and the defect size is $R_0 \approx 50$ Å. It is seen from Fig. 1 that the dependence $I(q)$ in the region between $q/Q \approx 0.0085$ ($q \approx 0.04$ Å^{-1}) and $q/Q \approx 0.01$ differs from $I_A \approx q^{-4}$. At $q/Q \approx 0.01$, the dependence is again described by $I_A \approx q^{-4}$.

Along the [0$\bar{1}$0] direction, with an increase of q, the intensity dependence changes from the Huang form to $I_{ST} \approx q^{-10/3}$ (Fig. 1). This shows that small-sized dislocation loops or looplike clusters are located on the (010) planes [7]. Since the $I_{ST} \approx q^{-5}$ dependence typical of dislocation loops was not observed at $q \gg R_0^{-1}$ [9], it is most probable that the observed dependence, $I_{ST} \approx q^{-10/3}$, is associated with the formation of nonspherical clusters in the sample.

In the neighborhood of the 220 relpoint, the q dependence of the scattering intensity, both along the [1$\bar{1}$0] and [$\bar{1}$10] directions, is described by the equation $I_{ST} \approx q^{-(2-B)}$. This fact indicates that the scattering under

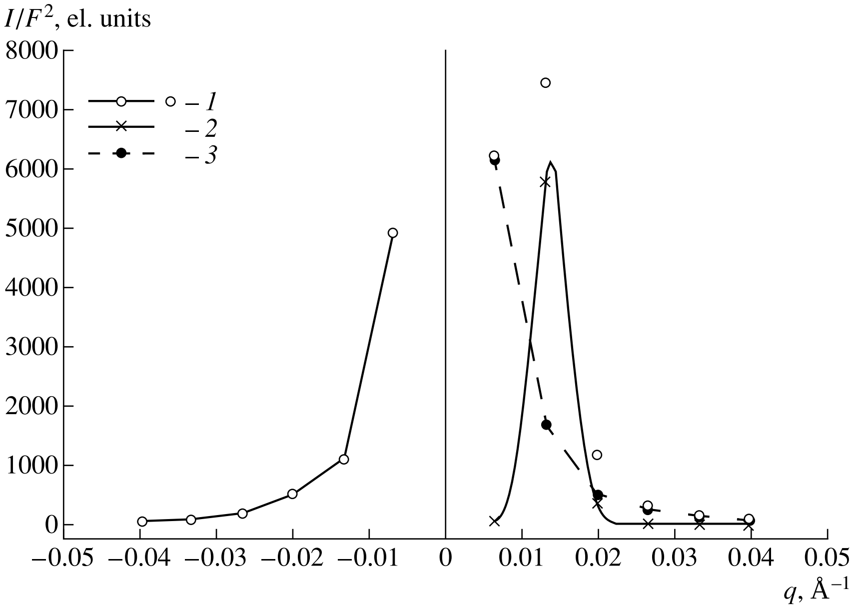

Fig. 2. Intensity of X-ray diffuse scattering from planar interstitial defects in a V_3Si single crystal as a function of q in the vicinity of the 040 relpoint in the [010] direction; the intensity of the regular reflection is shown by a solid line at $q = 0$: (*1*) the experimental points; (*2*) the points of the theoretical curve for the additional maximum caused by the local tetragonal distortions of the lattice parameters in the vicinity of defects; (*3*) the points of the difference curve between the experimental and calculated data.

consideration is caused by defects aligned in the [001] direction. Averaging the values along the $[1\bar{1}0]$ direction perpendicular to the **H** vector (Fig. 1), we obtain the value $B = 0.3$. At $q/Q \approx 0.017$ (corresponding to $q \approx 0.062$ Å^{-1}), the dependence $I_{ST} \approx q^{-(2-B)}$ is changed to $I_{ST} \approx q^{-4}$. If defects are located along the separated lines of the finite length L_0, the dependence $I_{ST} \approx q_1^{-(2-B)}$ (according to [7]) should be valid only at $q \ll \pi/L_0$, whence it follows that the size of these defects should obey the condition $L_0 \ll \pi/q \ll 50$ Å.

In the immediate vicinity of the 040 (Fig. 2) and 330 relpoints, additional maxima are observed along both **H** vectors on the side of larger Bragg angles. This is a characteristic indication of the existence of the lattice instability associated with intraphase fluctuations. The degree of distortions in the lattice parameters of the cubic matrix was determined from the reflections observed in the vicinity of the 220, 040 (Fig. 2), and 330 relpoints in the **H** directions. In all three cases, the lattice parameters of the cubic matrix $a = b = 4.7286$ Å decreased to $a = b = 4.7163$ Å.

It is well known that if the inclusions of a new phase appear in inhomogeneous solid solutions. Then, if the average atomic volumes of the phases are different, the formation of anisotropic inclusions of the new phase is energetically more favorable [7]. In this case, at a certain orientations of these inclusions with respect to crystallographic axes, the elastic energy of the system drastically decreases. With an increase of inclusions dimensions, the local distortions in the vicinity of defects also increase. If the structures of the phases are identical, these distortions give rise to a formation of satellites around each relpoint of the matrix. If the phases have different structures, the scattering from the regions of the new phase does not contribute to the scattering amplitude in the neighborhood of the relpoints of the matrix [7].

As was demonstrated above, the inclusions of the new phase in a V_3Si single crystal are located along the [001] direction. According to [7], the lattice parameters in the planes corresponding to this direction should remain equal to the lattice parameters of the matrix. Tetragonal distortions appear only along the directions perpendicular to these planes. This is confirmed by the fact that localized tetragonal distortions of the lattice parameters of the matrix along the [010]- and [110]-directions are observed only in the vicinity of defects. Only the *c*-parameter of the cubic matrix remains unchanged (4.7286 Å). That is why the close value of the ratio of the lattice parameters of the matrix observed for these regions ($c/a = 1.0026 \pm 0.00005$) to the corresponding value determined in [1] is not accidental.

The detection of an additional reflection due to tetragonal distortion in the vicinity of the 040 relpoint along the [010] direction, provided the determination of the symmetric component and elimination of the asymmetric component of the scattering intensity. The latter is proportional to the change in the unit-cell volume $\Delta\tau$. The scattering intensity shown in Fig. 2 is higher on the side of larger angles ($\Delta\tau > 0$), which indicates that the formation of interstitials is preferable [7]. This fact

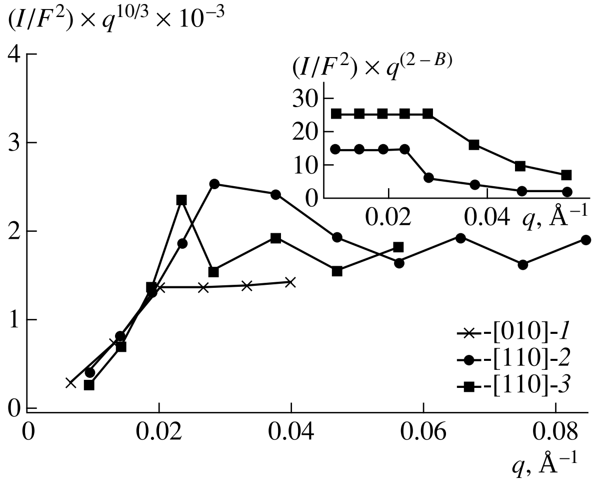

Fig. 3. Typical q dependence of the intensity of X-ray diffuse scattering from a V_3Si single crystal corresponding to the inclusions of the new phase randomly arranged in the (010) planes and to inclusions that start forming a spatially periodic distribution in the (110) planes. Points indicate the values experimentally measured in the vicinity of the (*1*) 040, (*2*) 220, and (*3*) 330 relpoints.

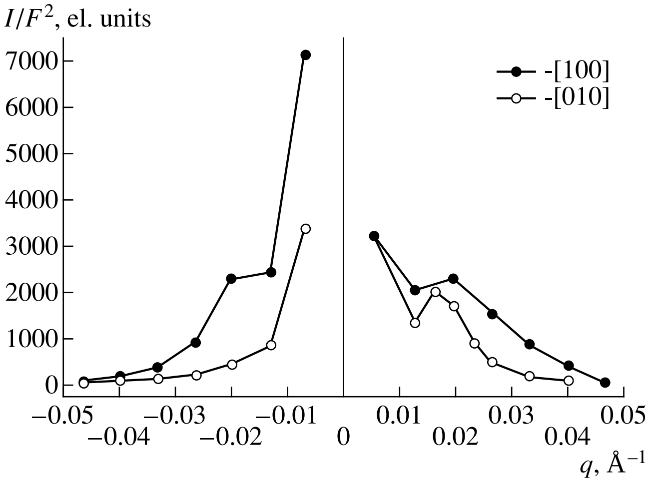

Fig. 4. Intensity of X-ray diffuse scattering from a V_3Si single crystal as a function of q corresponding to the spatially periodic concentration distribution of the particles of the new phase in the vicinity of the 330 relpoint; the intensity of the regular reflection is shown by a solid line at $q = 0$; points indicate the experimentally measured values.

confirms the presence of particles of the new phase in the system. For the symmetric component of the intensity, the dependence $T_H \approx q^{-2}$ changes to $I_{ST} \approx q^{-10/3}$ (Fig. 3) at the same q values as in Fig. 1.

After the separation of analogous reflections caused by the tetragonal distortion, the dependence of the intensity in the vicinity of the 220 and 330 relpoints along the [110] direction can be written as $I_{ST} \approx q^{-(2-B)}$ (Fig. 3, the inset). This dependence breaks down at $q = 0.024$–0.028 Å^{-1}, thus indicating possible lengths of the lines, $L_0 \ll 130$ Å. For the 220 relpoint, $B = 0.3$, as determined above. For the 330 relpoint, $B = 1.0$, which is three times higher than that for 220. The latter result is consistent with the data on the ratio of the additions M' reported in [3]. With a further increase in q along the [110] direction, the intensity of diffuse scattering in the vicinity of the 220 and 330 relpoints starts oscillating about the curve $I_{ST} \approx q^{-10/3}$ (Fig. 3). Note that oscillations in the vicinity of the 330 relpoint are observed at lower values of q than those in the vicinity of 220. In the vicinity of the 330 relpoint, satellites are located on both sides of the [100]-direction and are located at the equal distances from the main line, whereas along the [010] line, they are observed only from the side of larger angles (Fig. 4). In the vicinity of the 220 relpoint, no satellites along these directions are observed.

RESULTS AND DISCUSSION

Since the diffraction pattern shows effects associated with atomic displacements in the unit cell, the change in the structure amplitude caused by the presence of defects their concentration in the sample under study should be rather high. This is also evidenced by the value $B = 1$ determined in the vicinity of the 330 relpoint [7].

Apparently, the high concentration of strong defects in the V_3Si single crystal should lead to their elastic interactions and ordering. This, in turn, provides a certain orientation of the inclusions of the new phase, for example, along the [001]-direction. The separated lines have finite lengths L_0, which do not exceed 130 Å in some planes and 50 Å in some other planes. Partial ordering is also responsible for the spatially periodic distribution of the defect concentration due to self-organization [10]. According to [11], this fact accounts for the presence of satellites along the [100] and [010] directions in the vicinity of the 330 relpoint. Oscillations of the scattering intensity about the curve $I_{ST} \approx q^{-10/3}$ along the [110] direction in the vicinity of the 220 and 330 relpoints (Fig. 3) are also indicative of a certain tendency to the ordered mutual arrangement of inclusions in the (110) plane. The law $I_{ST} \approx q^{-10/3}$, observed along certain directions, indicates that planar pileups of randomly distributed defects in the planes perpendicular to the above directions [7]. Thus, it was found that randomly arranged planar inclusions have the size $R_0 \approx 50$ Å and are located in the (010) planes (Fig. 1). It is likely that in the (110) planes, the spatially periodic concentration distribution of the inclusions of the new phase takes place. It can be assumed that the sample under study contains two systems of lines of aligned defects. This assumption is consistent with the data reported in [3] (Fig. 3). Probably, “threads” of a nucleating superconducting phase observed belong to one of these systems.

To summarize, the results obtained in this study demonstrate that a V_3Si single crystal is, in fact, an essentially complex inhomogeneous system containing the regions or particles of the new phase, which are either randomly distributed in space or aligning to form spatially periodic distributions in the (110) planes. The latter inclusions give rise to localized tetragonal distortions of lattice parameters of the matrix ($c/a = 1.0026$), which is a characteristic sign of the lattice instability.

REFERENCES

1. B. W. Batterman and C. S. Barrett, Phys. Rev. **145**, 296 (1966).
2. A. M. Glogston and V. Jaccarino, Phys. Rev. **121**, 1357 (1961).
3. N. N. Stupina and A. A. Katsnel’son, Kristallografiya **42** (3), 488 (1997) [Crystallogr. Rep. **42** (3), 442 (1997)].
4. N. N. Stupina and A. A. Katsnel’son, Kristallografiya **34** (6), 1502 (1989) [Sov. Phys. Crystallogr. **34** (6), 899 (1989)].
5. C. J. Sparks and B. Borie, *Local Atomic Arrangements Studied by X-ray Diffraction*, Ed. by J. B. Cohen and J. E. Hilliard (Gordon and Breach, New York, 1966), p. 5.
6. R. W. James, *The Optical Principles of the Diffraction of X-rays* (Bell, London, 1962; Mir, Moscow, 1966).
7. M. A. Krivoglaz, *X-ray and Neutron Diffraction in Nonideal Crystals* (Naukova Dumka, Kiev, 1983).
8. L. R. Testardi and T. B. Bateman, Phys. Rev. **154**, 402 (1967).
9. P. H. Dederichs, Phys. Rev. B **4**, 1041 (1971).
10. A. I. Olemskoĭ and A. V. Khomenko, Zh. Éksp. Teor. Fiz. **110**, 2144 (1996) [JETP **83**, 1180 (1996)].
11. A. G. Khachaturyan, *Theory of Phase Transitions and Structures of Solid Solutions* (Nauka, Moscow, 1974).

Translated by T. Safonova

Crystallography Reports, Vol. 45, No. 4, 2000, pp. 655–660. Translated from Kristallografiya, Vol. 45, No. 4, 2000, pp. 715–721.
Original Russian Text Copyright © 2000 by Afanas'ev, Chuev, Imamov, Lomov.

REAL CRYSTAL STRUCTURE

Structural Characteristics of Multicomponent GaAs–$In_xGa_{1-x}As$ System from Double-Crystal X-ray Diffractometry Data

A. M. Afanas'ev*, M. A. Chuev*, R. M. Imamov, and A. A. Lomov****

** Institute of Physics and Technology, Russian Academy of Sciences,*
ul. Krasikova 25a, Moscow, 117218 Russia
*** Shubnikov Institute of Crystallography, Russian Academy of Sciences,*
Leninskiĭ pr. 59, Moscow, 117333 Russia

Received June 29, 1998

Abstract—The article continues a series of publications on the technologically important multilayer $In_xGa_{1-x}As$–GaAs/GaAs system with the 3-, 6-, and 9 nm-thick layers (quantum wells). The collimation system of the incident beam is improved. The dimensions of quantum wells and the interfaces between these wells are determined. The qualitative picture of quantum well "spreading" is described. The experimental diffraction reflection curves are measured from three different parts of the specimen. Their analysis shows how homogeneous the structure grown is. *© 2000 MAIK "Nauka/Interperiodica".*

INTRODUCTION

Earlier [1–4], we demonstrated the possibilities of the standard double-crystal X-ray diffractometry in the analysis of the GaAs–$In_xGa_{1-x}As$-type systems with the nanometer-thick layers. The existence of such layers with well developed boundaries predetermine a large number of oscillations on the diffraction reflection curve within the range of ten thousand of angular seconds. In this case, the reflection diffraction curve contains a large volume of information on the structure parameters. The use of the adequate mathematical apparatus allows the determination not only of the main parameters of the structure layer (set by the growth conditions), but also of the characteristics of interfaces between these layers. Such curves provide a unique possibility to control structural dimensions within several nanometers for the layers located far from the surface. Thus, double crystal X-ray diffractometry is one of the most important and perspective methods for analyzing multilayer structures with nanometer-thick layers.

The present article continues our studies of the GaAs–$In_xGa_{1-x}As$ systems and differ from the earlier publications [1, 4] by the dimensions of the main layers and the modified growth conditions. We also improved the experimental method by using a less divergent X-ray beam and a more sophisticated scanning system. The study of different regions of each specimen allowed us, first, to estimate the surface homogeneity of the heterosystem and, second, to compare the diffraction reflection curves from various regions, and thus to estimate the method resolution. We managed to show that the method used provides the reliable detection of variations in the layer thicknesses within fractions of a nanometer.

EXPERIMENTAL

The multilayer $In_xGa_{1-x}As$–GaAs/GaAs structure was grown by the method of molecular-beam epitaxy (MBE) on a RIBER-32P setup described elsewhere [1]. We studied a multilayer structure depicted in Fig. 1. Various quantum wells, i.e., $In_xGa_{1-x}As$ ($x = 0.12$) layers, had different indium content, the thickness of GaAs layers was 50 nm, and the substrate temperature was 470°C.

The experiment was performed on a computer-controlled (via a MATEX controller) triple-crystal diffractometer with parallel crystals providing the quasidispersionless $(n, -m)$ geometry. The diffraction reflection curves were obtained from the (004) planes. The incident X-ray beam was formed by a grooved threefold Ge(004) monochromator, which provided a higher angular resolution of the method without a noticeable decrease of the recorded intensity in comparison with the intensity obtained from a flat monochromator with the single reflection. The collimated X-ray beam had the crossover 200 μm in width and 4 mm in height. In order to reduce the contributions from the background and diffuse components to the total scattering signal, we also used a horizontal slit with the angular aperture of 8 angular minutes in front of the detector. The radiation source was a 1.1 kW X-ray tube with a copper anode. Similar to [1], the specimen surface deviated from the diffracting planes (the wedge angle) by 3°. Since the Bragg angle for the chosen reflection was ~33°, the angular position of the detector during scanning (±4 angular minutes and higher) was corrected for the dependence of the angular positions of the Bragg scattering component on the asymmetry coefficient β. Instead of traditional $\theta/2\theta$ scanning, we used $\theta/(1+\beta)\theta$ scanning. The diffraction reflection curves

GaAs	50 nm
InGaAs	3 nm
GaAs	50 nm
InGaAs	6 nm
GaAs	50 nm
InGaAs	9 nm
GaAs buffer	300 nm
Substrate	

Fig. 1. Schematic profile of a multilayer $In_xGa_{1-x}As$–GaAs structure corresponding to the growth conditions.

were recorded at a step of 5 angular seconds; the central part of the curve was recorded at a step of 1 angular second. The intensities were measured in the statistical mode (up to 1000 pulses at each point of the curve). The minimum and the maximum recording times were 2 and 100 s, respectively.

Reflection diffraction curves from the (400) plane of the specimen were measured in several regions of the plate surface (vertical primes) in Fig. 2 (*1* and *2* in the plate center and *3* at its edge); the location of these regions on the plate surface is shown in the inset in Fig. 2.

METHOD OF ANALYSIS

Mathematical modeling of the experimental data was performed by the method described in [1]. Each of the layers were characterized by thickness l_j, crystal-lattice parameter a_j, and the static Debye-Waller factor $f_j = \exp(-w_j)$ (setting the degree of the layer amorphization). As the initial approximation, we used the structure parameters set by the growth conditions. Solid lines in Fig. 2 illustrate the calculations for a seven-layer model with variable quantum-well parameters l_j, a_j, and f_i and the GaAs-layer parameters l_j and f_i (layers 1, 3, and 5 in Fig. 1). The lattice parameters for the last layers were considered to be equal to the corresponding parameters of the substrate. The variation of these parameters did not improve the fitting quality, and their deviation from the growth parameter only slightly exceeded their root-mean square error. We also varied the Debye–Waller factor in the buffer. The results of fitting are shown in Fig. 2; the layer parameters obtained and their root-mean square deviations are listed in Table 1.

The model used allowed us qualitatively describe all the details of the diffraction reflection curve, despite the fact that this curve was rather complicated and had a large number of oscillations. However, the quantitative evaluation of fitting by the χ^2 criterion (equal to 5.8, 3.4, and 3.7 for the central *1* and *2* and the peripheral *3* regions of the plate, respectively) showed the necessity of further improvements. Although in the modern theory of experimental data, processing the model is considered to be satisfactory if the χ^2-value lies in the range $\chi^2 = 1 \pm \sqrt{2/n_f}$, where $n_f = n - n_p$ is the number of the degrees of freedom in fitting, n is the number of the experimental points, and n_p is the number of the varying parameters [5]. In our case, this interval was 1 ± 0.05, with the so-called first-order error (i.e., the risk to reject the model with $\chi^2 = 5$ and at the same time to make a mistake) being negligibly small (of the order of 10^{-40}) [5].

Table 1. Layer parameters in a seven-layer model

j	Region 1 ($\chi^2 = 5.8$)			Region 2 ($\chi^2 = 3.4$)		
	l_j, nm	$\Delta a_\perp/a_j$, %	f_j	l_j, nm	$\Delta a_\perp/a_j$, %	f_j
1	50.9(2)	0	0.85(3)	50.8(1)	0	0.78(2)
2	4.4(3)	0.96(7)	0.89(4)	4.5(2)	0.96(4)	0.87(3)
3	52.4(2)	0	0.97(3)	52.5(2)	0	0.98(2)
4	7.2(2)	1.19(4)	0.94(2)	7.4(1)	1.11(2)	1.00(2)
5	51.4(2)	0	0.88(2)	50.9(1)	0	0.83(2)
6	10.9(2)	1.15(4)	0.82(3)	11.1(2)	1.13(2)	0.80(2)
Buffer			0.88(3)			0.83(2)

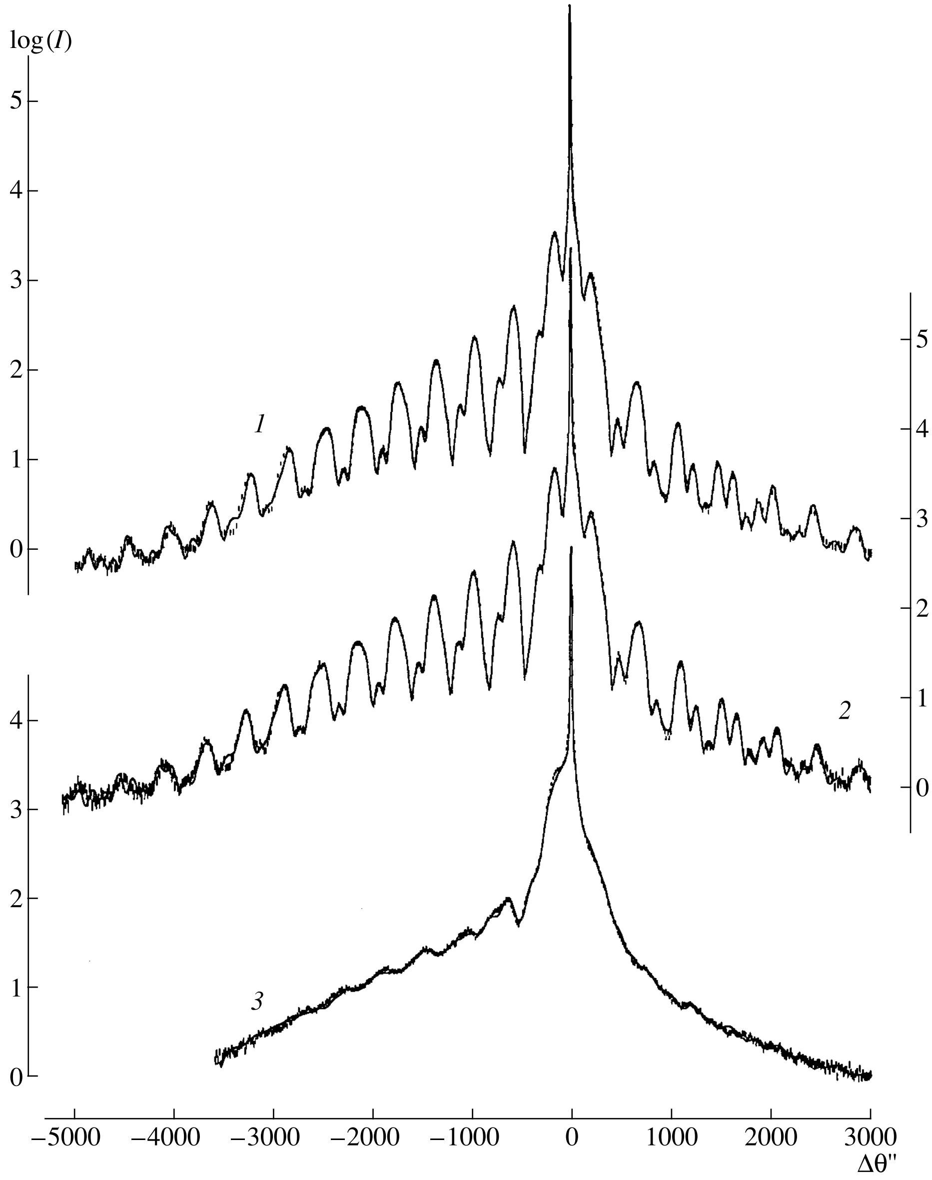

Fig. 2. Experimental diffraction reflection curves (vertical bars) of the multilayer $In_xGa_{1-x}As$–GaAs/GaAs structure ($x = 0.13$) measured from different regions of the specimen and the calculated curves (solid lines) for the seven-layer model ($\chi^2 = 5.8$, 3.4, and 3.7, respectively). The regions *1* and *2* are located at the layer center and region *3*, at its edge.

Thus, in this situation, we had to search for more adequate models.

With this aim, we introduced into consideration some additional layers at the boundaries between the quantum wells and the main layers [1], and an additional layer on the specimen surface. The initial parameters l_j of these additional layers were taken to be equal to 1 nm, whereas the values of the parameters a_j and f_i were taken to be equal to half-sums of the corresponding parameters for the neighboring layers. In the course of subsequent fitting, we varied all the parameters of both initial and additional layers. In this case, some parameters for the lower- and upper sublayers of the 3nm-thick layer were somewhat ambiguous, i.e., the root-mean square deviations of the parameters of these sublayers exceeded their average values. Therefore, such layers were rejected from the further analysis. This resulted in a much better agreement for the twelve-layer model (seven initial and five additional boundary sublayer, Table 2). In this case, the value of the parameter χ^2 decreased to 1.30 and 1.26 for the regions 1 and 2, respectively.

Thus, the fitting quality was so high that the experimental and theoretically calculated curves on the drawing scale showed no noticeable differences. Therefore, in such cases the results are usually represented in the

Table 2. Layer parameters in a twelve-layer model

j	Region 1 ($\chi^2 = 1.30$)			Region 2 ($\chi^2 = 1.26$)		
	l_j, nm	$\Delta a_\perp/a_j$, %	f_j	l_j, nm	$\Delta a_\perp/a_j$, %	f_j
1	2.9(1)	0	0.45(2)	2.8(1)	0	0.39(3)
2	49.3(1)	0	0.92(1)	49.7(1)	0	0.87(1)
3	5.0(1)	0.86(2)	0.84(1)	4.5(2)	0.95(4)	0.85(2)
4	51.4(1)	0	0.95(1)	50(1)	0	0.96(1)
5	3.3(6)	0.84(7)	0.87(1)	2.8(9)	0.2(1)	0.94(2)
6	3.6(8)	1.4(1)	0.99(3)	5.5(7)	1.23(4)	1.00(2)
7	3.2(3)	0.28(7)	1.00(2)	2.6(2)	0.4(2)	0.94(4)
8	46.6(6)	0	0.93(1)	46.5(9)	0	0.87(1)
9	3.9(3)	0.14(3)	0.80(2)	4.1(6)	0.15(5)	0.87(2)
10	7.7(2)	1.41(3)	0.79(1)	8.7(3)	1.23(2)	0.83(1)
11	3.6(1)	0.41(4)	0.94(2)	2.9(2)	0.44(8)	0.84(2)
Buffer			0.96(2)			0.88(1)

form of the normalized residual differences

$$\sigma_i = \frac{I_i^{(e)} - I_i^{(c)}}{s_i},$$

where $I_i^{(e)}$ and $I_i^{(c)}$ are the observed and the calculated intensities and s_i is the experimental error. Figure 3 shows the σ_i values for two regions of the specimen for the seven- and twelve-layer models. The twelve-layer model describes the experimental data much better: almost all the σ_i layers fit the interval from –3 to +3, in full accordance with the theory of high-quality fitting.

It should also be noted that the determination of the distribution profiles for the parameters is not unique, because in the experiment, one measures only the intensity of the reflected wave whereas, within the framework of the method, it is almost impossible to extract any information on the wave phase. If the region with the distorted parameters is rather small (about several monolayers), one should use the method described in [6], which provides the determination of all the equivalent solutions. The number of possible equivalent solutions increases as 2^N, where N is the number of layers. In our case, the structure consists of about a thou-

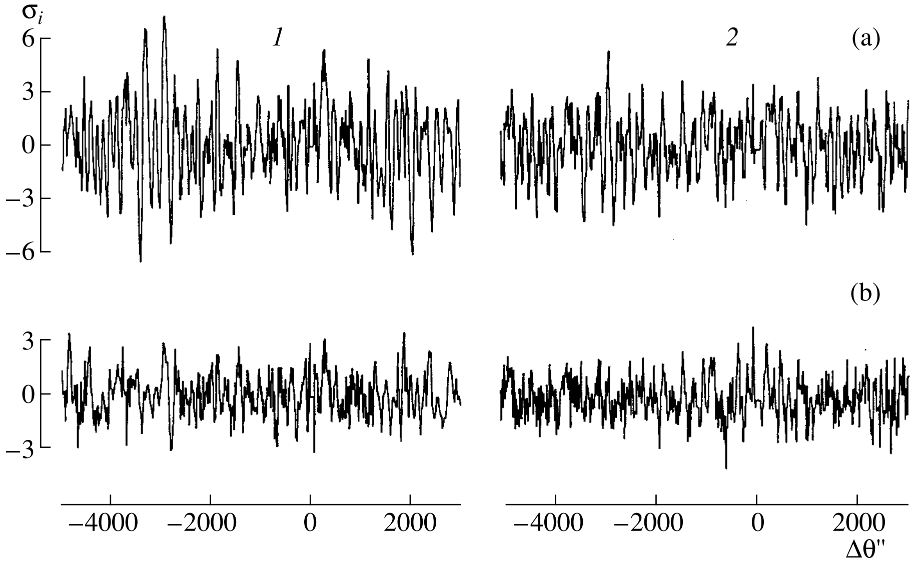

Fig. 3. Deviations σ of the calculated diffraction reflection curve from the experimental one obtained from regions *1* and *2* for the (a) seven- and (b) twelve-layer models.

Table 3. Indium content in structure layers (in monolayer units)

Region 1					Region 2				
seven-layer model		twelve-layer model			seven-layer model		twelve-layer model		
j	y_j	k	y_j	y_k	j	y_j	k	y_k	y_j
2	1.06(1)	3	1.07(1)	1.07(1)	2	1.06(1)	3	1.06(1)	1.06(1)
		5	0.73(3)				5	0.14(4)	
4	2.10(3)	6	1.21(2)	2.11(5)	4	2.03(4)	6	1.67(2)	2.07(6)
		7	0.22(3)				7	0.26(5)	
		9	0.13(6)				9	0.15(2)	
6	3.09(2)	10	2.68(4)	3.18(9)	6	3.10(2)	10	2.64(3)	3.11(4)
		11	0.37(5)				11	0.32(1)	

sand of monolayers, and the number of such equivalent solutions is enormous. One can assume that among these solutions there should also be some solutions that adequately describe the structure studied. Moreover, there are also some random solutions with close χ^2 values. To prove that the solutions obtained are unique, we performed some additional studies. First of all, in the transition to the twelve-layer model, the additional sublayers were introduced either gradually (one by one) in different sequences, or by groups in different combinations and sequences. All the parameters in the solutions thus determined were arbitrarily varied within 15% of their average value. Then, these values were considered as starting values again, and a new cycle of fitting was made. In all the cases, the solutions “came back” to the starting variant and no additional close solutions were revealed. This procedure will be described in the forthcoming article in more detail.

It should be indicated that the experimental diffraction reflection curve similar to those shown in Fig. 2 (~2000 points) is recorded for 24 h: their processing on a Pentium-200 computer took from two to several hours, depending on the number of the layers analyzed.

DISCUSSION OF RESULTS

As is seen from Fig. 2, the reflection diffraction curve from region *3* lying at a distance of 1 mm from the plate edge is strongly diffused and shows no features characteristics of the curves from regions *1* and *2*. This fact alone, without any additional mathematical analysis, indicates that region *3* is characterized by pronounced deviations of the structure from the structure set by the growth conditions. The mathematical analysis confirms this obvious conclusion. The fitting within the seven-layer model (solid line in Fig. 2) shows that in 3- and 6 nm-thick layers, the In-content is either very low, or is distributed along the layer thickness, so that, within this model, these layers cannot be seen. As to the 9 nm-thick layer, it contains only 25% of deposited indium, whereas the remaining indium is distributed over the structure thickness.

For two other regions of the plate located at the distances of ~5 and 10 mm from the plate edge, the parameters of the multilayer structure are rather close to one another. It is seen from Table 1 that the parameters of the main Ga-containing layers correspond to the growth conditions, the thicknesses of most of the layers correspond (within 5%) to the values set by the growth conditions. As to the quantum wells, or the $In_xGa_{1-x}As$ layers in the seven-layer model, they are thicker than it was expected: a layer expected to be 3 nm-thick is thicker by a factor of 1.5, and the layers expected to be 6- and 9 nm-thick are thicker for about 20%). However, the variation of the interplanar spacings is less than predicted on the basis of the indium concentration (12%). Such indium concentration should provide the spacing variation within $\Delta a/a = 1.65\%$. In this connection, it was expedient to determine the total indium content y_j in the quantum wells, because this quantity can be controlled during structure growth. The variations in the crystal-structure parameter a_j, caused by the substitution of gallium by indium, can readily be related to the indium concentration (Vegard’s law) and, most importantly, to the total indium content in the layers using the relationship:

$$\frac{\Delta a_\perp}{a} = \frac{a_{\mathrm{InGaAs}}(x) - a_{\mathrm{GaAs}}}{a_{\mathrm{GaAs}}} \cdot \frac{1+\nu_{\mathrm{InGaAs}}(x)}{1-\nu_{\mathrm{InGaAs}}(x)},$$

where $\nu_{\mathrm{InGaAs}}(x)$ is Poisson’s ratio for $In_xGa_{1-x}As$. The calculations performed by the above formula are listed in Table 3. It is seen that the total indium contents in these layers coincide, within the error, with the content dictated by the growth conditions.

The twelve-layer model allows one to interpret the structure of quantum wells and the indium distribution in the layers. As follows from Table 2 (see also Fig. 4), the 9 nm-thick layer consists of the central core with the dimensions close to those set by the growth conditions (for region *2*, within an error, the corresponding values coincide), but with somewhat reduced indium content. For both regions, this central part contains about 80% of the total indium content, whereas the remaining 20%

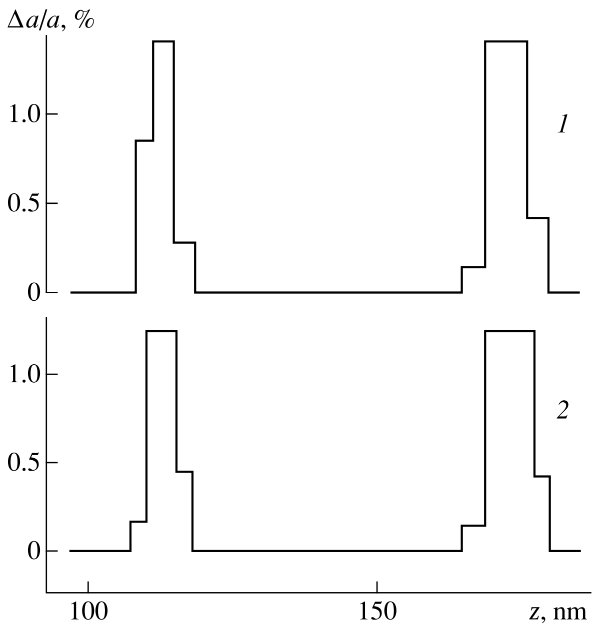

Fig. 4. Profiles of the lattice-parameter variation over the structure depth and in the direction normal to the surface $\Delta a_{\perp}/a$ for the central regions of the specimen (*1* and *2*) for a 12-layer model.

of indium are distributed within 3–4 nm distance from the central part, with 2/3 of this amount being located at the boundary far from the surface and 1/3, at the boundary close to it.

The quantum-well parameters for a 6 nm-thick $In_xGa_{1-x}As$ layer are essentially different from those set by the growth conditions. Its structure varies from point to point on the surface, and, as is seen from Table 2 and Fig. 4, this is associated mainly with the character of indium distribution in the quantum well, although, within the error, the total indium content (parameter y_j, Table 3) remains constant. For a 3 nm-thick layer, no more detailed information on the indium distribution was obtained. However, the average layer thickness and the indium content (or the variation of the interplanar spacing) can be determined. These parameters for different points on the surface are rather close (Tables 1–3). In both cases, the layer is “spread” for 4.5 nm, i.e., is 1.5 times thicker than was expected from the growth conditions.

Thus, the main qualitative results of our analysis are as follows. (1) The growth conditions (470°C) provide the formation of a 9 nm-thick homogeneous $In_xGa_{1-x}As$ layer with slightly diffused edges; (2) the indium distribution in a 6nm-thick $In_xGa_{1-x}As$ layer varies from point to point on its surface; (3) the total indium content in all the layers corresponds to the content set by the growth conditions. It should be emphasized that the indium distributions in quantum wells are determined quite reliably. Thus, the use of the structure parameters determined at point 1 for the description of the experimental data at point 2 considerably deteriorates the fitting quality— the parameter χ^2 increases from 1.26 to 3.8, i.e., by more than three times.

CONCLUSION

The above analysis demonstrates the possibilities provided by the standard method of double crystals diffractometry for determining the parameters of multilayer structures with nanometer-thick layers, under the condition that the method used in the mathematical analysis is adequate. This is associated, first and foremost, with the high angular resolution of the method. The intensity of diffraction scattering considerably exceeds the intensities of diffuse scattering and secondary radiation in the methods of X-ray standing waves [7]. Thus, the information obtained with the aid of the above method is very rich and allows one to establish fine details of the multilayer structure. It should also be indicated that the volume of the information extracted from the diffraction reflection curves can be considerably increased by using powerful X-ray sources such as generators with rotating anodes or synchrotron radiation.

ACKNOWLEDGMENTS

The authors are grateful to V.G. Mokerov for preparation of specimen preparation.

This study was supported by the Russian Foundation for Basic Research, project no. 96-02-16417a and the Interbranch Scientific and Technological Program *Physics of Solid State Nanostructures*, project no. 98-3009.

REFERENCES

1. A. M. Afanas’ev, M. A. Chuev, R. M. Imamov, *et al.*, Kristallografiya **42** (2), 1 (1997) [Crystallogr. Rep. **42** (3), 467 (1997)].
2. A. M. Afanas’ev, A. A. Zaĭtsev, R. M. Imamov, *et al.*, Kristallografiya **43** (1), 139 (1998) [Crystallogr. Rep. **43** (1), 129 (1998)].
3. A. M. Afanas’ev, A. A. Zaĭtsev, R. M. Imamov, *et al.*, Kristallografiya **43** (4), 677 (1998) [Crystallogr. Rep. **43** (4), 628 (1998)].
4. A. M. Afanas’ev, M. A. Chuev, R. M. Imamov, *et al.*, Kristallografiya **43** (5), 926 (1998) [Crystallogr. Rep. **43** (5), 872 (1998)].
5. H. Cramer, *Mathematical Methods of Statistics* (Princeton Univ., Princeton, N.J., 1946; Mir, Moscow, 1975).
6. A. M. Afanas’ev and S. S. Fanchenko, Acta Crystallogr., Sect. A: Found. Crystallogr. **44**, 25 (1988).
7. A. M. Afanas’ev, P. A. Aleksandrov, and R. M. Imamov, *X-ray Diffraction Diagnostics of Submicron Layers* (Nauka, Moscow, 1989).

Translated by L. Man

Crystallography Reports, Vol. 45, No. 4, 2000, pp. 661–669. Translated from Kristallografiya, Vol. 45, No. 4, 2000, pp. 722–730.
Original Russian Text Copyright © 2000 by Vdovin, Shcherbachev, Mironov, Parry, Parker.

A Study of Structural Perfection of Interfaces in Si/SiGe Superlattices

V. I. Vdovin*[1], K. D. Shcherbachev, M. Mironov***, C. P. Parry***,**
and E. H. C. Parker***

** Institute for Chemical Problems of Microelectronics, B. Tolmachevskiĭ per. 5, Moscow, 109017 Russia*
*** Moscow State Institute of Steel and Alloys, Leninskiĭ pr. 4, Moscow, 117936 Russia*
**** Department of Physics, University of Warwick, Coventry, CV4 7AL, UK*

Received July 28, 1998; in final form, November 23, 1998

Abstract—A complex investigation into the structural perfection of the Si/SiGe superlattices grown by molecular-beam epitaxy at different temperatures of the Si substrate has been carried out by high-resolution X-ray diffraction analysis, secondary ion mass spectrometry (SIMS), and transmission electron microscopy (TEM). It is demonstrated that the combination of these methods makes it possible to describe in sufficient detail the distributions of the strains and Ge concentrations in the elastically strained superlattices and also to evaluate the sharpness of the layer interfaces. It is shown that the densitometry of electron microscope images of the superlattice cross-sections permits characterization of the relative sharpness of the layer interfaces and a qualitative representation of the Ge distribution throughout the thickness of the SiGe layers. *© 2000 MAIK "Nauka/Interperiodica".*

INTRODUCTION

The relaxation of misfit stresses in elastically strained epitaxial Si/SiGe heterostructures leads to the smearing (disturbance of planarity and sharpness) of layer interfaces on the nanometer scale. These transformations of the interfaces can be caused by different processes accompanying the epitaxial growth of SiGe layers, including the Ge segregation, the interdiffusion, and the development of wavy roughness at the surface of a growing layer. The investigation into the structural perfection of interfaces calls for the use of different experimental techniques, which should be sensitive to the crystal lattice deformation and the Ge content in a solid solution and enable one to directly examine the interfaces. The X-ray diffraction analysis, the secondary ion mass spectrometry (SIMS), and the transmission electron microscopy (TEM) are the techniques most frequently employed for the study of multilayer heterostructures. In the present work, we undertook a complex investigation of the Si/SiGe superlattices by using the aforementioned techniques, with the aim of revealing the structural perfection of superlattice.

EXPERIMENTAL

Superlattices involving five periods of alternating 3-nm-thick $Si_{1-x}Ge_x$/Si and 30-nm-thick Si layers with the expected Ge content $x = 0.22$ in a solid solution were grown on Si(001) substrates by molecular-beam epitaxy using a VG Semicon V90S apparatus at different substrate temperatures in the range 550–810°C. A 225-nm-thick Si buffer layer was preliminarily grown on the substrates, and a 200-nm-thick Si cap layer was grown on the superlattices.

X-ray diffraction analysis. The high-resolution X-ray diffraction experiments were carried out on a Philips MRD diffractometer (X-ray source power, 1.5 kW; tube with a copper anode). The high resolution was achieved by using a fourfold Ge(220) Bartel monochromator consisting of two double Ge(220) slit monochromators with the (n, n) arrangement, which provides a high monochromatization of a beam (dispersion, $\sim 10^{-5}$). The beam diffracted by the studied sample was analyzed with a double Ge(220) slit monochromator. For this configuration, the divergence of primary and diffracted beams was equal to ~12″. The structure parameters of superlattices were determined by computer simulated rocking curves experimentally recorded in the receiving slit and triple-crystal modes. The reciprocal lattice maps in the neighborhood of the [[004]] and [[224]] points were constructed for analysis of stresses.

Secondary ion mass spectrometry. The Ge depth profiles were determined by the SIMS technique with an ultralow energy of the O_2^+ ion beam. Measurements were performed on an EVA 3000 instrument with a unique floating low-energy gun, which permits one to obtain the O_2^+ ion beams with a minimum energy of 150 eV and a diameter of ~50 μm [1]. The depth resolution was estimated using a high-quality delta layer [2]. At an ion primary beam energy of 500 eV, the res-

---

[1] *e-mail: icpm@mail.girmet.ru*

olutions for the leading and trailing SIMS edges in a Ge layer were equal to 0.3 and 1.3 nm, respectively. Superlattices similar to those studied in the present work, were investigated in [3]. It was shown that the concentration profiles of Ge in samples grown at different substrate temperatures are different, and these differences are not caused by instrumental errors of the technique.

Transmission electron microscopy. The direct TEM examination of the superlattice cross-sections prepared by the ionic etching was carried out on a JEOL 200CX microscope (accelerating voltage, 200 kV). The thicknesses of layers in the superlattices were preliminarily measured accurate to within ±0.5 nm from electron microscope images with the use of a Videoplan image analysis system. In this case, the location of layer interfaces was visually determined from the “jump” of the density. The concentration inhomogeneity of the SiGe layers was qualitatively evaluated from the distribution of the transmitted electron beam intensity in the cross-sectional plane {110}. The distribution of the beam intensity was determined from the negative density measured on a Microdensitometer 3CS unit.

In the TEM analysis, the superlattice cross-sections were examined in a bright field by using multibeam and double-beam (reflections $\mathbf{g} = \langle 220 \rangle$, $\langle 111 \rangle$, and $\langle 004 \rangle$) diffraction modes. The examination of the superlattices in the multibeam (the electron beam almost coincides with the [110] zone axis) and double-beam (with reflection $\mathbf{g} = \langle 004 \rangle$) diffraction modes is preferable for measuring the layer thickness, because the effect of sample deviation is eliminated from consideration. The images with the most uniform distribution of the contrast over the sample were obtained with the reflection $\mathbf{g} = [004]$ ($s < 0$). This mode was employed for recording the images for the densitometric analysis.

The microdensitometry of electron microscope image negatives is usually applied to determine the distribution of the electron beam intensity over the sample [4]. In the present work, we attempted to use densitograms for analysis of the composition inhomogeneity and the sharpness of the SiGe layer interfaces in the superlattices. In the densitometer, the negative was scanned by way of its uniform displacement with respect to the stationary light beam (perpendicular to the negative plane) along the straight line (normal to the superlattice surface). A narrow beam was cut with a rectangular slit from a plane light beam passing through the negative. The intensity of the narrow beam was measured using an optical wedge, and the profile of the negative density was recorded. The following parameters were used in the experiments: effective slit width (with allowance made for the magnification of the microdensitometer objective lens), 45 μm; effective slit height, 200 μm; optical wedge, 1.00D; magnification, 10 : 1, 20 : 1, and 50 : 1. The minimum requirements to the negative quality involve the correspondence of the studied image density to a linear portion in the curve of blackening density, and the correspondence between the density ranges of the negative and the optical wedge. The densitometric technique was tested with reference samples, the best of which was the negative with the image of a pointer located above the luminescent screen in the electron microscope. This reference sample was a narrow (1 mm wide) bright strip with sharp edges and uniform density.

RESULTS

High-Resolution X-ray Diffraction

Inspection of the $\mathbf{Si_{1-x}Ge_x}$ layers for pseudomorphism. The stress relaxation in the superlattices studied was analyzed using the symmetrical (004) and asymmetrical (224) reflections. The reflection of the substrate and the satellites of the superlattice are clearly seen in the reciprocal lattice maps in the neighborhood of the [[004]] and [[224]] points (Fig. 1). Note that the $SL \pm 1$ and $SL \pm 2$ satellites lie in the line passing through the (224) reflection of the Si substrate, and this line is parallel to the [001] direction (Fig. 1b). According to [5], this arrangement of the satellites in the reciprocal space upon asymmetric recording indicates that the superlattice is fully strained. Therefore, the superlattices under consideration are fully strained, and the layers of the $Si_{1-x}Ge_x$ solid solution are pseudomorphous.

Evaluation of layer thickness and Ge concentration in the $\mathbf{Si_{1-x}Ge_x}$ solid solution. The layer thickness and the mean Ge concentration in the SiGe layers were determined from the data obtained in the receiving slit mode. Figure 2 depicts the rocking curves for two superlattices grown at the lowest and highest substrate temperatures. These curves exhibit the satellites up to the seventh order, which suggests a high structural perfection of both superlattices. The rocking curves simulated on the basis of the dynamic diffraction theory [6] are also displayed in Fig. 2. A wide halo of diffuse scattering was observed for all the samples. Hence, the rocking curves were simulated with the static Debye–Waller factor including the coherent scattering losses. These curves were calculated using the thicknesses of the Si and $Si_{1-x}Ge_x$ layers, the Si cap, and the Ge concentration in the solid solution, which were obtained in the course of the optimization procedure. This procedure is based on the Levenberg–Marquardt method [7] and involves the minimization of the functional

$$F = \frac{1}{n-1}\sum_{i}^{n}\frac{(I_i^{\mathrm{theor}} - I_i^{\mathrm{exp}})^2}{I_i^{\mathrm{exp}}},$$

where n is the number of points in the rocking curve, and I_i^{theor} and I_i^{exp} are the calculated and measured intensities (in pulses) at the ith point. The structure was separated into the layers, each described by the following parameters: the thickness, the crystal lattice strain in the growth direction, and the static Debye–Waller

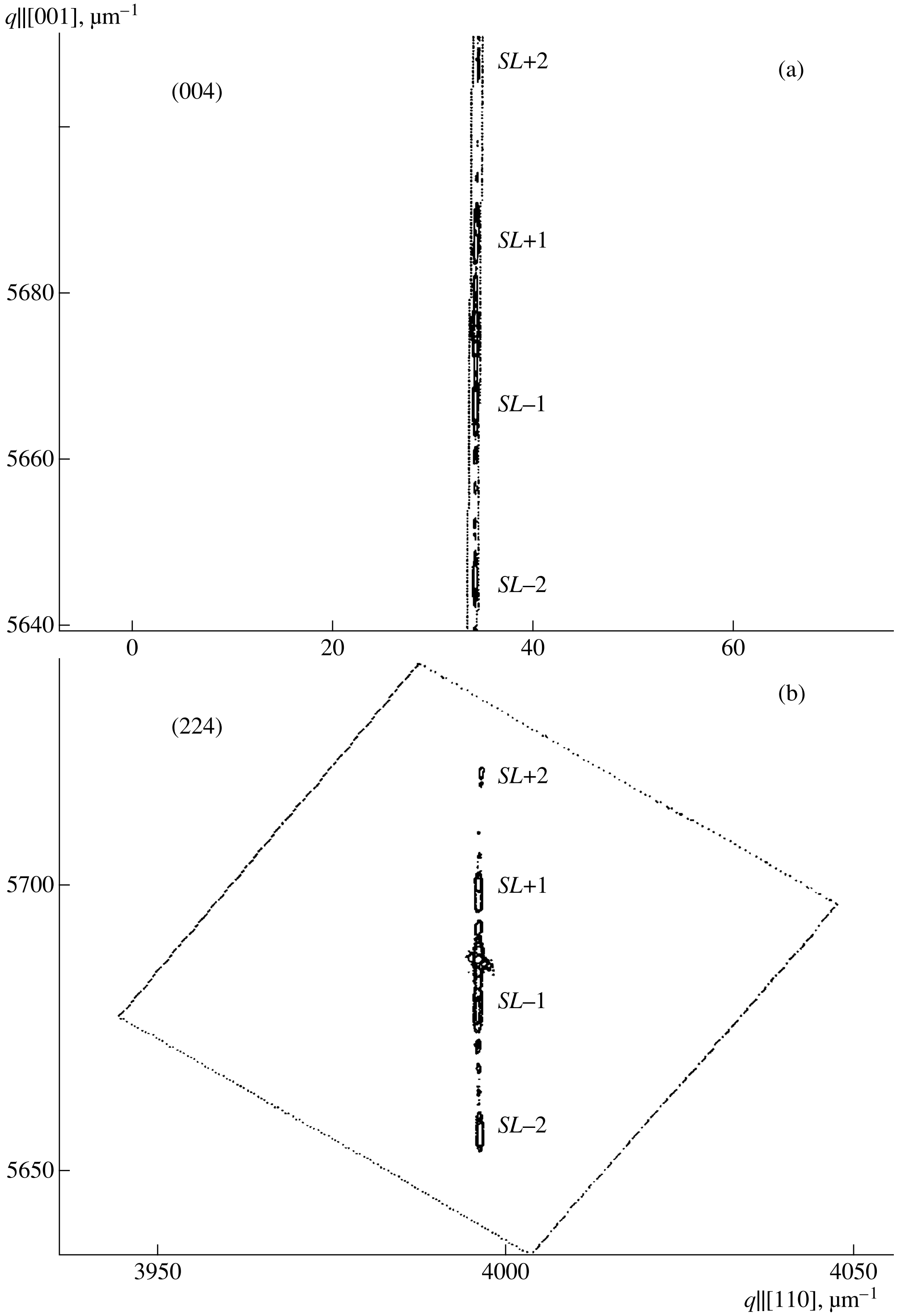

Fig. 1. Reciprocal lattice maps in the neighborhood of (a) [[004]] and (b) [[224]] points for sample 35/27.

factor. In order to decrease the number of variables, it was assumed that the layer parameters do not vary from period to period. The diffuse scattering was approximated by a Lorentzian, which made it possible to improve the convergence of the optimization procedure. The static Debye–Waller factors for the superlattice layers appeared to be larger than 0.99. Therefore, the substrate is responsible for the diffuse scattering. Table 1 lists the structure parameters of the Si/Si$_{1-x}$Ge$_x$ superlattices, which were determined from the optimization procedure.

The Ge concentration in the solid solution layers was evaluated from the strain $\varepsilon_\perp$ within the bilayer

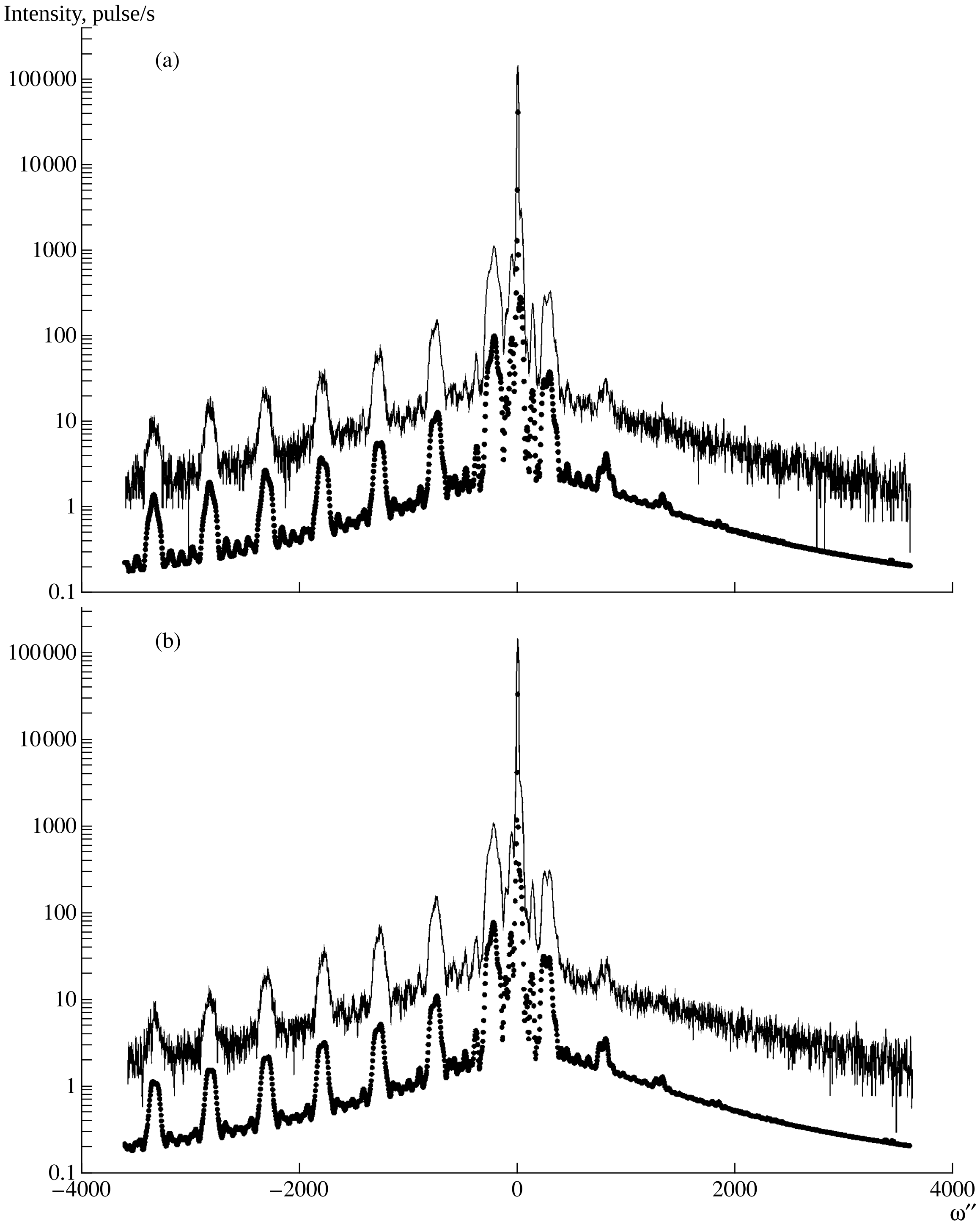

Fig. 2. Experimental and calculated rocking curves for the samples grown at temperatures of (a) 550 and (b) 810°C. (004) reflection. For clarity, the calculated curves are shifted with respect to the experimental curves.

approximation of the elasticity theory

$$\frac{a_{\mathrm{SiGe}} - a_{\mathrm{Si}}}{a_{\mathrm{Si}}} = \varepsilon_{\perp}\frac{C_{11}^{\mathrm{SiGe}}}{C_{11}^{\mathrm{SiGe}} + 2C_{12}^{\mathrm{SiGe}}},$$

$$C_{ij}^{\mathrm{SiGe}} = C_{ij}^{\mathrm{Si}} + \Delta C_{ij}\delta,$$

$$\Delta C_{ij} = C_{ij}^{\mathrm{Ge}} - C_{ij}^{\mathrm{Si}}.$$

Here, $a_{\mathrm{SiGe}} = a_{\mathrm{Si}} + 0.02\delta + 0.0026\delta^2$ (nm) [3], where δ is the Ge concentration (in relative units), and a_{Si} = 0.54309 nm.

Table 1. Structure parameters of the Si/$Si_{1-x}Ge_x$ superlattices

Sample	Substrate temperature, °C	Layer	Thickness, nm	Ge, %	$\varepsilon_\perp^*$	$\langle\varepsilon_\perp\rangle$**
35/27	550	Si	33.1	0	0	7.8×10^{-4}
		SiGe	4.0	22.6	0.0152	
		Si-cap	225.0	0	0	
35/31	650	Si	33.1	0	0	7.6×10^{-4}
		SiGe	4.0	22.2	0.0149	
		Si-cap	222.0	0	0	
35/25	700	Si	33.5	0	0	7.8×10^{-4}
		SiGe	4.0	22.6	0.0152	
		Si-cap	222.0	0	0	
35/28	810	Si	33.3	0	0	7.9×10^{-4}
		SiGe	4.0	23.5	0.0158	
		Si-cap	223.0	0	0	

* $\varepsilon_\perp = \dfrac{a_\perp^{\text{layer}} - a^{\text{Si}}}{a^{\text{Si}}}$, where $a_\perp^{\text{layer}}$ is the lattice parameter of the layer in the direction perpendicular to the sample surface, and a^{Si} is the lattice parameter of silicon. It is assumed that the substrate is unstrained.

** $\langle\varepsilon_\perp\rangle$ is the strain averaged over the superlattice thickness.

The C_{11} and C_{12} elastic moduli were taken from [8]

	Si	Ge
C_{11} (10^{10} Pa)	16.58	12.85
C_{12} (10^{10} Pa)	6.39	4.83

The strains $\varepsilon_\perp$ (Table 1) were converted to the intrinsic strains of the solid solution layers $\varepsilon_\parallel^{\text{layer}}$ and $\varepsilon_\perp^{\text{layer}}$:

$$\varepsilon_\parallel^{\text{layer}} = \frac{a_{\text{Si}} - a_{\text{SiGe}}}{a_{\text{SiGe}}},$$

$$\varepsilon_\perp^{\text{layer}} = \frac{a_{\text{Si}}(1 + \varepsilon_\perp) - a_{\text{SiGe}}}{a_{\text{SiGe}}},$$

where a_{Si} is the lattice parameter of silicon, and a_{SiGe} is the lattice parameter of the unstrained $Si_{1-x}Ge_x$ layer, calculated from the Vegard law.

The stresses σ_{xx} in the interface plane were determined from the Hooke law [9]

$$\sigma_{xx} = \varepsilon_\parallel^{\text{layer}} = (C_{11} + C_{12}) + \varepsilon_\perp^{\text{layer}} C_{12}.$$

The intrinsic strains and stresses σ_{xx} in the interface plane are given in Table 2. Note that, for sample 35/28, a stress of –1.51 GPa is in reasonable agreement with the stress (–1.28 GPa) obtained from the Raman spectrum in the range 500–530 cm^{-1} [10].

Analysis of the quantitative structure parameters for the given superlattices demonstrates that they were grown with a high reproducibility in the thickness of all the layers. A certain scatter in the Ge content in the solid solution and also in the mean strain of the superlattice indicates no correlation between these quantities and the substrate temperature.

Secondary Ion Mass Spectrometry

The Ge depth profiles in one superlattice period for three samples are shown in Fig. 3. There is a clear tendency for the broadening of the profiles with an increase in the substrate temperature. The major feature of the profile shapes is the presence of two linear portions in the peak slope corresponding to the Si-on-SiGe interface: the concentration varies in the range from 4×10^{21} to 8×10^{20} cm^{-3} in portion *1* (near the maximum of the peak), and from 8×10^{20} to 5×10^{19} cm^{-3} in portion *2*. At the same time, the other peak slope is approximated by the linear portion *3* that corresponds to the change in the concentration from 4×10^{21} to 5×10^{19} cm^{-3}.

Transmission Electron Microscopy

Figure 4 demonstrates the TEM images of cross-sections of the superlattices whose rocking curves are represented in Fig. 2. The absence of dislocations in the superlattices is in agreement with the data of X-ray diffraction analysis. The main difference in the structural features of the studied samples resides in the sharpness of layer interfaces in the superlattices. As can be seen in the sample grown at a temperature of 550°C, the sharpnesses of the upper (Si-on-SiGe) and lower (SiGe-on-Si) interfaces of the SiGe layers are identical. At the same time, in the sample grown at a temperature

Table 2. Intrinsic strains and stresses σ_{xx} in the interface plane

Sample	$\varepsilon_{\perp}^{\text{layer}}$	$\varepsilon_{\parallel}^{\text{layer}}$	σ_{xx}, GPa
35/27	6.54×10^{-3}	-8.52×10^{-3}	–1.46
35/31	6.41×10^{-3}	-8.36×10^{-3}	–1.43
35/25	6.54×10^{-3}	-8.52×10^{-3}	–1.46
35/28	6.79×10^{-3}	-8.86×10^{-3}	–1.51

of 810°C, the upper interfaces are sharper than the lower interfaces.

The densitograms of the reference sample and one SiGe layer in the real superlattice are compared in Fig. 5. The densitogram of the reference sample exhibits a peak with a flattened maximum and linear slopes, which are well approximated by straight tangents (Fig. 5a) whose slope angles (α_A and α_B) are equal to each other (Table 3). In the general case, the slope angles of tangents depend on the negative contrast, instrumental parameters (magnification of densitogram, slit width, etc.), and the sharpness of the corresponding interface in the image. The full width at half maximum (FWHM) corresponds to the stripe width (pointer projection) in the negative.

The characteristic feature of the densitograms of the SiGe layers in the superlattice (Fig. 5b) is that, in the peaks, the slope *A*, corresponding to the lower layer interfaces (SiGe-on-Si), is well approximated by a straight line. On the other hand, the slope corresponding to the upper layer interfaces (Si-on-SiGe) involves two portions *B* and *C*, each also approximated by a short straight line. The portion *B* near the maximum of the peak is always steeper than the lower portion *C*. The peak tails (portions *C*) considerably differ in shape and length along the direction of epitaxial growth. The slope angle of a tangent to the portion *B* (α_B) is always less than that of a tangent to the portion *A* (α_A). Since the slope angle of the tangent to the peak slope depends on the sharpnesses of the corresponding interface in the negative, all other factors (conditions of recording the densitograms) being the same, it can be assumed that the sharpness of the lower and upper SiGe layer interfaces are different. Note that the inequality $\alpha_A > \alpha_B$ indicates that the SiGe-on-Si interface is sharper.

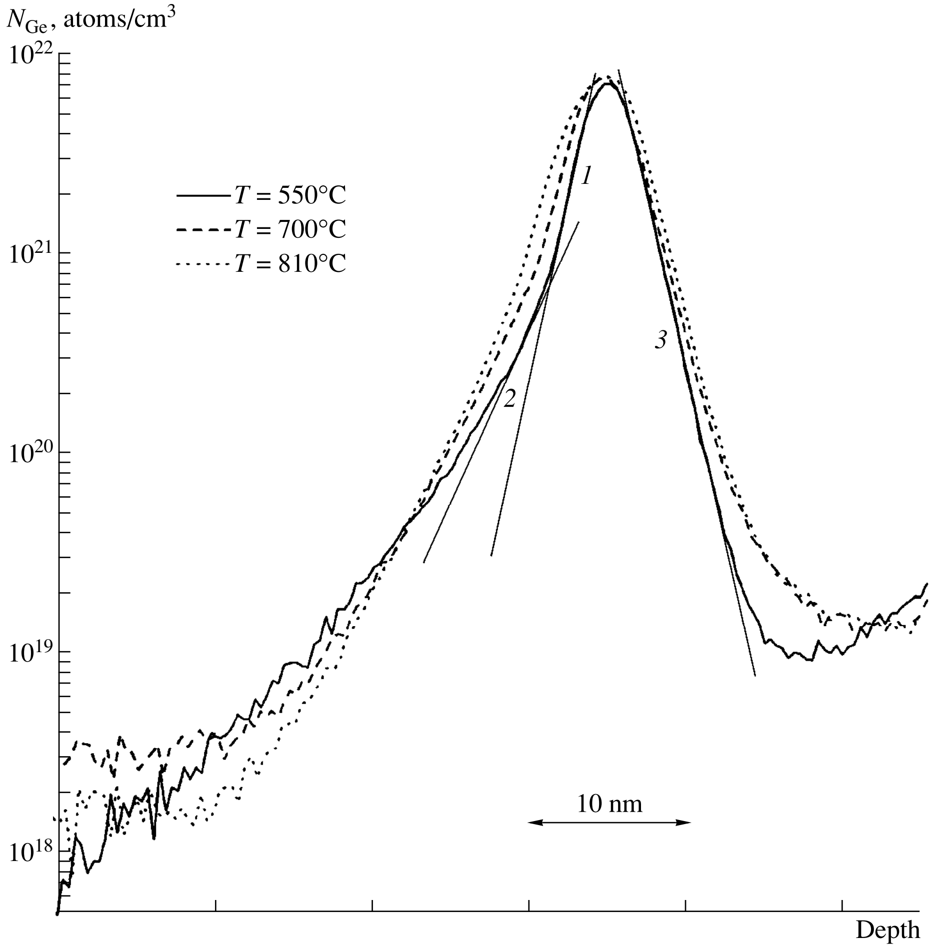

Fig. 3. SIMS Ge profiles in the region of the period closest to the surface for superlattices grown at different temperatures.

The densitometric analysis and measurements of the SiGe layer thickness in the superlattices were carried out for three samples grown at temperatures differing by about 200 K (Table 3). The layer thickness was determined from the electron micrographs with the use of the image analysis system. For five layers each in the superlattices, the thickness was measured at 100 points shifted along the layer. In superlattices 35/27 and 35/30 grown at relatively low temperatures, the scatter in thickness is absent or falls within the limits of experimental error (±0.5 nm). A substantial scatter in thickness (from 4.0 to 7.0 nm) is found for superlattice 35/28. For this sample, we analyzed the nonuniformity of the SiGe layer thickness along the direction of epitaxial growth. In order to determine the layer thickness more correctly, the measurements were conducted with densitograms recorded for each of five layers upon scanning of the negative along the same line. The full widths at half maximum are as follows: 5.5 nm for three layers inside the superlattice, 6.0 nm for the upper layer, and 6.5 nm for the lower layer. Analysis of the slope angles of tangents to the peaks demonstrates that the α_A angles for all the SiGe layers are identical within the limits of experimental error, whereas the α_B angles turn out to be different. The α_B angles are the smallest for the layer adjacent to the substrate and are approximately the same for the other layers.

Taking into account the above scatter in the parameters of the SiGe layers in the direction of the epitaxial growth, different superlattices were compared using the data (layer thicknesses and the slope angles of tangents to the peaks) obtained for the middle SiGe layers. The results of the corresponding measurements are presented in Table 3. It can be seen that an increase in the substrate temperature leads to an increase in the layer thickness and a deterioration of the interface sharpness. Note that the smearing of the upper layer interfaces is considerably larger than that of the lower interfaces.

The nonuniformity of the thickness of the middle SiGe layer in the growth plane was analyzed for sample 35/28. For this purpose, a series of densitograms was recorded at points shifted with a step of 20 nm along the layer within a region of length 0.5 μm. The data obtained show that, within the limits of experimental error, the α_A angles in all the densitograms are virtually identical. The mean α_A angle is equal to 86.9° ± 0.5°. For other peak slopes corresponding to the Si-on-SiGe interfaces, the scatter in the α_B angles is equal to ~3° (Table 3). The scatter in the layer thicknesses measured from the full width at half maximum is small, and the mean thickness is equal to 5.5 ± 0.5 nm.

DISCUSSION

The SIMS concentration profiles of Ge on the semilog scale are identical for all the periods in the superlattice for each sample. This allows us to use the profiles of one period in the superlattices for comparison of different samples (Fig. 3). As follows from comparison of the profiles for different samples, an increase in the temperature leads to the broadening of peaks. In this case, the slope of linear portions *1* and *3* in the peaks decreases, which suggests an increase in the smearing of the upper and lower SiGe layer interfaces. At the same time, the slope of linear portions *2* increases.

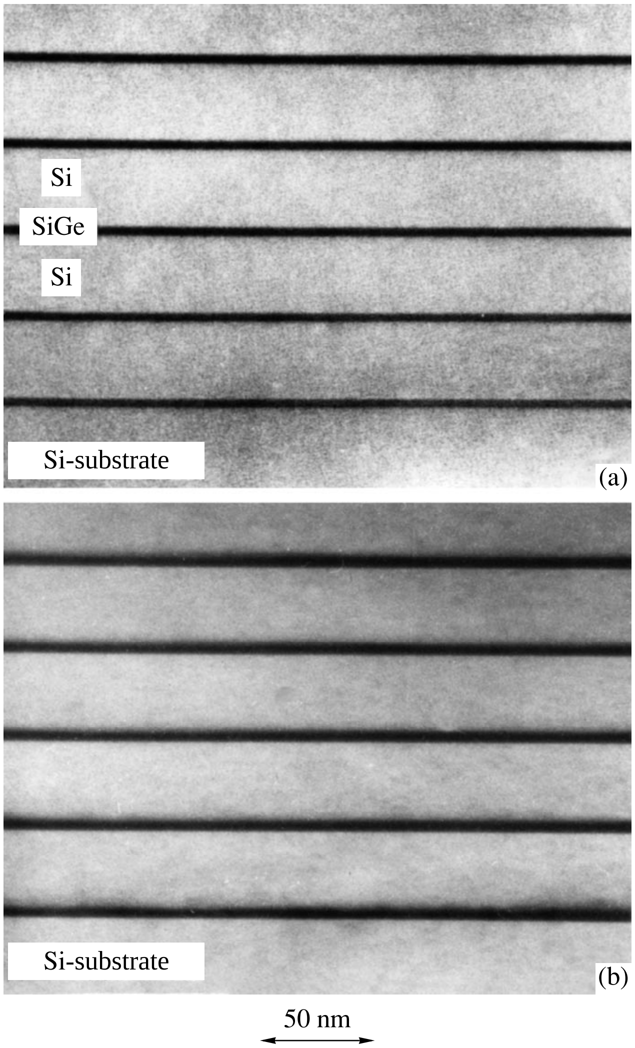

Fig. 4. TEM micrographs of the cross-sections of the superlattices grown at temperatures of (a) 550 and (b) 810°C.

It should be noted that the shapes of the SIMS profiles and densitograms resemble each other. Since the blackening density of the negative is proportional to the logarithm of the product of the illumination intensity (the electron beam intensity *J*) into the exposure time [11], the densitogram, in actual fact, is the dependence of log*J* on the coordinate along the normal to the superlattice surface. This makes it possible to qualitatively compare the densitograms with the Ge depth profiles of layers. Comparison demonstrates that the peaks in the experimental curves of both types exhibit a similar asymmetry, and there is a well-defined correlation

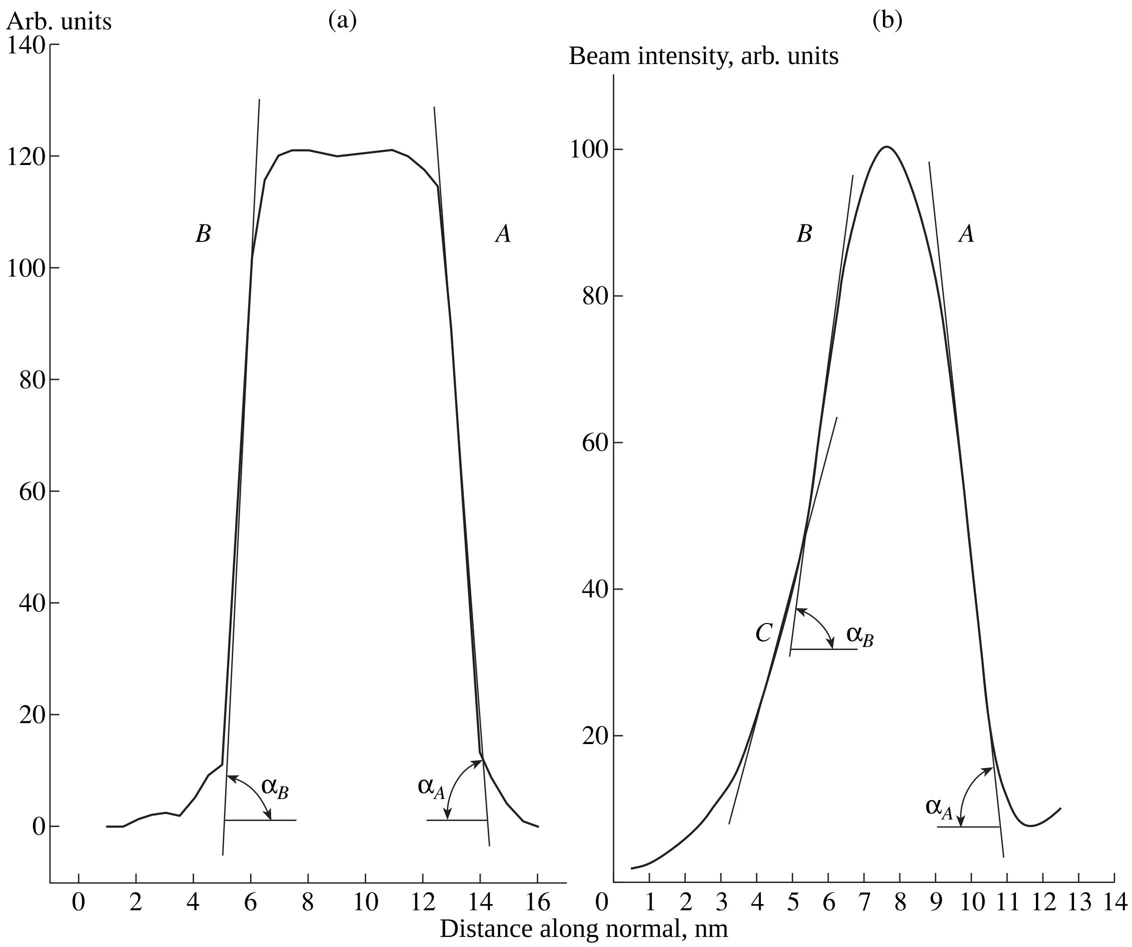

Fig. 5. Densitograms of the images of (a) reference sample and (b) SiGe layer in the real superlattice. Scanning direction in the layer densitogram corresponds to the motion of the light beam from surface to substrate along the normal to the surface.

between the slopes of three linear portions in these peaks and the temperature of epitaxial growth. Under conditions of diffraction contrast, the intensity of the passed electron beam is proportional to the Ge concentration in the solid solution (the larger the Ge content in the SiGe layer, the higher the beam intensity). Consequently, the concentration distribution of Ge in the layer can be qualitatively judged from the densitometric profile.

Table 3. Densitometric characteristics of the middle layer in the SiGe/Si superlattice

Sample	Growth temperature, °C	FWHM, ±0.5 nm	α_A, ±0.5°	α_B, ±0.5°
Reference sample			88.5	88.5
35/27	550	4.0	87.5–88.0	87.5–88.0
35/30	750	4.2	87.0–87.5	86.0–86.5
35/28	810	5.5	86.5–87.0	82.0–85.5

The SiGe layer thicknesses calculated from the high-resolution X-ray diffraction data differ from those directly measured by the densitometric technique (Tables 1, 3). Only for the sample grown at a temperature of 550°C, both methods lead to the same thickness (4.0 nm). At higher substrate temperatures, the SiGe layer thickness does not change according to the X-ray diffraction data, whereas the TEM and SIMS data indicate a pronounced increase in the layer thickness up to 5.5 nm (at 810°C). This difference is explained by the fact that the X-ray diffraction analysis is the integral method, and its sensitivity to a weak change in the strain profile with a change in the concentration profile of Ge in a particular thin SiGe layer is appreciably less compared to those of the TEM and SIMS techniques.

The set of the data obtained permits us to make certain conclusions concerning the nature of phenomena occurring at the interfaces in the superlattices in the course of their growth. The presence of two linear portions *1* and *2* (corresponding to the Si-on-SiGe interfaces) in the slopes of the SIMS and densitometric profiles is the characteristic indication of the Ge segregation at the surface of the growing SiGe layer [12]. The smearing of the Ge profile at the opposite interface is likely brought about by the germanium diffusion.

CONCLUSION

The combination of TEM, SIMS, and high-resolution X-ray diffraction techniques enabled us to describe in sufficient detail the distribution of the strains and the Ge concentration in the Si/SiGe superlattices and to evaluate the sharpness of interfaces. Different sensitivities of the methods to lattice strain and (or) the Ge content lead to considerable differences in the thicknesses of the SiGe layers and the Ge content, which were obtained by a particular technique. Comparison of these data shows that virtually all germanium is localized within the grown layer (according to the X-ray diffraction data), and the smearing of the Ge profile (according to the SIMS and TEM data) results in insignificant strain gradients in the interface regions, which are not recorded by the high-resolution X-ray diffraction technique. At the same time, the last method revealed that the samples under consideration are fully strained.

It was demonstrated that the densitometric profile of electron microscope images of the superlattices reflects the change in the logarithm of the Ge concentration in the solid solution and can be used for the qualitative evaluation of the Ge distribution over the layer thickness. The correct photographic recording of real superlattices and reference samples (the use of the same photosensitive material and simultaneous development) provides a way of applying the densitometric analysis of images to the characterization of the interface sharpness.

ACKNOWLEDGMENTS

This work was supported by the Russian Foundation for Basic Research, project no. 96-02-18608.

REFERENCES

1. M. G. Dowsett, N. S. Smith, R. Bridgeland, *et al.*, in *Secondary Ion Mass Spectrometry, SIMS*, Ed. by X. A. Benninghoven *et al.* (Wiley, Chichester, 1997).
2. M. G. Dowsett, G. Rowlands, P. N. Allen, *et al.*, Surf. Interface Anal. **21**, 310 (1994).
3. O. A. Mironov, P. J. Phillips, E. H. C. Parker, *et al.*, Thin Solid Films **306**, 307 (1997).
4. A. F. de Jong and K. T. F. Janseen, J. Mater. Res. **5**, 578 (1990).
5. G. Bauer, J. Li, and E. Koppensteiner, J. Cryst. Growth **157**, 61 (1995).
6. C. R. Wie, T. A. Tombrello, and T. Vreeland, Jr., J. Appl. Phys. **59**, 3743 (1986).
7. *Numerical Recipes in C: The Art of Scientific Computing*, Ed. by W. H. Press *et al.* (Cambridge Univ. Press, Cambridge, 1995), 2nd ed.
8. A. Segmuller and M. Murakami, in *Treatise on Materials Science and Technology*, Ed. by K. N. Tu and R. Rosenberg (Academic, New York, 1988), Vol. 27, p. 143.
9. J. F. Nye, *Physical Properties of Crystals* (Clarendon, Oxford, 1964), p. 322.
10. O. A. Mironov, P. J. Phillips, E. H. C. Parker, *et al.*, Proc. SPIE-Int. Soc. Opt. Eng. **3182**, 216 (1997).
11. W. Krug and H. Weide, *Wissenschaftliche Photographie in der Anwendung* (Akademische Verlagsgesellschaft, Leipzig, 1972; Mir, Moscow, 1975).
12. S. Fukatsu, K. Fujita, H. Yaguchi, *et al.*, Appl. Phys. Lett. **59**, 2103 (1991).

Translated by O. Borovik-Romanova

Crystallography Reports, Vol. 45, No. 4, 2000, pp. 670–675. Translated from Kristallografiya, Vol. 45, No. 4, 2000, pp. 731–737.
Original Russian Text Copyright © 2000 by Alshits, Lyubimov.

Orientation of Optical Axes in Absorptive Crystals with Arbitrary Permittivity Tensors

V. I. Alshits and V. N. Lyubimov

Shubnikov Institute of Crystallography, Russian Academy of Sciences,
Leninskiĭ pr. 59, Moscow, 117333 Russia

Received June 18, 1998

Abstract—The direct relation has been established between the orientations of the optical axes and the components of the inverse complex permittivity tensor of an absorptive crystal possessing an arbitrary symmetry. The particular forms of the general relationships for triclinic crystals, characterized by an arbitrary degree of absorption, are obtained for crystals of all the other symmetry systems. The relationships obtained acquire a substantially simplified form for weakly absorptive crystals. The consideration is based on the relationship established for the components of the inverse permittivity tensor in the Cartesian coordinates and the diadic form of this tensor, which is related to the directions of the optical axes. *© 2000 MAIK "Nauka/Interperiodica".*

INTRODUCTION

As is well known [1–3], the optical properties of absorptive crystals are considerably different from those of transparent crystals. Absorption cannot be reduced to a simple decrease of the wave intensities during their propagation, and results in qualitatively new characteristics of electromagnetic wave fields. It is especially clearly seen in the directions close to optical axes. The waves of two different independent polarizations propagating along these directions have not only the same phase velocities, but also the same absorption coefficients. Two independent waves can always propagate along any direction in an anisotropic crystal. In the general case, these waves have different velocities and absorption coefficients. While a transparent optically anisotropic crystal has one or two optical axes, an absorptive crystal has four such axes. The absorption-induced optical axes drastically change the wave-field pattern [1–3].

As is well known, all the optical properties of absorptive crystals are determined by complex permittivity tensor. For triclinic crystals, this tensor has twelve independent parameters—six components of the real part and six component of the imaginary one. In particular, these twelve components also determine the orientations of the optical axes of the crystal. However, the determination of the orientations of the optical axes from the given components of the complex permittivity tensor for a triclinic crystal with an arbitrary absorption has not been solved as yet. In the present article, we aimed to close this gap.

Below, we study the geometry of optical axes in an absorptive crystal of an arbitrary symmetry. The general relationships obtained for triclinic crystals with an arbitrary degree of absorption are then analyzed for crystals of higher crystal systems. We also consider the case of weakly absorptive crystals, for which all the relationships are considerably simplified. The complicated calculations for low-symmetric (triclinic and monoclinic) crystals are associated with the fact that the real and the imaginary parts of the complex permittivity tensor cannot be reduced to the diagonal form in the same coordinate system, whereas the orientations of the optical axes of the crystal are directly determined by this complex tensor. We shall establish the direct relation between the components of the inverse permittivity tensor and the orientations of the optical axes of an absorptive crystal of an arbitrary symmetry. Our approach is based on the relationship established for the components of the inverse permittivity tensor given in the Cartesian coordinate system and the diadic form of the tensor. We shall show that the complex vectors of the diadic representation and the directions of the optical axes are related by a rather simple way.

INITIAL RELATIONSHIPS IN THE FEDOROV FORMALISM

To solve the problem of optical-axis orientations formulated above, we have to study the behavior of the complex refractive indices N of electromagnetic waves harmonic both in time t and space $\mathbf{r}$, which propagate along the wave normal $\mathbf{m}$ with a frequency of ω:

$$\begin{bmatrix}\mathbf{E}\\ \mathbf{H}\end{bmatrix} \equiv \begin{bmatrix}\mathbf{E}(\mathbf{r}, t)\\ \mathbf{H}(\mathbf{r}, t)\end{bmatrix} = \begin{bmatrix}\mathbf{E}_0\\ \mathbf{H}_0\end{bmatrix} e^{i\omega[(N\mathbf{m}\mathbf{r}/c) - t]}, \qquad (1)$$

where $\mathbf{E}$ and $\mathbf{H}$ are the vectors of alternating electric and magnetic fields, $\mathbf{E}_0$ and $\mathbf{H}_0$ are their amplitudes, and c is the velocity of light in vacuum.

In absorptive anisotropic media, the Maxwell equations satisfied by the wave fields of Eq. (1) are reduced to the following vector equations [1, 2]:

$$\begin{aligned} \mathbf{D} &= (\hat{\varepsilon} + i\hat{\varepsilon}')\mathbf{E} = -N[\mathbf{mH}], \\ \mathbf{H} &= N[\mathbf{mE}], \end{aligned} \tag{2}$$

where $\mathbf{D}$ is the electric induction, and $\hat{\varepsilon} + i\hat{\varepsilon}'$ is the complex permittivity tensor whose imaginary part determines absorption.

Eliminating the electric field E from Eqs. (2), we arrive at the expression for the magnetic field H:

$$\mathbf{H} = -N^2[\mathbf{m}, \hat{B}[\mathbf{mH}]], \tag{3}$$

where $\hat{B}$ is the inverse permittivity tensor of a crystal

$$\hat{B} = (\hat{\varepsilon} + i\hat{\varepsilon}')^{-1} = \hat{\beta} - i\hat{\beta}', \tag{4}$$

which is both complex and symmetric and, thus, non-Hermitian.

For the further analysis, it is convenient to use the formalism suggested by Fedorov [1] and represent the tensor $\hat{B}$ in the diadic form,

$$\hat{B} = a + b(\mathbf{C}_1 \cdot \mathbf{C}_2 + \mathbf{C}_2 \cdot \mathbf{C}_1), \tag{5}$$

where a is any of the eigenvalues of the tensor $\hat{B}$, and the dot between the complex vectors $\mathbf{C}_1$ and $\mathbf{C}_2$ symbolizes the diadic multiplication. For some problems, the explicit form of scalars a and b and vectors $\mathbf{C}_1$ and $\mathbf{C}_2$ is unessential [1], but for the problems formulated above, it is very important to establish the concrete relationships between these parameters and the tensor components B_{ij} set in the Cartesian coordinates.

Substituting the tensor $\hat{B}$ in diadic form Eq. (5) into (3), we have

$$\{a - (1/N^2) + b(\mathbf{p}_1 \cdot \mathbf{p}_2 + \mathbf{p}_2 \cdot \mathbf{p}_1)\}\mathbf{H} = 0, \tag{6}$$

where, for the sake of brevity, we introduced the notation $\mathbf{p}_{1,2} = [\mathbf{mC}_{1,2}]$. Eq. (6) yields the expressions for the refractive indices and the polarization vectors of isonormal waves

$$1/N_{\pm}^2 = a + b(\mathbf{p}_1\mathbf{p}_2 \pm \sqrt{\mathbf{p}_1^2\mathbf{p}_2^2}), \tag{7}$$

$$\mathbf{H}_{\pm} \parallel \mathbf{p}_1\sqrt{\mathbf{p}_2^2} \pm \mathbf{p}_2\sqrt{\mathbf{p}_1^2}. \tag{8}$$

It is seen from Eq. (7) that the degeneracy condition, i.e., the condition for the coincidence of the complex refractive indices of two isonormal waves ($N_+ = N_-$), is fulfilled either at $\mathbf{p}_1^2 = 0$ or at $\mathbf{p}_2^2 = 0$ only for the following propagation directions

$$\mathbf{m}_{1,2}^{\pm} = \frac{\mathbf{C}_{1,2}\sqrt{\mathbf{C}_{1,2}^{*2}} + \mathbf{C}_{1,2}^{*}\sqrt{\mathbf{C}_{1,2}^{2}} \pm i[\mathbf{C}_{1,2}\mathbf{C}_{1,2}^{*}]}{|\mathbf{C}_{1,2}|^2 + |\mathbf{C}_{1,2}^2|}. \tag{9}$$

Subscripts 1 or 2 and the signs "+" or "–" in the left- and the right-hand sides of Eq. (9) are chosen in the same way. Both isonormal waves propagating along any of the four directions $\mathbf{m}_{1,2}^{\pm}$ (9) have the same phase velocities and the same absorption coefficients.

The diadic form of the tensor $\hat{B}$, Eq. (5), and expression (9) for the directions of the optical axes determined by this diadic form are not related to any concrete coordinate system, but, in practice, the tensor $\hat{B}$ for crystals is always set by its components B_{ij} ($i, j = 1, 2, 3$) in a certain crystallophysical coordinate system [4].

In this study, we aimed to determine the orientations of the optical axes of absorptive crystals of different systems characterized by the tensor B_{ij} set by its components in a Cartesian coordinate system. Using Eq. (9), we have to express the complex vectors $\mathbf{C}_{1,2}$ in terms of the components B_{ij}, which can be done if we manage to establish the relation between the diadic and the coordinate forms of the tensor $\hat{B}$.

ORIENTATIONS OF OPTICAL AXES IN ABSORPTIVE CRYSTALS OF DIFFERENT SYSTEMS

1.Triclinic Crystals

A. The case of arbitrary absorption. In this case, no specific constraints on the components of the tensor B_{ij} are imposed. According to Eq. (5), these components can be written in the Cartesian coordinate system as

$$B_{ij} = a\delta_{ij} + b\{(\mathbf{C}_1)_i(\mathbf{C}_2)_j + (\mathbf{C}_2)_i(\mathbf{C}_1)_j\}, \tag{10}$$

where $i, j = 1, 2, 3$, δ_{ij} is the unit matrix, and the scalar a is any of the roots of the characteristic equation of the tensor B_{ij}:

$$|B_{ij} - a\delta_{ij}| = 0. \tag{11}$$

Six equations of type (10) and condition (11) allow us to express the scalar b and the components of the complex vectors ($\mathbf{C}_{1,2}$) in terms of the components B_{ij}. Omitting the algebraic details,[1] we only indicate here the final results valid for the general case of a triclinic crystal with an arbitrary inverse tensor of the complex dielectric constant:

$$b = D_{31}/2, \tag{12}$$

$$\mathbf{C}_{1,2} = (B_{13} \pm R_{13}, B_{23} \mp R_{23}, B_{33} - a)/\sqrt{D_{31}(B_{33} - a)}. \tag{13}$$

Hereafter, we use the following notation for the differences between the diagonal components of the

---

[1] The numerical algorithm for solving the problem under consideration is given elsewhere [5].

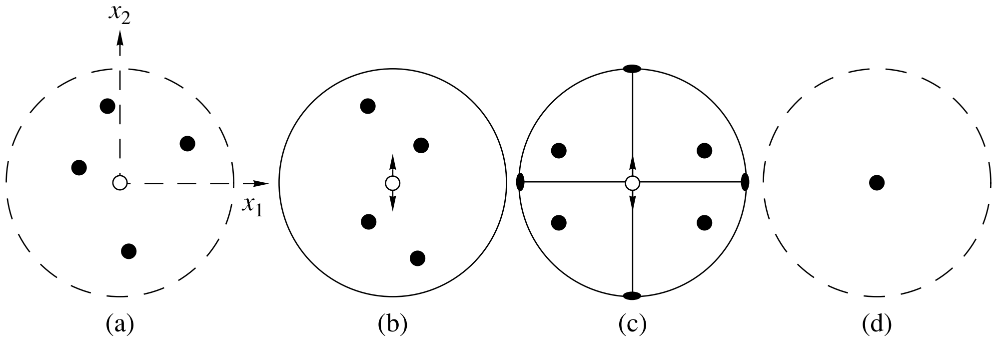

(a) (b) (c) (d)

Fig. 1. Configurations of optical axes (stereographic projections) in absorptive crystals of different systems: (a) triclinic crystals (classes $G = \bar{1}$, 1); (b) monoclinic crystals ($G = 2/m$, 2, m); (c) orthorhombic crystals ($G = mmm$, $mm2$, 222), (d) absorptive and nonabsorptive crystals of intermediate systems. For (a–c), the highest-order symmetry elements of the groups G in the corresponding systems are shown in the standard notation used in [4].

tensor B_{ij}:

$$D_{ij} = B_{ii} - B_{jj}. \tag{14}$$

The radicals R_{i3} in Eq. (13) have the form

$$R_{i3} = \sqrt{B_{i3}^2 - (B_{ii} - a)(B_{33} - a)}. \tag{15}$$

The radicals R_{13} and R_{23} in Eq. (13) are related as

$$R_{13}R_{23} = B_{12}(B_{33} - a) - B_{13}B_{23} \tag{16}$$

because the scalar a satisfies the characteristic equation (11).

The tensor B_{ij}, which, in the general case, has three eigenvalues [see Eq. (11)], can be represented in diadic form (5), (10), (12), and (13) by three different but equivalent methods.

The above general relationships can be somewhat simplified in the system of coordinates in which the tensor β_{ij} (4) is diagonal. Then, only the diagonal components of the tensor β_{ij} have the nonzero values

$$\beta_{11} \equiv \beta_1, \quad \beta_{22} \equiv \beta_2, \quad \beta_{33} \equiv \beta_3. \tag{17}$$

In this case, the nondiagonal components of the tensor B_{ij} are determined by the tensor β'_{ij} (4) alone,

$$B_{12} = -i\beta'_{12}, \quad B_{13} = -i\beta'_{13}, \quad B_{23} = -i\beta'_{23}. \tag{18}$$

In triclinic absorptive crystals, the orientations of four optical axes $\mathbf{m}_{1,2}^{\pm}$ can be established from the given components of the tensor B_{ij} with the aid of Eqs. (9) and (13). In the general case, each of the complex vectors $\mathbf{C}_1$ and $\mathbf{C}_2$ generates a pair of optical axes $\mathbf{m}_1^{\pm}$ and $\mathbf{m}_2^{\pm}$, respectively, with these four directions being nonequivalent (Fig. 1a).

B. The case of weak absorption. In this case, general relationships (11)–(16) are considerably simplified. Using the system of coordinates in which the tensor β_{ij} is diagonal, i.e., Eqs. (17) and (18) are valid, we can assume that the absolute values of all the components of the tensor β'_{ij} are much less than those of the diagonal components β_i (17). Under these conditions, formulas (11)–(16) yield the following approximate relationships:

$$a = \beta_2 - i\beta'_{22}, \quad b = (d_{31} - id'_{31})/2, \tag{19}$$

$$\mathbf{C}_{1,2} = \mathbf{m}_{1,2} + i\mathbf{c}'_{1,2}, \tag{20}$$

where the following notation is used

$$d_{ij} = \beta_i - \beta_j, \quad d'_{ij} = \beta'_{ii} - \beta'_{jj}. \tag{21}$$

The real vectors $\mathbf{m}_{1,2}$ in (20) have the sense of the directions of optical axes in the absence of absorption

$$\mathbf{m}_{1,2} = (\pm\sin\alpha, 0, \cos\alpha), \tag{22}$$

where

$$\sin\alpha = \sqrt{d_{21}/d_{31}}, \quad \cos\alpha = \sqrt{d_{32}/d_{31}}. \tag{23}$$

The vectors $\mathbf{m}_1$ and $\mathbf{m}_2$ are symmetrically located in the coordinate plane x_1x_3 and form an angle of 2α (Figs. 2a, 2b). Without any loss of presentation generality, the coordinate system can be chosen in such a way that the diagonal components β_i are numbered as follows:

$$\beta_1 \le \beta_2 \le \beta_3, \tag{24}$$

whereas the radicals in (23) are real. The vectors $\mathbf{c}'_{1,2}$ in (20) arise due to absorption

$$\mathbf{c}'_{1,2} = \left(\pm\kappa - \tilde{\beta}'_{13}, \pm\tilde{\beta}'_{12} - \tilde{\beta}'_{23}, \tilde{\kappa}\right). \tag{25}$$

The components of these vectors are linearly dependent on the absorption parameters, i.e., on the components of the tensor β'_{ij}

$$\begin{aligned} \kappa &= (d'_{31}/d_{31} - d'_{21}/d_{21})\sin\alpha, \\ \tilde{\kappa} &= (d'_{31}/d_{31} - d'_{32}/d_{32})\cos\alpha, \end{aligned} \tag{26}$$

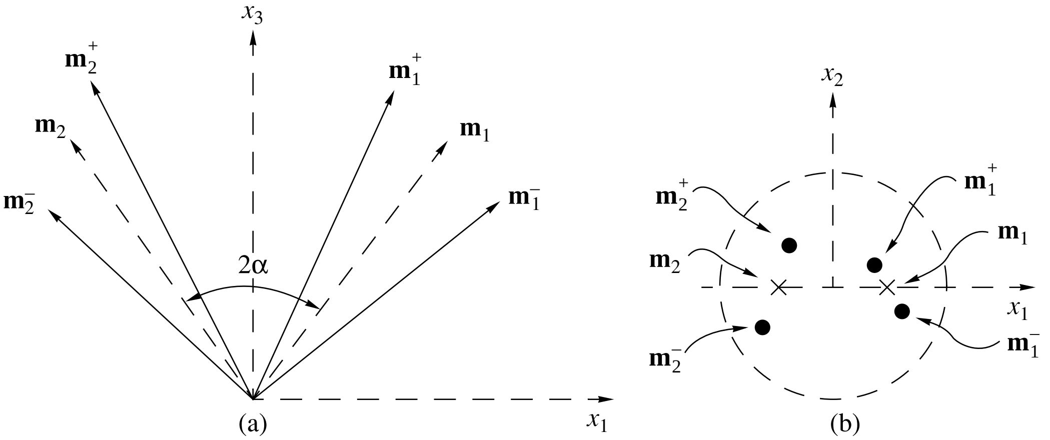

Fig. 2. Optical axes $\mathbf{m}_1$ and $\mathbf{m}_2$ in a transparent triclinic crystal and their splitting ($\mathbf{m}_1 \longrightarrow \mathbf{m}_1^\pm$, $\mathbf{m}_2 \longrightarrow \mathbf{m}_2^\pm$) due to "switching-on" of absorption: (a) spatial configuration (only the vectors $\mathbf{m}_1$ and $\mathbf{m}_2$ lie in the x_1x_3 plane); (b) stereographic projection.

$$\tilde{\beta}'_{12} = \beta'_{12}/\sqrt{d_{31}d_{21}}, \tag{27}$$

$$\tilde{\beta}'_{i3} = \beta'_{i3}/\sqrt{d_{31}d_{32}} \quad (i = 1, 2). \tag{28}$$

The absorption parameters κ and $\tilde{\kappa}$ (26) depend on the diagonal components of the tensor β'_{ij} alone and have the nonzero values for crystals of the lower and intermediate systems. At the same time, the parameters $\tilde{\beta}'_{12}$ (27) and $\tilde{\beta}_{i3}$ (28), which are determined by the nondiagonal components of the tensor β'_{ij}, have the nonzero values only for crystals of lower systems—$\tilde{\beta}'_{i3}$ for triclinic and $\tilde{\beta}'_{12}$ for monoclinic and triclinic ones.

The above approximate relationships allow us to find the directions of four optical axes $\mathbf{m}^\pm_{1,2}$ for weakly absorptive triclinic crystals. Thus, vector $\mathbf{C}_1$ (20) generates a pair of optical axes whose directions are set by the relationship

$$\mathbf{m}_1^\pm = \mathbf{m}_1 \pm [\mathbf{m}_1\mathbf{c}'_1], \tag{29}$$

where the vectors $\mathbf{m}_1$ and $\mathbf{c}'_1$ are set by the relationships (22) and (25). The second term in the right-hand part of (29) describes splitting of the optical axis (with the direction $\mathbf{m}_1$) of a transparent triclinic crystal under the effect of absorption. Using relationships (22) and (25), we can directly relate this splitting to the components of the tensor β'_{ij} characterizing absorption:

$$[\mathbf{m}_1\mathbf{c}'_1] = \left\{\left(\tilde{\beta}'_{23} - \tilde{\beta}'_{12}\right)\cos\alpha, \left(\kappa - \tilde{\beta}'_{13}\right)\cos\alpha - \tilde{\kappa}\sin\alpha, \left(\tilde{\beta}'_{12} - \tilde{\beta}'_{23}\right)\sin\alpha\right\}. \tag{30}$$

The second pair of the optical axes is set by the formula

$$\mathbf{m}_2^\pm = \mathbf{m}_2 \pm [\mathbf{m}_2\mathbf{c}'_2], \tag{31}$$

where the term describing splitting can be set by relationship (30) with the following substitution:

$$\sin\alpha \longrightarrow -\sin\alpha, \quad \kappa \longrightarrow -\kappa, \quad \tilde{\beta}'_{12} \longrightarrow -\tilde{\beta}'_{12}, \tag{32}$$

so that we have

$$[\mathbf{m}_2\mathbf{c}'_2] = \left\{\left(\tilde{\beta}'_{23} - \tilde{\beta}'_{12}\right)\cos\alpha, -\left(\kappa + \tilde{\beta}'_{13}\right)\cos\alpha + \tilde{\kappa}\sin\alpha, \left(\tilde{\beta}'_{12} + \tilde{\beta}'_{23}\right)\sin\alpha\right\}. \tag{33}$$

As is seen from (31), the angle formed by the optical axes $\mathbf{m}_1^+$ and $\mathbf{m}_1^-$ is proportional to the absorption parameters and set by the formula

$$\widehat{\mathbf{m}_1^+\mathbf{m}_1^-} = 2\left|[\mathbf{m}_1\mathbf{c}'_1]\right|. \tag{34}$$

The optical axes $\mathbf{m}_1^+$ and $\mathbf{m}_1^-$ are oriented symmetrically with respect to the initial axis $\mathbf{m}_1$, with all three vectors, $\mathbf{m}_1^+$, $\mathbf{m}_1^-$, and $\mathbf{m}_1$, being located in one plane.

In a similar way, the angle between the optical axes $\mathbf{m}_2^+$ and $\mathbf{m}_2^-$ is

$$\widehat{\mathbf{m}_2^+\mathbf{m}_2^-} = 2\left|[\mathbf{m}_2\mathbf{c}'_2]\right|. \tag{35}$$

The vectors $\mathbf{m}_2^+$, $\mathbf{m}_2^-$, and $\mathbf{m}_2$ also lie in one plane.

2. Monoclinic Crystals

For monoclinic crystals, the axis x_3 in the crystallophysical coordinate system is either parallel to the twofold symmetry axis or perpendicular to the symmetry plane (see [4]). In this case, the following components of the tensor B_{ij} go to zero

$$B_{13} = B_{23} = 0. \tag{36}$$

Then general characteristic equation (11) “splits.” It is convenient to choose one of two roots of the “split quadratic equation” as a parameter a:[2]

$$(B_{11} - a)(B_{22} - a) - B_{12}^2 = 0. \tag{37}$$

Then, expression (13) for the vectors $\mathbf{C}_{1,2}$ is simplified,

$$\mathbf{C}_{1,2} = (\pm\sqrt{a - B_{11}}, \mp B_{12}/\sqrt{a - B_{11}}, \sqrt{B_{33} - a})/\sqrt{D_{31}}. \tag{38}$$

For monoclinic crystals, the problem of optical-axis orientations for arbitrary absorption is solved with the use of relationships (9) and (38). Because of the symmetry, both pairs of the optical axes are equivalent (Fig. 1b), which can readily be seen if one takes into account that the components of the vectors $\mathbf{C}_1$ and $\mathbf{C}_2$ (38) differ only by their signs.

If absorption is weak, the expression for the vectors $\mathbf{c}'_{1,2}$ (25) is simplified:

$$\mathbf{c}'_{1,2} = \left(\pm\kappa, \pm\tilde{\beta}'_{12}, \tilde{\kappa}\right). \tag{39}$$

In this case, splitting of optical axes of a transparent monoclinic crystal is still determined by expressions (29) and (31), but with

$$[\mathbf{m}_1\mathbf{c}'_1] = \left(-\tilde{\beta}'_{12}\cos\alpha, \kappa\cos\alpha - \tilde{\kappa}\sin\alpha, \tilde{\beta}'_{12}\sin\alpha\right), \tag{40}$$

$$[\mathbf{m}_2\mathbf{c}'_2] = \left(\tilde{\beta}'_{12}\cos\alpha, -\kappa\cos\alpha + \tilde{\kappa}\sin\alpha, \tilde{\beta}'_{12}\sin\alpha\right). \tag{41}$$

Vectors (40) and (41) differ only by the signs of their components (the manifestation of the monoclinic symmetry).

3. Orthorhombic Crystals

In the standard crystallophysical coordinate system, with the coordinate axes parallel to the twofold symmetry axes or perpendicular to the symmetry planes, the complex tensor B_{ij} is diagonal, with the only nonzero components being

$$B_{11} \equiv B_1, \quad B_{22} \equiv B_2, \quad B_{33} \equiv B_3. \tag{42}$$

Under the assumption that $B_{12} = 0$ in (37) and (38), we arrive at the simplified equations

$$a = B_2, \tag{43}$$

$$\mathbf{C}_{1,2} = (\pm\sqrt{D_{21}}, 0, \sqrt{D_{32}})/\sqrt{D_{31}}. \tag{44}$$

The optical-axis orientations in orthorhombic crystals can be determined from (9) and (44). Because of the symmetry, all four optical axes are equivalent (Fig. 1c). This also follows from the fact that the difference between the vectors $\mathbf{C}_1$ and $\mathbf{C}_2$ reduces to different signs of only one of their components [see (44)].

If absorption is weak, the vectors $\mathbf{c}'_{1,2}$ can be written as

$$\mathbf{c}'_{1,2} = (\pm\kappa, 0, \tilde{\kappa}). \tag{45}$$

Splittings of the optical axes of a transparent crystal under the effect of absorption [see (29) and (31)] are determined by the vectors

$$[\mathbf{m}_1\mathbf{c}'_1] = -[\mathbf{m}_2\mathbf{c}'_2] = (0, \kappa\cos\alpha - \tilde{\kappa}\sin\alpha, 0). \tag{46}$$

The symmetry of orthorhombic crystals manifests itself in the above simple formula, relating the splittings of two different optical axes, $\mathbf{m}_1$ and $\mathbf{m}_2$.

4. Crystals of Intermediate Systems

The intermediate systems include the trigonal, tetragonal, and hexagonal crystals. In the standard crystallophysical setting, the x_3-axis is directed along the highest-order symmetry axis, the tensor B_{ij} is not only diagonal, but also has two coinciding principal values

$$B_1 = B_2. \tag{47}$$

In this particular case, relationship (44) takes the form

$$\mathbf{C}_1 \equiv \mathbf{C}_2 = (0, 0, 1). \tag{48}$$

---

[2] In this case, the “split eigenvalue” $a = B_{33}$ cannot be used, because it would lead to the 0/0-type indeterminate form, which requires a special consideration.

The vectors $\mathbf{C}_1$ and $\mathbf{C}_2$ of these crystals of intermediate systems are equal, real, and independent of the material characteristics. Under these conditions, the crystals have only one optical axis coinciding with the principal symmetry axis, irrespective of the degree of absorption (Fig. 1d)

$$\mathbf{m}_1 \equiv \mathbf{m}_2 = (0, 0, 1). \quad (49)$$

Obviously, this optical axis is not split.

DISCUSSION

Thus, if the components of the inverse permittivity tensor B_{ij} for an absorptive crystal of an arbitrary symmetry are known, it is possible to establish the orientations of its optical axes. The general relationships obtained do not depend on the absorption degree. However, it should be emphasized that if the components of the imaginary part of the tensor B_{ij} are of the same order of magnitude as the components of the real part, the electromagnetic waves can propagate only for rather small distances of the order of a wavelength.[3] In these cases, the role of absorption can be studied, e.g., on thin crystalline films or electromagnetic wave reflection from the surface of a bulky crystal.

The order of magnitude of the splitting angle of the optical axes in a transparent crystal caused by absorption is determined by the ratio $\sim\beta'/d$ [see Eqs. (34) and (35)]. Here β' is of the order of the component of the tensor β'_{ij} and d is of the order of the difference between the components of the tensor β_{ij} (d characterizes the anisotropy of the tensor β_{ij}). Thus, ~1° -splitting arises at $\beta'/d \approx 1/50$. This can happen, e.g., if $\beta' \approx 0.01$ and $d \approx 0.5$. The angles between the optical axes in absorptive crystals were also estimated in [6].

It should be indicated that in the limit of zero absorption, we always assumed that both optical axes in transparent crystals of lower systems were located in the coordinate plane x_1x_3 [see (22) and Fig. 2], which was determined by the fact that, in the coordinate systems considered, the diagonal components β_i were located in the order dictated by relationships (24).

Cubic crystals, being optically isotropic, required no consideration at all, because in these crystals, degenerate electromagnetic waves can propagate along any direction.

ACKNOWLEDGMENTS

The authors are grateful to A. F. Konstantinova for useful discussions. This study was supported by the Russian Foundation for Basic Research, project no. 98-02-16069.

REFERENCES

1. F. I. Fedorov, *Theory of Gyrotropy* (Nauka i Tekhnika, Minsk, 1976).
2. A. F. Konstantinova, B. N. Grechushnikov, B. V. Bokut', and E. G. Valyashko, *Optic Properties of Crystals* (Navuka i Tékhnika, Minsk, 1995).
3. A. M. Goncharenko, S. V. Grum-Grzhmaĭlo, and F. I. Fedorov, Kristallografiya **9**, 589 (1964) [Sov. Phys. Crystallogr. **9**, 504 (1964)].
4. Yu. I. Sirotin and M. P. Shaskol'skaya, *Foundations of Crystal Physics* (Nauka, Moscow, 1975).
5. B. N. Grechushnikov and I. N. Kalinkina, in *Covarian Methods in Theoretical Physics. Optics and Acoustics. Collection of Articles* (Inst. Fiziki, Minsk, 1981), p. 102.
6. A. I. Okorochkov and A. F. Konstantinova, Kristallografiya **30**, 105 (1985) [Sov. Phys. Crystallogr. **30**, 57 (1985)].

Translated by L. Man

---

[3] The collapse (annihilation) of optical axes considered in [1] corresponds just to such situations. Collapses arising due to random degeneracy (only if the specific relationships for the complex components B_{ij} are valid) are not very probable.

Crystallography Reports, Vol. 45, No. 4, 2000, pp. 676–677. Translated from Kristallografiya, Vol. 45, No. 4, 2000, pp. 738–739.
Original Russian Text Copyright © 2000 by Golovin, Morgunov, Julikov, Dmitrievskiĭ.

PHYSICAL PROPERTIES OF CRYSTALS

Aging-Induced Shift of the Optical Quenching Maximum of the Magnetoplastic Effect in NaCl Crystals

Yu. I. Golovin, R. B. Morgunov, S. E. Julikov, and A. A. Dmitrievskiĭ
Tambov State University, ul. Internatsional’naya 33, Tambov, 392622 Russia[1]

Received June 8, 1998

Abstract—The shift of the optical quenching maximum due to the magnetoplastic effect in NaCl crystals caused by one-year aging at $T = 293$ K after heat treatment has been found. It was established that the spectral characteristics of crystal sensitivity to light were changed and, at the same time, the crystals became insensitive to magnetic fields. © *2000 MAIK “Nauka/Interperiodica”.*

In [1], the displacement of dislocations in ionic crystals during their exposure to a dc magnetic field (MF) in the absence of external mechanical loading have been established. Later, it was also established that this magnetoplastic effect (MPE) can be suppressed if, prior to the MF application, a crystal free of “fresh” dislocations was illuminated by the ultraviolet light of a certain wavelength with the quantum energy E being substantially less than the forbidden band gap [2]. The most probable cause of the effect of the UV light on the magnetoplastic effect is a change in the state of the point defects that cease to oppose the dislocation motion in MF [2]. The bell-like shape of the dependence of mean dislocation paths on energy in magnetic fields [2] allows one to considere this dependence as a prototype of the absorption curve of the point defects studied. It is well known that the absorption spectra of point defects are sensitive to their state and change after thermal, electric, and other types of crystal treatment [3]. The present paper was aimed to study the effect of aging in dislocation-free NaCl crystals at $T = 293$ K on the spectral characteristics of the optical quenching of the magnetoplastic effect.

The magnetoplastic effect was experimentally studied in nominally pure NaCl single crystals annealed for 5 days at 700 K and cooled to $T = 293$ K at a mean rate of 1–2 K/min. Some of these crystals (NaCl(I)) were studied immediately after the thermal treatment. The other part of the crystals (NaCl(II)) were kept for one year at T = 293 K and then studied. Edge dislocations were introduced by the standard method of scratching. Their dislocation displacements were measured upon double chemical etching of the samples. Before the dislocation introduction, the crystals were illuminated for 15 min with a monochromatic light of the wavelength $\lambda = 400$–800 nm. Two fundamentally different methods were used to initiate displacement of dislocations—(i) MF pulses of the duration 10 ms and the amplitude 7 T all the experiments and having the form of half-period of a sinusoid; (ii) rectangular mechanical compression pulses of duration 200 ms and the amplitude 400 kPa. In the first case, the external factor facilitated dislocation depinning only from the magnetosensitive pinning centers. The dislocations then moved under the effect of random fields of internal stresses. In the second case, the uniform field of mechanical stresses provided depinning of dislocations from all the pinning centers and their motion in a certain direction. The magnetic-field and mechanical-stress values were such that the mean paths of dislocations, L_f and L_m, under the MF and mechanical loading effects, were the same in crystals not preliminarily subjected to photoexposure, i.e., in “dark” crystals, we had $L_f = L_m = L_0$.

In the first run of the experiments, we studied the effect of light on the dislocation paths L_f and L_m. The preliminary photoexposure of NaCl(I) crystals decreased L_f and increased L_m in comparison with L_0; the most pronounced deviations in both cases being achieved (similar to [2]) at $\lambda = 350 \pm 20$ nm (Fig. 1). In NaCl(II) crystals, the preliminary photoexposure decreased both L_f and L_m in comparison with L_0, with the maximum deviation of L_f and L_m from L_0 being achieved at $\lambda = 250 \pm 20$ nm (Fig. 1). Thus, the effect of light on the dislocation paths initiated by the magnetic field was dependent on the thermal pre-history of the crystals.

In the second run of the experiments, we used MF pulses instead of photoexposure. Since an MF pulse was switched-on prior to the introduction of “fresh” dislocations, then, similar to photoexposure, it could affect only the state of point defects. This effect can be estimated from the changes in dislocation paths L_{f0} initiated by the second MF pulse in comparison with paths L_0 in crystals not subjected to the effect of a MF prior to dislocation introduction. It has been established that in NaCl(I) crystals, $L_{f0} < L_0$, whereas in NaCl(II) $L_{f0} = L_f$ (Fig. 2), i.e., in the crystals kept for a year after heat treatment at $T = 293$ K, the maximum of optical

---

[1] *e-mail: golovin@main.tsu.tambov.ru*

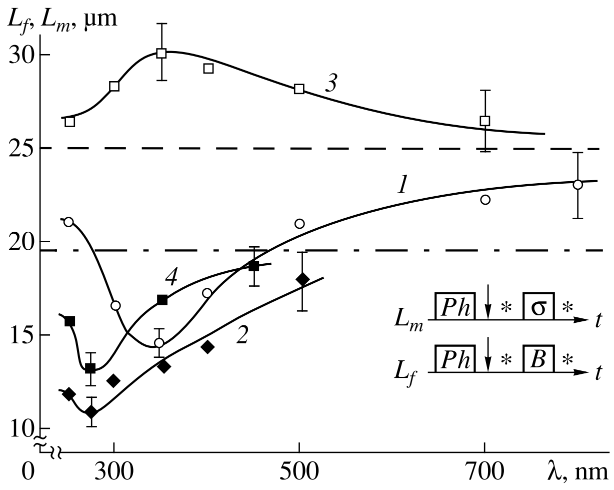

Fig. 1. Mean paths of dislocations, L_f (*1*, *2*) and L_m (*3*, *4*), whose motion was initiated by a MF pulse and mechanical loading, respectively, as functions of the wavelength λ of the light used for the preliminary photoexposure. (*1*, *3*) NaCl(I) crystals; (*2*, *4*) NaCl(II) crystals. Dashed and dot-dashed lines indicate dislocation paths L_0 in NaCl(I) ("dark") and NaCL(II) crystals, respectively. In inset: the sequence of procedures in the experiments in MF and under mechanical loading. Arrows indicate introduction of dislocations, star indicates etching, *B* is a MF-pulse, and *Ph* is a photoexposure.

quenching of magnetoplastic effect is shifted to the short-wavelength range and the point defects become insensitive to a magnetic field.

Apparently, a year storage of crystals at a constant temperature can lead only to the relaxation of metastable states of point defects. The corresponding changes in the response of the crystals to light and magnetic fields are likely to be mutually related. We measured the absorption spectra of crystals in a Hitachi spectrophotometer and detected no absorption maxima in the range studied. This bears witness to a small concentration of magnetosensitive defects and the high sensitivity of the method of "dislocation" probing of point defects used in our experiments.

Thus, the magnetosensitive defects in NaCl crystals are long-lived metastable complexes. The products of their relaxation are insensitive to magnetic fields, but change their state under ultraviolet light.

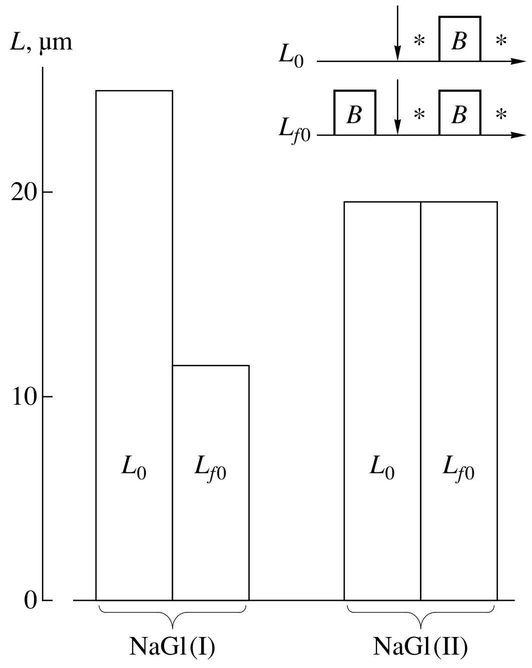

Fig. 2. Dislocation paths L of MF-pulse-initiated dislocation motion in NaCl(I) and NaCl(II) crystals; L_0 and L_{f0} are paths without and with the application of a magnetic field, respectively, before the introduction of dislocations. In inset: the sequence of procedures used in measuring L_0 and L_{f0}. For notation see Fig. 1.

ACKNOWLEDGMENTS

This study was supported by the Russian Foundation for Basic Research (grant no. 97-02-16074).

REFERENCES

1. V. I. Alshits, E. V. Darinskaya, T. M. Perekalina, and A. A. Urusovskaya, Fiz. Tverd. Tela (Leningrad) **29**, 467 (1987) [Sov. Phys. Solid State **29**, 265 (1987)].
2. Yu. I. Golovin, R. B. Morgunov, M. V. Badylevich, and S. Z. Shmurak, Fiz. Tverd. Tela (St. Petersburg) **39**, 1389 (1997) [Phys. Solid State **39**, 1232 (1997)].
3. C. Zaldo, J. García Sole, and F. Agullo-López, J. Mater. Sci. **17**, 1465 (1982).

Translated by A. Darinskiĭ

Crystallography Reports, Vol. 45, No. 4, 2000, pp. 678–681. Translated from Kristallografiya, Vol. 45, No. 4, 2000, pp. 740–744.
Original Russian Text Copyright © 2000 by Zalesskiĭ, Gubkin, Perekalina, Khimich.

PHYSICAL PROPERTIES OF CRYSTALS

Nuclear ^{57}Fe Relaxation in Fe^{2+}-Containing $NiFe_2O_4$ and $CoFe_2O_4$ Single Crystals

A. V. Zalesskiĭ, M. K. Gubkin, T. M. Perekalina, and T. A. Khimich
Shubnikov Institute of Crystallography, Russian Academy of Sciences,
Leninskiĭ pr. 59, Moscow, 117333 Russia

Received August 10, 1998

Abstract—Spin-lattice (T_1) and spin-spin (T_2) relaxation times of ^{57}Fe nuclei in the single-crystal $NiFe_2O_4$ and $CoFe_2O_4$ ferrites containing Fe^{2+} ions have been studied in the temperature range of 4.2–100 K by a spin-echo technique. The peaks of relaxation rates T_1^{-1} and T_2^{-1} caused by the presence of Fe^{2+} ions were observed for both ferrites in the ranges 38–42 and 28–32 K, respectively. The analysis of the results obtained with invocation of the data on ferromagnetic resonance and the measurements of the temperature dependence of resistivity shows that the mechanism of nuclear relaxation responsible for “impurity” peaks T_1^{-1} and T_2^{-1} is a slow relaxation process caused by electron exchange $Fe^{2+} \longleftrightarrow Fe^{3+}$, characterized by a low activation energy. © *2000 MAIK “Nauka/Interperiodica”.*

INTRODUCTION

The nuclear relaxation in magnetic oxides in the presence of paramagnetic impurity ions is determined mainly by the transfer of the energy of nuclear spin oscillations to the lattice, because of the interactions between the nuclei and impurity ions, whose energy state is determined by the exchange and the crystal fields. Such interactions are especially strong for certain ions of the iron group with partly “quenched” orbital momentum (Fe^{2+}, Co^{2+}).

The most often encountered impurity in ferrite single- and polycrystals affecting their properties (e.g., resistivity ρ and high-frequency behavior) is a divalent Fe^{2+} ion. These ions also affect the processes of nuclear relaxation in magnetic oxides. The temperature dependence of the spin-lattice (T_1^{-1}) and spin-spin (T_2^{-1}) relaxation rates for all the ferrites with Fe^{2+} ions for ^{57}Fe nuclei studied had the peaks. Such peaks were observed to magnetite Fe_3O_4 [1], where Fe^{2+} ions occupy 1/3 of the total amount of iron ions, in $Y_3Fe_5O_{12}$ garnet [2], in impurity-containing hematite α-Fe_2O_3 [3], in hexagonal barium ferrite $BaFe_{12}O_{19}$ [4], and also in lithium ferrite $Li_{0.5}Fe_{2.5}O_4$ [5].

There are two approaches to the interpretation of the relaxation mechanism, which are based on the so-called slow and fast relaxation theories. These theories were developed in the sixties to interpret the anomalies in the temperature dependence of the ferromagnetic-resonance (FMR) linewidth ΔH in ferrites. The detailed consideration of these problems can be found elsewhere [6, 7]. Later, these theories were used to interpret the nuclear relaxation, because both damping of the electron spins in FMR and nuclear relaxation in NMR are caused by the relaxation properties of an impurity ion determined by its relaxation time τ.

In our case the relaxation rate 1/τ describes interaction between Fe^{2+} ion and the lattice. It is also possible to introduce the frequency ω_{AB}, which is the measure of the exchange interaction between Fe^{2+} ions occupying “octahedral” (*B*) positions in the spinel structure and Fe^{3+} ions occupying the “tetrahedral” (*A*) sites (the *AB*-interactions are the determining interactions in spinel ferrites). According to the slow relaxation theory, the frequency ω of an external alternating magnetic field, which at resonance is equal to the NMR frequency, should be comparable with 1/τ but, at the same time, considerably lower than ω_{AB}. In other words, the following condition should be fulfilled:

$$\omega_{AB} \gg 1/\tau \approx \omega. \tag{1}$$

Contrary to the slow relaxation theory, the fast relaxation theory is developed under the assumption that the interaction of Fe^{2+} ions with the lattice is so pronounced that the 1/τ is comparable with ω_{AB} and is considerably higher than ω. In other words, this theory requires the fulfillment of the condition:

$$\omega_{AB} \approx 1/\tau \gg \omega. \tag{2}$$

According to [6, 7], even the FMR experiments give no grounds to determine which of these two theories should be applied to each concrete situation. The situation is even much more complicated for NMR experiments.

In the present paper, we describe the first study of the nuclear relaxation in Fe^{2+}-containing nickel and cobalt ferrite single crystals in the temperature range from 4.2 to 100 K. The study was undertaken to clarify the applicability of the existing theories to describe the impurity mechanisms of nuclear relaxation, and also to confirm that the fluctuations in local magnetic fields caused by $Fe^{2+} \longleftrightarrow Fe^{3+}$ electron exchange are responsible for the observed relaxation processes. To solve the formulated problems, we invoke the FMR data and measured resistivity of one of the single crystals at different temperatures.

SAMPLES AND EXPERIMENT

We studied Verneuil grown nickel and cobalt ferrite single crystals [8]. The disklike or platelike samples were cut out from homogeneous parts of the boules and had an arbitrary crystallographic orientation. The chemical analysis showed that the crystals had the compositions $Ni_{0.76}Fe^{2+}_{0.19}Fe^{3+}_{2.03}O_4$ and $Co_{0.89}Fe^{2+}_{0.18}Fe^{3+}_{1.95}O_4$. For the sake of brevity, hereafter we shall use the formulas $NiFe_2O_4$ and $CoFe_2O_4$. The number of Fe^{2+} ions in the $NiFe_2O_4$ and $CoFe_2O_4$ ferrites amounted to 8.5 and 8.4% of the total number of iron ions. The samples for NMR experiments were 1 to 2 g in weight. They were placed into a measuring coil so that the rf field was in the disk plane. The NMR was observed by a spin-echo method in the zero external field with the aid of a pulsed spectrometer manufactured by the Institute of Radioengineering and Electronics of the Russian Academy of Sciences. The temperature was controlled within ±0.1 K by blowing helium vapors.

With the change of the temperature, the value of T_1 changed by almost three orders of magnitude, therefore the longitudinal relaxation time was measured by different methods (because of the spectrometer limitations). Thus, high T_1 values (>5 ms) were measured by the method of the restoration of the longitudinal component of nuclear magnetization, with an increase of the repetition period of exciting pulse pairs (the saturation method). For T_1 values less than 5 ms, we used the so-called stimulated echo method (three-pulse method). The transverse relaxation time, T_2, was measured by the decay of an echo amplitude with an increase of time between two exciting pulses. The error in the measurements of T_1 and T_2, determined mainly by the signal-to-noise ratio, was 20–50%.

The resistivity was measured by a conventional dc four-probe method.

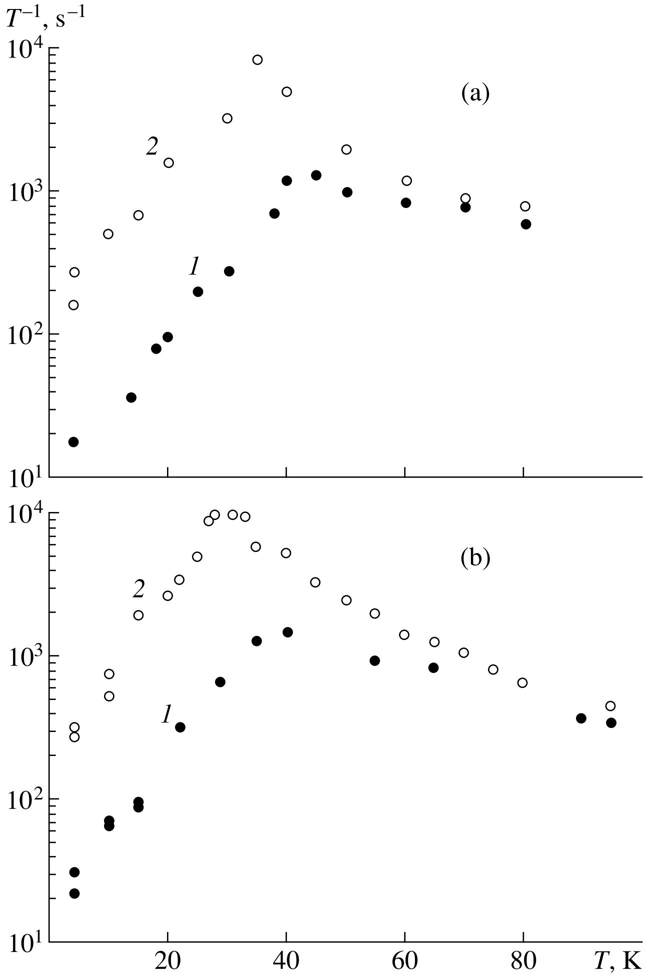

Fig. 1. Rates of (*1*) longitudinal and (*2*) transverse relaxation rates of ^{57}Fe nuclei (T_1^{-1} and T_2^{-1}, respectively) in (a) $NiFe_2O_4$ and (b) $CoFe_2O_4$.

RESULTS AND DISCUSSION

Figures 1a and 1b show the relaxation rates T_1^{-1} and T_2^{-1} measured for $NiFe_2O_4$ and $CoFe_2O_4$, respectively, in the interval of temperatures from 4.2 to 100 K. The relaxation rates were measured for ^{57}Fe nuclei at the *A*- and *B*-positions in the spinel structure. The resonance frequencies of ^{57}Fe for the *A*- and *B*-positions for these ferrites, in the interval of 4.2–77 K, are located at 71 and 76 MHz, respectively. Within the experimental error (30–50%), the T_1 and T_2 values for *A*- and *B*-sites are indistinguishable, therefore the experimental points in Figs. 1a and 1b can be attributed to any of iron positions. The temperature dependences of T_1^{-1} and T_2^{-1} for both ferrites are almost identical (both quantitatively and qualitatively). For both ferrites, the T_1^{-1} and T_2^{-1} maxima are located at 40 ± 2 and 30 ± 2 K, respectively. At the temperatures exceeding the peak temperatures,

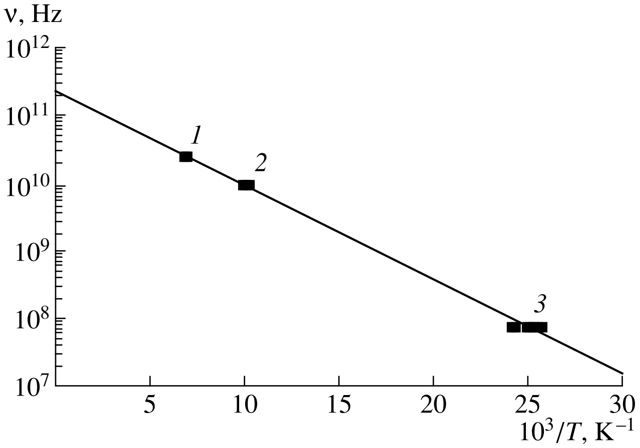

Fig. 2. The frequencies of the magnetic resonance $\nu = \omega/2\pi$ and the temperature positions of the ΔH (FMR) and T_1^{-1} (NMR) maxima for a $NiFe_2O_4$ crystal in the Arrhenius coordinates. (*1*), (*2*) FMR data [10], (*3*) the region of the T_1^{-1} peak in the ^{57}Fe NMR experiment. The straight line corresponds to the activation energy $E = 0.027$ eV.

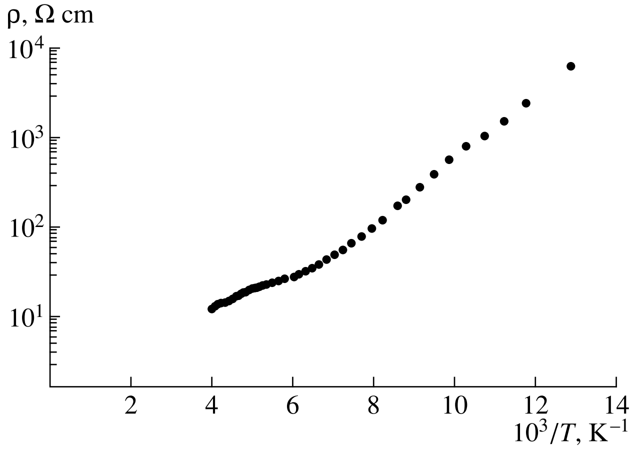

Fig. 3. Temperature dependence of resistivity ρ of a $NiFe_2O_4$ single crystal.

$T_1 \approx T_2$; at lower temperatures, $T_1/T_2 \approx 10$. The similar behavior of the relaxation time are observed in magnetite [1], where Fe^{2+} ions play the main part in the relaxation processes. To analyze the results, we use the standard expressions for relaxation times in the form given in [9]:

$$\frac{1}{T_1} = \gamma_n^2[\overline{H_x^2} + \overline{H_y^2}]\frac{\tau}{1+\omega^2\tau^2}, \quad (3)$$

$$\frac{1}{T_2} = \gamma_n^2\left[\overline{H_z^2}\tau + \overline{H_y^2}\frac{\tau}{1+\omega^2\tau^2}\right], \quad (4)$$

where γ_n is a nuclear gyromagnetic ratio, $\overline{H_x^2}$, $\overline{H_y^2}$, $\overline{H_z^2}$ are mean-square components of a fluctuating magnetic field at the nucleus, and τ is the correlation time of the general theory [9]; the physical sense of τ for our case will become clear later. It follows from (3) that T_1^{-1} has a maximum at $\omega\tau = 1$.

Now, return to the applicability of the fast and slow relaxation theories. Similar to (3), the final formulas for ΔH in the FMR and T_1 in the NMR in both theories contain the Loretzian factor responsible for the maximum of ΔH or T_1^{-1}, but the frequencies ω in these theories have different senses. In the fast relaxation theory, ω is the measure of the exchange energy (denoted above by ω_{AB}), while in the slow relaxation theory, ω is the observation frequency of FMR or NMR. Then, one of the most important properties follows, which provides the establishment of the applicability of these theories. According to condition (2), the temperature position of the maximum in the slow relaxation theory is independent of the observation frequency. On the other hand, the slow relaxation theory [condition (1)] predicts this dependence with due regard of the fact that τ is the temperature-dependent quantity.

To solve the problem of applicability of both theories, consider the FMR study of $NiFe_2O_4$ [10]. The sample used in [10] had the composition $(Ni_{0.75}Fe^{2+}_{0.25}Fe^{3+}_2O_4)$, i.e., was almost the same as our sample, which justifies the comparison of these data. Galt and Spenser [10] observed the peaks of ΔH at the temperatures 145 and 100 K and at the frequencies 24 and 9.2 GHz, respectively.

We assume that τ is determined by the activation mechanism and depends on temperature by the Arrhenius law:

$$\tau = \tau_\infty \exp(E/kT), \quad (5)$$

where k is the Boltzman constant, and E is the activation energy. Under this assumption, the logarithm of ω is a linear function of the reciprocal temperature of the maxima of ΔH and T_1^{-1}. It is seen from Fig. 2 that such a linear dependence really takes place. Thus, in this case, the relaxation mechanism satisfies the requirements of the slow relaxation theory, whereas the activation mechanism is responsible for the temperature behavior of τ.

As follows from the graph in Fig. 2, $E = 0.027 \pm 0.001$ eV and $\tau_\infty = (7.3 \pm 1) \times 10^{-13}$ s. The dependence (5) with such parameters is characteristic of the electron exchange $Fe^{2+} \longleftrightarrow Fe^{3+}$ in ferrites (the so-called “hopping” or “jumping” mechanism). For example, the parameters for electron hopping in magnetite are $E = 0.03$–0.055 eV [1, 7], $\tau_\infty = 3.7 \times 10^{-13}$ s [1]. Thus, the parameter τ acquires the meaning of the time of electron hopping. This mechanism is known to be responsible for a high conductivity of Fe^{2+}-containing ferrites [7]. Compare the E value obtained from the magnetic resonance data with the activation energy obtained from conductivity measurements. Figure 3 shows the measured resistivity ρ of a $NiFe_2O_4$ single crystal plotted in the lnρ, $1/T$ coordinates. The approximation by a straight line yields the averaged activation energy $E_\rho = 0.06 \pm 0.01$ eV. The E and E_ρ are of the same order of magnitude and differ by about 2 times. This difference can be explained by the fact that the E_ρ was measured in the steady-state mode, while E was measured in a microwave field. It is also conceivable that along with the hopping mechanism $Fe^{2+} \longleftrightarrow Fe^{3+}$, there exists a certain parallel conductivity mechanism.

The relationship $T_1 \approx T_2$, which holds at $T > 50$ K, is explained by the fact that, with an increase of the temperature and the distance from the peak of T_1^{-1}, the time of electron hopping τ decreases so that the condition $\omega\tau \ll 1$ becomes valid. As follows from (3) and (4), in an isotropic fluctuating field, $\overline{H_x^2} = \overline{H_y^2} = \overline{H_z^2}$, the above condition results in the equality of the longitudinal and the transverse relaxation times, T_1 and T_2.

On the other hand, with an increase of the distance from the value of T_1^{-1}, under conditions of the exponential increase in τ, the value of T_2^{-1} continues increasing because of the contribution of the longitudinal field component H_z into T_2 (the so-called secular or adiabatic contribution [9]). As follows from (4), this contribution results in a higher value of the T_1/T_2 ratio, which attains a certain limiting value. This contribution shifts the T_2^{-1} peak to somewhat lower temperatures than the temperature of the T_1^{-1} peak.

Concluding the discussion, consider the physics of the slow relaxation process under the conditions where the impurity channel of nuclear relaxation is provided by the electron exchange $Fe^{2+} \longleftrightarrow Fe^{3+}$.

The valence exchange between the Fe^{2+} and Fe^{3+} ions in this modification of the slow relaxation theory plays the role of quantum transitions, changing the population in a two-level system. The oscillations of a magnetization under the action of a microwave field change the angles between the magnetization and the local symmetry axes for nonequivalent B-sites and also change the energy levels of an ion $Fe^{2+} \longleftrightarrow Fe^{3+}$ pair, thus providing a certain preferable direction of transitions, which is also dependent on the applied microwave field. The transitions delayed with respect to the changes in the microwave field provide the energy dissipation into the lattice. The mean time τ, necessary for the valence exchange, is the characteristic of a relaxation time of the impurity Fe^{2+} ion. Historically, it was the first mechanism suggested for the interpretation of the temperature dependence of ΔH in FMR in ferrites [11].

CONCLUSIONS

The $NiFe_2O_4$ and $CoFe_2O_4$ crystals with the same concentration of impurity Fe^{2+} ions (8.5% of the total number of iron ions) show the identical temperature variations of the spin-lattice, T_1, and spin-spin, T_2, relaxation times of ^{57}Fe nuclei with the maxima of T_1^{-1} and T_2^{-1} rates at 40 ± 2 and 30 ± 2 K, respectively. The impurity peaks can be explained within the theory of slow relaxation, with the time of electron hopping $Fe^{2+} \longleftrightarrow Fe^{3+}$ being the parameter of the impurity relaxation. The value of the activation energy obtained by various methods support the idea that the electron exchange determines the temperature behavior of the nuclear relaxation times.

ACKNOWLEDGMENTS

This work was supported by the Russian Foundation for Basic Research, project no. 98-02-17197.

REFERENCES

1. T. Mizoguchi and M. Inoue, J. Phys. Soc. Jpn. **21**, 1310 (1966).
2. M. P. Petrov and A. P. Paugurt, Fiz. Tverd. Tela (Leningrad) **12**, 2829 (1970).
3. A. V. Zalesskiĭ, V. G. Krivenko, V. S. Lutovinov, *et al.*, Zh. Éksp. Teor. Fiz. **86**, 1891 (1984).
4. A. V. Zalesskiĭ, V. G. Krivenko, A. V. Kunevich, *et al.*, Fiz. Tverd. Tela (Leningrad) **29**, 1107 (1987).
5. L. L. Buishvili, S. V. Ivanov, A. V. Kunevich, *et al.*, Fiz. Met. Metalloved. **56**, 94 (1983).
6. A. G. Gurevich, *Magnetic Resonance in Ferrites and Antiferromagnetics* (Nauka, Moscow, 1973), Chap. 9.
7. S. Krupička, *Physik der Ferrite und der verwandten magnetischen Oxide* (Academia, Prague, 1973; Mir, Moscow, 1976).
8. A. A. Askochenskiĭ, Candidate's Dissertation in Phys.–Math. Sci. (Moscow, 1976).
9. C. P. Slichter, *Principles of Magnetic Resonance* (Harper and Row, New York, 1963; Mir, Moscow, 1967).
10. J. K. Galt and E. G. Spenser, Phys. Rev. **127**, 1572 (1962).
11. A. M. Clogston, Bell Syst. Techn. J. **34**, 734 (1955).

Translated by A. Zalesskiĭ

Crystallography Reports, Vol. 45, No. 4, 2000, pp. 682–686. Translated from Kristallografiya, Vol. 45, No. 4, 2000, pp. 745–750.
Original Russian Text Copyright © 2000 by Shtykov, Vij, Barnik, Nguyen.

LIQUID CRYSTALS

Dielectric and Pyroelectric Studies of an Antiferroelectric Liquid Crystal

N. M. Shtykov*, J. K. Vij, M. I. Barnik*, H. T. Nguyen*****

** Shubnikov Institute of Crystallography, Russian Academy of Sciences,*
Leninskiĭ pr. 59, Moscow, 117333 Russia
*** Department of Electronic and Electrical Engineering, Trinity College,*
University of Dublin, Dublin 2, Ireland
**** Centre de la Recherche Paul Pascal, Avenue A. Schweitzer, 33600 Pessac Cedex, France*

Received December 7, 1998

Abstract—Polymorphism and polar properties of an antiferroelectric (*R*)-2-methylheptyloxycarbonylphenyl-4-[(4-decyloxy-3-fluoro)benzoyloxy]benzoate liquid crystal are studied. The phases are identified, and the phase transition points are determined. Dielectric constant, dielectric losses, and pyroelectric properties are studied for the orthogonal smectic *SmA* and tilted smectic SmC_α^*, SmC^*, SmC_γ^*, and SmC_A^* phases. The temperature dependence of spontaneous polarization is measured by the repolarization current technique and integration of the pyroelectric constant. *© 2000 MAIK "Nauka/Interperiodica".*

INTRODUCTION

At present, a large variety of chiral liquid–crystalline (LC) compounds with tilted smectic C-phases (SmC^*) possessing ferroelectric properties have been synthesized for research and optimization of display characteristics [1]. Ferroelectricity in LCs was predicted by Meyer in 1974 [2], and in 1975, the first ferroelectric LC compounds were synthesized [3]. About a decade later, LC compounds with antiferroelectric properties were discovered among tilted chiral C-smectics [4]. A number of specific features (e.g., tristable switching) provide their widespread use in display technology and make them more advantageous than ferroelectric LCs [5]. In this connection, extensive search for new compounds of this type is now underway.

The most widespread subphases of antiferroelectric LCs are the ferroelectric SmC^*, the antiferroelectric SmC_A^*, and the ferrielectric SmC_α^*, SmC_γ^*, FI_L, and FI_H phases. Structural and physical properties of the latter phases were studied to a lesser degree [6]. Usually, the subphases are studied by the methods of X-ray and IR spectroscopy [7, 8], high resolution calorimetry [9], electrooptic measurements [10], dielectric relaxation spectroscopy [11], and many other methods [12].

Below, we describe the study of polymorphism of antiferroelectric LCs by measuring dielectric constant ε', dielectric losses ε'', and pyroelectric constant. The study was performed on a new ester with ferro-, antiferro-, and ferrielectric phases which is based on 4-(4-hydroxybenzoyloxy)alkylbenzoate and 4-(4-alkoxy-3-fluoro)benzoic acid synthesized by one of the authors (Nguyen).

EXPERIMENTAL

The LC compound under study, (*R*)-2-methylheptyloxycarbonyl-phenyl-4-[(4-decyloxy-3-fluoro)benzoyloxy]benzoate (JCR541), with the molecular structure shown in Fig. 1, has a number of polar and nonpolar phases. The points of the phase transitions were determined by the method of differential scanning calorimetry (DSC) in the range 96–118°C. The DSC spectrum (Fig. 2) displays a double exothermic peak consisting of the two merged peaks formed at the temperatures of 114.4 and 114°C, and the two single peaks at 104.5° (SmC^*–$SmFI^*$ transition) and 103°C ($SmFI^*$–SmC_A^* transition), with $SmFI^*$ being one of the ferroelectric phases. The existence of the double peak can be indicative of the transition from *SmA* to SmC^* via the SmC_α^*

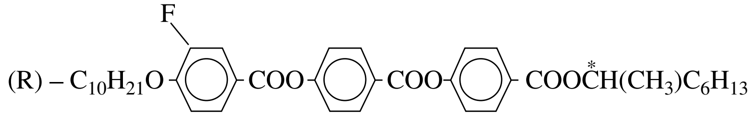

Fig. 1. Structural formula of a JCR541 liquid–crystal.

1063-7745/00/4504-0682$20.00 © 2000 MAIK "Nauka/Interperiodica"

phase, existing within a narrow temperature range 114–114.4°C. The complete sequence of phase transitions for JCR541, including the crystalline (*Cr*) and isotropic (*I*) phases, may be written as:

$$Cr\text{–}89.3\text{–}SmC_A^*\text{–}103\text{–}SmFI^*\text{–}104.5\text{–}SmC^*$$

$$\text{–}114\text{–}SmC_\alpha^*\text{–}114.4\text{–}SmA\text{–}128.5°\text{C–}I.$$

The cells for pyroelectric and dielectric measurements were fabricated from glass plates with a conductive indium tin oxide (ITO) layer applied onto one side. The planar LC orientation was attained by rubbing polyamide films deposited onto the electrodes. The working area of cells was 4.5×4.5 mm^2, their thickness was $d \approx 9 \pm 0.5$ μm.

The real ε' and the imaginary ε'' parts of dielectric constant were measured on a HP-4192A impedance analyzer at a measuring voltage of 0.1 V and the bias voltage ranging within 0–13 V. The temperature dependence of spontaneous polarization was studied by the repolarization current [14] and pyroelectric [15] techniques. Polarization switching was induced by alternating rectangular voltage pulses (±10 V, frequency 100 Hz).

Pyroelectric properties were measured by the method described in [15]. The temperature dependence of the pyroelectric constant, γ(*T*), was measured under sample cooling from the *SmA* phase. The temperature dependence of polarization was determined by integrating the pyroelectric constant [16] and measuring the repolarization currents.

RESULTS AND DISCUSSION

Figure 3 presents the temperature dependences of the spontaneous polarization P_s determined from repolarization current measurements made under LC sample cooling from 118 to 96°C and heating from 96 to 102°C. In *SmA* phase, spontaneous polarization is due to the electroclinic effect. With a decrease in temperature, it first steeply rises in the vicinity of the points of the SmA–SmC_α^* and the SmC_α^*–SmC^* phase transitions and then gradually increases in the *SmC** phase. At the temperature of 102°C, the spontaneous polarization drops to the level of ~$1/3P_{sm}$ (where P_{sm} is the maximum value of the spontaneous polarization in the *SmC** phase) and then, with the further temperature decrease, approaches zero. In the antiferroelectric SmC_A^* phase, $P_s = 0$, which signifies that the measuring voltage (10 V) is too low to induce the SmC_A^*–SmC^* transition in an electric field. A decrease of spontaneous polarization at 102°C and not at the temperature of the *SmC**–*SmFI** phase transition (104.5°C) is explained by the shift of the phase transition point in an electric field. The spontaneous polarization in the *SmFI** phase equals ~$1/3P_{sm}$, which shows that it is the well-known ferrielectric SmC_γ^* phase.

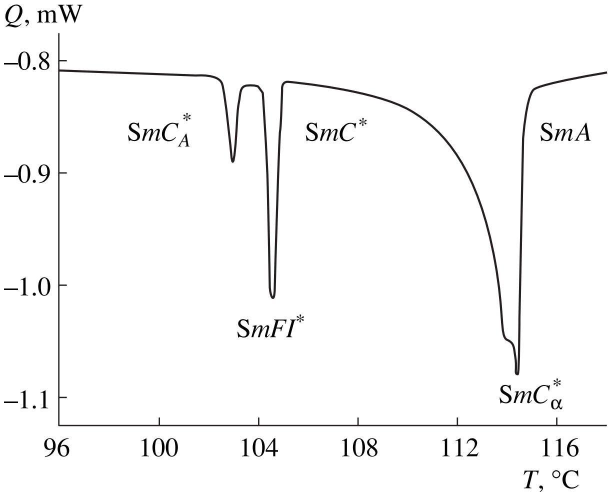

Fig. 2. DSC spectrum from a JCR541 sample (19.9 mg) during its cooling; *Q* is the heat flux.

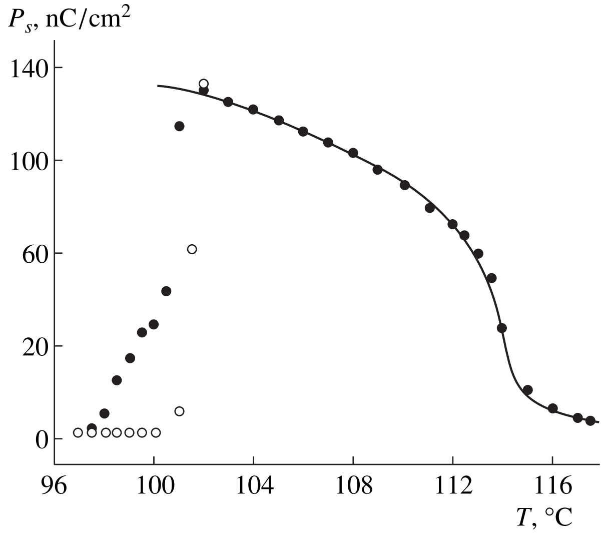

Fig. 3. The temperature dependence of spontaneous polarization of the JCR541 compound obtained by repolarization current method during cooling (●) and heating (○) or by the pyroelectric method (–) during cooling of the LC cell.

The measurements during heating of the LC showed no spontaneous polarization P_s in ferrielectric phase. Only close to the transition point to the ferroelectric *SmC** phase, spontaneous polarization sharply increases and attains the maximum value equal to the spontaneous polarization P_{sm} for the *SmC** phase. Such temperature behavior of the polarization may evidence the morphotropic nature of the ferrielectric SmC_γ^* phase in the LC.

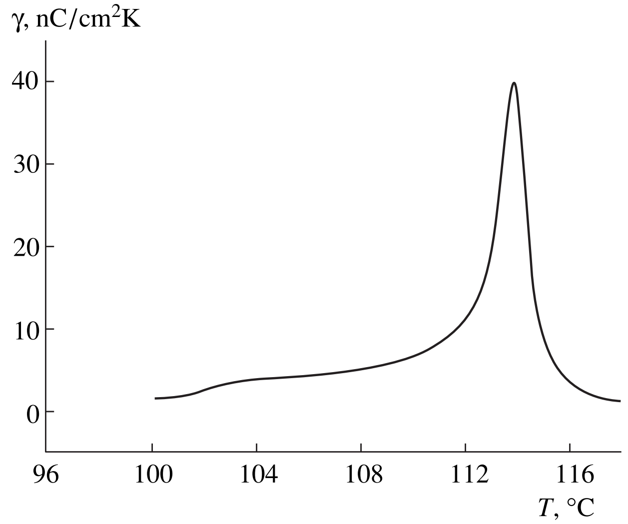

Fig. 4. Pyroelectric constant of the JCR541 compound as a function of temperature during cooling of the LC cell. The voltage of an applied dc field is 10 V.

The temperature dependence of the pyroelectric constant is shown in Fig. 4. Close to the SmC_α^*–SmC^* phase transition, the pyroelectric constant reaches its maximum (~40 nC/cm^{2}K) and then gradually decreases with cooling of the *SmC** phase. In the transition range from the *SmC** to the SmC_γ^* phase, the curve has a bending point, and the pyroelectric constant drops faster in the SmC_γ^* than in the *SmC** phase. The temperature dependence of spontaneous polarization, in the ferroelectric *SmC** phase obtained by integration of the pyroelectric constant (Fig. 3, solid line), agrees with the results obtained in repolarization measurements. However, the data obtained by both methods for the ferrielectric SmC_γ^* phase are inconsistent, which cannot be explained at the moment.

Dielectric constant ε of chiral tilted smectics is determined by two low-frequency orientational processes (modes), namely, the Goldstone mode,

$$\Delta\varepsilon_{GMC} = 2\pi C^2\chi_0^2/Kq^2, \tag{1}$$

associated with molecular rotation around the helicoid axis at constant tilt angle of the molecules in smectic layers, and the soft mode,

$$\Delta\varepsilon_{SMC} = 2\pi C^2\chi_0^2/[Kq^2 + 2\alpha(T_C - T)], \tag{2}$$

associated with the change in the tilt angle [17]. In the *SmA* phase, there is no Goldstone mode, and, therefore, the dielectric constant is determined by the soft mode alone,

$$\Delta\varepsilon_{SMA} = 4\pi C^2\chi_0^2/[Kq^2 + \alpha(T - T_C)]. \tag{3}$$

In Eqs. (2) and (3), α is the first Landau coefficient in the expansion of the free-energy density in powers of the orientational parameter of the transition, i.e., in the angle of the LC director tilt with respect to the smectic-layer normal, T_C is the temperature of the *SmA*–*SmC** transition, *K* is the elastic constant, *q* is the wavevector modulus of the chiral structure, *C* is piezoelectric coefficient, and χ_0 is dielectric susceptibility associated with the noncollective mechanisms of polarizability. Figure 5 depicts the real ε' and the imaginary ε'' parts of dielectric constant of the JCR541 compound measured at the frequency of 1 kHz at various temperatures. An increase of ε' in the *SmA* phase, as the temperature decreases is determined by the contribution of the soft mode (3), with the maximum ($\Delta\varepsilon_{SMA} \approx 40$) at the temperature of the *SmA*–SmC_α^* phase transition. With the further decrease of the temperature of the SmC_α^* phase, the contribution of the soft mode rapidly decreases Eq. (2) with the distance from the *SmA*–SmC_α^* transition. However, the total dielectric constant continues increasing because of the Goldstone-mode contribution. The SmC_α^*–SmC^* phase transition is not accompanied by a substantial change in the ε' value or its temperature dependence. In the *SmC** phase, the most pronounced contribution to the dielectric constant comes from the Goldstone mode Eq. (1), whose temperature dependence is determined mainly by the temperature dependence of the modulus of the wavevector *q* of the chiral structure. In the region of the transition from the ferroelectric *SmC** to the ferrielectric SmC_γ^* phase, the dielectric constant and the dielectric losses decrease monotonically. It is worth noting that the *SmC**–SmC_γ^* transition in thin oriented cells occurs at a lower temperature (103°C) than in the bulk sample (104.5°C) used in the studies of phase transitions by DSC technique. In the ferroelectric SmC_A^* phase, both ε' and ε'' continue decreasing and become almost equal to the corresponding values in the *SmA* phase. It should be emphasized that neither the SmC_γ^*–SmC_A^* nor the SmC_α^*–SmC^* phase transitions were recorded on the ε'(*T*) and ε''(*T*) curves.

To study the effect of an electric field on the dielectric constant and the phase transition points of LC, we measured the temperature dependence of the real and the imaginary parts of the dielectric constant at various bias voltages V_b (Fig. 6). The Goldstone mode is suppressed by the dc bias voltage, which is seen from a decrease of ε' and ε'' in the SmC_α^*, *SmC**, and SmC_γ^* phases. The soft mode in the vicinity of the *SmA*–SmC_α^* transition also decreases with the bias voltage according to the law $\Delta\varepsilon_{SMA} \approx 4\pi(C\chi_0)^{4/3}E_b^{-2/3}/3b^{1/3}$, where *b* is the second Landau coefficient in the expansion of the free energy density in powers of the orientational parameter of the transition, and E_b is the bias field [18]. Moreover, with an increase in bias voltage, the dielectric-constant maxima are shifted towards lower temperatures. This shift seems to be associated with the shift of the temperature of the SmC^*–SmC_γ^* transition in an electric field as in the case of antiferroelectric MHPOBC (4-(1-methylheptyloxycarbonyl)phenyl 4'-octyloxybiphenyl-4-carboxylate) [19], where the ferrielectric SmC_γ^* phase is also located between the ferroelectric SmC^* and the ferrielectric SmC_A^* phases. It is noteworthy that at lower temperatures in the transition from SmC^* to SmC_γ^*, and then also to the SmC_A^* phase, the ε' and ε'' dielectric parameters monotonically (and not jumpwise) decrease within the temperature interval of several degrees centigrade. The examination of LC textures in a polarizing microscope within this temperature range showed that the LC layer is a system of alternating linear domains of adjacent phases parallel to the smectic layers. Thus, one can state that, similar to the case of 3MC2PCPOPB (4'-(3-methoxycarbonyl-2-propoxycarbonyl)phenyl-4-(4-[*n*-octyloxy]phenyl)benzoate) [20], two adjacent phases coexist in this case. The dielectric constant measured in this range is, in fact, the average of the values for ferro- and ferrielectric phases or for ferri- and antiferroelectric ones. The absence of clearly pronounced phase transitions in the temperature dependence of the dielectric parameters follows from the fact of phase coexistence. The temperature dependence of the dielectric constant and spontaneous polarization exhibit hystereses in the vicinity of the SmC^*–SmC_γ^* phase transition during heating–cooling cycles.

The suppression of the Goldstone mode by a bias field provides the manifestation of the soft-mode peak related to the SmA–SmC_α^* transition (114.4°C). An increase of the bias voltage shifts this peak towards higher temperatures. For the SmA–SmC^* transition, the shift of the phase transition point induced by an electric field is estimated as [21]

$$\begin{aligned}(T_m - T_c)^{3/2} &= (\Delta T_{mc})^{3/2} \\ &= (3\sqrt{3}\chi_0\varepsilon_0 C/4\alpha d)(b/\alpha)^{1/2}V_b = s_T V_b,\end{aligned} \tag{4}$$

where T_m and T_c are the temperatures of the phase transition in an applied electric field and in the zero field, respectively; $\varepsilon_0 = 8.85 \times 10^{-12}$ F/m is dielectric constant in vacuum; and the coefficient s_T is of the order of 0.02 $\mathrm{K}^{3/2}/\mathrm{V}$ [21]. Using this s_T value for the SmA–SmC_α^* transition, we arrive at the following estimate of shift of the phase transition point at V_b = 13 V: $(\Delta T_{mc})^{3/2} = 0.02 \times 13 = 0.26$ or $\Delta T_{mc} = (0.26)^{2/3} \approx 0.4$ K, which agrees with the experimental value (Fig. 6).

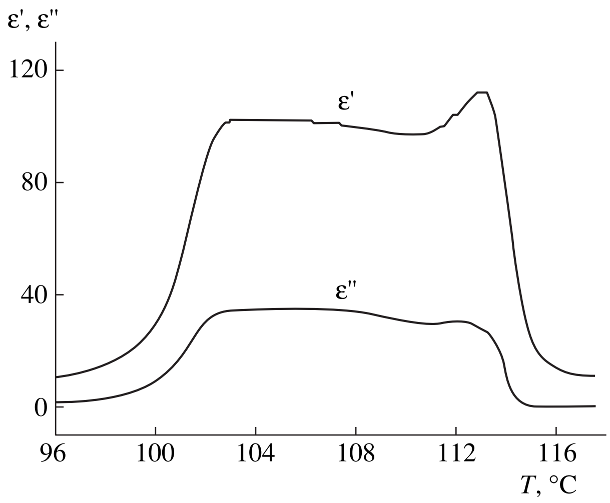

Fig. 5. Real ε' and imaginary ε'' parts of the dielectric constant of the JCR541 compound as functions of temperature (no bias field was applied).

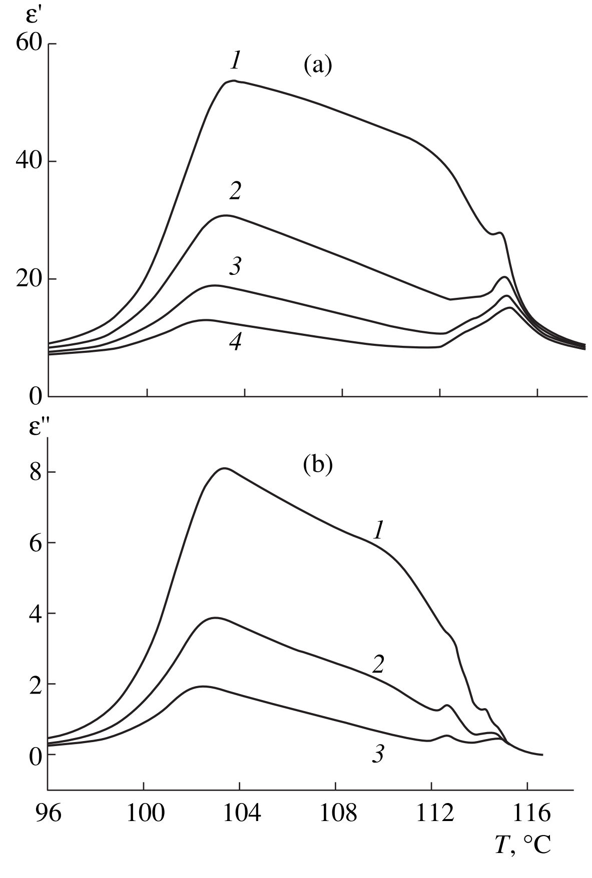

Fig. 6. Real ε' and imaginary ε'' parts of the dielectric constant of the JCR541 compound as functions of temperature. The bias voltage V_b: (a) 7 (*1*), 9 (*2*), 11 (*3*), and 13 V (*4*) and (b) 9 (*1*), 11 (*2*), and 13 V (*3*).

Figures 6 and 7 show that the bias field provides the determination of another dielectric constant peak at ~112.7°C, which seems to be determined by the contribution of the soft mode in the vicinity of the SmC_α^*–

*SmC** transition shifted to the lower temperatures due to the effect of an applied electric field.

CONCLUSIONS

The measurements of the dielectric constant and dielectric losses associated with the low-frequency soft mode showed the shift of the phase transition points in the JCR541 compound in an applied electric field: the points of the SmC^*_α–*SmC** and the *SmC**–SmC^*_γ transitions are shifted to lower temperatures, while the point of the *SmA*–SmC^*_α transition is shifted to a higher temperature. The types of the phases are identified, and the temperature dependences of the pyroelectric constant and spontaneous polarization are studied for all the phases. Spontaneous polarization of the ferroelectric *SmC** phase unwound by external electric field at the lower temperature limit of the range of its existence is about 120 nC/cm^2, whereas that of the ferrielectric SmC^*_γ phase is about 40 nC/cm^2.

ACKNOWLEDGMENTS

The work was supported by the INTAS and the Russian Foundation for Basic Research, project no. 95-128, and the Russian Foundation for Basic Research, project no. 98-02-17071.

REFERENCES

1. J. W. Goodby, R. Blinc, N. A. Clark, S. T. Lagerwall, M. A. Osipov, S. A. Pikin, T. Sakurai, K. Yoshino, and B. Zeks, *Ferroelectric Liquid Crystals* (Gordon and Breach, Philadelphia, 1991).
2. R. B. Meyer, Paper Presented at the 5th International Conference on Liquid Crystals (Stockholm, 1974).
3. R. B. Meyer, L. Liebert, L. Strzelecki, and P. Keller, J. Phys. (Paris) **36**, L69 (1975).
4. A. D. L. Chandani, T. Hagiwara, Y. Suzuki, *et al.*, Jpn. J. Appl. Phys. **27**, L729 (1988).
5. H. Moritake, A. Tagawa, M. Ozaki, and K. Yoshino, Jpn. J. Appl. Phys. **30**, 2377 (1991).
6. K. H. Kim, K. Ishikawa, H. Takezoe, and A. Fukuda, Liq. Cryst. **16**, 185 (1994).
7. A. Ikeda, Y. Takanishi, H. Takezoe, *et al.*, Jpn. J. Appl. Phys. **30**, L1032 (1991).
8. B. Jin, Z. Ling, Y. Takanishi, *et al.*, Phys. Rev. E **53**, R4295 (1996).
9. K. Ema, H. Yao, I. Kawamura, *et al.*, Phys. Rev. E **47**, 1203 (1993).
10. E. Gorecka, A. D. L. Chandani, Y. Ouchi, *et al.*, Jpn. J. Appl. Phys. **29**, 131 (1990).
11. K. Hiraoka, H. Takezoe, and A. Fukuda, Ferroelectrics **147**, 13 (1993).
12. A. Fukuda, Y. Takanishi, T. Isozaki, *et al.*, J. Mater. Chem. **4**, 997 (1994).
13. V. Faye, J. C. Rouillon, C. Destrade, and H. T. Nguyen, Liq. Cryst. **19**, 47 (1995).
14. V. M. Vaksman and Yu. P. Panarin, Mol. Cryst. Liq. Cryst. Sci. Technol., Sect. C **1**, 147 (1992).
15. J. W. O'Sullivan, Yu. P. Panarin, and J. K. Vij, J. Appl. Phys. **77**, 1201 (1995).
16. N. M. Shtykov, J. K. Vij, and M. I. Barnik, Mol. Cryst. Liq. Cryst. Sci. Technol., Sect. C **11**, 181 (1999).
17. Ph. Martinot-Lagarde and G. Durand, J. Phys. Lett. **41**, L43 (1980).
18. Yu. P. Kalmykov, J. K. Vij, H. Xu, *et al.*, Phys. Rev. E **50**, 2109 (1994).
19. K. Hiraoka, A. D. L. Chandani, E. Gorecka, *et al.*, Jpn. J. Appl. Phys. **29**, 1473 (1990).
20. H. Moritake, N. Shigeno, M. Ozaki, and K. Yoshino, Liq. Cryst. **14**, 1283 (1993).
21. L. M. Blinov, L. A. Beresnev, and W. Haase, Ferroelectrics **181**, 187 (1996).

Translated by A. Zolot'ko

Crystallography Reports, Vol. 45, No. 4, 2000, pp. 687–688. Translated from Kristallografiya, Vol. 45, No. 4, 2000, pp. 751–752.
Original Russian Text Copyright © 2000 by Vasil'eva, Randoshkin.

THIN FILMS

Growth of Forsterite Epitaxial Layers from PbO–B_2O_3-Based Fluxes

N. V. Vasil'eva and V. V. Randoshkin

Laboratory of Magnetooptoelectronics at the Mordovian State University, Saransk, Russia

Received February 24, 1998

Abstract—Forsterite layers are grown by the method of liquid phase epitaxy from supercooled PbO–B_2O_3-based fluxes. © *2000 MAIK "Nauka/Interperiodica".*

Chromium-activated Mg_2SiO_4 single crystals [1–3] are promising material for tunable lasers and, in particular, for fabricating radiation sources for high-speed fiber-based communication lines. The falerication of integrated circuits based on such sources requires the production of single-crystal layers with optical waveguides.

In order to grow single-crystal layers of various materials, one often uses the PbO–B_2O_3-based fluxes as parent phases [4–8]. The present study was aimed to grow single-crystal forsterite layers by the method of liquid-phase epitaxy (LPE) from such a flux.

The compositions of the starting charges are given in table. A sample in a platinum crucible was melted in air and heated for about 10 h at a temperature of 1000–1100°C, for sample homogenization. Then, the heater was switched off, the sample was cooled in the furnace and its cooling curve was recorded. Then, the sample was heated again at a constant heater power and its heating curve was recorded within the same time period (Fig. 1). The data obtained provided the determination of the temperature range of possible epitaxial growth of forsterite.

The optimum conditions for epitaxial growth of forsterite were determined as follows. A sample of forsterite single crystals of known weight was placed into a feux for 10–90 min at various temperatures, and rotated there at a velocity of 40–150 rpm. Upon cooling, single crystals were taken out of the furnace, washed with boiling 25% nitric acid, and weighed again. Since the crystals had irregular shapes, the growth rate of epitaxial layer (epilayer) was characterized by the relative increase Δm in the crystal weight,

$$v = (m_2 - m_1)/t,$$

where m_1 and m_2 are the crystal weights prior to and upon growth of the layer. Growth rates of 0.01–0.1 mg/min were measured on crystals which initially weighed 40–90 mg.

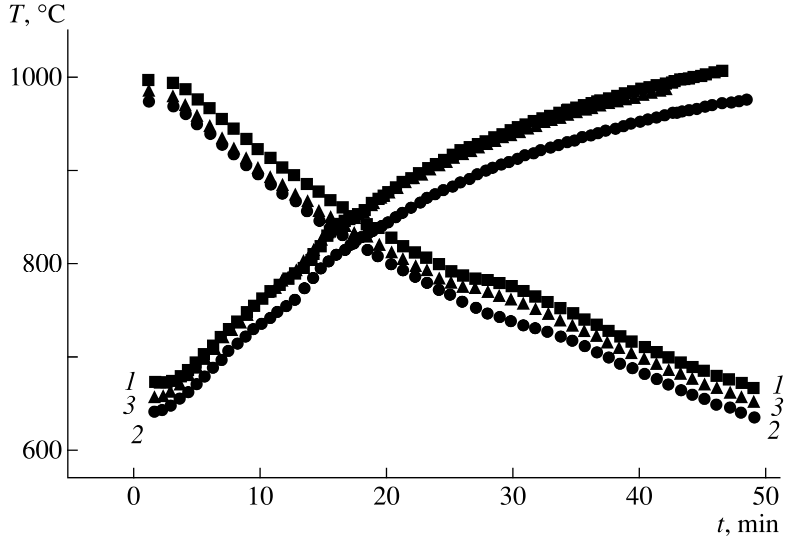

Fig. 1. Typical heating and cooling curves for compositions *1–3* (see table).

1063-7745/00/4504-0687$20.00 © 2000 MAIK "Nauka/Interperiodica"

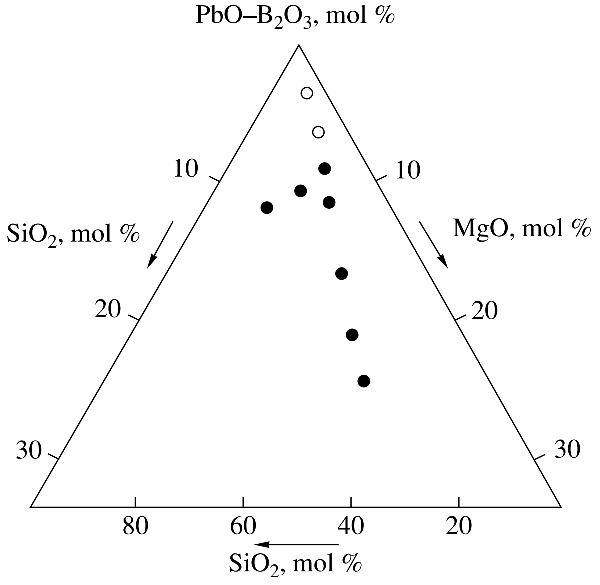

Fig. 2. Fragment of the composition triangle of the pseudoternary (PbO–B_2O_3)–MgO–SiO_2 system.

The results of the growth experiments are mapped onto the composition triangle of the pseudoternary system (PbO–B_2O_3)–MgO–SiO_2 (Fig. 2). The compositions which provide the growth of forsterite epilayers are shown by solid circles; the compositions unsuitable for such growth are indicated by open circles. It is seen that epilayers can be grown from both stoichiometric and SiO_2-enriched nutrients.

Flux compositions at which cooling and heating curves were recorded

Experiment	Composition, mol %			
	PbO	B_2O_3	MgO	SiO_2
1	84.1	4.9	7.3	3.7
2	85.0	5.0	5.0	5.0
3	85.0	5.0	3.7	7.3

Thus, the conditions for growth of single-crystal forsterite epilayers from supercooled PbO–B_2O_3-based fluxes by the LPE method are established. The results obtained seem to be promising for of growing epilayers of more complicated compositions.

ACKNOWLEDGMENTS

The authors wish to thank E. V. Zharikov and Yu. M. Papin for providing us with forsterite single crystals.

REFERENCES

1. H. Takei and T. Kobayashi, J. Cryst. Growth **23**, 121 (1974).
2. Weiya Jia, Lizhu Lu, B. M. Tissue, and W. M. Yen, J. Cryst. Growth **109**, 329 (1991).
3. Y. Yamaguchi, K. Yamaguchi, and Y. Node, J. Cryst. Growth **128**, 996 (1993).
4. V. A. Timofeeva, *Crystal Growth from Flux* (Nauka, Moscow, 1978).
5. V. A. Timofeeva, *Physicochemical and Methodical Grounds for Search for New Technical Crystals by Growth from Flux* (Nauka, Moscow, 1990).
6. P. A. Arsen'ev, Kh. S. Bagdasarov, and V. V. Fenin *Growth of Single Crystal Films for Quantum Electronics* (Izd. Mosk. Énerg. Inst., Moscow, 1981).
7. *Elements and Devices Based on Cylindrical Magnetic Domains* (Énergiya, Moscow, 1987).
8. V. V. Randoshkin and A. Ya. Chervonenkis, *Applied Magnetooptics* (Énergoatomizdat, Moscow, 1990).

Translated by A. Mel'nikova

Crystallography Reports, Vol. 45, No. 4, 2000, pp. 689–694. Translated from Kristallografiya, Vol. 45, No. 4, 2000, pp. 753–758.
Original Russian Text Copyright © 2000 by Bublik, Kol'tsov, Nemirovskiĭ, Yurchuk.

Defect Formation in Subsurface Be^+- and Se^+-Doped GaAs Layers

V. T. Bublik, G. I. Kol'tsov, A. V. Nemirovskiĭ, and S. Yu. Yurchuk
Moscow State Institute of Steel and Alloys (Technical University), Leninskiĭ pr. 4, Moscow, 117936 Russia

Received May 14, 1998

Abstract—The structure of subsurface Be^+ and Se^+ doped GaAs layers was studied by the X-ray diffraction technique. The implantation of Be^+ ions into gallium arsenide substrates causes the formation of distorted layers with elastic strains. With an increase of the energy of implanted ions from 50 to 100 keV, the maximum distortion remains almost constant, whereas the thickness of the distorted layer, with a lattice constant which exceeds that of the host material, increases. At higher energies (≥150 keV), the thickness of the distorted layer continues increasing, but the maximum strain drops. The Se^+ ions implantation into the GaAs substrates also provides the formation of layers distorted by positive tensile strain. The analysis of defect distributions and concentrations at various irradiation doses and the implanted-ion energies shows that the latter does not considerably affect these parameters. At the same time, an increase of the implanted-ion dose from 5×10^{14} to 5×10^{15} cm^{-2} increases the strains observed. The role of the Frenkel-pair annihilation and ion channeling in the formation of a defect layer is also discussed. © *2000 MAIK “Nauka/Interperiodica”.*

INTRODUCTION

The design and manufacturing of electronic devices with the use of ion implantation techniques calls for precise data concerning the distribution of the implanted dopant. The processes involving the diffusion-induced redistribution of the dopant in the course of the post-implantation annealing are determined, to a large extent, by the concentration of defects arising during the ion implantation and the profile of their distribution. Radiation defects cause distortions in the crystal lattice and can affect the direction of the dopant flux in the course of the diffusion-induced dopant redistribution, which accompanies activating annealing. The defects in the semiconductor substrate, their structural state, and their distribution over the distorted-layer depth affect the activation of implanted dopants. This is especially important for the $A^{III}B^{V}$ compounds, such as GaAs. Moreover, the implantation-induced defects also cause the changes in the electrical characteristics of semiconductors.

It is most expedient to study the distortions in a semiconductor crystal by the nondestructive method of high-resolution X-ray diffractometry method sensitive to the slightest changes in the lattice constant of the material. Analyzing the variations in the lattice constants of atomic layers located at different depths of the crystal from the diffraction reflection curves, one can estimate the concentration and distribution of point defects.

This paper is aimed to study the defect formation in GaAs layers implanted with Be^+ and Se^+ ions, in particular, to reveal the relationship between the characteristics of defect formation and the implanted-ion energy to determine the optimum implantation conditions and the limitations imposed on the mass of implanted ions.

EXPERIMENTAL

We studied the (100)GaAs plates implanted with 50, 100, 150, and 250 keV Be^+ ions at a dose of 5×10^{14} cm^{-2} (which is lower than the amorphization dose at all the ion energies indicated above). We also studied similar plates implanted with 100, 150, and 200 keV Se^+ ions at a dose of 5×10^{14} cm^{-2} and with 150 keV Se^+ ions at a dose of 5×10^{15} cm^{-2}. The implantation was performed at the HVE-350 facility (with an angle of 7° between the normal to the surface and the incident beam). To avoid the substrate heating, we used low densities of the ion flux.

The studies were performed on a UAR-PP-80.001 spectrometer. The rocking curves were measured in the dispersion-free scheme of a double-crystal X-ray diffractometer with the single symmetric Bragg reflection in the $(n, -n)$ geometry. The monochromators were high-quality (100)Ge crystals.

Rocking curves were modeled using the computer program based on the algorithm suggested in [1]. We constructed the deformation profiles and use them to estimate the total number of Frenkel defects from the experimental data the influence of Frenkel defects on the lattice constant [2].

The normalization of model curves for strains determined from the rocking curves with respect to the actual defect concentration was performed in the following way. Since upon implantation, no misfit dislocations were observed between the layer and the sub-

1063-7745/00/4504-0689$20.00 © 2000 MAIK “Nauka/Interperiodica”

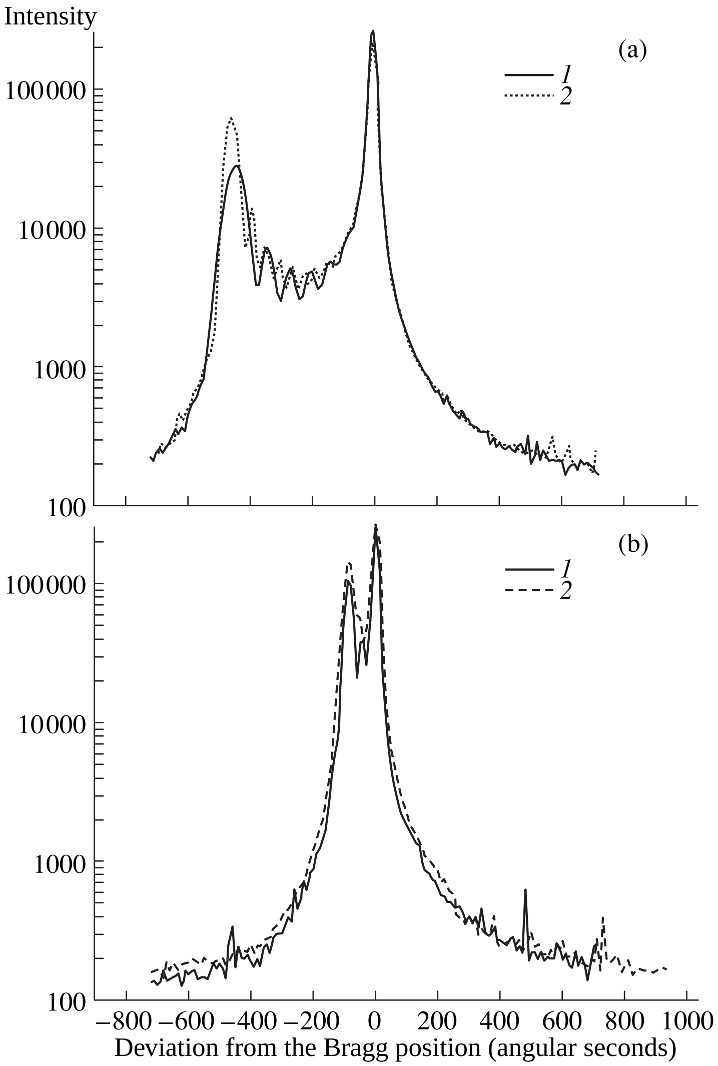

Fig. 1. X-ray rocking curves for GaAs implanted with 50- and 100-keV Be^+ ions (panel a, curves *1* and *2*), 150 and 250 keV (panel b, curves *1* and *2*).

strate, the tensor β_{ii}, describing the lattice mismatch and determined by the point-defect concentration, is expressed in terms of lattice strain ε_{zz} along the direction normal to the surface

$$\beta^0_{zz} = q_3\varepsilon_{zz}, \tag{1}$$

where ε_{zz} is the strain in the direction normal to the surface and q_3 is the factor dependent on the surface orientation. In our case, this factor can be written as [3]

$$q_3 = \frac{C_{11}}{C_{11} + 2C_{12}},$$

where C_{11} and C_{12} are the components of the elastic rigidity tensor in the matrix notation. For GaAs, we have $q_3 = 0.5$. Finally, the concentration of the Frenkel defects was determined from the strain by the formula

$$N_{\text{strain}} = \frac{\Delta a/a}{\Delta r/r}N, \tag{2}$$

where $\Delta a/a$ is the strain determined from the X-ray rocking curves, and $\Delta r/r$ is the relative change in the lattice constant caused by a single Frenkel defect. Since the relative change in the radii of a vacancy and a host atom equals approximately –0.15, and the relative difference in the sizes of an interstitial and tetrahedral pores equals approximately +0.3, then $\Delta r/r$ is about 0.15 [2]. Here, N is the number of atoms per 1 cm^3 of GaAs (4.66×10^{22} cm^{-3}).

In addition, we performed the Monte-Carlo calculations of the defect-distribution profiles for the aforementioned implantation doses [4] under the assumption that the average energy of atomic displacements in GaAs lattice is 9.45 eV [5].

The results of X-ray diffraction studies and calculations were compared with the depth profiles of the dopant distribution based on the secondary ion mass spectrometry (SIMS) data.

RESULTS AND DISCUSSION

The rocking curves from the GaAs plates implanted with Be^+ ions are shown in Fig. 1a (curves *1* and *2*). At the ion energy equal to 50 keV, the rocking curve had two peaks corresponding to the reflections from the substrate and the distorted layer. Between these peaks, one observes interference intensity oscillations of the reflected beam. For 100-keV ions, the oscillation period decreases, whereas the intensity peak due to the distorted layer increases, which indicates that the thickness of the distorted layer increases (Fig. 1b). However, the diffraction pattern does not undergo any qualitative changes.

The rocking curves in Figs. 1a and 1b were used to calculate the strain profiles. The distributions of the Frenkel defects calculated by Eq. (2) are shown in Fig. 2. The defect-concentration profile reproduces the strain profile [these profiles linearly depend on one another, see Eq. (2)]. It is clear that higher energies provide an increase in the layer thickness rather than the strain magnitude. Figure 2 also shows the Frenkel-defect distributions calculated from the rocking curves and the corresponding data of the Monte-Carlo calculations.

The defect distributions obtained by the Monte-Carlo calculations have a clearly pronounced bell-like shape. The peak of the profile shifts deeper into the crystal at higher energies. The profile broadens, and the peak height reduces with an increase of the ion energy. However, the area under the curve shows that the total number of defects per ion increases for higher ion energies.

The strain profiles obtained from the X-ray diffraction data for the samples implanted with 50- and 100-keV ions differ from those obtained from the Monte-Carlo modeling. The former are characterized by higher defect concentrations in the close vicinity of the surface and do not exhibit any peaks, which can be explained by the fact that the concentration of defects remaining in the crystal is determined not only by their generation in collisions with high-energy particles, but also by the annihilation of Frenkel defects (vacancies and interstitials) in the sublattices during irradiation. The annihilation rate of defects in the sublattice is proportional to the vacancy concentration in the *A* sublattice and to the concentration of interstitials A_i. A similar relationship is also valid for the *B* sublattice. Thus, we have

$$\nu_A = [V_A][A_i]k_1;\quad \nu_B = [V_B][B_i]k_2,$$

where $\nu_{A,\,B}$ is the annihilation rate for the Frenkel pairs in the *A*(*B*) sublattice and *k* is the constant characterizing the reaction rate.

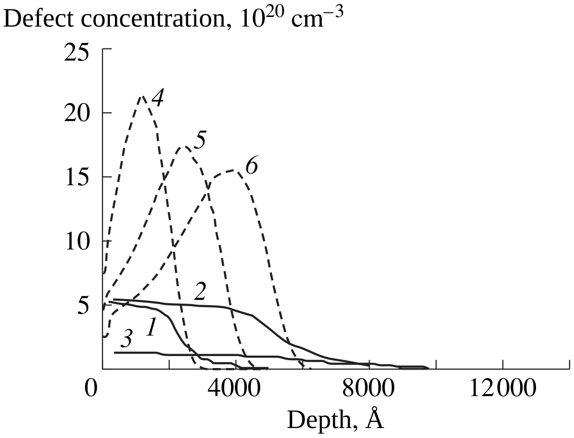

Fig. 2. Comparison of the defect concentration obtained from the X-ray data (solid curves *1*–*3*) and the model defect distributions calculated by the Monte-Carlo method (dashed lines *4*–*6*) for implantation with to 50-keV (curves *1*, *4*), 100-keV (curves *2*, *5*), and 150-keV ions (curves *3*, *6*).

However, we did not observe any intense diffuse scattering from the microscopic defects. This means that the process responsible for lower defect concentration is annihilation rather than cluster formation. The total annihilation rate for Frenkel defects is $\nu_A + \nu_B = \nu$. Apparently, it is the rate of the second-order reaction proportional to $[V_A]^2 + [V_B]^2$ (under the assumption that $[V_A] \sim [A_i]$ during Frenkel defect formation).

The Be-distribution profiles obtained by SIMS are shown in Fig. 3, curves *1*–*3*. The depth corresponding to the profile peak increases with energy almost proportionally to $\sqrt{E}$, whereas the peak height decreases. For all the ion energies, the peaks of the Be distribution are located deeper than the peaks on the Monte-Carlo profiles. The depth of the Monte-Carlo peaks is proportional to ion energies. The difference in the distribution profiles for dopants and defects is also associated with the phenomenon of channeling the more pronounced, higher, ion energy. Channeling is seen on the "tail" of the defect concentration profile on the side of more pronounced depths and increases with energy. At the ion energy of 150 keV (Fig. 1b), the rocking curve undergoes significant changes compared with the rocking curves for 50- and 100-keV ions. The peak intensity corresponding to the distorted layer increases, and the peak itself rapidly approaches the peak due to the substrate. A further growth of ion energy up to 250 keV results in no qualitative changes in the rocking curve, although the intensity of the peak due to distorted layer continues increasing.

Comparing the profiles in Fig. 2, one can clearly see some characteristic features of their variation.

For implantation with 50-keV ions, results in the formation of three distinct ranges on the profiles. I. The range, where the strain remains almost unchanged ($d \leq$

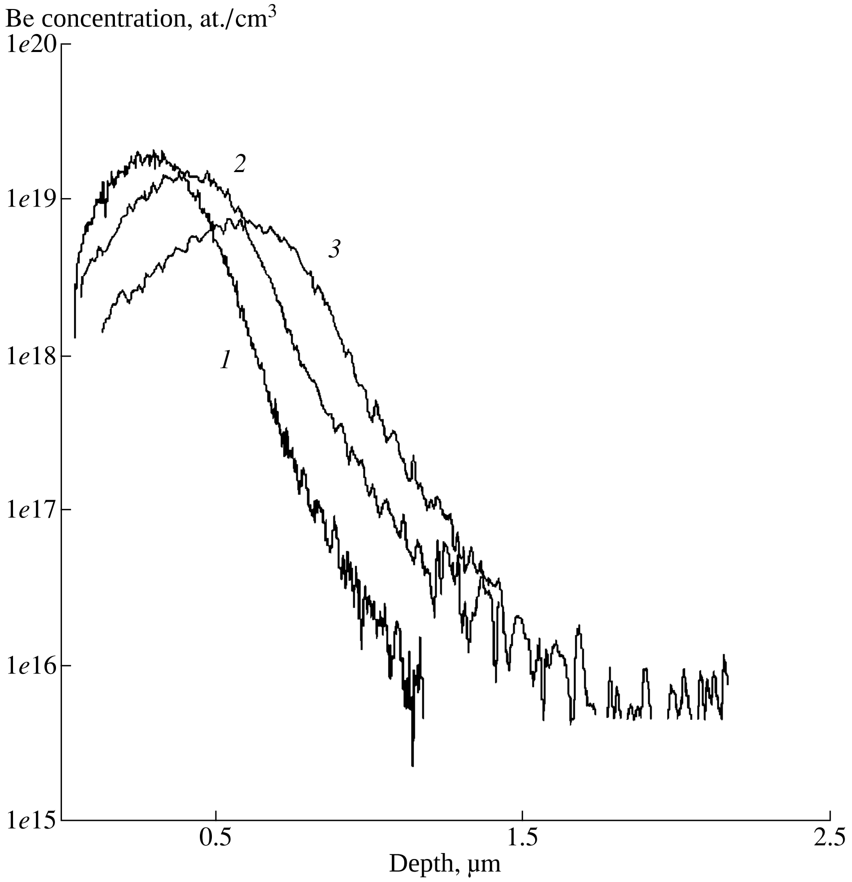

Fig. 3. Be$^+$ distribution in the GaAs substrate obtained by SIMS upon implantation with 50-keV (*1*), 100-keV (*2*), and 150-keV ions (*3*).

2000 Å); II. the range of the steep strain decrease ($2000 \leq d \leq 3000$ Å); III. the range of the gradual strain decrease.

Compared with the previous cases, the strain profile for implantation with 150 keV Be$^+$ ions (Fig. 2, curves *3*, *6*) is characterized by the drastic decrease of the maximum strain (approximately by a factor of 2.5). As a result, the profile changes its shape, region II is absent, and the strain gradually decreases throughout the depth of the layer.

For implantation with 100 keV Be$^+$ ions, the first range ends at the depth twice as deep as that of the profile corresponding to 50 keV ions. The energy increases by a factor of two (d is about 4000 Å). The second (crossover) region broadens and is feebly marked ($4000 \leq d \leq 7000$ Å), and, finally, the third region is located at $7000 \leq d \leq 9000$ Å.

For implantation with 150 keV ions, it is difficult to distinguish the above three ranges, but the depth of the profile "tail" remains the same as in the case of 100 keV ions ($d \leq 9000$ Å).

One can assume that the third range is associated with channeling. This effect can be prevalent at ion energies exceeding 150 keV for light Be$^+$ ions with a small covalent radius.

It is clear from Fig. 2 that the first range ends at the same position as the calculated Monte-Carlo defect distribution profile.

Considerable discrepancies between profiles, determined from the X-ray rocking curves and Monte-Carlo calculations, also affect the estimations of the concentration level of defects. Modeling of implantation with 50- and 100-keV ions yields the defect concentration four times, exceeding the values determined from the X-ray diffraction data. At 150 and 250 keV ion energies, the difference is even more pronounced. This disagreement seems to be caused by certain drawbacks of the TRIM program used for the Monte-Carlo calculations, where the recombination of radiation defects and the effects of rechanneling.

Thus, the strain profile undergoes qualitative changes with an increase of the ion energy. For 50- and 100-keV ions, the thickness of the layer containing most Frenkel defects increases proportionally to the ion energy. The X-ray diffraction data indicate that the total number of defects in the distorted layer also increases proportionally to the ion energy. The number of defects calculated by the Monte-Carlo method grows much more slowly, but nevertheless it considerably exceeds the values obtained from the X-ray diffraction data. This indicates the important role played by the annihilation processes in forming the defect distribution profile.

At higher energies, the annihilation becomes less important, and channeling begins to dominate in the formation of a defect profile. Under these conditions, the total number of Frenkel defects decreases much faster than in the Monte-Carlo calculations.

Now, consider the defect formation during implantation with larger Se^+ ions having a larger mass than Be^+ ions. In this case, the effects of channeling should not be less important in the ion-energy range of 100–200 keV.

The rocking curves for the samples implanted with Se^+ ions of energies of 100, 150, and 200 keV, at a dose equal to 5×10^{14} cm^{-2}, are presented in Fig. 4a, curves *1–3*. For higher energies of Se^+ ions, we also observed a slight decrease in the strains, and, thus also, in the concentration of Frenkel defects. The strain decreased by 4% with an energy increase from 100 to 150 keV and by another 4% with the energy increase up to 200 keV. The typical strain profile is shown in Fig. 5. In contrast to doping with beryllium ions, the profile has only two first regions. In this case, the "tail" associated with channeling can hardly be distinguished.

The comparison of strain profiles for implantation with 100-keV Be^+ and Se^+ ions demonstrates that the thickness of the distorted layer, Se^+, corresponding to the first profile range, is almost twice less at nearly the same strain. It is clear that the total number of Frenkel defects per layer for implantation with Se^+ ions is also twice as small. For the same target (GaAs), the doses and the energies of implanted ions and the number of arising defects are almost the same (at $E_i \gg E_d$, where E_i is the ion energy and E_d is the threshold energy for the defect formation). In addition, a dose of 5×10^{14} cm^{-2} of Se^+ ions is close to the amorphization dose at the aforementioned energy. All these facts allow us to suggest that half the number of residual Frenkel defects arising, due to implantation with Se^+ ions, is explained by fact that the defect concentration increases, and therefore the interdefect spacing decreases, thus providing a more intense annihilation. Finally, this leads to the mentioned difference in the residual defect concentration. Thus, the annihilation processes play an important role in the formation of the implanted layer structure.

Note that all the rocking curves have shoulders from the side of larger angles, which was ignored when calculating the corresponding profiles. This shoulder is most pronounced at the rocking curve from the sample implanted with 150 keV ions, at a dose equal to 5×10^{14} cm^{-2} (Fig. 4a, curve *2*). The shoulder can arise due to coherent scattering by a layer with the lattice constant less than that of the substrate, or due to the diffuse scattering by "interstitial" microscopic defects. Using the triple-crystal scheme, we measured the intensity distribution along the direction perpendicular to the

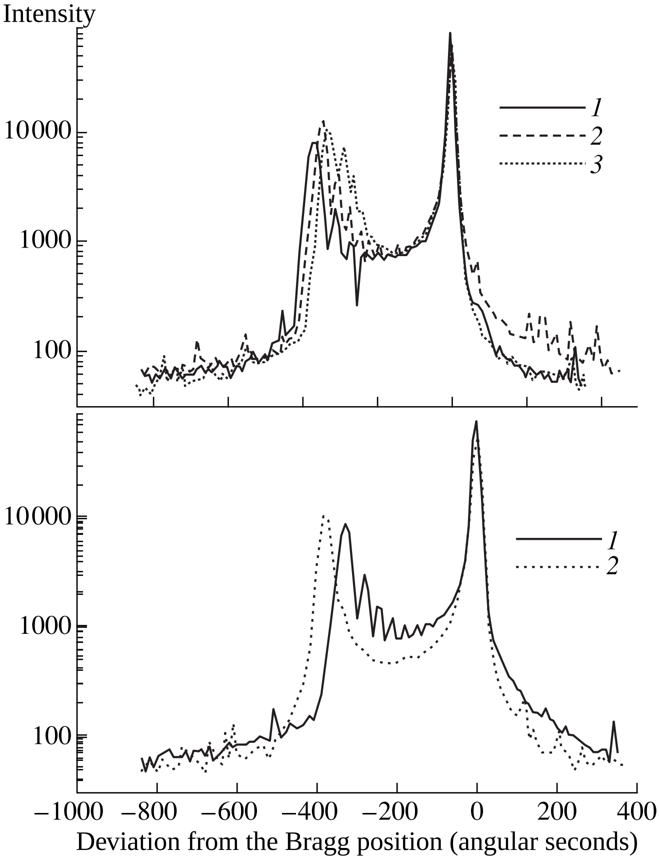

Fig. 4. X-ray rocking curves for GaAs implanted with Se^+ ions (a) with the energies (*1*) 100 keV, (*2*) 150 keV and (*3*) 200 keV at a dose of 5×10^{14} cm^{-2} and (b) with 150 keV Se^+-ions at doses (*1*) 5×10^{14} cm^{-2} and (*2*) 5×10^{15} cm^{-2}.

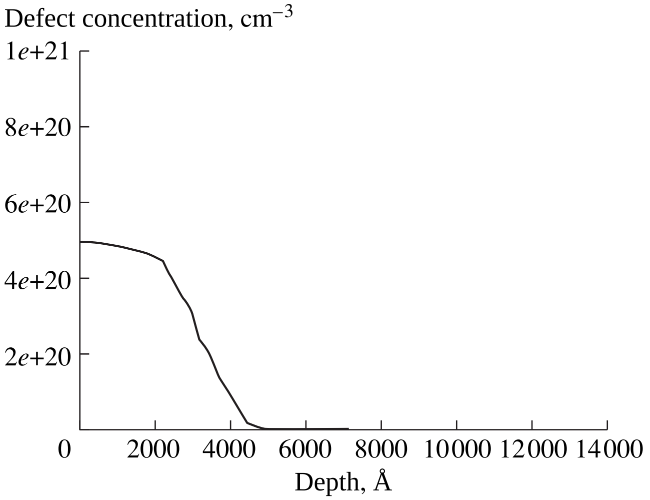

Fig. 5. Typical profile of defect distribution for the sample implanted with 100 keV Se^+ ions at a dose of 5×10^{14} cm^{-2}.

reciprocal lattice vector, at angles characterizing the sample deviation from the exact Bragg position corresponding to the shoulder location. At this cross section, one can see a narrow peak centered along the direction of the reciprocal lattice vector in the vicinity of the reciprocal lattice, where almost no diffuse scattering is observed. This indicates that a vacancy-enriched layer is formed at the crystal surface upon ion implantation.

The rocking curves for samples implanted with 150-keV Se^+ ions at doses of 5×10^{14} and 5×10^{15} cm^{-2} are shown in Fig. 4b, curves *1* and *2*.

These curves also exhibit the peaks due to the substrate and the distorted layer separated by 330″ and 375″ at the implantation doses 5×10^{14} and 5×10^{15} cm^{-2}, respectively. The intensities of reflection peaks for these two samples are almost equal and are independent of the implantation dose. With an increase of the implantation dose, the peak due to the distorted layer is shifted toward angles smaller by 45″. If a dose increases by a factor of ten, the strain and the number of residual defects increases by only 14%. This also shows that defect annihilation plays a considerable role in the formation of the distorted layer.

CONCLUSIONS

Implantation with ions of small and moderate masses of the layers having the orientation inconsistent with channeling, the formation of defect-enriched layer is affected by two mechanisms that manifest themselves differently during implantation with Be^+ and Se^+ ions.

In implantation with Be^+, both annihilation of radiation-induced defects and channeling are important, but the latter becomes more pronounced at higher ion energies. At ion energies exceeding 150 keV, channeling becomes the key factor determining the number of residual radiation-induced defects.

During implantation with Se^+ ions with the energy ranging within 100–200 keV, channeling almost does not affect the defect formation. In this case, at doses close to or higher than the amorphization dose, annihilation of radiation defects and the mean free path of dopants determine the number and the distribution of radiation defects in the implantation layer, respectively.

REFERENCES

1. C. R. Wie, T. A. Tombriello, and T. Vreeland, J. Appl. Phys. **59** (11), 3743 (1986).
2. V. T. Bublik and M. G. Milvidskiĭ, Materialoved., No. 1, 21 (1997).
3. Yu. P. Khapachev and F. N. Chukhovskiĭ, Kristallografiya **34** (3), 785 (1989).
4. V. S. Vavilov, Usp. Fiz. Nauk **167** (4), 407 (1997) [Phys. Usp. **167** (4), 387 (1997)].
5. F. Reyhaud and B. Legros-de Mauduit, Radiat. Eff. **88** (1–2), 1 (1985).

Translated by K. Kugel

Crystallography Reports, Vol. 45, No. 4, 2000, pp. 695–697. Translated from Kristallografiya, Vol. 45, No. 4, 2000, pp. 759–761.
Original Russian Text Copyright © 2000 by Sorokin, Krivandina, Zhmurova, Lyamina, Sobolev.

CRYSTAL GROWTH

Growth of Single Crystals and Optimization of Anionic Transport in $La_{1-x}Nd_xF_3$ Solid Solutions with Tysonite-type Structure by Isovalent Substitutions

N. I. Sorokin*, E. A. Krivandina*, Z. I. Zhmurova*, O. I. Lyamina, and B. P. Sobolev***

** Shubnikov Institute of Crystallography, Russian Academy of Sciences,*
Leninskiĭ pr. 59, Moscow, 117333 Russia[1]

*** Kurnakov Institute of General and Inorganic Chemistry, Russian Academy of Sciences,*
Leninskiĭ pr. 31, Moscow, 117907 Russia

Received September 8, 1998

Abstract—The study of the effect of isomorphous isovalent substitution on the fluoride-ion conductivity in $La_{1-x}Nd_xF_3$ solid solutions was aimed at optimizing the anionic transport in solid electrolytes with the tysonite-type (LaF_3) structure. A series of $La_{1-x}Nd_xF_3$ single crystals with $0.1 \le x \le 0.9$ was grown for the first time by the Bridgman–Stockbarger method in the fluorinating atmosphere. The ionic conductivity was measured at frequencies ranging from 5 to 500 kHz by the method of impedance spectroscopy (with the use of graphite contacts). The conductivity is maximal at the composition $La_{0.37}Nd_{0.63}F_3$. *© 2000 MAIK “Nauka/Interperiodica”.*

INTRODUCTION

Earlier [1], to establish the effect of lattice geometry of the solid solution with the tysonite-type structure (LaF_3) on the fluoride-ion conductivity σ, we measured the conductivity of LaF_3, NdF_3, and three solid solutions $La_{1-x}Pr_xF_3$ with x = 0.25, 0.5, and 0.75. The results obtained in [1] and the known conductivity data for RF_3 (R = La, Ce, Pr, Nd) and $La_{1-x}Pr_xF_3$ solid solutions show that the conductivity σ of tysonite-type materials is maximal for the ions with the radius r_{cat} = 1.270–1.285 Å (the r_{cat} values are given in the Shannon system of ionic radii, where the fluoride ion has the radius r_{F^-} = 1.19 Å [2]). Below, we report our further study of tysonite-type solid electrolytes [1] using the method of isomorphous isovalent substitution aimed to optimize the fluoride ion transport in $La_{1-x}Nd_xF_3$ ($0.1 \le x \le 0.9$) single crystals with continuously varying cation radius r_{cat} from 1.3 (La^{3+}) to 1.249 Å (Nd^{3+}).

EXPERIMENTAL

According to the phase diagram, the LaF_3–NdF_3 is a pseudobinary system forming the continuous series of $La_{1-x}Nd_xF_3$ solid solutions which can be obtained as single crystals [3]. A number of $La_{1-x}Nd_xF_3$ single crystals were grown from LaF_3 (special-purity grade) and NdF_3 (reagent-purity grade) starting materials. Prior to growth, the LaF_3 and NdF_3 melts were fluorinated to remove oxygen. Single-crystal boules 10 mm in diameter and 20 mm in length were grown in a helium atmosphere by the Bridgman–Stockbarger method. Special-purity PbF_2 (5 wt %) added to the starting charge served as fluorinating agent. Graphite crucibles were pulled down at the rate of 5.15 ± 0.15 mm/h.

Electric properties were measured on the samples 10 mm in diameter and 2 mm in thickness, which were cut from the central parts of the boules normally to the growth direction. Chemical composition of the samples differed from the calculated one by not more than 0.3–0.7 mol % and was checked by X-ray fluorescence analysis examining the La-L_β and Nd-L_α lines on a Carl Zeiss VRA-33 analyzer (Cr anode, 30 kV accelerating voltage, 30 mA current).

Electrical measurements were made in a vacuum of $\sim 10^{-1}$ Pa in the temperature range 293–716 K. Fluoride ion conductivity was determined by the complex impedance method. The impedance was measured at the frequencies 5 Hz–500 kHz on a Tesla BM-507 impedance meter. The electrodes were prepared from the DAG-580 graphite paste.

RESULTS AND DISCUSSION

The temperature dependence of conductivity for all the $La_{1-x}Nd_xF_3$ samples has a kink in the temperature range T_C = 415–500 K. All the dependences of conductivity σ on the reciprocal temperature consist of two lin-

---

[1] *e-mail: sorokin1@mail.ru*

Temperatures T_C, constants A, and enthalpy constant $\Delta H_{m,\,v}$ for $La_{1-x}Nd_xF_3$ single crystals

Composition	T_C^*, K	$T < T_C$		$T > T_c$	
		log A, Ω^{-1} cm^{-1} K	$\Delta H_{m,\,v}$, eV	log A, Ω^{-1} cm^{-1} K	$\Delta H_{m,\,v}$, eV
LaF_3 [1]	405	3.90	0.408	2.56	0.301
$La_{0.89}Nd_{0.11}F_3$	415	3.3(3)	0.386(2)**	2.46(7)	0.316(8)
$La_{0.78}Nd_{0.22}F_3$	420	3.5(2)	0.40(1)	2.27(7)	0.299(8)
$La_{0.71}Nd_{0.29}F_3$	445	3.2(3)	0.38(2)	2.7(1)	0.34(1)
$La_{0.60}Nd_{0.40}F_3$	430	3.82(3)	0.432(2)	2.46(6)	0.316(5)
$La_{0.53}Nd_{0.47}F_3$	435	3.5(2)	0.41(1)	2.15(7)	0.294(7)
$La_{0.42}Nd_{0.58}F_3$	490	3.2(1)	0.38(1)	2.1(1)	0.27(1)
$La_{0.37}Nd_{0.63}F_3$	500	3.4(1)	0.359(8)	2.1(1)	0.230(9)
$La_{0.21}Nd_{0.79}F_3$	470	3.4(1)	0.37(1)	1.94(9)	0.23(1)
$La_{0.11}Nd_{0.89}F_3$	475	3.4(1)	0.387(1)	1.9(1)	0.241(7)
NdF_3 [1]	445	4.56	0.46	2.85	0.31

* The values calculated by the formula $T_C = (\Delta H_1 - \Delta H_2)/k(\ln A_1 - \ln A_2)$.

** Standard deviations are given in brackets.

ear segments—where $T < T_C$ and where $T > T_C$, which obey the Arrhenius–Frenkel equation

$$\sigma = (A/T)\exp(-\Delta H_{m,\,v}/kT),$$

where A is a constant and $\Delta H_{m,\,v}$ is the enthalpy of migration of fluoride vacancy. The T_C, A, and $\Delta H_{m,\,v}$ values are given in table.

The figure shows the conductivity of the $La_{1-x}Nd_xF_3$ as a function of composition at 500 K. In the composition range $0 < x < 0.5$, the conductivity is almost constant, but then it starts increasing and attains the maximum at $x = 0.63$. The average cationic radius in $La_{0.37}Nd_{0.63}F_3$ showing the highest conductivity is $r_{cat} = (1-x)r_{La^{3+}} + xr_{Nd^{3+}} = 1.267$ Å, which is consistent with the average cationic radius $r_{cat} = 1.27–1.285$ Å determined in our earlier study [1]. This confirms the important role of the dimensional factor on the charge transport in tysonite-type structures with a charge homogeneity in the cationic sublattice.

Isostructural LaF_3 and NdF_3 compounds and their solid solutions $La_{1-x}Nd_xF_3$ are trigonal, sp. gr. $P\bar{3}c1$, $z = 6$ [4–6]. The cation positions in the $La_{1-x}Nd_xF_3$ structure are statistically occupied by La^{3+} and Nd^{3+} ions. As found in [7–9], the transport of fluoride ions proceeds by a migration of mobile fluoride vacancies over various nonequivalent lattice positions.

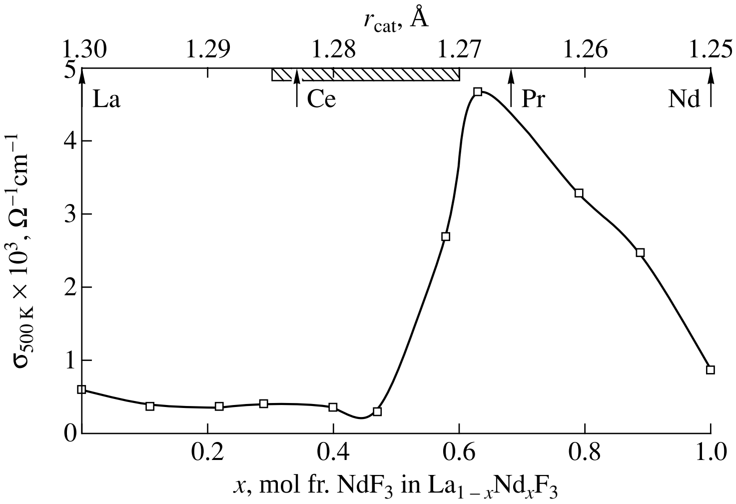

Conductivity as a function of the composition of the $La_{1-x}Nd_xF_3$ solid solutions at 500 K. The hatched region corresponds to $r_{cat} = 1.27–1.285$ Å.

The substitution of La^{3+} by Nd^{3+} does not lead to the formation of new fluoride vacancies. Yet, since the ionic radii of substituted cations and substituents are different, the parameters of the tysonite lattice change from $a = 7.1862$, $c = 7.3499$ Å in LaF_3 to $a = 7.0299$, $c = 7.1959$ Å in NdF_3 [10]. The analysis of the A and $\Delta H_{m,v}$ for various compositions shows that $La_{0.37}Nd_{0.63}F_3$ has the lowest activation enthalpy of conductivity ($\Delta H_{m,\,v} = 0.36$ eV at $T < T_C$ and $\Delta H_{m,\,v} = 0.23$ eV at $T > T_C$) and, consequently, also the lowest potential barrier for fluoride ion migration. This fact seems to determine the optimum fluoride-ion conductivity of the $La_{1-x}Nd_xF_3$ solid solution with $x = 0.63$.

ACKNOWLEDGMENTS

The authors acknowledge the assistance of D. N. Kuranov, O. A. Nikeeva, and M. V. Fominykh, students of the Lomonosov State Academy of Fine Chemical Technology.

REFERENCES

1. N. I. Sorokin and B. P. Sobolev, Kristallografiya **39** (1), 114 (1994) [Crystallogr. Rep. **39** (1), 101 (1994)].
2. R. D. Shannon, Acta Crystallogr., Sect. A: Cryst. Phys., Diffr., Theor. Gen. Crystallogr. **32**, 751 (1976).
3. B. P. Sobolev, Doctoral Dissertation in Chemistry (Russian Academy of Sciences, Moscow, 1978).
4. M. Mansmann, Z. Kristallogr. **122**, 375 (1965).
5. B. Maximov and H. Schulz, Acta Crystallogr., Sect. B: Struct. Sci. **41**, 88 (1985).
6. I. P. Kondratyuk, A. A. Loshmanov, L. A. Muradyan, *et al.*, Kristallografiya **33** (1), 105 (1988) [Sov. Phys. Crystallogr. **33** (1), 57 (1988)].
7. G. A. Jaroszkiewicz and J. H. Strange, J. Phys. C **18**, 2331 (1985).
8. A. F. Aalders, A. F. M. Arts, and H. W. den Wijn, Phys. Rev. B **32**, 5412 (1985).
9. I. Brach and H. Schulz, Solid State Ionics **15**, 135 (1985).
10. O. Greis and T. Petzel, Z. Anorg. Allg. Chem. **404**, 1 (1974).

Translated by A. Mel'nikova

Crystallography Reports, Vol. 45, No. 4, 2000, pp. 698–703. Translated from Kristallografiya, Vol. 45, No. 4, 2000, pp. 762–767.
Original Russian Text Copyright © 2000 by Tsvetkov, Tomilenko, Khranenko, Yurkin.

Study of Inclusions and Causes of Their Formation during Growth of Barium Metaborate Crystals

E. G. Tsvetkov, A. A. Tomilenko, G. G. Khranenko, and A. M. Yurkin

Institute of Mineralogy and Petrography, Siberian Division of the Russian Academy of Sciences,
Novosibirsk, Russia

Received August 10, 1998; in final form, August 9, 1999

Abstract—The complex study of barium metaborate crystals has been undertaken with the aim to determine the conditions of their growth with the minimum density of inclusions. It is shown that almost all the inclusions are multiphase formations of the melt type, and, in addition to the mixture of the main components of the quasieutectic composition, they can also be enriched with gas-forming impurities not removed during barium metaborate synthesis. It is shown that the amount and the composition of melt-like inclusions in crystals depends on the removal of by-products of the reactions used for barium metaborate synthesis from the system, the patterns of the convective flows in the flux, the character of its flow under the interface, the axial temperature gradient in the solution, and the temperature fluctuations at the crystallization front. *© 2000 MAIK “Nauka/Interperiodica”.*

INTRODUCTION

Single crystals of the low-temperature modification of barium metaborate (β-BaB_2O_4, BMB) are widely used as highly effective converters of lasing radiation in optoelectronic engineering [1]. This explains the high requirements of the structural quality of BMB used in the preparation of various elements for nonlinear optics.

One of the most typical defects in BMB crystals grown from viscous flux under specific conditions [2] are various inclusions [2–6]. These inclusions are almost always located in the central axial zone of the crystals, and, under unfavorable conditions at a certain stage of crystal growth, they can also be formed in the whole crystal bulk. Therefore, the study of these inclusions in BMB crystals, depending on the synthesis and growth conditions, is quite timely and will provide the establishment of the relationship between various technological processes in the cycle and the optimization of this cycle for growth of crystals with the minimum inclusion density.

Earlier, it was reported that such inclusions are enriched with sodium [5]. Some authors also assumed the presence of CO_2 in these inclusions [4] and the formation of solid-phase inclusions in the form of small elongated (presumably BMB) crystals. [3, 6].

Among the possible causes of inclusion capture by BMB crystals are nonoptimum temperature distribution and considerable temperature fluctuations in the flux [3–5], its poor stirring and high viscosity [4], and the evolution of dissolved gases at the crystallization front [5].

Below, we report our study of the conditions, providing the formation and accumulation of impurities in fluxes and also of these inclusions, their formation and composition.

EXPERIMENTAL

BMB crystals were grown from 80 ± 2 mol % BMB solutions in the Na_2O melt by the Czochralski technique. BMB synthesis was performed using high-purity or chemically-pure BaO, $BaCO_3$, $Ba(CH_3COO)_2$, B_2O_3, and H_3BO_3. The weights in the corresponding proportions were thoroughly mixed and sintered in a platinum crucible at the given temperature. To follow the synthesis dynamics, the sintered mass was regularly weighted to determine the content of gaseous products (impurities) not removed from the mixture. Then, three probes of this mass were taken for the X-ray phase analysis performed with the use of a TUR-62M diffractometer. The synthesis was completed with mixture melting and kept for 40–50 h at 1150°C. Formally, the BMB synthesis can be described by the reactions

$$Ba(CH_3COO)_2 + 2H_3BO_3 + 2O_2 \longrightarrow BaB_2O_4 + 6H_2O\uparrow + 2CO_2\uparrow, \quad (1)$$

$$BaCO_3 + 2H_3BO_3 \longrightarrow BaB_2O_4 + 3H_2O\uparrow + CO_2\uparrow, \quad (2)$$

$$BaO + 2H_3BO_3 \longrightarrow BaB_2O_4 + 3H_2O\uparrow. \quad (3)$$

The BMB melt thus obtained was quenched by pouring it into a platinum crystallization vessel outside the furnace with the addition of the corresponding amount of Na_2CO_3 (the starting compound of the solvent). Then the crystals were grown. The apparatus, methods, and growth conditions for BMB crystals were reported earlier [2]. The microthermometric studies of the melt-like inclusions were performed in a specially designed microthermometric chamber filled with an inert gas (Ar) [7]. The chemical composition of crystalline inclusions was determined by the method of X-ray microanalysis with the use of a JSM-35 scanning electron microscope–analyzer and a CAMEBAX microprobe.

The chromatographic analysis of the gases evolved as the material was heated on a chromatographic setup for the simultaneous detection of CO_2, CO, N_2, H_2, H_2O, O_2, etc. The setup was assembled using three industrial LKhM-80 chromatographs and was supplied with specially designed devices for the thermal and mechanical extraction of the gases [8]. In this case, annealing of the samples (grind fragments of BMB crystals with high inclusion density) was performed in a stepwise manner ($\Delta T \approx 100°C$) in the temperature range 200–900°C. The analysis of the gaseous and solid inclusions was performed by the method of the Raman spectroscopy on a RAMANOR U-1000 one-channel spectrometer, with the use of an Ar-laser by the method described elsewhere [9].

RESULTS AND DISCUSSION

Inclusions in BMB crystals. BMB crystals grown by different techniques from the charge prepared under various crystallization conditions had different densities and distributions of inclusions [regions of different (foreign) phases of different dimensions]. It was established that all the boules of the BMB crystals had a considerable amount of inclusions with the characteristic distribution over the crystals and, at the same time, also had a rather large volume zones free of any inhomogeneities. All the crystals had, to a larger or lesser degree, a divergent “column” of inclusions in the central axial (“subseeding”) zone of the boule. Usually, the inclusions density was higher in the axial part and was surrounded with an external layer, where the inclusion density was much lower. In the axial part of the column, one usually observed vertical chain structures and sometimes also thin channels with a diameter up to 100–200 μm extended for tens of millimeters from the seed into the crystal depth. In the external layers of such columns, the foreign-phase inclusions formed the volume–zonal distribution with the threefold axial symmetry.

Some BMB boules had belts of inclusions, which sometimes had the form of island accumulations in the peripheral subsurface zone. In the cases where cellular substructures were formed at the interface, we also observed the zones of continuous fields of foreign-phase inclusions in the boules formed as a result of a cellular growth. These fields also had local density maxima with the threefold symmetry.

The examination of polished plates sawn from the zones of the maximum inclusion densities in the crystals grown showed that all the inclusions can reliably be related to the melt type. Only some of them resembled 0.5 mm-long solid-phase inclusions (microcrystals) [3, 6]. The morphologies of the melt-like inclusions (multiphase formations) were rather diverse and, in many respects, resembled morphology described in [4, 5]. The crystallized melt is an aggregation of microcrystals of various phases, which deform the gas-phase bubble with an increase in the temperature of up to 430°C; the inclusions undergo phase transitions, and the texture of a finely grained aggregate is changed. An increase up to 750°C results in the start of the solid-phase recrystallization, accompanied by its clarification and gradual change of the grain shape and dimensions. At the 770°C, the first sign of melting appears. The crystalline phases decrease in dimensions and become mobile. The first solid phase, still existing upon recrystallization, disappears at 800°C. The dimensions of all the other phases decrease and at 820°C, the gas bubble and the last crystalline phase almost simultaneously disappear, i.e., inclusions become homogeneous. Upon homogenization at 860°C, one observes phase refaceting with the formation of an isometric negative crystal; finally, at 940°C, the total dissolution of the BMB matrix forming their walls begins. Upon quenching, the formation of a gas bubble is observed in all the inclusions. The melt (or glass) is stable up to 580°C; then its rapid crystallization starts.

Being “pushed” to the surface, the materials of the foreign phases both subjected and not subjected to heating behave in different ways. The heated crystalline phases remain the same upon “opening,” whereas unannealed phases are gradually “swelling.” This process occurs within several hours upon opening and seems to be associated with the hydration process. This conclusion is confirmed by the Raman spectroscopy (Fig. 1). In the range 800–1400 cm^{-1}, the Raman spectra of unopen and unannealed inclusions have only one intense line at 1326 cm^{-1} (Fig. 1, curve *d*). The unannealed inclusions were studied within 2 h upon their opening, and showed two more lines at 1052 and 1351 cm^{-1} (Fig. 1, curve *c*); upon 20 days after their opening in air, only the last two rather intense lines are observed (Fig. 1, curve *b*). The disappearance of the line at 1326 cm^{-1} indicates the composition of the inclusion changed due to hydration of the corresponding solid phases. The foreign inclusions heated up to 820°C showed no characteristics lines upon their opening in the range studied (Fig. 1, curve *e*).

The X-ray microanalysis showed that the inclusions consist mainly of Ba and Na (B and C could not be quantitatively measured). Being recalculated to the oxide form, the content of the components recorded during the analysis was: BaO 62.1, Na_2O 6.9,

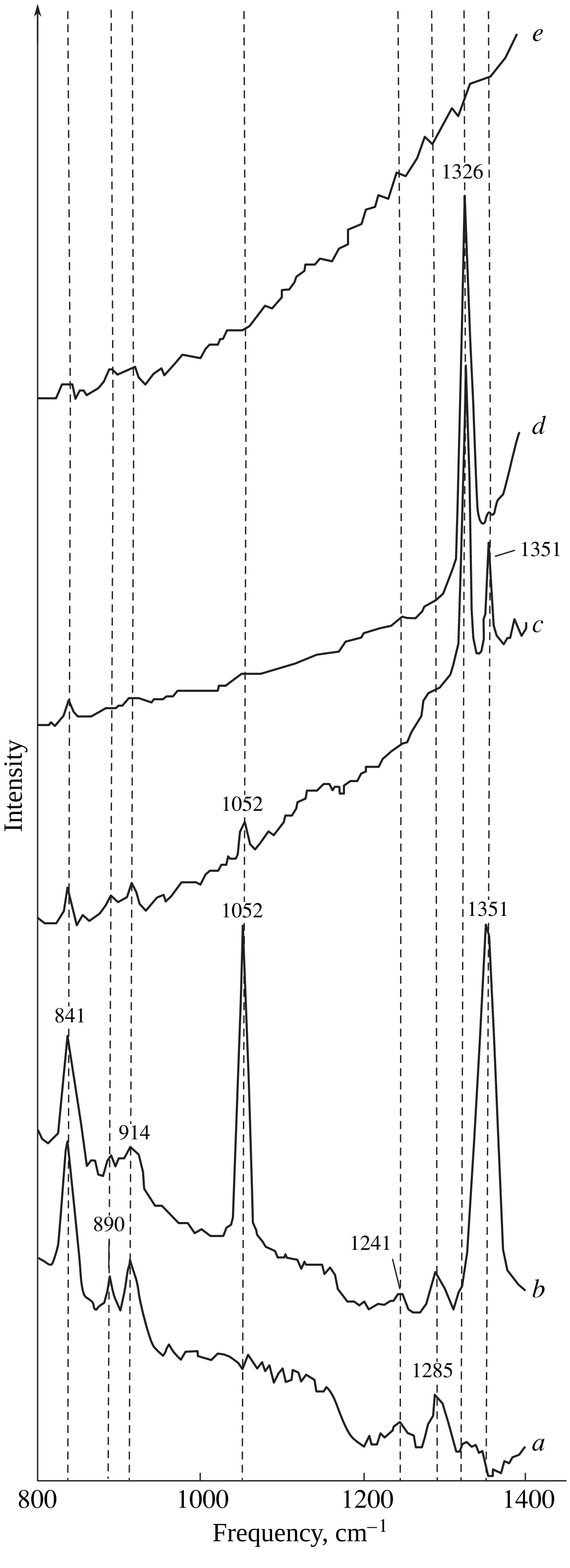

Fig. 1. Infrared spectra of: (*a*) a BMB crystal, (*b*, *c*) unheated open melted inclusion stored (*b*) for more than 20 days in air and (*c*) for not more than 2 h, (*d*) unheated unopen melted inclusion and (*e*) inclusion heated up to 820°C, quenched, and then open.

SiO_2 0.37, Al_2O_3 0.22, Cl 0.1, MgO 0.08, K_2O 0.04, and CaO 0.03 wt %. On the whole, the Ba and Na content do not reflect their ratio in the crystalline phases in the eutectic crystallization of the drops of the depleted solutions caught by the crystal in the quasibinary BaB_2O_4–$BaB_2O_4 \cdot Na_2O$ system [5]. A special scanning mode provided the detection of carbon in foreign phases in some crystals in the amount considerably exceeding the background value (Fig. 2).

The comparison of the batches of crystals grown from the solutions obtained with the use of BMB, synthesized by different reactions, showed that the amount of melted inclusions can considerably vary. However, the amount of such inclusions increases if one uses complex barium salts and decreases the time of the corresponding reaction. The content of the gaseous products not removed from foreign phases was determined by the chromatographic analysis. Figure 3 shows the results of such analysis for the crystal grown with the use of BMB synthesized by reaction (1) for 20 h. The sample was prepared from the cellular zone of the crystal and had a high density of foreign inclusions. Prior to the analysis, it was ground and kept out in the air for more than 30 days. The intense dehydration at the beginning of the sample heating was followed by an intense evolution of CO_2, with the maximum at 600°C. The data of homogenization, Raman spectroscopy, and X-ray microprobe analysis led us to assume the existence of a certain hydrated form of sodium–barium carbonate (conditionally, $Na_xBa_y[CO_3]_z \cdot nH_2O$) as a modified solid-phase inclusion, binding the gas-forming impurity components accumulated in front of the crystallization phase. This assumption is confirmed by the character and the temperature range of H_2O separation, and the character of CO_2 evolution during stepwise annealing, which indicates the thermal decomposition of low-temperature carbonate phases. We also observed the evolution of CO (in less quantities), correlating with the CO_2 content. The above fact of the intense hydration of the material of unheated inclusions seems to be associated with its partial hydration from the very beginning. Upon opening, the sample was further hydrated up to the saturation of the corresponding crystal-hydrate forms with water. This leads to an assumption that the flux contained some residual water not removed during crystal growth. The control analysis of the BMB samples, without visual inclusions, showed much less intense (by two orders of magnitude) gas evolution, which seems to be associated with the removal of adsorbed atmospheric vapors from the sample. Other components of the gas mixture which evolved during sample heating were either absent or had the “trace” concentrations.

BMB synthesis. We performed the comparative analysis of various variants of the BMB synthesis in order to estimate their contribution into the impurity content in fluxes and their effect on the density of inclusions and their nature. The conditions for the analysis and the main results are indicated in table.

The BMB synthesis, according to reaction (1), is hindered by product degassing, as seen from a relatively large mass fraction of impurities compared with that observed in reactions (2) and (3) for comparable times. The main impurity is carbon separated during $Ba(CH_3COO)_2$ decomposition, and slowly burning away under the conditions of a relative oxygen deficit in the muffle furnace. Therefore, the synthesis by reaction (1) of the product with 99.95 wt % BMB content requires at least two days, whereas its synthesis by reactions (2) and (3) yields the same result for only one day. The necessity of a thorough, maximum removal of carbon in the solid-phase BMB synthesis is dictated by the fact that its complete removal from the melt requires prolonged annealing at ~1200–1300°C and is accompanied, as showed the analysis, by the active transport of $NaBO_2$ (and possibly also B_2O_3) and the change of the given flux composition.

The X-ray microprobe analysis of the product samples show the presence of both BMB modifications at the synthesis temperatures higher than 950°C, whereas at lower temperatures, only the low-temperature β-BaB_2O_4 modification is synthesized. Melting of the low-temperature modification, with the short-time overheating of the melt up to 1200°C and its subsequent quenching, shows the metastable crystallization of β-BBO. If melting occurs prior to complete occurrence of the synthesis reaction, the impurities still contained in the mixture enter the melt and are captured there by a growing crystal as inclusion components.

Causes of inclusion capture. The major cause of the capture of any inclusions by a growing crystal is its deficient feeding caused by the presence of impurities pushed away to the crystallization front. In distinction from the total deficiency in feeding, resulting in growth cessation, the local deficient feeding results in the formation of various systems of inclusions—from individual inclusions to their periodic structures. The model schemes of inclusion capture were considered earlier, e.g., in [10].

Insufficient local feeding seems to be caused by the interaction between the free and forced convections in the solution bulk, which, in turn, is determined by the temperature distribution in the system and the parameters of the crystal motion. Thus, under certain conditions, localization of inclusions at the crystallization front with respect to the closed solution zone [2] would result in its fast depletion and the formation of a concave interface, the periodic capture of individual inclusions, which is more intense the more pronounced the temperature fluctuations at the crystallization front are. At the same time, since the free convection dominates in the solution, some stagnation zones can be formed in its bulk. The saturation of these zones increases, and, finally, results in the unnormalized supersaturation of the solution as the crystal and the mass capture of impurities accumulated at the crystallization front [2]. The atomic structure of a nonsingular growth surface of BMB crystals provides its morphological instability and the mass capture of inclusions.

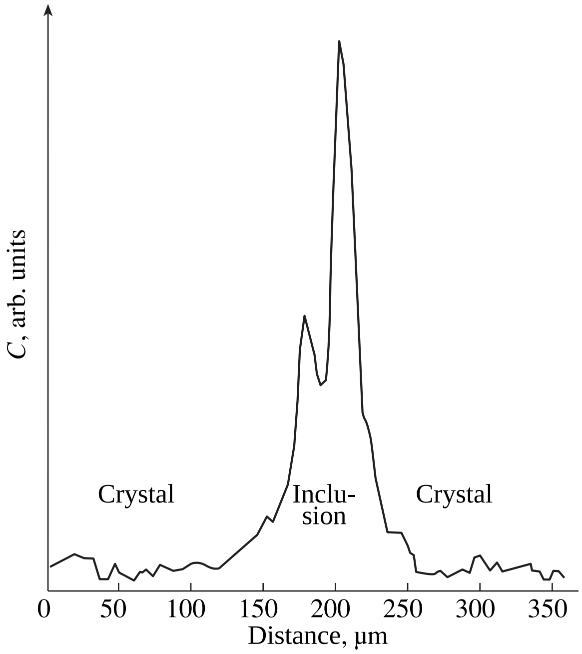

Fig. 2. X-ray microprobe carbon profile obtained by probe scanning through the BMB zone containing a melt inclusion.

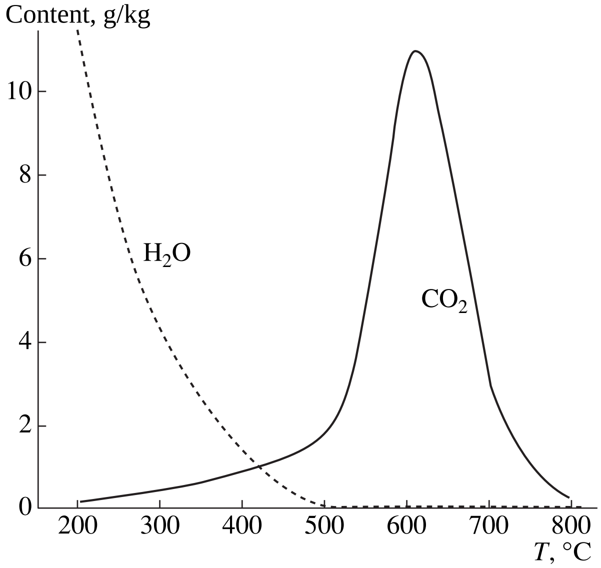

Fig. 3. Gas evolution from a BMB sample subjected to stepwise annealing.

Our experiments showed that, under the given thermal conditions, the free flow of the saturated solution under the crystallization front is attained due to the optimization of the velocity of crystals rotation [2].

Conditions and results of BMB synthesis

Composition of starting mixture	Synthesis temperature, °C	Time of synthesis, h	Results of the X-ray phase analysis*	Impurity content, wt %**	Notes
$Ba(CH_3COO)_2 + H_3BO_3$	$\frac{950/\text{bottom}}{1000/\text{top}}$	2	BMB $\alpha + \beta$	0.82	Continuous black carbon layer on the surface
Continuation of synthesis	$\frac{950/\text{bottom}}{1000/\text{top}}$	4	BMB $\alpha + \beta$	0.56	Island-like black-grey layer on the surface
	$\frac{950/\text{bottom}}{1000/\text{top}}$	20	BMB $\alpha + \beta$	0.33	Individual black inclusions
	$\frac{950/\text{bottom}}{1000/\text{top}}$	42	BMB $\alpha + \beta$	0.08	Clean (white) surface without visible trances of carbon
$Ba(CH_3COO)_2 + H_3BO_3$	$\frac{750}{800}$	16	BMB β	0.48	Surface coated with grey island-like layer
β-BMB (melting)	1200	5	BMB β	0.14	Crystallized grey melt
$BaCO_3 + H_3BO_3$	$\frac{850}{900}$	20	BMB β	0.15	Clean surface
Continuation of synthesis	$\frac{900}{950}$	25	BMB $\alpha + \beta$	0.08	Clean surface
$BaO + H_3BO_3$	$\frac{950}{1000}$	20	BMB α	0.06	Clean surface

* The X-ray phase analysis of all the three sampling yields the same result.
** Averaging over all the three probes.

This provides crystal growth with the minimum capture of inclusions, and the selection from all the boules only those that can give the material of a high optical quality. Of great importance is also the axial temperature gradient, which not only increases the crystallization pressure and the efficiency of impurity pushing, but also provides a lower solution temperature prior to the attaining supersaturation in the stagnation zones of free-convective cells. All these factors open new possibilities for reproducible growth of bulk single crystals with a minimum inclusion density.

CONCLUSIONS

Most inclusions in BMB crystals consist of the crystallized flux of the quasieutectic composition. If the gas-forming impurities are removed from the material synthesized in the solid phase only partly, the gas inclusions content in flux is rather high, and the total number of inclusions in the crystal considerably increases.

The BMB synthesis should be performed with the use of the oxide forms (not hydrated and salt ones) of the starting components (BaO and B_2O_3) (which are the real sources of inclusions in the melt and in crystals). If, for reason, one has to use such crystals, the synthesis should be performed until the complete removal of the gas-forming components from the system, with due regard of the kinetics of the corresponding reactions under the given conditions.

The synthesis of only low-temperature BMB modification, with all the precautions made against the growth of its low-temperature modification, occurs at $T < 900°C$. Under such conditions, the use of the oxide forms of the components, the gas-forming impurities are removed from the synthesis product within 25–30 h. The use of the salt forms requires not less than 40–50 h for obtaining the same result.

The considerable decrease of the inclusion content in BMB crystals is provided by the mutually related optimization of the thermal and dynamic parameters of crystallization, determining the configuration of the interphase surface and the feeding mode, e.g., a decrease of the velocity of the crystal rotation to 1–2 rpm under the axial temperature gradients in the subsurface zone of the solution equal to ~8–10°C/mm, etc.

REFERENCES

1. V. G. Dmitriev, G. G. Gurzadyan, and D. N. Nikogosyan, *Handbook of Nonlinear Optical Cryslals* (Springer, Berlin, 1997), p. 245.
2. E. G. Tsvetkov and A. M. Yurkin, Kristallografiya **43** (3), 1142 (1998) [Crystallogr. Rep. **43** (3), 1080 (1998)].

3. A. Jiang, F. Cheng, Q. Lin, *et al.*, J. Cryst. Growth **79**, 963 (1986).
4. L. K. Cheng, W. Bosenberg, and C. L. Tang, J. Cryst. Growth **89**, 553 (1988).
5. R. S. Feigelson, R. J. Raymakers, and R. K. Route, J. Cryst. Growth **97**, 352 (1989).
6. A. B. Bykov, V. V. Dozmarov, and O. K. Mel'nikov, Kristallografiya **39** (4), 720 (1994) [Crystallogr. Rep. **39** (4), 651 (1994)].
7. N. Yu. Osorgin and A. A. Tomilenko, USSR Inventor's Certificate No. 1,562,816, Byull. Izobret., No. 17 (1990).
8. N. Yu. Osorgin, *Chromatography Analysis of Gas Phase in Minerals* (*Methods, Apparatus, Metrology*) (Izd. Inst. Geol. Geodez. Sib. Otd. Akad. Nauk SSSR, Novosibirsk, 1990).
9. J. Dubessy, B. Poty, and C. Ramboz, Eur. J. Mineral. **1**, 517 (1989).
10. A. A. Chernov, E. I. Givargizov, Kh. S. Bagdasarov, *et al.*, *Modern Crystallography Vol. 3. Crystal Growth* (Nauka, Moscow, 1980; Springer, Berlin, 1984).

Translated by L. Man

Crystallography Reports, Vol. 45, No. 4, 2000, p. 704. Translated from Kristallografiya, Vol. 45, No. 4, 2000, p. 768.
Original Russian Text Copyright © 2000.

PERSONALIA

Al’bert Anatol’evich Katsnelson (On the Occasion of His 70th Birthday)

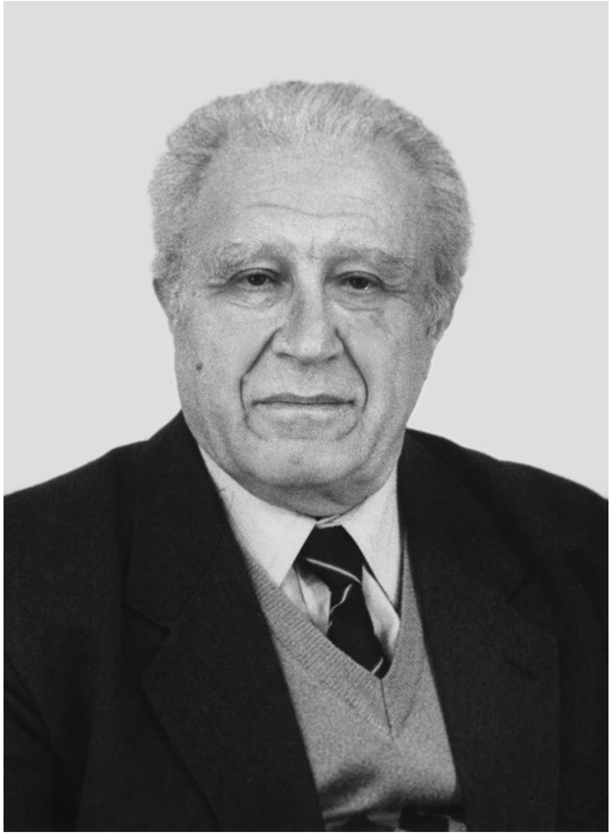

On April 14, 2000 Al’bert Anatol’evich Katsnelson, a prominent Russian scientist, an honored scientist of the Russian Federation, an honored professor of Moscow University, a winner of the Fedorov Prize of the Academy of Sciences of the USSR, professor of the Department of Solid State Physics of the Physics Faculty of Moscow State University, celebrates his seventieth birthday.

Professor Katsnelson made a considerable contribution to the development of solid state physics. He guided extensive studies in the field of atomic ordering, the theory of local atomic order, the electron theory of imperfect crystals, X-ray diffraction by imperfect crystals, multiwave interference transmission of X-rays in ideal and real crystals, and X-ray diffraction and physics of open nonequilibrium solid-state systems. Currently, he concentrates on the experimental and theoretical studies of the metal–hydrogen systems, in which the oscillation-type phase and structural transformations were first discovered.

For almost half a century, Katsnelson has been working in Moscow University, and for about thirty years he has been a professor of this university. In fact, he created a scientific school. More than 60 of his former students defended candidate dissertations, of them, seven became Doctors of Sciences. Katsnelson published eleven textbooks and monographs (three of them were translated into English and published in the United States) and more than 400 articles in Russian and international journals. His textbooks and monographs are popular among students, postgraduates, and researchers working in the field of solid state physics. Katsnelson is deeply engaged in pedagogical activity. He developed several new courses of lectures, which are always popular with the audience.

Professor Katsnelson is a member of the International Informatization Academy. He was awarded an honorary diploma of the International Association for Hydrogen Energy and the title of Soros Professor.

Katsnelson is a member of specialized qualification councils for the conferment of scientific degrees and an expert of several international and Russian science foundations.

Al’bert Anatol’evich Katsnelson meets his jubilee absorbed in new ideas and plans. The Editorial Board of *Kristallografiya*, the scientists of Moscow University, colleagues, and friends congratulate Al’bert Anatol’evich on his birthday and wish him good health and many years of fruitful activity, and happiness.

Translated by I. Polyakova